International Topical Meeting on
MICROWAVE PHOTONICS

Technical Digest
Including **High Speed Photonics Components** Workshop

October 12-14, 1998
Sarnoff Corporation, Princeton, New Jersey

MWP'98

IEEE

IEEE LASERS AND ELECTRO-OPTICS SOCIETY LEOS

MTTS

SARNOFF Corporation

Program at a Glance

	8:30 9:00 9:30	10:00	10:30 11:00 11:30	12:00 12:30 1:00	1:30 2:00 2:30	3:00	3:30	4:00 4:30	5:00 5:30	6:00 6:30 7:00 7:30
Oct 12 (Mon)	**MA** Plenary Session	Break	**MB** Fiber Wireless Systems (6 papers)	Lunch	**MC** Modulators (6 papers)		Break	Poster Session (18 papers)	Reception	
Oct 13 (Tue)	**TuA** Photonic Beamforming I (5 papers)	Break	**TuB** Photonic Beamforming II (6 papers)	Lunch and Panel Session	**TuC** Lasers (5 papers)	Break	**TuD** Photodetectors (6 papers)		Postdeadline Paper Session	Banquet
Oct 14 (Wed)	**WA** Novel Techniques (5 papers)	Break	**WB** Novel Systems (5 papers)	Lunch	**Workshop** High Speed Photonics Components					

REPORT DOCUMENTATION PAGE

Form Approved
OMB No. 0704-0188

1. AGENCY USE ONLY (*Leave Blank*)	2. REPORT DATE	3. REPORT TYPE AND DATES COVERED
	October 1998	Final Technical

4. TITLE AND SUBTITLE
Technical Digest of the
1998 International topical Meeting on Microwave Photonics
MWP'98

5. FUNDING NUMBERS
G
N00014-99-1-0114

6. AUTHORS
Multiple

7. PERFORMING ORGANIZATION NAME(S) AND ADDRESS(ES)
Institute of Electrical and Electronics Engineers, Inc.
445 Hoes Lane, P.O. Box 1331
Piscataway, NJ 08855-1331

8. PERFORMING ORGANIZATION REPORT NUMBER

9. SPONSORING / MONITORING AGENCY NAME(S) AND ADDRESS(ES)
Office of Naval Research
Ballston Centre Tower One
800 North Quincy Street
Arlington, VA 22217-5660

10. SPONSORING / MONITORING AGENCY REPORT NUMBER

11. SUPPLEMENTARY NOTES

12a. DISTRIBUTION / AVAILABILITY STATEMENT
APPROVED FOR PUBLIC RELEASE

12b. DISTRIBUTION CODE

13. ABSTRACT *(Maximum 200 words)*

The wideband, low loss transmission capability of optical systems has led to considerable interest in their use for distributing and controlling microwave signals in applications such as antenna remoting, wideband cable television distribution, optically controlled phased arrays and microwave signal processing. The use of microwave sub-carrier multiplexing on dark fiber systems also may be of importance in the near future, and to realize multi-gigabit optical communication systems, microwave design techniques must be used. The International Topical Meeting on Microwave Photonics is intended to present recent advances in the multi-disciplinary research area, ranging from novel devices to systems deployed in the field.

14. SUBJECT TERMS
microwave optical fiber links and systems, millimeter wave optical fiber links and systems, optically controlled microwave devices, optically controlled millimeter wave devices, microwave aspects of optical signal processing, optical distribution of signals in microwave systems, ultra-fast optoelectronic microwave measurements, optical control and beam shaping of phased array antennas, microwave sub-carrier multiplexing optical systems, high-speed light modulation and detection devices

15. NUMBER OF PAGES
266

16. PRICE CODE

17. SECURITY CLASSIFICATION OF REPORT	18. SECURITY CLASSIFICATION OF THIS PAGE	19. SECURITY CLASSIFICATION OF ABSTRACT	20. LIMITATION OF ABSTRACT
Unclassified	Unclassified	Unclassified	UL

International Topical Meeting on

Microwave Photonics

MWP'98

October 12–14, 1998
Sarnoff Corportion
Princeton, New Jersey

Technical Digest

(including **High Speed Photonics Components** Workshop)

Contents

Message from the Conference Chairmen iii

Committee Organization Information iv

Message from the Technical Program Committee Chairman v

Technical Program Schedule vii

Technical Sessions

MA1 Plenary Session: Broadband Fiber-Radio Access Networks 1
MB Fiber Wireless Systems 5
MC Modulators 29
P Poster Session 51
TuA Photonic Beamforming I 115
TuB Photonic Beamforming II 135
TuC Lasers 153
TuD Photodetectors 173
WA Novel Techniques 195
WB Novel Systems 211

Workshop: High Speed Photonics Components 231

Author Index 249

1998 INTERNATIONAL TOPICAL MEETING ON MICROWAVE PHOTONICS TECHNICAL DIGEST

IEEE Catalog Number 98EX181
ISBN 0-7803-4936-9 (softbound)
ISBN 0-7803-4937-7 (microfiche)
Library of Congress Number 98-85266

1998 International Topical Meeting on Microwave Photonics

Message from the Conference Chairmen

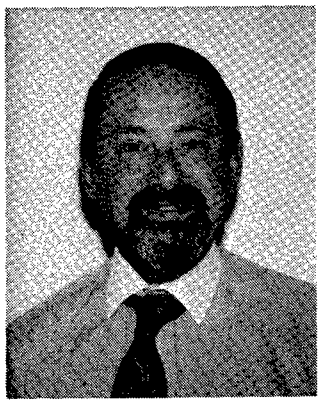

Peter R. Herczfeld
Drexel University

Chi H. Lee
University of Maryland

Welcome to MWP'98, which is jointly sponsored by the IEEE Lasers and Electro-Optics Society and the IEEE Microwave Theory and Techniques Society. For the first time the meeting is held in an industrial research center that has contributed significantly to the advance of microwave photonics. We are indebted to Sarnoff Corporation for offering its beautiful campus and superb facilities for this meeting.

This meeting is intended to bring together scientists and engineers who are interested in microwave photonics. They will present recent advances and exchange freely ideas in this multi-disciplinary research area, ranging from novel devices to systems deployed in the field.

This meeting is one in the series of meetings that began with the first LEOS Summer Topical Meeting in 1991 at Newport Beach, California on "Optical Millimeter Interactions: Measurements, Generation, Transmission and Control." This was followed by another meeting two years later—the 1993 meeting on Optical Microwave Interactions at Santa Barbara, California—before it became international (Cernay-la-Ville, France, 1994; Keystone, Colorado, USA, 1995; Kyoto, Japan, 1996; Duisburg, Germany, 1997).

We are particularly pleased to be witnessing steady growth of this field. For example, in 1991 most of the papers were in the device area with a very small pool of contributed papers. This year there are many papers on system applications in addition to the traditional device papers, which were selected from a much larger paper pool. Although it is interesting to note that many early contributors are still active in this field, it is even more gratifying to see many newcomers who are the new blood for the field.

As the meeting's general co-chairs, we would like to thank all those who have contributed to the success of this meeting, including the speakers, the panelists, the Technical Program Committee and meeting organization committee. Help provided by the LEOS staff is gratefully acknowledged.

This meeting is partially supported by the following federal agencies: U.S. Air Force, U.S. Army, U.S. Navy, and NSF.

1998 International Topical Meeting on Microwave Photonics

1998 International Topical Meeting on Microwave Photonics

Message from the Technical Program Committee Chairman

Charles H. Cox III
MIT Lincoln Laboratory

On behalf of the technical program committee, I would like to add our welcome to MWP98. These are exciting times for microwave photonics: the fruits of our initial researches are being applied to systems and new research is providing the basis for enhanced performance in the present as well as for wider applications in the future.

We have tried to have the technical program for MWP98 meet the growing needs of our field in two key ways. One way is that we tried to have a balanced technical program, both between microwaves and photonics as well as among devices, links and systems. To this end the technical program committee was divided into two sub-committees, each of which was composed of members who are experts in the individual disciplines as well as those with expertise across both disciplines.

The other way we have tried to meet the growing needs of the field is to expand the length of the conference. The strength and number of submitted papers (78) permitted us to expand the length of the conference by half a day so that a reasonable percentage of papers could be accepted—we finished at 73% acceptance.

We hope you have a technically challenging and interesting visit to MWP98.

1998 International Topical Meeting on Microwave Photonics
Technical Program Schedule

Monday, 12 October 1998

8:30am – 10:00am
MA Plenary Session
Presider: P. Herczfeld, Drexel University, Philadephia, PA

8:30am – 8:40am
Welcome by P. Herczfeld, Drexel University, Philadelphia, PA

8:40am – 8:50am
Welcome by C. Lee, University of Maryland, College Park, MA

8:50am – 9:10am
Special Remarks by Michael Ettenberg, Sarnoff Corporation, Princeton, NJ

8:30am – 9:50am (Plenary Speaker)
MA1 Broadband Fibre-Radio Access Networks
A. Seeds, University College London, London, UK

9:50am – 10:30am BREAK

10:30am – 12:00noon
MB Fiber Wireless Systems
Presider: D. Novak, University of Melbourne, Parkville, AUSTRALIA

10:30am – 10:45am
MB1 All Optoelectronic Generation and Detection of Millimeter-Wave Signals
T. Nagatsuma, N. Sahri, M. Yaita, T. Ishibashi, N. Shimizu and K. Sato, NTT Systems, Kanagawa, JAPAN

10:45am – 11:00am
MB2 Millimeter-Wave Multi-Channel CDMA Fiber-Radio
G. H. Smith, A. Nirmalathas and D. Novak, University of Melbourne, Parkville, AUSTRALIA

11:00am – 11:15am
MB3 Multicarrier Disbribution of Multiplex Digital Compressed TV Channels Using a Harmonic Laser Source at 38 GHz
D. Mathoorasing, S. Bouchoule and C. Kazmierski, OPTO+, Marcoussis, FRANCE and D. Tanguay, J. F. Cadiou, P. Legaud and E. Penard, France Telecom, Lannion, FRANCE

11:15am – 11:30am
MB4 A Novel Fiber-Optic Millimeter-Wave Uplink Incorporating 60GHz-Band Photonic Downconversion with Remotely Fed Optical Pilot Tone Using an Electroabsorption Modulator
T. Kuri, K. Kitayama and Y. Ogawa, OKI Electric Industry, Co., Ltd., Tokyo, JAPAN

Monday, 12 October 1998

11:30am – 11:45am
MB5 A Photoconductive Correlation Receiver For Wireless Digital Communications
E. E. Funk, S. Ramsey, C. H. Lee and J. Craven, University of Maryland, College Park, MD

11:45am – 12:00noon
MB6 Packaging For Millimetre Wave Fibre-Radio Modules
C. R. Pescod, G.M. Auker, P. T. Sharp, R. G. Sirett and T. P. Young, GEC-Marconi Research Centre, Essex, UK

12:00noon – 1:30pm LUNCH

1:30pm – 3:20pm
MC Modulators
Presider: W. Bridges, California Institute of Technology, Pasadena, CA

1:30pm – 1:55pm (Invited)
MC1 Electroabsorption Waveguide Modulators for High Performance Analog Fiber Links
P. K. L. Yu, R. B. Welstand, G. L. Li, W. X. Chen, and J. T. Zhu, University of California, San Diego, CA and S. A. Pappert, C. K. Sun, and R. Nguyen, SPAWAR System Center, San Diego, CA and Y. Z. Liu, Fermionics Laser Technology, Simi Valley, CA

1:55pm – 2:10pm
MC2 Polarization-Insensitive Multiple-Quantum-Well Traveling-Wave Electroabsorption Modulators with 18 GHz Bandwidth and 1.2 V Driving Voltage at 1.55 μm
S. Z. Zhang, Y. J. Chiu, P. Abraham and J. E. Bowers, University of California, Santa Barbara, CA

2:10pm – 2:25pm
MC3 Error Free Full Duplex Optical WDM-FDM Transmission Using an EA-Transceiver
A. Stohr and D. Jager, Gerhard-Mercator-Universitat, Duisburg, GERMANY and K. Kitayama, Communication Research Laboratories, Tokyo, JAPAN

2:25pm – 2:50pm (Invited)
MC4 Synthesis of the Optical Modulator Response
C. Laliew, S. Lovset, X. Zhang, and A. Gopinath, University of Minnesota, Minneapolis, MN

2:50pm – 3:05pm
MC5 Linearization of a Broadband Analog Optical Link Using Multiple Wavelengths
E. Ackerman, MIT Lincoln Laboratory, Lexington, MA

3:05pm – 3:20pm
MC6 Broadband Linearization of Externally Modulated Fiber-Optic Links
Y. Chiu and B. Jalali, University of Southern California, Los Angeles, CA

Monday, 12 October 1998

3:20pm – 4:00pm **BREAK**

4:00pm – 5:00pm
Poster Session

P1 **Microwave Fiber Optic Link Antenna Remoting Trade Study Measurements**
I. L. Newberg, Raytheon Systems Company, Los Angeles, CA

P2 **Tax Calibration of Optical Scattering Parameter Test Set**
B. Elamaran, R. D. Pollard and S. Iezekiel, University of Leeds, England, UK

P3 **Hybrid Fiber-Radio Systems in the mm Wave Range: A Comparison Between Available Optical Sources**
J. F. Cadiou, D. Tanguay, E. Penard and P. Jaffre, France Telecom, Lannion, FRANCE and H. Schmuck, Alcatel Alshtom Corporate Research Center, Stuttgart, GERMANY and E. Vergnol and D. Mathoorasing, OPTO+, Marcoussis, FRANCE

P4 **A New Optical Distribution Approach For Millimeter Wave Radio**
T. Marozsak, T. Berceli, G. Jaro, A. Zolomy, A. Hilt, S. Mihaly, E. Udvary, Z. Varga, Technical University of Budapest, Budapest, HUNGARY

P5 **Microwave Multichannel System with a Sideband Injection Locking Scheme in the 60 GHz-Band**
C. G. Schaffer, FH Lubeck, Lubeck, GERMANY and R. P. Braun, G. Grosskopf, F. Schmidt and M. Rohde, Heinrich-Hertz-Institut fur Nachrichtentechnik Berlin GmbH, Berlin, GERMANY

P6 **Interferometric Modulators Linearized to Arbitrary Order**
M. E. Marhic, Northwestern University, Evanston, IL

P7 **Seamless Integration of Fiber Optic Networks and Millimeter-Wave Wireless Access Using Nonlinear Photo-Detection Scheme**
M. Tsuchiya, T. Hoshida and K. Nishikawa, University of Tokyo, Tokyo, JAPAN

P8 **Sensitivity Analysis of Optical SSB Generation Using a Dual-Electrode Mach-Zehnder Modulator**
A. Nirmalathas, G. H. Smith and D. Novak, University of Melbourne, Parkville, AUSTRALIA

P9 **Fiber to the Air (FTTA) System Using Optical Coherence Coded Multiplexing Scheme**
K. Tsukamoto, S. Obata and S. Komaki, Osaka University, Suita-shi, JAPAN

P10 **Integrated Optics Photonic Mixer for an All-Optical Implementation of a Millimeter and Sub-millimeter Wave Oscillator**
S. Dubovitsky, V. Chuyanov, S. Garner and W. H. Steier, University of Southern California, Los Angeles, CA

Monday, 12 October 1998

P11 **Low Close-To-Carrier Noise Systems**
M. Nawaz and T. P. Young, GEC Marconi Research Centre, Essex, UK

P12 **Large Area, High Speed Phototube with a GaAsP Photocathode and GaAs Metal-Semiconductor-Metal Anode**
T. A. Yost and P. Herczfeld, Drexel University, Philadelphia, PA and V. Contarino, Naval Air Warfare Center Aircraft Division, Patuxent River, MD

P13 **Optical Single-Sideband Modulation with Delay Pre-Distortion for Fiber-Radio Applications**
R. A. Griffin, P. M. Lane and J. J. O'Reilly, University College London, London, UK

P14 **Modeling of Chirping Laser Diodes for Microwave Generation and Transmission Over Dispersive Fibres**
W. Freude, P. Palai and I. A. Sukhoivanov, Universitat Karlsruhe, Karlsruhe, GERMANY

P15 **Nonlinear Biasing of MZ-EOM Devices to Experimentally Reduce Chromatic Dispersion Effects in Antenna Remoting Up-Converting Fiber-Optic Links**
J. M. Fuster, J. Marti, V. Polo, F. Ramos and J. L. Corral, Universidad Politecnica de Valencia, Valencia, SPAIN

P16 **Photorefractive Phased Array Beamforming with True-Time-Delay Processing**
A. Kiruluta, P. E. X. Silveira, G. Kriehn, S. Weaver and K. Wagner, University of Colorado, Boudler, CO

P17 **High Performance Long-Wavelength Velocity-Matched Distributed Photodetectors For RF Fiber Optic Links**
T. Chau, S. Mathai, A. Rollinger, M. C. Wu and T. Itoh, University of Southern California, Los Angeles, CA and D. L. Sivco and A. Y. Cho, Lucent Technologies, Bell Laboratories, Murray Hill, NJ and D. C. Scott and T. A. Vang, TRW, Redondo Beach, CA

P18 **A Genetic Algorithm for the Design of All-Optical Microwave Filters**
T. A. Cusick, S. Iezekiel and R. Miles, University of Leeds, Leeds, UK

5:00pm – 6:00pm **RECEPTION**

Tuesday, 13 October 1998

8:30am – 9:55am
TuA Photonic Beamforming I
Presider: R. Esman, Naval Research Laboratory, Washington, DC

8:30am – 8:55am (Invited)
TuA1 Microwave Phase Conjugation Using Optically Interconnected Arrays
Y. Chang and H. R. Fetterman, University of California, Los Angeles, CA and B. Tsap, Pacific Wave Industries, Los Angeles, CA, and I. L. Newberg and S. K. Panateros, Hughes Aircraft Co., Los Angeles, CA

8:55am – 9:10am
TuA2 Optical Distribution of Reference Signals to a Digital Beamforming Antenna
J. Onnegren and L. Pettersson, National Defence Research Establishment, Linkoping, SWEDEN

9:10am – 9:25am
TuA3 Volume Array With Optical Feeds
A. D. Carr and P. J. Tittensor, GEC-Marconi Research Center, Essex, UK

9:25am – 9:40am
TuA4 Experimental Demonstration of a Fiber Optic Rotman Beamformer
R. A. Sparks and N. Slawsby, ANRO Engineering, Inc., Maynard, MA and J. Prince and J. Munro, MIT Lincoln Laboratory, Lexington, MA

9:40am – 9:55am
TuA5 Photonic Integrated Beamformer for Phased-Array Antennas
J. Stulemeijer, Delft University, Delft, THE NETHERLANDS

9:55am – 10:30am BREAK

10:30am – 12:00noon
TuB Photonic Beamforming II
Presider: J. Brock, TRW, Redondo Beach, CA

10:30am – 10:45am
TuB1 Optical Processing of 44 GHz Microwave Signals in an Adaptive Nuller
P. A. Schulz, R. A. Brown and S. R. Henion, MIT Lincoln Laboratory, Lexington, MA

10:45am – 11:00am
TuB2 Microwave Phase Detection for Angle of Arrival Detection Using a 4-Channel Optical Downconverter
P. D. Biernacki, A. Ward, L. T. Nichols and R. D. Esman, Naval Research Laboratory, Washington, DC

11:00am – 11:15am
TuB3 Optical Phase Locked Loop (OPLL) Module for Use as a 9 GHz Source in Phased Array Communications Antennas
L. N. Langley, M. D. Elkin, C. Edge and M. J. Wale, GEC-Marconi Materials Technology, Towcester, UK and U. Gliese, Technical University of Denmark, Lyngby, DENMARK and X. Huang and A. J. Seeds, University College London, London, UK

Tuesday, 13 October 1998

11:15am – 11:30am
TuB4 Developments in Photonic Beam-Forming
M. F. Lewis, P. Sample and R. A. Wilson, DERA, Worcestershire, UK

11:30am – 11:45am
TuB5 New Variable Phase Shifter Array Using Resonator with Graded Reflectivity Mirror for Single-Control Steerable Phased Array Antenna
B. Dingel and M. Izutsu, Communication Research Laboratory, Tokyo, JAPAN

11:45am – 12:00noon
TuB6 Double Heterodyne Filtering of Received Signals in Optically Time-Delay Controlled Antennas
S. Tonda-Goldstein, L. Pastur, D. Dolfi, J. P. Huignard, T. Merlet, O. Maas, J. Chazelas, Thomson – CSF, Orsay, FRANCE

12:00noon – 1:30pm LUNCH and Panel Discussion
Panel Discussion Abstract
The committee has arranged for a panel of technical leaders to discuss "What Photonics Can Do For Me" by focusing on the role of photonics in today's systems and the direction for future growth. This panel will discuss the role of broadband photonics in the commercial arena and in military systems. The present list of speakers at the panel discussion includes:

Michel Schaler – Dassault Electronics, FRANCE
Dr. Masayuki Izutsu – Communications Research Laboratories, JAPAN
Dr. Stephen Pappert – NR&D, USA
Dr. Caroline Gee – Ortel Corporation, USA
Dr. Gregory L. Tangonan (Panel Leader) – HRL Laboratories, USA

1:30pm – 2:55pm
TuC Lasers
Presider: N. Dagli, University of California, Santa Barbara, CA

1:30pm – 1:55pm (Invited)
TuC1 Advanced Microwave Photonic Devices for Analog Optical Links
D. Jager, A. Stohr, and R. Heinzelmann, Gerhard-Mercator University, Duisburg, GERMANY

1:55pm – 2:10pm
TuC2 Broadband, Directly Modulated Analog Fiber Link With Positive Intrinsic Gain and Reduced Noise Figure
C. H. Cox, III, H. V. Roussell, R. J. Ram, R. J. Helkey, MIT Lincoln Laboratory, Lexington, MA

2:10pm – 2:25pm
TuC3 Novel Integrated Laser Devices with Greatly Enhanced Quantum Efficiency and Intrinsic RF Matching for Low Loss, Broadband Opto-Microwave Applications
S. G. Ayling, D. R. Wright, M. Allenson, K. P. Hilton and G. W. Smith, Defence Evaluation Research Agency, Malvern, UK

Tuesday, 13 October 1998

2:25pm – 2:40pm
TuC4 Two-Section Integrated Quantum-Confined Stark Effect Tuned Laser with Uniform Frequency Modulation Response from 30kHz to 6GHz
X. Huang and A. J. Seeds, University College London, London, UK and J. S. Roberts, University of Sheffield, Sheffield, UK and A. P. Knights, University of Surrey, Guildford, UK

2:40pm – 2:55pm
TuC5 Clock Source-Limited Low Jitter, Subterahertz Signal Generation from Mode-Locked Semiconductor Laser Controlled by Phase Lock Loop (PLL) With Photonic Downconversion
E. Hashimoto and A. Takada, NTT Optical Network Systems Labs., Kanagawa, JAPAN and Y. Katagiri, NTT Opto-electronics Labs., Tokyo, JAPAN

2:55pm – 3:30pm BREAK

3:30pm – 4:45pm
TuD Photodetectors
Presider: F. DeBorgies, Thomson-CSF/LCR, Orsay, FRANCE

3:30pm – 3:45pm
TuD1 Distributed Millimeter-Wave InGaAs Metal-Semiconductor-Metal Photodetector
E. Droge, E. H. Bottcher, St. Kollakowski, A. Strittmatter and D. Bimberg, Technishce Universitat Berlin, Berlin, GERMANY and O. Reimann, Brandenburgische Technische Universitat Cottbus, Cottbus, GERMANY and R. Steingruber and A. Umbech, Heinrich-Hertz-Institute fur Nachrichtentechnik Berlin GmbH, Berlin, GERMANY

3:45pm – 4:00pm
TuD2 Distibuted Balanced Photodetectors for High Performance RF Photonic Links
M. S. Islam, T. Chau, A. R. Rollinger, S. Mathai, W. R. Deal, T. Itoh and M. C. Wu, University of California, Los Angeles, CA and A. Nespola, Politecnico di Torino, Torino, ITALY

4:00pm – 4:15pm
TuD3 1.55 μm Absorption, High Speed, High Saturation Power P-I-N Photodetectors Using Low-Temperature Grown GaAs
Y. J. Chiu, S. Z. Zhang, J. E. Bowers and U. K. Mishra, University of California, Santa Barbara, CA

4:15pm – 4:30pm
TuD4 Large-Signal Compression Measurements in High-Current P-I-N Photodiodes with +11 to +20 dBm Output Microwave Power
K. J. Williams and R. D. Esman, Naval Research Laboratory, Washington, DC

4:30pm – 4:45pm
TuD5 12dB Current Modulation by 1.55 μm Light Irradiation in Integrated Optically Controlled HEMT
K. Shimomura, T. Sakai and Y. Nitta, Sophia University, Tokyo, JAPAN

Tuesday, 13 October 1998

4:45pm – 5:00pm
TuD6 Bandwidth Characteristics of InP/InGaAs Uni-Traveling-Carrier Photodiodes
N. Shimizu, NTT Optical Network Systems Laboratories, Kanagawa, JAPAN and
N. Watanabe, T. Furuta and T. Ishibashi, NTT Systems Electronics Laboratories, Kanagawa, JAPAN

5:00pm – 6:00pm **POSTDEADLINE PAPER SESSION**

6:00pm – 8:00pm **BANQUET**

Wednesday, 14 October 1998

8:30am – 9:55am
WA Novel Techniques
Presider: K. Kitayama, Communications Research Laboratory, Koganei-shi, JAPAN

8:30am – 8:55am (Invited)
WA1 The Opto-Electronic Oscillator: Prospects for Extending the State-of-the-art in Reference Frequency Generation
L. Maleki, JPL, Pasadena, CA

8:55am – 9:10am
WA2 Photonic Time-Stretch: A Potential Solution for Ultrafast A/D Conversion
B. Jalali, A. S. Bhushan and F. Coppinger, UCLA, Los Angeles, CA

9:10am – 9:25am
WA3 Photonic RF Frequency Shifter Based on Highly Chirped Mode-Locked Fiber Laser
J. U. Kang, M. Y. Frankel and R. D. Esman, Naval Research Laboratory, Washington, DC

9:25am – 9:40am
WA4 A Novel Topology of Tuneable Optical Radio Frequency Notch Filter Using a Chirped Fibre Grating
W. Zhang, J. A. R. Williams and I. Bennion, Aston University, Birmingham, UK

9:40am – 9:55am
WA5 Signal-ASE Noise Filtering in Optical Millimeter-Wave Radio-over-Fiber Links
R. A. Griffin, P. M. Lane and J. J. O'Reilly, University College London, London, UK

9:55am – 10:30am **BREAK**

Wednesday, 14 October 1998

10:30am – 11:55am
WB Novel Systems
Presider: S. Pappert, NCCOSC, San Diego, CA

10:30am – 10:55 (Invited)
WB1 Coherent Fiber-Optic Links for Transmission and Signal Processing of Microwave and Millimeter-Wave Signals
U. Gliese, Technical University of Denmark, Lyngby, DENMARK

10:55am – 11:10am
WB2 2-Gbit/s Phase Shift Keying Based on Optical Delay Switching for Microwave Optical Link
S. Fukushima, T. Ohno, Y. Doi, Y. Matsuoka and H. Takeuchi, NTT Optoelectronics Laboratories, Kanagawa, JAPAN

11:10am – 11:25am
WB3 Simultaneous Electro-Optical Upconversion to 60 GHz of Uncoded OFDM Signals
M. Sauer, K. Kojucharow, H. Kaluzni, D. Sommer and W. Nowak, Dresden University of Technology, Dresden, GERMANY

11:25am – 11:40am
WB4 Fading-Free Transport of 60GHz-Optical DSB Signal in Non-Dispersion Shifted Fiber Using Chirped Fiber Grating
K. Kitayama, Communication Research Laboratory, Tokyo, JAPAN

11:40am – 11:55am
WB5 Generation, Routing, and Detection of 100 GSa/s Arbitrary Analog Optical Waveform Packets Using Analog Optical TDM
P. Toliver, R. Runser, K. Deng, I. Glesk and P. Prucnal, Princeton University, Princeton, NJ

11:55am – 1:30pm LUNCH

1:30pm – 3:00pm WORKSHOP: High Speed Photonics Components

1 **State of the Art Laser Sources for High Bit Rate, Long Haul Fiber Optic Communications Systems**
W. D. Johnston, Jr., Lucent Technologies—Bell Labs, Murray Hill, NJ

2 **Workshop on $LiNbO_3$ Broadband Modulators**
W. K. Burns, Naval Research Laboratory, Washington, DC

3 **Recent Progresses in High Frequency, High Power Photodetectors**
M. C. Wu, T. Itoh, T. Chau, S. Islam, S. Mathai, A. Rollinger, and A. Nespola, University of California, Los Angeles, CA

4 **45 GHz Wide Bandwidth InGaAs/InP Photoreceiver**
A. Joshi, X. Wang, and D. Mohr, Discovery Semiconductors, Inc., Cranbury, NJ and A. Paollela, Lockheed Martin CPC, Newtown, PA and W. Stacey, Raytheon Advanced Device Center, Lexington, MA

BROADBAND FIBRE-RADIO ACCESS NETWORKS

A. J. Seeds

Department of Electronic and Electrical Engineering,University College London,
Torrington Place, London, WC1E 7JE, England. a.seeds@eleceng.ucl.ac.uk.

ABSTRACT

The paper will discuss architectures for providing broadband wireless access using optical fibre signal transport systems. Recent advances in microwave modulated optical signal generation using optical phase lock loops and fibre grating lasers and in signal detection using optically controlled heterostructure phototransistors will also be described.

1. INTRODUCTION

Changes in working patterns make it attractive to be able to offer wireless access both within and outside buildings. Whilst the use of diffuse field infra-red access is attractive for within-building applications, problems of scattering/attenuation in fog and foliage obstruction suggest that this is unlikely to prove a reliable technology for outdoor use. Microwave access can offer reliable performance both indoors and outdoors, allowing a single communications interface to be used with substantial gains in simplicity and cost.

Raw data rate requirements increase from of order 40 kb/s to > 150 Mb/s in moving from standard telephony to high resolution video systems. The increased data rates coupled with scarcity of allocable spectrum will require the use of much higher carrier frequencies than those in the 0.9 and 1.8 GHz bands currently used for cellular voice and cordless telephone access [1]. Initially, allocations at around 29 GHz may be used for broadband access services with evolution to frequencies in the range 62 GHz to 66 GHz for such systems as the European Union RACE Mobile Broadband System (MBS). The European Union has also allocated spectrum between 40.5 GHz and 42.5 GHz for Multipoint Video Distribution Services (MVDS). Propagation considerations at these frequencies will require base station separations of a few hundred metres at most. The problem of feeding such a large number of base stations and the complexity of base station equipment therefore needs careful attention.

Digital optical fibre systems now carry the bulk of terrestrial long distance communications traffic and work is under way to bring fibre into the local network. The broadband low loss transmission properties of fibre [2] also suggest broadband wireless access architectures, where transmit and receive signals are modulated onto optical carriers for transport between the base stations and a central site where most of the electronic processing is carried out, thus yielding a significant reduction in base station complexity.

2. SYSTEM ARCHITECTURES

A baseband transport architecture, although simplifying the optical transmission requirements and allowing either analogue or digital transmission, requires multiple channel modulators/demodulators and frequency generation at each base station. Channel re-allocation must be carried out by distributing appropriate control signals to the base stations with the baseband data.

The complexity of the base stations can be reduced significantly by moving to the architecture of Figure 1. Here all signals are modulated/demodulated at the central site and the multi-channel ensemble is up/down-converted by a millimetre-wave local oscillator at each base station. This architecture requires analogue optical transmission of IF signals and a stable millimetre-wave source at each base station but remotes much of the system complexity to the central site.

Frequency generation can be remoted entirely using the architecture of Figure 2. Here IF downlink signals are up-converted to the required millimetre-wave transmit frequency and modulate an optical source at the central site. A millimetre-wave modulated optical signal is also distributed to the base station to down-convert received signals to a convenient IF which directly modulates the uplink laser. The base station functions are thus simplified to transmit and receive amplification and uplink down-conversion and laser modulation at the expense of requiring millimetre-wave optical modulation, transport and demodulation techniques. The architecture allows frequency generation and allocation to be carried out entirely at the central site and facilitates the provision of multiple and reconfigurable services from a single network of base stations. These advantages have made it the subject of intensive investigation worldwide [3-6].

0-7803-4936-9/98/$10.00

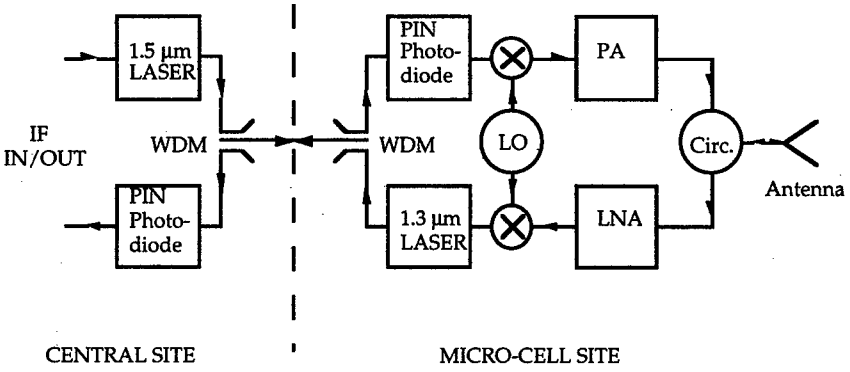

Figure 1: IF transport architecture.

An important objective for practical systems is to include capability to remote several base stations from separate tapping points on a single optical fibre bus, thus improving the utilisation of installed fibre. This can be achieved in the architectures of Figures 1 and 2 by using wavelength division multiplex, with the architecture of Figure 2 allowing additional flexibility through simultaneous use of sub-carrier multiplex techniques.

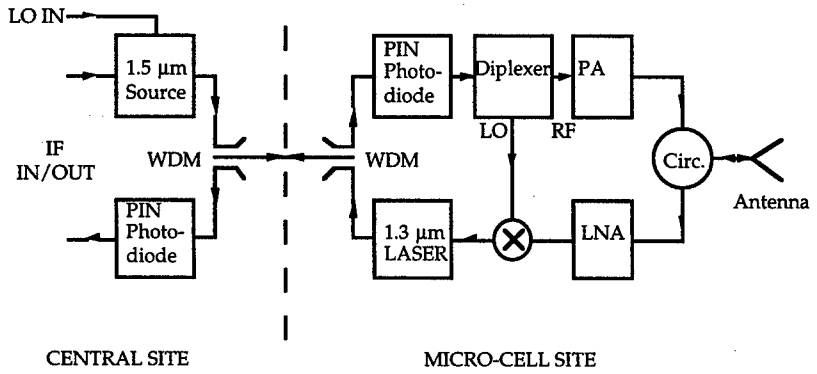

Figure 2: Millimetre-wave transport architecture.

3. SOURCES

For intensity modulation schemes the only suitable directly modulated source is the semiconductor laser, and bandwidths in excess of 30GHz have been demonstrated [7]. External modulators can offer reduced dispersion penalties through low chirp operation. Mach-Zehnder interferometric modulators have been realised in both lithium niobate [8] and III-V semiconductor technologies [9] with bandwidths exceeding 50 GHz. However, if it is desired to use a millimetre-wave transport architecture with standard telecommunications fibre of dispersion 17 ps/(nm.km) the dispersion limited transmission distance will be only a few km [10]. The use of laser heterodyne techniques [11] with baseband modulation applied to only one of the laser outputs enables this limitation to be greatly eased since the dispersion penalty then applies only to the base-bandwidth. Such an approach requires either two carefully stabilised narrow linewidth lasers or an optical phase-lock loop (OPLL) to correlate the phase noise between the two lasers. Semiconductor lasers are preferred as sources due to their compactness, efficiency and relatively low cost, but their wide linewidths (typically 5MHz to 50 MHz for commercially available DFB devices) require loops having extremely wide bandwidths and short loop propagation delays [12], which are very difficult to implement. Figure 3 shows an architecture that we have developed which overcomes this limitation, the heterodyne optical injection phase-lock loop (OIPLL).

A microwave reference signal at the required carrier frequency or one of its sub-harmonics frequency modulates the master laser (ML) producing sidebands, one of which is used to injection lock the slave laser (SL). The half wave (H) and quarter wave (Q) beam plates in conjunction with the optical isolators (I), polarising beam splitter (PBS) and non-polarising beam splitter (NBS) combine the master and slave laser outputs on the photodetector producing the heterodyne electrical output to drive a narrow bandwidth phase-lock loop, ensuring optimum tuning of the slave laser

for phase noise suppression. Initial tests of this system using lasers with a beat linewidth of 36 MHz (beyond the limits for reliable operation of a conventional OPLL using bulk optics) have yielded microwave carriers with phase noise better than - 93 dBc/Hz at 100 kHz offset and locking ranges greater than 20 GHz.

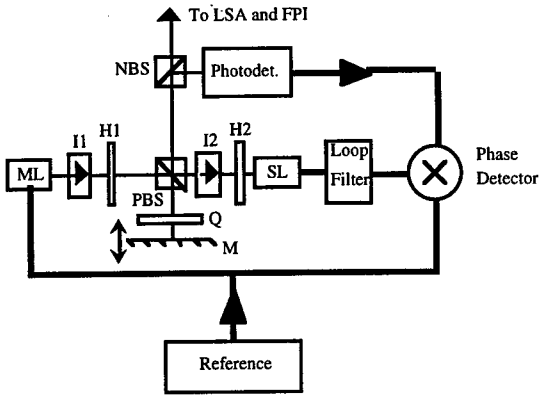

Figure 3: Heterodyne optical injection phase-lock loop.

An alternative strategy is to package the laser with a suitable line narrowing element. Figure 4 shows such a device, a fibre grating laser (FGL) [13].

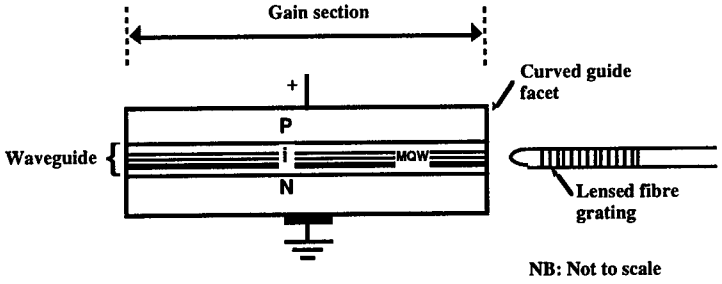

Figure 4: Fibre grating laser.

Such lasers have linewidths of < 50 kHz at an output power of 1 mW, > 40 dB sidemode suppression and high temperature stability (< 2 GHz/K), since most of the resonant cavity is within the fibre. The narrow linewidth permits a high performance OPLL to be constructed with loop propagation delay up to 20 ns, so that conventional fibre-based construction techniques can be used.

4. DETECTORS AND DEMODULATORS

For millimetre-wave transport architectures depletion layer photodetectors are preferred and -3dB bandwidths in excess of 100 GHz have been reported [14]. Two-terminal edge-coupled heterostructure bipolar transistor (HBT) detectors having unity current gain frequencies exceeding 30 GHz have also been reported [15] and offer the important attraction of an internal gain mechanism since high gain multi-stage amplifiers are difficult to realise at millimetre-wave frequencies.

The alternative approach of using the optical signal to control or introduce signals directly into microwave devices has been of limited application owing to the very poor optical responsivities of most microwave devices [16]. The geometry of both edge-coupled and normal incidence illuminated HBTs is well adapted to combining high optical responsivity with good microwave performance. In an experiment on opto-electronic mixing of a 3 GHz RF modulated optical signal with a 2.5 GHz electrical local oscillator, using an edge-coupled device [17] we achieved an IF output 7 dB above that obtainable at RF with a 100% quantum efficient photodiode and 14 dB above that expected for such a photodiode combined with a double balanced diode mixer. These results confirm the excellent potential of the HBT as an optically controlled device for use within the architectures of both Figures 1 and 2.

5. CONCLUSION

Broadband wireless access using IF or millimetre-wave optical transport offers the attractions of simplified base station architecture and suitability for both indoor and outdoor use using a common communications interface. Key challenges for the future are to determine optimum component technologies for the proposed systems and to develop volume manufacturing techniques capable of reducing the system acquisition costs to acceptable levels. A substantial contribution to this objective could come from monolithic integration of optical sources and receivers in opto-electronic integrated circuit (OEIC) form.

6. ACKNOWLEDGEMENTS

The author would like to thank his academic and industrial colleagues for their many contributions to the work described here. Special thanks are due to Dr. D. Wake (BT Laboratories) for the supply of DFB lasers and edge-coupled HBTs. Work at University College London has been supported by the United Kingdom Engineering and Physical Sciences Research Council, Nortel, the United States Air Force Office of Scientific Research, the United States Army, the UK-Israel Science and Technology Fund and the United Kingdom Ministry of Defence.

REFERENCES

1 A. J. Cooper, Fibre radio for the provision of cordless/mobile telephony services in the access network", *Electron. Lett.*, 26, pp. 2054-2056, 1990.

2 A. J. Seeds, "Optical transmission of microwaves" in Review of Radio Science, ed. W. R. Stone, Oxford, New York, pp. 335-360, 1996.

3. J. J. O'Reilly, P. M. Lane, M. H. Capstick, H. M. Salgado, R. Heidemann, R. Hofstetter and H. Schmuck, "RACE R2005: Microwave Optical Duplex Antenna Link", *IEE Proc.*, 140 Pt. J., pp. 385-391, 1993.

4. K. Kitayama, T. Kuri, H. Yokoyama and M. Okuno, "60 GHz millimetre-wave generation and transport over OFDM fiber-optic networks", in Int. Top. Mtg. Microwave Photonics, Kyoto, 1996, pp. 49-52.

5. R. P. Braun, G. Grosskopf, D. Rohde and F. Schmidt, "Optical millimetre-wave generation and transmission experiments for mobile 60 GHz band communications", *Electron. Lett.*, 32, pp. 626-628, 1996.

6. Z. Ahmed, D. Novak, R. B. Waterhouse and H. F. Liu, "37 GHz fibre-wireless system for distribution of broadband signals", *Trans. IEEE*, MTT-45, pp. 1431-1435, 1997.

7. R. S. Tucker and I. P. Kaminow, "High frequency characteristics of directly modulated InGaAsP ridge waveguide and buried heterostructure lasers", *J. Lightwave Tech.*, LT-2, pp. 385-393, 1984.

8. K. Noguchi, H. Miyazawa, and O. Mitomi, "75 GHz broadband Ti:$LiNbO_3$ optical modulator with ridge structure", *Electron. Lett.*, 1994, 30, pp. 949-951.

9. R. G. Walker in IEE Colloq. on Microwave Opto-electronics, London, 1994.

10. R. Hofstetter, H. Schmuck and R. Heidemann, "Dispersion effects in optical millimetre-wave systems using self heterodyne method for transport and generation", Trans. IEEE, MTT-43, pp. 2263-2269, 1995.

11. A. J. Seeds, "Coherent techniques in analogue signal transmission", in Analogue Optical Fibre Communications, ed. B. Wilson, Z. Ghassemlooy and I. Darwazeh, Institution of Electrical Engineers, London, 1995, pp. 33-50.

12. R. T. Ramos and A. J. Seeds, "Delay, linewidth and bandwidth limitations in optical phase-locked loop design", *Electron. Lett.*, 26, pp. 389-391, 1990.

13. F. N. Timofeev, S. Bennett, R. Griffin, P. Bayvel, A. J. Seeds, R. Wyatt, R. Kashyap and M. Robertson, "High spectral purity millimetre-wave modulated optical signal generation using fibre grating lasers", in IEEE MTT-S Int. Microwave Symp., Baltimore, 1998, pp. 1221-1224.

14. D. G. Parker, P. G. Say and A. M. Hansom, "110GHz high efficiency photo-diodes fabricated from indium tin-oxide/GaAs", *Electron. Lett.*, 23, pp. 527-528, 1987.

15. D. Wake, D. J. Newson, M. J. Harlow and I. D. Henning, "Optically biased edge coupled InP/InGaAs heterostructure photo-transistor", *Electron. Lett.*,29, pp. 2217-2218, 1993.

16. A. J. Seeds, "Microwave opto-electronics", *Optical and Quantum Electronics*, 25, pp. 219-229, 1993.

17. C. P. Liu and A. J. Seeds, "Noise performance of a two-terminal InP/InGaAs heterojunction phototransistor opto-electronic mixer", in Int. Top. Mtg. Microwave Photonics, Kyoto, 1996, pp. 123-125.

ALL OPTOELECTRONIC GENERATION AND DETECTION OF MILLIMETER-WAVE SIGNALS

T. Nagatsuma, N. Sahri, M. Yaita, T. Ishibashi, N. Shimizu*, and K. Sato*

NTT System Electronics Laboratories,
3-1 Morinosato Wakamiya, Atsugi, Kanagawa 243-0198, Japan
Tel. +81 462 40 2252, Fax. +81 462 40 4041, e-mail: ngtm@aecl.ntt.co.jp

**NTT Optical Network Systems Laboratories,*
1-1 Hikarinooka, Yokosuka, Kanagawa 239-0847, Japan

I. Introduction

Recently, photonics in millimeter-wave applications such as fiber-optic links for wireless systems and optoelectronic measurements has attracted great interests[1-3]. This is partly because the use of optical fibers in place of conventional metallic cables and waveguides would make such systems simple, flexible, and cost-effective. The use of 1.3- or 1.55-μm wavelength-based optoelectronic materials and devices, e.g., lasers, detectors, and modulators is essential from a practical point of view.

In this paper, we demonstrate the first, to our knowledge, all-optoelectronic 1.55-μm-based approaches to radiate and receive continuous millimeter-wave signals. 60-GHz millimeter-wave signals with power of more than 10 dBm, generated with an actively mode-locked laser diode[4] and a uni-travelling-carrier photodiode[5], are emitted from an antenna and are electro-optically detected with a CdTe electric-field sensor with high sensitivity.

II. Experimental Setup

Figure 1 shows the experimental setup for both the generation and detection of millimeter-wave signals using all 1.55-μm-based optoelectronic techniques. The optical signal is generated with a subharmonically mode-locked laser diode (MLLD) integrated with an electroabsorption modulator. The MLLD is drived at 30 GHz to generate the second harmonic, 60 GHz. The optical signal is boosted with an optical fiber amplifier, and is focused onto the uni-travelling-carrier photodiode (UTC-PD) which is prepared in an on-wafer manner. The main feature of the UTC-PD is a large pulse-shaped output voltage of >2 V with a wide bandwidth of >100 GHz.

The output signal of the UTC-PD is delivered to a horn antenna through a V-band air-coplanar/coaxial probe (Cascade-Microtech) and a coaxial-to-rectangular- waveguide converter. The millimeter-wave signals radiated from the antenna are focused with Teflon lens into an electric-field sensor made of a <110> oriented CdTe crystal (3 mm cube) to be measured with electro-optic (EO)

0-7803-4936-9/98/$10.00

sampling technique. A photograph of the electric-field sensor is shown in Fig. 2. An optical fiber and a collimator lens are attached to the CdTe crystal, through which the optical sampling pulses propagate and are reflected back at a mirror-coated end surface.

The sampling pulses are generated by a passively-mode-locked fiber ring laser with 0.7-ps pulse width and 40-MHz repetition rate. The fiber laser is phase-locked with the MLLD. Polarization change in the CdTe crystal due to the focused electric field is converted to a photocurrent (EO signal) with the integrated polarization detection module (Fig.3)[6]. Electro-optically detected 60-GHz millimeter-wave signals are displayed on a scope with an acquisition time of 0.1 - 1 second.

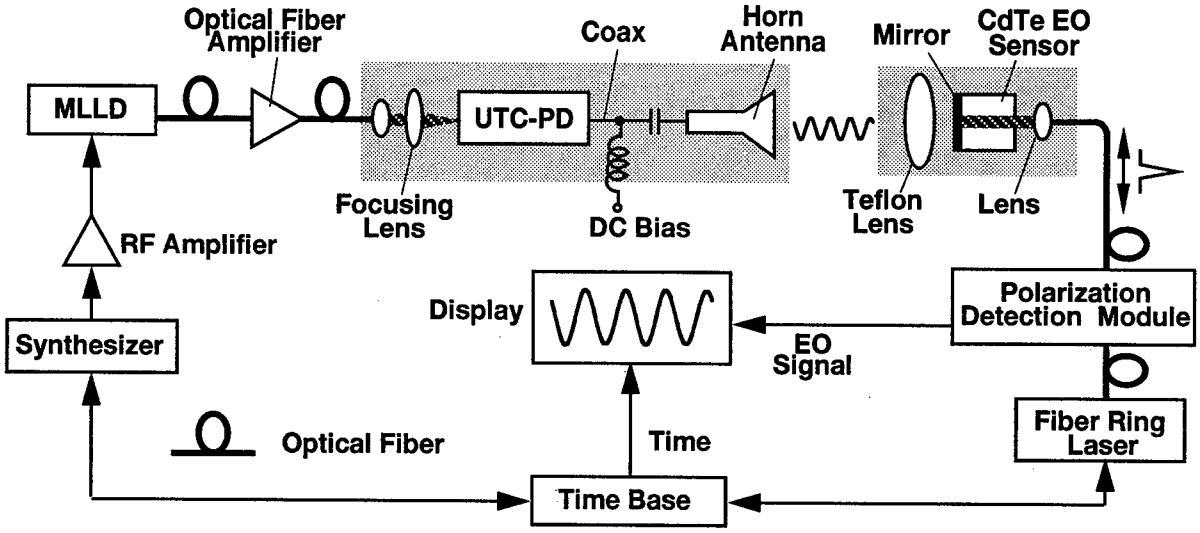

Fig. 1 Experimental setup for all-optoelectronic millimeter-wave radiation and detection. Components in the shaded areas can be integrated into compact fiber-remoted emitter and receiver.

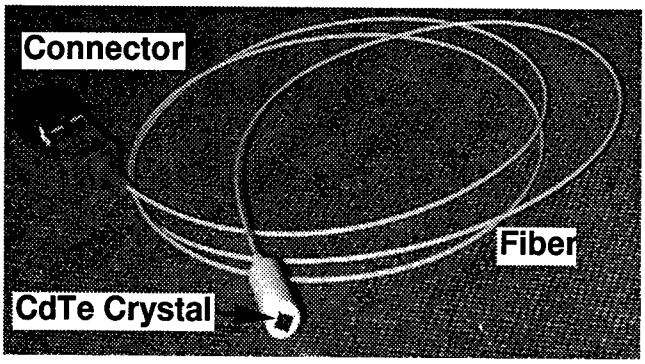

Fig. 2 Photograph of a fiber-coupled EO sensor head.

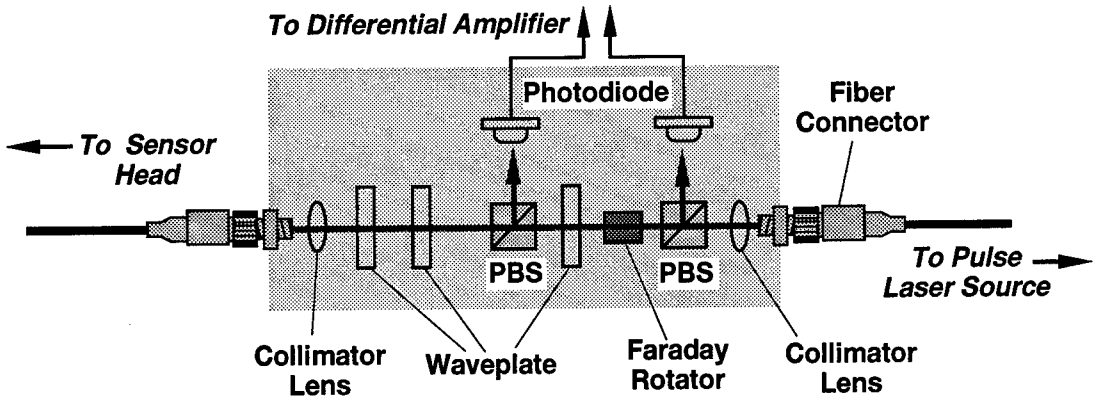

Fig. 3 Schematic of the electro-optic polarization detection module.

III. Results

Figure 4 shows the autocorrelation traces of optical signals from the MLLD for different applied RF powers. When the RF power increases, the pulses become narrower down to less than 2 ps. The power of millimeter-wave signals generated by the UTC-PD is measured with a power meter (Anritsu ML4803A) at the input end of the horn antenna. The output power of the UTC-PD chip, calibrated by taking into account losses (~4.5 dB) due to probes, cables, connectors, bias-T and transitions, is plotted against DC photocurrents as shown in Fig. 5. Efficient generation of 60-GHz signals is achieved with the quasi-sinusoidal pulse-shaped waveform of the optical pulses (Fig.4(a)). RF conversion efficiency from optical to millimeter-wave signal is close to that estimated from the DC responsivity (~0.3 A/W) of the UTC-PD. The highest obtained power is 12 dBm, which is comparable to that of solid-state electronic devices, for the photocurrent of 30 mA.

Figure 6 shows the measured 60-GHz waveforms for different photocurrents. Minimum detectable power in the detection scheme is less than -30 dBm, which can be further improved by optimizing the electro-optic detection system. It is also shown that the radiated electric field increases almost linearly with the photocurrent at least up to 30 mA.

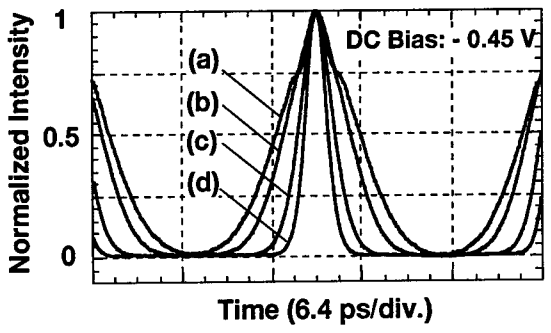

Fig. 4 Autocorrelated traces of optical pulses generated by the mode-locked laser diode for different RF powers, 10 dBm(a), 12 dBm(b), 16 dBm(c), and 18 dBm(d).

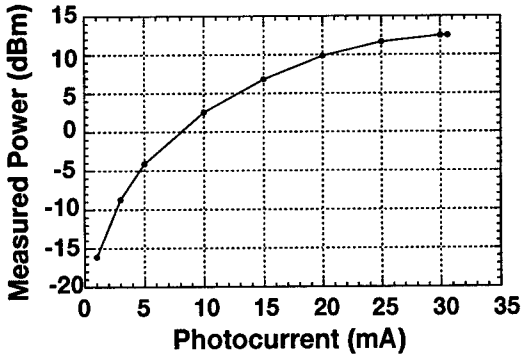

Fig. 5 Dependence of the generated 60-GHz-signal power on the total photocurrent.

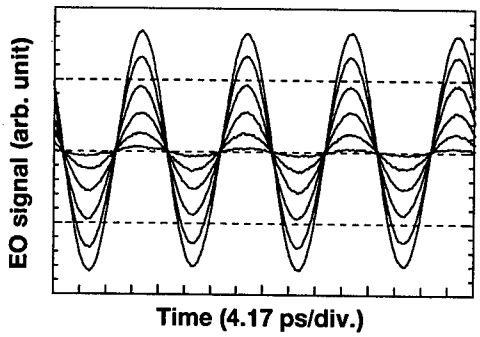

Fig. 6 Measured 60-GHz waveform for different photocurrents,1, 5, 10, 15, 20, 25 mA.

IV. Conclusion

We have demonstrated radiation and detection of 60-GHz millimeter-wave signals using all 1.55-μm-based optoelectronic techniques. High output power of over 10 dBm has been obtained. Fiber-optic millimeter-wave detector based on EO sampling has also been demonstrated with a minimum detectable power of less than -30 dBm. These results can be developed to compact fiber-optic emitters and receivers applicable in millimeter-wave measurements and communications.

Acknowledgment

The authors would like to thank T. Takizawa and M. Shinagawa for their help in experiment, and J. Yamada, K. Yamasaki, and I. Kobayashi for their encouragement and discussion.

References

[1] H. Schmuck, and R. Heideman, "High Capacity Hybrid Fibre-Radio Field Experiments at 60 GHz," Tech. Dig. Microwave Photonics, TU4-3, pp. 65-68, Kyoto (1996).

[2] N. Sahri, T. Nagatsuma, N. Shimizu, M. Yaita, T. Otsuji, "Characterization of > 300 GHz Transistors Using a Novel Optoelectronic Network Analyzer," Tech. Dig. XIth Intern. Conf. Ultrafast Phenomena, ThA2, Germany (1998).

[3] D. M. Mittleman, R. G. Baraniuk, and M. C. Nuss, "Applications of Terahertz Imaging," Tech. Dig. Contemporary Photonic Technologies, pp.81-84, Tokyo (1998).

[4] K. Sato, I. Kotaka, Y. Kondo, and M. Yamamoto, "Active mode-Locking at 50-GHz Repetition Frequency by Half-Frequency Modulation of Monolithic Semiconductor Lasers Integrated with Electroabsorption Modulators," Appl. Phys. Lett., 69, pp. 2626-2628 (1996).

[5] T. Ishibashi, N. Shimizu, S. Kodama, H. Ito, T, Nagatsuma, and T. Furuta, "Uni-Traveling-Carrier Photodiodes," Tech. Dig. Ultrafast Electronics and Optoelectronics, pp.166-168, Incline Village (1997), also in OSA TOPS on Ultrafast Elcetronics and Optoelectronics Vol. 13, pp. 83-87(1997).

[6] T. Nagatsuma, "Electro-Optic Testing Technology for High-Speed LSIs," IEICE Trans. Electron., E79-C, pp.482-488 (1996).

MILLIMETER-WAVE MULTI-CHANNEL CDMA FIBER-RADIO

G.H. Smith, A. Nirmalathas, and D. Novak

Australian Photonics Cooperative Research Centre, Photonics Research Laboratory, Department of Electrical and Electronic Engineering, The University of Melbourne, Parkville VIC 3052, Australia.

Tel: +61 3 9344 6525 Fax: +61 3 9344 6678 Email: grsm@ee.mu.oz.au

Abstract: We investigate experimentally and theoretically the transmission of multi-channel millimeter-wave CDMA signals in a fiber-radio system. The use of optical SSB modulation enables transparency of the optical link to CDMA signal propagation, while channel cross-talk is due to the CDMA codes.

I. Introduction

Radio access at millimeter-wave (mm-wave) frequencies offers the large bandwidth required for the future provision of broadband services. In such systems optical fiber links are being proposed as a means of connecting the antenna base stations (BSs) to a central office (CO), which acts as a centralized exchange for signal routing and processing. If mm-wave optical fiber links are also incorporated, up/down-conversion to/from the required radio frequency can be performed at the CO rather than at each BS. Previous investigations of mm-wave fiber-radio systems have focused on the frequency division multiple access (FDMA) air interface, an access scheme in which users or cells are assigned different radio frequencies. Subcarrier multiplexing in the optical link can be used to implement FDMA in a mm-wave fiber-radio system [1].

Recently however, there has been considerable interest in code division multiple access (CDMA) radio systems for both cellular mobile and satellite communications. CMDA radio networks offer a number of advantages including larger capacity, increased tolerance to multipath propagation effects, and can better cope with the asynchronous nature of multimedia data traffic [2,3]. It has also been shown in lower radio frequency demonstrations that since a smaller carrier-to-noise ratio is required in CDMA systems, less stringent characteristics are required of the optical link components [4,5]. In this paper we investigate the transmission of CDMA radio signals in a multi-channel mm-wave fiber-radio system and demonstrate the first broadband multi-channel mm-wave CDMA fiber-radio system operating at 39.2 GHz. We also develop an accurate model to simulate the CDMA fiber-radio system in order to investigate the transparency of the mm-wave optical link to CMDA signal propagation.

II. Experiment

Fig. 1 illustrates the mm-wave CDMA fiber-radio system that was implemented. At these higher mm-wave frequencies, it is difficult to obtain direct up and down frequency conversion of the large bandwidth spread-spectrum CDMA signals. Instead, we propose a scheme that incorporates a two-step upconversion process from baseband to an intermediate frequency (IF) and finally to a mm-wave frequency, as indicated in Fig. 1. Such a scheme also allows the mm-wave and IF components to be shared between a large number of

0-7803-4936-9/98/$10.00

radio channels at the CO. The optical *cw* output from a DFB laser was modulated by two mm-wave broadband radio CDMA signals via an optical single-sideband (OSSB) generator [4,5]. These signals were created from two 10 Mb/s, 2^{15}-1 data pseudorandom bit sequences which were spread in the frequency domain by two 320 Mb/s Gold code chip sequences. These Gold code chip sequences were derived from the modulo-2 sum of (5,3) and (5,4,3,2) maximum length sequences [3].

The CDMA spread spectrum baseband signals were combined and used to modulate the phase of a 2.5 GHz local oscillator in order to generate an IF binary phase-shift-keyed CDMA signal. This sub-carrier signal was further upconverted to 39.2 GHz using a mm-wave subharmonically-pumped image-reject mixer (SHPIRM), amplified to +10 dBm and applied to the OSSB generator. An erbium doped fiber amplifier (EDFA) was used to increase the optical power before transmission over 30 km of standard single-mode optical fiber (SSMF). At the remote BS, the mm-wave signals were detected by a high-speed photodiode (PD). The CDMA signals were then amplified and transmitted over a 3 m radio link using specially

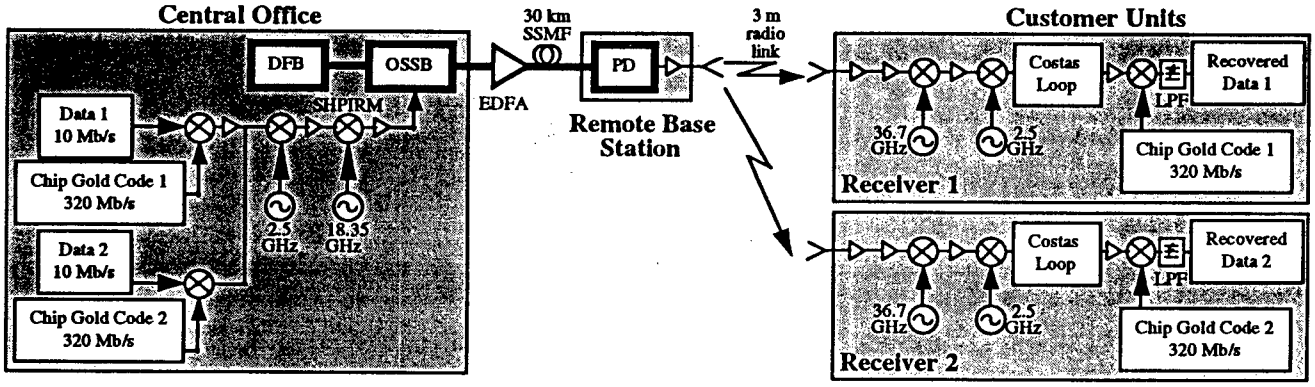

Fig. 1. Experimental setup of multichannel mm-wave CDMA fiber-radio system

designed broadband mm-wave microstrip patch antennas with gains of 5 dBi [6]. At the customer units (CUs) the received mm-wave signals were first downconverted to 2.5 GHz before being passed through a Costas Loop, which reproduced the two spread spectrum baseband signals. Each 10 Mb/s data channel was then recovered by mixing the spread spectrum baseband signals with the corresponding Gold code.

Fig. 2c shows the measured eye diagram of the received data for one channel in the mm-wave multi-channel CDMA system. In addition, Fig. 2a shows the electrical back-to-back measurement for a single channel (with no optical or radio link included) and Fig. 2b shows the eye-diagram for a single channel CDMA fiber-radio system. A bit-error-rate (BER) of less than 10^{-9} was achieved for each channel in the multi-channel CDMA fiber-radio system, although BER curves could not be measured due to the limited dynamic range of the Costas Loop used to recover the data. We expect however, a fiber dispersion-induced rf power penalty of less than 1.5 dB, which we measured previously for a fiber-radio system transporting a similar mm-wave frequency signal over a comparable fiber length using optical SSB modulation [7]. Also, in this demonstration the rf power loss in the radio link due to signal attenuation was 87 dB.

III. Theory

In Figs. 2a-c, the ripple observed in the measured eye-diagrams was due to the phase responses of the low pass filters (LPFs) at the output of the Costas Loops in the CUs. In order to confirm our experimental results and further investigate the transmission of multi-channel CDMA signals over optical fiber, we developed a model to simulate the entire mm-wave CDMA fiber-radio system. The model was based on the simulation package "GOLD" (Gigabit Optical Link Designer [8]) with additional components created in Labview in order to generate the CDMA codes and Costas locking circuits. For simplicity, the optical and electronic components in the system were all modeled as ideal and noise-free. Figs. 3a-c present the simulated received eye-diagrams for the CDMA fiber-radio system corresponding to the experimental conditions shown in Figs. 2a-c. The theoretical predictions show good agreement with our measurements.

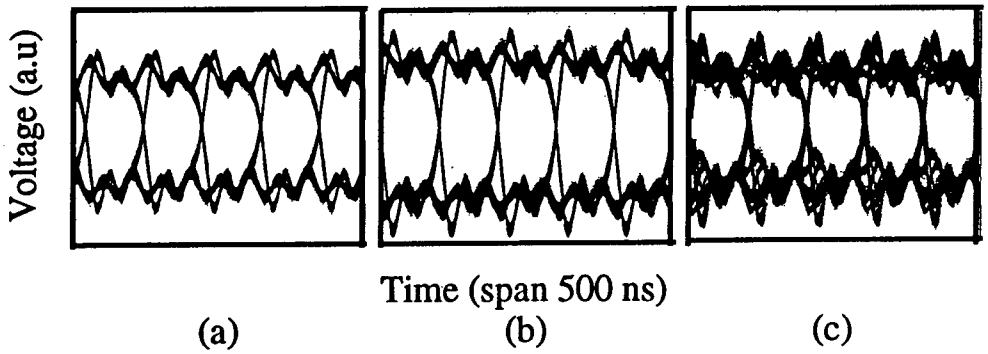

Fig. 2. Measured eye diagrams: (a) single channel electrical back-to-back; (b) single channel, and (c) two channel after 30 km SSMF and 3 m radio link

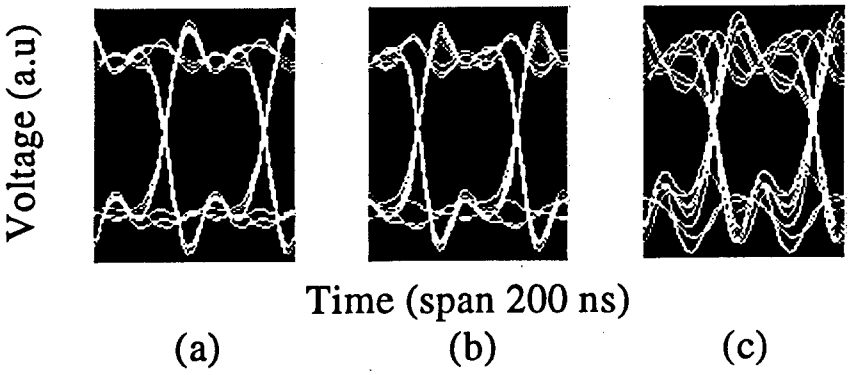

Fig. 3. Simulated eye diagrams: (a) single channel electrical back-to-back; (b) single channel, and (c) two channel after 30 km SSMF and 3 m radio link

In a multi-channel CDMA system, the measure of the rejection of other channels within a particular channel is determined by the ratio of the autocorrelation to cross-correlation for the codes used. For the Gold codes implemented in this experiment, a ratio of 0.36 was achieved. In the two channel eye-diagram, cross-

talk effects arising from this finite ratio of 0.36 are observed as additional noise on the "0"s and "1"s, as can be seen in Figs. 2c, 3c. In order to reduce this cross-talk it is necessary to use longer chip sequences.

IV. Conclusions

We have investigated the transmission of mm-wave multi-channel CDMA signals in a fiber-radio system incorporating this access scheme. In the fiber-radio system demonstrated, two 10 Mb/s data channels were converted to 320 Mb/s direct-sequence CDMA signals and transmitted at 39.2 GHz over 30 km of SSMF and a 3 m radio link. This multi-channel CDMA fiber-radio system was also modeled with theoretical predictions confirming our system measurements. It was found that transportation of the CDMA signals over optical fiber using optical SSB modulation overcomes possible dispersion penalties. In addition, the observed eye closure in a multi-channel CDMA environment is due to crosstalk effects related to the CDMA codes used in the system, and is independent of the optical link.

Acknowledgments

The authors thank Dr. Jim Harvey, MNA for the mm-wave transceiver units and Dr Rod Waterhouse, RMIT University for the broadband mm-wave patch antennas. They also thank Jennifer Yates and Michael Cahill for useful discussions, and Dr John Archer and CSIRO TIP for their support.

References

[1] G.H. Smith, D. Novak, and C. Lim, "A Millimeter-Wave Full-Duplex WDM/SCM Fiber-Radio Access", Proc. Optical Fiber Commun. Conf., San Jose, USA, pp. 18-19, February 1998.

[2] S. Glisic and B. Vucetic, Spread Spectrum CDMA Systems for Wireless Communications, Artech House, 1997.

[3] R. Prasad, CDMA for Wireless Personal Communications, Artech House, 1996.

[4] V. O'Byrne, "Digital cellular in the fiber-optic access network", *Proc. Optical Fiber Commun. Conf.*, USA, pp. 83-84, February 1992.

[5] S.L. Woodward and S. Ariyavisitakul, "Transmission of CDMA signals over an analog optical link", *Proc. Int. Conf. on Commun.*, USA, pp. 344-348, 1997.

[6] G.H. Smith, D. Novak, and Z. Ahmed, "Novel Technique For Generation Of Optical SSB With Carrier Using A Single MZM To Overcome Fiber Chromatic Dispersion", Proc. IEEE International Topical Meeting on Microwave Photonics, Kyoto, Japan, Post-Deadline Paper 2, December 1996.

[7] G.H. Smith, D. Novak, and Z. Ahmed, "Technique For Optical SSB Generation To Overcome Dispersion Penalties In Fiber-Radio Systems", Electron. Lett., pp. 74-75, January 1997.

[8] S.D. Targonski, R. B. Waterhouse, and D.M. Pozar, "Design Of Wideband Aperature-Stacked Patch Antennas", to appear in IEEE Trans. Ant. and Prop.,September 1998.

[9] G.H. Smith and D. Novak, "Full-Duplex Fiber-Wireless System Using Electrical and Optical SSB Modulation For Efficient Broadband Millimeter-Wave Transport", Proc. IEEE International Topical Meeting on Microwave Photonics, Duisburg, Germany, pp. 223-226, September 1997.

[10] G.J. Pendock, "WDM Transmission Simulator", Proc. Optoelectronics and Communications Conference, Seoul, Korea, pp. 296-297, July1997.

MULTICARRIER DISTRIBUTION OF MULTIPLEX DIGITAL COMPRESSED TV CHANNELS USING A HARMONIC LASER SOURCE AT 38 GHZ

D. Mathoorasing(1), D. Tanguy(2), J. F Cadiou(2), P. Legaud(2),

E. Penard(2), S. Bouchoule(1), C. Kazmierski(1)

(1)**OPTO +**
Groupement d'Intérêt Economique
Route de Nozay, F-91 460 Marcoussis
France Telecom, CNET- DTD/SSC
(2)France Telecom, CNET, 2 route Tregastel, 22301 Lannion, France

Email: dean.mathoorasing@cnet.francetelecom.fr

Abstract

ACTS FRANS project is investigating alternative optical mm-wave source solutions for implementing ATM radio over fibre network. In this context, we have demonstrated that multicarrier operation with 16 QAM data signals on a optical non-linear laser at 38 GHz can be achieved. Several TV channels have been distributed through a 9 km standard fibre link using this optical source with less than 0.5 dB penalty

Introduction

While fiber to the home is still prohibitive, radio over fiber network can be combined with existing network to allow full coverage, fast setting up of new services fast and overall cost optimization. Besides, most telephone and cable industries has refocused on less expensive fiber to the curb and hybrid fiber coax which combines the fiber's advantages and share the costs amongst many customers. The development of future radio over the fibre communication is framed in a completely integrated perspective where the analysed solutions can fully be embedded in the network to provide broadband communication. As a consequence, this technique must be able to tackle multicarrier operation as well and time division multiplexed signals. Many self-standing complementary systems[1,2,3] can be used to distribute data signals centered at the millimeter wave frequency from the central station to several base stations where the signal is radiated to the customers through directive antennas. In this paper, we demonstrate that multicarrier distribution of MPEG digital video data signal on an optical harmonic laser mixer at 38 GHz has been achieved with penalty less than 0.5 dB.

Millimeterwave Multicarrier distribution of the optical source at 38 GHz

Fig 1 shows the multicarrier compressed digital video distribution over a radio over fibre network using a DFB laser as optical mm-wave source[4]. Each carrier containing several digital video channels is received from the satellite through an antenna then downconverted at DC1 to an IF 1.589 GHz signal. The signal is downconverted at DC2 to 800MHz. On each carrier there is a set of digitally TV channels multiplexed in time. The carriers are spaced 10 - 15 MHz apart. The multicarrier signal is centered at 800 MHz The signal is then fed into the optical source through the IF port. The coding of each channel is MPEG. The optical source is

0-7803-4936-9/98/$10.00

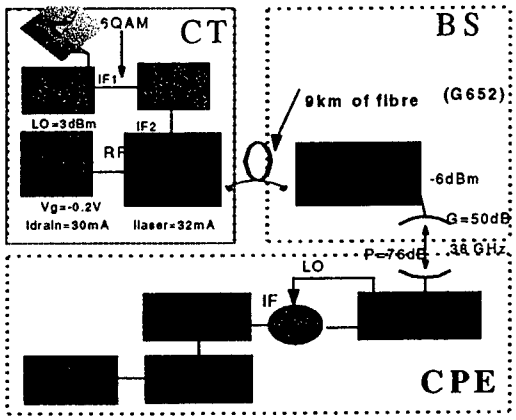

Fig 1: Multicarrier digital video distribution over an optical radio fibre network using an optical source laser

Fig 1 shows the multicarrier compressed digital video distribution over a radio over fibre network using a DFB laser as optical mm-wave source[4]. Each carrier containing several digital video channels is received from the satellite through an antenna then downconverted at DC1 to an IF 1.589 GHz signal. The signal is downconverted at DC2 to 800MHz. On each carrier there is a set of digitally TV channels multiplexed in time. The carriers are spaced 10 - 15 MHz apart. The multicarrier signal is centered at 800 MHz The signal is then fed into the optical source through the IF port. The coding of each channel is MPEG. The optical source is also modulated at the LO port to transpose the IF signal on the fourth LO harmonic frequency at 38 GHz. The 38GHz propagates in a link of 9 km of fibre and a radio link of 2 m. The signal is divided in two paths. The first one is used to extract the LO frequency to demodulate the signal frequency on the 2nd path. The demodulation signal is analyzed by the carrier selector and the demultiplexer before being decoded and displayed on a video screen. In this demonstration the number of carriers was limited to 4.
Fig 2 a,b. show the multicarrier electrical spectrum at the input of the optical source and at the output of the radio link after demodulation at 38 GHz respectively.

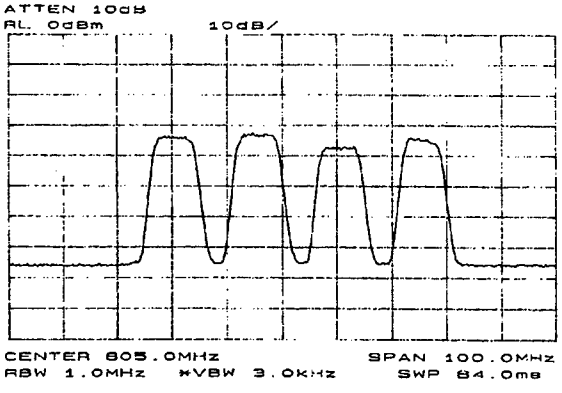

Fig.2 a Input multicarrier digital video signal

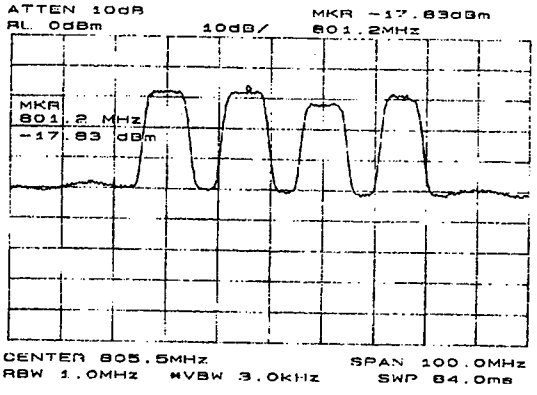

Fig 2.b Output multicarrier digital video signals after the fibre radio network

First, 16 QAM BER measurements at 25 Mbit/s has been performed in two cases: The first one with only one carrier (the other carriers turned off) and the other on the same carrier with the three other carriers turned on.
To fully demonstrate the optical source capability, compressed digital video channels on multiple carriers coming from a satellite has been used to feed the data signal on the input of the optical laser source. The output of the optical radio after demodulation is displayed on a video screen as shown on fig 1. A selector allows to choose the carrier and the TV channel and then the MPEG data signal is decoded before being displayed on the video screen. The TV channels distribution demonstration after the radio link of 9 km of standard fibre at 38 GHz was successful. The BER has been measured for three different conditions as shown on fig 4.

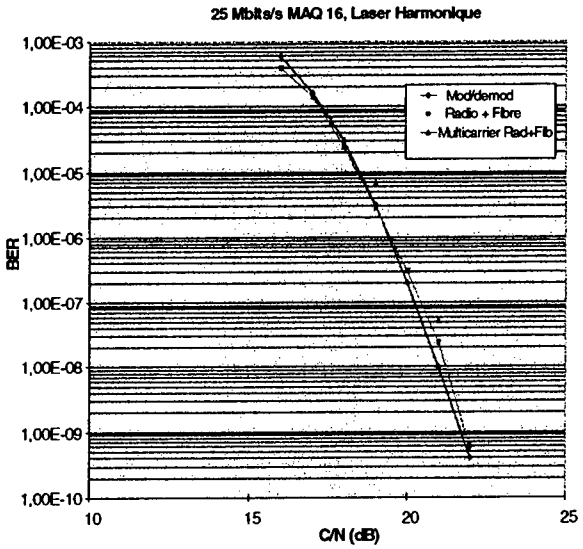

Fig 3. BER measurements for modulator and demodulator back to back, for the whole system (radio+fibre network) on one channel and the other turn off and with the other channels turrned on

This allows to show the degradation caused by the radio fibre link and alsoby the multicarrier operation. The radio fibre link, using the optical source, when operating in multicarrier operation(4 carriers) had a penalty of 0.5 dB. With one carrier, the penalty is slightly lower. On the video monitor no image distortion could be noticed on any channel.

Conclusion

We have demonstrated a 38 GHz millimeterwave distribution of multicarrier compressed digital video signals at 25 Mb/s 16QAM data signal over 9 km of standard fiber using an optical laser source. We showed also a penalty as low as 0.5 dB when operating with 4 carriers. This result is quite promising for the the tailoring of low cost distribution network(<20km) based on radio over fibre concept.

Acknowledgements: This work has been partly financed by European ACTS project FRANS. We would like to express our gratitude to A. Ougazzaden for the wafer furniture.

References

[1] J. Park, W.V Sorin and K. Y Lau, " Elimination of the fibre chromatic dispersion penalty on 1550nm millimetre-wave optical transmission," Electron. Lett., Vol 33, 1997, pp 512-513

[2] G. H Smith, D. Novak and Z. Ahmed, ," Technique for optical SSB generation to overcome dispersion penalties in fibre-radio systems," Electron. Lett., Vol 33, 1997, pp 74-75
[3] .E. Vergnol , ...Design of an integrated lightwave millimetric single side band source, Submitted to Journal of Lightwave Technology and French Patent Pending fr 9705362.
[4] D. Mathoorasing , C. kazmierski, D. Tanguy,"Patent CNET 02754"

A Novel Fiber-Optic Millimeter-Wave Uplink Incorporating 60GHz-Band Photonic Downconversion with Remotely Fed Optical Pilot Tone Using an Electroabsorption Modulator

Toshiaki Kuri,Ken-ichi Kitayama,*and* Yasunori Ogawa†
Communications Research Laboratory, MPT,† Oki Electric Industry, Co., Ltd.
4-2-1, Nukui-Kitamachi, Koganei, Tokyo 184-8795, JAPAN
Phone:+81-42-327-6331 /Facsimile:+81-42-327-7035 /E-mail:kuri@crl.go.jp

I. Introduction

To transmit millimeter(mm)-wave signals between a central station (CS) and many base stations (BSs), a radio-on-fiber system is very attractive, because of low transmission loss, extremely wide bandwidth, availability of optical amplifiers, and so on. Many radio-on-fiber systems have been proposed [1] $\sim$ [4]. To accelerate an initial deployment commercially, the low cost BS will be the key. The external modulation technique provides one of the best solutions because of the simple configuration [5]. We have already reported the fiber-optic mm-wave downlink system using 60GHz-band external modulation [6]. The same modulation technique is also applicable to the uplink system.

In this paper, the novel fiber-optic mm-wave uplink incorporating 60GHz-band photonic downconversion with the remotely fed optical pilot tone from the CS by using the EA modulator is presented. The error-free 156Mb/s-DPSK 60GHz-band mm-wave signal transport over 50km-long standard single-mode fibers (SMFs) is successfully demonstrated. This system has an advantage that neither a light source nor any mm-wave sources are required at the BS, leading to a simple BS configuration.

II. Uplink Using Photonic Down-Conversion

Figure 1 shows the experimental setup of the fiber-optic mm-wave uplink. It consists of a wireless terminal (WT), a BS, two SMF links, and a CS. The WT is a 60GHz-band radio station, which generates a 156Mb/s-DPSK 59.6GHz signal and transmits it from the mm-wave antenna to the remote BS. The BS has a mm-wave antenna, a mm-wave amplifier, a polarization controller (PC), the 60GHz-band EA modulator (EA Mod. 1) for the photonic downconversion, Erbium-doped fiber amplifiers (EDFAs), and an optical bandpass filter (BPF). The CS has an optical pilot tone generator, a photodetector (PD) and a demodulator. The optical pilot tone generator consists of a distributed feedback laser diode (DFB LD), another 60GHz-band EA modulator (EA Mod. 2), another EDFA, and a 57.0GHz mm-wave source. The 50km-long SMFs were used as downlink and uplink fibers.

A 156Mb/s-DPSK 59.6GHz signal from the WT is received, amplified and applied to the EA Mod. 1 in the BS. The optical pilot tone modulated with 57.0GHz at the CS is transmitted through the downlink SMF, amplified and fed to the EA Mod. 2. Its spectrum is schematically shown in Fig. 2(a). Here, λ_c represents the wavelength of optical carrier from the DFB LD, and $\Delta\lambda_l$ and $\Delta\lambda_r$ correspond to the frequencies of 57.0GHz and 59.6GHz for the mm-wave source at the CS and the received mm-wave signal, respectively. The PC is used to adjust the polarization of optical pilot tone to that of the EA modulator to maximize the modulation efficiently. Figure 2(b) shows the uplink optical signal generated by the photonic downconversion of the pilot tone with the applied 59.6GHz signal. After amplified by the EDFA, two upper sideband spectra at $\lambda_c + \Delta\lambda_l$ and $\lambda_c + \Delta\lambda_r$ are filtered out by the BPF and transmitted over the uplink SMF to the CS. At the demodulator in the CS, the beat generates 156Mb/s-DPSK intermediate frequency (IF) signal ($\Delta\lambda_r - \Delta\lambda_l$ which corresponds to the frequency of 2.6GHz) with the square-law detection of the PD. The optically direct-detected signal is demodulated to recover the data and the clock.

0-7803-4936-9/98/$10.00

III. Experimental Results and Discussion

To investigate the power sensitivity of the uplink system, the electrical powers of the received mm-wave signal and the optically detected IF signal were measured for some points of the received optical power. For measurement, the spectrum analyzer (HP 8565E) and its mixer (HP 11974V) were used, which had the average noise power density of −140dBm/Hz (typ.). The result is shown in Fig. 3. The conversion efficiency, which is defined by the power ratio of the detected IF and the received mm-wave signals, is constant up to the received mm-wave power of −63dBm. Above the received mm-wave power of −63dBm, the power of IF signal levels off. This is due to the saturation of mm-wave amplifier (RF Amp.) before the EA Mod. 1 in the BS. From the table in Fig. 3, the conversion efficiency is proportional to the square of received optical power.

The single sideband (SSB) phase noise at 10kHz apart from the carrier of detected IF signal was measured for the received mm-wave power of −65dBm. For measurement, the utility (HP 85671A) installed in HP 8565E was used. As shown in Fig. 4, the SSB phase noise of −85dBc/Hz was achieved in the higher optical power. Since the 57.0GHz oscillator output in the CS has the SSB phase noise of −86dBc/Hz, the degradation due to introduction of fiber-optic link is negligible. But the phase noise became worse in the lower optical power due to the thermal noise. The noise power density in the lower optical power is flat and dominated by the thermal noise, and the shot noise is dominant in more than −5dBm.

The phase noise was also measured for the constant IF signal power of −60dBm. Figure 5 shows the results. For each received optical power, the received mm-wave power was adequately arranged to keep the same detected IF signal power. As the received mm-wave power becomes stronger, both the phase noise and the noise power density are improved and less optical power is required. To keep the good quality of performance, it is desirable from Fig. 5 that the received mm-wave signal power is more than −90dBm. Judging from Figs. 4 and 5, if the received optical power is 3dBm which is conventionally the maximum allowable power into the PD, the margin of about 15dB should be estimated, taking the shot-noise-induced-penalty into consideration.

Figure 6 shows the optical power level diagram of the system. Here, the optical carrier (λ_c=1554.0nm) and the optical lower sideband signal (1553.5nm) were eliminated by using the narrow BPF for the optical upper sideband (USB, 1554.5nm). The mm-wave signal power applied into the EA Mod. 2 was 0.9dBm and its phase noise was −93dBc/Hz at 10kHz apart from the carrier. The modulation depths of optical signals at $\lambda_c + \Delta\lambda_l$ and $\lambda_c + \Delta\lambda_r$ for the optical carrier at λ_c were about 85% and 45% with the reverse bias voltage of −1.35V and −1.80V, respectively, resulting in the overall modulation depth of 53% (=45%/85%) for the uplink optical signal. For simplicity, a coaxial cable and an attenuator instead of free-space propagation. The total amount of mm-wave attenuation between the WT and the BS was 68dB.

Figure 7 shows the BERs after 50km-long SMF transmission and the back-to-back. The spectra of the optical pilot tone and the uplink optical signal are also shown in Figs. 7(a) and (b), respectively. No floor of the BER was observed. The minimum received optical power to get the BER of 10^{-9} was −20.5dBm after the 50km-long SMF transmission for the perfect polarization-matching condition. The power penalty of 1.5dB from the optical back-to-back is only due to the amplified spontaneous emission noises of EDFAs because this system is essentially free from fiber dispersion effect. Comparing with the BER for the imperfectly polarization-matching condition after the 50km-long SMF transmission, the polarization dependence loss (PDL) of the EA Mod. 2 was less than 1dB as shown in Fig. 7.

When the BER of 10^{-9} was achieved, the received mm-wave power was −65dBm. It is found from Fig. 3 that the detected IF signal power is about −62dBm, because of the conversion efficiency of about 3dB for the optical power of −20.5dBm. If the BER of 10^{-5} is allowed, the dynamic range will

expand to more 10dB, as a result of the margin of 5dB for required minimum optical power. In this case, the system is still in the thermal noise limitted. Moreover, when the optical power of 3dB is received and the margin of 15dB for shot-noise-penalty is took into account as mentioned in Fig. 5, the dynamic range will increase totally by no less than 40dB because the minimum received mm-wave power is about -105dBm. When the BER of 10^{-5} without error correction cording is achieved, for example, the transmission of video signals will be possible. From the above, it is expected that the WT in this system can be a mobile station with high data rate and slow mobility as one of short-distance radio applications.

IV. Conclusion

The fiber-optic mm-wave uplink incorporating 60GHz-band photonic down-conversion with remotely fed optical pilot tone using the EA modulator has been newly proposed. The power management of the system has been discussed by measuring the conversion efficiency, the SSB phase noise and the noise power density. Then, error-free 156Mb/s-DPSK 59.6GHz mm-wave signal transport over 50km-long SMFs has been successfully demonstrated. Here, the photonic downconversion has been also successfully performed. This technique will promise to realize the fiber-optic mm-wave access network in near future, also including mobile wireless stations.

Acknowledgments

The authors wish to thank T. Ushikubo, S. Seki and M. Akiyama of Oki Electric Industry, Co., Ltd. for collaborating in this experiment. Their thanks are also due to H. Fukuchi and Y. Furuhama of CRL for their encouragement.

References

[1] D. Wake, *et. al.*, *IEEE Trans. Microwave Theory Tech.*, vol. 43, no. 9, pp. 2270–2276, Sep. 1995.

[2] R. Heidemann, *et. al.*, in *Proc. of MIOP'93, 7th Exhibition and Conference for Ultra High Frequency Technology*, pp. 251–254, 1993.

[3] K. Kitayama, *et. al.*, in *Proc. GLOBECOM'96*, London, pp. 2162–2169, Nov. 1996.

[4] T. Kuri, *et. al.*, *Electron. Lett.*, vol. 32, No. 23, pp. 2158–2159, Nov. 1996.

[5] K. Kitayama, in *IEICE Technol. Rep. 2nd MWP*, MWP97-25, pp. 92–98, Feb. 1998.

[6] K. Kitayama, *et. al.*, in *OFC'98 Dig.*, San Jose, CA, TuC, pp. 14–15, Feb. 1998.

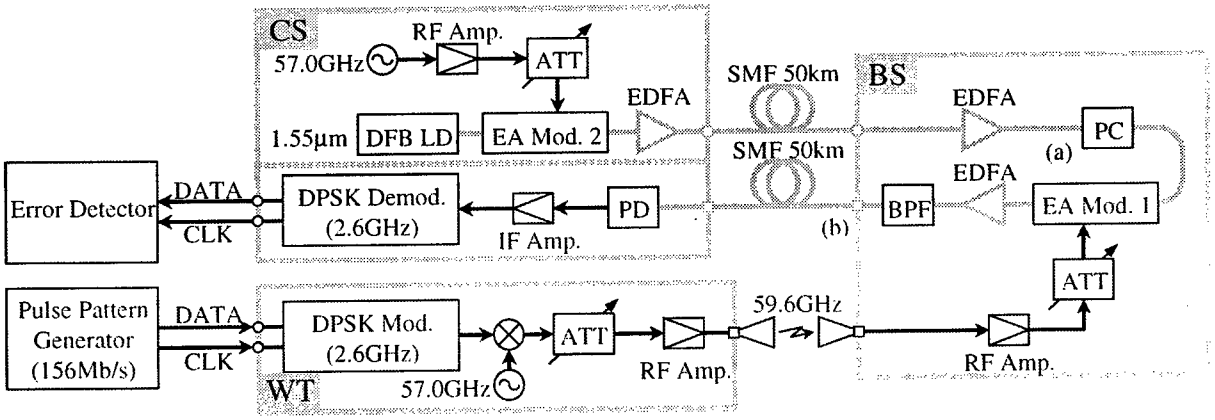

Fig. 1. Experimental setup.

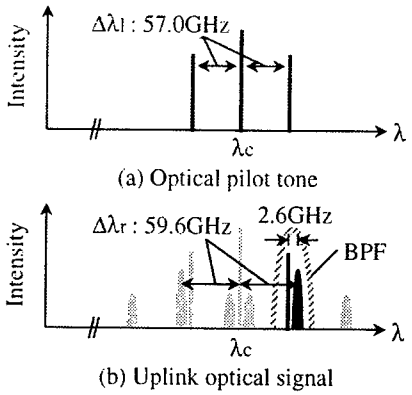

Fig. 2. Optical spectrum design.

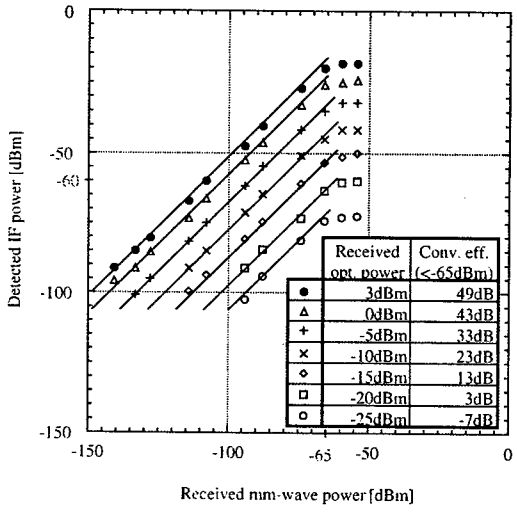

Fig. 3. Detected IF signal power vs. received mm-wave signal power

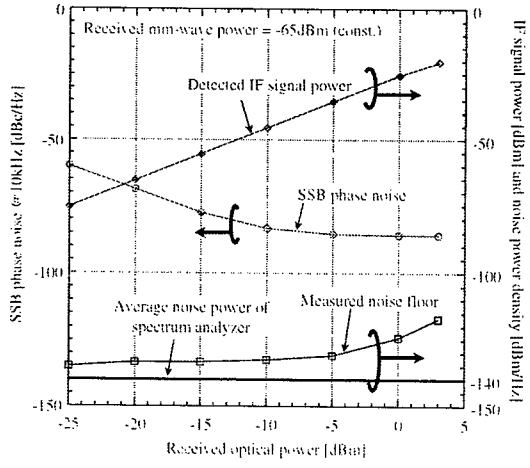

Fig. 4. SSB phase noise and noise power density (1)

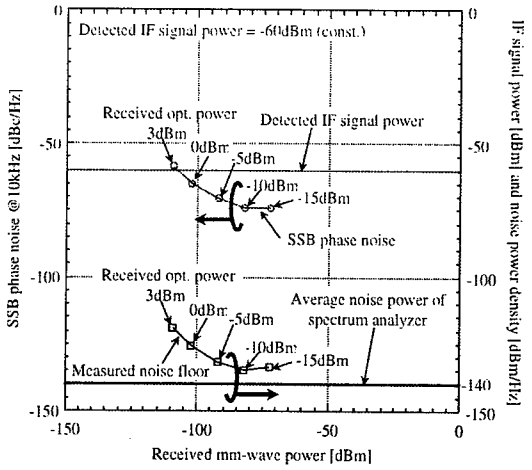

Fig. 5. SSB phase noise and noise power density (2)

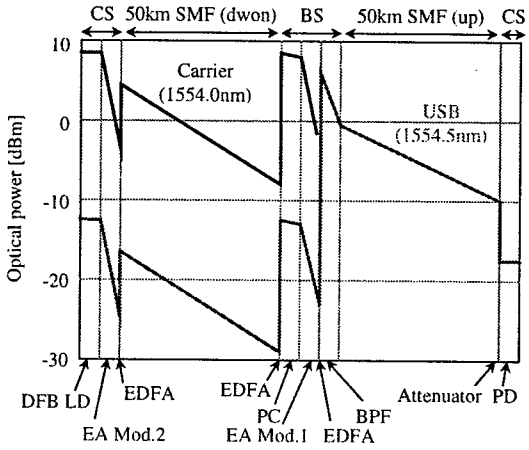

Fig. 6. Optical power level diagram.

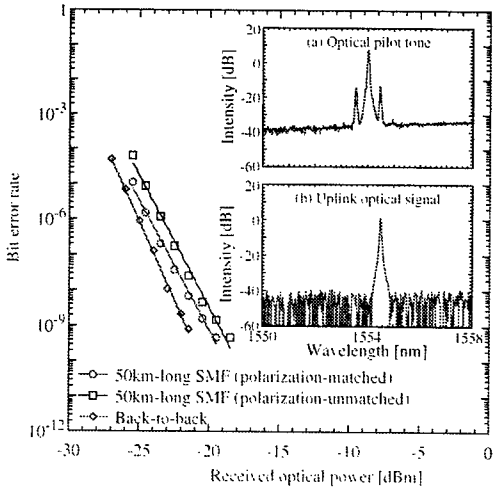

Fig. 7. BERs and spectra of optical signals.

A PHOTOCONDUCTIVE CORRELATION RECEIVER FOR WIRELESS DIGITAL COMMUNICATIONS

Eric E. Funk, Scott Ramsey, Chi H. Lee, and John Craven*

Joint Program for Advanced Electronic Materials,
Department of Electrical Engineering,
and
Laboratory for Atomic, Molecular, and Optical Science and Engineering,
University of Maryland,
College Park, MD 20742

*U.S. Department of Defense

ABSTRACT

We demonstrate an impulse radio architecture which employs a GaAs photoconductive switch in performing correlated reception. Results show a bit-error-rate of better than 10^{-8} at 38 Mb/s and excellent interference rejection.

I. INTRODUCTION

Wireless digital communications systems now commonly employ spread-spectrum (SS) modulation and correlated reception. Due to the demand for higher data rates and greater security, spread-spectrum bandwidths of approximately 1 GHz are now being considered. Signal processing at these bandwidths is difficult and costly with conventional electronics. Hence, some unique approaches are being considered.

Impulse radio [1] is one such technique that is now being investigated. Impulse radio is based on the transmission of precisely timed short RF pulses, typically one to three RF cycles long, near a 1 GHz center frequency. The presence or position of these pulses is used to transmit information; there is no carrier conversion involved.

Impulse radio offers a potentially less expensive/easier means of realizing large (> 100 MHz) spread-spectrum bandwidths and, in turn, higher processing gains when compared to digital signal processing (DSP) techniques presently in use in direct sequence (DS) and frequency hopped (FH) systems. A well designed impulse radio system can exploit the large available processing gain for the purposes of signal security. In addition, the large signal bandwidth has been shown to effectively mitigate frequency selective fading [2] which leads to an overall reduction in the fade margin of the link budget.

However, some of these advantages are traded against some difficult receiver design requirements. Most importantly, the impulse radio receiver must accept interference over the full signal bandwidth. Interference from the full VHF and UHF broadcast and two-way radio bands can easily mask the impulse radio signal in a receiver with poor dynamic range.

We believe that correlated reception [3] using photoconductive gating is an ideal approach to dealing with the impulse radio signal. Photoconductive switching technology [4], with its high speed, low jitter, and large dynamic range is ideally suited to both generating and gating these RF bursts. In this work, we demonstrate the performance of a photoconductive switch as the key component in a 38 Mb/s correlation receiver.

0-7803-4936-9/98/$10.00

II. DEMONSTRATION SYSTEM

The transmitter and correlation receiver are shown in Fig. 1. In the transmitter, a clock signal drives a step-recovery diode (SRD), generating a train of unipolar pulses at 38 MHz repetition rate. These unipolar pulses are then on/off keyed (OOK) by a synchronized 38 Mb/s binary message. A single pulse is used per bit *for this demonstration*, however multiple pulses per bit could also be used with a DS code. Finally, the OOK pulse train is amplified in a broadband amplifier and radiated by a broadband reciprocal bow-tie antenna. Alternatively, the transmitted signal could be generated by use of a photoconductively switched antenna [5].

In the receiver, a reciprocal bowtie antenna feeds a gating photoconductive switch. The fast gating function acts as a correlator on the received impulse train. The gated signal is amplified in a broadband low-noise amplifier and passed through a microwave crystal diode detector before threshold detection.

Our photoconductive switch consists of a small interdigitated capacitor on an undoped GaAs microstrip line with finger width and spacing of 30 μm. The capacitance is low enough to give more than 20 dB of off-state isolation. The switch is triggered by a 810 nm Ti:sapphire laser pulse train which is synchronized to the incoming RF pulses. A trigger energy of 900 pJ/pulse is used with the soft-focus of a 15 cm focal length lens.

The gating function is most easily characterized under DC bias, where the switch produces a 500 ps full width at half maximum pulse. Shorter gating could be obtained by use of other photoconducting materials, however, for this application, the 500 ps window is more than sufficient.

There are three primary features of our switch. First, the switch mitigates interference by providing isolation between the antenna and detector during the large interval when there is no impulse radio signal present. Second, during the brief intervals when a signal is present, it provides a gated signal to the threshold detector. Third, it ensures a large dynamic range, by providing a 1 dB input compression point of greater than 24 dBm (measured at 1 GHz). While certain high dynamic range mixers can match this compression point, the required LO drive signal is large enough to cause significant coupling of the LO into the IF port, rendering their performance unacceptable in a carrier-free baseband system.

The experimental setup described above was tested in our laboratory by performing an uncoded bit-error-rate test (BERT) with a 38 Mb/s pseudo-random bit sequence (PRBS). In order to assess resistance to narrowband interference, a strong 1 GHz CW signal was added to the environment from a nearby transmitter.

With a received power of -35 dBm at the antenna terminals (measured by integration of the received waveform) and no added interference from the CW transmitter, a bit-error-rate (BER) of better than 10^{-8} was measured. A typical return-to-zero (RZ) "eye diagram" measured at the output of the gate is also shown as an inset in Figure 2.

A 1 GHz CW signal was then added to the environment from a nearby transmitter. Figure 2 shows the measured BER vs. the signal-to-interference ratio (SIR) at the receiving antenna. Note that excellent BER performance is achievable even with an SIR of less than 0 dB. For example, an SIR of only –6 dB is required to achieve a BER of 10^{-6}. At this BER, the interference power is 1.2 μW. This shows how the processing gain that results from the large bandwidth of our signal can be used to provide interference resistance.

The results and evaluation discussed above show the capability of the photoconductive receiver to mitigate narrowband interference in an impulse radio system. This feature is essential since spectrum is shared with many other comparatively narrowband signals. We emphasize that this measurement was specifically designed to assess resistance to a very strong interferer and, by no means, represents the sensitivity limit.

III. CONCLUSION

Unlike most conventional spread-spectrum receivers, our receiver performs correlated reception of the signal at the receiver front-end on a broadband (700 MHz RF bandwidth) signal. This is accomplished without high-speed A/D converters which would otherwise limit the dynamic range of the system. We can also achieve one-to-one improvement in interference resistance by lowering our data rate. For example, we could operate at 12 kb/s with a SIR of -41 dB.

Although a laboratory laser was used for this initial demonstration, the switch geometry is being re-designed to operate with compact lasers such as Q-switched laser diodes[6]. This would make such a system realizable in a very compact package.

We also note that in this work, we have attempted to focus on interference-limited reception in the case of ideal synchronization. As such, we have run the transmitter and receiver from the same clock. Ultimately, the photoconductive switch would serve as a drop-in technology in a system where a tracking loop is employed to maintain wireless synchronization of clocks.

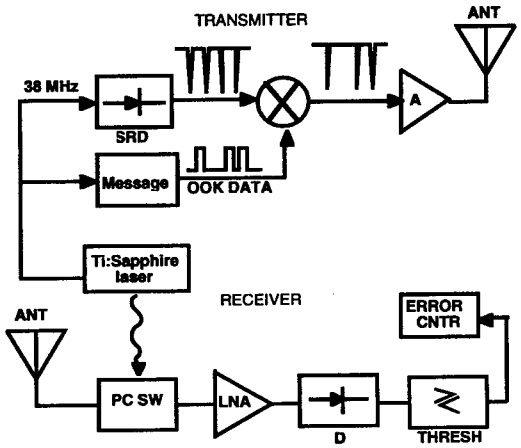

Figure 1. System architecture. SRD: step-recovery diode circuit, A: power amplifier, ANT: broadband antenna, PC SW: photoconductive switch, LNA: low noise amplifier, D: diode detector, THRESH: threshold detector.

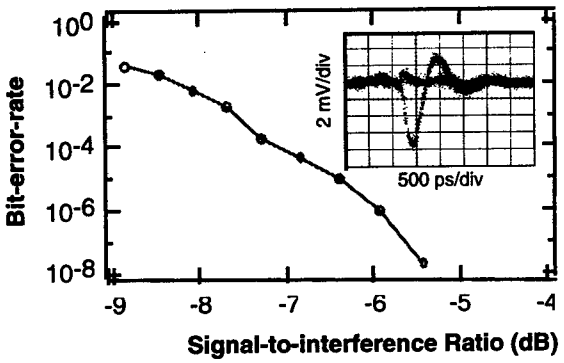

Figure 2. 38 Mb/s system performance. Measured BER vs. SIR signal-to-interference ratio (SIR). Inset: Eye-diagram measured at output of the photoconductive switch.

REFERENCES

[1] Moe Z. Win, and Robert A. Scholtz, "Impulse Radio: How it Works," IEEE Communications Letters, vol. 2, pp. 36-38, Feb. 1998.

[2] Moe Z. Win and Robert A. Scholtz, "On the robustness of ultra-wide bandwidth signals in a dense multipath environment," IEEE Communications Letters, vol. 2, pp. 52-53, Feb. 1998.

[3] Andrew J. Viterbi, *Principles of Spread Spectrum Communications*, New York: Addison-Wesley Publishing Company, 1995.

[4] C. H. Lee, "Picosecond optics and microwave technology," IEEE Trans. Microwave Theory and Tech., vol. 38, no. 5, pp. 596-607, 1990.

[5] Eric E. Funk and Chi H. Lee, "Free-Space Power Combining and Beam Steering of Ultra-Wideband Radiation Using an Array of Laser-Triggered Antennas," IEEE Trans. Microwave Theory Tech., vol. 44, pp. 2039-2042, November 1996,.

[6] B. J. Thedrez, S. E. Saddow, Y. Q. Liu, C. Wood, R. Wilson, and C. H. Lee, "Experimental and theoretical investigation of large output Q-switched AlGaAs semiconductor lasers," IEEE Photon. Technol. Lett., vol. 5, pp. 19-22, Jan. 1993.

Packaging For Millimetre Wave Fibre-Radio Modules

C R PESCOD, G M AUKER, P T SHARP, R G SIRETT & T P YOUNG

GEC-Marconi Research Centre, West Hanningfield Road, Chelmsford, Essex, CM2 8HN, England.

Abstract: A 27.75-29.32GHz millimetre wave fibre-radio antenna unit is reported which distributes 622Mbit/s downlink and 40Mbit/s composite TDMA uplink ATM multimedia signals to/from customer premises equipment (CPE) located within a 500m range. Coherent optical signals are used to distribute downlink transmit and LO signals. The uplink millimetre wave signal is downconverted to a 615MHz IF for transmission on an intensity modulated optical link to the central station.

I. Introduction

As part of the ACTS AC083 (FRANS) programme, the consortium has been building a fibre-radio network for distribution of multimedia services to domestic users supported by a fibre infrastructure. Opto-systems require a great deal of electronics in them, and packaging is a key feature in making such products viable.

The FRANS mm-wave 622Mbit/s ATM fibre/radio network consists of five parts as shown in Figure 1. These include the optical mm-wave source, passive optical network (PON), antenna unit (AU), free space mm-wave radio link (500m maximum range) and the customer premises subscriber equipment (CPE). Coherent heterodyne optical transmission techniques have been adopted to minimize the effect of fibre dispersion on the 27.875GHz 622Mbit/s 16 QAM downlink signal. TDMA is used in the uplink (centred on 29.26GHz) to combine data from the CPEs. The optical uplink uses a laser diode which is directly modulated by the downconverted 40Mbit/s FSK 615MHz IF uplink signal.

MRC's role was to develop low cost softboard technology to integrate Tx and Rx mm-wave subsystems onto a single substrate along with the optical, electrical and rf subsystems, producing a rugged package for field trials.

II. System Design

The FRANS AU demodulates the coherent optical signals (generated by the Alcatel-SEL mm-wave optical source) that are incident on the AU photodetector, amplifies and filters the wanted lower sideband downlink and local oscillator (LO) signals, while rejecting the unwanted upper sideband downlink signal. The downlink signal (27.75 to 28.0 GHz) is then coupled to a patch antenna array where the 622Mbit/s QAM mm-wave signal is transmitted on a free-space radio link to the CPEs. The LO signal (29.875 GHz) is used internally to downconvert the received uplink signal (29.2 to 29.32 GHz) which is then transmitted to the central station on a 615MHz IF optical link.

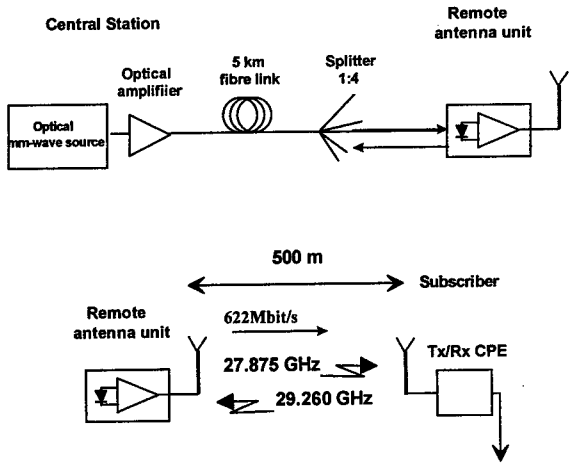

Figure 1 FRANS mm-wave fibre/radio system (downlink: 622Mbit/s ATM, uplink: 40Mbit/s TDMA composite from all CPEs)

Hybrid and monolithic reactively matched millimetre-wave photodiodes have been developed by Thomson-CSF and GEC-Marconi for use in the AU. The softboard techniques described below were used to effect a transition from the coplanar output of the photodiode to the microstrip used in the AU (shown in top right section of figure 1).

III. AU Softboard Substrate Design and Processing

A softboard substrate integration technology has been developed which enables the various active and passive optical and electrical components to be integrated into a compact AU, offering potential cost reductions compared with conventional alumina substrate based microwave integrated circuits (MICs). A substrate copper etching process has been developed to fabricate tracks and gaps of 50±5μm. Test filter structures have

0-7803-4936-9/98/$10.00

been fabricated and characterised which confirm the suitability of the processing technique.

A range of softboard substrate test circuits have been designed, built and characterised. These include passive microstrip filters (based on filter layout information provided by University of York), photodiode and MMIC amplifier test jigs incorporating coplanar waveguide (CPW) to microstrip transitions and patch antenna test jigs. Figure 2 shows an 8 resonator LO filter test jig.

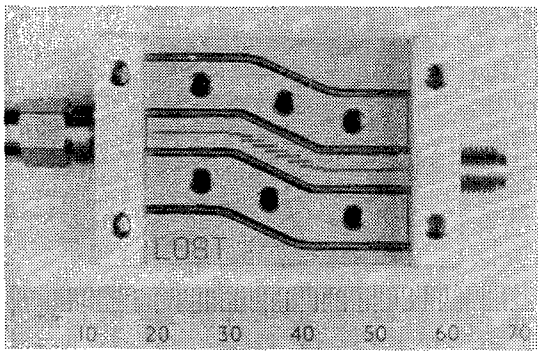

Figure 2 mm-wave LO Filter Test Jig

A downlink/LO diplexer has been implemented (based on a UoY design) which uses 6 resonator downlink and LO filters. The frequency response of the diplexer implemented using the MRC softboard technology is given in Figure 3.

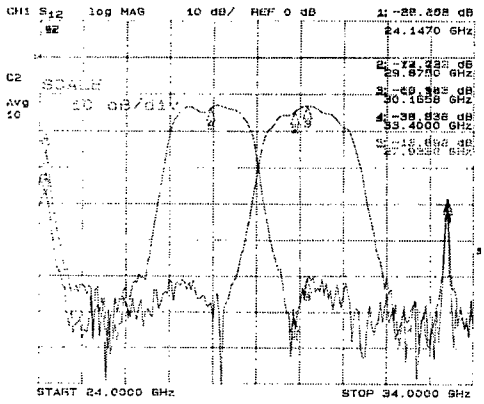

Figure 3 Downlink/LO Diplexer Passband and Rejection Characteristics

IV. Integrated Millimetre Wave Active/Passive Substrate

Figure 4 shows the fully integrated millimetre wave module and its screening lid. This circuit combines all of the AU optical/millimetre wave active/passive functions on a single softboard substrate. Downlink functions include: PIN waveguide photodiode, low noise MMIC amplifier, downlink/LO diplexer, LO MMIC amplifier, downlink MMIC driver and power amplifiers and the MMIC amplifier d.c. bias decoupling circuits. Uplink functions include: low noise MMIC amplifier, bandpass filter, MMIC mixer and IF filter. The screening lid is required to improve cross-channel isolation.

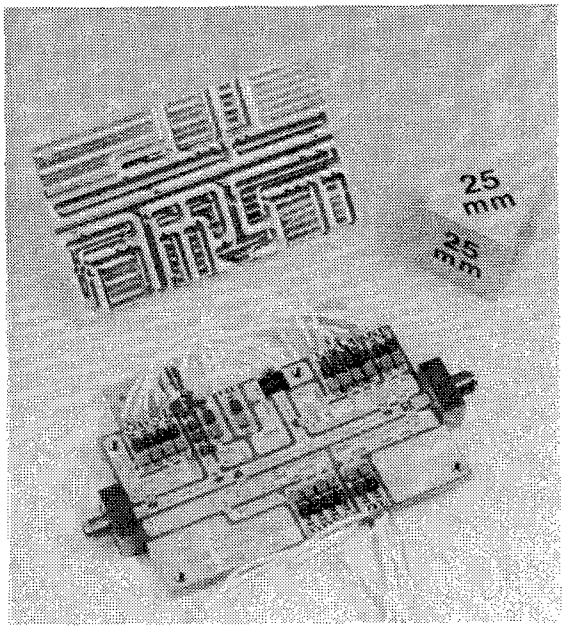

Figure 4 Integrated Softboard Substrate Optical/Millimetre Wave Downlink/Uplink Module

V. Ruggedised Antenna Unit

The ruggedised AU consists of five modules and the package, these include: the mm-wave module, the downlink and uplink patch antennas, the IF uplink laser module, the power conditioning and bias control circuits. Figure 5 shows these integrated in the ruggedised package. Figure 6 shows a front view of the AU with the patch antenna radomes inset in to the front panel.

Field trials are scheduled to start during October 1998 and preliminary results will be presented.

Conclusion

A system module to deliver ATM services from a fibre network and broadcast them to domestic customers has been produced and test results will be presented at the Conference. Particular emphasis is laid here on the packaging and particularly the microwave packaging needed to support an opto-electronic function such as this.

Acknowledgements

We wish to thank the other FRANS collaborators for their contribution to this activity, particularly, Francois Deborgies (Thomson-CSF), Peter Duthie (GMMT),

Mike Page-Jones (Univ. of York), Steffen Kudszus (Fraunhoffer Inst.), Martin Mittrich (Alcatel-SEL), Pierre Jaffre (CNET) and Harald Schmuck (Alcatel-SEL). We acknowledge EU support through the ACTS programme.

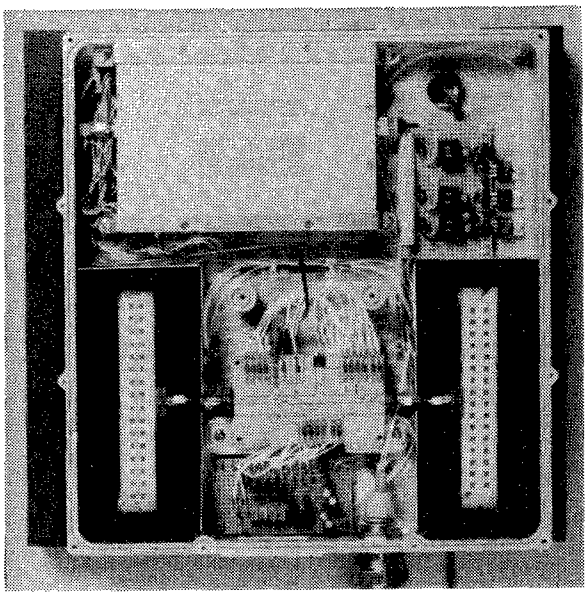

Figure 5 Internal View of Rugged AU Showing IF Laser Module, Patch Antennas & Power Module

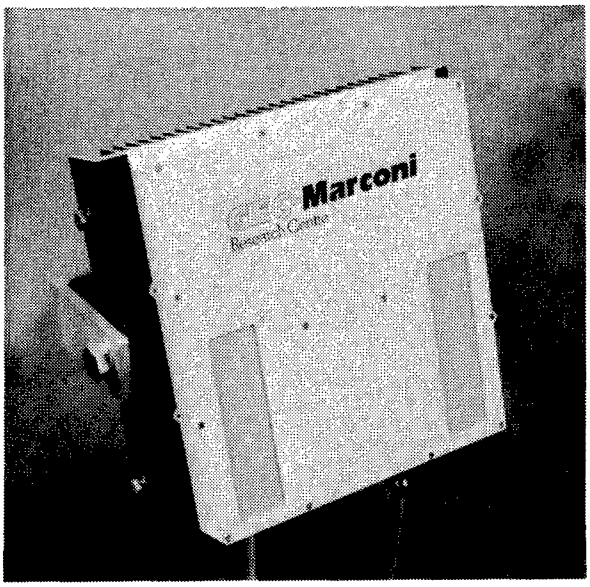

Figure 6 Fibre Radio Module with Patch Antenna Radomes (Rx on left, Tx on right)

Electroabsorption Waveguide Modulators for High Performance Analog Fiber Links

P. K. L. Yu, R. B. Welstand, G. L. Li, W. X. Chen, J. T. Zhu,
University of California, San Diego; Department of ECE; La Jolla, CA 92093-0407
Tel: 619 534 6180; FAX: 619 534 0556; email: yu@ece.ucsd.edu
S. A. Pappert, C. K. Sun, R. Nguyen
SPAWAR System Center, San Diego, CA 92152-5001
Y. Z. Liu
Fermionics Laser Technology; 4555 Runway Dr.; Simi Valley, CA 93063

Summary

Analog fiber optic links have been shown to be useful in antenna remoting and active phased array applications.[1] Semiconductor electroabsorption (EA) waveguide modulators can be used in these links in view of their potential for low voltage operation, large bandwidth, and monolithic integration with other components.[2] Important considerations of an optical modulator for analog applications are RF efficiency and the spurious free dynamic range (SFDR). In our prior work[3], we demonstrated dual-function properties of a Franz-Keldysh effect waveguide which can function as a modulator and as a detector. As an electroabsorption modulator, a fiber optic link with a -17.4 dB RF loss and a 124 $dB/Hz^{4/5}$ sub-octave SFDR, as depicted in Fig. 1, is obtained with electrical biases in the 2-3 V range. As a waveguide photodetector, a 0.45 A/W fiber coupled responsivity, photocurrents up to 20 mA, and an output third-order intercept of > 34.5 dBm, are achieved at -7V. As extensions of this work, we present (a) the results on the novel bias control of the electroabsorption waveguide modulator for maximum RF efficiency based upon the behavior of the modulator photocurrent, (b) the progress in the study of high SFDR electroabsorption waveguide modulator based upon a combination of the Franz-Keldysh effect (FKE) and Quantum Confined Stark effect (QCSE).

(A) Novel bias control of the EA modulator for adaptation to environmental changes

While prior work[3] emphasizes the simplification of the antenna feed network shown in Fig. 2, we note that the photocurrent generated during electroabsorption modulation can be useful for an adaptative bias control of the modulator, as schematically depicted in Fig. 3. For an EA modulator, the RF efficiency and the multi-octave SFDR can be optimized at the same bias. The optimum bias voltage for maximum RF efficiency can *shift* during operation due to changes such as ambient temperature, polarization and optical power levels, especially with the modulator placed at the antenna site. Therefore it is necessary to adjust the bias dynamically to maintain the maximum RF efficiency and SFDR.

The RF link gain is proportional to the square of the modulator slope efficiency, therefore, one expects, under certain operating conditions, the optimum bias voltage for maximum RF efficiency to be identical to the bias voltage for maximum slope of the modulator transfer curve. Under stable operating conditions, with the modulator not saturated by the optical power, the sum of modulated light coupled to the detector and light absorbed in the modulator is assumed constant. The photocurrent that flows in the biased semiconductor EA modulator depends only on the bias voltage, V_m. Thus the change in modulator photocurrent, I_m, is complementary to the change in modulator transmission, especially near the critical bias voltage. $V_{m,m}$, defined as the bias point for the largest slope in I_m with respect to V_m, will drift in response to changes in

0-7803-4936-9/98/$10.00

operating conditions such as temperature, polarization and optical power levels. Consequently, by finding the bias voltage where dI_m/dV_m is largest, one can track the optimum bias for maximum RF efficiency. This concept suggests a new approach to control the modulator bias for maintaining maximum RF link gain under changing operation conditions.[4] Link gain measurements are performed on an InGaAsP/InP modulator and compared to the I_m versus V_m curve. Same measurements are made for several laser wavelengths and for different input polarizations. We show that $V_{m,m}$ tracks maximum RF link gain (G_{RF}) and thus can be used for controlling the modulator bias voltage for maximum RF efficiency, as depicted in Fig. 4. This method is applicable to FKE as well as QCSE EA modulators.

(B) Transfer curve and projected SFDR of combined FKE-QCSE EA modulators

We have developed a methodology to analyze the linearity of the transfer characteristic of electroabsorption waveguide modulator. We found that a superlinear transfer curve can be obtained using a combination of the FKE and the QCSE. In this design, the differences in the FKE and QCSE absorption-voltage relationships are used to perform optical nonlinear cancellation.

The experimental structure consists of a 0.15 μm thick InGaAsP (λ_g = 1.49 μm) and five InGaAs/InP quantum wells (68 Å well) grown by MOCVD. At an optical wavelength of 1.544 μm, these represent detuning energies of 28 mV and 20 meV, respectively. Rib-loaded waveguide modulators are fabricated and devices cleaved at different lengths are measured. Fig. 5 shows the DC transfer curve obtained from a device with a cleave length of 105 μm. Note that the TE polarization has a larger modulator photocurrent and a smaller transmission than does the TM polarization for biases greater than 1.2 V. We attribute this to the QCSE which predominantly operates in the TE polarization.

It is observed that this combination of EA absorption produces a very linear transfer curve. Fitting this curve with the theoretical design curve, a close match is observed and indicates a simultaneous suppression of both second- and third-order nonlinearities at 1.64 V. The projected SFDR of this device is depicted in Fig. 6, where a multi-octave SFDR of 118 dB in a one Hz noise bandwidth is predicted. The simulation assumes a detector DC photocurrent of 0.47 mA and a laser RIN of -165 dBc/Hz. Inspection of the higher order terms show that the dominant distortion is the third-order intermod rather than the second-order intermod.

The sensitivity of the linearized transfer characteristics is investigated over a range of temperature. The linearized modulator device is mounted onto a thermoelectric cooler (TEC), and several transfer curves are measured as a function of the device sub-mount temperature. The temperature is varied from 20 to 32 °C (± 0.5 °C). Fig. 7 shows the range (shaded area) of bias, over which the measured transfer curve maintains its apparent straight-line fit, as a function of TEC temperature.

Acknowledgement: This work is partially sponsored by DARPA, ONR, and MICRO of Calif.

References:

1. W.L. Glomb, Jr., 'Fiber optic links for antenna remoting', Proc. SPIE, Optical Technology for Microwave Application VI and Optoelectronic Signal Processing for Phased-Array Antennas III, 1992, **1703**, pp. 523-527.
2. N.M. Froberg, G. Raybon, A.M. Johnson, Y.K. Chen, T. Tanbun-Ek, R.A. Logan, A. Tate, A.M. Sargent, K. Wecht, P.F. Sciortino, Jr., 'Pulse generation by harmonic modulation of an intergrated DBR laser-modulator', Electron. Lett., 1994, **30**, pp. 650-651.

3. R. B. Welstand, S. A. Pappert, C. K. Sun, J. T. Zhu, P. K. L. Yu, "Dual-Function Electroabsorption Waveguide Modulator/Detector for Optoelectronic Transceiver Applications," Photon. Tech. Lett., 1996, 8, pp. 1540 – 1542.
4. G.L. Li, R.B. Welstand, W.X. Chen, J.T. Zhu, S.A. Pappert, C.K. Sun, Y.Z. Liu, and P.K.L. Yu, "Novel Bias Control of Electroabsorption Waveguide Modulator," Photonics Technology Letters, Vol. 10 (5) , pp. 672-674 (1998).

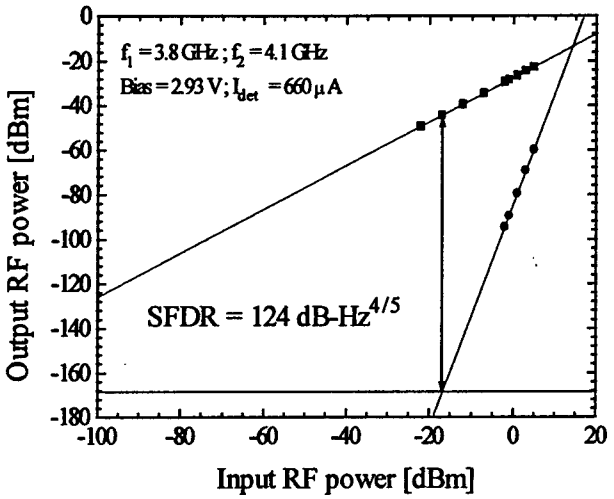

Fig. 1. Narrow bandwidth two-tone linearity measurement of the transceiver as a waveguide modulator showing fundamental (squares) and third-order intermodulation product (circles) signals. TM polarized light (37 mW) is incident onto the device (afer Ref. 3).

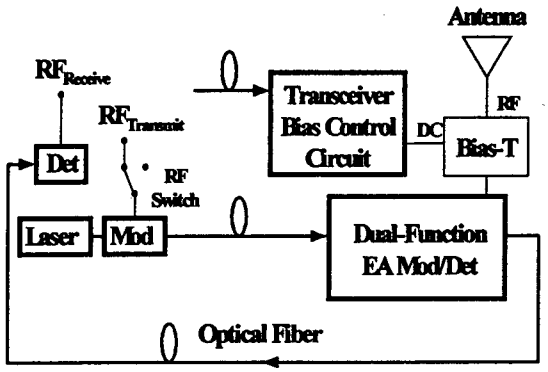

Fig. 2. Schematic of antenna feed network, including optoelectronic transceiver, remote laser, optical detector (Det), and modulator (Mod), used for transmit/receive applications (after Ref. 3).

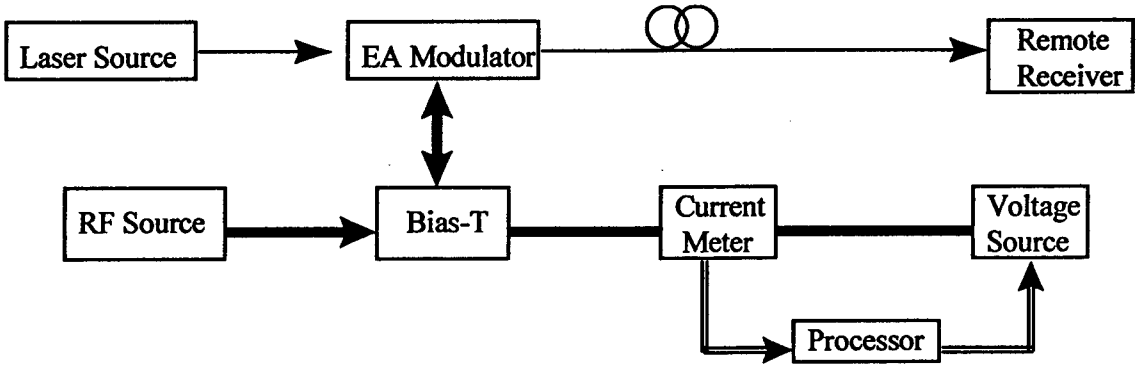

Fig. 3. Schematic diagram for implementing EA modulator bias control based upon the correlation between RF link gain and modulator DC photocurrent.

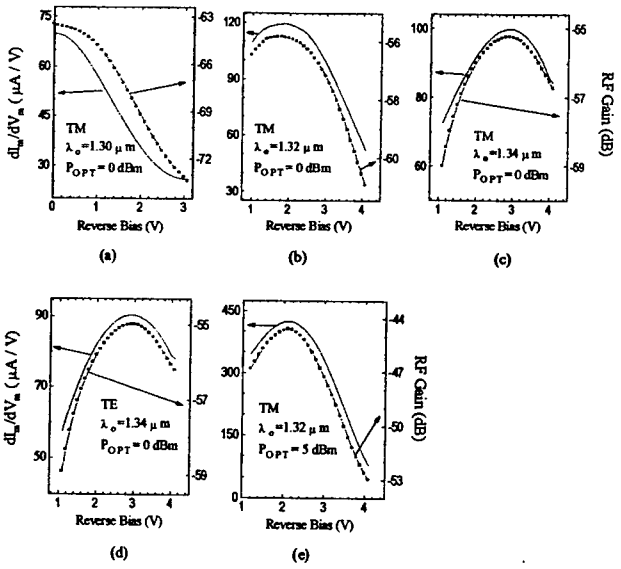

Fig. 4a to 4e, G_{RF}~V and dI_m/dV_m~V_m curves under different operating λ, optical power and polarization. The left axis is dI_m/dV_m (μA/V), the right axis is RF Gain (dB) (after Ref. 4).

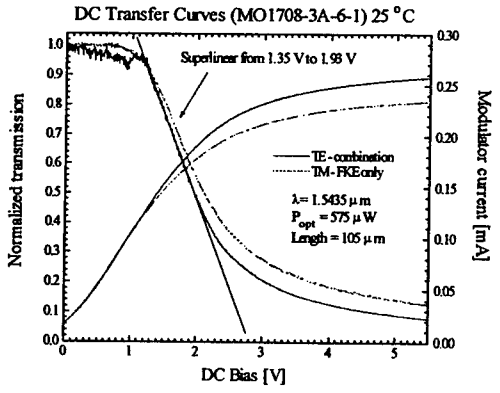

Fig. 5. Normalized DC transfer curves and modulator photocurrent for both TE and TM polarizations in the combination (FKE+QCSE) structure.

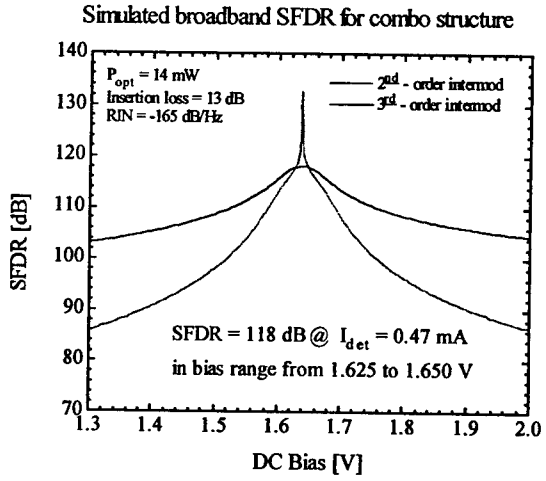

Fig. 6. Simulated SFDR in 1 Hz noise bandwidth of the DC transfer curve of Fig. 5, operating in TE polarization.

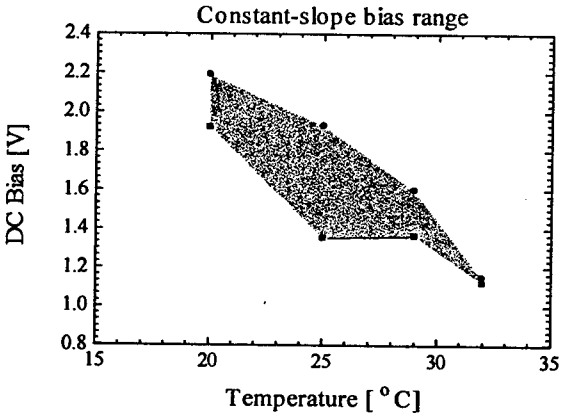

Fig. 7. Temperature dependence of constant-slope bias range for the combination (FKE+QCSE) structure.

Polarization-insensitive multiple-quantum-well traveling-wave electroabsorption modulators with 18 GHz bandwidth and 1.2 V driving voltage at 1.55 μm

Sheng Z. Zhang, Yi-Jen Chiu, Patrick Abraham, and John E. Bowers
Department of Electrical and Computer Engineering
University of California, Santa Barbara, CA 93106
Tel: (805) 893-5614, Fax: (805) 893-3262, zhang@opto.ucsb.edu

Abstract

Traveling-wave electroabsorption modulators (TEAM) fabricated with InGaAsP/InGaAsP quantum-wells show a modulation bandwidth of 18 GHz, and driving voltages of 1.20 and 1.28 V for 20 dB extinction ratio for TE and TM modes respectively at 1.55 μm.

Introduction

Electroabsorption (EA) modulators are very attractive devices for optical fiber communications because of their very low driving voltage, very high modulation efficiency and integratibility with lasers [1]. However conventional EA modulators are lumped-electrode devices, whose speed is limited by the total parasitics of the device, which restricts the device to very short length for high speed operation [1-3]. One way to overcome the parasitic limitation is by integrating passive waveguides with short absorption section [2]. However, this kind of device with short active region has low extinction ratio and requires relatively high driving voltage. On the other hand, a traveling wave electrode structure can overcome the RC limitation and allows longer device for the same speed. This can lower the driving voltage, increase the extinction ratio and increase the optical saturation power [4-5]. Here we demonstrate 1.55 μm traveling-wave EA modulators with 18 GHz bandwidth, 1.2 V driving voltage for MQW InGaAsP/InP EA modulators.

Design and Fabrication

The material structure consists of 10 strain-compensated InGaAsP quantum well (10.4 nm, 0.37% tensile strain) and InGaAsP barrier (7.6 nm, 0.5% compressive strain) sandwiched by 1.8 μm p-InP and 0.3 μm n-InP cladding layers. The material is grown by MOCVD. Prior to the other layers, a 0.5 μm n^+-InP layer was grown on the semi-insulating InP substrate for the n-contact. The material has a photoluminescence peak at 1495 nm at room temperature.

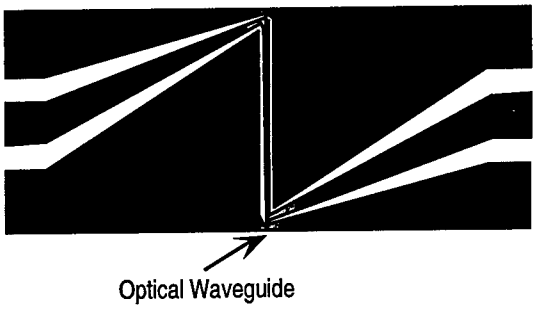

Fig. 1(a): Schematic diagram of the traveling wave electro-absorption modulator.

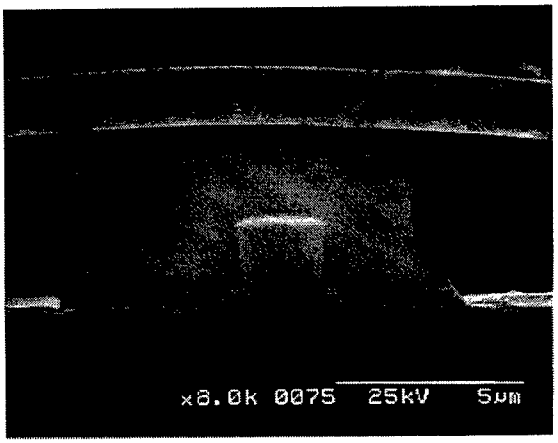

Fig. 1(b): Facet view of the device. A PMGI bridge is used to connect grounds from different sides of the waveguide.

0-7803-4936-9/98/$10.00

A coplanar waveguide (CPW) electrode structure is designed for both the microwave feed line region and the optical waveguide region [6]. Figure 1(a) shows the schematic diagram of the device. The ridge is formed by $CH_3/H_2/Ar$ reactive ion etch (RIE) followed by a $HCl:H_3PO_4$ wet etch to reduce the RIE damage. PMGI is used to passivate the side-wall and to reduce the capacitance due to the p-electrode on the optical waveguide. As shown in Figure 1(b), PMGI bridges are formed at both ends of the optical waveguide to connect grounds from different sides of the optical waveguide.

Measurement Results

A lens pair is used to couple light from fiber to the waveguide and vice versa. Figure 2 shows the fiber-to-fiber transmission versus reverse bias voltage for several wavelengths and for TE and TM polarization states. Because of proper bandgap engineering the device shows little dependence on the polarization. The 2 μm wide, 300 μm long device has driving voltages of 1.20 and 1.28 V for 20 dB extinction ratio for TE and TM modes respectively at wavelength of 1.55 μm. A fiber to fiber insertion loss of 13.6 dB is achieved at 1.57 μm for TM polarization in a device without antireflection coating.

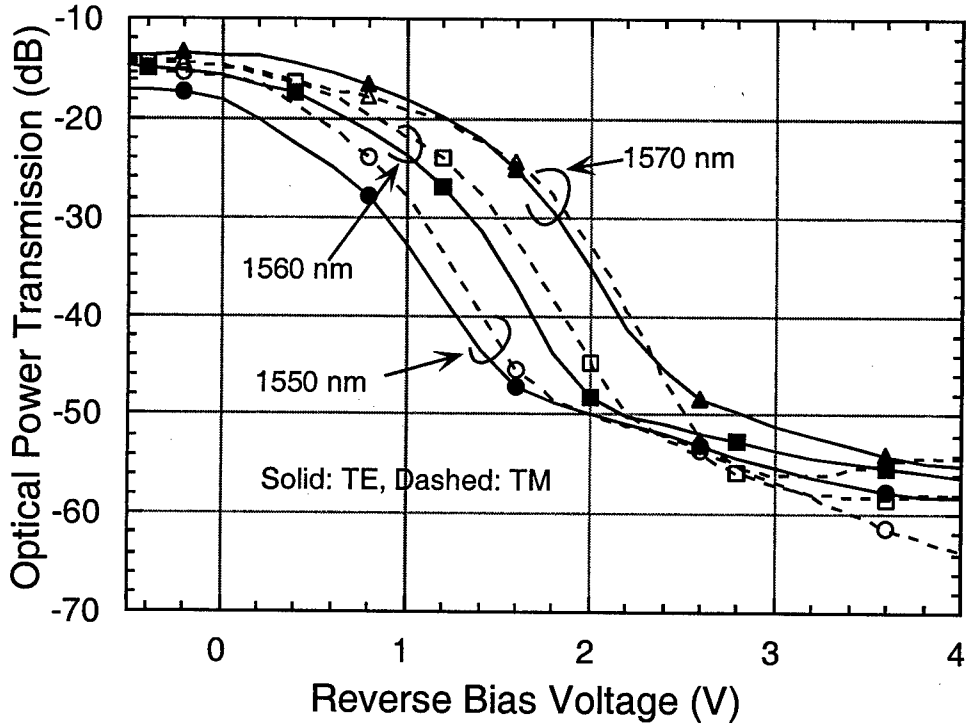

Fig. 2 Fiber-to-fiber transmission vs. reverse bias voltage for several wavelengths and for TE and TM polarization states. Solid: TE polarization, Dashed: TM polarization

High speed measurements are performed with an HP Lightwave Component Network Analyzer that measures up to 20 GHz. Two Cascade probes are used for microwave connection and one of the probes is terminated with a 50 Ω load. Figure 3 shows the measured response (in dBe) versus modulation frequency. With a 50 Ω termination, a 3 dBe bandwidth of 18 GHz is obtained, yielding a bandwidth to driving voltage (0.8 V for 10 dB extinction) ratio of 22.5 GHz/V. The bandwidth reduces to 10 GHz without 50 Ω termination. The reason for this large bandwidth reduction is the large reflection from the un-terminated port. The capacitance and the series resistance of the device deduced from the electrical S_{11} measurement are about 0.40 pF and 4.6 Ω, which infers RC limited bandwidths of 7 and 13 GHz for cases with and

without a 50 Ω termination. The larger bandwidth for the TEAM than that for the lumped device confirms that traveling-wave electrode structure can overcome the RC limitation.

Figure 4 shows the microwave S_{21} response (with triangles) measured with a network analyzer up to 40 GHz. The 3 dB drop occurs at 20 GHz, agrees well with the measured E-O response bandwidth of 18 GHz. This suggests that the device is operating with a traveling wave mode and the speed of the device is mainly limited by the microwave loss, which consists of propagation loss in the waveguide and impedance-mismatch induced reflection loss at the input and the output ports. The curve with circles in Fig. 4 shows the calculated response with CPW model while the curve with rectangles shows the calculated response with the RC model and with the R and C values deduced from the S_{11} measurement (here a 50 Ω load is included in the calculation).

To separate the microwave propagation loss from the impedance-mismatch induced reflection loss, microwave S_{21} for devices with lengths of 300, 400, 500 and 600 μm are measured. It is found that at 20 GHz, the 600 μm-devices have about 2.0 dB extra loss than 300 μm-devices. This suggests that for the 300 μm device, the propagation loss is about 2.0 dB, while the reflection loss is about 1.0 dB. Consequently, to improve the device bandwidth we need to reduce the propagation loss and increase the waveguide characteristic impedance so as to reduce the reflection loss.

Acknowledgements

The authors would like to thank DARPA for supporting this work under the Ultra Photonics Terabit TDM project.

References

[1] F. Devaux and A. Carenco, "Optical processing with electroabsorption modulators", *OFC'98 Technical Digest*, paper ThH3, p. 285, 1998.

[2] T. Ido, S. Tanaka, M. Suzuki, M. Koizumi, H. Sano, and H. Inoue, "Ultra-high-speed multiple-quantum-well electro-absorption optical modulators with integrated waveguides", *J. of Lightwave Tech.*, **14**, 2026, 1996.

[3] K. Wakita, K. Yoshino, I. Kotaka, S. Kondo, and Y. Noguchi, "High-speed, high efficiency modulator with polarisation insensitive and very low chirp", *Electron. Lett.*, **31**, 2041, 1995.

[4] K. Kawano, M. Kohtoku, M. Ueki, T. Ito, S. Kondoh, Y. Noguchi, and Y. Hasumi, "Polarisation-insensitive travelling-wave electrode electroabsorption (TW-EA) modulator with bandwidth over 50 GHz and driving voltage less than 2 V", *Electron. Lett.*, **33**, 1580, 1998.

[5] H. Liao, X. Mei, K. Loi, C. Tu, "Microwave structures for traveling-wave MQW electro-absorption modulators for wide band 1.3 μm photonic links". *Proceedings of the SPIE*, **3006**, 291, 1997.

[6] K. Giboney, M. Rodwell, and J. Bowers, "Traveling-wave photodetector theory", *IEEE Trans. Microwave Theory and Techniques*, **45**, 1310, 1997.

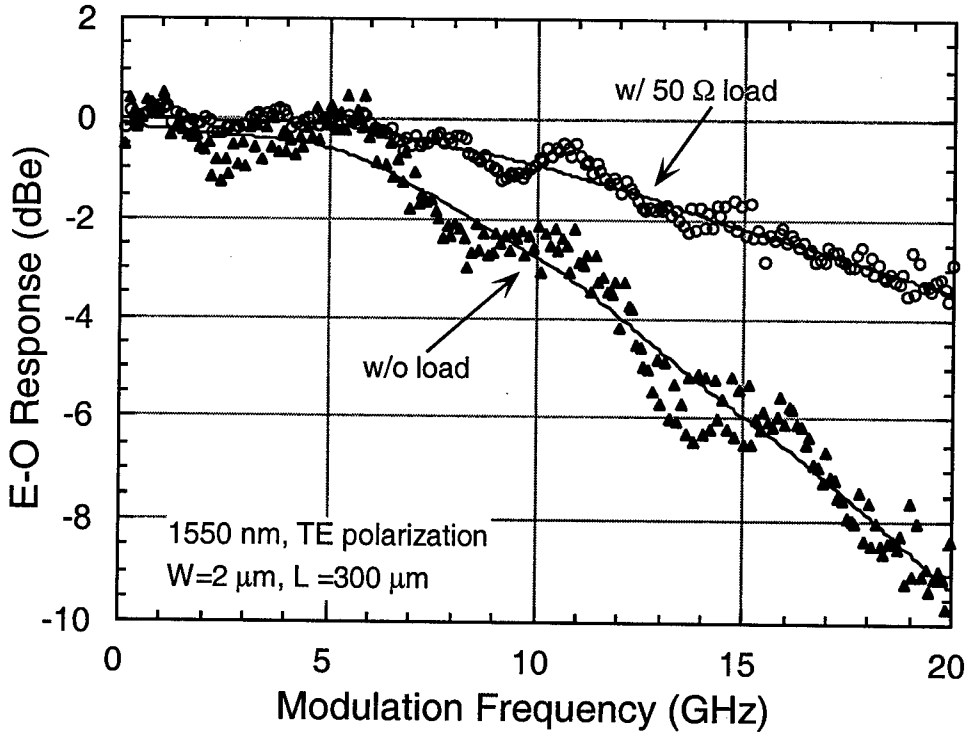

Fig. 3: Measured electrical-optical frequency response (in dBe) for different load terminations.

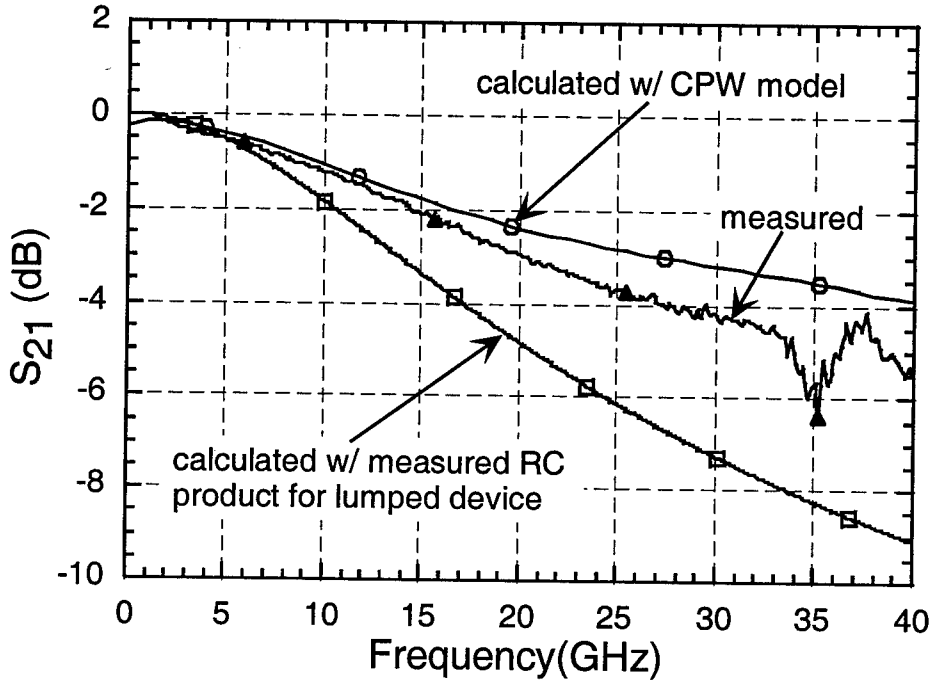

Fig. 4: Microwave S_{21} response of a traveling-wave EA modulator. Triangle: measurement, circle: calculated w/ CPW model, rectangle: calculated from measured RC product for lumped device.

ERROR-FREE FULL-DUPLEX OPTICAL WDM-FDM TRANSMISSION USING AN EA-TRANSCEIVER

Andreas Stöhr [1], Ken-ichi Kitayama [2] and Dieter Jäger [1]

[1] Gerhard-Mercator-Universität, FB9 - Optoelektronik, Kommandantenstraße 60, 47057 Duisburg, Germany
Phone: +49 203 379 - 2825, Fax: +49 203 379 - 2409, E.mail: stoehr@optorisc.uni-duisburg.de

[2] Communication Research Laboratories, 4-2-1 Nukui-kitamachi, Koganei-shi, Tokyo 184, Japan
Phone: +81 423 27 - 6209, Fax: +81 423 27 - 7035, E.mail: kitayama@crl.go.jp

I. Introduction

The penetration of optical fibers into the access arena, including an optical path to the subscriber as well as the successful implementation of fiber-wireless networks, strongly depends on the deployment of cost-effective optical transceivers. This transceiver acts as an interface between a broadband fiber optic network on the one hand and an existing copper infrastructure (fiber-copper) or a remote antenna unit (fiber-wireless) on the other hand. A cost-effective optical transceiver will most probably accelerate the introduction of broadband services into the public network. Most promising candidates in that respect are either hybrid or monolithically integrated optical transceivers performing full-duplex (simultaneous bi-directional transmission) access to an optic network.

Usually, a transceiver consists of many devices such as photodiodes (PDs), laser diodes (LDs), passive waveguides, wavelength multiplexers, etc. A very straightforward way in reducing the transceiver costs is to simply reduce the number of necessary optical components. This can be accomplished by using a single electroabsorption (EA) modulator not only for modulation but also for detection in order to provide up- and downlink data transmission simultaneously. In that case, the transceiver consists of only one optical component, an EA-modulator. Half-duplex transmission (non-simultaneous bi-directional transmission) using a vertical Fabry-Perot modulator was first reported in [1] and half-duplex transmission using a waveguide modulator was demonstrated recently [2]. In [3], full-duplex transmission using a waveguide EA-modulator was achieved in a frequency-division-multiplexed (FDM) analogue fiber-wireless system.

In this paper we propose the utilization of a waveguide EA-modulator as a full-duplex transceiver for WDM based optic networks. The modulation properties of a fiber-coupled 1.55 μm InGaAsP/InP waveguide EA-modulator such as extinction ratio, insertion loss and electrical bandwidth are experimentally determined and detection properties are analyzed in terms of responsivity and electrical bandwidth. Furthermore, the EA-transceiver is employed within an optical link and error-free full-duplex transmission is achieved.

II. EA-Transceiver

The device investigated in this paper is a high-speed waveguide EA-modulator with a MQW InGaAsP core layer, designed for 10 Gb/s operation at 1.55 μm wavelength. Extinction ratio and fiber-to-fiber insertion loss at 1.55μm wavelength are 12 dB and 7 dB, respectively. The responsivity of the fiber-coupled device is in excess of 0.4 A/W within the wavelength region of 1.52-1.54 μm. The

This work has been performed at CRL while A. Stöhr was a COE research fellow of CRL.

0-7803-4936-9/98/$10.00 © 1998 IEEE

frequency response of the EA-transceiver was measured separately for modulation and detection performance. As can be seen in Fig. 1, the 3 dB cut-off frequencies for modulation and detection are both in excess of 17GHz.

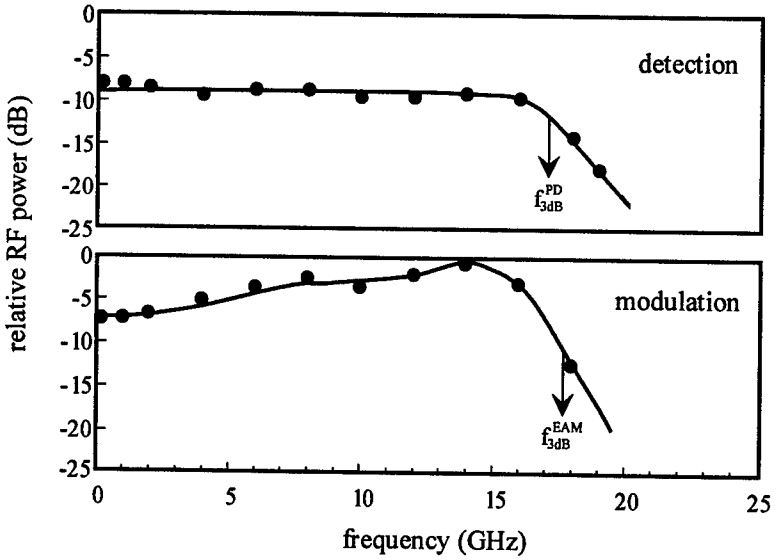

Fig. 1: Measured relative frequency responses at 0 V applied bias. Optical wavelengths in modulation and detection mode were 1560 nm and 1525 nm, respectively.

III. Transmission Experiment

The experimental set-up for verification of bi-directional full-duplex optical data transmission is shown in Fig. 2. Two LDs with wavelengths λ_1 and λ_2 are used for the downlink and the uplink data transmission, respectively. Both laser diodes are located within the central station, thus removing the need for a laser diode at the remote transceiver unit. The major advantage of using WDM is that responsivity of the EA-transceiver on the one hand and modulation index and optical losses on the other hand can be optimized separately. This leads to a distinct reduction of the up- and downlink RF insertion loss. For demonstration, we measured the RF insertion loss using carrier frequencies of

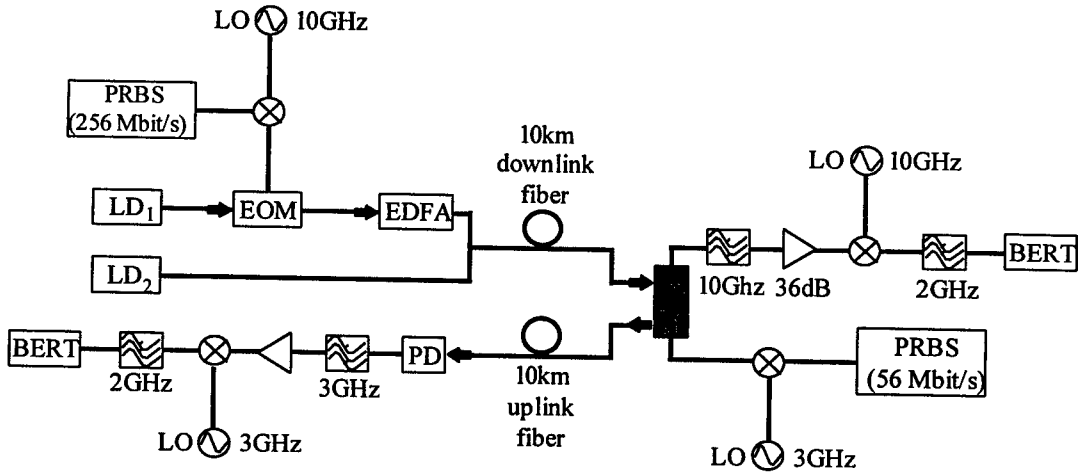

Fig. 2: Experimental set-up

3 GHz and 10 GHz for the up- and downlink, respectively, as well as 10 km of standard non-dispersion shifted single mode fiber. As the transceiver element we used the EA-waveguide modulator. In Fig. 3, the measured up- and downlink RF insertion losses are shown versus optical wavelength at different reverse bias applied to the EA-transceiver. Input RF power of both carriers was fixed to 0 dBm. From Fig. 3 it can be seen, that downlink RF insertion loss at any bias is smallest for a wavelength of about λ_1=1525 nm. This is because the responsivity of the EA-transceiver is highest at this wavelength (>0.4A/W @ 1525nm). The optimum wavelength for smallest uplink RF insertion loss strongly

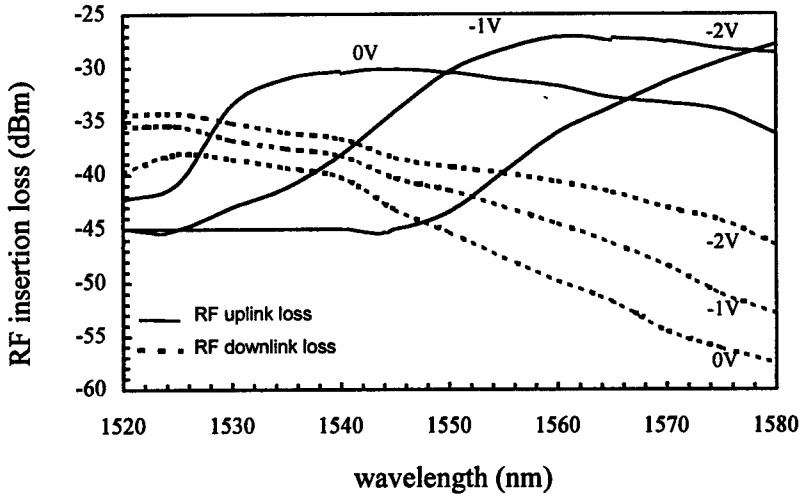

Fig. 3: Up- and downlink RF insertion loss versus wavelength.

depends on the bias applied to the EA-transceiver. Minimum uplink RF insertion loss is achieved at λ_2=1560 nm with a reverse bias of -1 V. These results clearly demonstrate the advantage of operating the EA-transceiver at different wavelengths simultaneously. By way of comparison, operating with a single LD at an intermediate wavelength of 1550 nm and a reverse bias of -1 V instead of using two LDs (1525 nm for the downlink and 1560 nm for the uplink transmission) increases the uplink RF insertion loss by 3.5 dB and the downlink RF insertion loss by 6.5 dB. A second advantage of using two wavelengths is the complete suppression of uplink-downlink mixing in the uplink.

To demonstrate full-duplex transmission we performed bit error rate (BER) measurements, using the set-up shown in Fig. 2. We used λ_1=1525 nm for the downlink and λ_2=1560 nm for the uplink transmission. Measured downlink BER of a 256 Mb/s PRBS versus received optical power at the EA-transceiver is shown in Fig. 4(a). In Fig 4(b) the BER of the uplink transmission using a 56 Mb/s PRBS is shown as a function of total RF power (carrier and data) for 3dBm and 0dBm optical power in the EA-transceiver. As can be seen, bi-directional full-duplex BER measurements better than 10^{-9} were achieved.

We would like to point out, that the maximum data rates for up- and downlink signals were limited by the microwave band-pass filters in the experimental set-up. In principle, higher data rates or a larger number of FDM channels are possible. The cut-off frequency of the EA-transceiver for both, detection and modulation is 17 GHz. The WDM-FDM approach is also of advantage when the EA-transceiver is

driven passively, i.e. without applied DC bias. However, in that case up- and downlink RF insertion losses are larger and we also found that intermodulation in the downlink is enhanced.

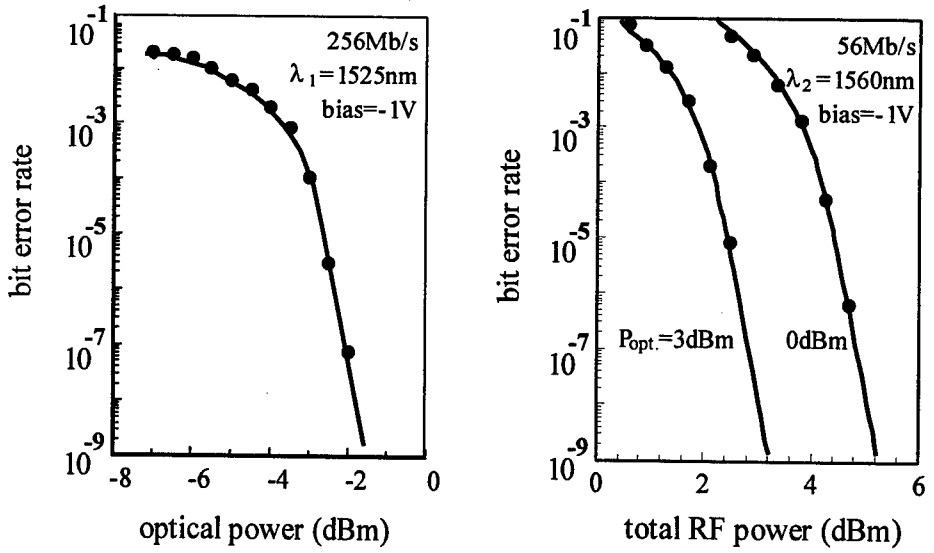

Fig. 4: Measured down- (a) and uplink (b) bit error rates (BERs).

IV. Conclusion

In summary, we determined the modulation and detection properties of a waveguide EA-transceiver experimentally. The fiber-coupled device exhibits an optical insertion loss of 7 dB. Maximum extinction ratio and responsivity are 12 dB and >0.4 A/W, respectively. The 3 dB cut-off frequency for both, modulation and detection is in excess of 17 GHz. Employing this transceiver we realized an optical WDM link over 10 km of standard single mode fiber. Up- and downlink RF insertion losses are -27 dB and -34 dB, respectively. Error-free (BER<10^{-9}) and full-duplex transmission of a 256 Mb/s downlink NRZ (2^{23}-1) data stream and a 56 Mb/s uplink NRZ (2^{23}-1) data stream was achieved.

V. Acknowledgment

The authors wish to thank T. Ushikubo of Oki Electric Industry Co., Ltd. for his useful discussions.

VI. References

[1] T.H. Wood, E.C. Carr, B.L. Kasper, R.A. Linke, C.A. Burrus, and K.L. Walker, **„Bidirectional Fibre-Optical Transmission Using a Multiple-Quantum-Well (MQW) Modulator/Detector“**, *in Electron. Lett.*, Vol. 22, No. 10, 1986, pp. 528-529

[2] R.B. Welstand, S.A. Pappert, C.K. Sun, J.T. Zhu, Y.Z. Liu, and P.K.L. Yu, **„Dual-Function Electroabsorption Waveguide Modulator/ Detector for Optoelectronic Transceiver Applications“**, *in IEEE Phot. Technol. Lett.*, Vol. 8, No. 11, 1996, pp. 1540-1542

[3] L. Noël, D. Wake, D.G. Moodie, D.D. Marcenac, L.D. Westbrook, and D. Nesset, **„Novel Techniques for High-Capacity 60GHz Fibre-Radio Transmission Systems“**, *in IEEE Trans. on Microwave Theo. and Techn.*, Vol. 45, No. 8, 1997, pp. 1416-1423

Synthesis of the Optical Modulator Response

Chanin Laliew, Sigurd Weidermann Lovseth, Xiaobo Zhang, Anand Gopinath
University of Minnesota
Department of Electrical and Computer Engineering
Minneapolis, MN 55455, USA

Abstract

Directional coupler modulator response may be synthesized by using a suitable coupling function, which may be determined by using Gel'fand-Levitan-Marchenko inverse scattering technique or by the inverse Fourier transform technique. The techniques provide possibility of designing coupler modulators with low switching voltages and better linearity. In this paper, the implementation of the coupling function for a linear modulator is outlined.

Summary

An optical directional coupler may be used to modulate light. However, in the uniform coupler, where the coupling is constant throughout the length of the device, the response is given by

$$\eta = \frac{1}{1+\left(\delta/\kappa\right)^2}\sin^2\left(\kappa z\sqrt{1+\left(\delta/\kappa\right)^2}\right)$$

where the response η is proportional to the optical power of the output signal, and $\delta = \Delta\beta/2$, with $\Delta\beta$ the difference in the propagation constants of the two coupled optical modes which is proportional to the applied voltage, z is the length of the device, and κ is the coupling constant. Thus, it is seen that the response of the uniform directional coupler modulator is highly nonlinear. However, it is possible to construct a directional coupler modulator with a response that differs dramatically from that of a uniform one, by varying the coupling function by means of a synthesis technique to obtain a given response function. The synthesis techniques that we use are the so-called Gel'fand-Levitan-Marcheko (GLM) inverse scattering technique and the inverse Fourier transform technique. The GLM technique yields exact results but it requires that the response function be rational and all the poles of this function must lie in the left half of the complex plane and be distinct. The inverse Fourier transform technique, on the other hand, gives approximate results, but any class of response functions can be used. The reader should refer to references [1] and [2] for more detailed explanation of these two techniques. As an example, the synthesized coupling function for the 3rd-order Chebyshev response function obtained by using the GLM technique and that for the ideal linear response function obtained by using the Fourier transform technique are shown in Fig.1(a) and in Fig.1(b), respectively.

0-7803-4936-9/98/$10.00

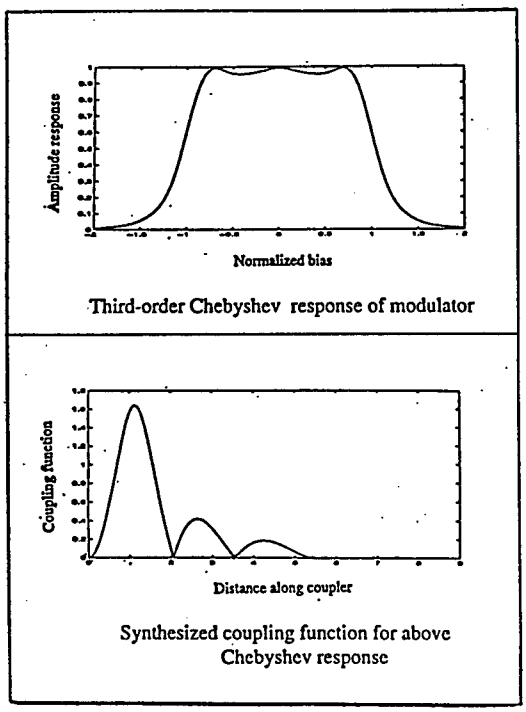

Fig. 1 (a)

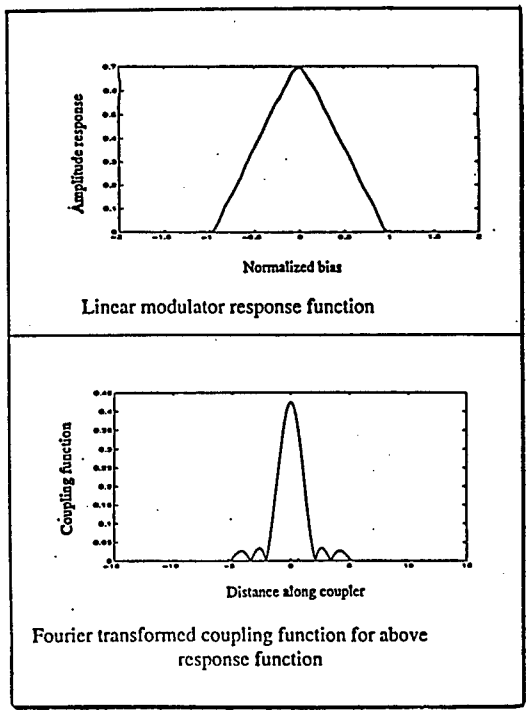

Fig. 1 (b)

Fig. 1 : Synthesized coupling functions of
(a) the 3rd-order Chebyshev response function and
(b) the linear response function

With the synthesized desired coupling functions as a starting point we then calculate the corresponding "shape" of the directional coupler modulators. We use $Al_{0.3}Ga_{0.7}As/GaAs$ structure for our modulators, which are designed to be operating at 1.3 μm wavelength. A schematic of such a modulator is shown in Fig. 2 below.

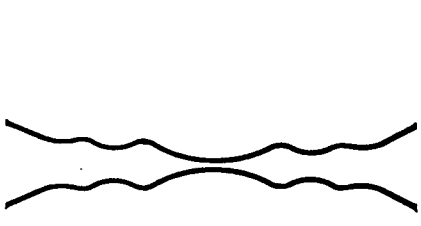

(a)

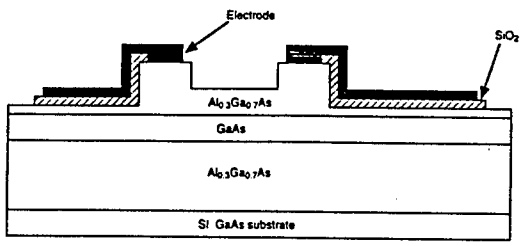

(b)

Fig. 2 : Schematic of the modulator : (a) top view and (b) cross section

In our project, we have built modulators with different kinds of response functions and with different lengths. An example of the measured response of an ideal "linear" modulator is given in Fig.3. While this is a dc result, we are in the process of making rf measurements, and we hope to present these at the meeting.

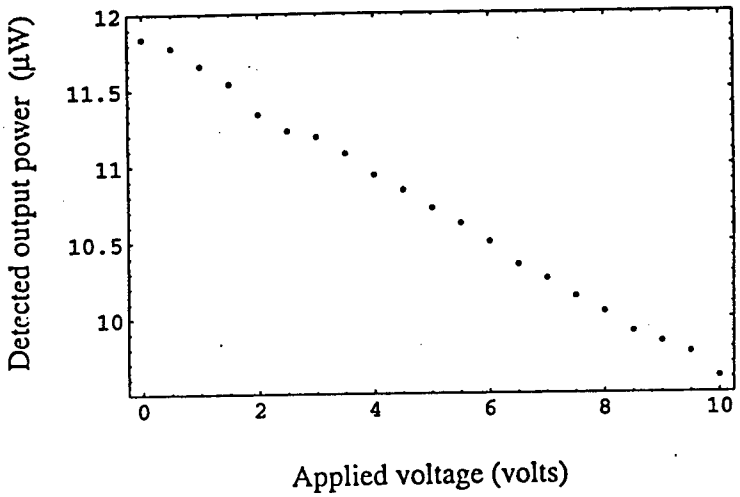

Fig.3 : Measured amplitude response of a linear modulator

The current design yields too high switching voltages for the modulators and now we are in the process of redesigning the modulators so that they will have a better performance.

In summary, our synthesis techniques have rendered optical directional coupler modulators that have a better linearity than the standard ones.

Acknowledgements

This project has been supported by DARPA.

References

[1] Sigurd Weidermann Lovseth, Chanin Laliew, Anand Gopinath : *Synthesis of Amplitude Response of Optical directional Coupler Modulators*, 1997 IEEE-MTT-S International Microwave Symposium Digest, Volume III, pp.1717-1720, June 1997

[2] Sigurd Weidermann Lovseth, Chanin Laliew, Anand Gopinath : *Amplitude Response of Optical Directional Coupler Modulators by Fourier Transform Technique*, 8th European Conference on Integrated Optics Proceedings, pp.230-233, April 1997

Linearization of a Broadband Analog Optical Link Using Multiple Wavelengths

Edward I. Ackerman

MIT Lincoln Laboratory

Abstract

Instead of balancing the RF signal voltage on two modulator electrodes, broadband linearization of a link can be more easily achieved when two wavelengths are simultaneously modulated using a standard single-electrode Mach-Zehnder modulator.

Introduction

It is possible to operate either a Mach-Zehnder or a directional-coupler modulator around a DC bias voltage at which the second derivative of the transfer function is zero; doing so eliminates distortion at the second-harmonic and second-order intermodulation frequencies, causing third-order distortion products to dominate and thus limit the dynamic range [1], [2]. Third-order distortion limits the broadband dynamic range achievable using commercially available $LiNbO_3$ modulators to roughly 110 $dB \cdot Hz^{2/3}$. To improve upon this, recent efforts have focused on the development of broadband "linearized" modulators, in which third-order distortion is minimized at the same DC bias voltage where no even-order distortion occurs. Figure 1 shows three previously proposed broadband linearized modulators (after [3]–[5]).

For frequencies above 2 GHz or so, where the modulator electrodes must be configured as transmission lines whose effective refractive index at RF frequencies closely matches the optical refractive index [6], there are inherent challenges associated with implementing any of the architectures shown in Fig. 1. Two of these approaches [Fig. 1(a) and(b)] require that the RF signal be split and applied in precise proportion to two different RF electrodes. To achieve broadband linearization at frequencies of 2 GHz or higher, therefore, the RF characteristics of the modulator's two traveling-wave electrodes (including RF attenuation per unit length, characteristic impedance, and guided wave velocity as determined by the effective RF refractive index) must match each another over the entire band of interest. This RF signal balancing gets progressively more difficult to accomplish with increasing signal frequency and/or percentage bandwidth.

To my knowledge the only broadband (greater than an octave bandwidth) linearized electro-optic modulator proposed thus far that does not require application of the RF signal to more than one electrode is the modified directional coupler design shown in Fig. 1(c). This configuration is the same as a straightforward directional coupler modulator [2], except for the incorporation of two additional DC-biased electrodes that impose controlled mismatches in the propagation constants between the optical waveguides in the coupling region [5]. In the 500-1000 MHz band a dynamic range of 111 $dB \cdot Hz^{4/5}$ has been demonstrated using this type of modulator [7]. Recently, an analytical model [8] has shown that modulator could achieve a dynamic range of 129 $dB \cdot Hz^{4/5}$ across a broad band and at high frequencies, but only if the mismatch between the RF and optical refractive indexes is counteracted by "re-phasing," which is essentially splitting of the RF among multiple shorter electrode segments—leading back to the electrode characteristic-matching issue.

Technical Approach

Figure 2 shows a new broadband linearization approach that uses a straightforward commercially available Mach-Zehnder electro-optic modulator with a single traveling-wave RF electrode and a single DC bias electrode. The Mach-Zehnder modulates two wavelengths of light simultaneously, and at the other end of the link a wavelength-division multiplexer (WDM) routes the two modulated wavelengths to separate detectors whose outputs are combined in an RF hybrid coupler. At the correct modulator bias voltage and the correct ratio of photodetector currents, both second- and third-order distortion are cancelled.

The curves in Fig. 3(a) show how the photocurrents at the individual detectors vary with modulator bias voltage (dashed lines), and how the current at the Δ output of the RF hybrid coupler varies with modulator bias (solid line). Figures 3(b) and (c) show second and third derivatives of these curves, respectively.

0-7803-4936-9/98/$10.00

These plots reflect the case where the ratio of photocurrents is maintained such that, at the modulator bias where both detector outputs have zero even-order distortion, the detectors deliver equal levels of third-order distortion to the hybrid coupler. Therefore, at this modulator bias and photocurrent ratio, the strongest distortion products at the hybrid coupler's Δ port are fifth-order.

This new linearization architecture is analogous to the dual-parallel Mach-Zehnder modulator configuration shown in Fig. 1(b), in which the RF signal is split in a specific proportion between two Mach-Zehnders that are fed a single optical carrier that has also been split in a specific proportion. In the new configuration only one Mach-Zehnder modulator is required because it has a different halfwave voltage (V_π) at the two wavelengths, so that an RF signal of magnitude v_M applied to the one electrode results in a different modulation depth v_M/V_π at the two wavelengths. Conceptually this dual-wavelength approach more closely approximates one described by Johnson and Roussell, who cancelled third-order (but not second-order) distortion by balancing two different *polarizations* of light that have different halfwave voltages in a lithium niobate Mach-Zehnder modulator [9].

An important advantage imparted by the new multiple-*wavelength* linearization approach is that inexpensive, commercially available fiber wavelength-division multiplexers can be used to route the two modulated wavelengths of light to separate photodetectors whose outputs are combined electrically (as in Fig. 2). Wavelength multiplexing to separate detectors enables precise maintenance of the desired ratio of RF signal powers to achieve distortion cancellation, even in the presence of unpredictable environmental factors such as stresses on the fiber that might induce variability in the relative losses at the two wavelengths [10].

Experimental Results

Using only commercial components I assembled a link in a configuration similar to the one shown in Fig. 2. For the optical sources I used an ATx Nd:YAG laser with 200 mW output power at 1320 nm and an Ortel InGaAsP DFB laser with 30 mW output power at 1550 nm. Both lasers had polarization-maintaining fiber pigtails. A WDM manufactured by PIRI coupled the inputs at the two different wavelengths into one polarization-maintaining fiber so that both optical carriers could be fed into the modulator. The modulator I used was a $LiNbO_3$ Mach-Zehnder device with one traveling-wave RF electrode and one DC bias electrode. At 1320 nm the manufacuterer (UTP) specified V_π of 4.7 V at DC and a 3 dB bandwidth of 3 GHz. A second WDM demultiplexed the modulated optical carriers, each of which I routed to a separate BT&D InGaAs photodiode detector. I was careful to match as closely as possible the lengths of the two fiber paths from the WDM to the detectors. I also followed both detectors with RF line stretchers and adjusted these to equalize the group delay measured (using a network analyzer) from the modulator input to either input of the RF hybrid coupler.

Before attaching the hybrid coupler (manufactured by Anzac, and specified for 2-2000 MHz operation) I connected the detector outputs to separate RF spectrum analyzers, and the modulator input to an RF signal generator set to 750 MHz. I varied the modulator's DC bias voltage and observed minima at the second-harmonic frequency (1.5 GHz) about every 4.7 V for the 1320 nm detector, and about every 6.8 V for the 1550 nm detector. At a modulator bias voltage of about –5.0 V it happened that the 1.5 GHz output from either detector was very near one of its minima.

With the modulator bias fixed at this second-order minimum, the next step was to set the ratio of RF powers at the hybrid coupler input ports. Figure 2 suggests one method involving amplifiers [10] for maintaining the two coupler inputs at the proper ratio for distortion cancellation. To achieve the proper ratio in the initial experiment I used a precision variable optical attenuator between the YAG laser and the 1320 nm input of the WDM. Feeding a two-tone RF input to the modulator, I varied the 1320 nm carrier attenuation until I observed a minimum in the measured output power from the Δ port of the hybrid coupler at the third-order intermodulation frequency.

Varying the link input power at the two RF tones (f_1, f_2), I measured the link output power at these tones, their sum frequency (f_1+f_2), and the third-order intermodulation frequencies ($2f_1-f_2$, $2f_2-f_1$). Fig. 4(a) shows the measured results for 499 and 501 MHz input tones, along with the measured noise output in a 1 MHz instantaneous bandwidth. Figure 4(b) shows results of the same measurement for input tones at 999 and 1001 MHz. In these plots hollow squares and circles represent measured data at the fundamental and third-order intermod frequencies for the link with only the 1550 nm laser on (this yields better performance than

the link with only the 1320 nm laser). When power at the second wavelength is present in proper proportion to the first wavelength, third-order distortion is suppressed, as shown by the solid triangles in the plots.

The plots show four of additional features worth mentioning: first, and most significantly, the spurious-free dynamic range is greater for the two-wavelength link, in accordance with its design; second, the two-wavelength link suppresses second-order distortion (represented on the plots by solid circles) incompletely, but to a degree sufficient to ensure that the dynamic range is third-order distortion limited; third, there is some noise figure penalty associated with the linearization, which has been true for every broadband linearized link that uses Mach-Zehnder modulators [11]; fourth, the same control settings (modulator bias and photocurrent ratio) yield linearization across an octave of bandwidth—i.e., at 500 MHz and 1 GHz, as shown in Fig. 4 (a) and (b), respectively. Amplification of the 1550 nm carrier, and a corresponding decrease in attenuation of the 1320 nm carrier, would enhance the link's dynamic range more profoundly.

Summary and Acknowledgments

Proposals for linearization of a fiber-optic link across more than an octave bandwidth have required precise balancing of the signal voltage levels on multiple electrodes in a custom modulator, which represents a significant implementation challenge. I have described a new link linearization method that uses a standard Mach-Zehnder $LiNbO_3$ modulator with only one RF and one DC bias electrode to linearize across greater than an octave bandwidth. Instead of balancing the voltages on two RF electrodes, this new technique uses the standard traveling-wave electrode to modulate two optical carriers, and it is the ratio of these optical carrier powers that is adjusted for distortion cancelling.

The author thanks Charles Cox and Pamela Haddad for helpful discussions, and Scott Henion, Harold Roussell, Mike Taylor, and John Vivilecchia for technical assistance. This work was sponsored by the Department of the Air Force under Contract F19628-95-C-0002. The views expressed in this paper are those of the author and do not reflect the official policy or position of the U.S. Government.

References

[1] I. Kaminow, "Optical waveguide modulators," *IEEE Trans. Microwave Theory Tech.*, vol. MTT-23, pp. 57-69.

[2] S. Kurazono, K. Iwasaki, and N. Kumagai, "A new optical modulator consisting of coupled optical waveguides," *Electron. Comm. Jap.*, vol. 55, pp. 103-109.

[3] H. Skeie and R. Johnson, "Linearization of electro-optic modulators by a cascade coupling of phase modulating electrodes," *Proc. SPIE*, vol. 1583, pp. 153-164.

[4] S. Korotky and R. DeRidder, "Dual parallel modulation schemes for low-distortion analog optical transmission," *IEEE J. Select. Areas in Commun.*, vol. 8, pp. 1377-1381.

[5] M. Farwell, Z. Lin, E. Wooten, and W. Chang, "An electrooptic intensity modulator with improved linearity," *IEEE Photon. Technol. Lett.*, vol. 3, pp. 792-795.

[6] R. Alferness, "Waveguide electrooptic modulators," *IEEE Trans. Microwave Theory Tech.*, vol. 30, p. 1121.

[7] J. Schaffner, J. Lam, C. Gaeta, G. Tangonan, R. Joyce, M. Farwell, and W. Chang, "Spur-free dynamic range measurements of a fiber optic link with traveling wave linearized directional coupler modulators," *IEEE Photon. Technol. Lett.*, vol. 6, pp. 273-275.

[8] U. Cummings and W. Bridges (California Institute of Technology, Pasadena), "Bandwidth of linearized electro-optic modulators," *J. Lightwave Technol.*, July 1998 (in press).

[9] L. Johnson and H. Roussell, "Reduction of intermodulation distortion in interferometric optical modulators," *Opt. Lett.*, **13**, p. 928, 1988.

[10] C. Cox and A. Yee, "RF gain stabilization of a directly modulated optical link using detector current normalization," *IEEE Microwave Theory Tech. Symp. Dig.*, p. 1117, 1994.

[11] W. Bridges and J. Schaffner, "Distortion in linearized electro-optic modulators," *J. Lightwave Technol.*, vol. 43, pp. 2184-2197.

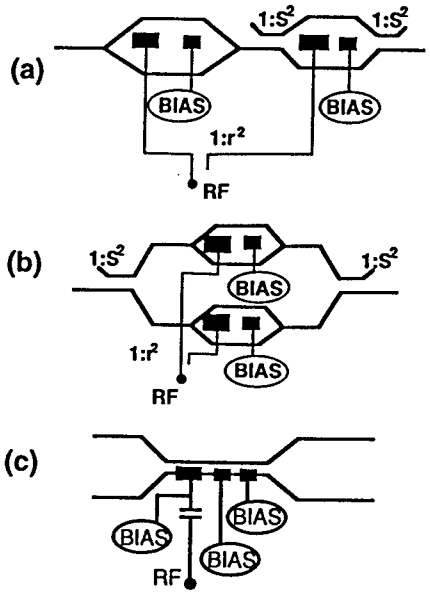

Fig. 1 Broadband linearized electro-optic modulator configurations: (a) series Mach-Zehnders [3]; (b) parallel Mach-Zehnders [4]; (c) modified directional coupler [5].

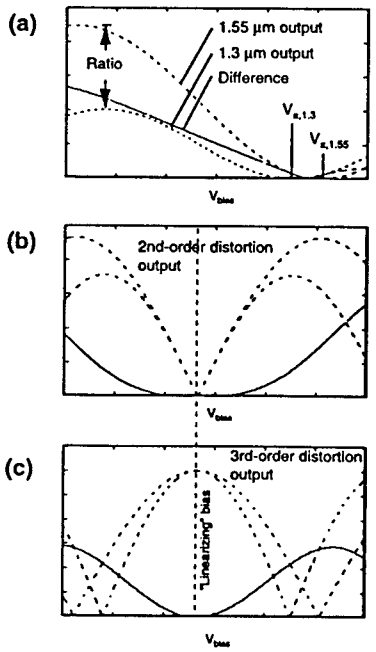

Fig. 3 (a) Photocurrent at the two individual detectors (dashed lines), and the current at the output of the RF hybrid coupler (solid line), as a function of the modulator bias;

(b) Second derivative of the photocurrent at the individual detectors (dashed lines), and at the output of the RF coupler (solid line), as a function of the modulator bias;

(c) Third derivative of the photocurrent at the individual detectors (dashed lines), and at the output of the RF coupler (solid line), as a function of the modulator bias.

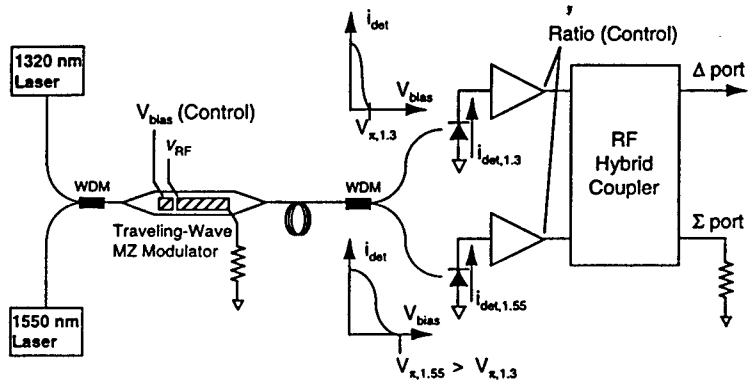

Fig. 2 New linearization architecture. Second- and third-order distortion are simultaneously minimized by precise control of the modulator bias and the ratio of signal powers carried by the two optical wavelengths.

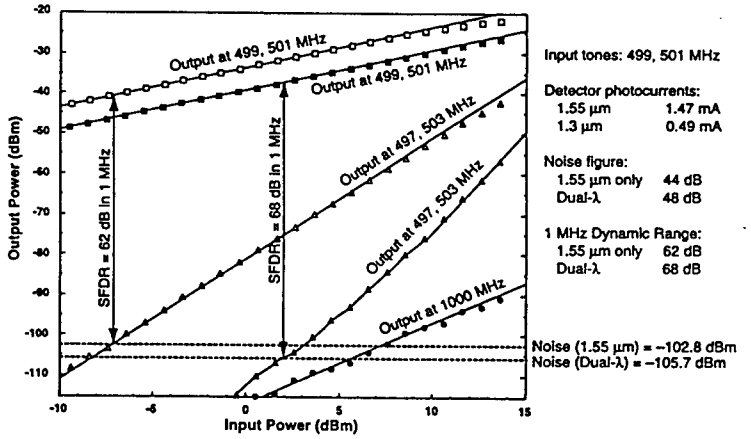

Fig. 4 (a) Link output noise (dashed line) and RF power measured at the fundamental (squares), second-order intermod (circles), and third-order intermod (triangles) frequencies as the RF input power at the fundamental frequencies (499 and 501 MHz) is varied. Hollow symbols represent the situation where only one of the wavelengths (1550 nm) is present; solid symbols represent two-wavelength operation at the proper ratio of detector photocurrents.

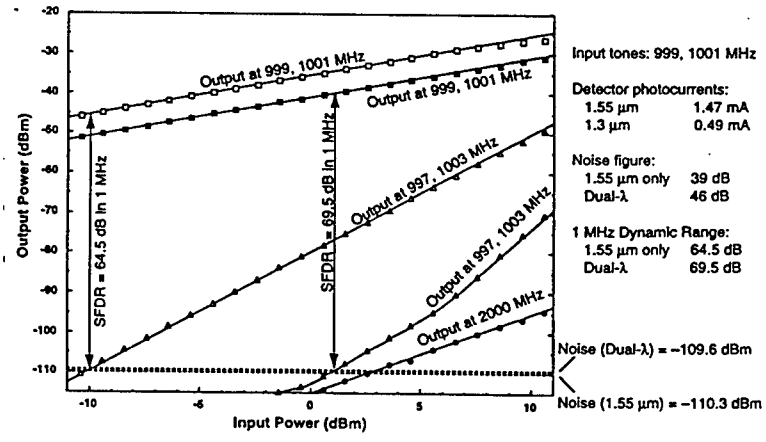

Fig. 4 (b) Same as (a), but with fundamental frequencies of 999 and 1001 MHz. Modulator bias and photocurrent ratio settings are unchanged from the 499 and 501 MHz measurement..

Broadband Linearization of Externally Modulated Fiber-Optic Links

Yun Chiu and Bahram Jalali
Electrical Engineering Department, UCLA, Los Angeles, CA 90095-1594
S. Garner and W. Steier
*Electrical Engineering Department, University of Southern California, Los Angeles, CA, 90089

Transmission of analog amplitude modulated (AM) signals puts stringent demand on the link linearity. Transmitter nonlinearities cause the modulated subcarriers to mix and generate intermodulation products, which usually fall into other channels. It is well known that externally modulated laser transmitters demonstrate higher dynamic range than direct modulated distributed feedback (DFB) laser transmitters. A prominent advantage of the external modulator is that it offers the quadrature biasing point where even-order distortions are nulled out.

To deal with the remaining odd-order terms of distortion, electronic linearization techniques have been conceived [1]. Fig. 1 shows the block diagram of a typical externally modulated fiber optic transmitter with parametric linearity feedback control. The linearizer has an *arcsine* transfer function that is the inverse of the raised cosine transfer function of the modulator. The purpose of the local feedback loop is to stabilize the transmitter against long term drifts.

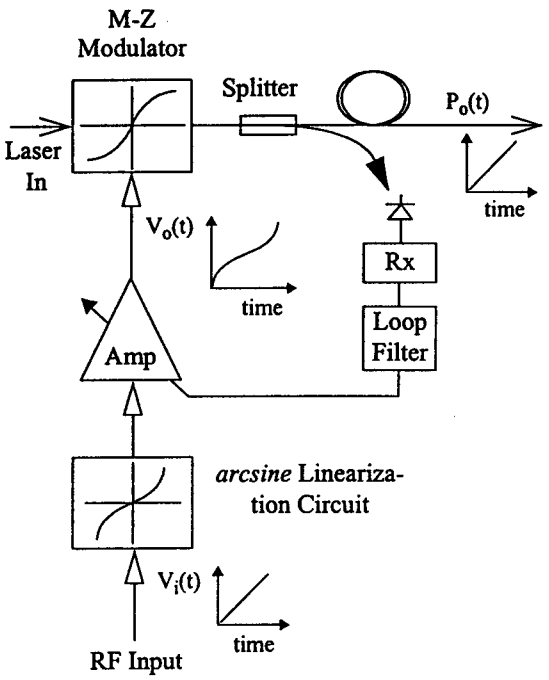

Fig. 1. Typical linearized externally modulated fiber optic transmitter.

The *arcsine* circuit generates odd-order harmonics that cancel those of the modulator biased at the quardrature point. Traditionally, such circuits have been realized using diodes or bipolar transistors. They take advantage of the exponential transfer characteristics of such devices to generate odd-order harmonics[1] [2]. Field Effect Transistors (FETs), such as CMOS, have not been used due to their square-law behavior.

However, as most of the baseband signal processing is realized using low-cost scaled CMOS technology, more and more analog building blocks have been forced to look for CMOS solutions. The use of bipolar circuits simply bars the system integration and results in a higher manufacturing cost. On the other hand, the continuous decrease of the driving voltage of the optical modulator has made it possible to build low cost and highly-integrated modulator driver circuits based on the CMOS technology. This underscores the need for circuit architectures that provide the requisite linearization function using FETs. The challenge is to synthesize an *arcsine* transfer function using the square-law behavior of these transistors.

In this paper, we present the design of the first CMOS linearization circuit and its performance in an experimental externally modulated fiber optic link. The circuit provides an unprecedented 17dB of IMP3 suppression at an ultrahigh 49.6% modulation depth over a broadband from DC to 1.3GHz.

The FET-based *arcsine* circuit architecture is shown in Fig. 2. By subtracting the output current of a clipping amplifier (inner pair) from that of a linear amplifier (outer pair), the circuit synthesizes an *arcsine* function. It can be shown analytically that this circuit matches coefficients of the *arcsine* up to the fifth order. To the best of our knowledge, this has never been attained in a single circuit before. To improve the linearity of the linear amplifier, a voltage-biased class-AB architecture is used. A fully balanced version of the CCDP based predistortion circuit is constructed by combining two *arcsine* core circuits with PMOS current mir-

0-7803-4936-9/98/$10.00

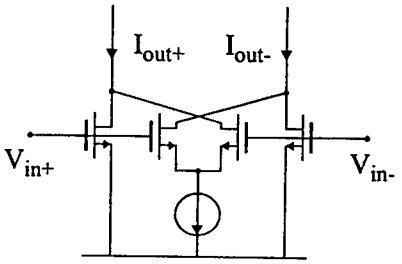

Fig. 2. The proposed circuit for generating the *arcsine* transfer function using field effect transistors.

rors.

The circuit was fabricated using MOSIS 0.6-μm CMOS process. To characterize its performance, an experimental link was set up. The link consists of a 1.3-μm Nd:YAG solid-state laser, a $LiNbO_3$ Mach-Zehnder modulator (with V_π = 2.5 V at DC and 2.5 GHz bandwidth) biased at quadrature operating point, and a PIN diode photodetector (with bandwidth 1.5 GHz).

Two tone transmission experiments were performed with and without the predistortion circuit. Fig. 3 shows the two-tone output spectrum at 1.3 GHz under an ultrahigh modulation index, β = 49.6%. The circuit provides 17 dB suppression of the IMP3. This is the best linearization performance ever obtained at such a high modulation index. We found that the performance is indepen-

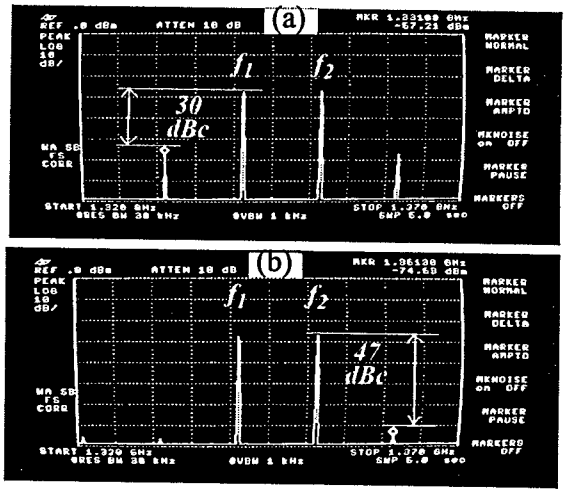

Fig. 3. Two-tone IMP3 spectrum at 1.3 GHz at the modulation index of 49.6%. (a) without linearization and (b) with linearization showing an IMP3 suppression of 17dB.

dent of modulation frequencies in the range DC - 1.3 GHz.

To determine the SFDR of the experimental link, extrapolation was performed on the measured IMP3 data [3], as shown in Fig. 4. The basic link without linearization showed an SFDR of 85 dB, which was increased to 99 dB after linearization. This indicates a 14 dB improvement of the link SFDR, the highest value reported up to date. This result was obtained in our experimental link with noise floor of -124 dBm/Hz. In a high performance link with lower noise floor, an even greater improvement will be obtained.

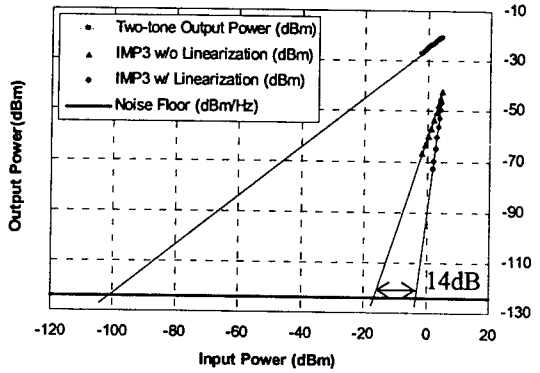

Fig. 4. Extrapolation of the measured two-tone IMP3 result at 1.05 GHz.

The first low-cost broadband CMOS linearization circuit has been built and evaluated. Measurement results show broadband performance from D.C. to above 1.3 GHz, which makes it highly attractive for the 1-GHz CATV application planned in the near future.

In general, the proposed circuit architecture works with all field effect devices including MESFET and HEMT. Implemented with these devices instead of CMOS, the same circuit can operate at much higher frequencies.

REFERENCES

[1] M. Nazarathy, J. Berger, A. J. Ley. I. M. Levi and Y. Kagan, "Progress in Externally Modulated AM CATV Transmission Systems," *Journal of Lightwave Technology*, Vol. 11, No. 1, Jan. 1993.

[2] L. Zhang, H. Hua, J. Lee and F. Harlow, "Ten-GHz MMIC Predistortion Circuit For Improved Dynamic Range of Broadband Analog Fiber-Optic Link," *Microwave and Optical Technology Letters*, Vol. 11, No. 6, Apr. 1996.

[3] J. H. Schaffner and W. B. Bridges, "Intermodulation Distortion in High Dynamic Range Microwave Fiber-Optic Links with Linearized Modulators," *Journal of Lightwave Technology*, Vol. 11, No. 1, Jan. 1993.

MICROWAVE FIBER OPTIC LINK ANTENNA REMOTING TRADE STUDY MEASUREMENTS

Irwin L. Newberg
Raytheon Systems Company
P.O. Box 92426
RE, Bldg. R07, M/S P539
Los Angeles, CA 90009
Phone: (310) 334-6834, Fax: (310) 607-5699
e-mail: inewberg@west.raytheon.com

Abstract

This paper summarizes measurements made to evaluate the use of commercial off-the-shelf microwave fiber optic links for transmitting and receiving RF signals for antenna remoting in testing of electronic warfare and radar systems.

Introduction

This paper presents the results of measurements made in a trade study of a microwave fiber optic link for potential use in remoting RF signals for testing RF systems in aircraft. The trade study results were used to determine the end-to-end RF performance parameters (gain, noise figure and dynamic range) that can currently be achieved using RF fiber optic links for antenna remoting of wide bandwidth (0.1 to 18 GHz) RF signals. The purpose of the trade study was to evaluate both transmission and reception of these signals into and out of an anechoic chamber for use in testing systems/functions of Electronic Warfare (EW); Radar; and Communication, Navigation and Identification (CNI) equipment installed in aircraft. Commercial-off-the-shelf (COTS) components were assembled into a fiber optic link that was tested for use in transmission of RF signals to radar transmitter and receiver hardware mounted on equipment carts in the chamber.

The results of the trade study showed that the current COTS fiber optic microwave links could not meet the needed RF performance for either receiving or transmitting. It was determined that the required performance could be met by moving the RF generation and receiving equipment onto the equipment carts in the chamber, and using digital fiber optic links to send signals into the chamber for use in RF signal generation and to send digitized RF signals out of the chamber for use in RF signal monitoring and evaluation.

I. Summary of Measurements

Table 1 is a summary of the measured link performance data; no RF amplifiers were included as part of the link being measured.

Table 1. Summary of RF/Photonic Link Performance Measurements

Frequency Range, GHz	0.045 to 18	Dynamic Range	
Loss, dB	40	Linear, dBc*/Hz	150
Noise Figure, dB	46	Spur Free, dBc/Hz$^{2/3}$	108
1-dB Compression Point, dBm	22	2nd Harmonic, dBc	44
Third Order Intercept Point, dBm	33		
*dBc: dB relative to the carrier			

The parameters listed in the table are a composite of those measured over the entire frequency range and are for the link. These were the key parameters needed to evaluate the link performance for transmitting signals to the chamber and receiving signals from the chamber, where signal monitoring and evaluation could be accomplished. Using these fiber optic link measured parameters, the overall loop performance with associated RF amplifiers, transmitters and receivers was calculated.

The following figures give selected data plots that were recorded during the test and used with other measured data to calculate the parameters in Table 1. Many other plots were taken to obtain the composite data in Table 1.

Figure 1 gives the link amplitude and phase response over the frequency range. Figure 2 gives the third order intermodulation products for one frequency in the frequency range of interest. Figure 3 gives the second harmonic measurement at a particular frequency in the frequency range.

0-7803-4936-9/98/$10.00

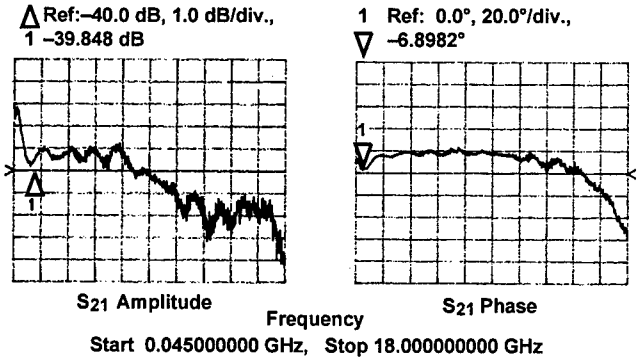

Figure 1. Link Amplitude and Phase vs. Frequency

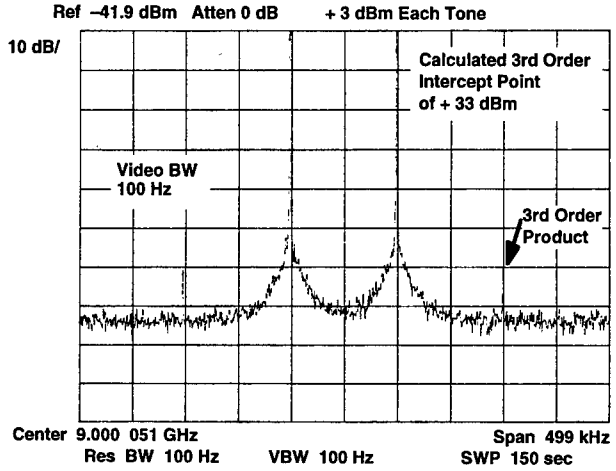

Figure 2. Link Intermodulation Test Showing Third Order Products Down 60 dB

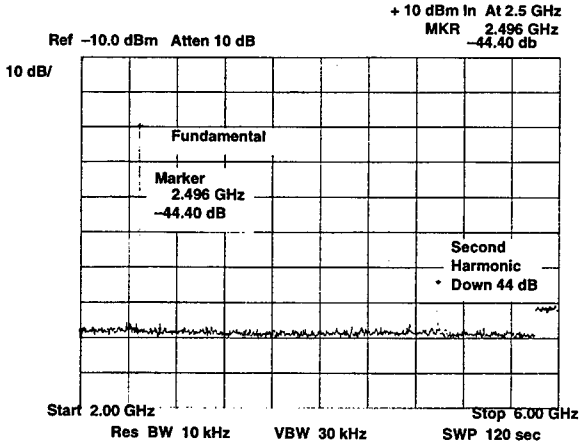

Figure 3. Link Test Showing Second Harmonic Down 45 dB

II. Description of Test Setup

Figure 4 is a block diagram of the fiber optic link. A solid state CW YAG laser shown at the upper left supplies an optical signal through an 8-way optical signal splitter to a lithium niobate Mach-Zehnder external modulator. The external modulator also receives the RF input signal that amplitude modulates the laser light. The external modulator has a DC

bias voltage supplied by the bias controller circuit. The DC bias keeps the modulator output light level centered between maximum output and no output when there is no RF modulation. The inputs to the bias circuit come from couplers at the modulator outputs. A small amount (1%) of light coupled off each of the modulator outputs is sent to low frequency photodiode detectors to read slow light level changes that are sent as a dc level to the bias controller. The modulator output then goes to two series cables representing fiber cable lengths used for antenna remoting. One cable was 500 ft and the other cable was 200 ft. These represented a typical cable run with the associated connectors.

The operating parameters for the COTS link were as follows: The external modulator had a $V\pi$ of 10 volts at 10 GHz and 4 dB optical loss. Optical power of 10 mW into the modulator was from one output of an 8-way optical power splitter. The photodiode dc current out was 1 mA.

Figure 5 shows the fiber optic link used during the testing. Some of the block diagram components of Figure 4 are called out in Figure 5.

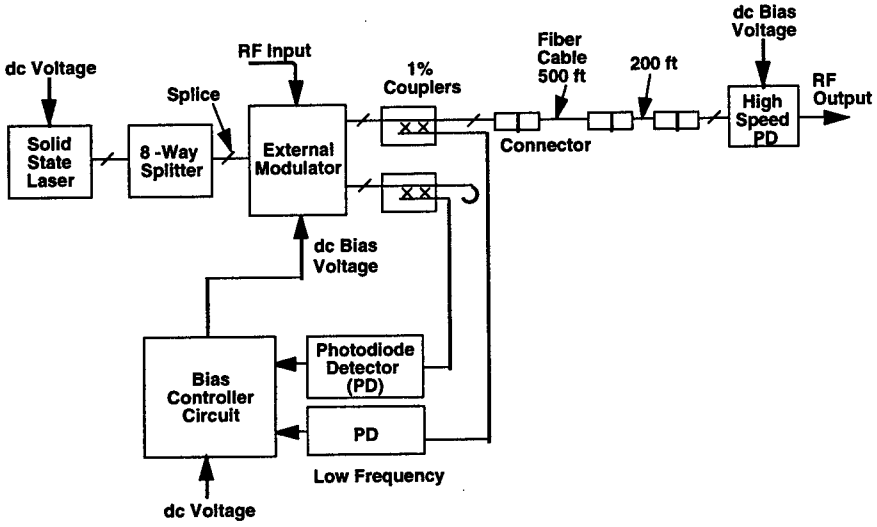

Figure 4. Fiber Optic Link Block Diagram for Test Measurements

III. Comments on the Trade Study

The data showed that some type of loop calibration signal will probably be required for precise amplitude and phase measurements. This is particularly true for phase, because the long fiber cable will change in phase with temperature. The use of two links was not tested in the study, but two links for receiving both vertical and horizontal antenna signal polarization would be used. Calibrating signals for two links may still be needed even though the relative phase between the two links will probably be small, since the fiber for both links would be collocated in fibers in the same cable.

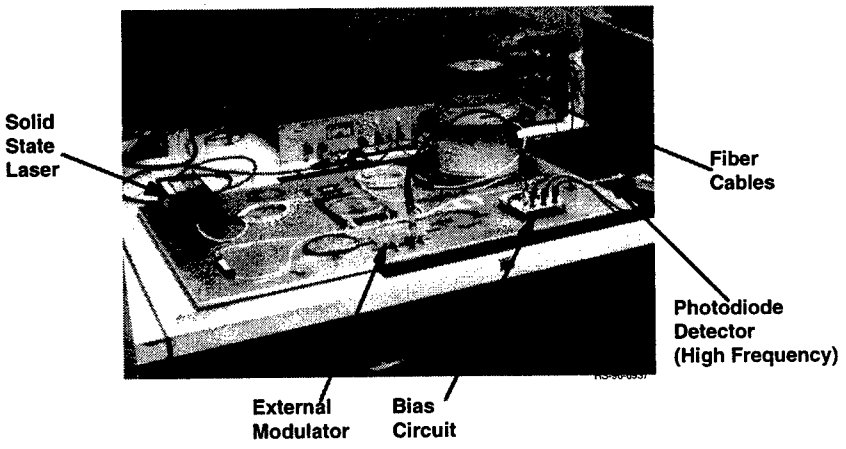

Figure 5. Photo of Optic Link Showing Components of Block Diagram

The particular solid state laser used was a YAG single optical line laser. It was determined in the testing that the laser had lines appearing in the RF spectrum at around 8.5 and 17 GHz, which were low but still visible in the RF frequency range of interest. The fact these lines did exist in a so-called single line laser was verified with the laser vendor. Because of these lines, these particular types of laser would require some type of feedback cancellation circuit to attempt to reduce the lines below the link RF noise level. Semi-conductor laser sources do exist that do not have these mode lines that show up in the RF output. These lasers have lower optical output power, and thus more lasers would be needed. External modulation was used for this link because of the wide bandwidth required.

Although the components used in the fiber optic link are spread out for convenience in these tests, the components could be packed in a compact way for mounting in the equipment. Also, not all components shown in the block diagram (Figure 4) may be needed. In particular, the 8-way splitter was used to simulate sharing the output optical power between several modulators.

IV. Loop Demonstration

A simple demonstration of the entire loop—transmission of RF signals from the signal generation and receiving RF equipment to the carts with equipment in the chamber, then back over the RF fiber optic link to a receiver—was performed.

Figure 6 shows the demonstration configuration that represents the RF signal source and receiver (network analyzer) located in an area remote from the chamber. The TWT represents the transmission carts, the RF absorber box represents the chamber, and the fiber optic link is the one used for the measurements. The two horns in the chamber box for radiation and reception represent the transmitting and receiving antenna. The demonstration was over a 7 to 12 GHz frequency range that was limited by the RF antenna horns used.

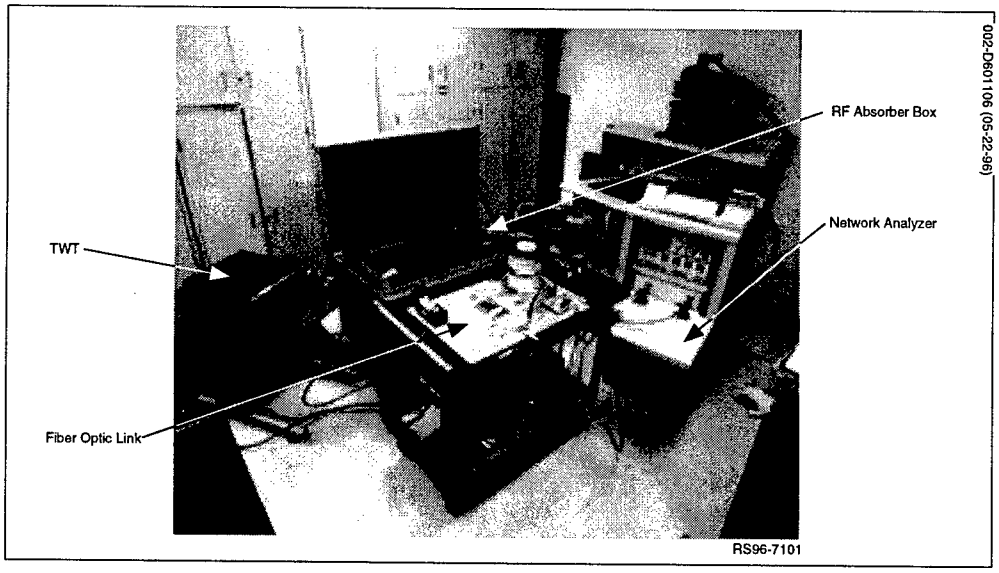

Figure 6. Demonstration Configuration for Fiber Optic Link Loop Demonstration

TA*x* Calibration of Optical Scattering Parameter Test Set

Balasundaram Elamaran, Roger D. Pollard and Stavros Iezekiel

Institute of Microwaves and Photonics,
School of Electronic and Electrical Engineering,
The University of Leeds,
Leeds LS2 9JT, England.

Tel: +44-113-2332093, Fax: +44-113-2332032, e-mail: eenbe@leeds.ac.uk

Abstract- The thru-attenuator-*x* (TA*x*) family of calibration techniques has been implemented for a two-port optical test set. A wide variety of results demonstrating the good performance of these techniques applied to optical components are presented.

I. INTRODUCTION

There is an increasing need to develop accurate and efficient techniques for the small-signal characterization of the microwave modulation response of the optical components used in microwave fibre-optic links, optical beamformers and all-optical microwave signal processing. Existing approaches to lightwave network analysis are relatively primitive when compared with those available for microwave network analysis. Measurements of the modulation *S*-parameters [1] of microwave fiber-optic components are mostly implemented using simple normalization calibration techniques, although the optical equivalent of the microwave one-port offset shorts and matched load calibration technique has also been investigated [2]. The first method is not accurate due to its simplicity, while the second is disadvantaged because the *S*-parameters of the calibration standards need to be known. These limitations can be overcome if a two-port calibration theory is applied, as originally proposed in [3], in which bilateral electro-optic networks were suggested for application to a two-port test set arrangement. Simulated and measured results of optical one-port measurements using the bilateral electro-optic network and a 'blackbox approach' have been presented [4]. However, the viability of the bilateral network for two-port measurements is yet to be validated, even though the optical equivalent of microwave thru-reflect-line techniques [5] for error correction was outlined in theory [3]. An optical equivalent of thru-match-reflect (TMR) calibration technique has been implemented [6], albeit with numerous connect-disconnect cycles having to be carried out manually during calibration and measurement. Since then, a generalized algorithm for implementing all of the thru-reflect-line (TRL) family of calibration techniques has been proposed, and measurement results presented applied to microwave components [7]. In this paper, the TA*x* family of techniques are implemented in the optical domain for the first time, and their performance compared among themselves and with the commercially used response and isolation calibration.

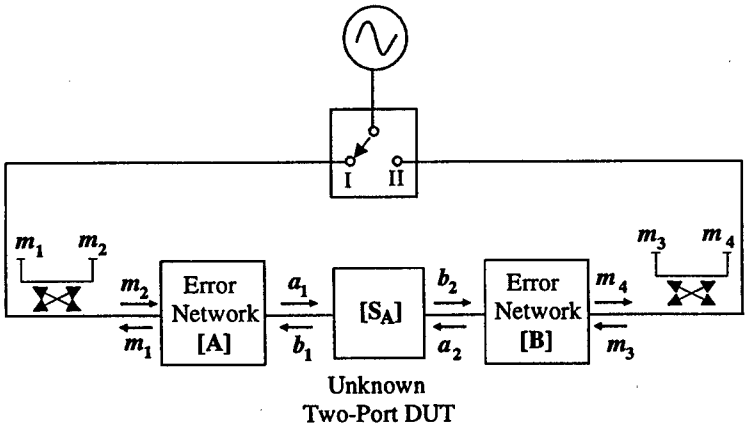

***Figure 1** Schematic of the reduced two-port error networks assuming cross coupling is negligible between the two measurement ports.*

0-7803-4936-9/98/$10.00 © 1998 IEEE

II. THEORY

The systematic errors in a network analyzer can in general be reduced to two equivalent two-port networks [5], one on each side of the measurement ports, as shown in Fig. 1. From this model, there are eight error terms to be determined for calibrated measurements to be taken. This leads to the so called eight-term calibration techniques, the most popular of which are the TRL family. These techniques calculate seven of the error terms normalized to the eighth. It can be proved that this normalization does not affect subsequent measurements of *S*-parameters of a device under test [DUT]. The most generalized form of the TRL calibration algorithm proposed by Heuermann and Schiek [7] is, for convenience, the technique utilised here for the experiments.

III. EXPERIMENTAL RESULTS

The two-port optical test set configuration is shown in Fig. 2. The output of the external modulator in the lightwave component analyzer is passed through a 2-way optical switch into the dual directional coupler associated with either Port 1 or Port 2. The incident and reflected lightwaves at both ports are then sampled in turn by the lightwave receiver via a 4-way optical switch.

Four different sets of calibration standards have been used, namely TAR, TAN, TAF and TAF$_K$. The thru (T) and attenuator (A) are used as the first and second standards respectively, while the final standard is chosen from one of the following: mirror reflects (R), a symmetrically reflecting network (N) and one or more Fresnel (F) reflects. The third standard is normally considered to be unknown, but with identical reflection coefficients at both ports. However, a slight variation of the calibration theory which assumes the third standard to be a known [7] one-port at either port 1 or 2 is also implemented using the Fresnel standard, since the Fresnel reflection can be calculated. This case is denoted by F$_K$.

The attenuator (A) standard is constructed using a dual directional coupler by terminating two of its four ports with matched loads. The reflect (R) standard used was a dielectric coated mirror with a theoretical reflection of 95% (-0.2 dB). The symmetrically reflecting network (N) standard was constructed using a similar configuration to the one used for the attenuator standard, by replacing the matched loads with dielectric coated mirrors. It has symmetrical, but frequency dependent reflection and transmission coefficients. This property is useful in determining any dependency of the calibration accuracy on the *S*-parameter values of the third standard.

The uncalibrated measurements were de-embedded using the algorithm in [8]. Each calibration was implemented in turn, and various optical components - optical two-ports and double one-ports - were measured to verify the calibrations over a wide dynamic range. Typical results are shown in Figs. 3, 4 and 5. The measured results obtained for the same components with response and isolation calibration, which is the common commercially used technique, are also presented for comparison. The calibrated results of the magnitudes of S_{11}^{oo} of the dielectric coated mirror, S_{11}^{oo} of the Fresnel reflect and S_{12}^{oo} of a 20 dB attenuator are presented. Here, the superscript *oo* denotes optical modulation *S*-parameters. For the S_{21}^{oo} performance, a dual directional coupler in a recirculating delay line loop structure is used. This structure has a frequency dependent transmission coefficient. The calibrated measurements of the deviation from linear phase of the reflection coefficient of a mirror at the end of a length of fibre, and the transmission phase of a 20 dBo attenuator are also shown.

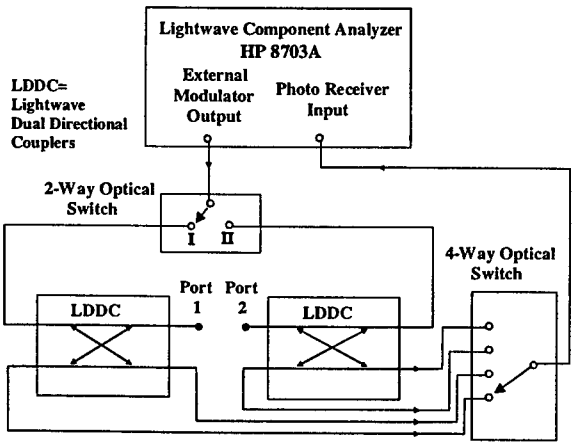

Figure 2 The measurement configuration

IV. DISCUSSION and CONCLUSIONS

Figs. 3(a) and (b) compare the reflection magnitude performance from the TA*x* family of calibration techniques with regard to magnitude measurements. It is seen that for reflection measurements, the TAR and TAF calibration techniques give values very close to the nominal values of the DUTs, and are also flat over the whole frequency range within ±0.05 dBo, which is better than the measurement with the response and isolation calibration. Also, the commercially used technique gives erroneous results for the reflection measurements, as does the TAF_K calibration which makes use of a third standard (the Fresnel reflect) which is assumed to be known. The TAN calibration, which was implemented using a symmetrical network with frequency dependent reflection and transmission coefficients as the third calibration standard, produces a varying frequency response for DUTs which have a flat frequency response. This error is most likely due to the magnitude dependent reflection intensity noise (RIN) of the laser, and leads one to conclude that it is better to use frequency invariant components as calibration standards. Hence, the TAR and TAF techniques have a definite advantage over the other TA*x* techniques and also over the response and isolation calibration. However, it should be noted that the TAN technique also gives acceptable results as long as a frequency invariant symmetrically reflecting network (N) standard is used. Figs. 4(a) and (b) compare the forward and reverse transmission magnitude performance from the calibrations. All the techniques provide good agreement for the S_{21}^{oo} response of the recirculating delay line. The results for the different techniques vary for S_{12}^{oo} measurement of the 20 dBo attenuator, but are well within the connection repeatability errors.

Fig. 5 compares the phase performance from the TA*x* techniques. Fig. 5(a) compares the deviation from linear phase of the reflection coefficient of an offset mirror standard. The TAN technique produces highly nonlinear reflection phase measurement, whereas the other techniques provide measurements with nonlinear deviations less than ±0.5°. Fig. 5(b) shows that the transmission phase is linear within ±1° over most of the frequency range. Overall, it is seen that the reflection measurements are more sensitive to calibration accuracy than the transmission measurements.

The slightly degraded performance with increasing frequency observed for most of the calibration techniques is due to the modulated signal power from the external modulator decreasing gradually by about 8 dB at 20 GHz from its value at 1 GHz. This raises the possibility that an attenuator used in the calibration results in a signal at the photoreceivers which is at or below the noise floor. The measurements here have been implemented by sequentially sampling the measurement quantities rather than simultaneously, which increases the effects of noise. Better performance can be expected with simultaneous measurements.

V. ACKNOWLEDGMENTS

The authors are grateful to the Hewlett-Packard Company, Santa Rosa, USA for sponsoring this project. B. Elamaran thanks Filtronic Comtek Plc., UK and the UK Overseas Research Scholarship scheme for their financial support.

REFERENCES

[1] R.W. Wong, P. Hernday, M.G. Hart, G.A. Conrad, "High-speed lightwave component analysis," *Hewlett-Packard J.*, vol. 40, no. 3, pp. 35-51, June 1989.

[2] D.D. Curtis and E.E. Ames, "Optical test set for microwave fiber-optic network analysis," *IEEE Trans. Microwave Theory Tech.*, vol. MTT-38, pp. 552-559, May 1990.

[3] S. Iezekiel, C.M. Snowden and M.J. Howes, "Scattering parameter characterization of microwave optoelectronic devices and fiber-optic networks," *IEEE Microwave and Guided Wave Letters*, vol.1, no. 9, pp. 233-235, Sep. 1991.

[4] B. Elamaran, R. D. Pollard, S. Iezekiel, "Simulation and Implementation of Lightwave Component Characterization using a Bilateral Electro-optic Network," *IEEE Trans. on Microwave Theory Tech.*, vol. MTT-45, pp. 1492-1495, Aug. 1997.

[5] H.J. Eul, B. Schiek, "A generalized theory and new calibration procedures for network analyzer self-calibration," *IEEE Trans. Microwave Theory Tech.*, vol. MTT-39, pp. 724-731, Apr. 1991.

[6] A.H. Quoc and S. Tedjini, "Measurement & calibration procedure for the characterization of the scattering parameters in microwave fiber-optic devices," *Proc. 24th European Microwave Conf.* (Nice, France), pp. 934-939, 1994.

[7] H. Heuermann, B. Schiek, "Robust algorithms for Txx network analyzer self-calibration procedures," *IEEE Trans. Instru. Measurements*, vol. IM-43, pp. 18-23, Feb. 1994.

[8] H. Heuermann, B. Schiek, "Procedures for the determination of scattering parameters for network analyzer calibration," *IEEE Trans. Instru. Measurements*, vol. IM-42, pp.528-531, Apr. 1993.

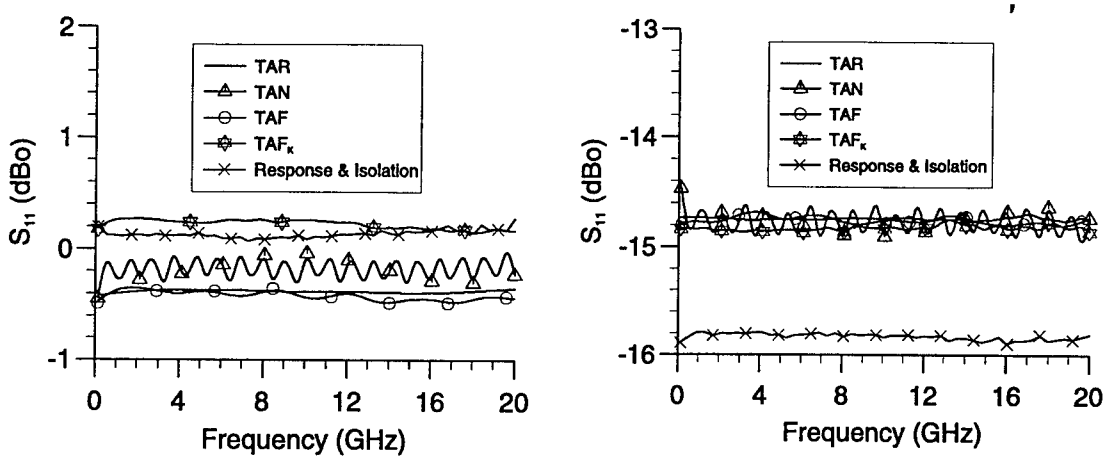

Figure 3 TAx calibrated optical magnitude measurements (a) S_{11}^{OO} of a -0.2 dB reflect at Port 1 (b) S_{11}^{OO} of a Fresnel reflect at Port 2

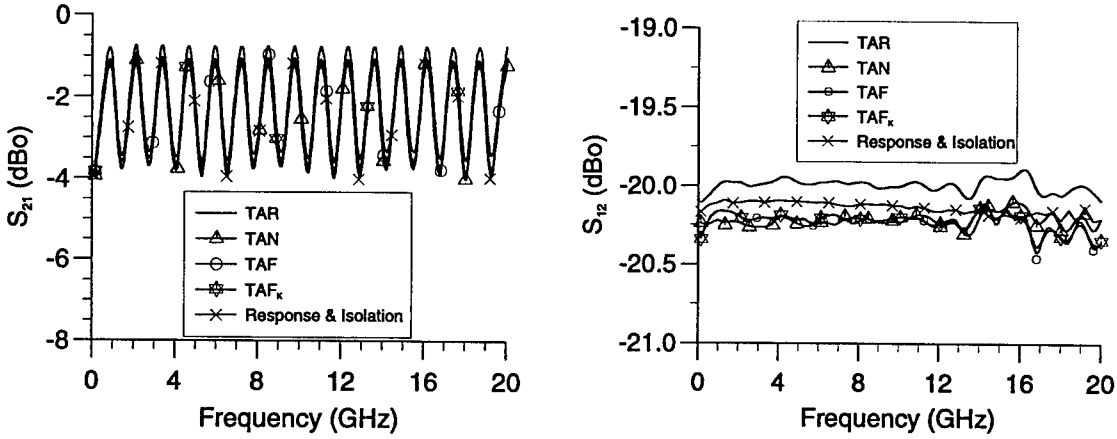

Figure 4 TAx calibrated optical magnitude measurements (a) S_{21}^{OO} of a recirculating delay line loop (b) S_{12}^{OO} of a -20 dB attenuator

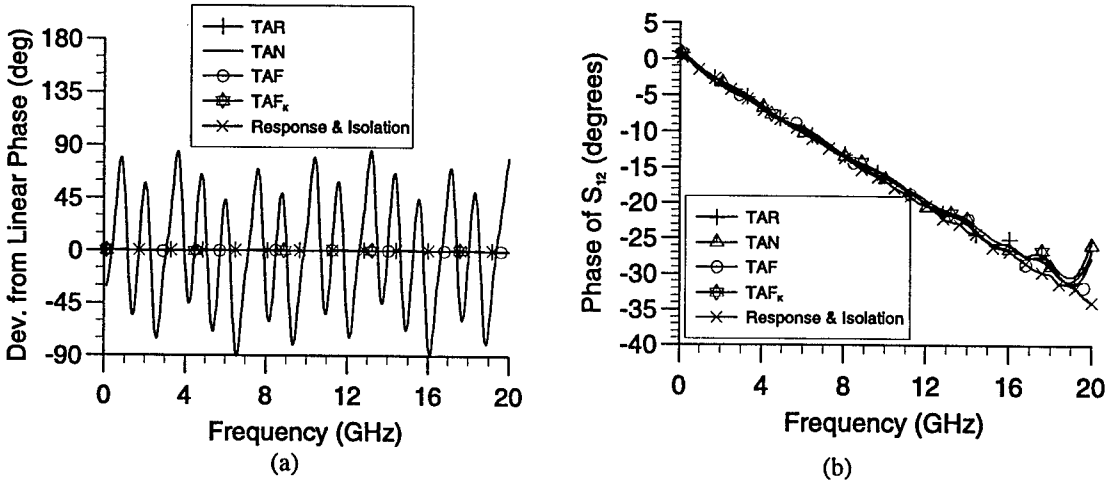

Figure 5 TAx calibrated optical phase measurements (a) Deviation from Linear Phase of S_{11}^{OO} of a -0.2 dB reflect at the end of a length of fibre at Port 1 (b) Phase of S_{12}^{OO} of a -20 dB attenuator

Hybrid fiber-radio systems in the mm wave range : A comparison between available optical sources

J.F. Cadiou*, D. Tanguy*, E. Pénard*, P. Jaffré*, H. Schmuck**, E. Vergnol***, D. Mathoorasing***
* France telecom BD CNET/DTD/AEA
** Alcatel Alsthom CRC, Stuttgart
*** OPTO+, Marcoussis

Introduction :

Wireless communications are nowadays a way of life all over the world because people like the idea of being contacted everytime and everywhere. Such systems have experienced an enormous growth over the last decade, and beside, the explosion of multimedia services, among them INTERNET have motivated the demand for high capacity services. Wireless and high bit rate systems lead naturally towards the synergy between radio and optical networks (1)(2). Applications of those techniques can be shared in two different parts, including indoor (IC) and outdoor communications (OC). For ICs, cabling offices, houses, and public premises can be avoided by installing wireless link, this is the aim of DECT or HIPERLAN systems. Also for very small area ERO (European Radiocommunication Office) have identified the 59-62 GHz frequency band which is well suited for such applications (small size area, simplified frequency plan, frequency re-use, broadband ...). For OC, wireless local loop can be an economical way to provide services without the need of cabling buildings, houses, ...This is the goal of the project -Fibre Radio ATM Network and Services- (FRANS) (3), included in European ACTS program, as part of more advanced Integrated Broadband Network (IBC).
In this context radiowave signal containing subscribers informations can be delivered by an optical media to the Radio Access Point, and then distributed over the area. Identified frequency bands for such systems are 28 and 40 GHz. A typical FTTR system (Fiber To The Radio) is described in fig 1.

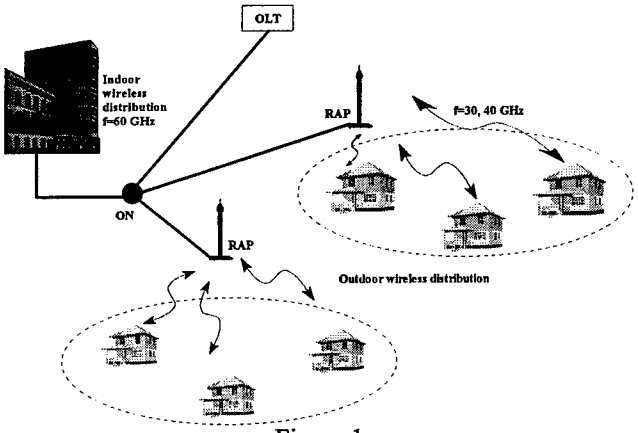

Figure 1

From the optical node (ON) radiowave signal is distributed towards the radio access point (RAP) for diffusion of multimedia services such as digital TV programs, Rapid Internet, Telephony, datas. The need for efficient millimeter wave optical sources is then clearly identified, and these components and systems have to be completely transparent to the radio signal particularly to the modulation format (QAM, QPSK, FSK), to the high frequency modulation scheme (28, 40 60 GHz). Chromatic dispersion compensation, modulation efficiency and transparency to the modulation format are the major key points taken into account in the developpement of mm wave range optical sources. In the first part of this paper we will first introduce the different sources we have tested, in the second part, systems performances will be described and in the last section a comparison between sources will be realised and argumented.

Part 1 : 3 different mm optical sources : Description

Harmonic DFB laser :

The source is a high resonance frequency MQW VUG DFB laser used as harmonic generator and upconverter (4). The laser is driven by a Local Oscillator (LO) signal in the range of 5/10 GHz and mm wave frequency is then generated by harmonic conversion. The laser is integrated with transimpedance amplifier presenting to input ports : The LO port and the IF (Intermediate Frequency) radio signal port. By biasing the laser in its non linear zone the radiowave signal is

0-7803-4936-9/98/$10.00

upconverted at frequency n×LO+IF. Chromatic dispersion can partly be compensated by combination of the high FM modulation index of the laser (300-600 MHz-mA) and a dispersive media (4). Simulations and measurements on G652 fibers at 1.55 μm wavelength are showing that a quasi constant detected level (3 dB ripple) at 38 GHz can be reached over 2-20 km range. This technique also allows the use of complex modulation such as QAM or QPSK modulation scheme and fig 2 shows a typical BER diagram at 25 Mbits/s for 16 QAM transmission over 9 km fiber and 4 m radiowave link at 38GHz. Emission and reception antennas have respectively 5 and 25 dB gain.

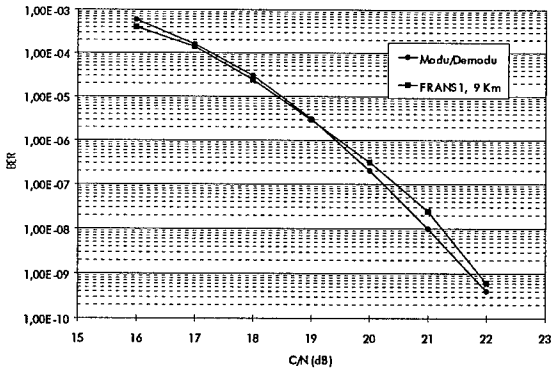

Figure 2

No excess degradation is observed in comparison to the reference modem curve. (FRANS1 : Label of the laser)

Single Side Band Source (SSB) :

Dispersion compensation is realised in this source by the SSB technique, implemented in a fully integrated laser-modulator structure (5). The structure of the device is an asymetric MMI followed by two very high speed electro-absorption modulators (>35 GHz bandwidth) in each arm of the interferometer. Millimeter wave signal is then applied on each arm with a phase difference of $\pi/2$, resulting in single side band optical spectrum without dedicate tuning optical filter as shown on figure 3. SSB suppression ration can be better than 13 dB.

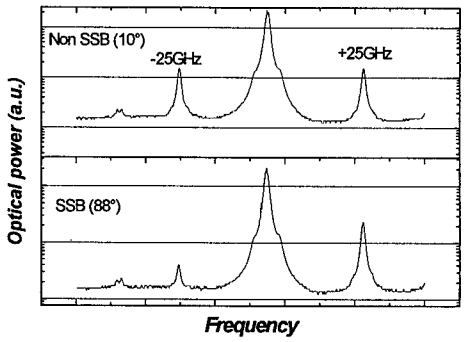

Figure 3

Propagation was performed as a function of fiber length over 50 km of G652 fiber, and experimentally 2 dB ripple remains. SSB source has also the advantage of being transparent to the modulation format.

Self Heterodyne (SH) mm wave source :

This source type which also offers a chromatic dispersion compensation, is principally based on a single laser in combination with an intensity modulator. By applying a double sideband modulation scheme (6) optical carriers are provided which can generate by coherent mixing a high purity mm-wave signal with frequencies up to more than 100 GHz. Depending on the system requirements, several approaches can be realised showing different complexity with regard to the number and the performance of their implemented components (7).

In the FRANS field trial a most complex version of the SH technique is foreseen for implementation. This approach realises the full advantages for the delivery of multi-channel mm-wave signals as long as the system is transparent to modulation format. Furthermore, like the case of the non-linear laser, this configuration enable an intrinsic generation of electrical reference signals usable at the base station or subscriber site.

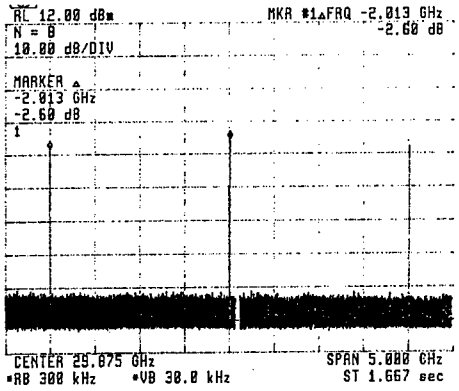

Figure 4

Figure 4 shows the typical electrical spectrum at the base station with the reference line at 29.875 GHz and the unmodulated side bands with 2 GHz frequency offset.

Part 2 : System performances, characteristic figures

Different performances are summarized in table 1 to 3 for the three different solutions presented in the first section. Phase noise, stability, C/N measurements are realised first on the detected LO, and on the other hand on the radio wave signal (SB) at 31.88 GHz, common peltier modules are used to stabilised temperature of the device. C/N measurements are expressed in a 225 MHz bandwidth which corresponds to the useful information band for 622 Mbits/s 16 QAM radiowave signal. Standard SMF fiber length is 10 km with 1:4 splitter and -0.9 dBm optical power in front of PIN.

C/N performances

C/N (dB)	Local oscillator	Lower sideband
VUG	37.1	35.3
SSB	None	42.9
SH	37.0	36.3

Table 1

LO Phase noise measurements

Phase noise (dBc/Hz)	VUG	SSB	SH
1 KHz	-68	-79	-77
10 KHz	-69	-82	-88
100 KHz	-95	-103	-98
1 MHz	-112	-108	-110
10 MHz	-115	-123	-118

Table 2

LO and Sidebands measured electrical power

Electrical power (dBm)	VUG	SSB	SH
LO	-38.8	None	-28.3
Side band	-38.2	-34.2	-31.3
LO variations, 50 h	< +/- 1.5 dB	Unavailable	<+/- 1.5 dB
SB variations, 50 h	< +/- 1.0 dB	Unavailable	<+/-0.8 dB

Table 3

For the different sources mm wave signal 3 dB linewidth is better than 10 Hz and is limited by the resolution of the spectrum analyser.

Part 3 : Discussions

C/N considerations:

C/N are better than 35 dB and then allows the use of complex modulation scheme such as 16 QAM without noise floor for low bit rate (see fig 2). For more complex modulations (32, 64 QAM) C/N figure can be a limitation because such modulation schemes require excellent SNR. SSB source is 6 dB better because no up conversion or mixing process is involved in this technique. Moreover we have used in our experiments a non optimised device because of a low output optical power and results should be improved after high speed packaging of the chip.

Phase Noise considerations :

Phase noise have been measured at 28.88 GHz using spectrum analyser, table 2 shows that SSB and SH techniques are providing very similar results at frequency offsets from 1 KHz to 10 MHz. For the non linear laser source phase noise have 10 dB penalty in the range 1 KHz-10 KHz due to phase error multiplication in the up-conversion process. Rms Phase Noise (PN) has been measured and it clearly shows that it increases linearly with the harmonic order (From 3° initial to 9° on H4). However this inherent PN degradation can be cancelled by mixing the received RF signal with coherent LO. The main drawback is the radiation of the LO which could be a limitation in terms of spectral occupation. The second solution is to use a high spectral purity oscillator in order to conserve a good signal caracteristic after the multiplication process. This point becomes essential with the modulation complexity increase. (16-64 ... QAM).

Power stability considerations :

Power fluctuations have not been measured for the SSB source because of the unpigtailed configuration and the unsufficient stability of our experimental test-bed over 50 hours. Power fluctuations for both sources VUG and SH (see table 3) are in the same range and compatible with the specifications of the ACTS FRANS project. In terms of detected power, SH source is more efficient source compared to SSB or Non linear Laser. The 10 dB power penalty for the VUG is due to the upconversion process, but for the SSB the detected power should be strongly improved by optimising design parameters of the integrated structure (Losses in the MMI, More powerful laser, Suitable coatings ...).

Conclusion :

Three different mm wave optical sources have been presented and compared in terms of SNR, detected RF power, power fluctuations and Phase Noise. For the *PN considerations*, VUG is limited by the inherent problems of the non linear process. *The PN* can be cancelled wih the drawback of higher spectral occupation. *SNR performances* are in the same range for the three sources and better than 35 dB. *Power stability* could be improved, but are less than +/- 1.5 dB and are fulfilling FRANS specifications. *The detected RF power* is better for SH and SSB, but loss conversions in the harmonics process are lowering power at 29.88 GHz. *In terms of complexity*, VUG and SSB are equivalent techniques (monolithic semiconductor devices). SH source have, at the moment a higher complexity, however its integration is planned and should also provide a compact and potentially low cost mm wave source.

Acknowledgements :

This work have been supported by EEC in the ACTS FRANS project for VUG and SH mm-wave optical sources.

References :

(1) : Outdoor and Indoor applications for broadband local loop with fiber supported mm-wave radio systems, M. Goloubkoff et al, IEEE MTT-S 97, TU1B-3, Denver 1997.

(2) : Picocell chips shape the future of wireless links, D. Wake et al, BT Engineering, vol 16, pp 10.6-11.2, july 1997.

(3) : Demonstrating the enabling Technology for Broadband Wireless Local Loop: ACTS FRANS and other Hybrid Fibre Radio Trials, R. Heidemann, M. Mittrich, H. Schmuck, E. Penard, International Symposium on Service and Local Access ISSLS, 22-27.3.1998, Venice, Italy

(4) : Wide band optoelectronic upconverter for radio over fibre applications at 28/38/60 GHz, D. Mathoorasing et al, ECOC'96, WeP. 22, Oslo 1996. Patent CNET: N° 02754

(5) : Design of an integrated lightwave millimetric single side band source.E. Vergnol et al, to be published in Journal of Lightwave Technology (july 98) and French Patent Pending FR 9705362.

(6) : Microwave Optical Duplex Antenna Link (MODAL), J .J. O'Reilly et al, IEE Proc Part J, Vol 140, N°6, pp 385-391, December 1993.

(7) : Optical mm-wave Source Configurations for Hybrid Fibre Radio Systems, H. Schmuck, R. Heidemann, European Conference on Network&Optical Communications NOC'98,Manchester, June, 23-25, 1998.

A NEW OPTICAL DISTRIBUTION APPROACH FOR MILLIMETER WAVE RADIO

T. Marozsák, T. Berceli, G. Járó, A. Zólomy, A. Hilt, S. Mihály, E. Udvary, Z. Varga

Technical University of Budapest, Dept. of Microwave Comm.
H-1111 Budapest, Goldmann György-tér 3, Hungary,
Tel.: (36)-1-463-4142, Fax: (36)-1-463-3289

Introduction

The mobile communication systems tends to use the millimeter wave region in picocellular applications [1, 2]. The signal distribution system uses single mode fiber for transmission of the millimeter wave carrier. These solutions requires expensive devices for optical-electrical conversions. The fiber dispersion is also an important limiting factor which is difficult to overcome [3, 4]. Our approach utilizes a low frequency microwave reference signal for distributing the millimeter wave carrier and this way it is not affected by the distortion problem, relatively simple and utilizes inexpensive devices.

Abstract

In the proposed picocellular radio system a microwave reference and subcarrier multiplexed radio signals are distributed optically. The millimeter-wave carrier is generated by phase locking technique. This approach is not affected by dispersion and utilizes inexpensive devices.

I. System Proposal

The local base stations (LBS) are extended by several picocell transceivers (PTR) which are connected to the LBS with simple single mode fiber (Fig. 1). The LBS makes the channel selection for the communication channels and transmits both a reference signal and the information modulating subcarriers to the PTR-s. In the PTR the millimeter wave (MMW) carrier is generated based on the transmitted microwave reference signal and radiated by an antenna after mixing with the subcarriers.

The millimeter wave carrier generation multiplies the microwave reference with N, thus produces $N \times f_{ref}$ frequency carrier. The most simple solution for multiplying is to use varactor diodes, but when N is high, strong amplification is necessary at millimeter wave. For that reason the PLL techniques are more preferable [5]. Several PLL method can be used like heterodyne stabilizer applying harmonic mixer, subharmonic locking utilizing frequency dividers or high harmonic output oscillator. The phase noise of the low microwave reference has vital importance, since the frequency multiplication even in idealized cases increases the phase noise with 20logN [dB] in the band of the oscillator output signal.

II. Experimental results

Simplified version of the system was built for verification. The LBS was simplified to be able to transmit one information channel having 50 MHz bandwidth. As a reference f_{ref}=1055 GHz was chosen with 390 MHz IF subcarrier and hence, 1445 GHz microwave subcarrier. The laser diode was a simple Fabry Perot type operating at 1310 μm and it was matched reactively the 50 Ω system impedance in the band of the microwave reference signal and subcarriers. Its threshold current was 70 mA and had -120dB/Hz RIN@85mA.

The photodetector in the PTR is followed by a branching filter which separates the microwave reference signal from the subcarriers. The MMW carrier generation is based on a harmonically locked oscillator with a frequency divider by 8 in the PLL (Fig. 2). The oscillator was designed to have high level of harmonics at the output. The system utilizes the third harmonic which was at 25.32 GHz following from the foregoing. In the second order loop a 1GHz mixer was used as phase detector.

A. Design of the harmonic VCO

A new method was developed for the design of the harmonic VCO. The VCO produces high third harmonic output according to the system requirements.

The investigated simplified oscillator configuration consists of a nonlinear amplifier ($A(g)$) and a linear feedback network ($K(\omega)=K_r(\omega)+jK_i(\omega)$) as it is shown in Fig. 3 [6]. The nonlinear characteristic of

0-7803-4936-9/98/$10.00

the amplifier is shown in Fig. 4. In a transistor oscillator the transconductance of the active device corresponds to the amplifier and all other elements (transistor parasitics and external circuit elements) are involved to the feedback circuit.

The high level of the harmonics are generated by driving the active element of the oscillator circuit into saturation or/and below pinch-off at the positive and negative peaks of the output signal, respectively [7]. This operation is illustrated in Fig. 4 if only the fundamental is assumed to be feed back to the amplifier input.

This strongly nonlinear operation is achieved by applying strong feedback. The operation point and thus the output harmonic content can be adjusted by varying the transfer function of the feedback circuit (and thus X_1) and the gate bias voltage (V_0) of the active device. The output harmonic content can be calculated by using harmonic balance method. Applying the nonlinear U_{GS}-I_{DS} characteristic of the used NE13783 type MESFET from NEC Fig. 5.a and Fig. 5.b shows the magnitude of the fundamental (B_1) and the third harmonic, respectively, at the output of the amplifier versus the magnitude of the input (gate) signal (X_1) and the gate bias voltage (V_0). The fundamental is maximum if the output signal is nearly symmetric (i.e. output signal is symmetrically truncated).

The signal levels at the 50 Ohm output load can be determined by calculating the transfer function from the transistor current generator to the 50 Ohm load resistor. The measured frequency and power of the realized oscillator at the fundamental and at the third harmonic are presented in Fig. 6.a and Fig. 6.b. The signals were measured after a branching filter which was designed to separate the fundamental from the 3rd harmonic. The calculated signal levels are close to the measured ones. The stability and the soft build-up condition of the oscillation were also derived.

B. Measurement of the system

Measurements were performed on the generated MMW carrier and information transmission. (Figs. 7-10). The optically transmitted microwave reference was produced by a crystal stabilized oscillator (SSB phase noise -94dBc@1kHz). The measurements show no significant phase noise degradation with the optically transmitted reference (Fig. 8). The subcarrier multiplexed signal transmission was also measured (see Fig.10) where the higher order mixing products and the intensity noise of the FP laser degrades the signal to noise ratio but even so it was more than 110 dB/Hz.

Conclusion

A new method was presented to distribute and generate MMW signals using inexpensive subcarrier multiplexed optical transmission in picocellular communication systems. It is based on optically transmitted microwave subcarriers and a frequency reference signal. The MMW carrier is produced by a PLL including a MMW harmonic VCO in the transceivers. The advantages of this method are the relatively low cost, small sensitivity for the fiber dispersion and the application of only wide-spread inexpensive microwave and optical components.

Acknowledgment

The work was financed by the "FRANS" program of the European Union and Hungarian National Scientific Research Fund 'OTKA' No. T017295, F024113, T014300, T019839 and T019857.

References

[1] D.Wake, D.G.Moodie : "Passive Picocell - prospects for increasing the radio range", IEEE Topical Meeting on Microwave Photonics, MWP'97 Digest, pp.269-271, Duisburg, Germany, September 1997.[2] L. Noël, D. Wake, D. G. Moodie, D. D. Marcenac, L. D.

[2] Westbrook, D. Nesset : "Novel Techniques for High-Capacity 60-GHz Fiber-Radio Transmission Systems" IEEE Trans. Microwave Theory Tech., vol. 45, pp. 1416-1423, August, 1997

[3] H.Schmuck : "Comparison of optical millimeter-wave system concepts with regard to chromatic dispersion", Electronics Letters, Vol.31, No.21, pp.1848-1849, 12th October 1995.

[4] G.H.Smith, D.Novak, Z.Ahmed: "Overcoming Chromatic-Dispersion Effects in Fiber-Wireless Systems Incorporating External Modulators", IEEE Trans. on MTT, Vol.45, No.8, Part II, pp.1410-1415, August 1997.

[5] T. Berceli, "A new approach for optical millimeter wave generation utilizing locking techniques", IEEE MTT-S, International Microwave Symposium Digest, Vol. III, pp. 1721-1724, Denver, USA, June 1997

[6] V. Bíró: "Nonlinear Oscillations in Feedback Systems", ISBN-963-05-3425-8 Akadémiai Kiadó, Budapest, Hungary, 1985.

[7] A. Zólomy, V. Bíró, T. Berceli, G. Járó, A. Hilt: "Design Of Harmonic Oscillators For Millimeter Wave Signal Generation In Optical Systems", accepted to the 28th EuMC, Amsterdam, 1998.

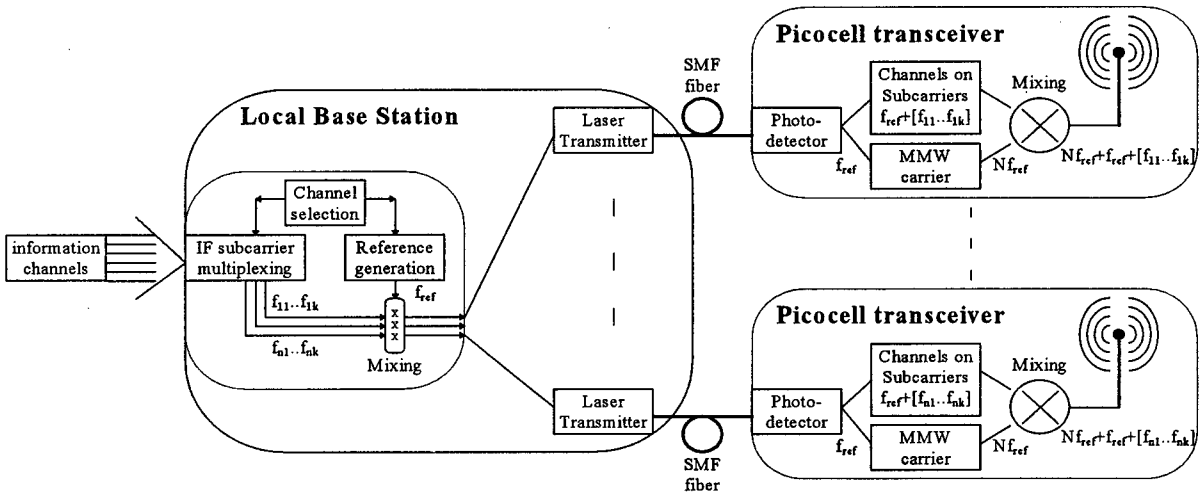

Fig. 1, System concept

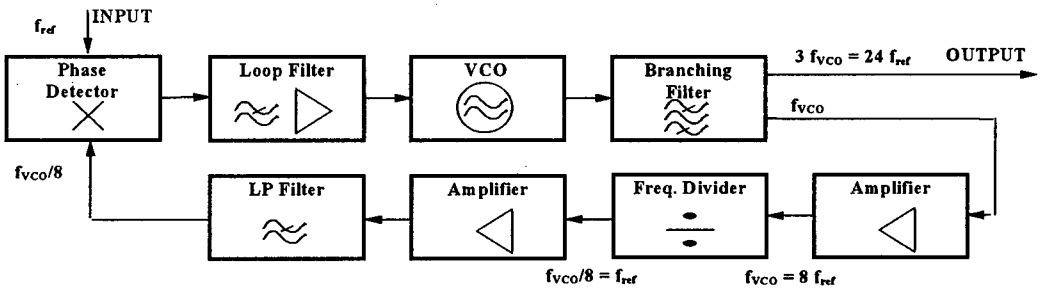

Fig. 2, Block diagram of the MMW reference PLL

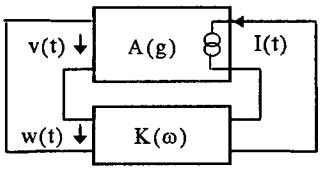

$$I(t) = Re\left\{\sum_{k=1}^{N} B_k \exp\left(j\left(k\omega t + \Psi_k\right)\right)\right\};\ V(t) = Re\left\{\sum_{k=1}^{N} X_k(t)\exp\left(j\left(k\omega t + \varphi_k(t)\right)\right)\right\}$$

$$B_k = B_k\left(X_1, X_2 \ldots X_N, \varphi_1, \varphi_2 \ldots \varphi_N, \omega\right)$$

$$\Psi_k = \Psi_k\left(X_1, X_2 \ldots X_N, \varphi_1, \varphi_2 \ldots \varphi_N, \omega\right)$$

Fig. 3, Simplified model of the VCO

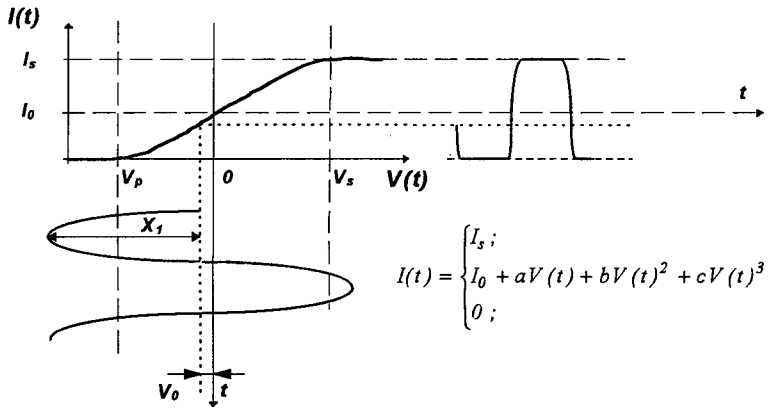

$$I(t) = \begin{cases} I_s; & V_s \le V(t) \\ I_0 + aV(t) + bV(t)^2 + cV(t)^3; & V_p < V(t) < V_s \\ 0; & V(t) \le V_p \end{cases}$$

Fig. 4, Harmonic generation by the truncation of the VCO output signal

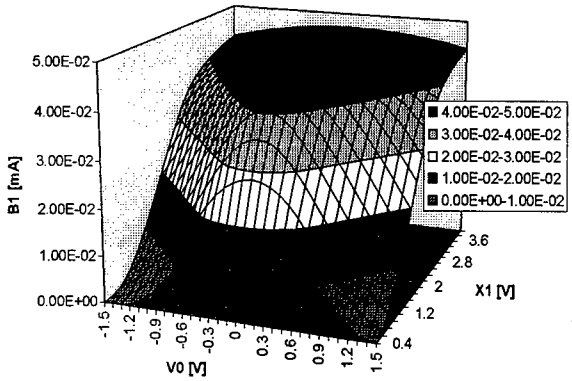

Fig. 5.a , Fundamental magnitude

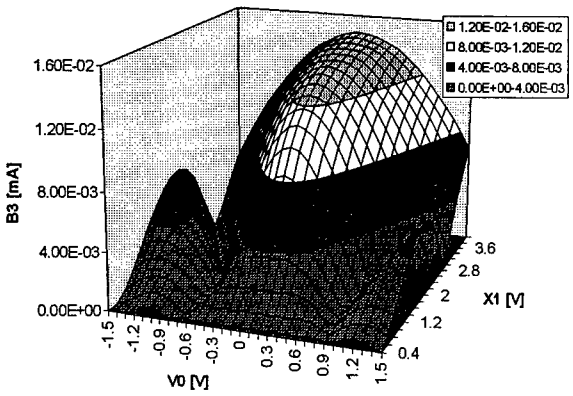

Fig. 5.b , 3rd harmonic magnitude

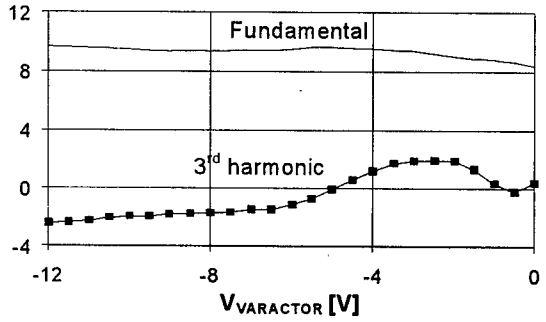

Fig. 6.a, Fundamental and 3rd harmonic power [dBm]

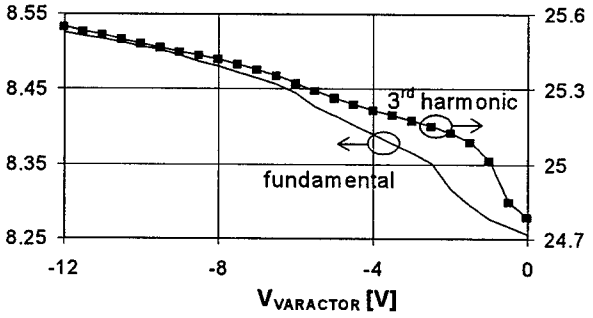

Fig. 6.b, Fundamental and 3rd harmonic freq. [GHz]

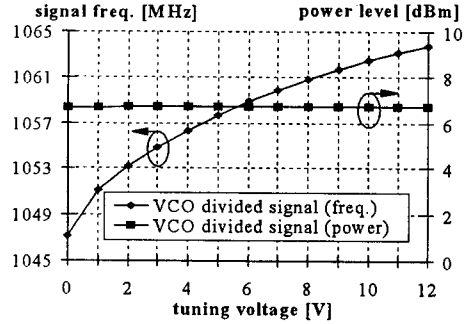

Fig. 7, Frequency and power dependence of the output signal of the digital divider

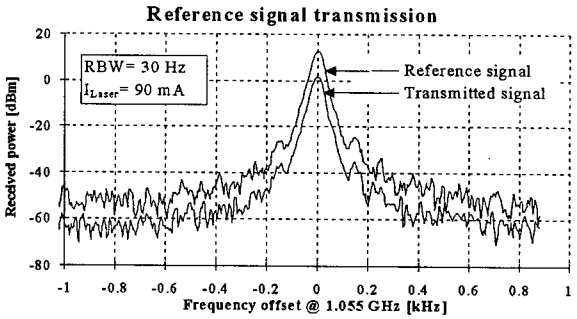

Fig. 8, Power spectra of the original reference signal and the optically transmitted reference signals

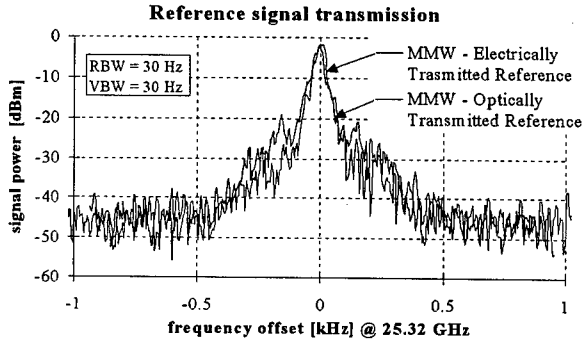

Fig. 9, Spectrum of the MMW carrier (MMW signal @ 25.32 GHz)

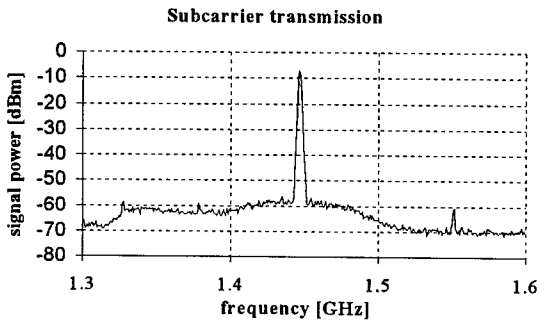

Fig. 10, Microwave subcarrier@390MHz

Microwave Multichannel System with a Sideband Injection Locking Scheme in the 60 GHz-Band

C.G. Schäffer, FH Lübeck, Stephensonstr. 3, 23562 Lübeck
schaeffer@fh-luebeck.de
R.-P. Braun, G. Grosskopf, F. Schmidt, M. Rohde
Heinrich-Hertz-Institut für Nachrichtentechnik Berlin GmbH
Einsteinufer 37, 10587 Berlin, Germany

Abstract: In the 60 GHz band a frequency range of 1 GHz is allocated for use in picocellular communication systems. Electrical and optical frequeny multichannel schemes with a sideband injection locked source are investigated theoretically and experimentally.

I. Introduction

The combination of fibre optics and millimeter wave techniques offers advantages for broadband mobile communication systems as well as for the remote control of phased array antennas. Additionally to the long distance low loss transmission and large bandwidth of the fibers, the remote generation of the millimeter wave signals is a powerful advantage.
The microwave signals are generated by heterodyning the optical waves of a Signal Laser LDS_i and the Reference Laser LDR at the photodiode in the Optic/Millimeterwave Converter OMC (Fig. 1). The two lasers are located in the control station and the sideband injection locking technique is used to get a stable microwave signal in the 60 GHz-band with low phase noise [1, 2]. LDS1 and LDR are locked to modulation sidebands of the Master Laser LDM which is subharmonically modulated by OSC1. For data transmission a subcarrier (fs_1), which is phase modulated by a 155 Mbit/s data signal in the OQPSK format modulates the injection current of LDS1. The two optical signals are added and fed into a standard single mode fiber.
For applications in communication systems the optical control station must have multichannel capability. The different channels can be generated with an optical or an electrical frequencymultiplex scheme. The spectral behaviour of both systems is investigated with a dynamic model (van der Pol differential equation) of the injection locked lasers.

II. Optical Frequency Multiplex System

The dual frequency source (LDS1, LDR) at the control station is extended by a further signal laser (LDS 2) for the additional data channel. Frequency matching to the channels in the 60 GHz band is carried out in the control station with subcarrier modulation of the two data channels. From results of the simulation no influence between the modulated signal lasers LDS_i is expected as long as the channel spacing is greater than 110 MHz for a 155 Mbit/s data signal i.e. no spectral overlapping exists. A raised cosine spectrum with a rolloff factor of 0.4 is assumed. The spectral efficiency is about 1.4 bit/s/Hz. In the experiment the channel spacing is 140 MHz and the modulation index of the two data channels is equal. The bit error rate (BER) measurements in channel 1 and 2

0-7803-4936-9/98/$10.00

were carried out with and without modulation in the neighbouring channel (Fig.2). In all four cases nearly identical results were obtained i.e. the BER is less than 10^{-9} for a receiver input power greater than -59 dBm. For decreasing channel spacings a penalty in the BER is observed.

III. Electrical Frequency Multiplex System

The injection current of LDS 1 in the dual frequency source (Fig. 1) is modulated by the composed signal of the two or more subcarriers with constant frequency spacing of 140 MHz. Each subcarrier is modulated with the OQPSK data signal. As a result of the simulation of the injection locked lasers the frequency modulation of directly modulated semiconductor lasers is converted into optical phase modulation. The phase deviation can be represented by the ratio of the original FM deviation to the locking half bandwidth. Where the first is proportional to the amplitude modulation index of LDS1 and the second is proportional to the injected power. The phase deviation in the locking range must be less than $\pi/2$. For values above $\pi/2$ the phase noise of the generated microwave is increasing. The phase noise in a QPSK modulated system limits the achievable BER [3]. Therefore in an electrical frequency multiplex scheme the average phase deviation of all channels must be less than $\pi/2$. But for a BER of 10^{-9} a certain value of amplitude modulation index is necessary, in our demonstrator i_{mod}/channel>1mA. For modulation currents of approximately 3 ·· 4 mA the phase deviation is $>\pi/4$ and the BER increases rapidly.

IV. Conclusion

For multichannel systems in the 60 GHz band low phase noise is achieved by the sideband locking technique. Optical frequency multiplex schemes offer maximum signal-to-noise ratio but for each baseband channel an additional signal laser LDS is required. In electrical frequency multiplex schemes the maximum phase deviation of the signal laser limits the number of of data channels per signal laser.

Acknowledgement

Part of the work was carried out within the national research project PHOTONIK II supported by the Bundesministerium für Bildung, Forschung und Technologie and by the city of Berlin. The authors are grateful to R. Meschenmoser and G. Villino from Bosch Telecom for their support.

References:

[1] R.-P. Braun, G. Grosskopf, D. Rohde, F. Schmidt, "Optical millimetre wave generation and transmission experiments for mobile 60 GHz band communications", El. Letters, Vol. 32, No. 7, pp.626-628,1996.

[2] R.-P. Braun, B. Strebel, "Coherent optical fibre transmission using injection locked lasers", IEE Colloquium on 'Advances in coherent optic devices and technologies', London, Dig. No. 1985/30, paper 12, March 1985.

[3] C. Schäffer, "Limitation of the Transmission of mm-Wave Signals in Single Mode Fibers due to Fiber Dispersion", Workshop "Mobile Millimeter Communications", TU Dresden, 12.5.-13.5.1997.

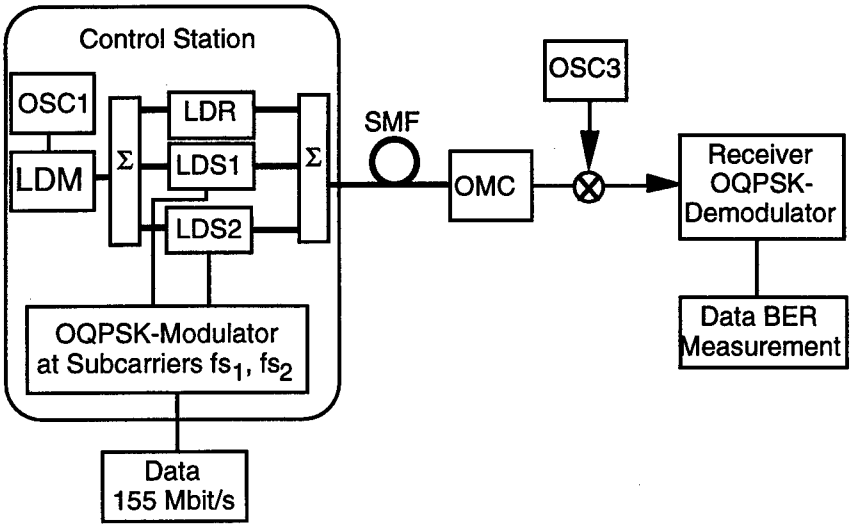

Fig. 1: Experimental Setup: LDM: Master Laser, LDR: Reference Laser, LDS: Signal Laser, OSC1: f=3.2GHz, Subcarrier Frequencies fs_1= 0.56 GHz, fs_2= 0.7 GHz, OSC3: f=63.07GHz, OMC: Optic/Millimeterwave Converter, SMF: Single Mode Fiber.

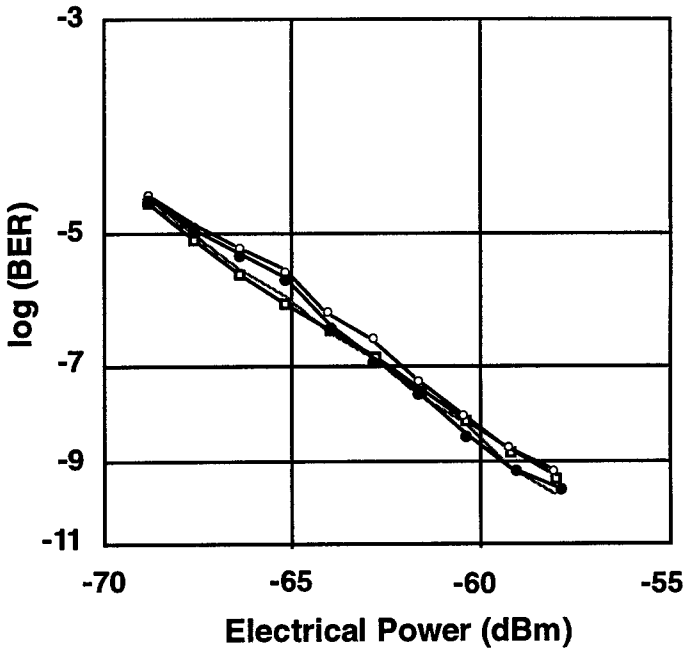

Fig. 2: Bit error rate vs. electrical power at the OQPSK receiver input. Modulation: 155 Mbit/s, PRBS. BER in CH1, CH2 without modulation(-•-). BER in CH2, CH1 without modulation(—). BER in CH1, both channels with modulation(-o-). BER in CH2, both channels with modulation (-□-).

Interferometric Modulators Linearized to Arbitrary Order

M. E. Marhic

Department of Electrical and Computer Engineering
Northwestern University
2145 N. Sheridan Rd., Evanston, Il 60208

I. Introduction.

When designing optical modulators it is generally desired to obtain a linear relationship between the applied voltage V and the output light intensity I, or output field E. Using the Mach-Zehnder interferometer (MZI) as a basic component, designs have been found which are free from harmonic distortion up to the fifth order [1,2]. Here we introduce a novel interferometric architecture which in principle allows us to suppress the generation of harmonics to any arbitrary order. We will prove this theoretically for either intensity, or field amplitude modulation, and we will provide explicit procedures for calculating the optical parameters.

II. Generalized interferometers.

We consider the arrangement of Fig. 1. An optical wave with angular frequency ω is incident from the left. It is then split M ways by the $1XM$ splitter. The M resulting waves pass through M phase modulators, and are then recombined by the $MX1$ combiner, which is the same as the $1XM$ splitter used backwards.

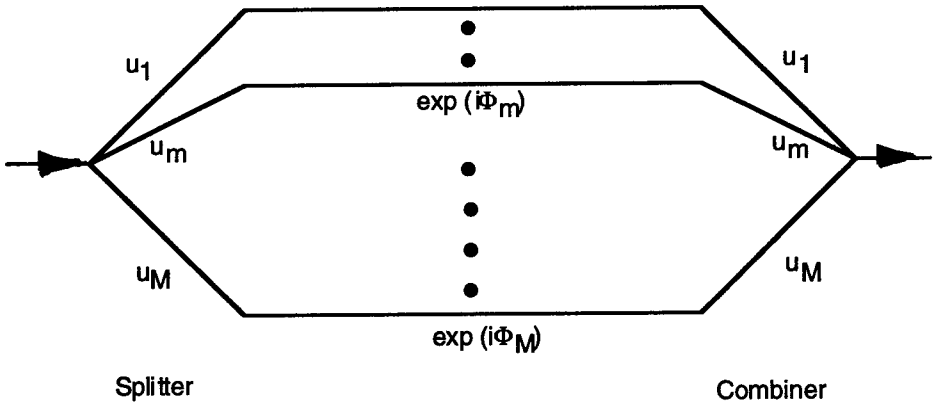

Figure 1: Layout of the generalized interferometers.

The symbol appearing next to each segment is its amplitude transmission coefficient. We assume that u_m is real, and that $\Phi_m = \phi_m + \nu_m V$, where ϕ_m and ν_m are real constants. Then the total amplitude transmission coefficient of the interferometer is given by

$$t_i = \sum_{m=1}^{M} u_m^2 e^{i(\phi_m + \nu_m V)}. \tag{1}$$

Power conservation indicates that we must have $|t_i|_{max} = \sum_{m=1}^{M} |u_m^2| \leq 1$.

III. Intensity modulator linearization.

In analog communication systems using intensity modulation (IM) and direct detection (DD), it is generally desirable to have to have a linear modulator, i.e. we would like to have the modulator transmittance T to be such that

$$T = (a + bV) = a(1 + x) = T(x), \tag{2}$$

where a and b are real constants, and $x = bV/a$ is a dimensionless variable proportional to V. We need $0 \leq a \leq 1$.

We are going to show that, by matching the first M terms of power series expansions of two functions of x (coming from Eq.(1) and Eq.(2)), we can suppress spurious harmonics up to order M. We proceed by matching the power series of t, rather than T. The desired form for t is obtained by taking the square root of Eq.(2). We choose for simplicity the real positive square root; then

$$t(x) = [T(x)]^{1/2} = a^{1/2}(1 + x)^{1/2} = \sum_{p=0}^{\infty} c_p x^p, \tag{3}$$

0-7803-4936-9/98/$10.00

where c_p are the coefficients of the power series expansion, given by

$$c_0 = a^{1/2}; \qquad c_p = \frac{1}{2}(\frac{1}{2} - 1) \cdots (\frac{1}{2} - p + 1)(p!)^{-1} a^{1/2}, \quad p \geq 1. \tag{4}$$

Since $T(x)$ must be real, we may choose $M = 2(N+1)$, and group guides in pairs, with the same u_m^2's and opposite Φ_m's (this is actually equivalent to using $(N+1)$ MZI's in parallel). Then Eq. (1) can be rewritten as

$$t_i(x) = \sum_{n=0}^{N} \left[\alpha_n \cos(\mu_n x) + \beta_n \sin(\mu_n x)\right], \tag{5}$$

where $\mu_n = (a/b)\nu_n$, $\alpha_n = 2u_n^2 \cos\phi_n$, and $\beta_n = -2u_n^2 \sin\phi_n$. Expanding $t_i(x)$ in power series with respect to x, we obtain

$$t_i(x) = \sum_{n=0}^{N} \left[\alpha_n \sum_{k=0}^{\infty} (-1)^k \frac{(\mu_n x)^{2k}}{(2k)!} + \beta_n \sum_{k=0}^{\infty} (-1)^k \frac{(\mu_n x)^{2k+1}}{(2k+1)!}\right]. \tag{6}$$

If we now compare Eqs.(3) and (6), we see that in order for the first $2(N+1)$ expansion coefficients to match, the following set of equations has to hold:

$$\sum_{n=0}^{N} \alpha_n (\mu_n)^{2m} = (-1)^m (2m)! c_{2m} = c'_m, \quad m = 0, 1, ..., N; \tag{7}$$

$$\sum_{n=0}^{N} \beta_n (\mu_n)^{2m+1} = (-1)^m (2m+1)! c_{2m+1} = c"_m, \quad m = 0, 1, ..., N. \tag{8}$$

With such an arrangement, spurious harmonics will be suppressed up to order $(2N+1)$ (included). To proceed further, we need to make some choices about which parameters can be assumed to be fixed, and which ones are to be considered as unknowns to be solved for.

If we assume that a and the μ_n's are known, then Eqs.(7) and (8) are two independent sets of $(N+1)$ linear equations, respectively for the $(N+1)$ unknowns α_n and β_n. This system of equations generally has a unique, real solution.

Eq.(7) can be viewed as a vector equation of the form $\mathbf{P} \cdot \alpha = \mathbf{c}'$, where: α is the vector of components α_n; $\mathbf{c}'$ is the vector of components c'_m; $\mathbf{P}$ is the matrix of elements $P_{m,n} = (\mu_n)^{2m}$. We can formally write the solution in terms of determinants, or use numerical techniques to obtain it.

In order for the network to be physically realizable, we must have $|t_i|_{max} = \sum_{n=0}^{N} (\alpha_n^2 + \beta_n^2)^{1/2} \leq 1$. Not all choices of a and μ_n's lead to a suitable solution, however some can be found by trial and error.

For example, for $a = 1/2$, $N = 3$, $\mu_0 = 0.79$, $\mu_1 = 3.03$, $\mu_2 = 6$, $\mu_3 = 8$, we find that: $\alpha_0 = 0.745$, $\alpha_1 = -0.042$, $\alpha_2 = 0.0033$, $\alpha_3 = -0.00043$, $\beta_0 = 0.570$, $\beta_1 = -0.037$, $\beta_2 = 0.0033$, $\beta_3 = -0.00043$, $|t_i|_{max} = 0.9999$. We note that $\alpha_n \simeq \beta_n$, and that the larger n, the closer they are.

Fig. 2 shows that the resulting $T(x) - T_i(x)$ corresponding to this case is indeed very small near $x = 0$: its magnitude is less than 10^{-4} for $-0.4 \leq x \leq 0.4$, and no ripples are present. This shows that the elimination of all harmonics up to the seventh, is accomplished without adding an undue amount of distortion from higher harmonics. The case $N = 2$, with the same first three μ_n's, is shown for comparison.

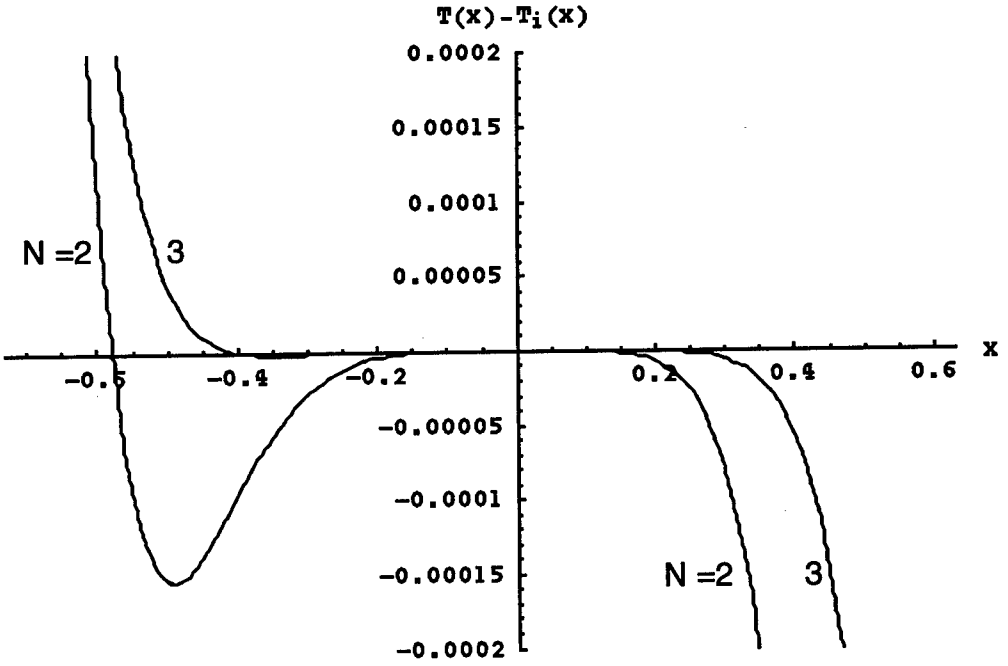

Figure 2: Plot of $T(x) - T_i(x)$, for $N = 2$ and 3.

IV. Amplitude modulator linearization.

4.1. Analog coherent systems. In analog communication systems using coherent detection, the receiver RF voltage is proportional to the envelope of the amplitude of the incident light. For linear operation of the entire system, one would thus like to have a modulator generating output field E proportional to V, i.e. with $t = c + dV = c(1 + x) = t(x)$, where $x = dV/c$. We may use the same procedure as in section II, but now the coefficients of expansion of $t(x)$ are simply $c_0 = c_1 = c$, and $c_p = 0$ for $p > 1$. We need $\mu_0 = 0$, which leads to $\alpha_0 = c_0$, and $\alpha_n = 0$ for $n \geq 1$. β_0 is undetermined, and the number of equations in (8) needs to be reduced by one, by dropping the last one (then elimination of odd harmonics will take place up to the $(N-1)$st). The solution is then similar to that of section II; physically realizable solutions have been found here as well.

4.2. Optical single sideband. In other communication systems, it would be beneficial to have single-sideband (SSB) transmission, possibly without carrier [3]. This cannot be obtained with the previous modulator designs, because they always produce two sidebands. One way to obtain optical SSB is to use two modulators which generate output field E proportional to V, driving them $\pi/2$ out of phase, and combining the outputs. Here we must now show explicitely the time dependence of the modulating voltages. Denoting time by τ, we assume that one modulator is modulated by $V_0 \cos(\Omega\tau)$, and the other one by $V_0 \sin(\Omega\tau)$. The output fields of the two modulators are combined with a $\pi/2$ optical phase shift. Hence the total output field is of the form

$$E_{tot} = E_0 e^{i\omega\tau} \left[dV_0 \cos(\Omega\tau) + idV_0 \sin(\Omega\tau)\right] = E_0 dV_0 e^{i(\omega+\Omega)\tau}, \tag{9}$$

where E_0 is the input field amplitude, and d is a constant. Since the only frequency component is at $(\omega + \Omega)$, a single sideband is generated (and the carrier is suppressed.)

We would thus now like to have a modulator with $t = dV$. We can let $x = V$ to reuse some notations of section III. We now have $c_0 = 0$ and $c_1 = d$. $t_i(x)$ can be generated solely by means of sine functions, and their weights determined from Eq.(8); the β_n's are obtained as in 4.1.

We define the modulation slope S as

$$S = \left[\frac{dt_i(x)}{dx}\right]_{x=0} = d\sum_{n=1}^{N} \beta_n \mu_n = d. \tag{10}$$

When there is a single term in the series, it can be implemented efficiently by an MZI with identical electrodes in the two arms, driven by V and $-V$. Assuming that the 1X2 and 2X1 couplers are symmetric and have no excess loss, we have $\beta_1 = 1$. The phases can be adjusted so that t_i is of the form

$$t_i = \frac{-i}{2}\left(e^{i\nu_1 V} - e^{-i\nu_1 V}\right) = \sin(\nu_1 V) = \sin(\mu_1 x). \tag{11}$$

The modulation slope for this MZI is $S_1 = \frac{dt_i}{dx} = \mu_1$. This can serve as a basis for comparison for other structures.

Generally d is not known at the outset. We note, however, that the β_n's are proportional to d (Eq.(8)), and this indicates that we can then proceed as follows to optimize d. We first assume an arbitrary value for d, which is $d' = 1$, and solve for the resulting values of the β'_n's. We then impose an additional condition corresponding to lossless couplers, namely $\sum_{n=1}^{N} |\beta_n| = 1$, which is ideal from an optical standpoint. We then let $d = d'/C = 1/C$, where $C = \sum_{n=1}^{N} |\beta'_n|$; this leads to $\beta_n = \beta'_n/C$, which now satisfy the additional condition. S is then simply equal to $d = 1/C$.

As an example, we have done this explicitely for $N = 4$, and $\{\mu_1, \mu_2, \mu_3, \mu_4\} = \{1, 3, 5, 7\}$. For $d' = 1$, we find that: $\beta'_1 = 1.196$; $\beta'_2 = -0.0797$; $\beta'_3 = 0.00957$, $\beta'_4 = -0.00069$. This leads to: $C = 1.286$, $\beta_1 = 0.930$; $\beta_2 = -0.062$; $\beta_3 = 0.00744$; $\beta_4 = -0.00054$. The fact that the β_n's decrease approximately in exponential fashion indicates that the required $1X4$ splitter could be made by connecting in series 1X2 couplers with nearly the same coupling fraction, which would make implementation practical.

We find that $d = 1/C = 0.777$. This indicates that the modulation slope of this linearized modulator is somewhat smaller than that of the basic MZI (which would be 1 here). In fact it can be shown that this is a tradeoff inherent in the linearization scheme.

V. Conclusion.

We have introduced a novel family of interferometric modulators, in which M parallel waves travelling between a $1XM$ splitter and an $MX1$ combiner are independently phase modulated by a voltage V. We have shown that, because of the many degrees of freedom of the system, it is possible to choose some of them in such a way as to approximate a desired modulation characteristic. In particular, we have shown that an intensity or amplitude modulator can always be linearized to arbitrary order if the phase modulation depth in each arm is given. This work is theoretical, and does not include important practical considerations about stability, dynamic range, and maximum modulation voltages, which will impose other constraints, and ultimately determine the extent to which these ideas may be useful in practice.

References

[1] Y. Wang-Bulic, "A Linearized Optical Modulator for Reducing Third-Order Intermodulation Distortion," J. Lightwave Technol. **10**, p. 1066 (1992).

[2] W. K. Burns, "Linearized Optical Modulator with Fifth-Order Correction," J. Lightwave Technol. **13**, p. 1724 (1995).

[3] M. Y. Frankel and R. D. Esman, "Optical Single-Sideband Suppressed-Carrier Modulator for Wide-Band Signal Processing," J. Lightwave Technol. **16**, p. 859 (1998).

SEAMLESS INTEGRATION OF FIBER OPTIC NETWORKS AND MILLIMETER-WAVE WIRELESS ACCESS USING NONLINEAR PHOTO-DETECTION SCHEME

M. Tsuchiya, T. Hoshida* and K. Nishikawa
Department of Electronic Engineering, Univ. of Tokyo
Hongo 7-3-1, Tokyo 113-8656, Japan
*presently with Fujitsu Laboratories

Abstract

It would be attractive if the functionality of millimeter-wave (mm-wave) wireless transmitters could be integrated in an existing fiber optic access network for signal transmission of baseband and/or intermediate frequencies. It would be further desired if one were able to utilize the optical signals in the network without any O/E or E/O conversions. We have pointed out that such seamless integration of mm-wave wireless accessibility to a fiber optic system can be implemented by the mm-wave photonic methods such as the optical feeding technique of mm-wave signals from distant local oscillators and the optoelectronic mixing technique at the photo-detection stage in an antenna base station. Furthermore, we have proposed and demonstrated experimentally that the requirement on the base station components for the seamless integration can be drastically relaxed by employing a novel optoelectronic mixing technique called as nonlinear photo-detection.

First of all, let us consider possible modes of optical links in a mm-wave wireless system. Figure 1 shows a schematic illustration of general architecture of a mm-wave wireless apparatus, which consists of four basic elements: signal processing circuits at baseband and/or intermediate frequencies (IF), a mm-wave local oscillator (LO), mm-wave front-end including amplifiers and an antenna, and a mm-wave mixer. There are three kinds of connections between the mm-wave mixer and one of the other three. Use of a fiber-optic link to each of those connections leads to specific advantages from mm-wave photonics point of view. For instance, a low-loss fiber-optic link at the mm-wave connection between the mixer and the mm-wave front-end (denoted as Link-A in Fig. 1) makes it possible to separate an antenna base station from other components than a mm-wave front-end and therefore has been one of the most well known concept in mm-wave photonics [1].

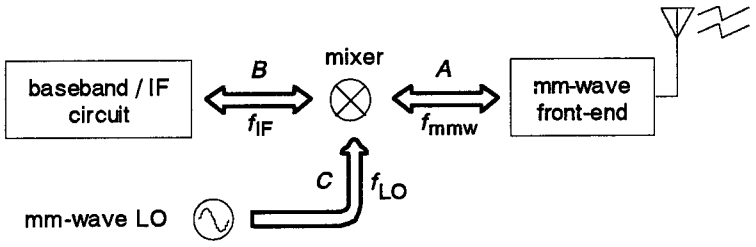

Fig. 1 General architecture of a mm-wave wireless apparatus. Connections A, B and C handle modulated mm-waves wireless signals, IF signals, and a mm-wave LO signal, respectively.

One should note here that a fiber-optic link for the connection between the mixer and the signal source (denoted as Link-B in Fig. 1) offers an interesting possibility: seamless integration of a mm-wave wireless transmitter and/or receiver to an existing fiber optic network. Here, the considerable candidates for such networks are CATV, telephone, local area networks, and so on. The seamless integration is possible, especially in the cases of down links, since the optical IF band and/or baseband signals used in the fiber optic network can be fed directly to the mm-wave mixer in Fig. 1 without

0-7803-4936-9/98/$10.00

employing any additional O/E or E/O conversions.

Figure 2 shows schematically, as an example, a concept of coax-wireless-hybrid fiber optic CATV system. Here, the mm-wave wireless access functionality is attached to a conventional fiber-optic CATV network. The wireless accessibility thus provided is beneficial for some specific customers who are suffering from difficulties in construction of wired access or prefer mobile access. This architecture, however, could be improved in terms of complexity and cost of antenna base station hardware if another fiber-optic link (Link-C) were applied to the system [2,3]. Otherwise, the connection between the mixer and the LO are still electrical and a mm-wave local oscillator and a mm-wave mixer are required at each antenna base station, resulting in the complexity and high cost.

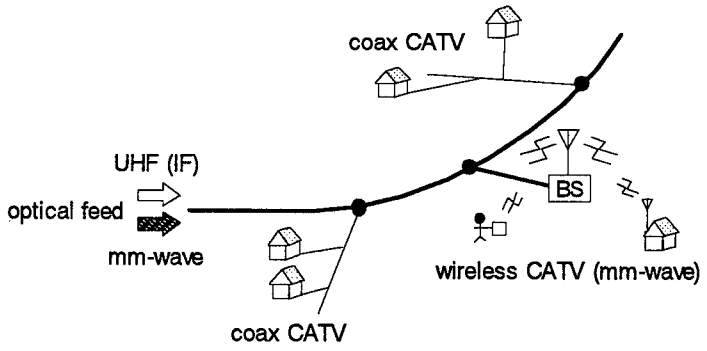

Fig. 2 A concept of coax-wireless-hybrid fiber optic CATV system where mm-wave wireless access capability is added to an ordinary fiber-optic CATV network. Thick solid lines indicate fiber optic links while think solid lines are coaxial cables. UHF and mm-wave LO signals are optically fed from a central office. One can make the system fiber-chromatic-dispersion-tolerant by taking advantages of the hybrid-type optical mm-wave link.

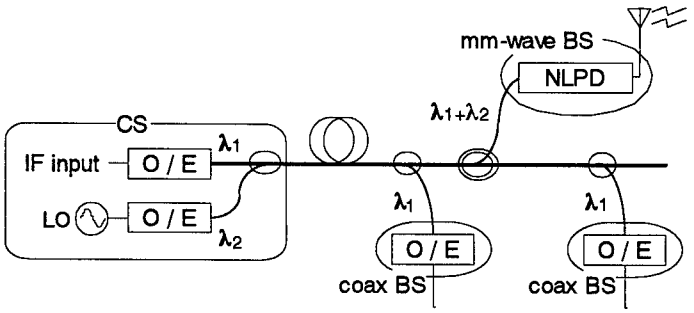

Fig. 3 Schematic diagram of a coax-wireless-hybrid fiber optic CATV system employing the nonlinear photo-detection scheme. The tow color optical carriers are utilized to feed optical IF and mm-wave LO signals.

Through Link-C the mm-wave LO signal is optically delivered from the central station. The two parallel links can be confined into a single optical fiber by taking advantage of the wavelength division multiplexing technique. The assembly of mm-wave local oscillators at the central station provides not only the simplification of antenna base station hardware but also flexibility of the system: the mm-wave carrier frequency can be re-allocated rather easily without any change in the antenna base station hardware, which would be difficult if a local oscillator were fixed at each antenna site.

In addition, we would like to point out that the proposed system is fairly immune to the fiber chromatic dispersion penalty because of the following reasons. First, the mm-wave bandwidth limitation induced by the fiber chromatic dispersion effect is less serious for Link-C than for Link-A. This is because the bandwidth of LO signal is much smaller than those of mm-wave signals modulated by IF or baseband signals [4]. Second, the chromatic dispersion penalty can be even eliminated if one delivers the LO signal in the form of two-mode optical signal. Such optical two mode signals can be generated, for instance, by the optical suppressed carrier modulation method [5]. Third, regarding Link-B, the fiber chromatic dispersion has much less influence because the signal frequency (IF) is much lower.

In the most straightforward method for such dual-optical-feeding scheme, however, one needs two optical connections between two optical fiber outlets and two photo-detectors as well as two mm-wave connections between the photo-detectors and a mm-wave mixer. These many couplings cause much loss and keep an antenna base station still sophisticated and expensive. We have proposed and demonstrated previously [6,7] a method where a single photo-diode under low-bias conditions serves as an O/E converter and an optoelectronic mixer simultaneously. We have called it as nonlinear photo-detection (NLPD) scheme for the optoelectronic mm-wave mixing. One expects that by the NLPD scheme an antenna base station can be drastically simplified and therefore the whole system, too. Figure 3 shows a schematic diagram of a coax-wireless-hybrid fiber optic CATV system employing the NLPD scheme.

A feasibility of such a hybrid fiber-wireless system was validated experimentally as follows. The setup for the experiments is shown in Fig. 4. The optical IF signal was generated by driving a distributed feedback laser diode (λ = 1552 nm) with an electrical 700 MHz IF signal modulated by a baseband signal encoded into 156 Mbit/s BPSK format. The mm-wave signal (58 GHz) was prepared by the optical suppressed carrier modulation method with conjunction of a cw laser diode (λ = 1564 nm) and a $LiNbO_3$ Mach-Zehnder modulator. The two optical wavelengths were set apart to avoid beat noise generation. Those two optical signals were combined by an optical coupler, transmitted through a non-dispersion-shifted fiber link, and fed to a waveguide photo-diode. The photo-diode was biased so that the nonlinearity was enhanced while the high speed response was maintained properly [6,7]. The electrical mm-wave signal thus generated was amplified and emitted through a V-band horn antenna with a 25 dB gain into the free space. A mm-wave receiver was constructed by using another horn antenna and a homodyne demodulator. The baseband signal obtained by the receiver was coupled into a sampling oscilloscope for eye diagram measurement or into an error detector for bit error rate evaluation.

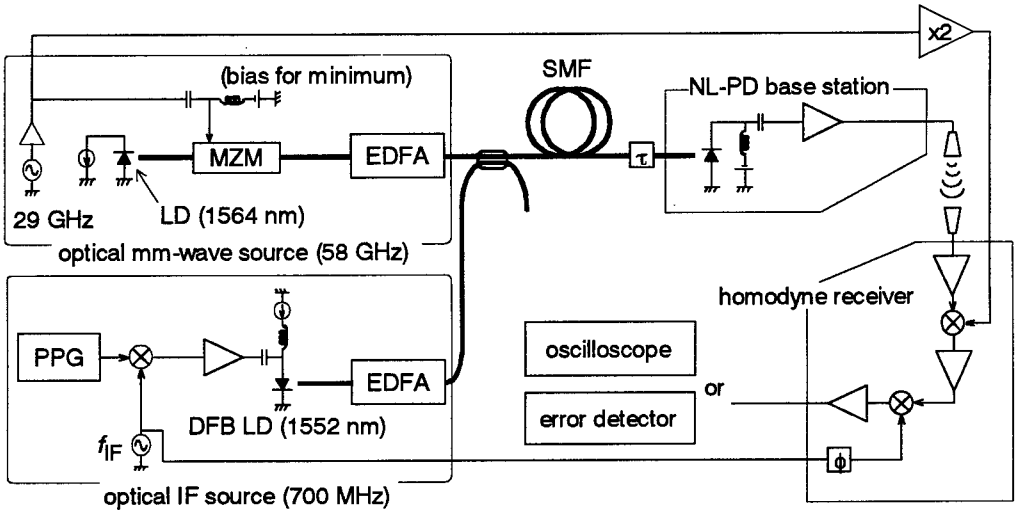

Fig. 4 Experimental setup for fiber-optic / mm-wave wireless digital transmission.

Figures 5 show eye diagrams obtained after transmission over (a) a 0-km link and (b) a 30-km fiber link, respectively, under a condition where the mm-wave path was back-to-back. Clear eye opening indicates that the data was transmitted with negligible error rate. It should be noted here that successful transmission over a 30-km non-dispersion-shifted fiber for mm-wave frequencies around 60 GHz has been achieved, which is rather difficult by a normal optical mm-wave photonic link configuration employing a double side band optical intensity modulator and an ordinary photo-detector because of the fiber chromatic dispersion effect. The transmission bandwidth was confirmed up to IF of 1.7 GHz, which was limited by the bandwidth of IF amplifier, indicating the broadband nature of the NL-PD scheme.

Furthermore, an error-free operation was successfully demonstrated for a 3-m free-space wireless link. What is interesting here is that the error-free transmission was achieved for a photo-diode bias of 0 V where a bias source is not necessary. Although a power amplifier was used in the base station at the present stage as shown in Fig. 4, it would be possible to eliminate it and make the antenna base station passive [8], free from any electric supply in other words, if the nonlinear photodetector could be operated at higher power levels. It would be a subject to be studied in the future.

In summary, we have proposed a novel millimeter-wave wireless access scheme employing a millimeter-wave photonic

technique called nonlinear photo-detection scheme. In the framework of this method, the functionality of millimeter-wave wireless down link is easily attached to existing baseband or intermediate frequencies fiber optic networks. Furthermore, wireless feed of 156 Mbit/s BPSK data on 58 GHz carrier has been successfully demonstrated as a preliminary feasibility study of the concept of seamless attachment of mm-wave wireless accessibility.

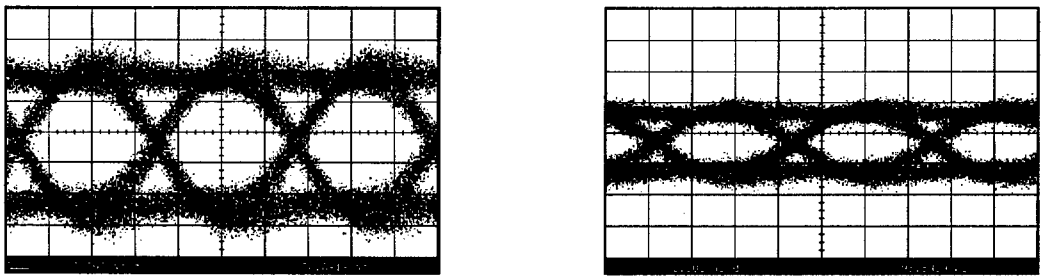

(a) (b)

Fig. 5 Eye diagrams for 156 Mbps digital signals of BPSK format obtained after transmission over (a) 0-km optical link and (b) 30-km non-dispersion-shifted fiber link. Millimeter-wave path was back-to-back for the both cases. Optical power of mm-wave and IF signals were 1 and 0.5 mW, respectively. The bias voltage of photo-diode was 0 V. Vertical axis : 500 mV/div.

Acknowledgment

The authors would like to thank Prof. Kamiya of Univ. of Tokyo for his encouragement.

References

1. For instance, J. O'Reilly and P. Lane: Remote delivery of video services using mm-wave and optics, IEEE J. Lightwave Technol., **12**, pp.369-375 (1994).
2. H. Ogawa and Y. Kamiya: Fiber-optic microwave transmission using harmonic laser mixing, optoelectronic mixing, and optically pumped mixing, IEEE Trans. Microwave Theory Tech., **39**, pp. 2045-2051 (1991).
3. L. Noel, D Marcenac and D. Wake: 120 Mbit/s QPSK radio-fibre transmission over 100 km of standard fibre at 60 GHz using a master/slave injection-locked DFB laser source, Electron. Lett., **32**, pp. 1895-1897 (1996).
4. Note that the fiber chromatic dispersion effect is two-fold: periodic variation of transmitted signal intensity appears as functions of (a) transmission distance as well as (b) carrier frequency. The discussion on the chromatic dispersion penalty in the manuscript is based on the latter aspect.
5. H. Schmuck : Comparison of optical millimetre-wave system concepts with regard to chromatic dispersion, Electron. Lett., **31**, pp. 1848-1849 (1995).
6. T. Hoshida, M. Tsuchiya and T. Kamiya: Millimeter-wave upconversion by nonliner-photodetection using a carrier generated from a remote mode-locked semiconductor laser, Technical Digest of International Topical Meeting on Microwave Photonics (MWP'97), Duisburg, 1997, **FR1-3**, pp.197-200 (1997).
7. T. Hoshida and M. Tsuchiya: Broadband millimeter-wave upconversion by nonlinear photo-detection using a waveguide p-i-n photodiode, IEEE Photonics Technol. Lett., **10**, pp. 860-862 (1998).
8. D. Wake, D. Johansson and D. G. Moodie: Passive picocell - a new concept in wireless network infrastructure, Electron. Lett., **33**, pp. 404-406 (1997).

P8

SENSITIVITY ANALYSIS OF OPTICAL SSB GENERATION USING A DUAL-ELECTRODE MACH-ZEHNDER MODULATOR

A. Nirmalathas, G. H. Smith, and D. Novak

Australian Photonics Cooperative Research Centre, Photonics Research Laboratory
Department of Electrical and Electronic Engineering,
The University of Melbourne, Parkville VIC 3052, Australia.
Tel: + 61 3 9344 4936, Fax: + 61 3 9344 6678,
Email: a.nirmalathas@ee.mu.oz.au

ABSTRACT:

Data transmission in a mm-wave optical link incorporating optical SSB modulation via a dual-electrode modulator, has been modeled. Simulations of received eye-diagrams show that the SSB generator is tolerant to errors in phase and power level of the drive signals: ± 5 ° and 3 dB respectively.

I. Introduction

Wireless systems operating at millimeter-wave (mm-wave) frequencies have attracted much interest as a means of providing broadband access for future multimedia applications. Optical fiber has emerged as the ideal medium for the distribution of the mm-wave radio signals, from a central exchange to the remote antenna base stations. The simplest technique for the transmission of data at mm-wave frequencies for such fiber radio systems is a direct-detection scheme incorporating an external modulator. However, the transportation of such a signal over optical fiber can lead to complete cancellation of the detected rf power after the fiber link. This occurs due to the optical modulation side-bands experiencing different amounts of phase delay as a result of fiber chromatic dispersion. The resulting degradation of the carrier-to-noise ratio (CNR) severely limits the achievable fiber link distance in mm-wave fiber radio systems [1,2].

Optical single side-band (OSSB) with carrier modulation can significantly reduce the effect of fiber dispersion [3]. We have demonstrated a simple technique for the generation of OSSB modulation which employs a dual-electrode Mach-Zehnder modulator (MZM). When this modulator is biased at quadrature with two rf signals applied to the electrodes which are equal in power and 90° out of phase, we have shown that one optical side-band can be suppressed. The modulation scheme can be used to transport mm-wave optical signals over fiber lengths > 50 km [2].

In order to achieve very good suppression of the unwanted optical side-band in our OSSB generator, the power differences between the electrical drive signals or any phase shift away from the required 90°, should be minimized. When the unwanted side-band is only partially suppressed, the detected rf power will vary as a function of fiber length, causing a reduction in the achievable CNR. In this paper, we present a detailed investigation of the sensitivity of the OSSB generation scheme to variations in the drive conditions of the modulator. An optical mm-wave transmission link employing this modulation scheme has been modeled and the effect of phase and rf power level differences in the driving conditions of the modulator, is investigated. In particular we consider the effect of these errors on the recovered data after the fiber link.

II. OSSB Generator Model and Simulations

Fig. 1 shows a schematic of the OSSB generator employing a dual-electrode MZM. The transfer function of the MZM is given by Eqn. 1, where E_{in} is the optical input signal and E_{out} is the output optical signal from the MZM. The input voltages applied to the rf ports (V_1 and V_2) are normalized with respect to V_π, the switching voltage of the MZM.

$$E_{out}(t) = E_{in}(t)\left[e^{j\frac{\pi V_1(t)}{2}} - e^{j\frac{\pi V_2(t)}{2}}\right] \quad \ldots (1)$$

0-7803-4936-9/98/$10.00

A 155 Mb/s BPSK data signal was imposed on a 38 GHz rf carrier. The input signals to the MZM can be expressed as:

$$V_1(t) = \frac{1}{2} + \frac{A}{2}\cos\left(\omega_{rf} t + \theta + \Delta\theta + m(t)\right)$$
$$V_2(t) = \frac{1}{2}\cos\left(\omega_{rf} t + m(t)\right) \quad \ldots (2)$$

where *m(t)* corresponds to the BPSK data modulation. The data modulation is used to study the effect of variations in rf power and phase difference of the two MZM drive signals, on the recovered data eye-opening. In order to suppress the lower optical modulation side-band, the phase between the two mm-wave signals was set to 90°. To investigate possible phase differences between the applied drive signals, a phase deviation from this condition, $\Delta\theta$ in Eqn. 2, was varied from -90° to +90°. To simulate possible differences in the power levels of the two applied signals, an attenuator was placed in one of the arms ($A=1$ for equal amplitudes).

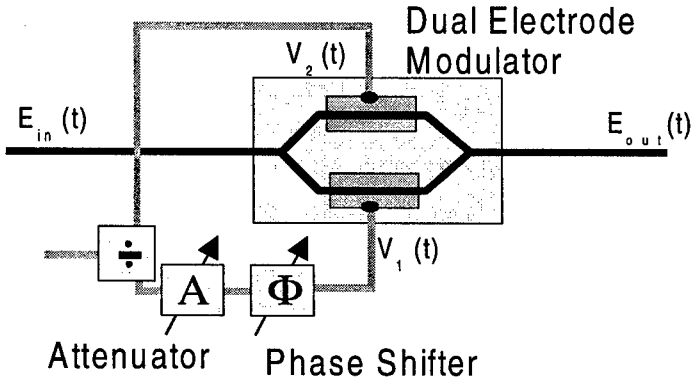

Figure 1: Schematic of the OSSB generator

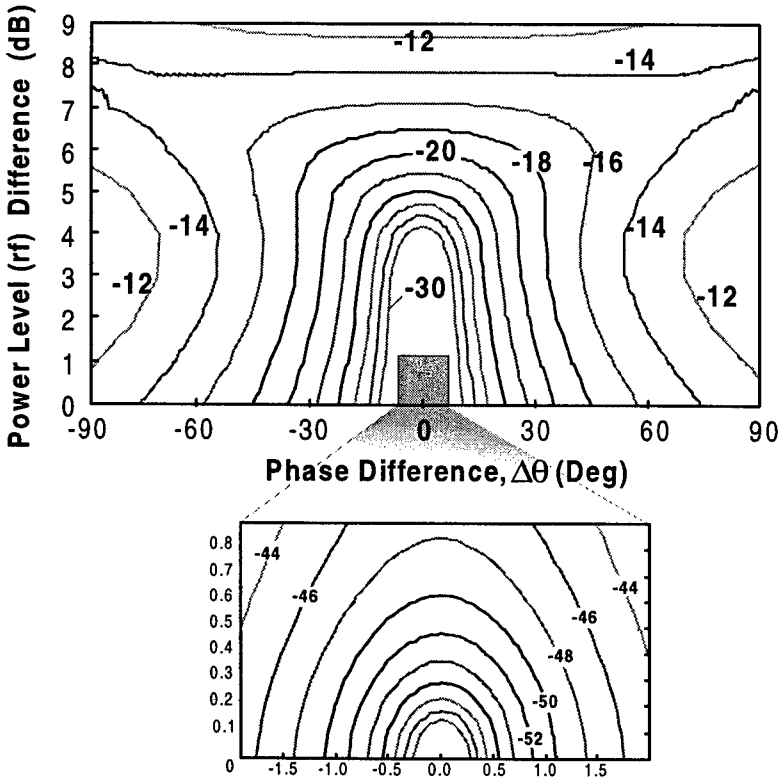

Figure 2: Contour plots of lower side-band suppression as a function of differences in rf power level and phase between the two signals applied to the MZM.

The effect of power level and phase variations on the suppression of the unwanted optical side-band was first investigated. The side-band suppression is defined as the ratio of optical power in the unwanted side-band relative to the optical carrier power level. At the ideal operating conditions of equal drive levels and 90° phase shift, the lower optical side-band is perfectly suppressed (> 250 dB). Fig. 2 shows the contours of the lower side-band suppression ratio from -30 dB to -12 dB in steps of 2 dB, as a function of differences in power levels and phase shift of the MZM drive signals. The close-in view of the most sensitive region is shown below the main curve. When the phase and power levels deviate from the optimum conditions, the suppression reduces rapidly. However, it can be seen that good suppression ratios in excess of -30 dB, can be realized for phase errors of ± 5° and rf power level differences of ± 3 dB. The power in the required (upper) optical side-band is also affected by errors in phase and rf power levels, as shown in Fig. 3. In fact, when the power level difference is 3 dB, the upper side-band optical power is increased by 2.4 dB, while still sustaining good suppression (~40 dB) of the lower side-band. However, the non-zero MZM chirp that results when the rf drive powers differ [2,4] must also be taken into account. It is envisaged that even with a finite MZM chirp, the 2.4 dB improvement in the wanted side-band may improve the power budget considerably.

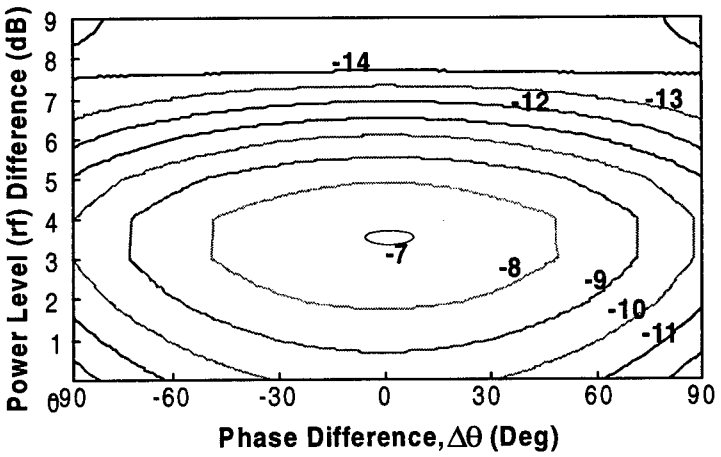

Figure 3: Contour plots of upper side-band suppression as a function of differences in rf power level and phase between the two signals applied to the MZM.

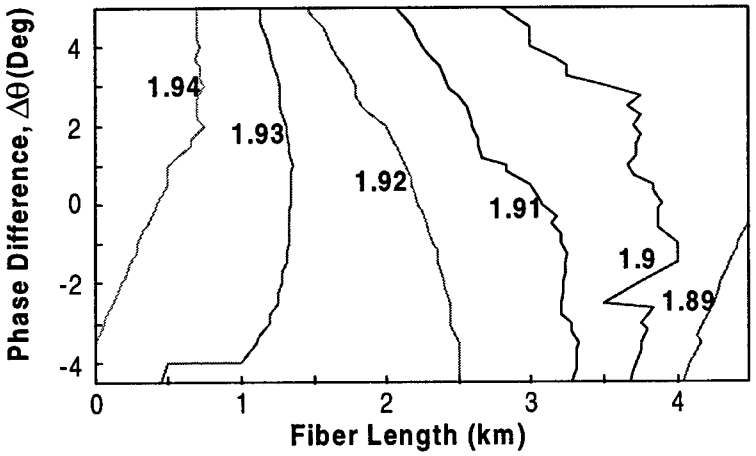

Figure 4: Contour plots of eye-opening as a function of phase difference between the two MZM drive signals and fiber distance (rf power levels of MZM drive signals are equal).

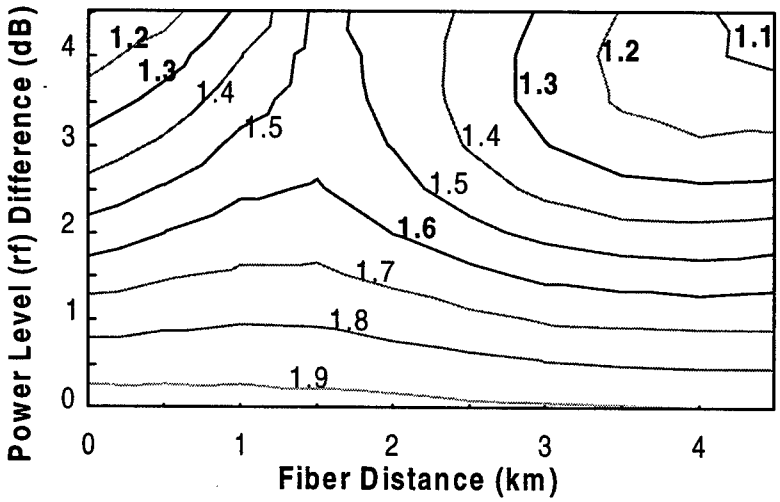

Figure 5: Contour plots of eye-opening as function of rf power level difference between the two MZM drive signals and fiber distance ($\theta = 90°$, $\Delta\theta = 0°$).

The eye-diagram of the received signal was then analyzed as a function of optical fiber length and errors in the MZM drive signals' power levels and phase. Fig. 4 shows contours of the eye-opening (Volts) as a function of phase error and fiber length, when the rf power level difference in the drive signals was kept at zero. It can be seen that at a fixed length of fibre, changes in $\Delta\theta$ of $\pm$ 4.5 cause only a $\pm$ 5.2% change in the eye-opening of the received signal. Fig. 5 shows the same eye-opening contours but as a function of rf power level difference when the phase error was set at zero. For any fixed power level difference, the eye-opening of the received signal is improved for certain lengths of fiber, confirming the interplay between MZM chirp and increased optical power in the wanted side-band. It should be noted that for a fiber length of 2.5 km with dispersion parameter of D = 17ps/nm/km, a conventional intensity modulated link at 38 GHz (double side-band) will experience an rf power loss in excess of 40 dB [2]. The curves in Fig. 4 and 5 confirm that the OSSB technique successfully overcomes the dispersion induced penalty.

III. Conclusion

We have investigated theoretically, the tolerance of an optical SSB signal generator incorporating a dual-electrode MZM, to errors in phase and power levels of the signals driving the MZM. Our simulations of a mm-wave optical link have shown that no appreciable eye-penalty occurs for errors in phase and power level of the drive signals: $\pm$ 5° and 3 dB respectively.

IV. References

[1] Gliese et al., *IEEE Trans. Microwave Theory Tech.*, vol. 44, pp. 1716- 1724, 1995.
[2] Smith et al., *IEEE Trans. Microwave Theory Tech.*, vol. 45, pp. 1410- 1415, 1997.
[3] Park et al., *Electron. Lett.*, vol. 33, pp. 512-513, 1997.
[4] A. Djupsjobacka, *IEEE Photon. Technol. Lett.*, vol. 4, pp. 41-43, 1992.

Fiber To The Air (FTTA) system using optical coherence coded multiplexing scheme

Katsutoshi Tsukamoto, Satoshi Obata and Shozo Komaki
Department of Communications Engineering, Faculty of Engineering, Osaka University
2-1 Yamada-oka, Suita-shi, 565-0871, Japan
Phone +81+6+879-7716, Fax. +81+6+879-7715, Email: tukamoto@comm.eng.osaka-u.ac.jp

1. Introduction

Microwave / Millimeter wave radio access systems using radio on fiber techniques have been extensively studied and developed[1]. These Fiber To The Air (FTTA) systems have many advantage such as the flexibility for radio air interfaces, mobile users accommodating capability, multicast capability and so on compared with conventional wired access systems, FTTH/ FTTC/ FTTB (Fig.1) [2,3]. In the FTTA system employing multiple-sector radio zone or constructed with some radio base stations (RBS) connected to one optic-fiber link, it is required to multiplex some radio signals with different / same frequencies in the fiber link. So this paper proposes Fiber To The Air (FTTA) system using optical coherence coded multiplexing (CCM) scheme which is a kind of code division multiple access operated in optical frequency domain and applied to optical digital transmission system[4]. The scheme can provide the transparent capability for radio frequency and needs no time synchronization between transmitter and receiver. The theoretical analysis of received carrier to noise plus interference ratio shows the improvement on the number of accommodated RBS.

Fig. 1 FTTA system.

2. System Configuration

Figure 2 illustrates the configuration of the reverse link of the CCM-FTTA. A laser light is divided into the signal and the phase reference components, and the former is modulated by the received radio signal and frequency encoded (FE), that is coherence encoded. The phase reference component used at the coherent detector of the receiver, is transmitted over another fiber link, but the two components can be transmitted on a fiber link by use of polarization multiplexing, frequency multiplexing and so on. In the case of multiple sector system in a radio zone, multiple modulators and FEs are equipped at a RBS but needs only one laser. At the receiver of the control station, the signal light is decoded at the FD with its same code as the transmitter and detected together with the reference light by a balanced mixing photodetector (BMPD), then becomes the original radio signal at the output of the BPF. Other signals from other RBSs are also detected and contaminates the desired signal as an interference noise, but their power level are reduced by coherence decoding.

Figure 2 also illustrates the principle and configuration of the FE and FD. The modulated light is divided into several frequency components at the frequency divider. Next the phase of each components is shifted randomly at the phase mask with its P.N. sequence pahse patern. At FE, the correlation between the signal light and the reference light is extremely reduced as the frequency resolution of the phase mask increases. These phase-randomized signal components are gathered again and transmitted to the receiver. The FE needs a broadbandness of the signal light, that is realized by FP-LD, SLD, or pre-moduling with high frequency signal.

Fig. 2 Configuration of the reverse link of the CCM-FTTA.

3. Non-uniform chip width phase mask

To improve the carrier to interference power ratio at the receiver, we should increase the process gain of the CCM by increasing frequency resolution of the FE, but the non-uniform spectrum of the optical carrier limits the sufficient power reduction of interference noises at the output of the BMPD. So we propose the non-uniform chip width phase mask shown in Fig. 3. By use of the FE and FD using the proposed phase mask, all frequency components have the same power , hence those with their randomized phases each other are effectively smoothed out at the output of the BMPD, thereby the CIR is improved.

0-7803-4936-9/98/$10.00

Fig. 3 Non-uniform chip width phase mask

4. Analysis of CINR and discussion

We theoretically analyze the carrier to interference plus noise ratio (CINR). In the analysis, we consider two kinds of the interference noises, one is the interference noise generated from the signal and reference, and another is the cross-interference noise occurred by the interference among the signal of deferent RBSs. We also consider the shot noises, the relative intensity noise of laser and the receiver thermal noise. Figure 4 shows the relation ship between the code length and the CINR. The proposed phase mask improves the CINR compared with the use of the conventional equalized chip-width phase mask and its improvement is increased as the code length increases. Figure 5 shows the number of connectable RBS versus the chip bandwidth. The RBS number is improved as the chip bandwidths decrease, but in the case of that of less than 1GHz, the improvement is saturated because of the additive noise. When 3 sector radio zone (L=3), the proposed phase mask relaxes the required chip bandwidth up to 6 times.

5. Conclusion

Fiber To The Air (FTTA) system using optical coherence coded multiplexing (CCM) scheme with a new type of phase mask has been proposed. The theoretical analysis of CINR shows the improvement on the CINR and the number of accommodated RBS.

Fig. 4 Relationship between code length and CINR.

Fig. 5 Number of connectable RBS vs. chip bandwidth.

References

[1] For example, IEEE Trans. MTT, 45,8 (1997).

[2] S.Komaki, K.Tsukamoto, S. Hara and N.Morinaga, "Proposal of Fiber and Radio Extension Link for Future Personal Communications," Microwave and Optical Technology Letters, vol. 6, no., pp. 55-60, Jan. 1993.

[3] H. Harada, H.J.Lee, S.Komaki, and N. Morinaga, "Performance Analysis of Fiber-optic Millimeter-Wave Band Radio Subscriber Loop", IEICE Trans. on comm., vol.E76-B, no.9, pp1128-1135, Sept.1993.

[4] R. A. Griffin, D. D. Sampson, David A. Jackson, "Coherence Coding for Photonic Code-Division Multiple Access Networks", IEEE J.Lightwave Technol.,Vol.13 No.9, pp.1826-1837. Sep. 1995.

Integrated Optics Photonic Mixer for an All-Optical Implementation of a Millimeter and Sub-millimeter Wave Oscillator

S. Dubovitsky, V. Chuyanov, S. Garner, W. H. Steier

Department of Electrical Engineering

University of Southern California

Los Angeles, CA 90089-0483

The extremely high bandwidth of optical signals that can be transported in small lightweight optical fibers and processed by integrated optics components make photonics well suited for distribution of "RF" radiation. It is logical and desirable to extend photonics to the generation of RF signals. For example, in the gigahertz or tens of gigahertz frequency regime Yao and Maleki have demonstrated an opto-electronic oscillator[1]. However, the frequency range of opto-electronic generation is limited by the response time of the photodetectors and electronic components which are difficult to push beyond few tens of GHz. Another opto-electronic approach better suited for generation of higher frequencies is based on heterodyne generation of RF radiation by beating two laser beams on a very fast photodetector[2]. It is also difficult to extend this approach, because high speed of the photodetectors dictates low efficiency and small size, i.e. low maximum power. Consequently for efficient generation of millimeter and sub-millimeter waves, which are useful for environmental monitoring, astrophysical observations, and secure communications, an all-optical method is highly desirable.

We propose to use an extended electro-optic interaction between the two guided-wave IR beams in a nonlinear optical waveguide as the method for generation of polarization at the difference RF frequency. The electro-optic interaction is fast and the distributed waveguide interaction enables high efficiencies and higher total power. In addition, use of fiberoptics and integrated optics enables local generation of RF beams from the remotely located IR sources.

The design of the proposed optical mixer (Figure 1) is based on a recently demonstrated $LiNbO_3$ wave-coupled electrooptic modulator[3]. Two infrared inputs separated by the sub-mm frequency are coupled into an electro-optic (EO) waveguide. Due to a second order nonlinear interaction ($\chi^{(2)}$) a polarization wave at the difference frequency is induced in the medium. The medium polarization is sensed by the transmission line electrodes and coupled to an array of antennas which in turn radiate the sub-millimeter wave in the phase-matched direction. The radiation patterns of the dipole antennas deposited along the interface of two dielectric half-spaces are directed into the half-space with higher dielectric constant and therefore most of the power goes into the substrate. This precludes use of LiNbO3 for generation of sub-millimeter waves because of its high loss (~60 cm^{-1})[4].

To solve the problem of efficient radiation of the generated waves, we propose to use a different material system: electrooptic thin film polymer waveguide deposited on top of a low loss substrate. In such a system, generation of the polarization is performed by one material, namely thin film electrooptic polymer, but the radiation and propagation of the RF wave are governed by the substrate material, which can now be tailored for low absorption at the RF frequency of interest. RF absorption of the polymer is less important because the RF wave sees only a very short distance(L_s) in the polymer before it is radiated away by the antennas. The geometry of Fig 1 assumes the polymer is poled perpendicular to the plane and therefore the generated polarization is correct to couple into the mode supported by transmission line that delivers power to antenna and rotates the polarization by 90° for more efficient radiation.

Phase matching and terahertz loss(α) are the key factors driving the design of the device. The maximum useful length of each transmission line electrode (L_S) is determined by the minimum of either the coherence length(L_c) or the loss length($1/\alpha$). The coherence length is determined by the velocity mismatch between the infrared waves propagating in the waveguide and the RF wave traveling along the electrodes; $L_c = \lambda_{RF}/(n_{eff}(IR) - n_{eff}(RF)$. The optical velocity is given by the effective index [$n_{eff}(IR)$] of the mode in the optical waveguide, whereas the sub-mm velocity

0-7803-4936-9/98/$10.00

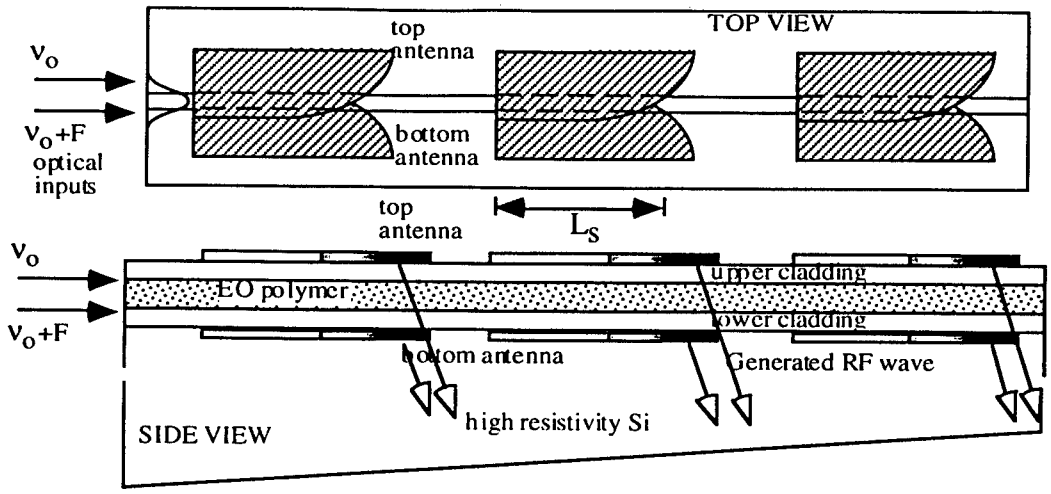

Figure 1. Schematic view of terahertz wave generator.

depends on the effective index [n_{eff}(RF)] of the transmission line mode. Limited data is available on the index of refraction of EO polymers in the sub-millimeter wavelength region but based on our data and extrapolations, we estimate L_c to be between 1mm to 2mm for 2.4 THz. From our measurements and published data we estimate the loss of relevant EO polymers to be in the range of 5 - 7 cm^{-1} [5]

Another important consideration is the spatial overlap between the optical waveguide mode and transmission line mode which determines how well the generated polarization will be picked up by the electrodes. Best overlap is achieved when the electrodes are placed as close to the waveguide as possible without introducing additional optical loss. We will present an analysis for the optimum design.

The efficiency of the electrooptic interaction can be estimated by using a standard parametric amplification analysis[6]. Assuming a 200 mW "pump" from Nd:YAG at ν_o and a tunable "signal" at $\nu=\nu_o$+2.4THz coming from a tunable DFB laser, we can calculate the amount of "idler" generated at 2.4 THz. We base our estimate of the second order nonlinear optical coefficient from measurement of the EO coefficient, r_{33}, since this measurement uses the approximately correct range of frequencies. Assuming r_{33}=30 pm/V, α=5cm^{-1}, L_c = 2 mm we calculate an efficiency of $\eta=1 \times 10^{-3}$ for a 2 cm long device. This is about three orders of magnitude better than photomixers which are severely input-power limited[2]. For every 10 mW of signal at 1.3 μm we generate 10 μW at 2.4 THz. The overall efficiency also depends on how well the antennas radiate the generated power away and how much gets absorbed by the substrate.

We will present measurements of relevant materials properties of candidate EO polymers and a detailed device design and performance estimate based on these properties. The fabrication issues will also be addressed

References

1. X. Steve Yao and Lute Maleki, J. Opt.Soc. Am. B, **13**, 1735, (1995)

2. S. Verghese, K. A. McIntosh and E. R. Brown, IEEE Trans. Microwave Theory Tech., **45**,1301, (1997).

3. W. B. Bridges, F. T. Sheehe and J.H. Schaffner, IEEE Photon. Technol. Lett., 3, 133, (1991)

4.*Handbook of optical constants of solids.*, Academic Press 1985.

5. Ajay Nahata, David H. Auston, Chengjiu Wu and James T Yardley, Appl. Phys. Lett., **67**,1358, (1358), 1995.

6.A.Yariv and P. Yeh, *Optical Waves in Crystals* , John Wiley & Sons, New York, 1984.

LOW CLOSE-TO-CARRIER NOISE SYSTEMS

M Nawaz & T P Young

GEC-Marconi Research Centre (mohammed.nawaz@gecm.com)
GEC-Marconi Research Centre (terry.young@gecm.com)

Abstract: A 100MHz distribution system is described with phase noise 1Hz from carrier around -130dBc rising slightly at 40°C. Far from carrier it saturates at -150dBc. Vibration at 0.24g generate noise spikes around -80dBc.

I. Introduction

Many optical communication systems require the distribution of high fidelity local oscillator signals. Here we report a system to distribute a high quality signal at 60MHz to 100MHz to 10 destinations and report on the basic close to carrier phase noise measurement made. It will be appreciated from the results presented that such links would not degrade even the most high fidelity oscillators.

II. System Design

The system used is shown in figure 1. A 20mW 1550nm Nortel DFB laser with a RIN better than -160dBc/Hz is spliced onto a dual output lithium niobate modulator produced by UTP. The splicing was polarization-maintaining (pm) to pm fibre. Both outputs from the modulator were used, since the absolute phase of the rf signal was unimportant. Each output from the modulator went into a 1:6 splitter (single mode, no polarization control). The loss of each link and channel through the system was optimized by hand to get the best uniformity across all 10 outputs. The remaining 2 channels were used for housekeeping and calibration.

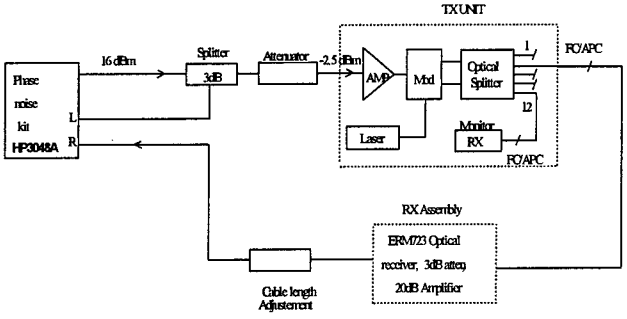

Figure 1: Basic Link Layout

The optical receiver (Epitaxx ERM 723) uses a high saturation photodiode, low noise linear amplifier followed by a 75Ω matching transformer. The output of the receiver is matched to 50Ω and further amplified. The single-mode fibre cable was of the loose construction type (BRUGG Telcom) filled with gel which should reduce the effects of vibration on the link.

Since the phase noise specification was one of the most important aspects of this system, care was taken to minimise noise at all stages of the design. Electrically, this meant ensuring low return loss into the preamplifier, into the modulator, at the receiver output and also providing low noise and stable power supplies. These issues were addressed at the design stage and considerable care was taken to assemble the precise combination of components reported. Optically, designing for low phase noise meant using low loss FC/APC connectors to minimize interface reflections. Care was also taken to select devices with bevelled or angle fibre coupling.

III. Phase Noise and Environmental Measurements

The phase noise measurements were performed using the HP3048A phase noise equipment. Figure 2 shows the transmitter and receiver units with 2.8km of fibre between them. Measurements have been taken at both 60MHz and 100MHz. The effect beyond 1kHz is simply an artefact of the delay in one arm of the phase noise measuring kit. The spike at 4Hz was not reproducible, most of the rest appear to be mains pick-up.

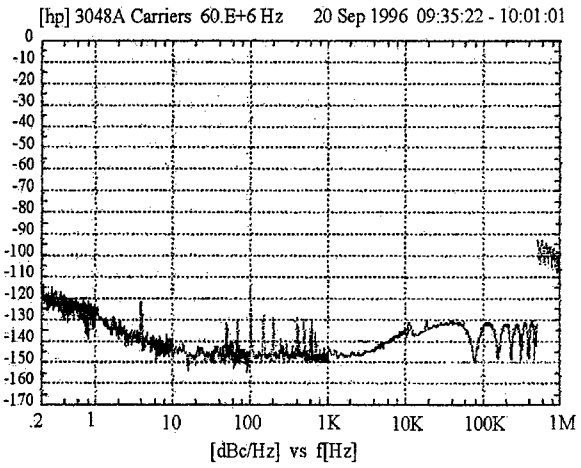

Figure 2: Phase Noise with 2.8km fibre length (60MHz)

0-7803-4936-9/98/$10.00 © 1998 IEEE

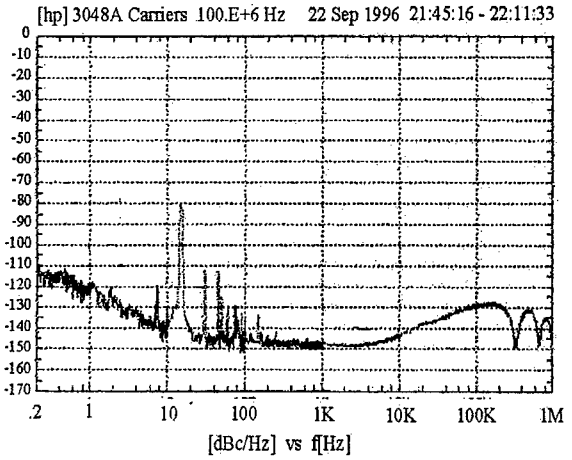

Figure 3: Phase noise: fibre vibrated at 0.24g at 15Hz

The link system with 600m of cable was put on a vibration table: firstly just the fibre was vibrated sinusoidally at 0.24g, then the transmitter assembly. The results at 100MHz are shown in figures 3 & 4 respectively for a 15Hz excitation

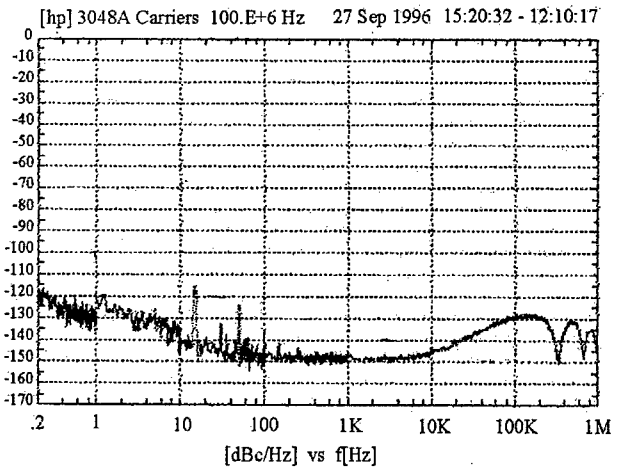

Figure 4: Phase noise: Transmitter vibrated at 0.24g at 15Hz

A rise of the noise floor in the environmental chamber used for these measurements was observed even without the vibration and this is attributed to a higher electrically noisy environment. This effect is shown in figure 5 (with the transmitter and receiver essentially back to back).

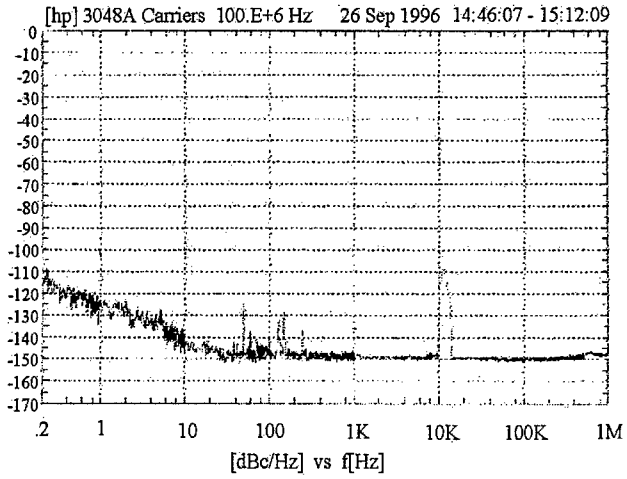

Figure 5: Phase noise measured in environmental chamber (room temperature, no vibration).

When the 600m of fibre was vibrated, peaks were seen at the fundamental vibration frequency and its harmonics. Levels as high as 60dB with respect to the noise floor are observed. This result was extremal and the measurement was frequency dependent. At 25Hz, for instance, the spike was <40dB high and it may be that a degree of mechanical resonance is being observed here. These preliminary results are hard to interpret, especially since the mechanical transfer function of the vibration stage and the fibre coil have not been characterized. However, the encouraging news is that the phase noise remains below -80dBc under worst conditions, remaining generally better than -100dBc. Clearly, the results will improve with shorter link lengths.

Figure 4 shows the transmitter alone being vibrated at 15Hz with a spike ~25dB high appearing (i.e. phase noise at -115dBc). This is an excellent result.

The temperature of the fibre was also varied. The close-to-carrier noise floor generally rose with rising temperature. These measurements were quite difficult to take because the phase variation with expanding fibre made it hard to keep the measurement kit in lock for the duration of the measurements. Figure 6 shows a result taken at 40°.

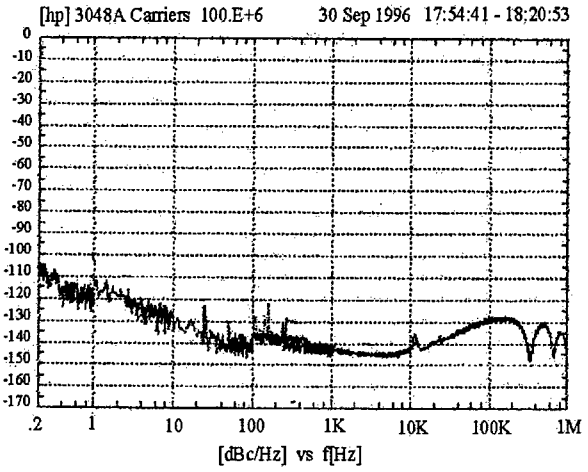

Figure 6: Phase noise for fibre heated to 40°C

Although the noise floor has risen by ~10dB in the 1Hz to 10Hz interval, it is hard to know how much is due to locking instabilities in the noise kit. A fuller experiment with two sets of coils to take out the delay changes is needed to be precise. However, over a temperate range from -20° to +40°, the noise floor never rose above -125dBc at 10Hz from carrier.

IV. Conclusions

Very low close-to-carrier phase noise results have been obtained on a 2.6km fibre link operating from 60MHz to 100MHz. This low noise has been obtained by using good electrical matching, low noise linear amplifiers and very low optical reflections at all interfaces. The gel-filled fibre cable design minimizes vibration induced noise.

The quality of phase noise suppression achieved through careful electrical and optical design means that the link has a much better characteristic than most sources in this range and will certainly not be the limiting noise source in distributing high quality signals.

The techniques used here are applicable to much higher frequencies and there is no reason why this level of phase noise should not be achieved in, for instance 10GHz systems, given careful design and selection of components. However, the CATV market which has produced such high quality components at low frequencies does not currently exist at higher frequencies and receivers, in particular, might have to be designed from scratch.

The thermal and vibration results are both interesting and reassuring. The vibration levels are much higher than one would observe for any fixed infrastructure (barring earthquakes) and bode well for mobile and airborne systems. Clearly more measurements are needed in this area, but the quality of off-the-shelf equipment is already capable of producing excellent results.

Acknowledgments

This research was sponsored by the Jindalee Over-the-Horizon Radar Network Project. We thank them for permission to publish.

Large Area, High Speed Phototube with a GaAsP Photocathode and GaAs Metal-Semiconductor-Metal Anode

Tamera A. Yost, Peter R. Herczfeld
Drexel University, Center for Microwave and Lightwave Engineering, Philadelphia, PA 19104

Vincent M. Contarino
Naval Air Warfare Center Aircraft Division, 22349 Cedar Point Rd., Patuxent River, MD 20670-5304

Abstract

This paper concerns the development of a large area (8 mm diameter), high speed (3 GHz) phototube with gain (170 Amps/watt) with applications in hybrid lidar-radar, free space optical communications and medical imaging.

0-7803-4936-9/98/$10.00

Introduction

This paper concerns the development of a large area, high speed, and high gain photodetector for use in the newly developing hybrid lidar-radar, free space optical communication, and medical imaging technologies. In particular, the lidar-radar system produces a blue-green optical pulse with a 3 GHz microwave envelope to significantly improve target contrast [1]. These technologies have clearly expressed a need for photodetectors that perform above and beyond those available today, such as avalanche photodiodes and photomultiplier tubes. Although these devices provide the needed large active area of cm^2 and gain of > 100, they are limited to a bandwidth of less than 1 GHz. The most promising device, the intensified photodiode or IPD shown in Figure 1, provides the large area and gain, but is limited in bandwidth to 2 GHz by virtue of the anode which is a vertical structure Schottky diode [2]. To achieve proper focusing of the incident electron beam diameter of 200 μm, the anode device must also have a large active area. To overcome the speed limitations of the vertical structure, the Schottky diode anode was replaced with a lateral interdigital metal-semiconductor-metal (MSM) device that allows higher speed while maintaining the large area. In this application, the MSM is bombarded by a beam of energetic electrons, which is the first known use of an MSM as an electron detector. Analysis of the gain and bandwidth of the IPD is presented where both the GaAsP photocathode thickness and the GaAs interdigital metal-semiconductor-metal device anode dimensions are optimized to provide a gain of a > 1000 and bandwidth of several gigahertz.

The commercially available IPD consists of an 8 mm diameter circular GaAsP photocathode, an electron focusing and accelerating assembly, and a GaAs Schottky diode as the anode as shown in Figure 1. Incident photons strike the surface of the GaAsP photocathode, the emitted beam of photoelectrons is accelerated by a kilovolt potential and focused to the anode by two electrostatic rings. An electron gain of greater than 10^3 is achieved via impact ionization of the semiconductor lattice of the anode.

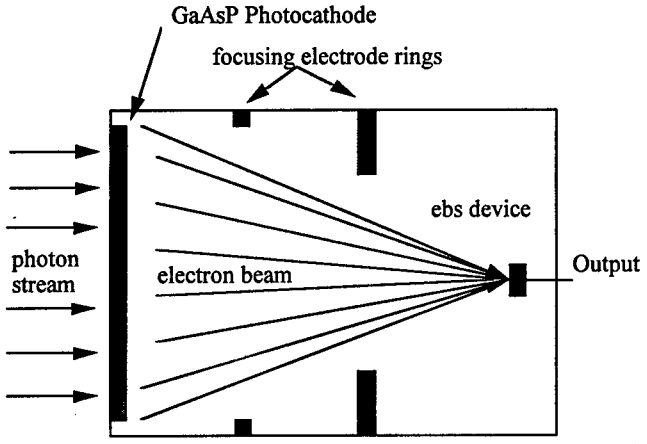

Figure 1. Block Diagram of Intensified Photodiode (IPD)

In considering the gain and bandwidth of the IPD, the thickness of the photocathode and the physical geometry of the MSM anode were optimized. The 8 mm diameter transmission mode photocathode exhibits quantum efficiencies greater than 40% and consists of a 0.6-1.0 μm $GaAs_{0.7}P_{0.3}$ active layer, a 500 angstrom AlGaAsP layer, and a Si_3N_4 quarter-wave anti-reflection

coating optimized for peak transmission at 550 nm [3]. An optimized 0.6 μm active layer maintains a quantum efficiency of > 35% while providing a bandwidth of approximately 10 GHz. The total area of the MSM was fixed at 300 μm^2 and the dimensions of the interdigital electrodes were optimized to achieve maximum bandwidth. It should be noted that for the MSM as an electron detector, carriers are generated not only in regions between the electrodes but also beneath them, which affects the gain and bandwidth. Therefore, a novel current transport model was developed to account for these additional carriers. For an MSM with an interdigital electrode thickness of 650 angstroms of titanium, electrode spacing of 5 μm and width of 4 μm, biased at 15 V, the model predicts an electron gain of 1150 for an incident electron beam energy of 8000 eV. The bandwidth of the MSM under the same conditions is simulated to be 3.1 GHz as shown in Figure 2, where the bandwidth is determined by the frequency at which the output current response has dropped to $1/\sqrt{2}$ (0.707) of the maximum.

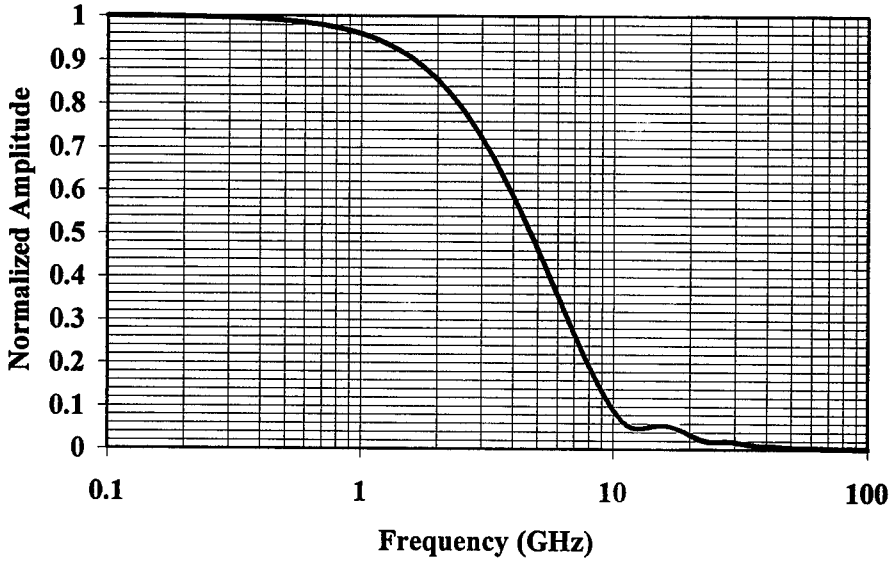

Figure 2. MSM Electron Detector Bandwidth

Conclusion

A photocathode thickness of 0.6 μm provides a quantum efficiency of > 35% while not limiting the IPD bandwidth. A bandwidth of 3.1 GHz and electron gain of 1150 can be achieved for an interdigital MSM with an electrode thickness of 650 angstroms of titanium, electrode spacing of 5 μm and width of 4 μm. The optimization of the photocathode and MSM anode predict an IPD responsivity of 170 A/W with a bandwidth of 3.1 GHz. The paper will discuss the design, fabrication, and evaluation of the large area, high speed and gain photodetector.

References

[1] Mullen, L.J.; Vieira, A.J.C.; Herczfeld, P.R.; Contarino, V.M, *IEEE Transactions on Microwave Theory and Techniques*, vol. 43, no. 9, pp. 2370-2377, Sept. 1995.

[2] LaRue, R.A.; Edgecumbe, J.P.; Davis, G.A.; Gospe, S.; Aebi, V., *SPIE Proceedings on Photodetectors and Power Meters*, vol. 2022, pp. 64-73, June 1993.

[3] Edgecumbe, J.P.; Aebi, V.W.; Davis, G.A, *SPIE Intl. Symp. On Electron Tubes and Image Intensifiers*, vol.1655, pp. 204-210, Feb. 1992.

OPTICAL SINGLE-SIDEBAND MODULATION WITH DELAY PRE-DISTORTION FOR FIBER-RADIO APPLICATIONS

R. A. Griffin, P. M. Lane and J. J. O'Reilly

Telecommunications Group, Department of Electronic and Electrical Engineering, University College London, Torrington Place, London WC1E 7JE

Introduction: Optical single-sideband (SSB) modulation has been demonstrated for the transport of millimeter-wave modulated signals in radio-over-fiber applications [1], [2]. Sideband suppression effectively eliminates carrier power fluctuations due to fiber chromatic dispersion, allowing operation over standard single mode fiber at 1550 nm. A remaining limitation for mm-wave links, however, is the generation of phase noise due to interaction between chromatic dispersion and laser phase noise [3]. Here we demonstrate an alternative SSB generation technique which allows delay pre-distortion, doubling the useable link length when phase noise limited.

Modulation: Optical SSB modulation can been achieved by driving a dual-electrode Mach-Zehnder modulator (MZM) with phase shifted electrical signals [1],[2]. Spectral components are produced at the optical carrier frequency f_0 and at $f_0 + f_{mm}$, where f_{mm} is the modulation frequency. Although optical SSB generation largely eliminates dispersion-induced power fluctuations, a further manifestation of chromatic dispersion which may limit link performance results from the interaction with laser phase noise. Dispersion generates a time delay between the carrier and sideband, causing a partial decorrelation of optical phase noise common to the two terms. The result for mm-wave modulation is an increase in the detected carrier phase noise for increasing span lengths. Since spectrally efficient digital modulation schemes are sensitive to carrier phase noise, dispersion-induced phase noise may impose a serious limitation on optical mm-wave transport [3].

An alternative approach to perform optical SSB generation employs two MZMs in parallel, as shown in Fig. 1. In this case, both modulators are biased at V_π, the point of minimum optical transmission. One modulator is driven with a mm-wave carrier at f_{mm}, while the second modulator is driven with subcarrier data at f_{IF}, generating spectral components at $f_0 \pm f_{IF}$ and $f_0 \pm f_{mm}$ with a suppressed optical carrier. A fiber Bragg grating (FBG) following the modulators is used as a band-stop filter to eliminate the term at $f_0 + f_{mm}$, ensuring minimal dispersion-induced signal power variation. Photodetection generates an upconverted data signal at frequency $f_{mm} \pm f_{IF}$; the generated image signal at $f_{mm} - f_{IF}$ may be removed by electrical filtering before the antenna.

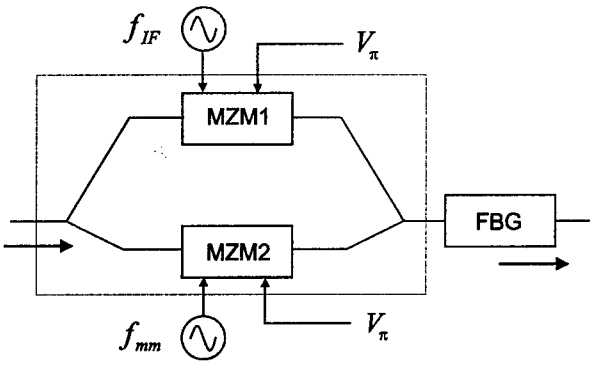

Figure 1: Schematic arrangement for SSB generation using two MZMs in parallel.

Although the optical filter requirements may be relaxed by including the filter in the lower branch of Fig. 1 [4], locating the filter externally provides the potential for integration of the two modulators in $LiNbO_3$ or III-V semiconductors. Integration will allow polarization matching, and allow precise control of the differential time delay of the two branches. By incorporating a longer optical path length in the upper branch, a delay pre-distortion can be achieved to compensate for the effect of chromatic dispersion.

Phase Noise: The phase variance for a mm-wave carrier generated by an optical time delay τ is given by $\sim 2\pi\Delta\nu\tau^2 BW$, where $\Delta\nu$ is the laser linewidth and BW is the electrical bandwidth [3]. The calculated power penalty due to generated phase noise is shown in Fig. 2 for a mm-wave link transporting 622Mb/s data encoded with 16-QAM at a 60 GHz carrier frequency, for a laser linewidth of 5 MHz. If the allowable power penalty due to phase noise generation is set at 0.1 dB, the link length is limited to 14 km. Delay pre-distortion of 115 ps applied to the upper arm of the modulator structure compensates for fiber dispersion, providing minimum degradation around 15 km. As

0-7803-4936-9/98/$10.00

shown in Fig. 2, pre-distortion allows a doubling of the fiber length within the 0.1 dB power penalty limit.

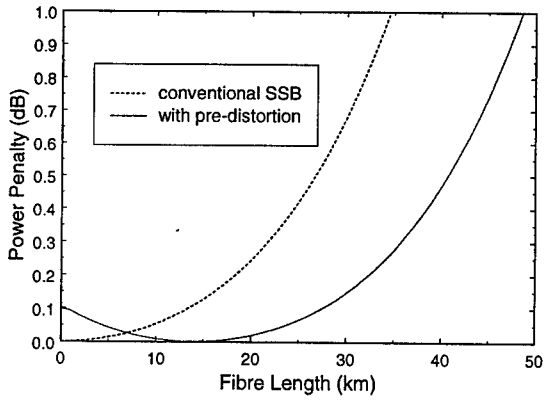

Figure 2: Power penalty for 16-QAM due to dispersion-induced phase noise.

Experiment: Optical SSB generation was performed by modulating a 1550 nm DFB laser with an 18 GHz carrier and an IF subcarrier around 1 GHz. A FBG with peak reflectivity 99.9% and FWHM 60 GHz was used to filter the upper optical sideband. The measured optical spectrum is shown in Figure 3. When the laser temperature was tuned optimally, the upper sideband at $f_0 + 18$ GHz was suppressed by more than 20 dB, ensuring less than 1 dB variation in detected carrier power due to fiber dispersion. For higher carrier frequencies the tolerance for laser wavelength control is relaxed. Using lasers and FBGs compatible with DWDM, stable operation can be anticipated without the need for feedback control.

To demonstrate transparent upconversion of data, a 28 Mb/s 16-QAM subcarrier signal at 1GHz was applied to MZM2. The spectrum of the detected upconverted signal at 19 GHz is shown in Fig. 4. The absence of 'spectral regrowth' confirms the linearity of the upconversion technique.

Conclusion: We have demonstrated a flexible optical SSB generation technique which employs two MZMs and a fiber Bragg grating. The arrangement allows integration of delay pre-distortion, which can compensate for carrier phase noise generated by fiber chromatic dispersion. Pre-distortion doubles the maximum fiber length which can be employed to transport high-rate, high-order digitally modulated data for mm-wave radio-over-fiber applications.

Acknowledgements: This work was funded by the European Commission ACTS project FRANS.

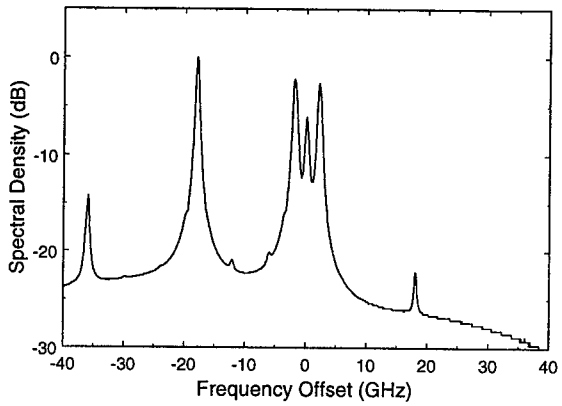

Figure 3: Optical spectrum of SSB signal, demonstrating > 20 dB suppression of the upper sideband.

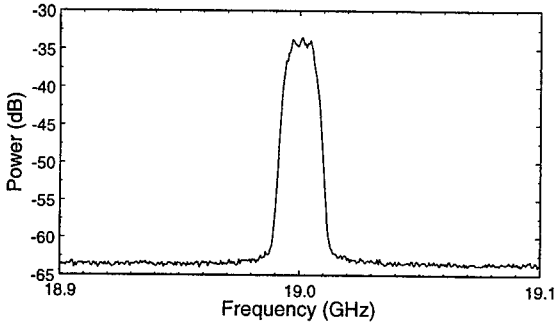

Figure 4: Electrical spectrum of 16-QAM subcarrier upconverted to 19 GHz.

References:

1. G.H Smith, D. Novak, and Z. Ahmed, "Technique for optical SSB generation to overcome dispersion penalties", *Electron Lett.*, vol. 33, pp. 74-75, 1997.
2. E. Vergnol, F. Devaux, D. Jahan, and Acarenco, "Fully integrated millimetric single-sideband lightwave source", *Electron Lett*, vol 33, pp.1961-3, 1997.
3. U. Gliese, S. Norskov, and T. N. Nielsen, "Chromatic dispersion in fiber-optic microwave and millimeter-wave links", *IEEE Trans Microwave Theor. Tech.*, vol 44, pp. 1716-1724, 1996.
4. M. Goloubkoff, E. Penard, D. Tanguy, P. Legaud, D. Mathoorasing, F. Devaux, and C. Minot, "Outdoor and indoor applications for broad-band local loop with fiber supported mm-wave radio systems", IEEE MTT-S International Microwave Symposium Digest, pp. 31-34, 1997.

MODELLING OF CHIRPING LASER DIODES FOR MICROWAVE GENERATION AND TRANSMISSION OVER DISPERSIVE FIBRES

Wolfgang Freude, Parthasarathi Palai*, Igor A. Sukhoivanov†
Institut für Hochfrequenztechnik und Quantenelektronik
Universität Karlsruhe, Kaiserstr. 12, D-76128 Karlsruhe, Germany
Tel: +49 721 608-2480 Fax: -2786
E-mail: W.Freude@etec.uni-karlsruhe.de

Abstract

For a sinusoidal modulation of the injection current we present optical and photocurrent spectra computed by a numerical large signal LD model, and compare the outcome to previous analytical and experimental results [2]. We also treat successfully some cases of overmodulation, where temporarily the current falls below threshold. For lower modulation frequencies and below-threshold currents the optical power becomes significantly determined by spontaneous emission; in these cases our present deterministic model fails.

I Introduction

The commercial impact of extended subscriber services with higher transmission capacity seems to be tremendous, if cost-effective means of connecting to subscribers can be employed. A very promising way is to upgrade existing copper or optical fibre cables by hybrid fibre radio networks, where wireless transmission channels employing the microwave and mm-wave frequency range 20...70 GHz bridge inexpensively the 'last mile' to a subscriber. The direct modulation of a laser diode (LD) has the potential to be very cost-effective, especially if harmonic upconversion by transmission over a fibre or any other suitable dispersive element is exploited [1] [2]. For an optimization of this technique a model of a chirping LD is needed, which we discuss in the following.

II Laser diode spectrum

The optical output field of a LD is represented by an analytic signal $a(t)$ with complex amplitude $A(t)$, phase $\varphi(t)$, and total output power $P_a(t)$ leaving the resonator (time t, angular optical frequency $\omega_0 = 2\pi f_0$, vacuum speed of light c, vacuum wavelength λ_0, frequency $f_0 = c/\lambda_0$, elementary charge e, Planck's constant h, time constant τ_R from finite resonator mirror reflectivities, photon lifetime $\tau_P = 3\,\mathrm{ps}$, effective carrier lifetime $\tau_{\mathrm{eff}} = 3\,\mathrm{ns}$, differential quantum efficiency $\eta_d = \tau_P/\tau_R = 0.28$, field confinement factor $\Gamma = 0.2$). Further, the normalized quantities $Z(t)$ for the photon number $N_P(t)$, $Y(t)$ for the carrier number $N_K(t)$ inside the active volume $V_K \approx 0.16 \times 3 \times 420\,\mu\mathrm{m}^3$, and $\Pi(t)$ for the injection current $I(t)$ (threshold values indexed by S, threshold current $I_S = 41\,\mathrm{mA}$, bias pumprate $\Pi_0 = 3$ with corresponding approximate DC values $Y_0 \approx 1$, $Z_0 \approx 2$, $Z_0 \sim P_{a0} = 18\,\mathrm{mW}$) are introduced,

$$a = A\,\mathrm{e}^{\mathrm{j}\omega_0 t},\quad A = |A|\,\mathrm{e}^{\mathrm{j}\varphi},\quad P_a = \frac{|a|^2}{2} = N_P \frac{hf_0}{\tau_R},\quad \Pi = \frac{I/e}{I_S/e},\quad Y = \frac{N_K/\tau_{\mathrm{eff}}}{I_S/e},\quad Z = \frac{N_P/\tau_P}{I_S/e},$$

$$E_G = \frac{I_S/e}{V_K/\tau_P}\,\Gamma\varepsilon_G,\quad G_N(Y,Z) = \frac{G(N_K,N_P)}{G_S(N_{KS},N_{PS})} = \frac{Y-Y_t}{1-Y_t}\,\frac{1}{1+E_G Z},\quad \omega_s = \frac{\varepsilon_G \Gamma P_{a0}}{\eta_d V_K h f_0} = \frac{E_G Z_0}{\tau_P}. \qquad (1)$$

Further parameters are the normalized gain G_N with the normalized transparency carrier number $Y_t = 0.82$, the normalized differential gain $\partial G_N/\partial Y = G_{Nd} \approx 1/(1-Y_t) = 5.56$, the threshold gain $\Gamma G_S \approx 1/\tau_P$, the gain saturation parameter $\varepsilon_G = 10 \times 10^{-17}\,\mathrm{cm}^3$, its normalized version $E_G = 0.075$, the adiabatic angular frequency shift $\omega_s = 2\pi \times 8.0\,\mathrm{GHz}$, the Henry factor of amplitude-phase coupling $\alpha = 3.5$, and the factor of spontaneous emission $Q = 10^{-4}$. We adopt the notation $X(t) = X_0 + X_1(t)$ for any quantity $X(t)$ dependent on time t around a constant operating point X_0; this formulation does *not* necessarily imply a small signal approximation for $X_1(t)$.

The quasi-stationary resonance frequency $\omega(t) = \omega_0 + \omega_1(t)$ of a single-mode field in a laser resonator with length L, effective modal refractive index n_e and effective modal group index n_{eg} is written as [3, Eq. (3.107)]

$$\frac{\omega}{c} n_e \cdot 2L = 2\pi q,\qquad q = 1,2,3,\ldots,\qquad n_{eg} = n_e + \omega\frac{\partial n_e}{\partial \omega},$$

$$\mathrm{d}(\omega n_e) = \frac{\partial(\omega n_e)}{\partial \omega}\,\mathrm{d}\omega + \frac{\partial(\omega n_e)}{\partial n_e}\,\mathrm{d}n_e = n_{eg,0}\,\mathrm{d}\omega + \omega_0\,\mathrm{d}n_e \stackrel{!}{=} 0, \qquad (2)$$

$$\mathrm{d}\omega = -\frac{\omega_0}{n_{eg,0}}\,\mathrm{d}n_e,\quad \omega_1 = \frac{\mathrm{d}\varphi}{\mathrm{d}t} = -\frac{\omega_0}{n_{eg,0}} n_{e,1}.$$

*On leave from Department of Physics, Indian Institute of Technology, New Delhi - 110016 Hauz Khas, India
†Chair for Physical Foundations of Electronic Technology, Technical University of Radioelectronic, Lenini-Prospekt 14, 310726 Kharkov, Ukraine

0-7803-4936-9/98/$10.00

For all practical cases (even for large signal modulation) the frequency and index deviations $\mathrm{d}\omega = \omega_1$ and $\mathrm{d}n_e = n_{e,1}$ from their stationary values remain small, $\omega_1/\omega_0, n_{e,1}/n_{e,0} \ll 1$. Introducing the effective modal group velocity $v_{eg} = c/n_{eg}$, the gain $G = v_{eg}g$, and the ususal definition of the Henry factor α, we therefore have

$$\alpha = -\frac{2\omega_0}{c}\frac{\partial n_e/\partial N_K}{\Gamma\partial g/\partial N_K} \approx -\frac{2\omega_0}{n_{eg,0}}\frac{\partial n_e/\partial N_K}{\Gamma\partial G/\partial N_K} = -\frac{2\omega_0}{n_{eg,0}}\frac{(\partial n_e/\partial N_K)\,\mathrm{d}N_K}{(\Gamma\partial G/\partial N_K)\,\mathrm{d}N_K} = -\frac{2\omega_0}{n_{eg,0}}\frac{n_{e,1}}{\Gamma G_1} > 0\,. \tag{3}$$

From Eqs. (2) and (3), the normalizations (Eq. (1)), and with the gain threshold value $\Gamma G_S = 1/\tau_P$, we find a conceptually very simple variant of the well known relation for the phase of the optical field [4],

$$\varphi(t) = 2\pi\int_0^t f(t_1)\,\mathrm{d}t_1\,, \quad \frac{\mathrm{d}\varphi}{\mathrm{d}t} = \omega_1 = \frac{\alpha}{2}\Gamma G_1 = \frac{\alpha}{2\tau_P}G_{N,1}\,, \quad G_{N,1} = \frac{\partial G_N}{\partial Y}Y_1 + \frac{\partial G_N}{\partial Z}Z_1 \approx G_{Nd}\cdot(Y - Y_0)\,. \tag{4}$$

With Eqs. (1) and (4), the normalized rate equations read:

$$\begin{aligned}
\tau_P\frac{\mathrm{d}Z}{\mathrm{d}t} &= [G_N(Y,Z) - 1]\,Z + QY, \qquad & \frac{\mathrm{d}\varphi}{\mathrm{d}t} &= \frac{\alpha}{2}\frac{1}{\tau_P}\frac{Y - Y_0}{1 - Y_t} \\
\tau_{\mathrm{eff}}\frac{\mathrm{d}Y}{\mathrm{d}t} &= -G_N(Y,Z)\,Z - Y + \Pi, & &= \frac{\alpha}{2}\left[\frac{1}{Z}\frac{\mathrm{d}Z}{\mathrm{d}t} + \omega_s\left(\frac{Z}{Z_0} - 1\right) + \frac{1}{\tau_P}\frac{QY_0}{Z_0}\left(1 - \frac{Y/Y_0}{Z/Z_0}\right)\right], \\
\Pi(t) &= \Pi_0 + (\Pi_0 - 1)m\sin(\omega_m t).
\end{aligned} \tag{5}$$

The pumprate Π is assumed to vary sinusoidally with a relative amplitude (modulation index) $m \geq 0$. For $Q \ll 1$, high bias pumprate $\Pi_0 \gg 1$ and modulation index $m < 1$, the carrier lifetime is strongly reduced below τ_{eff} by induced emission. Then, $|A| \sim \sqrt{Z}$ and φ can be found analytically,

$$\begin{aligned}
Z(t) &= Z_0\,[1 + m\sin(\omega_m t)]\,, \qquad Z_0 = \Pi_0 - 1, \qquad Q \ll 1\,, \\
\varphi(t) &= \frac{\alpha}{2}[\ln(1 + m\sin(\omega_m t)) + m\frac{\omega_s}{\omega_m}(1 - \cos(\omega_m t))].
\end{aligned} \tag{6}$$

For the relative optical spectra we calculated the Fourier transform of $\sqrt{2Z(t)}\,\mathrm{e}^{\mathrm{j}\varphi(t)}$ from either Eq. (5) for a period $1/f_m$ where the stationary state was already reached, or we used directly the analytical relations of Eq. (6). In both cases we subtracted any residual linear phase variation, i. e., any residual frequency offset. This is required because the fast Fourier transform routine implicitly assumes a strict periodicity, so any frequency offset (even by numerical inaccuracies) would be equivalent to a phase step at the boundaries of the chosen $1/f_m$-interval leading to artefacts in the computed optical spectrum. As a result, we found the complex coefficients c_n (c_0, $c_{\pm1}$, $c_{\pm2}$, …, $c_{\pm N}$) of the causal optical line spectrum for frequencies $f > 0$, where $|n| \leq N$ denotes the $2N$ lines $c_n\delta(f - f_0 - nf_m)$ on both sides of the optical carrier $c_0\delta(f - f_0)$ [2].

III Experimental and computed spectra

Detailed experimental data were previously reported in [2]. The measured current modulation indices m_i differed from the actual injection current modulation index m depending on f_m because of a bias-T. To illustrate the DFB laser data, Fig. 1 shows the DC characteristic in normalized coordinates; some measurement points (full circles) demonstrate the low influence of spontaneous emission. In Fig. 2, the computed small signal modulation response $10\log[\breve{Z}_1(f)/\breve{\Pi}_1(f)]$ is graphed for various operating points; $\breve{X}_1(f)$ represents the Fourier transform of $X_1(t)$. The parameters given above lead to a relaxation frequency of $f_r = 5.55\,\mathrm{GHz}$.

Small signal modulation $\mathbf{m_i = 0.13}$ The experimental photodetector (PD) current spectra, and the analytically computed spectra [2] coincided well with the numerically computed spectra using Eq. (5) or Eq. (6), as it was to be expected.

Large signal modulation $\mathbf{m_i = 0.66}$ We had measured formerly the product $\alpha f_s \approx 30\,\mathrm{GHz}$ [2]. Experiments and numerically computed PD current spectra coincided best using $\alpha = 3.5$ and $f_s = 8\,\mathrm{GHz}$. For comparable model parameters, the results from the *analytical* evaluation of Eq. (6) [2] as well as the present *numerical* computation based on Eq. (5) *or* on Eq. (6) practically coincide. In Fig. 3a, the optical power for lines of weight $P_{n\,\mathrm{opt}}/\,\mathrm{dB_0} = |c_n/c_0|^2$ is displayed as a function of the frequency deviation $\Delta f = f_0 + nf_m$ from the optical carrier (marked by ↓) for $m = 0.49$ @ $f_m = 1.95\,\mathrm{GHz}$. The corresponding $Z(t)$, $\varphi(t)$ for the stationary state are displayed in Fig. 4 during one period $1/f_m$ (marked by $m = 0.49$, thin lines, *left* φ-scale, $\Pi_0 = 3$, $Z_0 = 2$). The dotted curves starting at $Z = Z_0 = 2$ represent $Z(t)$ from Eq. (6) for comparison; obviously, the full rate equations Eq. (5), for

$m = 0.49$ @ $f_m = 1.95\,\mathrm{GHz}$, merely introduce a phase shift, but no significant distortion of the photon number $Z(t)$. Additionally, we computed numerically the PD current spectra [2] after a length $L = 12.8\,\mathrm{km}$ of a fibre with chromatic dispersion $C = 18\,\mathrm{ps}\,/\,(\mathrm{km\ nm})$ which converts FM into AM, see Table 1. It is to be seen that no significant difference exists between the analytically $(\cdots)$ and the numerically computed $[\cdots]$ results.

$f_m/\,\mathrm{GHz}$	$P_1/\,\mathrm{dB_0}$	$P_2/\,\mathrm{dB_0}$	$P_3/\,\mathrm{dB_0}$	$P_4/\,\mathrm{dB_0}$	$P_5/\,\mathrm{dB_0}$
1.95	−6.9 (−6.4) [−6.6]	−24 (−22) [−22]	−40 (−36) [−34]	−49 (−49) [−44]	−46 (−62) [−53]
2.52	−6.2 (−4.3) [−4.9]	−22 (−16) [−16]	−35 (−26) [−25]	−31 (−34) [−32]	−33 (−43) [−40]
3.52	−10 (−6.5) [−8.0]	−25 (−17) [−20]	−29 (−26) [−30]	−32 (−35) [−40]	−34 (−44) [−50]

Table 1.. Measured (analytically computed, $\alpha = 3$, $f_s = 10\,\mathrm{GHz}$ [2]) [presently computed, $\alpha = 3.5$, $f_s = 8\,\mathrm{GHz}$] PD current spectral powers for $m_i = 0.66$; with PD current amplitudes $|2I_k|$, the spectral powers are $P_k/\mathrm{dB_0} \mathrel{\widehat{=}} 10\lg(P_k/P_0) = 20\lg(|2I_k|/|I_0|)$

Overmodulation $\mathbf{m_i = 1.5}$ To increase the higher harmonics of the PD current after transmission through a dispersive fibre, the relative modulation current amplitude may be increased to $m_i = 1.5$ ($m = 1.11$ @ $f_m = 1.95\,\mathrm{GHz}$), so that the LD is also driven *below* threshold, and the analytical technique [2] cannot be applied any more. The corresponding $Z(t)$, $\varphi(t)$ are shown in Fig. 4 (marked by $m = 1.11$, thick lines, *right* φ-scale, $\Pi_0 = 3$, $Z_0 = 2$). The photon number function becomes distorted. Due to the steeper slopes of Z, the transient (first) term in the phase equations dominates, and results in much larger phase changes during one period. As a consequence, we expect a wider optical spectrum as can be seen in Fig. 3b (optical carrier marked by ↓). In Table 2 the measured and the numerically computed $[\cdots]$ results are compared. Measured and computed PD current spectra after a fibre length of $L = 12.8\,\mathrm{km}$ coincide very well for $f_m = 3.52\,\mathrm{GHz}$, while for $f_m = 1.95; 2.52\,\mathrm{GHz}$ the deviations are rather large.

$f_m/\,\mathrm{GHz}$	$P_1/\,\mathrm{dB_0}$	$P_2/\,\mathrm{dB_0}$	$P_3/\,\mathrm{dB_0}$	$P_4/\,\mathrm{dB_0}$	$P_5/\,\mathrm{dB_0}$	$P_6/\,\mathrm{dB_0}$	$P_7/\,\mathrm{dB_0}$	$P_8/\,\mathrm{dB_0}$
1.95	−25 [−0.3]	−30 [−8.9]	−33 [−14]	−35 [−17]	−38 [−19]	−40 [−22]	−43 [−25]	−48 [−29]
2.52	−7.4 [−0.3]	−20 [−7.2]	−13 [−11]	−17 [−13]	−21 [−16]	−26 [−19]	−28 [−23]	[−29]
3.52	−1.7 [−2.4]	−6.2 [−8.6]	−12 [−13]	−18 [−17]	−21 [−21]	[−24]	[−26]	[−28]

Table 2.. Measured [presently computed, $\alpha = 3.5$, $f_s = 8\,\mathrm{GHz}$] PD current spectral powers for $m_i = 1.5$; with PD current amplitudes $|2I_k|$, the spectral powers are $P_k/\mathrm{dB_0} \mathrel{\widehat{=}} 10\lg(P_k/P_0) = 20\lg(|2I_k|/|I_0|)$

For explaining these discrepancies, we refer for $f_m = 1.95\,\mathrm{GHz}$ to Fig. 4 (marked $m = 1.11$). From the dotted curve giving the instantaneous photon number Eq. (6) it is seen that the laser is driven below threshold. The numerically computed curves (thick lines) show a strong distortion for the photon number, which comes near to zero when the current falls below threshold. As soon as the induced emission decreases, the laser field becomes strongly influenced or even dominated by spontaneous emission, its statistics change from that of a LD to that of a LED; the spectral width increases significantly, and the LD coherence time decreases. Therefore, the optical phase must not be treated deterministically, and the deterministically computed optical spectrum Fig. 3b is not correct. The same effect is to be observed in Fig. 5a and Fig. 6 ($f_m = 2.52\,\mathrm{GHz}$, $m = 1.44$, thin lines; dotted curve for $Z(t)$ from Eq. (6); upper and lower time axes differ in scale because of different f_m). For a more appropriate description, the rate equations (5) should be supplemented with Langevin forces [5] [3] in this case.

The situation is different for $Z(t)$, $\varphi(t)$ with $f_m = 3.52\,\mathrm{GHz}$, $m = 1.11$ in Fig. 6 (thick lines, upper time scale). While the laser is still driven below threshold, the modulation frequency is much closer to the relaxation frequency $f_r = 5.55\,\mathrm{GHz}$ than before, and the delay between current and photon number inherent in the rate equations prevents that the photon number reaches or undershoots its threshold value. As a consequence, the statistics of the LD radiation do not change significantly, and the deterministic description Eq. (5) remains appropriate. The computed optical spectrum Fig. 5b (optical carrier marked by ↓) is broadened in comparison to Fig. 3a, and the associated PD current spectrum after a 12.8-km fibre coincides well with measurements, see Table 2 last line.

IV Conclusion

Above threshold and for low-frequency modulation $f_m \ll f_r$ with index $m \leq 0.66$ the evaluation of Eq. (6) is sufficient without regression to the rate equations. For larger f_m and m, the numerical analysis of Eq. (5) becomes necessary. When using the LD as an efficient harmonic upconverter, the injection current should temporarily fall below threshold, $m > 1$. The validity of the LD model Eq. (5) is assured, as long as the photon number does not approach threshold, which has to be checked in each case. If the photon number is very near or even falls below threshold, the statistics of the LD field change significantly, the deterministic description fails, and Langevin forces should be added to the rate equations.

V References

[1] Braun, R.-P.; Großkopf, G.; Schmidt, F.: Microwave generation and transmission using optical heterodyning or optical upconversion technique. Int. Top. Meeting Microwave Photonics. Kyoto (MWP 1996) TU3-6

[2] Freude, W., Braun, R.-P.; Großkopf, G.; Schmidt, F.: Microwave generation and transmission with chirping laser diodes and dispersive fibres. Int. Top. Meeting Microwave Photonics. Duisburg (MWP 1997) pp. 261–264

[3] Grau, G.; Freude, W.: Optische Nachrichtentechnik, 3. Aufl. Berlin: Springer-Verlag 1991

[4] Koch, T. L.; Linke, R. A.: Effect of nonlinear gain reduction on semiconductor wavelength chirping. Appl. Phys. Lett. 48 (1986) 613–615

[5] Petermann, K.: Laser diode modulation and noise. Dordrecht: Kluwer Academics Publishers 1988

VI Figures

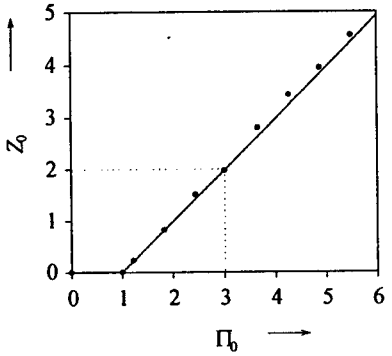

Fig 1. DC characteristic. (•) measured data

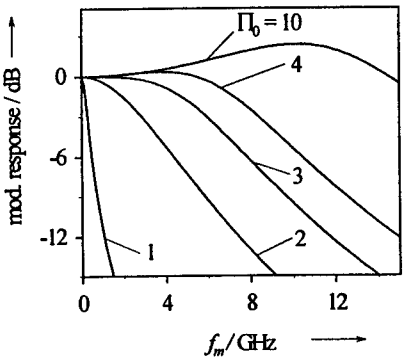

Fig 2. Small signal response $10\log[\breve{Z}_1(f)/\breve{\Pi}_1(f)]$

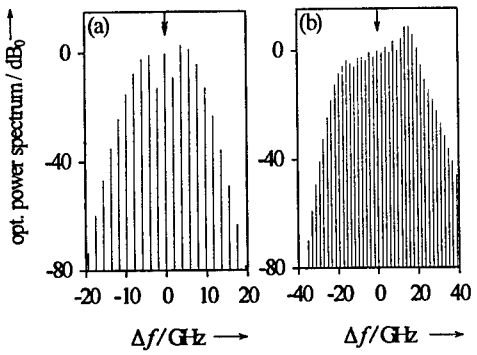

Fig 3. $f_m = 1.95\,\text{GHz}$ (a) $m = 0.49$ (b) $m = 1.11$

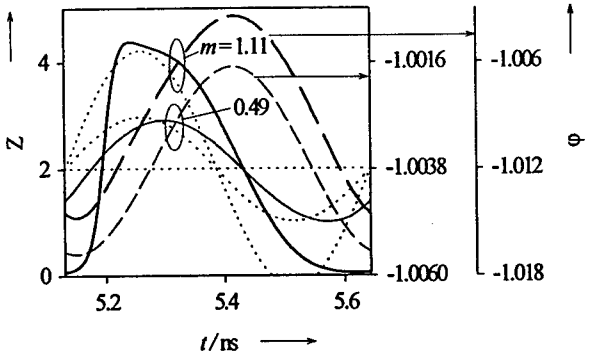

Fig 4. Z, φ; parameters of Fig. 3

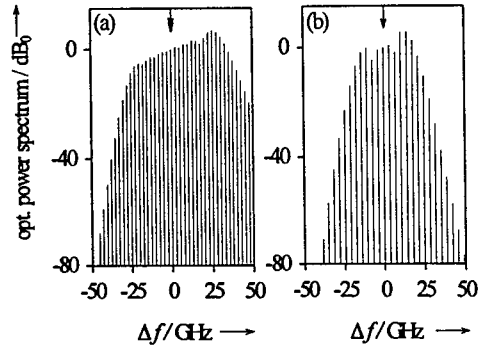

Fig 5. (a) $f_m = 2.52\,\text{GHz}$, $m = 1.44$, (b) $f_m = 3.52\,\text{GHz}$, $m = 1.11$

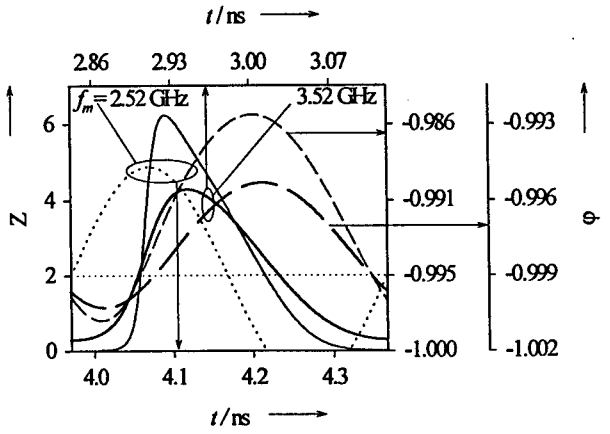

Fig 6. Z, φ; parameters of Fig. 5

Non linear biasing of MZ-EOM devices to experimentally reduce chromatic dispersion effects in antenna remoting up-converting fiber-optic links

J.M.Fuster, J.Marti, V.Polo, F.Ramos, J.L.Corral

Departamento de Comunicaciones, Universidad Politecnica de Valencia
Camino de Vera s/n, 46071 Valencia (SPAIN)
e-mail : jfuster@dcom.upv.es, jmarti@dcom.upv.es

Abstract: The authors investigate the reduction of the dispersion-induced power penalty in harmonic up-converting millimeter-wave fiber-optic links by biasing appropriately the Mach-Zehnder electrooptical modulator. Experimental results on the carrier supression effect are provided for three different types of bias.

Introduction

The generation and transmission of microwave/millimeter-wave signals using optical techniques is required in current applications involving hybrid photonic-microwave systems such as local multipoint distribution systems (LMDS) remote antenna links and mobile communications picocelular systems [1-2]. However, the performance of these systems is severely limited by the chromatic dispersion of standard single-mode fiber (SSMF) [3], which sharply limits the frequency-length product of fiber-optic links. To overcome this limitation several optical techniques such as chirped fiber gratings [4] and single sideband optical modulators [5] have been proposed.

On the other hand, several harmonic up-converting fiber-optic link schemes based on a single Mach-Zehnder electrooptical modulator (MZ-EOM) have been proposed to alleviate the frequency requirement on the local oscillator (LO) source [6]. The impact of biasing the MZ-EOM at the minimum transmission bias (MITB) point was theoretically outlined in [7], where it was shown that the dispersion-induced power penalty of the fiber-optic link may be sharply reduced when the second order harmonic of the LO source was considered to perform the harmonic upconversion with the MZ-EOM biased at the MITB point. Preliminary experimental results were reported in [8]. In this paper, we demonstrate that by biasing the MZ-EOM at the MITB point, the dispersion-induced power penalty is reduced, not only when considering upconversion through the second order harmonic of the LO source, but also for any other LO harmonic of a 2 + 4k order, with k = 0, 1, 2, ... Additionally, we also investigate the impact of biasing the MZ-EOM at the maximum transmission bias (MATB) point on the dispersion-induced power penalty. In this case we demonstrate that the dispersion-induced power penalty is reduced when upconverting with harmonics of a 4 + 4k order, with k = 0, 1, 2, ...

Theory

Figure 1 shows the block diagram of two different implementations of an antenna remoting fiber-optic link: one based on a conventional radio frequency (RF) modulated scheme (figure 1a), and the other based on an up-converting scheme (figure 1b).

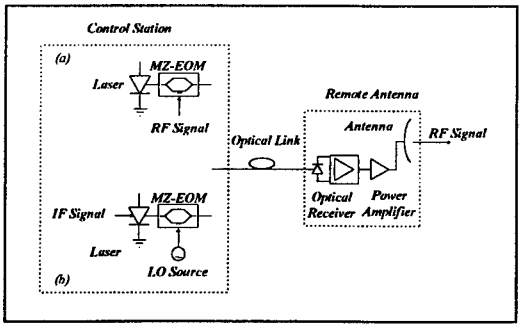

Figure 1. Remoting antenna system block diagrams, (a) conventional modulating scheme, (b) harmonic upconverting scheme.

In the conventional scheme, the RF signal to be radiated on the antenna is externally modulated onto the optical carrier (figure 1a). Alternatively, in the up-converting system, an intermediate frequency (IF) signal directly modulates the optical source, and photonic up-conversion is achieved through the LO signal driving the external modulator (figure 1b). In either case, the modulated or the up-converted RF signal is launched into the optical fiber and may be optically amplified if necessary. At the receiving end, the detected RF signal at the output of the photodetector is amplified by an RF power amplifier prior to be radiated.

In the conventional link (figure 1a), fiber-optic chromatic dispersion affects the transmission

0-7803-4936-9/98/$10.00

of millimeter-wave signals [3]. The detected RF current at the output of the photodetector is proportional to,

$$i_{phot} \propto \cos\left(\beta f_{RF}^2\right) \quad (1)$$

where β is,

$$\beta = \frac{\pi D \lambda^2 L}{c} \quad (2)$$

where L and D are the length and the dispersion factor of the optical fibre, respectively, λ is the optical wavelength and c is the speed of light in vacuum. The factor $\cos\left(\beta f_{RF}^2\right)$ in (1) results in a dispersion-induced power penalty that limits the frequency-length product of the fibre-optic link.

Moreover, when harmonic upconversion is performed (figure 1b), the MZ-EOM may be biased either at the quadrature bias (QB) point, which results in upconverted signals of frequency $f_{RF} = (2k+1)f_{LO} + f_{IF}$, with $k = 0, 1, 2, \ldots$, or at the MITB or at the MATB points, where the upconverted signal frequency is $f_{RF} = 2kf_{LO} + f_{IF}$, with $k = 0, 1, 2, \ldots$. Therefore, odd order harmonics of the LO source are employed for upconversion when the MZ-EOM is biased at the QB point, while even order harmonics are employed when the MZ-EOM is biased either at the MITB or at the MATB points. Selecting an appropriate power level for the LO signal powers the contribution of a particular harmonic.

When performing direct upconversion with the fundamental frequency of the LO source with the MZ-EOM biased at the QB point, the photodetected RF current is proportional to,

$$i_{phot} \propto m_i J_0(\alpha_{LO}) J_1(\alpha_{LO}) \cos\left((\omega_{LO} + \omega_{IF})t\right) \cdot \cdot \cos\left(\beta f_{IF} f_{RF}\right) \cos\left(\beta f_{LO} f_{RF}\right) \quad (3)$$

where m_i is the optical source modulating index, and α_{IF} and α_{LO} are given by,

$$\alpha_{IF} = \frac{\pi V_{IF}}{2V_\pi(f_{IF})} \qquad \alpha_{LO} = \frac{\pi V_{LO}}{2V_\pi(f_{LO})} \quad (4)$$

where V_{IF} and V_{LO} are the voltages of the IF and LO signals, respectively, and $V_\pi(f_{IF})$ and $V_\pi(f_{LO})$ are the half-wave voltages of the IF and LO signals, respectively. From (3), it may be observed that the dispersion-induced power penalty is also present when direct upconversion is performed. Assuming that $f_{RF} >> f_{IF}$, it may be stated that when f_{IF} is very low,

$$\cos\left(\beta f_{LO} f_{RF}\right) \rightarrow \cos\left(\beta f_{LO}^2\right) \approx \cos\left(\beta f_{RF}^2\right) \quad (5)$$

and fiber chromatic dispersion affects similarly in the up-converting QB case as in the conventional modulating case.

When the second order harmonic of the LO source is employed to perform the upconversion, the impact of fiber chromatic dispersion depends on the bias point of the MZ-EOM. If the modulator is biased at the MITB point, the photodetected RF current is proportional to,

$$i_{phot} \propto m_i J_1^2(\alpha_{LO}) \cos\left((2\omega_{LO} + \omega_{IF})t\right) \cdot \cdot \cos\left(\beta f_{IF} f_{RF}\right) \quad (6)$$

The $\cos\left(\beta f_{IF} f_{RF}\right)$ term in (6) results in a less dramatic dispersion-induced power penalty, provided that the argument of the cosine function depends on f_{RF} in the MITB case, instead of depending on f_{RF}^2 as in the QB case. Therefore, when MITB is considered, the first notch of the power penalty degradation is shifted to higher frequencies. Figure 2 shows the normalized RF power level detected against the RF frequency, for the conventional modulated case (dotted line), the upconverting QB case (dashed line) and the upconverting MITB case (solid line). Figures 2a, 2b and 2c, correspond to three different cases employing IF signals of 2, 1.5 and 1 GHz, respectively.

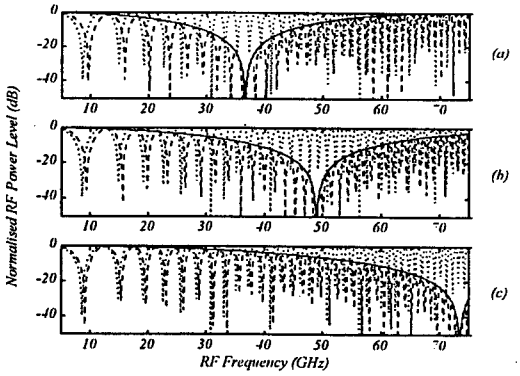

Figure 2. *Normalized RF power level against RF frequency. (a) f_{IF}=2GHz, (b) f_{IF}=1.5GHz, (c) f_{IF}=1GHz.*

From figure 2 it may be observed that the performance of the upconverting QB case tends to that of the conventional case when IF decreases, while the chromatic dispersion effects tend to vanish for the upconverting MITB case.

Moreover, considering upconversion through the second order harmonic of the LO source when the modulator is biased at the MATB point, the photodetector current is proportional to,

$$i_{phot} \propto m_i J_0(\alpha_{LO}) J_2(\alpha_{LO}) \cos\left((2\omega_{LO} + \omega_{IF})t\right) \cdot$$
$$\cdot \cos(\beta f_{IF} f_{RF}) \cos(\beta f_{LO} f_{RF}) \qquad (7)$$

which results in a severe dispersion-induced power penalty factor, similar to that of the upconverting QB case.

On the other hand, when upconversion through the fourth harmonic of the LO source is considered, the situation turns around. In this case, MATB is a better option than MITB regarding that the power penalty degradation factors are given by $\cos(\beta f_{IF} f_{RF})$ for the MATB case, and $\cos(\beta f_{IF} f_{RF}) \cos(\beta f_{LO} f_{RF})$ for the MITB case.

In general, it may be proved that the reduction of the chromatic dispersion effect in fiber-optic upconverting links is achieved by employing MITB when considering even harmonics of an order 2 + 4k (k = 0, 1, 2, ...), while MATB is the right option when considering even order harmonics of an order 4+ 4k (k = 0, 1, 2, ...). The explanation is given in figures 3 and 4. In both figures it is depicted the optical electric field spectra for both cases MITB and MATB against the normalized frequency. The LO and IF spectral components that contribute in each bias case to the generation of the RF frequency are remarked using arrows. The frequency of the RF signal is given by $f_{RF} = 2f_{LO} + f_{IF}$ in figure 3, and by $f_{RF} = 4f_{LO} + f_{IF}$ in figure 4.

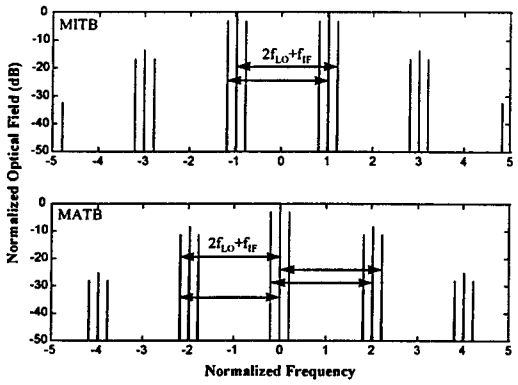

Figure 3. Simulated optical electric field spectra at the output of the MZ-EOM for the MITB and MATB cases, as a function of the normalized frequency. ($f_{RF} = 2f_{LO} + f_{IF}$).

The factor $\cos(\beta f_{IF} f_{RF})$ is related to the cases in which the RF signal is produced by two beats of the LO and IF frequency components. This corresponds to the MITB case of figure 3 (LO second order harmonic) and the MATB case of figure 4 (LO fourth order harmonic). On the other hand, the factor $\cos(\beta f_{IF} f_{RF}) \cos(\beta f_{LO} f_{RF})$ arises from the beat of four LO and IF frequency components, which corresponds to the MATB case of figure 3 (LO second order harmonic) and the MITB case of figure 4 (LO fourth order harmonic). This explanation may be extended to higher even LO harmonics. MITB is best suited when using harmonics of a 2 + 4k order (k = 0, 1, 2, ...), while MATB is the best election for harmonics of a 4 + 4k order (k = 0, 1, 2, ...).

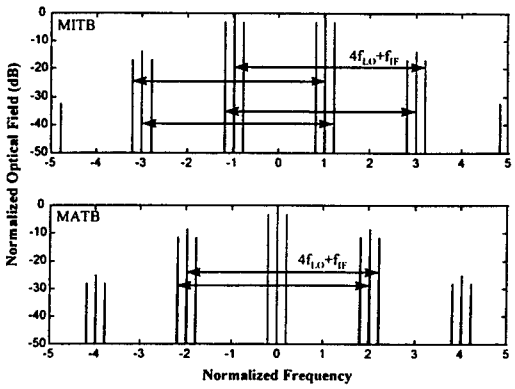

Figure 4. Simulated optical electric field spectra at the output of the MZ-EOM for the MITB and MATB cases, as a function of the normalized frequency. ($f_{RF} = 4f_{LO} + f_{IF}$).

Experiment

The setup of the antenna remoting fiber-optic link depicted in figure 1b has been mounted in the laboratory in order to demonstrate the reduction of the dispersion-induced power penalty.

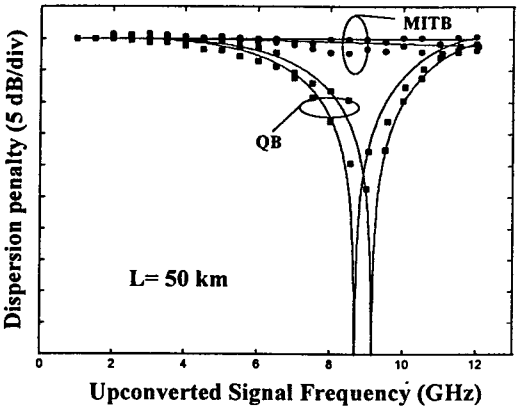

Figure 5. Normalized RF power level against the RF frequency for the upconverting QB case ($f_{RF} = f_{LO} + f_{IF}$)., and for the upconverting MITB case ($f_{RF} = 2f_{LO} + f_{IF}$).

Figure 5 shows the normalized RF signal power level detected at the output of a 50 km length fiber-optic link against the RF frequency, ranging from 1 to 12 GHz, when employing either the LO fundamental contribution to perform the up-conversion, or the second harmonic of the LO signal with the MZ-EOM biased at the MITB point.

Two IF signal frequencies (100 MHz and 1500 MHz) have been considered in order to demonstrate the influence of the IF signal frequency election on the optical link bandwidth. From figure 2 it can be observed that the chromatic dispersion effects tend to vanish when employing the second order harmonic of the LO source with MITB biasing, as predicted by the theory.

Figure 6 shows the normalized RF signal power level detected at the output of a 75 km length fiber-optic link against the RF frequency, ranging from 1 to 10 GHz, when employing either the LO fundamental contribution or the fourth harmonic of the LO signal with the MZ-EOM biased at the MATB point. From figure 6 it may be observed that the chromatic dispersion effects are also reduced in this case.

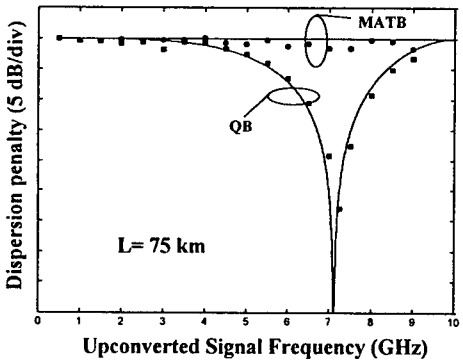

Figure 6. Normalized RF power level against the RF frequency for the upconverting QB case ($f_{RF} = f_{LO} + f_{IF}$)., and for the upconverting MATB case ($f_{RF} = 4f_{LO} + f_{IF}$).

Conclusion

The reduction of chromatic dispersion effects in antenna remoting up-converting fiber-optic links has been experimentally demonstrated employing even order harmonics of the LO signal source. Biasing the up-converting MZ-EOM device at the MITB point is required when employing harmonics of a 2 + 4k order (k = 0, 1 ,2 ,...), while MATB is the best election for harmonics of a 4 + 4k order (k = 0, 1 ,2 ,...). Moreover, the influence of the IF signal frequency on the overall optical link bandwidth has also been demonstrated. The transmission scheme proposed in this letter requires a LO signal of half, a fourth, a sixth, ... of the nominal frequency, and produces a notorious increase of the optical link bandwidth. Therefore, the MITB or MATB up-converting optical link is proposed as an alternative to the conventional modulating case for millimetre-wave transmission in antenna remoting systems.

Acknowledgements

The authors thank the Spanish Research Commission (CICYT) for funding the project TIC96-0611. This work was partially supported by Fringes S.A., and by Global Manufacturers' Services Valencia S.A.

References

[1] S.Komaki, K.Tsukamoto, M.Okada, "Requirements for radio-wave photonic devices from the viewpoint of future mobile radio system", *IEEE Trans. on Microw. Theory Tech.*, vol. 43, pp. 2222-2228, 1995.

[2] J.Park, A.F.Elrefaie, K.Y.Lau, "1550 nm transmission of digitally modulated 28 GHz subcarriers over 77 km of nondispersion shifted fiber", *IEEE Photon. Technol. Lett.*, vol. 9, pp. 256-258, 1998.

[3] H.Schmuck, "Comparison of optical milimetre-wave system concepts with regard to chromatic dispersion", *Electron. Lett.*, vol. 31, pp. 1848-1849, 1995.

[4] J.Marti, J.M.Fuster, R.I.Lamming, "Experimental reduction of chromatic dispersion effects in lightwave microwave/millimetre-wave transmissions employing tapered linearly chirped fibre gratings", *Electron. Lett.*, vol. 33, pp. 1170-1171, 1997.

[5] G.H.Smith, D.Novak, Z.Ahmed, "Technique for optical SSB generation to overcome fiber dispersion penalties in fiber-radio systems", *Electron. Lett.*, vol. 33, pp. 74-75, 1997.

[6] J.M.Fuster, J. Marti, V. Polo, J. L. Corral, "Fibre-optic microwave link employing optically amplified electro-optical up-converting receivers", *IEEE Phot. Technol. Lett.*, vol. 9, pp. 1161-1163, 1997.

[7] J.M.Fuster, J. Marti, J. L. Corral, "Chromatic dispersion effects in electro-optical up-converted millimetre-wave fibre-optic links", *Electron. Lett.*, vol. 33, pp. 1969-1970, 1997.

[8] J.M.Fuster, J. Marti, J.L.Corral, "Experimental reduction of chromatic dispersion effects in electrooptical upconverted millimeter-wave fiber-optic links", Optical Fiber Conference OFC'98, paper WM20, San Jose, 1998.

Photorefractive Phased Array Beamforming with True-Time-Delay Processing

Andrew Kiruluta, Paulo E. X. Silveira, Greg Kriehn, Sam Weaver and Kelvin Wagner
Optoelectronic Computing Systems Center, Department of Electrical and Computer Engineering
University of Colorado, Boulder, CO 80309-0525
1-303-492-7916 Andrew.Kiruluta@colorado.edu

We introduce a new optical approach to the problem of implementing true-time-delay (TDD) beamforming for a large N-element adaptive array that requires only 2 tapped delay lines (TDLs) instead of the conventional N TDLs. This new algorithm, BEAMTAP (Broadband and Efficient Adaptive Method for TTD Array Processing) is capable of processing very large phased array radar systems with thousands of receiving elements with GHz of bandwidth [1]. The corresponding digital processing load that would be required to solve such large, broadband adaptive array problems exceeds 10^{15} multiply-accumulate operations per second; well beyond the capability of current electronic systems.

Consider the BEAMTAP algorithm shown in Fig. 1. Each antenna element output $s_i(t)$ is multiplied at each resolved time step by a linear array of weights W_{ij} located along a given row of the weight matrix. Each product is then summed along the column with the corresponding products from the other array elements. The resulting sum is fed into a scrolling delay line with the overall output given by

$$o(t) = \sum_j \int \delta(t' - [t - j\tau]) Y_j(t') dt' = \sum_j Y_j(t - j\tau) = \sum_j \sum_i s_i(t - j\tau) W_{ij}^* \tag{1}$$

The $Y_j(t)$ are the partial sums incident on the tap-in delay line, and the scrolling detector continuously accumulates them. The weights in BEAMTAP are calculated using conventional LMS adaptation [2] [3] but with a reference signal applied to a tap-out delay line as shown. These weights are implemented as holographic gratings in a photorefractive crystal (PRC) volume, and each resolvable hologram acts as an interferometric time integrating multiplier in the form

$$W_{ij}^*(t) = \int_{-\infty}^{t} s_i^*(t_1) f(t_1 + (j - M - 1))\tau) dt_1 \tag{2}$$

Hence, the resulting LMS output is

$$\begin{aligned} o(t) &= \sum_j \sum_i \int \delta(t' - [t - j\tau]) s_i(t') \int_{-\infty}^{t'} s_i^*(t_1) f(t_1 + (j - (M-1))\tau dt_1 dt' \\ &= \sum_j \sum_i s_i(t - j\tau) \int_{-\infty}^{t} s_i^*(t_2 - j\tau) f(t_2 - (M-1)\tau) dt_2 \end{aligned} \tag{3}$$

This algorithm is nearly equivalent to the conventional time-delay-beam-forming (TDBF) except for the simple time shift $T = (M-1)\tau$ in the reference signal $f(t)$ which implies anticipation of the output $o(t)$. This apparent causality problem can be overcome by delaying a copy of the antenna signals $s_i(t)$ by T and using them to write the weights while the undelayed version is used for beamforming. The number of delay lines in this case has been dramatically reduced from N as required by the TBDF to just 2. An optical implementation of the BEAMTAP processor using holographic gratings in a PRC as the adaptive weights is shown in Fig. 2.

A low relative intensity noise (RIN) laser is required to feed an array of electrooptic modulators driven by the outputs of the antennas that convert an incident RF wavefront on each antenna into an optical field. These optical fields are launched by the fiber feed through an optical system and into

0-7803-4936-9/98/$10.00

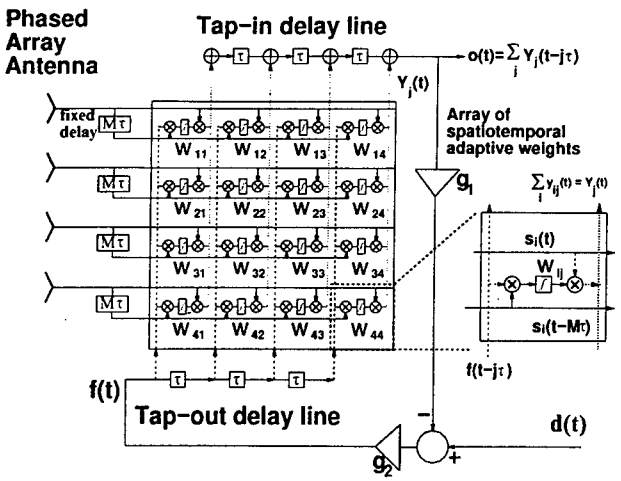

Figure 1: BEAMTAP algorithm for broadband squint-free true-time-delay beamforming using a single output tap-in delay line and a single feedback TDL for adaptive calculation of the weights within the array as integrated correlations. Time delay is not required within the array of weights.

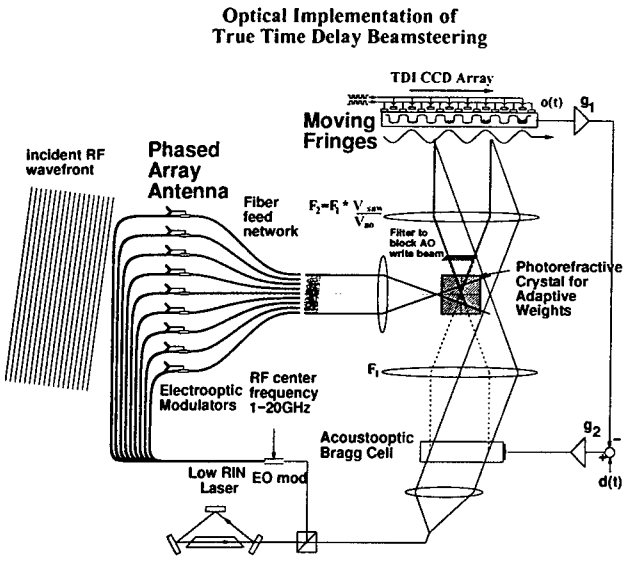

Figure 2: Signal flow for an optical BEAMTAP system utilizing 2 broadband adaptive beamformers that simultaneously form a main beam in the direction of any arriving desired signal $s(t)$ and then null out any narrowband jammers arriving on the sidelobes.

a PRC. Because of fiber length mismatches, the optical phase front is not necessarily planar but the photorefractive hologram can adapt to compensate for this distortion.

It is assumed that we have available a signal of similar correlation characteristics as the desired incident RF signals. The processor output is subtracted from this desired waveform $d(t)$ and applied to the reference AOD. The interference of the spatio-temporally modulated optical field from the fiber bundle with the steering signal in the AOD builds up a dynamic grating throughout the crystal volume that is Bragg matched to the angle-of-arrival of the incident radar signal. In conventional dynamic holography, the diffracted wave is not separable from the write beam. We provide read-write multiplexing by angle and polarization encoding; details of which can be found in [1] and [4].

Hence, any subsequently Bragg matched incident energy is diffracted toward the scrolling output detector where it is interferometrically detected using the undiffracted light from the AOD and time integrated in a traveling wave coordinate system. Hence, at each resolvable time instant, the scrolling detector is read out after a corresponding charge packet has traversed the length of the detector while accumulating charge and being delayed for each position. This scrolling delay line is implemented with a 1-dimensional CCD detector operating in time-delay-and-integrate (TDI) mode. In this mode, each photogenerated carrier is accumulated and shifted along at a constant velocity by the applied clock signal.

Photonic processing of microwave signals is often limited by the conversion of optically modulated signals into high frequency photocurrent usually using high speed point detectors, however, we need a scrolling accumulating detector such as a TDI CCD. GaAs based CCDs promise speeds in excess of 1 GHz while silicon CCDs are still limited to 100 MHz. In addition, all CCDs are inherently prone to bias build up and are full well shot noise limited which may reduce the overall dynamic range of the system. Other promising technologies we are investigating involve replacing the CCD with a traveling fridge detector [5]. In contrast to CCD technology, these traveling wave detectors promise to simultaneously maintain a high saturation level owing to a large detection volume and a high operating frequency well in excess of 1 GHz. Although the instantaneous bandwidth of the AOD and the CCD devices are at best about 1-2 GHz, the

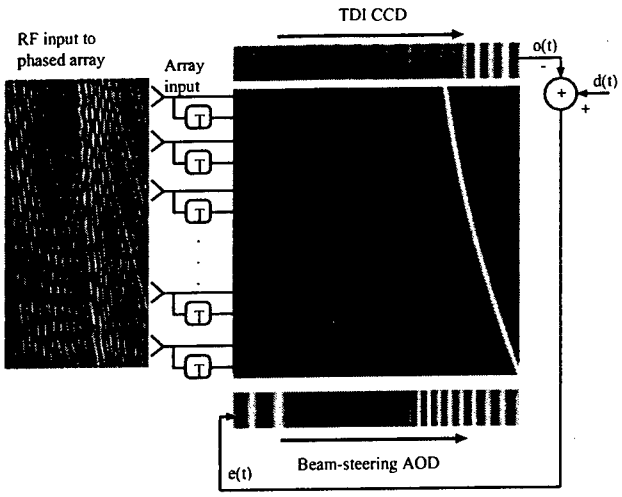

Figure 3: Simulation of BEAMTAP adaptation in the presence of a near-field chirp signal and two jammers: one in the near-field and the other in the far-field.

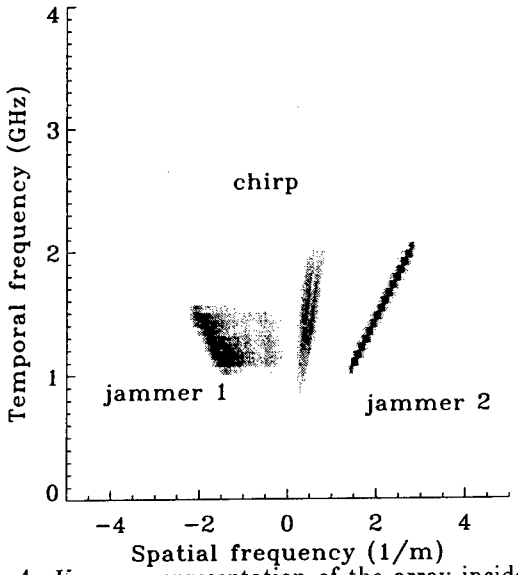

Figure 4: K-space representation of the array incident energy showing the spatio-temporal content of the linear chirp and the two jammers.

BEAMTAP optical system can operate at any 1 GHz bandwidth tunable throughout the bandwidth of the electrooptic modulators, which is typically 20-60 GHz using a single EO device as shown in Fig. 2, without the need for electronic mixers, which can be very lossy at such high frequencies.

A simulation of the BEAMTAP operation with jammer nulling is illustrated in Fig. 3. In this example the input consist of a chirp signal and two jammers. The desired signal is a repetitive near-field broadband spatio-temporal linear chirp spanning from 0.5 GHz to 1.5 GHz, and originating at a distance $5.2L$ from the antenna array, where L is the total array length. The jammers were produced from filtered Gaussian white noise sequences. The first jammer spans the frequency range 1 GHz to 1.5 GHz, located at a distance $L/2$ from the antenna array while the second jammer spans from 1 GHz to 2 GHz, and it is located in the far-field.

A k-space/frequency diagram representing the input signals is shown in Fig. 4. Notice that the chirp signal occupies a broad bandwidth both in time and space, as expected from a near-field source and since it is repetitive, it is sampled in frequency. The near-field jammer signal occupies a large spatial frequency bandwidth, while the far-field jammer occupies a broad time frequency range. Adaptation of our parameters (weights) should provide us detection of the desired output signal and nulling of the jammers for any combination of signal and multiple jammers, as long as their space/time spectra do not overlap and sufficient feedback gain is available.

The graph in the far left of Fig. 3 illustrates the spatio-temporal sequence of the input array signals, linear chirp plus jammers, followed by the graph representing the weights of the adaptive array after 1.02 μs of adaptation. 128 antenna elements and 128 time delays on each delay line were used on this simulation, providing us with an array of 128×128 adaptive weights. Their intensity is proportional to the local variation in the index of refraction of the PRC which constitutes the grating. Notice that the time and phase delays caused by the curved wavefronts of the near-field signal are exactly compensated for by the diffraction off of the curved grating slice in the PRC in a fully adaptive fashion. Similar gratings would compensate for delays associated with arbitrary array configuration, such as a conformal or flexible array, or additional delays or phases from the fiber feed network. The thin slice below the weights represents the local variation in the index of refraction in the AOD, which implements the tap-out delay line. The thin slice above the weights represent the accumulated output in the TDI CCD, the tap-in delay line.

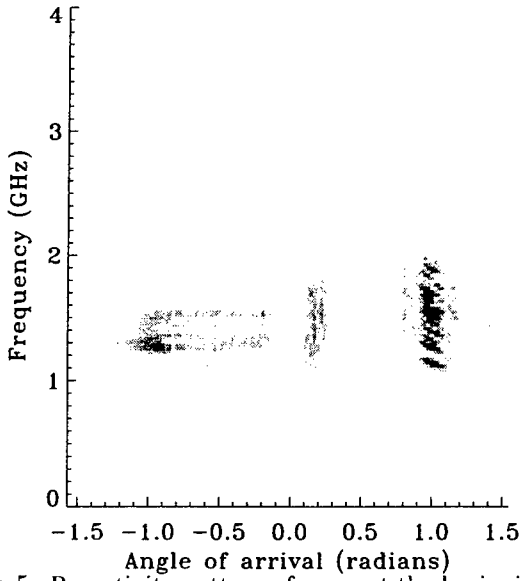

Figure 5: Receptivity pattern of array at the beginning of adaptation.

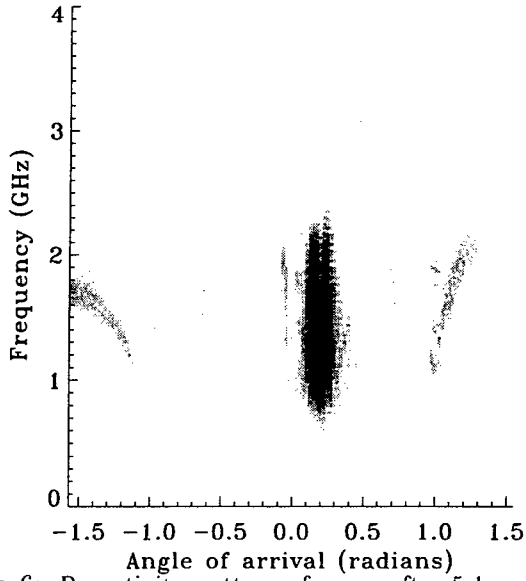

Figure 6: Receptivity pattern of array after 5.1 μs of adaptation.

Figure 5 shows the receptivity pattern at the beginning of adaptation, where the bright regions represent the combination of angles-of-arrival (AOA) and frequencies of signals to which the antenna array is sensitive. Notice that at first, the adaptive array responds to the presence of all signals. Figure 6 shows the same graph after 5.12 μs of adaptation. Notice that only the broadband near-field chirp is present, proving the presence of nulls in the space occupied by the jammers. Also notice the absence of beam-squint, indicated by the constant value of the AOA of the receptivity pattern due to the true time-delay signal representation.

For an antenna array with $N = 1000$ elements, bandwidth $B = 1$GHz and of length $L = N\lambda/2 = 15$m (requiring $M = BL/c = 50$ taps), this optical processor achieves a throughput of $NMB = 10^{14}$ analog multiplications, which is well beyond the capabilities of electronic approaches, providing strong motivation for the development of these optical techniques.

We wish to acknowledge the support by Dr. William Miceli of ONR and the Office of the Secretary of Defense through the MURI program grant no. N00014-97-1-1006. Useful discussions we had with S. Kraut, Dr. L. Griffiths, T. Weverka, and Dr. T. Sarto are gratefully acknowledged.

References

[1] R. T. Weverka, K. Wagner, and A. Sarto, "Photorefractive processing for large adaptive phased-arrays," *Applied Optics*, vol. 35, pp. 1344–1366, 1996.

[2] B. Widrow, P. Mantey, L. Griffiths, and B. Goode, "Adaptive antenna systems," *Proceedings of the IEEE*, vol. 55, p. 2143, 1967.

[3] B. Widrow and S. D. Stearns, *Adaptive Signal Processing.* Prentice-Hall, 1985.

[4] A. Sarto, K. Wagner, R. Weverka, S. Weaver, and E. Walge, "Wide angular aperture holograms in photorefractive crystals by the use of orthogonally polarized write and read beams," *Applied Optics*, vol. 35, no. 29, pp. 5765–5775, 1996.

[5] T. Merlet, D. Dolfi, and J. Huignard, "A traveling fridge photodetector for microwave signals," *IEEE J. Quant. Elec.*, vol. 32, pp. 778–783, 1996.

High Performance Long-Wavelength Velocity-Matched Distributed Photodetectors For RF Fiber Optic Links

T. Chau, S. Mathai, A. Rollinger, D. L. Sivco*, A. Y. Cho*, D. C. Scott[+], T. A. Vang[+], M. C. Wu, and T. Itoh
UCLA, Electrical Engineering Department,
66-147D Engineering IV, Box 951594
Los Angeles, CA 90095-1594
Tel: (310) 825-6859, Fax: (310) 825-6954, Email: wu@ee.ucla.edu
*Lucent Technologies, Bell Laboratories, Murray Hill, NJ 07974
[+]Photonics Technology Department, TRW, Redondo Beach, CA 90278

Abstract

Improved performance of InP-based long wavelength velocity-matched distributed photodetector (VMDP) with metal-semiconductor-metal photodiodes is experimentally demonstrated. A 3-dB bandwidth of 13 GHz and an external quantum efficiency of 0.57 A/W have been achieved.

I. Introduction

High power, high frequency photodetector is a key component for high performance microwave fiber optic links [1-3]. High optical power in externally modulated links can greatly enhance the link gain, signal-to-noise ratio, and spurious-free dynamic range [4]. In conventional photodetectors, there is a trade-off between the saturation photocurrent and the device bandwidth. High power device requires a large absorption volume, thus the device is usually large, resulting in large RC time or long carrier transit time that limits the device bandwidth. In contrast, conventional high-speed photodetectors with small RC time and small transit time usually have low saturation photocurrents. The velocity-matched distributed photodetectors (VMDP) is a novel type of travelling wave photodetector which can achieve both high bandwidth and high saturation power. It was first proposed in 1993 [6], and has been successfully demonstrated experimentally [1,5]. The successful fabrication of long-wavelength VMDP for use in 1.3 or 1.55 μm RF Photonics systems was first reported in [5]. In this paper, we report on the performance of improved long wavelength VMDP with new design and fabrication procedures. A 3-dB bandwidth of 13 GHz and an external quantum efficiency of 0.57 A/W have been achieved.

II. Device Structure and Fabrication

The schematic structure of the VMDP is illustrated in Figure 1. A passive (non-absorbing) optical waveguide is used to serially connect an array of periodically spaced metal-semiconductor-metal (MSM) photodiodes. Light in the optical waveguide is evanescently coupled to the MSM photodiodes. The photocurrents are added in phase and collected by a 50Ω coplanar strips (CPS) microwave transmission line. The active photodiodes are designed to have small optical confinement factor to keep them bellow saturation under high optical illumination. The bandwidth of the VMDP is limited by that of the individual photodiode, and the residual velocity mismatch. Since photocurrents are collected from many photodiodes along the transmission line, the individual photodiode does not need to have high quantum efficiency and therefore can be made small and fast. The MSM photodiodes serve two functions: generating photocurrents as well as providing the periodic capacitance loading needed for velocity matching. The VMDP design allows the passive waveguide, the active photodiodes, and the microwave coplanar strips to be independently optimized.

0-7803-4936-9/98/$10.00

The principle of the VMDP has been discussed in more detail in [1]. We have made three major changes: (1) mesa width reduction to reduce optical coupling loss from optical waveguide to active MSM photodiodes; (2) nitride passivation on mesa sidewall and underneath the large CPS electrodes to reduce dark current and improve device reliability; and (3) use of platinum in Schottky metal contacts to prevent gold diffusion at high power operation

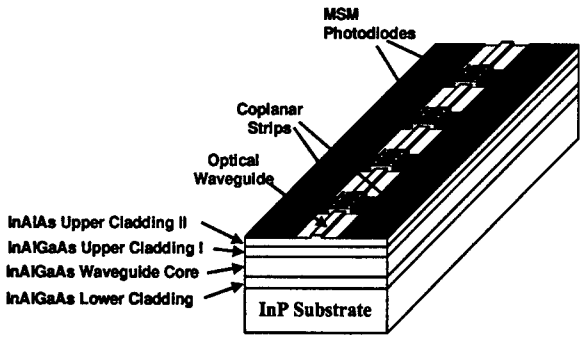

Figure 1. Schematic structure of long-wavelength velocity-matched distributed photodetector (VMDP)

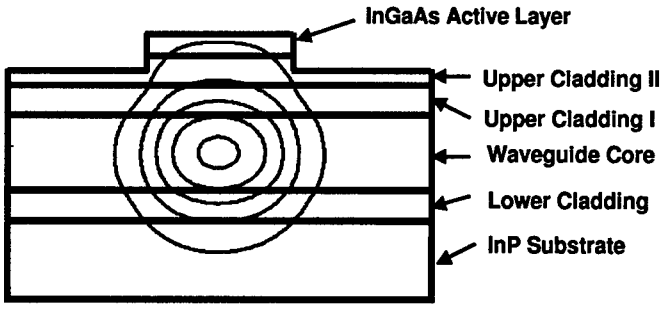

Figure 2. Contour plot of the fundamental mode profile in the photodiode region using BPM

Beam propagation method (BPM) is used to design and simulate the optical performance of the VMDP. Large-core optical waveguide is employed to reduce the coupling loss between the passive waveguide and the photodiode region as well as to reduce the optical power density in the absorption region. Only fundamental mode exists in both the passive waveguide and the photodiode regions. Figure 2 shows the optical field distribution of VMDP in the photodiode. Most of the optical energy concentrates in the waveguide core. The optical absorption and the coupling loss per photodiode for the VMDP shown in Fig. 1 are estimated to be 8.3% and 1.6%, respectively, by the BPM simulation.

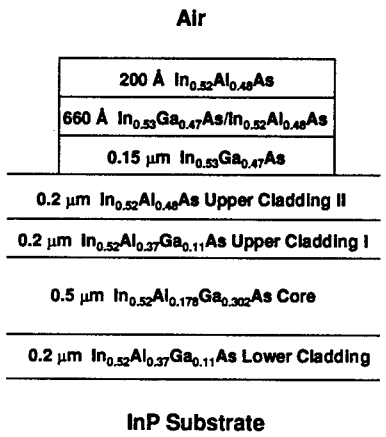

Figure 3. Cross section of VMDP wafer after mesa etching

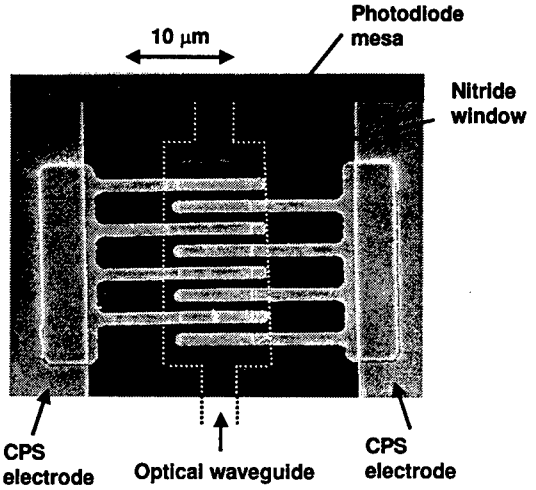

Figure 4. SEM picture of a single MSM photodiode of VMDP

The active MSM photodiodes consists of InGaAs absorption layer; InGaAs/InAlAs graded superlattice layers; InAlAs Schottky-barrier enhancement layer; and interdigitated fingers. The fabrication process is as followed: first, metal alignment markers are patterned on the substrate for subsequent process. Next, active mesas for photodiodes are defined by wet etching down to the InAlAs Upper Cladding II. Then optical ridge waveguide with ridge height

of 0.1μm is formed by wet etching. After mesa and waveguide etching, a Si_3N_4 passivation layer is deposited to protect the mesa edges. The nitride directly on top of the active mesas are opened for Schottky contacts. Interdigitated Ti/Pt/Au fingers with 1μm finger width and 1μm finger spacing are patterned in the open windows using optical lithography. Finally, the CPS microwave transmission line is fabricated using standard liftoff technique. The cross section of VMDP wafer after mesa etching is shown in Figure 3. Figure 4 shows the scanning electron micrograph (SEM) of a single MSM photodiode in the VMDP.

III. Device Characteristics

All devices under test are mounted on copper heat sinks. The temperature is set at 19 °C using a temperature controller. The VMDP exhibits very low dark current: 8.3 nA at 10V bias for a 1-mm-long VMDP with 13 photodiodes. The dark current has been reduced by 10 times compared to the VMDP in [5]. It is attributed to the nitride passivation which prevents the leakage currents through the sidewalls and the CPS electrodes. The external quantum efficiency is measured to be 0.4 A/W. With anti-reflection (AR) coating, it could reach 0.57 A/W. The dominant loss comes from the coupling from optical fiber to the VMDP. Figure 5 shows the DC responsivity of the new device. The responsivity of the VMDP in [5] is also shown for comparison.

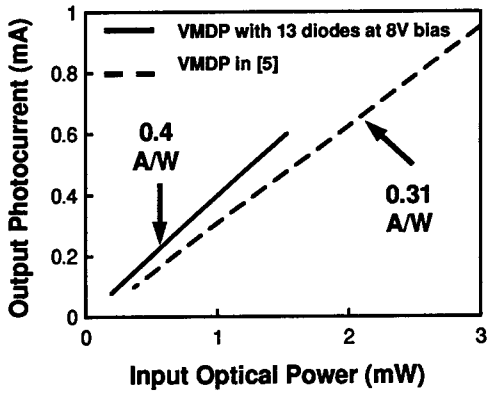

Figure 5. DC responsivity of VMDP (without AR coating)

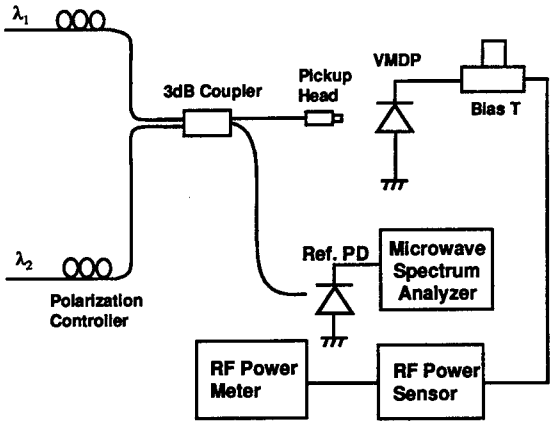

Figure 6. Schematic of optical heterodyne system setup for frequency response characterization of VMDP

The frequency response of the VMDP is characterized by optical heterodyne method [7,8]. The schematic of the experimental setup is shown in Figure 6. The system consists of two external cavity tunable lasers at 1.55μm, the frequency of each laser can be tuned in 1GHz step. The optical signals are combined by a 3dB coupler, and coupled to the VMDP using a fiber pickup head. The microwave signal generated by optical mixing in the VMDP is collected at the output end of the CPS by a 50GHz picoprobe (GGB Industries), which is connected to an RF power sensor and monitored by an RF power meter. The calibrated frequency response of long wavelength VMDP is shown in Figure 7. At 10 Volt bias, a 3dB bandwidth frequency of 13GHz is measured. By scaling down the MSM to deep sub-micron scale, much higher bandwidth (> 100 GHz) is expected.

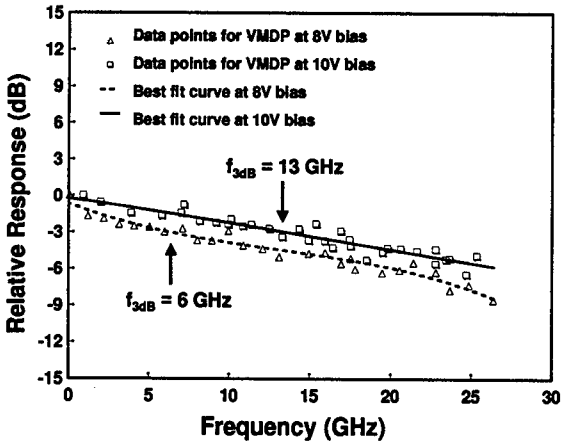

Figure 7. Measured frequency response of a long wavelength VMDP with 10 MSM photodiodes at different DC bias voltages

IV. Conclusion

In summary, we have experimentally demonstrated the improved performance of the long wavelength velocity-matched distributed photodetector (VMDP). A 3dB bandwidth of 13 GHz and a responsivity of 0.57 A/W have been achieved.

This project is supported by TRW, ONR MURI on RF Photonics, NRAO, Tracor and HRL under UC MICRO and JSEP.

References

[1]. L. Y. Lin, M. C. Wu, T. Itoh, T. A. Vang, R. E. Muller, D. L. Sivco, and A. Y. Cho, "High-power High-Speed Photodetectors. Design, Analysis, and Experimental Demonstration," IEEE Microwave Theory and Techniques, Vol. 45, pp1320-1331, 1997.

[2]. H. Jiang, J. T. Zhu, A. L. Kellner, P. K. L. Yu, Y. Z. Liu, "High-saturation-power waveguide photodetectors for analog fiber optic links," Proc. SPIE, Photonics and Radio Frequency, 7-8 August 1996, Denver, Colorado,Vol. 2844, pp. 120-124.

[3]. S. Jasmin, A. Enard, J.-C. Renaud, N. Vodjdani, "High-speed high-power waveguide photodetector with distributed absorption," Proc. SPIE, Photonics and Radio Frequency, 7-8 August 1996, Denver, Colorado,Vol. 2844, pp. 125-132.

[4]. C. H. Cox, III, "Gain and noise figure in analogue fiber-optic links," IEE Proceedings-J, Vol. 139, pp. 238-242, 1992.

[5]. T. Chau, L. Fan, D. T. K. Tong, S. Mathai, and M. C. Wu, "Long Wavelength Velocity-Matched Distributed Photodetectors," Proc. Conference on Lasers and Electro-Optics (CLEO), San Francisco, CA, May 3-8, 1998, p. 377.

[6]. M. C. Wu and T. Itch, "Ultrafast photonic-to-microwave transformer (PMT)," IEEE LEOS Summer Topical Meeting on Optical Microwave Interactions, Santa Barbara, California, USA, July 19-21, 1993

[7]. T. Hawkins, II, M. D. Jones, S. H. Pepper, and J. H. Goll, "Comparison of Fast Photodetector Response Measurement by Optical Heterodyne and Pulse Response Techniques," J. of Lightwave Technology, Vol. 9, pp. 1289-1294, 1991.

[8]. P. D. Hale, D. A. Humphreys, and A. D. Gifford, "Photodetector frequency response measurements at NIST, US, and NPL, UK: preliminary results of a standards laboratory comparison," Proc. SPIE Vol. 2149, pp. 345-356, 1994.

A Genetic Algorithm for the Design of All-Optical Microwave Filters

Thomas A. Cusick, Stavros Iezekiel, Robert E. Miles

Institute of Microwaves and Photonics, University of Leeds, Leeds, LS2 9JT, U.K.

tel: +44 113 2332093, fax +44 113 2332032, email: eentac@sun.leeds.ac.uk

Abstract *- Genetic algorithms are successfully employed to synthesize all-optical microwave filtering topologies. Unlike previous techniques, this allows investigations of new structures, and the inclusion of design factors such as physical size, component count or preferred values.*

I. INTRODUCTION

It is possible to implement signal processing functions on intensity modulated optical signals without transduction into the electrical domain, using optical waveguide structures. The structures considered here are composed of optical fiber 2×2 directional couplers, interconnected by fiber delays, to implement filtering functions at microwave frequencies. The delays are designed to be sufficiently long compared to the source coherence length, to ensure that incoherent optical interference takes place within the structures.

Techniques for the analysis of all-optical fiber structures for the processing of microwave frequency modulating signals, based on *z*-transform and signal flowgraph theory, are well known [1]. However the significant problem of structure *synthesis* has been less exhaustively investigated. The assumption of incoherent optical interference restricts the time domain output to positive values, thus preventing the reliable application of traditional digital filter design methods. Techniques have been proposed based on a state-space matrix representation of the problem [2] and on a modified Padé approximation [3], both leading to final designs which are relatively complex, incorporating several couplers, amplifiers and attenuators. The concatenation of a number of identical [4], and non-uniform [5], unbalanced Mach-Zehnder sections was suggested, to generate a symmetrical window response in the time domain. These resulted in simple passive structures, but included no attempt to minimize their physical size, the order of the response, or the number of optical components used and relied on the *a priori* selection of the form of the basic topology. In contrast, the genetic algorithm approach presented here overcomes these limitations, allowing the exploration of new topologies as solutions, as well as enabling the designers to meet specifications in an optimal fashion. The following section describes the application of a genetic algorithm to all-optical microwave filter design. Results are then presented, and the benefits and versatility of this approach discussed.

II. THE GENETIC ALGORITHM

Genetic algorithms [6] are computer based routines that mimic the process of 'survival of the fittest'. They are well-suited to the simultaneous optimization of several features of multivariable problems having complex solution spaces. As an illustration of the application of genetic algorithms to all-optical filter design, the synthesis of an optimized Mach-Zehnder lattice (see Fig.1), to perform an FIR filtering function, is outlined.

0-7803-4936-9/98/$10.00

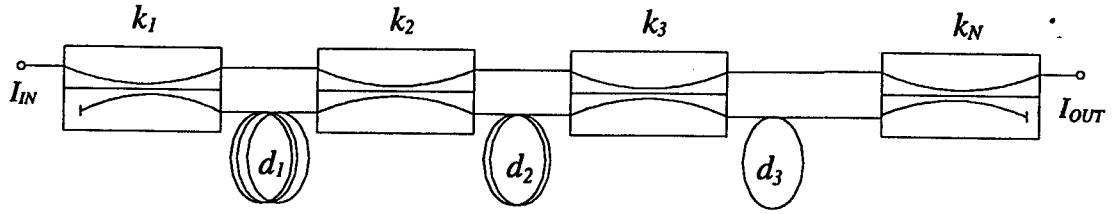

Fig. 1. The All-OpticalFiber Mach-Zehnder Lattice.

(i) **Initialization**: The problem is reduced to the optimization of a string of parameters, a *chromosome*, which uniquely identifies a particular solution. This consists of N, the number of couplers in the lattice, a list of the respective coupling coefficients ($k_1,\ldots,k_N$), and a list of the values of delay length difference between each pair of paths between adjacent couplers ($l_1,\ldots,l_{N-1}$) as multiples of the unit delay length. The coupling coefficients can be represented by floating point decimal values, and the delays by an integer multiple of the unit delay, which is dictated by the frequency of operation of the filter. An initial population of these chromosomes is generated using random values within predetermined limits, $1 < N < N_{MAX}$, $0 < k_i < 1$, $0 < l_i < l_{MAX}$.

(ii) **Fitness Function** : The *fitness* of each of these chromosomes is calculated; a measure of their suitability as solutions. This is done using an ideal filter specification [7]. The frequency response of each of the proposed filters is evaluated, and at equally spaced points in the passband and stopband, the response is compared to the specification. The fitness is enhanced for each point which meets the specification. For structures that meet the specification at all points, the fitness is further increased, and structures incorporating fewer couplers and shorter delays are awarded higher fitness ratings.

(iii) **Selection and breeding** : The best solution in the current generation is preserved (*elitist selection*), and chromosome pairs are selected to be parents by a process that is random but biased towards fitter individuals. *Offspring* can be produced in a variety of ways, the most common being *single-point crossover* [6]. Here a crossover point is randomly selected within the chromosome, and the genes after this point are exchanged.

(iv) **Mutation** : This is applied to each gene of each chromosome in the population, with every gene having an equal chance of being modified. If a gene is selected to undergo mutation, its value is randomly altered. This is to ensure that no region of the solution space becomes inaccessible to the algorithm.

(v) **Evolution** : After mutation has been applied, the offspring constitute the new generation. Steps (ii) to (iv) are repeated, until a predetermined number of generations has been generated and tested.

By having a population of solutions instead of a single one, several promising areas of the solution space can be simultaneously explored, and exploited with a view to finding a global maximum. This means that if they exist, families of solutions can be identified.

III. RESULTS AND DISCUSSION

An algorithm capable of working with FIR structures of any order was written in C, and run on a sun workstation. A population size of 1000 was chosen. The algorithm was applied to the design of a bandpass filter, with the specification (passband: 3.5-4.5 GHz, intensity (-3dBo)-(-5dBo); stopbands: 2.0-2.6 GHz, 5.4-6.0 GHz, intensiy <-25dBo) which is shown by the broken line in Fig.2. The genetic

algorithm generated a solution which included five couplers and four unit delays (Fig. 3 (a)). The simulated response is shown in Fig. 2 (solid line). This structure represents the set of most efficient FIR solutions to the problem in terms of number of couplers and delays used.

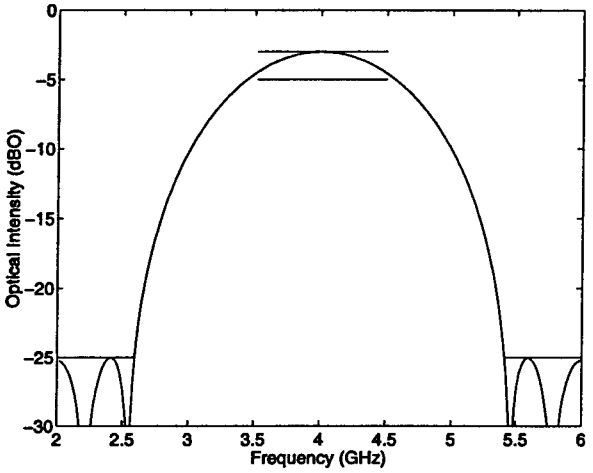

Fig. 2. Response of first structure produced by the algorithm.

A great advantage of the genetic algorithm solution to filter synthesis is the control that is possible over potential topologies. For example, in some cases the components to be used are restricted to a fixed set of preferred values. It is difficult to manufacture fused optical directional couplers to a prescribed coupling ratio, but the algorithm can be employed to ascertain the best combination and permutation of a set of couplers whose behaviors are already known, with a view to finding the solution to a particular design problem. This requires some modification of the breeding and mutation stages of the algorithm, to ensure that new solutions are acceptable. Fig. 3(b) shows an alternative solution to the previous design problem, using preferred coupler values : 0.1, 0.2...0.8, 0.9. To accommodate this restriction the structure requires an extra unit delay length.

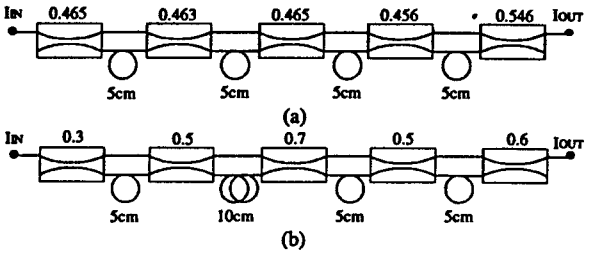

Fig.3.(a) Minimal and (b) preferred value structures.

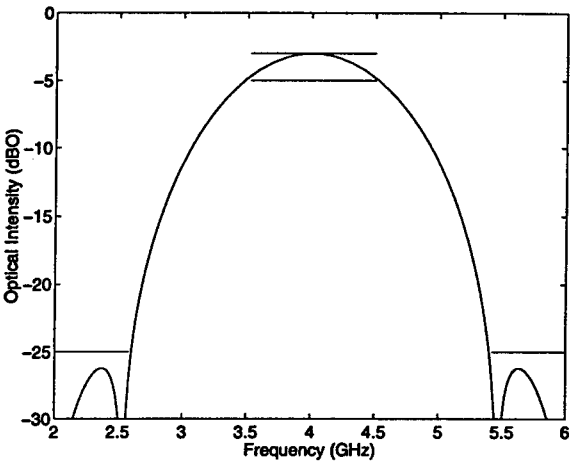

Fig. 4. Response of structure built using preferred component values.

Control over the delay lengths included in potential solutions is also useful. The assumption of incoherent operation within a structure is usually considered to be justified when the shortest delay length in the structure is less than the coherence length of the source. For sources with greater coherence lengths however, the assumption that incoherent interference takes place becomes increasingly unreliable [8]. It is possible, moreover, to construct a filter in which each individual delay length is comfortably greater than the coherence length of the source, but which contains two or more paths which are equal in length. This problem can be overcome by carefully selecting the delays in the structure, so that each one is at least a unit delay longer than the sum of all those preceding it. Fig. 5 shows a four coupler solution generated under these conditions, and its response and the specification (pass: 3.5-4.5 GHz, intensity (-3dBo)-(-6dBo); stop: 2.0-2.6 GHz, 5.4-6.0 GHz, intensiy<-20dBo) are shown in Fig.6.

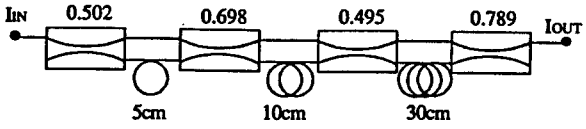

Fig. 5. Filter structure avoiding equal path lengths.

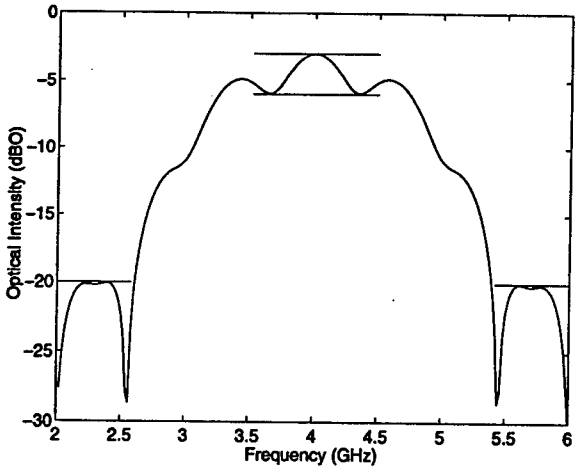

Fig.6 Response of structure shown in Fig.5.

Perhaps the most powerful aspect of these algorithms is their ability to optimize simultaneously several different attributes of a filter. Compromise between size, number of components and filter response can be easily worked into the fitness evaluation algorithm, and a weighting can be applied to each of them according to their relative importance. Physical size, for example, is especially of interest in problems where space is at a premium, such as integrated optics realizations.

In the examples presented in this summary the general form, if not the order, of the structure has been predetermined, hence like structures compete against one another. However, more sophisticated schemes may also subject the topology itself to optimization, rather than assuming a standard network.

IV. CONCLUSIONS

A new approach to the synthesis problem for all-optical microwave frequency filters has been suggested, which uses a genetic algorithm to generate the filter structure. The advantages of such an approach have been discussed. The algorithm has been implemented and tested on microwave bandpass filter specifications. The application of genetic algorithms has been demonstrated to be a viable approach for the synthesis of all-optical filter networks. The algorithm has been shown to have some advantages over previous suggested methods [2]-[5], producing sets of minimal solutions, and overcoming restrictions such as limited or fixed component values, and unwanted coherent interference effects. The method also benefits from being free of initial assumptions about the order or form of the filter structure, so that the topology itself can be subject to optimization.

References

[1] B.Moslehi, J.W.Goodman, M.Tur, H.J.Shaw, "Fiber Optic Lattice Signal Processing", Proceedings of the IEEE, vol.72, no.7, pp.909-930, 1984.

[2] E.C.Heyde, R.A.Minasian, "A Solution to the Synthesis Problem of Recirculating Optical Delay Line Filters", IEEE Photonics Technology Letters, vol. 6, no.7, pp.833-835, 1994.

[3] J.Capmany, J.Cascón, J.L.Martín, S.Sales, D.Pastor, J.Martí, "Synthesis of Fiber-Optic Delay Line Filters", Journal of Lightwave Technology, vol.13, no.10, pp.2003-2012, 1995.

[4] S.Sales, J.Capmany, J.Martí, D.Pastor, "Solutions to the synthesis problem of optical delay line filters", Optics Letters, vol.20, no.23, pp.2438-2440,1995.

[5] T.A.Cusick, S.Iezekiel, R.E.Miles, S.Sales, J.Capmany, "Synthesis of All-Optical Microwave Filters using Mach-Zehnder Lattices", IEEE Trans. MTT, vol.45, no.8, pp.1458-1462, 1997.

[6] Z.Michalewicz, *Genetic Algorithms+Data Structures=Evolution Programs,* Springer-Verlag, Berlin, 1994.

[7] D.A.Suckley, "Genetic algorithm in the design of FIR filters", IEE Proceedings-G, vol.138, no.2, pp.234-238, April 1991.

[8] H.Ho-Quoc, S.Tedjini, A.Hilt, "Optical Polarization Effect in Discrete Time Fiber-Optic Structures for Microwave Signal Processing", IEEE MTT-S Digest, pp.907-910, 1996.

DEMONSTRATION OF OPTICALLY CONTROLLED MICROWAVE PHASE CONJUGATION

Yian Chang and Harold R. Fetterman
Electrical Engineering Department
University of California, Los Angeles, CA 90095

Boris Tsap
Pacific Wave Industries, Inc.
10911 Weyburn Av. Suite 222, Los Angeles, CA 90024

Irwin L. Newberg and Steve K. Panaretos
Hughes Aircraft Co.
PO Box 92426, Los Angeles, CA 90009-2426

Abstract: We have demonstrated two-dimensional free space phase conjugation at $10.24GHz$ using an one-dimensional optically controlled phased array with a simple one-stage-mixing technique. Preliminary results are also obtained for an improved two-stage-mixing configuration.

Introduction

Since its first demonstration, phase conjugation has been studied intensively and has been well developed in the optical regime. In general, this technique utilizes the nonlinear susceptibility of a medium to reverse the phase factor of an incoming wave. The phase-conjugate wave propagates backward and has the same wavefronts as that of the incoming wave. This unique property is useful in many novel applications including automatic pointing and tracking, phase aberration corrections, and phase-conjugate resonators. Efforts to extend this technique to microwave and millimeter wave frequencies have encountered severe difficulties due to the small nonlinearity of natural materials and the low power density of sources in this regime. In the search for alternative media suitable for microwave and millimeter wave phase conjugation, artificial media were found to have much larger nonlinearities than that of natural materials. Using shaped microparticle suspensions [1] and MEMS structures [2], volume grating formation for microwave phase conjugation has been demonstrated with degenerate four-wave mixing techniques. However, these media intrinsically suffer from slow response time and are sensitive to surrounding conditions. Therefore, they are not suitable for any practical systems and applications. In this study, we have developed a new technique to achieve microwave phase conjugation using arrays of optically controlled antenna-coupled mixers as artificial nonlinear media. An 8-element array has been assembled using a simple one-stage-mixing configuration to demonstrate two-dimensional free space phase conjugation at $10.24GHz$. The results have clearly shown the retro-directivity and automatic phase correction characteristics of phase conjugation. Also in the study, a superior two-stage-mixing approach has been developed and its single element performance has been tested. These experiments have shown amplified conjugate-wave power up to 10 times of that of the incoming wave. This amplifying ability demonstrates the potential of such arrays to be used in novel communications applications.

0-7803-4936-9/98/$10.00

Concept

In this study, microwave circuits that combine antennas and microwave mixers effectively replace the nonlinear dipoles of a medium. The idea is to "sample" the incident wave at different positions of the wavefront and then generate phase-conjugate currents using microwave mixers. These currents will then excite a phase-conjugate field at each sampling point. The combined field of all elements will be the phase-conjugate wave of the incident beam. This sampling concept was proposed and examined in the 60's [3], but due to the lack of modern semiconductor [4] and photonic technologies, researchers did not have a practical way to realize the concept. To understand how the conjugate signal can be generated at each element using microwave circuitry, let's consider the incident electric field at the j^{th} element:

$$\mathbf{E} = \mathbf{A}(\mathbf{r}_j)e^{i(\omega t-\varphi_j)} + c.c., \text{ where } \varphi_j = \mathbf{k}\cdot\mathbf{r}_j + \varphi(\mathbf{r}_j)$$

The signal detected by the antenna and then sent to the RF port of the mixer can be written as:

$$V_{j1} \propto A(r_j)e^{i(\omega t-\varphi_j)} + c.c.$$

Now consider a 2ω signal delivered to the LO port of the mixer given by:

$$V_{j2} = Ce^{2i\omega t} + c.c.$$

This 2ω pump signal has to be delivered to all elements at the same amplitude and phase; otherwise the mixed output will contain a term other than V_{j1} that depends on j. If this happens, the sum of the excited field at each element will be distorted and will not form the conjugate beam. Optical control is the crucial technology implemented to carry this 2ω microwave pump signal in phase to all mixing elements because of its low loss, light weight, and small size compared to the microwave counterpart. Using difference frequency generation in a mixer, the IF output current can be written as:

$$I_C \propto e^{2i\omega t}\cdot e^{-i(\omega t-\varphi_j)} = e^{i(\omega t+\varphi_j)}$$

This current component has the conjugate phase $+\varphi_j$ instead of the input phase $-\varphi_j$. Therefore when it is delivered to the antenna, it will excite the conjugate field at $\mathbf{r}_j$:

$$\mathbf{E}_{Cj}(\mathbf{r}_j) \propto \mathbf{A}(\mathbf{r}_j)e^{i(\omega t+\varphi_j)} + c.c.$$

When the sampling spacing is less than $\lambda/2$, the combined field $\mathbf{E}_C = \sum_j \mathbf{E}_{Cj}(\mathbf{r})$ forms the phase-conjugate wave on the sampling surface and therefore everywhere. Computer simulation has shown that the quality of the conjugate wave is limited by the size of the conjugation surface, not the element spacing, as long as the inter-element spacing is less than $\lambda/2$.

In the previous discussion, there is no way to separate the unwanted V_{j1} leakage in the mixer from the desired conjugate signal because both are at the same frequency ω. A two-stage-mixing technique has been developed to solve this problem. In this scheme, V_{j1} is first mixed with an LO at $2\omega-\Delta$ through different frequency generation:

$$I_c' \propto e^{i(2\omega-\Delta)t}\cdot e^{-i(\omega t-\varphi_j)} = e^{i[(\omega-\Delta)t+\varphi_j]}$$

Since the desired signal is at $\omega-\Delta$, a bandpass filter can be used to block the leakage at ω. This intermediate signal is then mixed with an LO at Δ through sum frequency generation:

$$I_C \propto e^{i\Delta t}\cdot e^{i[(\omega-\Delta)t+\varphi_j]} = e^{i(\omega t+\varphi_j)}$$

This signal now carries the desired conjugate phase $+\varphi_j$ at the desired frequency ω. A second bandpass filter can be used to block the leakage at $\omega - \Delta$. Notice that by choosing Δ close to ω, no high frequency 2ω devices are required.

Demonstration

To demonstrate the above-mentioned concepts, we have built an optically controlled 8-element one-dimensional array using the one-stage-mixing technique. Figure 1 shows the configuration of each element. In this demonstration, the RF frequency is set at $10.24GHz$. A diode-pumped Nd:YAG laser is used as the light source. The optical wavelength is at $1319nm$, with a linewidth $\leq 5KHz$. The laser light is directed into a Mach-Zehnder optical modular and is modulated by the 2ω ($20.48GHz$) signal. The 2ω pump signal is delivered to each element using optical fibers. It is then extracted by a photodetector to be used as the LO signal for mixing. The amplitudes of all phase-conjugate elements are matched to within $\pm 2\%$. The phases are matched to within $\pm 0.2ps$ (0.2%).

To measure conjugate electric field distribution, a computer controls a receiving horn to scan the desired area. The detected signal is sent to a digital sampling oscilloscope and is compared to a fixed reference signal for both amplitude and phase measurements. Figure 2 shows the results of two illuminating sources. The first plot, marked as "Without Distortion", is obtained without anything in the microwave paths and it clearly demonstrates retro-directivity for each source. However, due to the diffraction effects of the small array, the wavefronts do not focus back to the sources. Note that the fainter fringes are caused by mixer leakage and can be eliminated by using a two-stage mixing technique. To demonstrate automatic phase

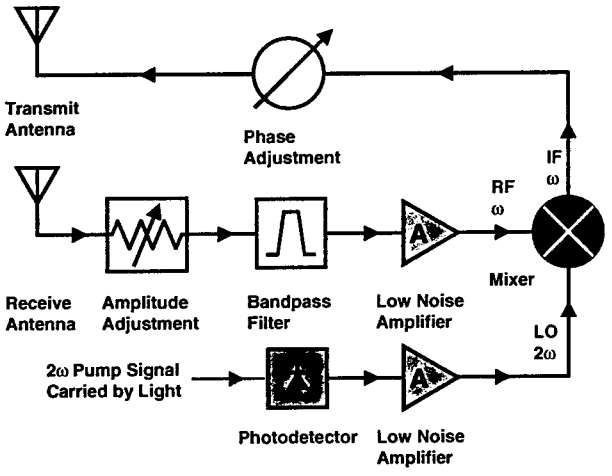

Figure 1. The configuration of the one-stage-mixing phase-conjugate element used in this study.

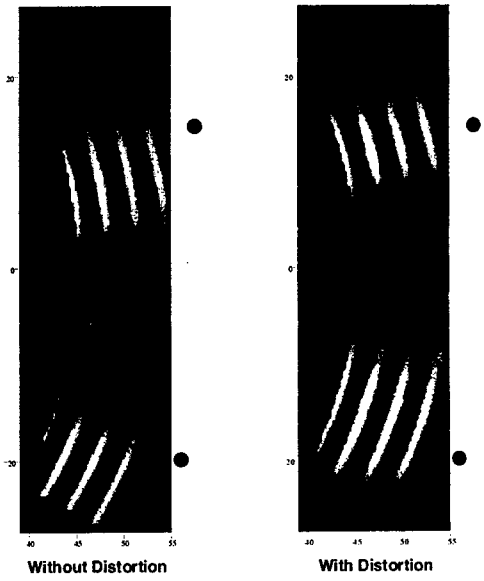

Figure 2. The contour plots of the phase-conjugate electric field of two sources marked by the black dots. The conjugator is located on the left of each plot. Brightness represents electrical field magnitude. The wavefronts (fringes) travels from left to right. They demonstrate retro-directivity and automatic phase correction when a distorting medium is inserted in front of the conjugator. Leakage signals, down by about 10 dB, also appear adjacent to the conjugate signals and are distorted by the distorting medium.

correction, a distorting material is placed in front of the conjugator and the conjugate field is shown in the second plot, marked as "With Distortion". By comparing the fringes of the two plots, automatic phase correction is clearly demonstrated in the phase conjugate beams while the phase information is destroyed in the leakage signals.

As mentioned earlier, a two-stage-mixing technique has been developed to solve the mixer leakage problem [5]. The configuration is shown in Figure 3. In the preliminary test we have chosen: $\omega = 7.1GHz$ and $\Delta = 3.1GHz$. The measured output phase (y) vs. input phase (x) is shown in Figure 4. It exhibits excellent agreement with the desired function $y = -x$ for phase conjugation. Figure 5 shows the measured output amplitude vs. input phase. It demonstrates the output amplitude is virtually independent of the input phase.

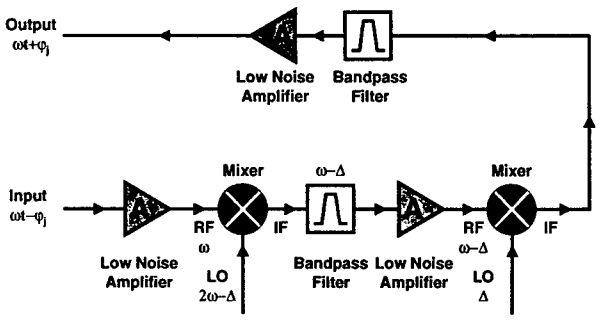

Figure 3. The configuration of the two-stage-mixing phase-conjugate element tested in this study.

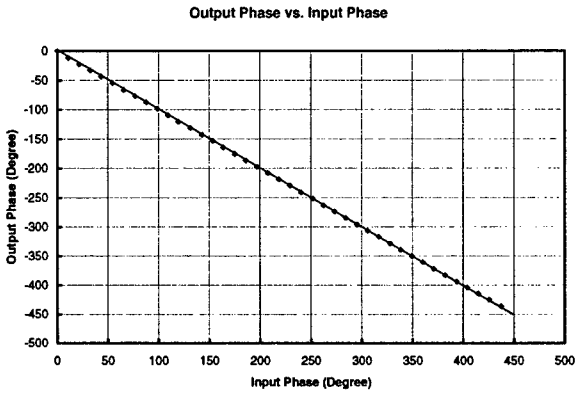

Figure 4. The measured output phase vs. input phase for the two-stage-mixing element. The straight line represents the desired function $y = -x$.

Conclusion

We have demonstrated two-dimensional phase conjugation at $10.24GHz$ with diffraction limited results using an optically controlled one-stage-mixing phased array. Preliminary results are also obtained for an improved two-stage-mixing configuration. By extending one-dimensional arrays into two-dimensional surfaces, complete three-dimensional wavefront reconstruction can be realized at microwave and millimeter wave frequencies.

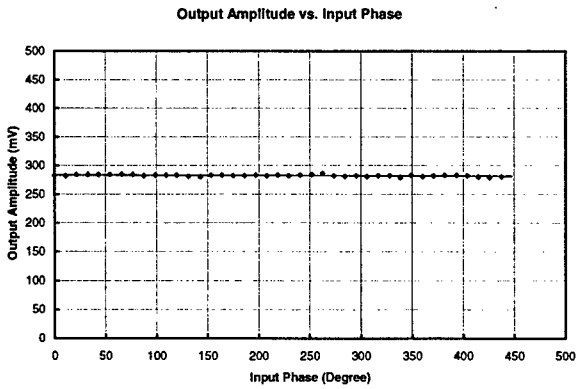

Figure 5. The measured output amplitude vs. input phase for the two-stage-mixing element.

This work was supported by DARPA and AFOSR under Dr. Howard Schlossberg.

References:

[1] R. Shih, H. R. Fetterman, et al., *Phys. Rev. Lett.*, vol. 65, no. 5, pp. 579-582, 1990.
[2] B. Tsap, K. S. J. Pister, and H. R. Fetterman, *Appl. Phys. Lett.*, vol. 70, no. 18, pp. 2475-2477, 1997.
[3] C. C. Cutler, R. Kompfner, and L. C. Tillotson, *Bell Syst. Tech. J.*, vol. 42, pp. 2013-2032, 1963.
[4] C. W. Pobanz, and T. Itoh, *Proceedings of 1995 IEEE MTT-S International Microwave Symposium*, New York, NY, USA: IEEE, vol. 2, pp. 905-908, 1995.
[5] B. D. Steinberg, *Microwave imaging with large antenna arrays : radio camera principles and techniques*, New York, NY, USA: Wiley, 1983.

Optical Distribution of Reference Signals to a Digital Beamforming Antenna

Jan Önnegren and Lars Pettersson

Defence Research Establishment (FOA), Box 1165, S-581 11 Linköping, Sweden
Phone: +46 13 37 80 00, Fax: +46 13 37 81 00, E-mail: janonn@lin.foa.se

***Abstract*—The use of fiberoptic techniques for distributing reference signals to a digital beamforming antenna has been investigated. An optical calibration network has been implemented and evaluated. The results are compared to other calibration methods.**

I. INTRODUCTION

With digital beamforming, DBF, very accurate beam control can be obtained and various array signal processing methods can be applied. This include multiple beams with very low sidelobes and adaptive pattern control, direction of arrival estimation, etc.

The different parts of a receiving DBF antenna are illustrated in Fig. 1. It consists of an array of antenna elements, a calibration network, receiver modules, AD-converters, digital down converters, channel equalizers, a digital beamformer and a control processor.

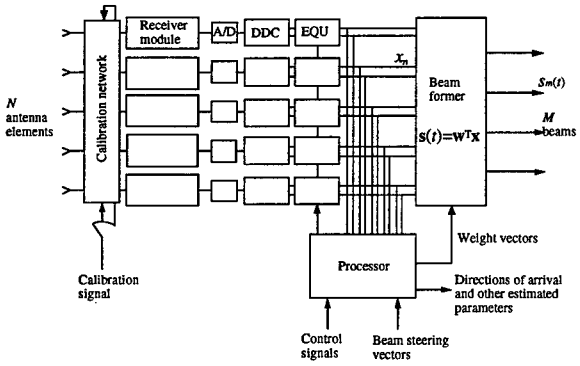

Fig. 1. Architecture of a DBF antenna system [1].

The internal calibration network is placed between the antenna elements and the receiver modules. The calibration signal must be stable in both phase and amplitude if low sidelobe levels should be achieved. Furthermore the reveiver module must be stable between two calibrations. Any relative phase errors $\Delta\theta$ (RMS) and relative amplitude errors ΔA (RMS) that remains after a calibration give rise to a relative sidelobe level (in dB).

$$\text{Relative sidelobe} = 10 \cdot \log\left(\frac{(\Delta A)^2 + (\Delta\theta)^2}{N \cdot \eta_A}\right) \qquad (1)$$

Where N is the number of antenna element (here N=12) and η_A is the antenna aperture efficiency ($\eta_A \approx 0.5$-1). Equation (1) shows that the optical calibration signal must be very stable in both phase and amplitude. If the sidelobe level should be less than -50 dB it requires that the relative amplitude variation (ΔA) is less than 0.1 dB (when $\Delta\theta$=0) or that the relative phase variation $\Delta\theta$ is less than 0.7° (when ΔA=0). To obtain this, the optical calibration network must have a good amplitude and phase stability over a long period of time.

The fiberoptical calibration network studied consists of a direct modulated semiconductor laser, fiber, optical coupler (1xN) and PIN diodes as detectors. Fig. 2 shows the optical calibration network and how the calibration signals (electrical and optical) are connected to the receiver module that should be calibrated.

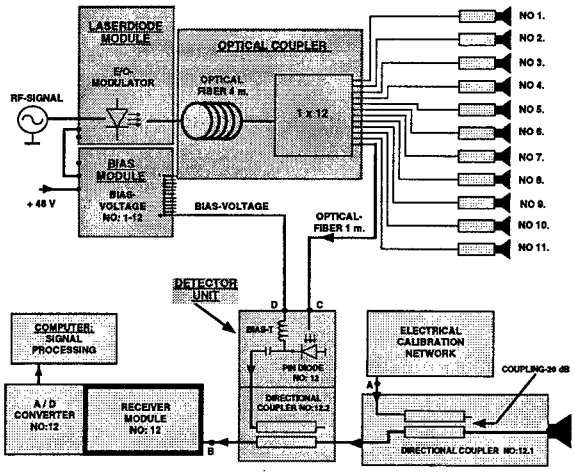

Fig. 2. Implementation of optical calibration network.

The calibration signal from the optical distribution network is fed to the receiver via a separate 20 dB directional coupler. Therefore it is made possible to compare optical and electrical calibration methods. The antenna operating frequency is 2.8-3.3 GHz, but the optical calibration network has a good performance from almost DC to around 5 GHz. If the frequency of the calibration signal is higher than 5 GHz, external modulators can be used instead of the direct modulated laser. To evaluate the optical calibration network it's temperature dependence has been experimentally evaluated in detail.

0-7803-4936-9/98/$10.00

II. TEMPERATURE DEPENDENCE OF PIN DIODES AND OPTICAL COUPLERS

The temperature dependence for the components in the optical calibration network in Fig. 2, for example the PIN-diode, laser, optical coupler, fiber, bias-T and directional coupler, has been evaluated separately.

The main temperature dependence for the PIN diode detector is due to the variation in the optical coupling efficiency between fiber and diode. The PIN diode (chip) itself has a very small temperature dependence that normally can be neglected.

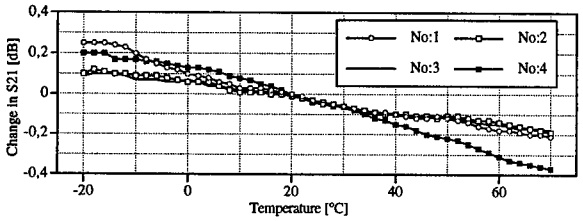

Fig. 3. Change in electrical power S21 as a function of temperature.

Fig. 3 shows the change in microwave transmission (S21) at 3 GHz for four PIN diodes of type B. The microwave power decrease with about 0.06 dB per 10°C.

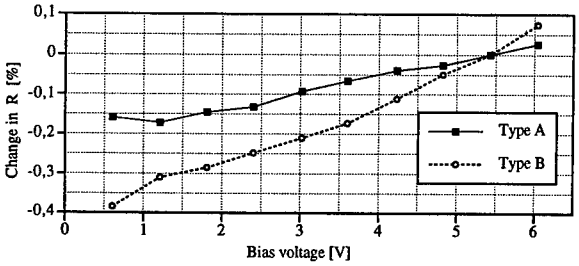

Fig. 4. Change in responsivity R as a function of bias voltage.

The responsivity R [A/W] for the PIN diode has a small bias voltage dependence. Figure 4 shows that the change in R is about 0.1 % per volt for a diode of type B (corresponding to a change in power of 0.0086 dB).

The temperature dependence for a singel mode fiberoptical coupler from ETEK has been evaluated. This coupler (see Fig. 5) is built of cascaded 2x2 couplers, to a total of 16 outputs. The coupler is manufactured with a "fused biconical taper" technique. During the measurement of the optical variation at the output of the coupler, the optical input polarisation has been held constant. The optical output variation with input polarisation has also been evaluated.

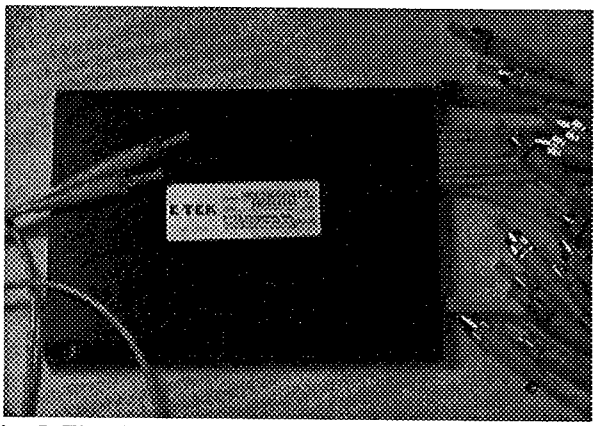

Fig. 5. The single mode optical coupler from ETEK.

The results from the temperature measurement on the optical coupler from ETEK can be seen in Fig. 6. The maximum change in the optical output power is less than 4% over a 90 °C temperature change, corresponding to a change in the electrical output power of 0.34 dB.

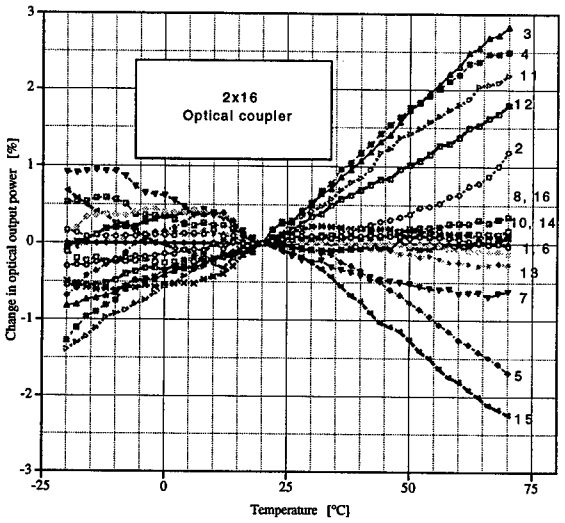

Fig. 6. Change in optical output power [%] as function of temperature for the optical coupler.

If smaller amplitude and polarisation variations is required, other types of optical couplers must be considered [2].

III. OPTICAL CALIBRATION NETWORK

The optical coupler, laserdiode module and the bias module was mounted in a "transmitter" box that can be seen in Fig. 7. The optical fiber between the laser diode

and optical coupler has been made as short as possible. This is because the optical polarisation variations at the input of the optical coupler must be minimised. Before the optical calibration network shown in Fig. 7 was mounted in the antenna, additional temperature measurements where carried out on the total system.

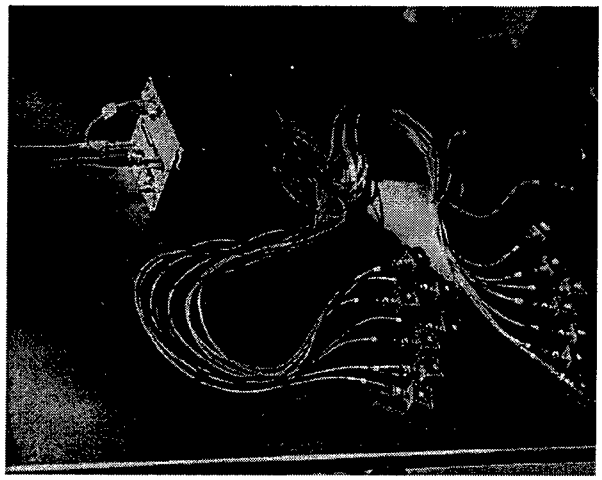

Fig. 7. The optical calibration network before it was mounted into the antenna.

The transmitter module shown in Fig. 8 was built around a laser diode module from Fujitsu (FLD3F7CX). This laser diode has extremely high slope efficiency (0.3 W/A in to fiber) and low relative intensity noise (-170 dB/Hz at 600 MHz). The module has a built-in series resistor of 20 ohm. This resistor gives the module a broadband microwave matching at the cost of additional link loss.

The measured link gain for the laser diode module is around -17 dB for frequencies below 4 GHz at 10 mW optical output power [3]. The 1x16 optical coupler gives an additional loss of 24 dB. Therefore the total link gain for the optical calibration network is around –41 dB, excluding the 20 dB directional coupler.

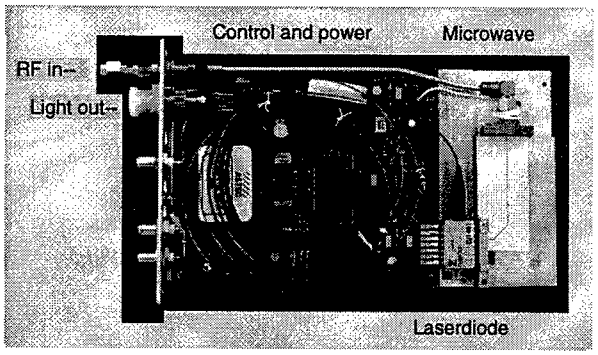

Fig. 8. The laser diode module.

IV. CALIBRATION EXPERIMENT

Figure 9 illustrates the alternatives that can used to calibrate the antenna. The three alternatives are: external calibration using a separate illuminating antenna, and internal electrical and optical calibration networks respectively. During a calibration only one signal is applied to the antenna.

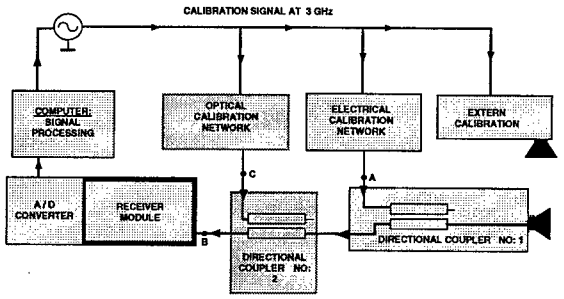

Fig. 9. The three calibration alternatives.

Once the optical calibration network is mounted into the antenna (see Fig. 10) it is difficult to verify the stability of the network because of the big temperature dependence in the receiver modules. One method to evaluate the performance of the optical calibration network is to compare the optical calibration results with the results from an internal electrical or external calibration.

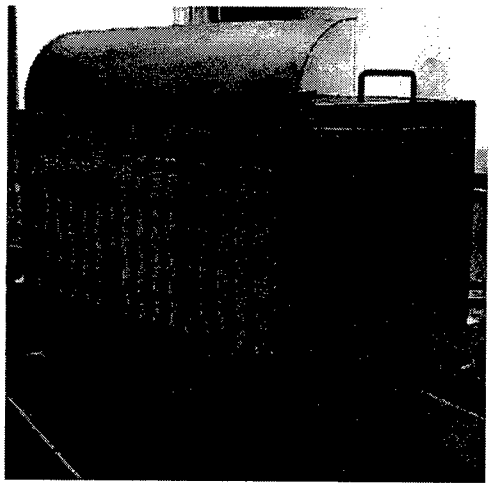

Fig. 10. S-band digital beamforming antenna.

Figure 11 shows calibration results for the optical calibration network, normalised to the results from an external calibration. During these measurements the room temperature varied between 18 °C and 22 °C. Each trace correspond to a measurement that is repeated once every hour. The variation between the seven traces is a quality

indicator of the optical calibration network, but the temperature variations of the striplines from the antenna elements to the directional coupler are also included in this variation.

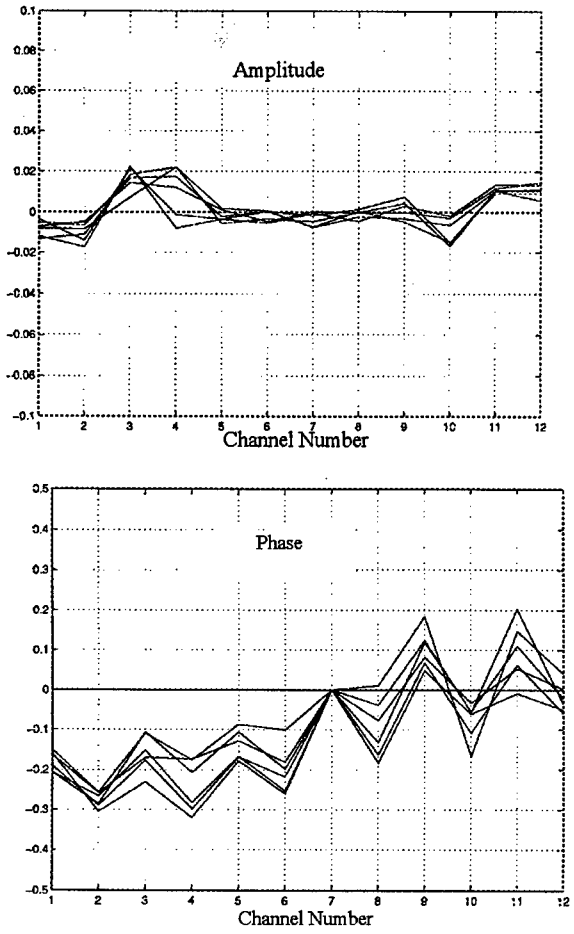

Fig. 11. Measured change in amplitude in dB (top) and phase in degree (bottom), using the optical calibration network.

The calibration results shown in Fig. 11 using the optical calibration network, during 7 hours and with 4°C room temperature variation, gave an accuracy of approximately 0.01 dB in amplitude and 0.2° in phase. The calibration network can thus be used to obtain very low sidelobes.

V. CONCLUSION

Calibration measurements on the antenna shows that both the electrical and optical calibration network fulfils the amplitude and phase requirements. Both calibration networks can be used to obtain a sidelobe level lower than -50 dB for a 12 element array.

The advantages with an fiberoptical calibration network compared to an electrical one are:

- Reference signals over a wide frequency range can be distributed (0-20 GHz).
- The optical fiber is flexible and temperature stable. This is of great importance in large antenna and if the antenna unit is separated.
- The calibration network studied can easily be extended to a larger number of elements. With a direct modulated laser the upper limit is some hundred antenna elements.
- No electromagnetic interference inside the antenna.

One disadvantage with an optical calibration network is the optical polarisation variation in the fibers, which is due to mechanical stress or temperature variations. Different types of normalisation techniques can be applied to minimise the corresponding amplitude and phase variations. One technique is to measure the PIN diode current and use this to compensate for the amplitude variations [4].

REFERENCES

[1] L.Pettersson, M. Danestig, U. Sjöström "An Experimental S-Band Digital Beamforming Antenna", IEEE Int. Symp. on Phased Array System and Technology, pp. 93-98, Boston, USA, 15-18 Oktober 1996.

[2] Y. Namihira et al."Incident polarization angle and temperature dependence of polarization and spectral response characteristics in optical fiber couplers", Applied Optics, Vol.30, No. 9, pp. 1062-1069, March 1991.

[3] J.Önnegren, A.Alping "A high Performance Fiber Optical S-band Radar Link", International Topical Meeting on Microwave Photonics, PDP pp. 13-14, Duisburg/Essen, Tyskland, September 1997.

[4] C. H. Cox III and A. C. Yee "RF Gain Stabilization of a Directly Modulated Optical Link using Detector Current Normalization", IEEE MTT-S, International Microwave Symposium Digest, Vol. 2, pp. 1117-1120, San Diego, USA, May 23-27, 1994.

VOLUME ARRAY WITH OPTICAL FEEDS

A D Carr P J Tittensor

GEC-Marconi Research Centre
West Hanningfield Road, Great Baddow, Essex CM2 8HN, U.K.

Abstract: Volumetric phased arrays offer full spherical coverage with phase-only control. To overcome problems of feed obstruction limitations, we report an array in which transmit power and signal are delivered to each element on fibre.

I. Introduction

Phased array antennas offer the opportunity for versatile power management and the potential for multiple beams, factors which are of continuing and increasing importance to systems applications such as radar, comms and EW. MRC has recently completed a study of conformal and volume arrays and the role of optics in feeding a signal and power to the latter is described. Conformal array elements are distributed over a curved, possibly spherical, surface while volume array elements are distributed randomly within a 3-D region. The various configurations offer the following benefits:

Planar Array

Pros	Cons
Established technology.	Limited scan range.
Fixed amplitude distribution.	Inefficient use of elements in multi-faceted array.
Phase only scan.	Gain falls with scan.
Single polarization elements can be used.	Bandwidth limited by grating lobes.

Conformal Array

Pros	Cons
Full cover (spherical array).	Must change amplitude and phase distributions when scanning beam.
Mounts on non-planar surface.	Must switch elements to cover wide angles. This limits EIRP.
Low sidelobes possible.	Bandwidth limited by grating lobes.
Cross-polar achievable with control of orthogonal polarizations.	

Volume Array

Pros	Cons
Full spherical coverage	Requires control of three orthogonal polarizations for spherical coverage with low cross-polar.
Phase-only control.	May require amplitude and phase control for very low sidelobes (less significant for larger arrays).
Higher EIRP because all elements contribute.	
Low sidelobe levels with amplitude control, or density tapering for large arrays.	
Bandwidth not limited by grating lobes.	

II. Implementation Of Volume Array

Volume arrays have been demonstrated experimentally with elements fed and supported by vertical coaxial cables. The elemental designs have included single-plane log periodic dipoles [1] and microstrip loop structures [2]. The presence of the metallic feeds introduces significant performance limitations since they restrict the possible radiation polarisation to be perpendicular to the feed axis thus precluding the use of full polarisation diversity and spherical field of scan. In addition the feed metallisation also causes some scattering of the perpendicular polarisation, it can constitute a large component of the array mass and can limit the minimum lateral element spacing. The replacement of metal feeds by dielectric glass fibre carrying RF modulated optical power offers a promising route to address these limiting factors and allow the full potential of volume arrays to be realised. The remainder of the paper describes a prototype dipole array, developed and demonstrated at Marconi Research Centre, which employs such fibre feeds to provide both RF signal and DC power to each element. The principle has been demonstrated so far for an array of single axis dipoles operating in transmit mode but

0-7803-4936-9/98/$10.00

possible routes to full polarisation and duplex operation will also be summarised.

III. Configuration of optically fed array - dipole

The demonstrator array comprises 16 dipole elements placed randomly within a volume of approximately 34 cm^3. The elements are mounted on top of varying length quartz rods. Each dipole consists of two metal arms separated by a quartz block which incorporates a high speed photodiode, photocell, capacitor, inductor and fibre interfacing. The RF intensity modulated optical signal (λ=1550nm) is delivered to each element via a standard singlemode fibre with a 45° mirrored end to reflect light up into the planar mounted photodiode. The purpose of the photocell is to provide a reverse bias of a few volts to the photodiode to achieve high speed operation. Each photocell is illuminated via a multimode (62.5/125 μm) fibre with power provided by an array of semiconductor diodes, one for each element. Uniform illumination of the full photocell area is essential for optimum operation and this is achieved by using an appropriate length glass block also with a 45° mirrored face to direct the beam down onto the planar mounted device. The maximum load current which can be supported by the photocell sets the limit for the mean photocurrent and hence optical power which is acceptable to fall on the photodiode and therefore the electrical power which can be radiated. Two other components are included on each dipole; a very small coil inductor to isolate the photocell from the photodiode at RF and a chip capacitor. Figure 1 shows a picture of the completed array.

Phasing of the elements was implemented by inserting appropriate length fibre patchcords selected from a set which covered a range in excess of a microwave wavelength in 0.5 mm increments (6.8° in electrical phase at the operating frequency). The phase was determined and adjusted relative to a reference by performing an RF/optical measurement on each element in an identical isolated environment. A modelled result for a 16 element array is shown in figure 2. Figure 3 compares the experimentally measured pattern with 11 of the 16 elements driven with the corresponding prediction. The limitation on number of driven elements was imposed by the availability of HeNe powering lasers and not by element functionality.

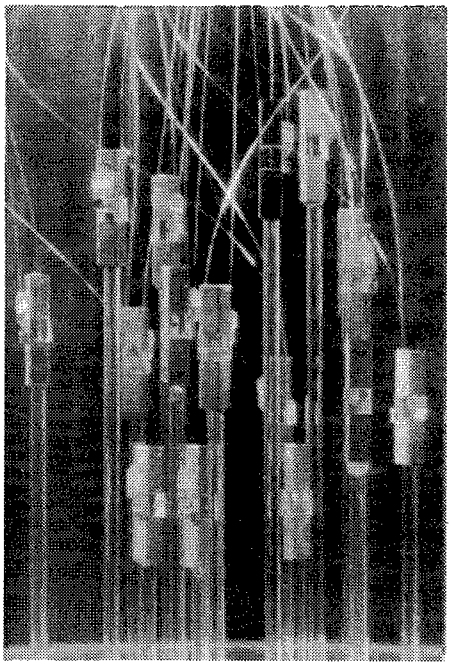

Figure 1: Photograph of 16 element volume array

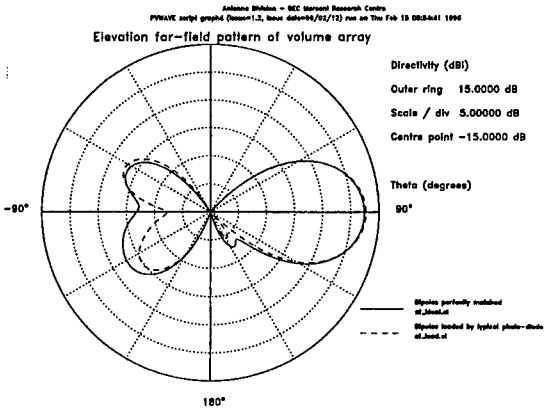

Figure 2: Predicted pattern for 16 element array

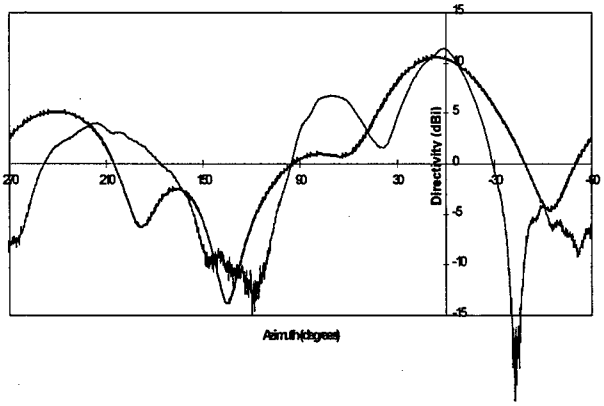

Figure 3: Comparison of modeled and measured patterns, 16 element array with 11 elements driven.

IV. Conclusions And Future Directions

Volume arrays may offer significant benefits for certain applications including the potential for full spherical coverage with phase only control, high EIRP and a wide bandwidth not limited by grating lobes. A 16 element prototype volume array has been demonstrated in transmit mode, in which both power and modulated signal are delivered to each element optically, thus overcoming one of their principal limitations in terms of feed obstruction.

Several areas of further development can be identified for the optically fed volume array. Practical applications will require higher radiated power per element. As discussed above this is primarily limited by the mean optical signal power at the photodiode which can be supported by the photocell. Enhancements to this could be achieved by increasing the visible source power, using several photocells in parallel or higher efficiency devices. Optically pulsed operation would also increase the peak radiated powers for some applications. Polarisation diversity may be implemented by appropriate choice of element design, for example a 3-D arrangement of crossed dipoles or a more novel structure such as a pyramidal log-periodic arrangement.

Duplex operation would require a signal modulator at each element which would therefore need to be compact, optically fed, capable of operating at microwave frequencies and ideally have a low drive voltage to obtain significant modulation depth without requiring electrical pre-amplification. Scanned operation would need to be addressed but here the optically fed nature would be directly compatible with advanced optical True Time Delay approaches to wideband beamforming.

Acknowledgements

The authors would like to acknowledge the support given to this work by DERA Malvern, and Mr A Fray's original proposals for this concept. We also acknowledge some early results obtained at MRC by Mr A J Aitken.

Reference

1. Tennant A, Fray A F, Adamson D B, Shelley M W, 1997, "Beam scanning characteristics of 64 element broadband volumetric array", Elect. Lett., 33, No. 24 2001-2002.
2. Wilden H, Ender J, "The crows nest antenna-experimental results", IEEE International Radar Conference, Radar '90, 280-285

EXPERIMENTAL DEMONSTRATION OF A FIBER OPTIC ROTMAN BEAMFORMER

R. A. Sparks, N. Slawsby, ANRO Engineering, Inc.*
63 Great Road, Maynard, MA 01754
Tel: (978) 897-2601; Fax: (978) 897-2642
and
J. Prince, J. Munro, Lincoln Laboratory, Massachusetts Instititute of Technology**
244 Wood Street, Lexington, MA 02173
Tel: (781) 981-5022; Fax: (781) 981-3905

INTRODUCTION

The fiber optic Rotman lens (FORL) is a lightwave analog of the well-known Rotman-Turner [1] microwave lens that has found extensive application in shipboard and airborne radar warning receiver systems operating over ultra-wide frequency bands. The lightwave embodiment first demonstrated by Cardone [2] implements true-time-delay beamforming using optical couplers and delay lines to achieve the appropriate amplitudes and phase shifts for a signal driving a linear array antenna. A similar scheme was described by Pappert [3],[4] for RF direction finding applications, and Curtis [5] subsequently demonstrated a holographic Rotman lens using diffractive optic elements in free space.

On transmit, the FORL system steers the beam in M-discrete directions by dividing the optical signal to fiber paths with appropriate time delay to N-antenna elements. On receive, the FORL behaves in a reciprocal manner, and since the beamforming process is linear, multiple simultaneous beams can be formed, one at each beam port corresponding to the angle of arrival of a wavefront incident on the aperture array elements.

SYSTEM DESCRIPTION

The FORL can be demonstrated in either the transmit or receive mode. For the transmit mode, the signal from a single laser is equally divided among the array elements, while in the receive mode each element requires a laser. A block diagram of the test system architecture is shown in Figure 1. The hardware was configured to operate in the transmit mode for cost considerations. Therefore, a single Fabry-Perot, directly modulated, laser transmitter provided the 1300 nm light source for the four pointing directions by sequentially connecting it to each beam port. The four array ports were terminated in packaged InGaAs photodiode optical converters specifically sized for a 30 cm overall length including pigtail, FC/APC and SMA connectors. The use of in-line bias tees with internal blocking capacitors enabled the reverse bias voltage to be established at each detector. RF amplifiers in all four channels provided signal gain over the 2.0 to 4.0 GHz frequency range. Mechanical line stretchers and fixed attenuators were inserted prior to the antenna to compensate for channel-to-channel phase and amplitude variations. Four equal length, flexible RF cables were used to feed the four columns of the antenna array.

The passive FORL beamformer, shown within the dashed lines of Figure 1, consists of eight commercially available 1x 4 single mode, fused biconic couplers and sixteen precision lengths of single mode fiber optic delay cables. The couplers were packaged in standard panel mount containers with all pigtails internal, connected by FC/APC's to bulkhead adapters. The delay line patchcords were specified with 900 um diameter plastic jackets, FC/APC connectors and an overall length tolerance of +/- 1 mm for beam pointing directions of +/- 45° and +/- 22.5°. The eight couplers were mounted in an L-shaped bracket with all beam ports, array ports and interconnections labeled. Each patchcord was uniquely identified with respect to its origin and termination. A photograph of the assembled beamformer is shown in Figure 2, and a view of the integrated system test hardware, including all power supplies, mounted in the antenna support housing is illustrated in Figure 3. Only the central four columns of the four-row, sixteen-column array antenna are connected to the beamformer. All other elements were terminated in matched loads.

* This work was sponsored by DARPA under Phase II SBIR Contract No. DAAH01-96-C-R085. ** This work was sponsored under Air Force Contract F19628-95-C-0002. Opinions, interpretations, conclusions, and recommendations are those of the authors and are not necessarily endorsed by the United States Air Force.

0-7803-4936-9/98/$10.00 © 1998 IEEE

MEASUREMENT AND TEST RESULTS

Ten couplers were purchased and evaluated for optical insertion loss and differential delay. Eight were selected for the beamformer based on their insertion loss uniformity which ranged from 6.3 +/- 0.1 dB to 7.0 +/- 0.5 dB. The delay variation for the best coupler was +/- 2 mm, and the worst coupler was +/- 8 mm. By subsequently measuring the absolute delay length for each coupler path, final corrections were made to the specified lengths of the interconnecting patchcords. In the four sets of precision delay cables the variation from the ideal lengths ranged from 0.7 mm to 2.7 mm. All delay measurements were carried out using the HP 8504 Precision Reflectometer including the optional reference extension kit and a special reference reflector fabricated for this application. The photonic beamformer was integrated as shown in Figure 2, and the optical insertion loss and delay of the assembled unit remeasured.

The responsivity of the optical converters was measured over a 5 GHz swept frequency range, and their differential optical lengths measured with the HP 8504. The three-stage RF amplifiers in each of the four channels, including line stretchers and antenna cables, were measured individually for amplitude and phase tracking over the 2.0 to 4.0 GHz frequency band. When subsequently integrated with the detector/bias tee combinations, the line stretchers were adjusted to equalize the delays for each channel using an RF network analyzer.

Following completion of all optical and RF tests at MIT Lincoln Laboratory, the test system was shipped to an outdoor antenna test range and mounted on the elevation-over-azimuth positioner for pattern testing. Figure 4 is a photograph of the front face of the four-row, sixteen-column planar antenna array [6] that had been provided under a CRDA with the Rome Photonics System Branch, Griffiss AFB, New York. Azimuthal patterns were recorded for each of the four (+/- 22.5° and +/- 45°) off-broadside beam pointing directions, and at 500 MHz frequency increments over the 2.5 - 4.0 GHz frequency range. The composite plots are presented in Figure 5. System noise, and more significantly, ground reflections, are evident in some of the patterns attributable to the outdoor antenna test range.

In subsequent tests the periphery of the antenna was wrapped with absorber and more accurately aligned with the positioner and the far field test horn. The resulting plots, compared with the computed patterns, were in excellent agreement with respect to main beam shape, sidelobes, null depths and null directions.

CONCLUSIONS

A breadboard demonstration of a four-beam port, four-array port fiber optic Rotman lens fabricated from commercially available optical components has been described. The photonic beamformer was tested with a 2.0 to 4.0 GHz array antenna and pattern results presented. The basic approach can be implemented for larger arrays [7], but more compact component packaging techniques are recommended. An eight-beam port prototype lens using planar waveguide optical couplers is currently under construction.

REFERENCES

[1] W. Rotman and R. F. Turner, "Wide-Angle Microwave Lens for Line Source Applications", *IEEE Trans. Antennas & Prop.*, vol. AP-11, pp.623-632; Nov.1963.

[2] L. Cardone, "Ultra-Wideband Microwave Beamforming Technique", *Microwave Journal*, pp.121-131; April 1985.

[3] S. A. Pappert, et al, "A Fiber Optics Matched Delay Filter for RF Direction Finding", *J. Lightwave Tech.*, Vol. LT-3, pp. 273-275; 1985.

[4] S. A. Pappert, "Ultra-Wideband Direction Finding Using Fiber Optic Transversal Filter", *NOSC Technical Report 1161*; March 1987.

[5] D. D. Curtis, "Holographic Rotman Lens for Phased Array Antenna Beamforming", *Proc. SPIE*, 2481; 1995.

[6] Final Technical Report (Draft), "Demonstration of Optical Time Delay Networks (OTDN) for Phased Arrays", Section 8.0, Contract No. F30602-91-C-0008; June 1996.

[7] K. E. Alameh, et al, "High Capacity Optical Interconnects for Phased Array Beamformers", *J. Lightwave Tech.*, Vol.13, pp. 1116-1120; June 1995.

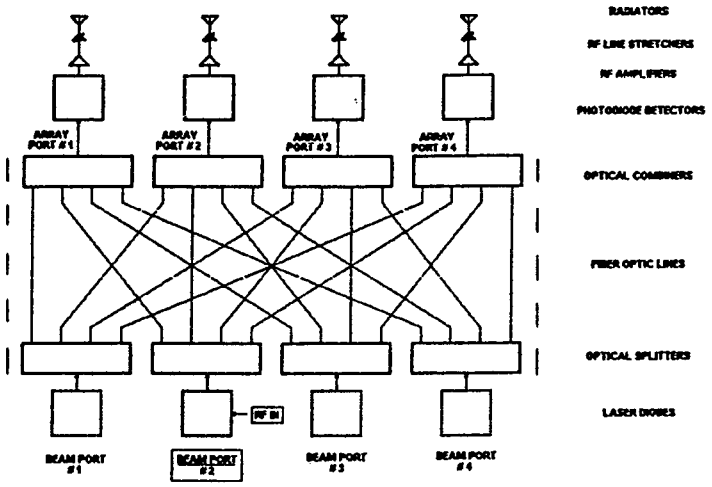

FIGURE 1 BLOCK DIAGRAM OF ASSEMBLED ROTMAN BEAMFORMER TEST SYSTEM

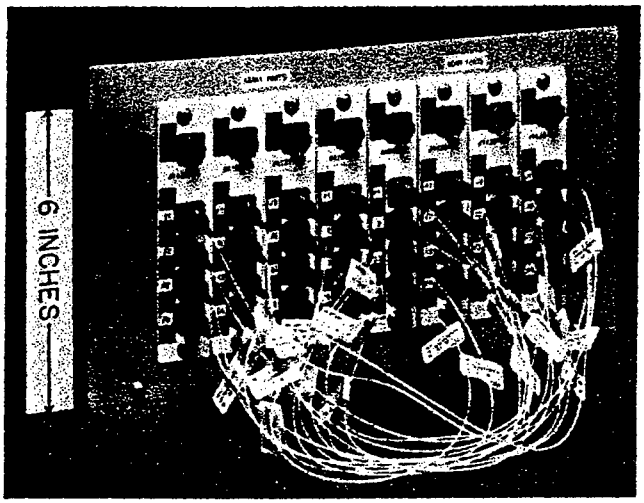

Figure 2 Four-Beam Port Fiber Optic Rotman Lens

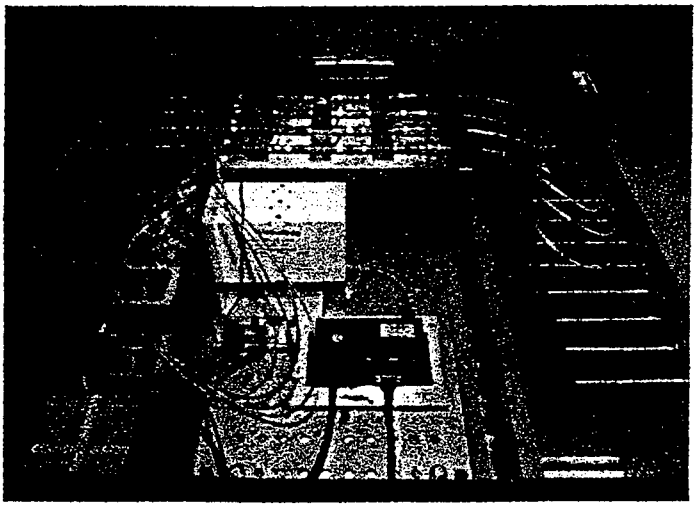

Figure 3 Photonic Rotman Beamformer System Test Hardware

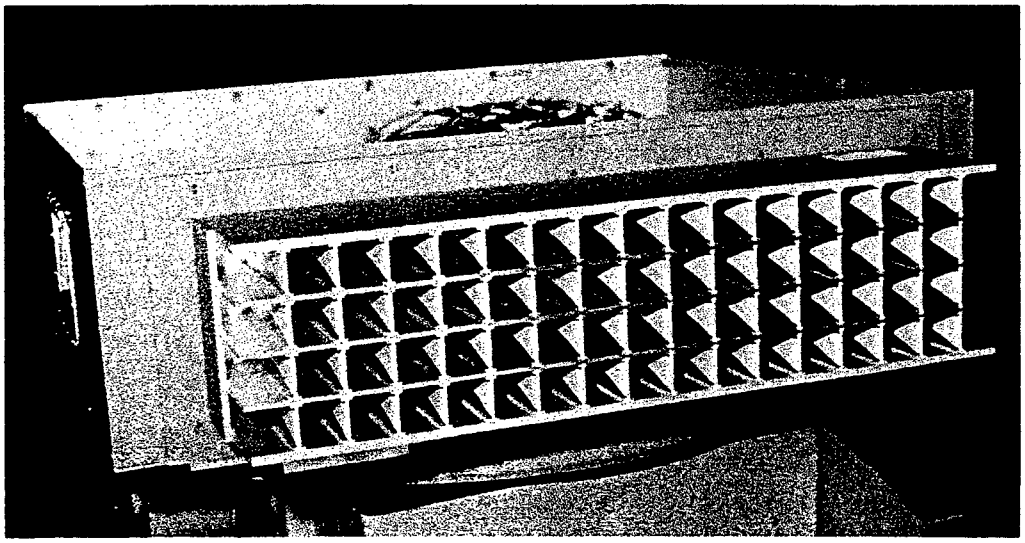

Figure 4 Four-Row, Sixteen Column Linear Array Test Antenna

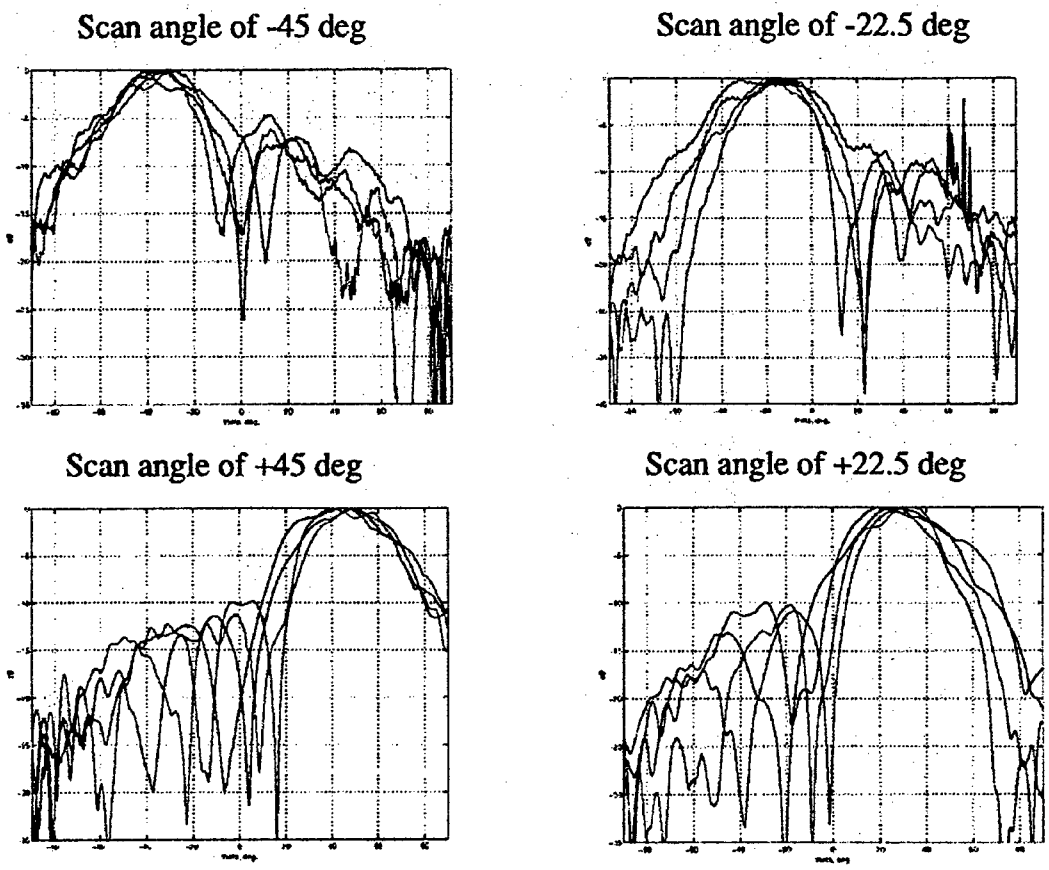

Figure 5 Composite Pattern Plots of Rotman Beamformer-Antenna

PHOTONIC INTEGRATED BEAMFORMER FOR PHASED-ARRAY ANTENNAS

J. STULEMEIJER[1] F.E. VAN VLIET[2] K.W. BENOIST[2] D.H.P. MAAT[3] M.K. SMIT[1]

[1]DELFT UNIVERSITY OF TECHNOLOGY, DEPARTMENT OF INFORMATION TECHNOLOGY AND SYSTEMS, TTT LABORATORY, PHOTONIC INTEGRATED CIRCUITS GROUP, POBOX 5031, 2600 GA DELFT, THE NETHERLANDS, J.STULEMEIJER@ITS.TUDELFT.NL
[2]TNO-PHYSICS AND ELECTRONICS LABORATORY, THE HAGUE, THE NETHERLANDS
[3]DELFT UNIVERSITY OF TECHNOLOGY, DEPARTMENT OF APPLIED PHYSICS, DELFT, THE NETHERLANDS

Feasibility of an extremely compact Photonic Integrated Circuit for controlling phase and amplitude of a 16-element phased-array microwave antenna has been demonstrated experimentally.

I. Introduction

Phased array antennas have been used since the beginning of the 70's and are now becoming increasingly important in satellite and mobile communications. A drawback for broad application of phased-array antennas is the large volume and weight of the RF electronic beamforming network. Photonics holds a great promise for reducing both weight and volume of these networks. Many experiments have been reported based on discrete optical components [1-3]. In this paper we report first experiments on an extremely compact (8.5x8mm) integrated beam-forming network for controlling phase and amplitude of a 16-element RF phased-array antenna.

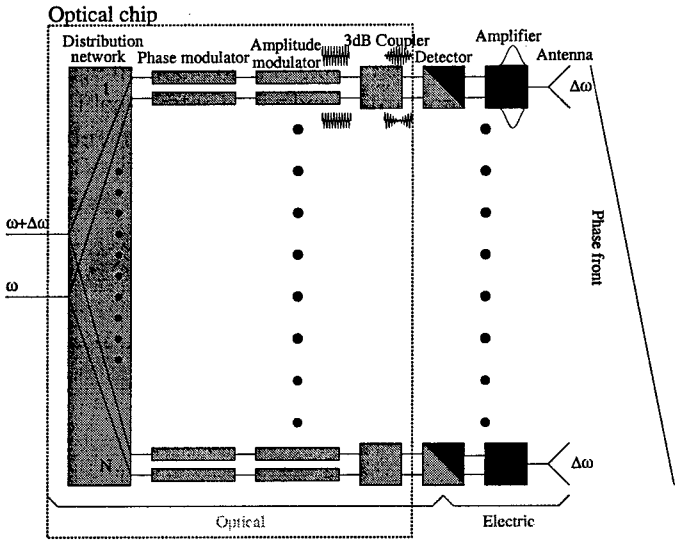

Figure1: Schematic view of the optical control of a phased array antenna.

II. Operation principle

Using a coherent detection scheme phase and amplitude of an optical signal can be directly transferred to a microwave signal by mixing this signal with an optical local oscillator signal. In this way modulation of phase and amplitude of a microwave signal can be performed using optical phase and amplitude modulators, which provides the module with an almost unlimited bandwidth; the frequency of the generated microwave signal can be chosen anywhere from a couple of MHz up to many GHz (only limited by the photodetector). Figure 1 illustrates the schematic of the photonic beam control network, which has been realized. The optical chip is shown within the dotted box. The chip has two inputs for two optical signals, one of which is modulated with the

0-7803-4936-9/98/$10.00

radar pulse. The two inputs are fed to a 2x16 power splitting network, the outputs of which are sorted in pairs. Each pair is connected to a phase and amplitude modulation section, after which the two signals are fed to a 3-dB-coupler. The RF-signals are obtained by coupling the signals coming out of the sixteen 3 dB couplers to a series of 16 balanced detector pairs. In the following we will shortly discuss the design and performance of the different elements.

III. Design and Experiments

We developed our circuit in a MO-VPE grown InP/InGaAsP/InP Double-Heterostructure as usual for operation in the long wavelength window (1550 nm) for optical communication. Ridge-type waveguides are etched with an optimized CH_4/H_2 Reactive-Ion-Etching process. For interconnection we use 2 μm wide waveguides, see figure 2A.

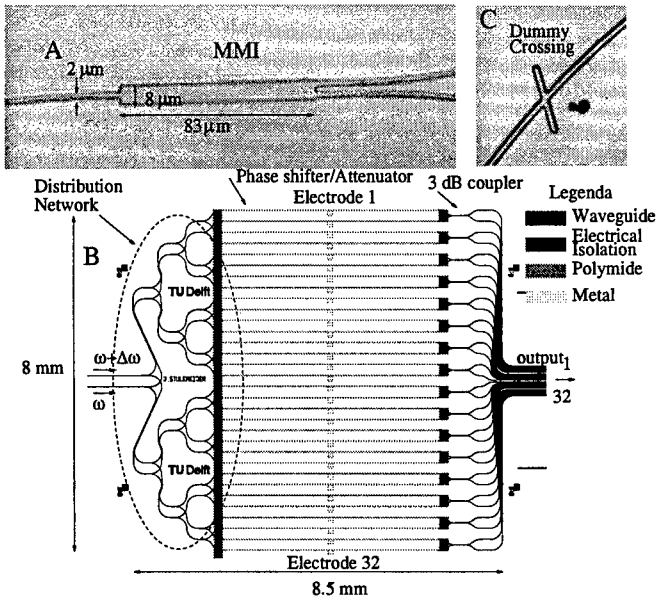

Figure 2: A) A MMI power splitter. B) Mask layout of chip. C) Dummy crossing to equalize output powers.

A. Passive waveguides

The chip was designed for use with TE polarized light, this does not impose any problems because the input lasers provide linearly polarized light. The total on chip loss was around 28 dB with a spread of 1.0 dB measured for input one to all outputs and input 2 to all outputs. Dummy waveguide crossings, see figure 2C, were introduced to eliminate loss differences between different paths.

Power splitters and 3 dB couplers have been realized by applying Multi-Mode Interference couplers [4]. These couplers consist of a wide multi-mode waveguide section as shown in figure 2A, which exhibits self-imaging properties.

The average on chip-loss is composed as follows. The theoretical splitting loss of a 1x16 splitter is 12 dB and the losses at a MMI mixer are 3 dB, leaving an excess loss of 13.1 dB. Test structures were included to measure the losses for straight waveguides, bends and waveguide crossings. Straight waveguides, of 2 μm width have a loss of 1.4 dB/cm. Measurements showed a maximum loss of 0.15 dB/90° for bend waveguides with radius of 250 μm. The loss was 0.15 dB for a crossing of waveguides under an angle of 60°. Combining the results of the test structures with the layout of the chip we expect the excess loss to be 4.1 dB. Part of the additional 9 dB is caused by a problem in the processing. Based on previous experiments on 1x16 splitters [5] we expect that the total excess loss can be below 6 dB.

B. Phase-modulation sections

Phase shifting is accomplished by utilizing refractive index changes due to the electro-optic effect. The doping profile of the chip is chosen in such a way that the InGaAsP waveguiding layer gets depleted when a

reverse bias is applied to the waveguide. This way the overlap between the electrical field and the optic field is maximal, for further details see [6].

In figure 3 it can be seen that 720 degrees of phase shift can be realized with a 4.9 mm long electrode by applying a negative voltage smaller then 20V (the losses get very high at such voltages see next section). The insertion loss, (without applied voltage) for a phase shifting section including the electrical isolation sections is about 1 dB. Taking into account the length of 4.9 mm of the phase shifting section it follows that the efficiency is 8.2 °/(V mm).

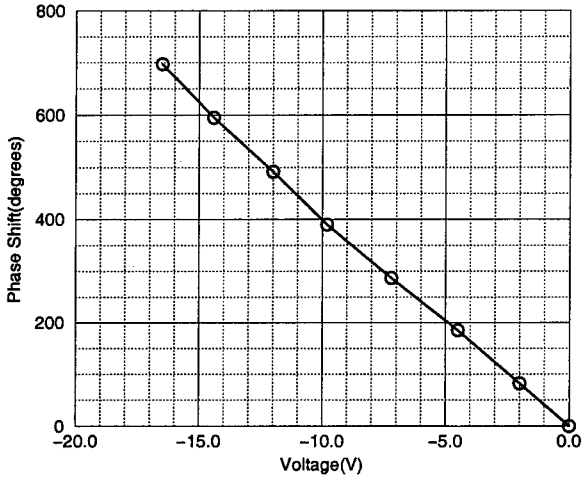

Figure 3: Phase shift as function of applied voltage.

C. Amplitude modulators

An advantage of the pin-type waveguide phase-modulator is that, with a proper design, it can be used also as an amplitude modulator using the electro-absorption effect which occurs at higher voltages due to the electrical-field induced shift of the band-edge. Figure 4 shows the attenuation as a function of the voltage, it is seen that an attenuation of over 15 dB can be achieved with an applied voltage of -20V.

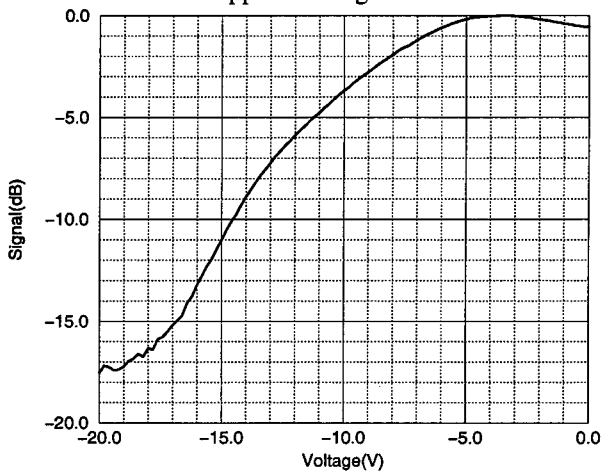

Figure 4: Attenuation as function of applied voltage.

A predefined value for amplitude and phase can be reached as follows. First the attenuation in both interfering arms has to be set by applying the same voltage to the phase/attenuation sections in both arms. Next the phase can be adjusted by changing the voltage on both arms relative to each other with a small amount.

IV. RF-Operation

Light from two different lasers was coupled into the two input waveguides. This was done by positioning two lensed fibers in front of the two input waveguides. The two external cavity lasers were tuned about 250 MHz apart and the output level of 0 dBm was boosted to 13 dBm using EDFAs. At one of the ouputs the light was coupled into a lensed fiber and guided to the detector. At the detector the light intensity level was about –60 dBm. After the detector a 40 dB electrical amplifier was used.

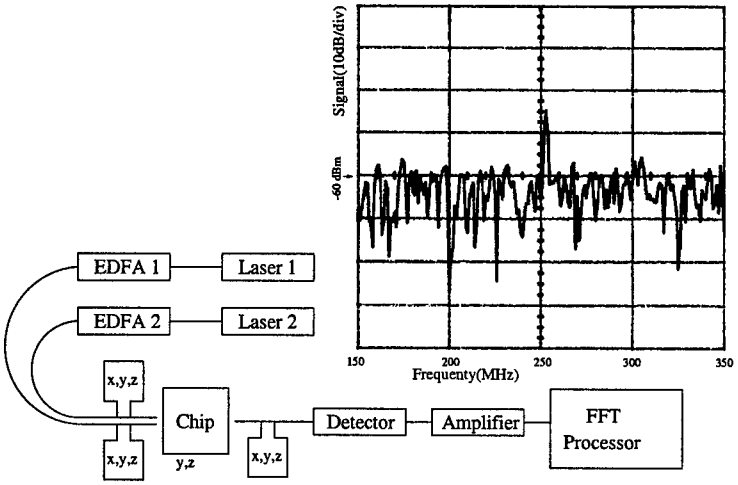

Figure 5: Measurement setup for light mixing.

The frequency generated by the mixing of the two optical signals can be chosen at any frequency between a few MHz and hundreds of GHz (only limited by the detector). A lower bound to the obtainable frequencies is set by the line width of the laser source. In our case the laser line width is 100 kHz. In our experimental setup the upper frequency was limited by our FFT-analyzer to 0.5 GHz. In this range the output level appeared to be virtually frequency independent. Figure 5 shows a recorded spectrum demonstrating the potential of our approach. The SNR is rather low since the intensity of the optical signal at the detector is so low that the signal is almost lost in the noise from the amplifier. We are presently working on reducing the fiber to chip loss and the on chip losses in order to reduce this problem.

V. Conclusion

We have realized a 2x32 distribution network integrated with phase shifting sections on an InP chip with record small dimensions (8.5x8mm). The on-chip loss is 28.1±1.0 dB. The phase/attenuation sections have a phase dynamic range of more than 360° and an attenuation dynamic range of almost 20 dB.

VI. Acknowledgments

We thank Phillips Opto-electronics for kindly providing us two micro-positioners. Further we thank E. Radius form KPN Research Optical Network Innovation group for the use of one of their EDFAs. Also we like to thank Frank van Putten from TNO-FEL for assistance during the measurements.

VII. References

[1] H. Zmuda, E.N. Toughlian, "Photonic Aspects of Modern Radar", Artech house, 1994

[2] A.J. Seeds, "Application of Opto-electronic Techniques in Phased Array Antenna Beamforming", Proceedings of the Microwave Photonics conference, 1997, pp. 15-20.

[3] J.J. Lee, et al.,"Photonic Wideband Array Antennas", IEEE-ANP, Vol. 43(9), pp. 966-982, 1995

[4] L.B. Soldano, E.C.M. Pennings, "Optical Multi-Mode Interference Devices Based on Self-Imaging: Principles and Applications", Journal of Lightwave Technology, Vol. 13(4), pp. 615-627, 1995.

[5] J. Stulemeijer, X.J.M. Leijtens, I. Moerman, M.K. Smit, "Photonic IC for Electronic Radar Beam Control", Proceedings of 1997 IEEE/LEOS Symposium Benelux Chapter, 1997, pp. 205-208.

[6] T. Uiterdijk, "Integrated Electro-Optical Switches On InP", PhD Thesis, Technical University Delft, 1997

OPTICAL PROCESSING OF 44-GHZ MICROWAVE SIGNALS IN AN ADAPTIVE NULLER

P. A. Schulz, R. A. Brown, and S. R. Henion
MIT Lincoln Laboratory, 244 Wood St, Lexington, MA 02173

Abstract

A seven-channel adaptive nuller using optics achieved 40-dB nulls, which is ~15 dB better than state-of-the-art microwave technology. The optics provided remoting and processing of signals in a 2-GHz band centered at 44.5 GHz.

Future satellite communications will require increased data rates and lower cost. Lower cost must be implemented in the satellite through less weight and lower power of the communications payload. The higher data rates will make the communication system more susceptible to jamming. To overcome the jamming threat, better anti-jam protection through such measures as stronger nulling capability should be designed into future satellite communications.

The optical nuller can achieve ~15 dB more jammer suppression than a nuller using current millimeter-wave technology. This achievement is a consequence of the design advantages available with the use of photonics, namely, inherent channel tracking after microwave-to-optical conversion. The improved channel tracking is a consequence of the very small fractional frequency width of the 2-GHz communication band relative to the 200 THz optical carrier. As a result, nulls of 40 dB across the 2 GHz EHF band are routinely obtained instead of ~25 dB nulls using microwave processing.

Optics also helps to reduce the weight and power requirements. Fiber optics is used to connect electronics protected within the satellite body to the antenna, which is exposed to the space environment. Because the microwave signal carried on optical fiber is only weakly affected by changes in the fiber environment, this remoting function is robust. In addition, the optical fiber is nearly lossless for typical intrasatellite distances under 100 m.

MIT Lincoln Laboratory has developed optical nuller technology that processes the signal to form a spatial null in the direction of a jammer (see Fig.1). The outputs of a multi-port receive antenna emulator provide one signal to each

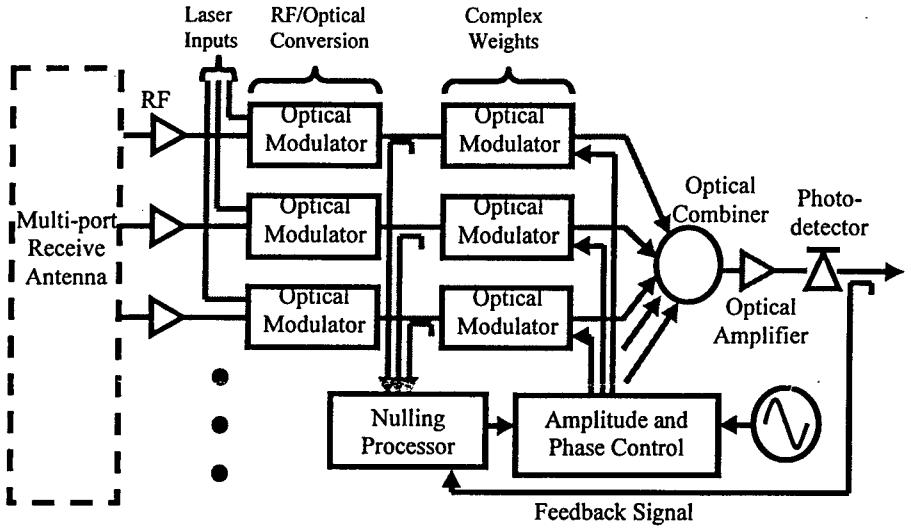

Figure 1. Optical nuller schematic. In the laboratory demonstration, an antenna emulator was used in place of the antenna and the correlator was not fully implemented.

channel of the optical nuller. Each channel has a low-noise amplifier followed by a Mach-Zehnder electro-optic modulator to upconvert the millimeter-wave signals to optical frequencies. Each channel has a second modulator to weight the signals in amplitude and phase to suppress interference. Phase is controlled with ferrite phase shifters for a 37-GHz tone. Amplitude is controlled with the bias voltage on the electro-optic modulator. Fiber combining with polarization

0-7803-4936-9/98/$10.00

combiners and 3-dB couplers acts to sum the signals prior to conversion from the optical to the microwave domain in a photodetector.

The only components that need to frequency track are the LNAs and the electro-optic modulators. Both of these components were commercially procured and no selection among components was required to achieve the required frequency tracking. After upconversion to optical frequencies the tiny fractional bandwidth means that frequency tracking is not a worry.

After characterizing the performance of the optical nuller, several nulling scenarios have been demonstrated with 40-dB suppression of a simulated jamming signal. With this setup an interfering source is simulated with the antenna emulator. The weighting is adaptively adjusted to suppress the interference. The suppression of the interference over the 43.5-45.5 GHz band is shown in Fig. 2 for one of the scenarios.

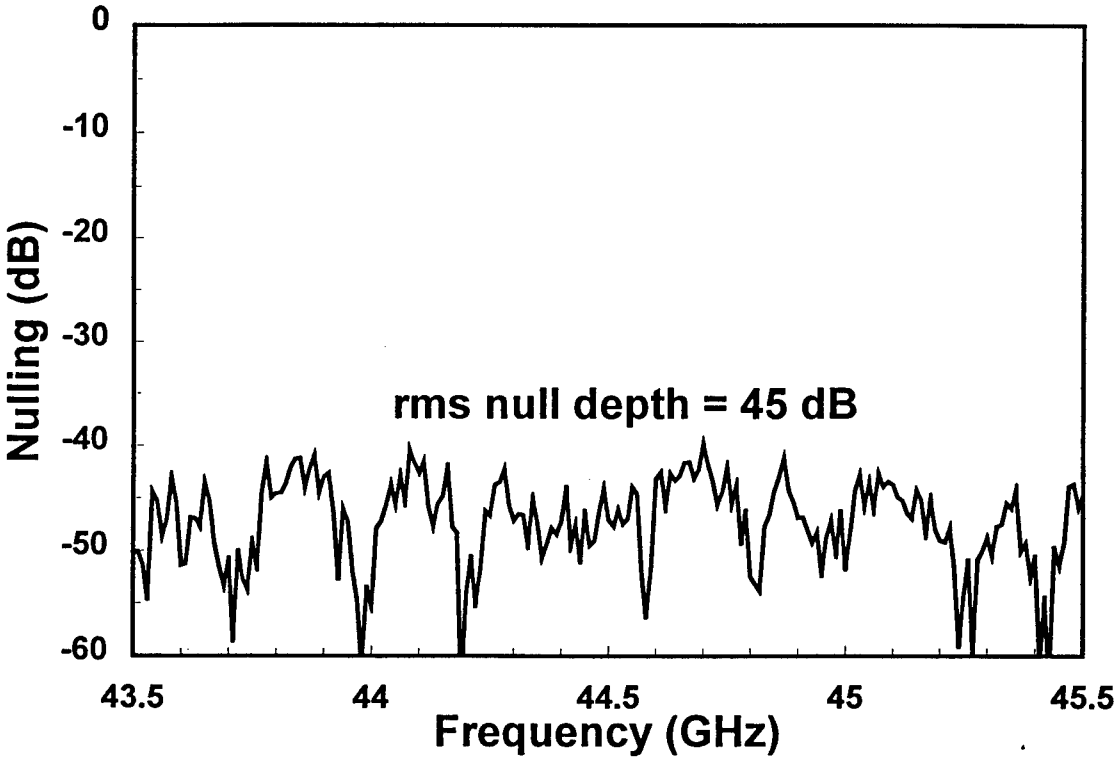

Figure 2. Optical nuller demonstration results. A broadband interfering source was suppressed by more than 40 dB over the 2-GHz band.

Microwave Phase Detection for Angle of Arrival Detection Using a 4-Channel Optical Downconverter

P. D. Biernacki, A. Ward, L.T. Nichols, R. D. Esman

Naval Research Laboratory, Code 5672
4555 Overlook Ave., S. W.
Washington, DC 20375-5338

Abstract: We present the first results of a 4-channel remotable optical downconverter used for phase detection of incoming signals up to 18 GHz. The phase information is related to angle of arrival detection.

I. Introduction

Fiber optic links maintain an advantage over traditional microwave transmit and receive systems in terms of multi-octave operation and RF isolation, and the ability to remote microwave signals great distances. For the first time, a 4-channel optical downconverter capable of detecting the relative microwave phase of incoming microwave signals up to 18 GHz is tested. The phase information can be related to angle of arrival detection. An optical downconverting link using cascaded modulators allows reduced weight at the antenna site since only a modulator (and possibly a microwave pre-amplifier) is needed at the sensor location while the LO drive and modulator, detectors, and any other signal processing components can be located elsewhere.

II. Optical Downconverting System

The 4-channel system is shown in Fig. 1. A 50 mW 1550 nm laser is amplitude modulated by a +24 dBm LO microwave source input to a Mach Zehnder modulator (MZM) biased at quadrature (V_π =20V). After passing through a polarization maintaining erbium-doped fiber amplifier (EDFA) capable of producing 500 mW of optical power, the LO modulated optical signal is split 4 ways providing a common feed for the four RF input signal

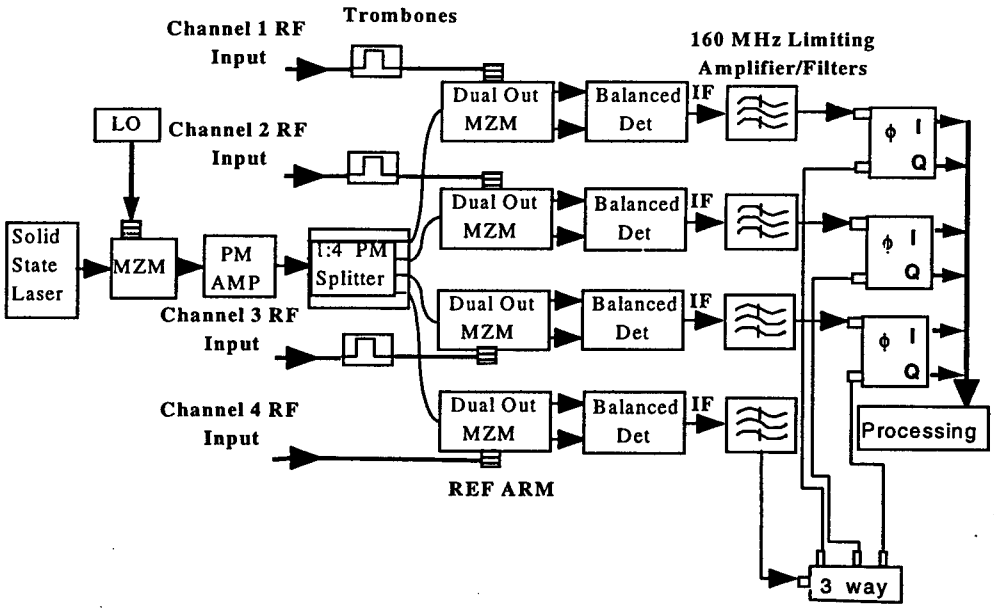

Figure 1. 4-channel configuration of the optical-microwave downconverter

0-7803-4936-9/98/$10.00 © 1998 IEEE

channels. Microwave-optical mixing of the LO signal with each separate RF channel results in a downconverted IF signal containing the phase of the original RF signal. Balanced p-i-n detectors with a bandwidth of 2 GHz are used to allow current addition of the IF photocurrent signal, and to cancel unwanted RIN and EDFA noise [1-2]. The IF signals are then amplified, filtered and processed to provide information on the phase of the original microwave signal. RF variable phase shifters (trombones) are used on three of the four RF input signals to provide arbitrary time delayed inputs.

III. Results and Discussion

To evaluate our system as a viable means for relative phase detection of incoming RF signals, the relative microwave-optical time delays through the system must be known. For example, in all 4 channels the relative microwave-optical time delay from the LO MZM signal input to the RF MZM is needed as well as the relative time delays from the RF MZM to the detector output. These time delays need to be known to provide a reference phase delay in each channel so that accurate phase information of the incoming RF signals can be measured.

The cascaded series modulator configuration gives an IF signal for each channel proportional to [3]:

$$IF \propto 2J_1(X_{RF})J_1(X_{LO})\cos[(\omega_{LO}-\omega_{RF})t + \theta(\omega_{LOCh(i)})-\theta(\omega_{RFCh(i)})], \quad (1)$$

$$X_{RF/LO}=\frac{\pi V_{RF/LO}}{V_{\pi RF/LO}(f_{RF/LO})}$$

where J_1 is the Bessel Function of order 1, V is the signal amplitude voltage, $V_\pi(f_{RF/LO})$ is the frequency dependent half wave voltage, $\omega_{LO} - \omega_{RF}$ is the downconverted IF signal (160 ± 15 MHz), and $\theta_{LOCh(i)}-\theta_{RFCh(i)}$ is the LO – RF phase difference in any channel (i). Assuming the time delay from the LO MZM input to the RF MZM input is identical in all 4 channels, the relative RF phase difference between two channels can be expressed as:

$$\Delta\phi=\theta(\omega_{RF(ref)})-\theta(\omega_{RFCh(x)}). \quad (2)$$

Therefore, the phase of any of the RF signals can be determined relative to any of the other channels. The I/Q (in phase, quadrature phase) phase detectors provide functional phase measurements of the incoming RF signals compared to a reference incoming signal [4].

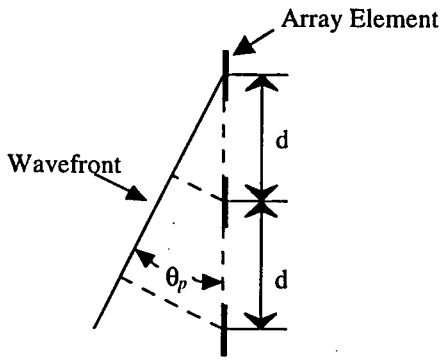

Figure 2. Wavefront incident on a linear array at an angle θ_p.

It is important to note that, as in traditional downconverted balanced detection, sufficient path length matching needs to be done only for the IF frequency (160 MHz). In our system the time delay from the LO input to the RF MZM was ≅ 244 ns (the EDFA provided 40 m of the fiber delay) and the time delays from the RF MZMs to detectors were ≅ 53 ns (10.6m). The trombones provided the necessary flexibility needed in testing our system.

An example application of this 4-channel phase detection system is determination of a signal's angle of arrival (AOA) to an antenna array [4]. The angle of arrival of an incoming plane wave can be determined by measuring the phase delay among the channels of the optical downconverter, as shown by Eq. (3),

$$\phi_n = 2\pi nd \sin\theta_p/\lambda \quad (3)$$

where ϕ_n is the phase delay of the n^{th} channel (far field conditions), d is the antenna element spacing (assuming a linear array), λ is the wavelength of the incoming plane wave, and θ_p is the angle of arrival of the free space traveling RF wave (Fig. 2). Assuming that the linear array elements are placed optimally (d = ½ λ), the electrical phase shift is given by Eq. (4),

$$\phi_n = \pi n \sin \theta_p \tag{4}$$

In the characterization of the optical downconverter, we used an RF synthesizer and trombones to introduce appropriate phase delays (ϕ_n) at the input port of each channel to simulate the arrival of a plane wave at an angle θ_p to our array. For AOA applications, electrical phase error limits the angular resolution of the optical downconverter. Additionally, broad band operation will require more sophisticated antenna spacing.

Taking the differential of Eq. 4, the angular resolution is given by Eq. (5),

$$\sigma_\theta = \sigma_\phi (\beta a \cos \theta_p)^{-1} \tag{5}$$

where σ_θ is the angular resolution, σ_ϕ is the electrical phase error, $\beta = 2\pi/\lambda$, and 'a' is the distance between the first

Figure 3. 160 MHz downconverted phase detection in 4-channels for an 18 GHz input RF signal.

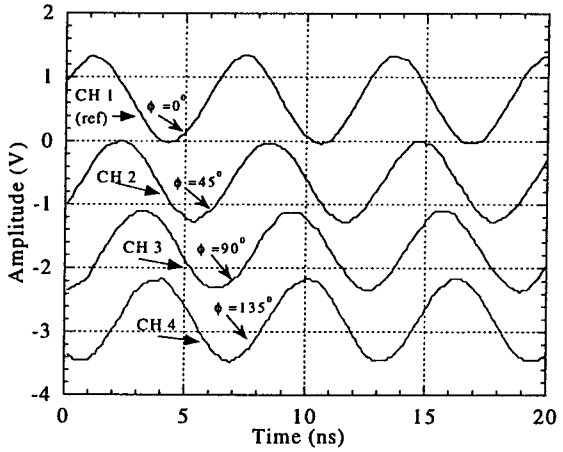

and last element in the linear array (in this case a = 2d =λ). Figure 3 shows the four channel downconverted signals at an IF of 160 MHz amplified by the limiting amplifiers. Channel 1 is used as the reference channel and the other

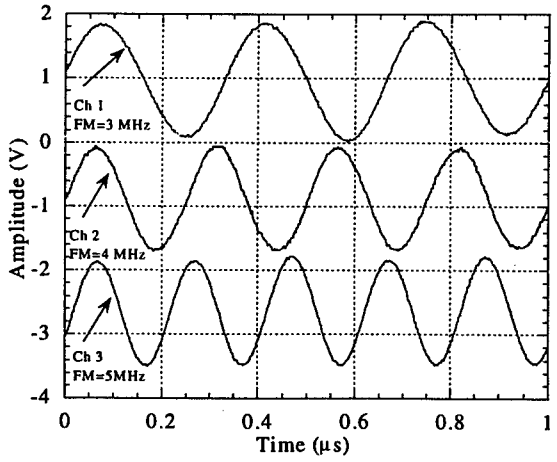

Figure 4. Simultaneous frequency modulation detection of the 18 GHz RF carrier at a rate of 3, 4, and 5 MHz in three of the downconverted channels.

three channels have their RF phase shifted by about 45°, 90°, and 135° at 18 GHz relative to channel one. These values would correspond to an angle of arrival of 14.5°, 27.5°, and 48.6° respectively. A RF power of -5 dBm was fed into each of the 4 channel MZM RF ports. With these power levels a phase stability of approximately 2° was measured using an oscilloscope.

For our simulated antenna conditions, using this RF signal at 18 GHz and an IF signal at 160 MHz, the optical downconverter has a calculated minimum resolution (at broadside) of $\sigma_\theta \cong 0.5°$ for our measured value of $\sigma_\phi = 2.0°$. Previously we have demonstrated input RF sensitivity of –66 dBm for a measured phase error of 2.0° (rms) [5].

Of particular interest is the ability of this system to also provide simultaneous phase or frequency detection between any of the 4 channels. This is useful for characterization of the sensitivity of such a system since it is generally easy to introduce FM modulation. In Fig. 4, three of the channels have their 18 GHz carrier frequency modulated at 3, 4, and 5 MHz relative to the reference channel. The I/Q video phase detectors see this frequency modulation as phase modulation providing a stable signal of the modulation wave.

IV. Conclusion

In conclusion, a 4-channel optical downconverter capable of detecting AOA has been tested. With a measured RF phase error of 2° (at 18 GHz) the phase error in AOA (at broadside) would only be 0.5°. This system shows promise as a viable alternative to traditional microwave systems since it has the ability to remote the input RF sensor location great distances from all other system components. Great flexibility is also shown by this system in its ability to also simultaneously detect RF phase or frequency in its independent channels.

Acknowledgement

This work was supported Office of Naval Research.

References

[1] G. L. Abbas, V. W. S. Chan, and T. K. Lee, "A dual-detector optical heterodyne receiver for local oscillator noise suppression," *J. Lightwave Technol.* vol. LT-3, pp. 1110-1122, 1985.

[2] K. J. Williams, and R. D. Esman, "Optically amplified downconverting link with shot-noise-limited performance," *IEEE Photon. Technol. Lett.*, vol. 8, pp. 148-150, 1996.

[3] G. K. Gopalakrishnan, W. K. Burns, and C. H. Bulmer, " Microwave-optical mixing in $LiNbO_3$ Modulators," *IEEE Trans. Microwave Theory Tech.*, vol. 41, pp. 2383-2391, 1993.

[4] Antenna Handbook Vol. III, "Antenna Applications," Edited by Y. T. LO and S. W. Lee, Ch. 25, pp. 21-23, 1993, Van Nostrand Reinhold.

[5] P. D. Biernacki, L. T. Nichols, K. J. Williams, D. G. Enders, and R. D. Esman, "A Two-channel Optical Downconverter for Phase Detection," accepted for publication in *IEEE Trans. Microwave Theory Tech.*

Optical Phase Locked Loop (OPLL) Module for use as a 9 GHz Source in Phased Array Communications Antennas

L N Langley, M D Elkin, C Edge and M J Wale,
GEC-Marconi Materials Technology, Caswell, Towcester, NN12 8EQ, UK;

U Gliese,
Technical University of Denmark, DK-2800 Lyngby, Denmark;

X Huang and A J Seeds
University College London, Torrington Place, London WC1E 7JE, UK.

Coherent optical beamforming [1] is particularly advantageous in multi-beam mobile phased array communications. Systems of this type employ a pair of phase locked optical carriers with a difference frequency equal to the required microwave signal. In this work a packaged diode-laser OPLL sub-system has been constructed for evaluation in a proof-of-concept optical beamforming system. The loop has been implemented with laser diodes, micro-optics and wide bandwidth electronics to give optimum phase noise performance. The laser diodes are designed for narrow linewidth, wide bandwidth and high FM-efficiency, whilst the main challenge in the construction of the packaged OPLL is the realisation of a high gain loop, with a small propagation delay.

OPLLs are of interest because of their potential to significantly reduce the relative phase noise of a pair of frequency-locked lasers, resulting in the optical generation of high spectral purity microwave signals. A schematic diagram of an OPLL is shown in figure 1. The system is similar in design to a conventional electronic phase locked loop. The optical microwave carrier output is generated from the beat signal formed between the two lasers, which is detected by the photodiode acting as an optical mixer. The resulting microwave signal is amplified and its phase is compared to the reference signal from the local oscillator. This process is performed using a microwave mixer, resulting in the loop phase error signal which is used to tune the frequency of the slave laser, forcing it to track the master laser with a frequency offset equal to the desired microwave frequency, therefore ensuring that the relative phase noise of the lasers is significantly reduced.

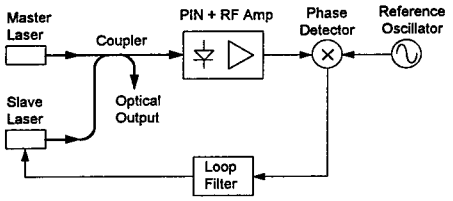

Figure 1: Schematic representation of an optical phase locked loop (OPLL)

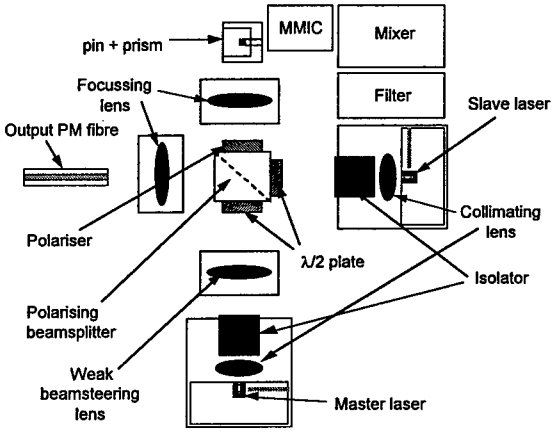

Figure 2: Schematic representation of the module

Several laboratory systems have been built using narrow-linewidth Nd:YAG lasers [e.g. [2]) but these devices are not well suited to communications equipment due to their large size and poor electrical efficiency. OPLLs based on semiconductor diode lasers can be much smaller, more rugged and more efficient. On the other hand, a diode-laser OPLL [3,4] requires much wider loop bandwidth and special attention is needed to the tuning characteristics and linewidth of the laser diodes. We have constructed a packaged diode-laser OPLL subsystem for evaluation in a proof-of-concept beamforming system. This involves optimization of the loop design, and development of custom single-frequency laser diodes with the necessary linewidth, frequency modulation and tuning characteristics. An important design parameter for the OPLL is the loop propagation delay, which must be minimised to give the necessary phase noise improvements. Consequently the physical dimensions of the OPLL must be reduced as much as possible. Therefore the optical parts of the OPLL consist of a micro-optic assembly, and the wideband loop feedback electronics have been implemented using discrete microwave components. Each laser has a miniature collimating lens and optical isolator. Other miniature lenses are used to focus the optical signals into the fibre and

0-7803-4936-9/98/$10.00

photodiode. A 20 GHz photodiode and a GaAs HEMT travelling wave amplifier MMIC are used in the front-end. A 4-14 GHz mixer is used to generate the phase error signal and the loop filter is a simple phase-lead low-pass RC design.

In order to achieve the subsequent optical phase-shift processing for antenna beamforming, the two optical signals must be arranged with orthogonal polarisation states. Semiconductor lasers emit light in the TE polarisation only, so $\lambda/2$ plates are used to rotate the polarisation of the laser beams. A polarisation beamsplitter is then utilised to divert a small proportion of the light onto the photodiode and generate the phase error signal. The larger proportion of the two beams is coupled into PM fibre for use in a coherent optical beamforming system. Efficient wavefront overlap of the two beams is required to give a strong microwave signal from the optical mixing in the photodiode. The resulting OPLL design has been implemented in a custom opto-electronic package suitable for use in an optically controlled phased array communications antenna system. The OPLL module implementation is represented in figure 2.

Loop propagation delay	400 ps
Loop gain	0.5 GHz
Loop bandwidth	70 MHz
Summed laser linewidth	6 MHz
Laser FM efficiency	2 GHz/mA
Total phase variance	0.05 rad^2
Phase variance (15 MHz bandwidth)	0.001 rad^2
CNR (1 Hz bandwidth)	95 dBc

Table 1: Key OPLL module parameters

Key design parameters and the measured performance of the loop have been summarised in table 1. The use of micro-optics has enabled a compact loop to be implemented, having a loop propagation delay of 400 ps. The locked OPLL output signal is shown in figure 3 for an LO frequency of 9 GHz. At this frequency the acquisition range is 400 MHz. The total measured phase noise variance is 0.05 rad^2 and that within the 15 MHz system bandwidth is 0.001 rad^2. The CNR is 95 dBc. Figure 4 shows the acquisition range for various LO frequencies indicating that the loop will operate from 7 to 14 GHz.

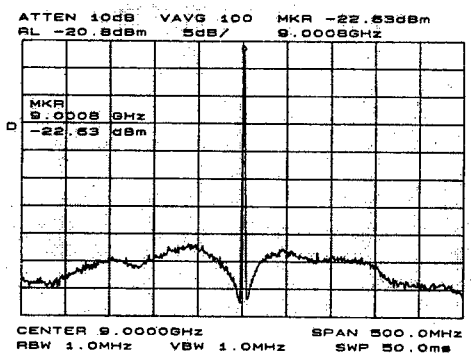

Figure 3: 9 GHz locked output signal

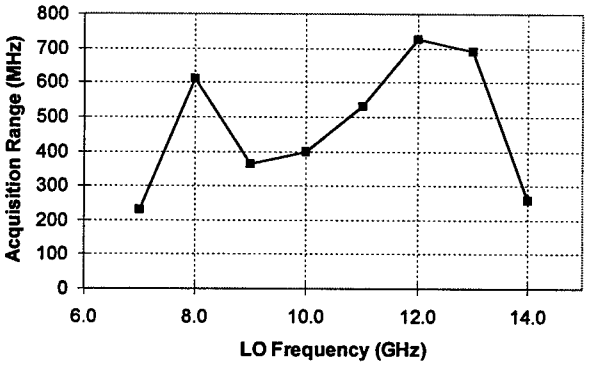

Figure 4: Acquisition range v. LO frequency

[1] W S Birkmayer, M J Wale, B Furch and T Jones, "A coherent optical beamforming network for satellite communications", *Workshop on Microwave Optoelectronics*, European Microwave Conference, Stuttgart, September 1991.

[2] M J Wale and M G Holliday, "Microwave signal generation using optical phase locked loops", Workshop on Microwave Optoelectronics, European Microwave Conference, Stuttgart, September 1991.

[3] U Gliese, T N Nielsen, M Bruun, E L Christensen, K E Stubkjaer, S Lundgren and B Broberg, "A wideband heterodyne optical phase-locked loop for generation of 3-18 GHz microwave carriers", *IEEE Photon. Technol. Lett.*, **4** (8), pp. 936-938, 1992.

[4] R T Ramos and A J Seeds, "Fast heterodyne optical phase-lock loop using double quantum well laser diodes", *Electron. Lett.*, **28** (1), pp. 82-83, 1992.

This work has been supported by the US Army CECOM under contract DAA-B07-95-C-D155. We thank L Coryell and Wright for support and useful discussions.

DEVELOPMENTS IN PHOTONIC BEAM-FORMING

M F LEWIS, P SAMPLE and R A WILSON
DERA, Malvern, Worcestershire, WR14 3PS, UNITED KINGDOM
Telephone: +44-1684-894872. Fax: +44-1684-896150. e-mail: aiohnstone@dera.gov.uk

Introduction

A previous paper [1] has described an optical beam-former which used a liquid crystal spatial light modulator (SLM) to impose the required microwave phase shifts on the output from one laser. This was subsequently combined with the output from a second laser, in a conventional beam-splitter arrangement, before being split into individual signals by a lenslet array for transmission by optical fibres. Optical detectors then recovered the laser difference frequency and phase, and microwave amplifiers raised the signal level before application to the elements of a phased array antenna.
A minor complication was the need to incorporate imaging optics between the SLM and lenslet array to avoid cross-talk through diffraction of the individual beamlets.
This free-space optical arrangement [1] which has been used to verify the principles of the beam-former, is quite compact, and has proved very reliable and stable in the laboratory, requiring no adjustments whatsoever over periods of many months. However, this paper describes a refinement which offers further advantages over the first implementation. By combining the two lasers with orthogonal polarisations in a commercial polarising beam splitter, the need for mechanical alignment stages was eliminated and the system made more compact and rugged. The combined laser outputs are passed over a *common path* through an SLM, which modifies the phase of only one polarisation component. The use of a polariser with axes at 45° to each polarisation vector allows the two components to be combined with a common polarisation component, as is necessary to recover the difference frequency on the subsequent photo-detectors. This configuration allows the output of the SLM to be fed directly into the lenslet array, minimising diffraction and eliminating the need for the imaging stage used in the original beam-former. The net result is a very compact and stable assembly with improved performance over the original beam-former because it uses fewer components and has a shorter and common optical path.
Measurements of the SLM phase control characteristic with varying polarisation are given, together with measurements of the overall performance.
As the liquid crystal SLM has a very slow response an alternative faster approach is also described, which uses a micro-machined silicon transducer to provide the control of phase.

Beam-former configuration

The new beam-former reported here makes use of a particular characteristic of a linear nematic liquid crystal phase control SLM, in that it only produces a phase shift of vertically polarised light while horizontally polarised components pass through the SLM unaffected.
Measurements were made on the SLM, which had been used in the previous beam-former [1] to determine the effect of angle of polarisation on the phase control characteristic. The results confirmed that the full range of phase control was available at 0° polarisation and there was a minimal effect on the orthogonal polarisation.
Figure 1 is a schematic of the new beam-former. Lasers 1 and 2 were Lightwave Electronics Model 125 units, each operating at a wavelength of 1.3 microns and providing an output power of 200mW into single mode optical fibre. The laser outputs are combined in a polarisation combiner manufactured by Optics For Research, (type number PFS-3-1310-Y-Z), with polarisations set such that Laser 1 is horizontally polarised at the SLM and Laser 2 vertically polarised. A single lens collimates the combined laser signals to produce a circular beam having a diameter of approximately 4mm. A standard anamorphic prism assembly, manufactured by Melles Griot, with a beam compression ratio of six to one, was used to reduce the beam height to 0.67mm to improve coupling to the linear fibre optic output array. A polariser was mounted at 45°at the output of the SLM so that the optical detectors could recover the laser difference frequency.

0-7803-4936-9/98/$10.00

As the beam-splitter of ref. [1] is absent in the new beam-former, it was possible to mount the lenslet array sufficiently close to the SLM so that there was negligible cross talk between channels due to diffraction. The actual dimension was 14mm, at which position there was negligible diffraction, as expected from the 250-micron diameter beamlets.
The output from one of the microwave detectors was used to stabilise the laser difference frequency against a stable microwave reference.
The phase control characteristic of the SLM was measured at a frequency of 1GHz and the results are shown in Figure 2 compared with those for the original beam-former. There is a very small difference between the two sets of results, confirming that the SLM does not influence the phase of the horizontally polarised laser signal.
Microwave output power levels from individual photodetectors were measured at 10GHz and a maximum of –16dBm was recorded, using 200mW lasers, compared with an equivalent figure of –39dBm, using 40mW lasers, for the original beam-former [1]. Allowing 14dB for the difference in laser powers, the new beam-former gave an increase in output power of 9dB over the original system.

Micro-machined silicon SLM

The liquid crystal SLM used in the above experiment is slow in operation, taking a fraction of a second to settle after a phase change. This may be acceptable in phased arrays used in telecommunications, but would be unsuitable for most phased array radars.
Micro-machined mirror arrays [2] provide a viable alternative to the liquid crystal device as an SLM. Already systems using thousands of bi-stable amplitude modulating mirrors are in production for display applications [3].
Consisting of a flat mirror suspended by flexure beams, as shown in Figure 3, and manufactured using micro-machining techniques, this form of SLM is highly efficient and directly applicable to the optical beam-former. The displacement of the mirror is controlled by an electrostatic charge, which is produced by an applied voltage of up to 20volts. A range of devices has been produced within DERA, e.g. using polysilicon and aluminium on nitride processes, having mirror sizes from 0.1mm to 1mm square. A typical sensitivity for a 0.1mm square polysilicon device is 18nm/volt, with a frequency response, which is shown in Figure 4, in excess of 50kHz.
The micro-machined SLM can be fabricated to match the single row of pixels and spacing of 250microns used in the original beam-former. Equally well, two-dimensional arrays can be made to meet larger antenna array requirements.

Optical beam-former using micro-machined SLM

One possible configuration incorporating the reflective micro-machined SLM is shown in Figure 5. The combining of the two orthogonal beams from Lasers 1 and 2 and subsequent beam shaping, is identical to the liquid crystal SLM beam-former described above.
The combined beam is applied to a polarising beam-splitter, which separates the two beams, one passing to a plane mirror, the other to the reflective SLM. Each beam also passes through a quarter-wave plate which rotates the polarisation through 90^{o} in a double pass. The pixels of the SLM have their relative positions set by control voltages, which vary the path length of each section of the beam, in this case every 250microns, to give a corresponding phase shift to each section of the beam. The two reflected beams are combined at the face of the beam-splitter, from which point they pass out through the lenslet array as in the beamformer of Figure 1.

Conclusions

The experimental compact beam-former has demonstrated that an improved performance, over the original system, can be obtained with a much simpler and more compact optical arrangement. Output power has improved by 9dB through the use of fewer optical components and alignment adjustments.
The SLM phase control range has been maintained without any degradation caused by passing both laser beams through the SLM.
The method of combining the two laser signals using the fibre polarising combiner, allows much more flexibility in shaping the beam before it is applied to the SLM, as the resulting optical format is common to both laser components.
The reflective micro-machined SLM provides a much higher speed of operation than the liquid crystal device and is readily incorporated into the optical beamformer. It will have many more applications

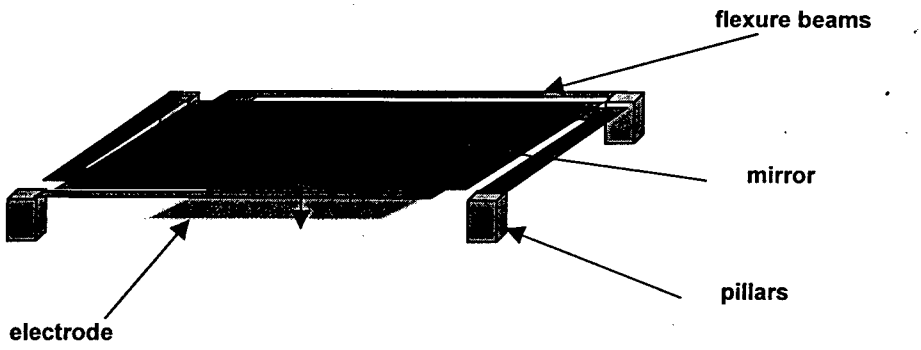

Figure 3 Micro-machined SLM Construction

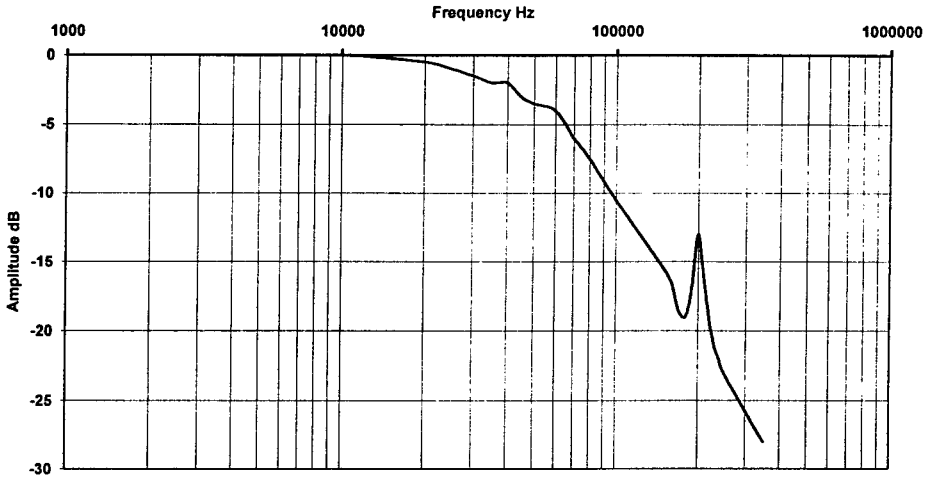

Figure 4 Frequency response of 0.1mm square polysilicon SLM

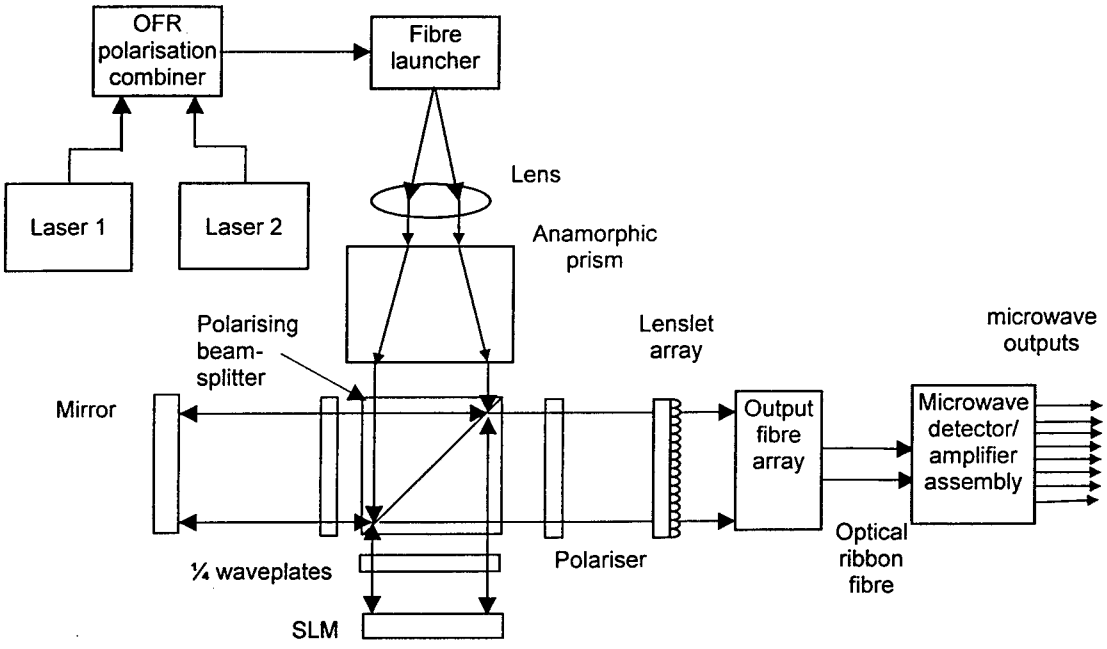

Figure 5 Schematic optical beam-former with reflective SLM

than just that of photonic beamforming, e.g. in pattern recognition and adaptive optical phase compensation.

References

1. M F Lewis, 'Coherent optical beam-forming', paper WE 1-3, pp23-26,Microwave *Photonics* (MWP'97), Sept.,1997, Duisburg/Essen, Germany.
2. Tsen-Hwang Lin, 'Implementation and characterization of a flexure-beam micro-mechanical spatial light modulator', Optical Engineering, pp 3643-3648, November 1994, Vol. 33 No. 11.
3. J M Younse, 'Projection display systems based on the Digital Micromirror Device™(DMD™)',in *Proc.* SPIE, Vol. 2641, pp. 64-75, July 1995.

Acknowledgement

Thanks to Alan Johnstone who provided useful assistance, and to Mike Ward and co-workers who produced the Micromachined Silicon devices used in this work.

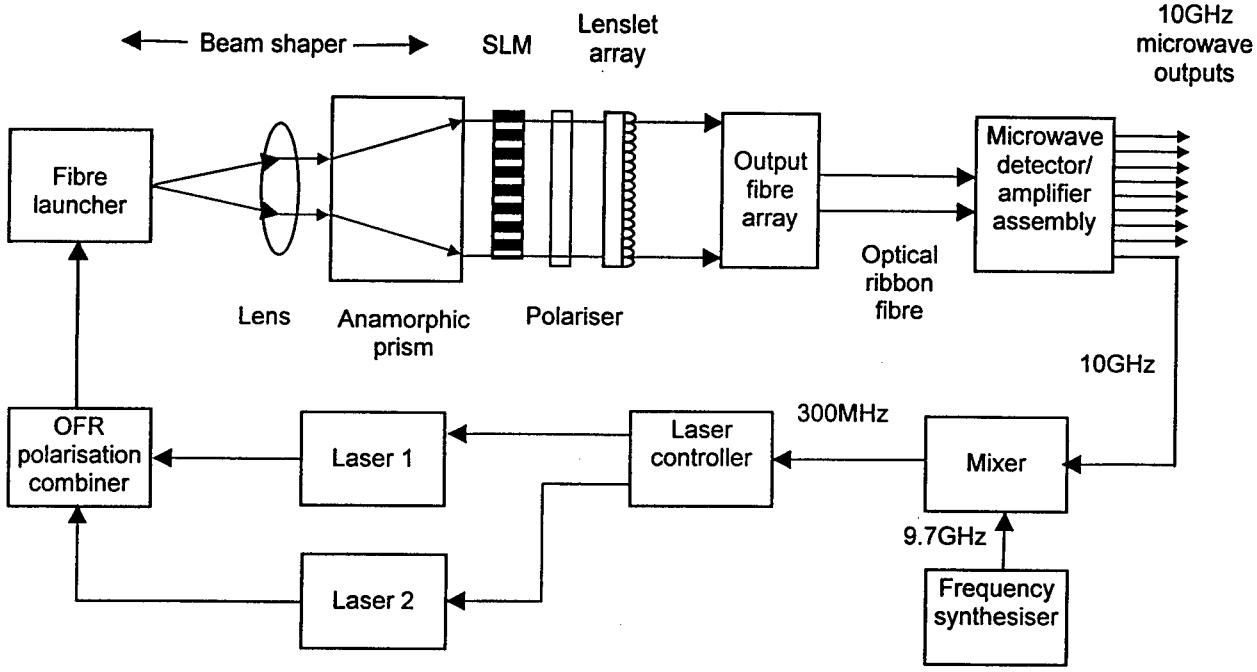

Figure 1 Schematic Optical beam-former with liquid crystal SLM

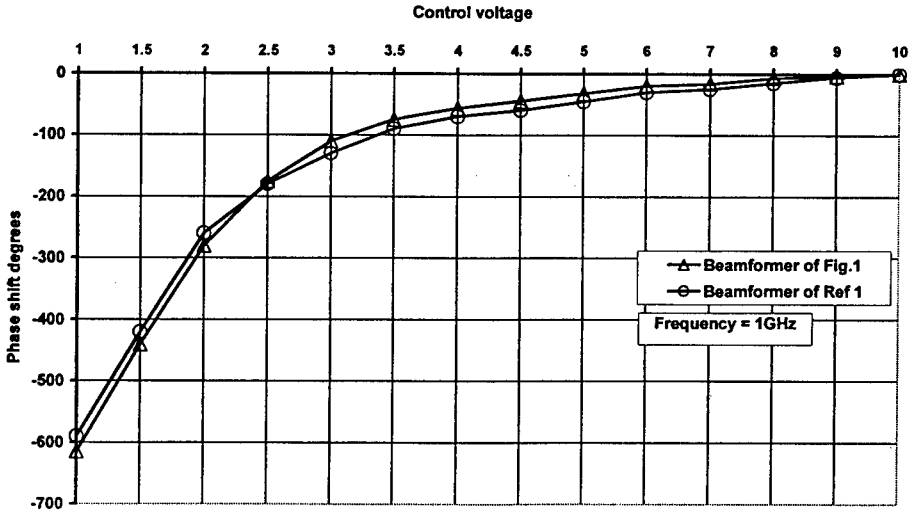

Figure 2 Beam-former phase control sensitivity

New Variable Phase Shifter Array using Resonator with Graded Reflectivity Mirror for Single-Control Steerable Phased Array Antenna

Benjamin B. Dingel and Masayuki Izutsu
Communication Research Laboratory (CRL), MPT
4-2-1 Nukui Kitamachi, Koganei, Tokyo 184-8795, Japan
Tel: (+81)-423-27-5647 Fax:(+81)-0423-27-6106 E-mail: bdingel@crl.go.jp

Abstract

We propose a novel, prism-like optical device using a Gires-Tournois resonator (GTR) whose front surface mirror is coated with a pre-defined reflectivity profile. It can function as variable linearly increasing phase shift array (LIPSA) for single-control microwave phased array antenna (PAA) using heterodyne configuration. One important feature of this device is that it requires only one parameter to automatically adjust the respective phase shift of the rest of the elements in the array. This feature can drastically reduce the number of components in PAA system. Numerical results showing the coating profile and phase response are discussed. The associated set-up for microwave phase array transmitter is also presented.

I. Introduction

With the rapid progress and development in mobile, wireless and satellite communication technologies, there is an increasing demand for new photonic-based variable phase shift or true time-delay mechanism that can make the phased array antenna (PAA) system simple, compact and lightweight.

Many optically-controlled microwave phased array antennas have been proposed using different schemes [1-2] that has improved many aspects of conventional antenna. Unfortunately, these optically-controlled antennas are still constraint by size, weight and volume due to (now!) numerous supporting optical and electronic devices necessary to control individually the N-delay lines or N-phase shifters in PAA. In general, an electronic control unit (ECU) per phase shifter, or a switch per delay-line is required for individual phase/time delay adjustment. Furthermore, a master computer, sophisticated algorithms, interface devices, and other supporting elements are required to assemble the beam forming network (BFN) which controls all ECUs or switches in PAA. This BFN becomes complex, huge and slow as the number of elements increases.

The main goal of this work is to propose a new photonic device which can function as variable linearly increasing phase shifter array (LIPSA) for PAA application. One important feature of this device is that it requires ONLY one parameter (as opposed to N parameters) to automatically adjust the respective phase shift of the rest of the elements in the array. Using this single device under an optical heterodyne arrangement, the phase-steerable PAA system can be made simple, compact, and lightweight. Some additional feature of this method are (1) absence of sophisticated computer and complicated beam forming control algorithms, and (2) possibility of a nanosecond steering speed.

II. Principle of the Proposed Device

Our proposed device is a modified Gires-Tournois resonator (GTR) [3] whose front surface is coated with pre-defined reflectivity profile. A conventional GTR[4] is basically an asymmetric Fabry-Perot resonator with partially reflecting front surface M1 and 100% reflecting back surface M2. Schematics of the proposed device where M1 of GTR is replaced by a graded-reflectivity mirror (GRM) R_n is shown in Fig. 1. For explanation and clarity purposes only, a beam splitter BS is included in Fig.1 in order to spatially separate the incident electric field, E_{inc} from the reflected electric field E_{ref} (or reflected beamlets B_1-B_n). Here n stands for the position along a coordinate (1-D for simplicity) in the surface of the coated mirror. Furthermore, the resonator length is chosen to be much smaller

0-7803-4936-9/98/$10.00

than the effective GRM's radii [5] so that plane wave approximation model can be employed.

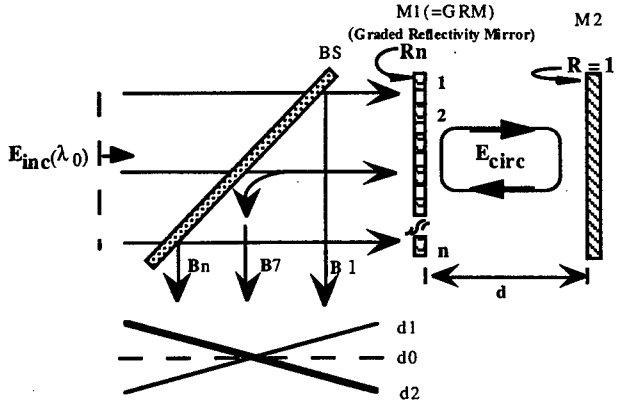

Fig. 1. Schematics of the proposed device---LIPSA using GT resonator with suitable graded or discrete reflectivity profile coated onto mirror M1. By simply changing the resonator length d, the output phase profile of the incident beam E_{inc} can be steered.

The complex reflection coefficient and the reflected phase shift Θ_n of the n-channel in the proposed device are given as [3]

$$\beta_n e^{i\Theta_n} = \frac{E_{ref}}{E_{inc}} = e^{j\psi_n}\left\{\frac{\rho_n + e^{j(\psi_n - 2\theta_n)}}{1+\rho_n e^{j(\psi_n-2\theta_n)}}\right\}, \beta_n = 1 \quad (1)$$

$$\Theta_n = -2tan^{-1}\left(\frac{tan(k\,d)\{Cos(\psi_n)+\sqrt{R_n}\} - Cos(\psi_n)\,tan(\psi_n)}{\{Cos(\psi_n)-\sqrt{R_n}\} + Cos(\psi_n)tan(\psi_n)\,tan(k\,d)}\right) \quad (2)$$

where β_n (=1) is the amplitude reflection coefficient, $\rho_n(=-R_n^{1/2})$ is the reflectance, $\theta_n = 2\pi\eta d/\lambda = k\eta d$, d is the resonator length, λ is the wavelength, η is the refractive index (=1 for simplicity) of the material inside the GTR, and ψ_n is phase angle of the n-channel due to coating in the array.

Given a well collimated monochromatic plane wave λ_0 incident normal to the proposed device, the uniform phase distribution of the incident wave can be transformed into specific phase shift pattern if the reflectivity across the front surface M1 is coated with suitable spatially varying reflectance R_n. In order to generate a linearly increasingly phase shift across the different channels, we impose five conditions. First, we assumed that incident beam and all the components are perfectly aligned to avoid beam walk-out during multiple reflections inside the resonator. Secondly, we used $\lambda_0/4$ multiple coating fabrication or technology on M1 so that $\psi_n = 2\pi n$. This leads to $Tan[\psi_n]=0$ and $Cos[\psi_n]=1$ for all n, and simplifies the reflected phase shift Θ_n into

$$\Theta_n = -2\,tan^{-1}\left(\frac{1+\sqrt{R_n}}{1-\sqrt{R_n}}tan(k\,d)\right). \quad (3)$$

Thirdly, we required that the coating profile R_n to be given by

$$R_n = \left\{\frac{(Tan[k_0 n\Delta l/2] - Tan[k_0 d])}{(Tan[k_0 n\Delta l/2] + Tan[k_0 d])}\right\}^2 \le 1 \quad (4)$$

with Δl being the parameter that need to be chosen to set the minimum phase shift and $k_0 = 2\pi/\lambda_0$ with λ_0 being the wavelength value used in the coating fabrication. For a given fixed Δl and k_o, there are many profiles R_n that can be generated depending on the initial choice of the resonator spacing $d = z_0$. Some of these profiles R_n are shown in Fig. 2. Coating profile may be continuous or discrete depending on the requirements of the application. A proper choice of the value of d is necessary to obtained a physically meaningful result in which the resultant R_n must be less than or equal to 1.

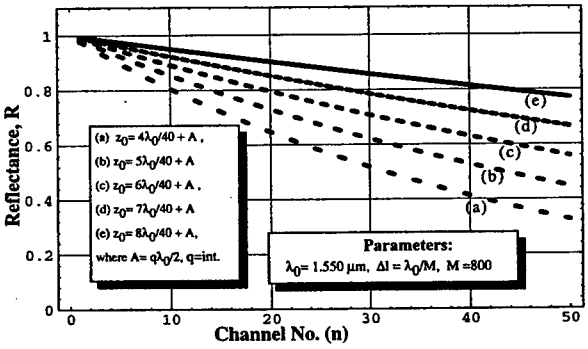

Fig. 2. The various reflectivity profiles R_n that can be coated onto M1 to obtain an increasing phase shift values for the reflected beamlets $(B_1\text{-}B_n)$ for different resonator spacing z_0 (q is integer).

By substituting (4) into (3), the resultant reflected phase shifts across the different channels can be expressed as

$$\Theta_n(\Delta l_0, z_o, \lambda_0, d, n) = -2\,tan^{-1}\left(\frac{tan\,(k_0\,n\,\Delta l/2)}{tan(k_0\,z_0)}tan(k\,d)\right) \quad (5)$$

where z_0 is again the initial resonator spacing used in the calculation of reflectance R_n and $k = 2\pi/\lambda$ with λ being the wavelength of the actual incident beam. Fourthly, we assumed that value of ΔL is very small in order that $\tan^{-1}(k_0\, n_{max}\Delta L/2) \sim k_0\, n_{max}\, \Delta L/2$. Lastly, we imposed that the parameters ΔL, z_0 d and n are chosen properly such that

$$\left|\frac{k_0\, n_{max}\, \Delta l/2}{tan(k_0\, z_0)}tan(k\,d)\right| \le w_0 \quad (6)$$

where w_0 defines the overall accuracy of the linearity and the maximum channel n_{max} for a given

z_0, d and ΔL. The value of w_0 is usually less than 0.5 so that $\Theta_n \sim \tan^{-1}(w_0) \sim w_0$ for all $n < n_{max}$. With these assumptions, Θ_n can now be written as

$$\Theta_n(\Delta l_0, z_o, \lambda_0, d, n) \approx -\frac{tan(k\,d)}{tan(k_0\,z_0)} k_0\,\Delta l\,n \quad (7)$$

which shows clearly the linear dependence of Θ_n on the channel number n. We will refer to this proposed device as LIPSA since it can function as variable linearly increasing phase shift array.

III. Properties of LIPSA

We can observe the following important features of LIPSA. First, LIPSA is functionally similar to a tiltable prism-like optical device. It requires only one parameter to automatically adjust the respective phases of the rest of the elements in the array. By simply changing d of LIPSA within a specified range Δd ($<\lambda_0$), the slope or tilt of the wavefront can be changed. An excellent linearity between Θ_n and channel n could be obtained up to certain maximum n_{max} as shown in Fig. 3.

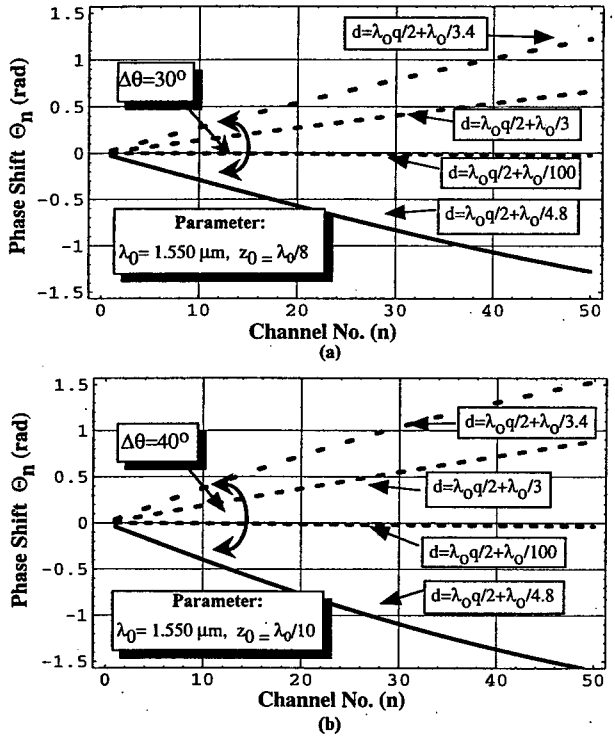

Fig. 3. Reflected phase shift of LIPSA as a function of channel n for different resonator spacing d. These curves are obtained using (5) that gives $\Delta\Theta \sim \pi/6$ when $z_o = \lambda_o/8$ (a) and $\Delta\Theta \sim 2\pi/9$ when $z_o = \lambda_o/10$ (b) (q is integer).

With regards to the angular deflection coverage of LIPSA, the maximum angular tilt $\Delta\Theta_{max}$ is a function of the choice of the coating profile due to z_o and channel number n_{max}. There is a trade-off between $\Delta\Theta_{max}$ and n_{max} which is contained in (6). As shown in Fig. 3, the $\Delta\Theta_{max}$ is equal to $\pi/6$ (=30 deg.) at n_{max}= 40 when $z_o = \lambda_o/8$ (a), and is equal to $2\pi/9$ (=40 deg.) at n_{max}=30 when $z_o = \lambda_o/10$ (b) given the same $w_0 = 0.47$ criterion.

The coating profile calculated with spacing z_0 is periodic with respect to a multiple of $\lambda_0/2$. This means that a profile generated with an initial spacing z_0 can be reproduced if a new spacing z is equal to z_0 plus $q\lambda_0/2$. Here q is an integer. Lastly, for a given fixed value of $q\lambda_0/2$ the choice of z_0 affects the effective channel number that can be used. The shorter the length z_0 the lower the number of channel before R approaches zero. This is clearly seen in the case of curve (a) compared with curve (e) found in Fig. 2.

Note that in the above discussion, we assumed that the incident λ is equal to wavelength used in the coating process ($\lambda=\lambda_0$ or $\Delta\lambda=0$). If the incident λ is detuned from λ_0 ($\Delta\lambda=\lambda-\lambda_0$), then the n_{max} will be lower and $\Delta\Theta_{max}$ will be narrower.

IV. Proposed Phased Array Transmitter

Our proposed phased array transmitter is based on phased-steering method using coherent optical heterodyning[6]. The set-up is made up of two parts; (1) the heterodyne module, and (2) the transmitter module. The heterodyne module consists of a modified Michelson interferometer (MI) in which one of the typical reflecting mirror is replaced by LIPSA, and a microwave or RF modulator (FM) is inserted in one arm of MI as shown in Fig. 4. Furthermore, a beam expander and lenses are used for collimation of the laser beam operating at λ_o.

As shown in Fig. 4, an incident light is beam expanded, collimated before it is split into two beam#1 and beam#2 of equal intensity by beamsplitter BS. Beam#1 propagates through arm L1, frequency shifted by an amount Ω by FM, reflected by M3, and frequency shifted Ω again as it travel back toward BS. While beam #2 propagates through arms L2, phase shifted by LIPSA and subsequently reflected back toward BS. Then both beams are coherently added, and detected by an array of PD that give an output normalized current signal i_n

$$i_n \propto \text{Const} \quad \text{Sin}^2\left[\frac{2\Omega t + \Theta_n(d)}{2}\right]. \quad (8)$$

This heterodyne module performs three generic tasks: (1) to introduce or superimpose the microwave or RF signal into the carrier wavelength (λ_o) using a modulator (FM), (2) to generate an optical linearly increasing phase shift difference inside MI using LIPSA and, (3) to convert these phase differences into microwave phase shifts at the detector output as given by (8).

These detected current signals i_n are then passed to transmitter module consisting of array of (i) photodetectors (PD), (2) receiver / transmitter (R/T) modules, and (iii) antenna for beam steering. Note again that under this arrangement, the optical phase shift Θ_n due to LIPSA functions as a spatially, linearly increasing microwave phase shifter array at the detector's output. In our derivation we assumed the whole system to be lossless, and the MI arm length difference is zero.

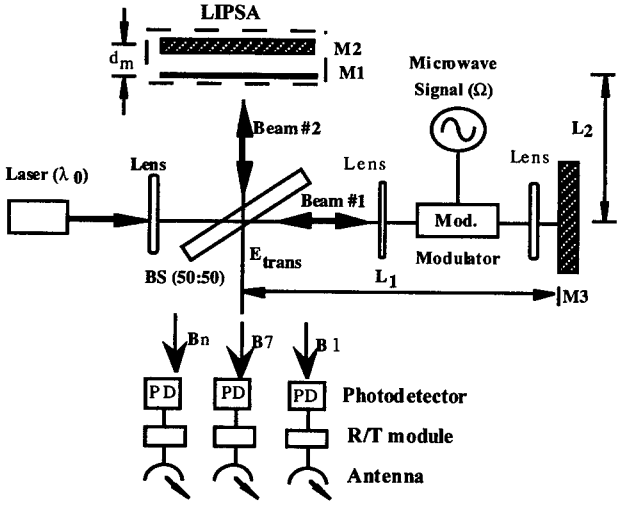

Fig. 4. Set-up for microwave phase array transmitter in which LIPSA is used as microwave phase shifters in Michelson interferometer arrangement for coherent optical heterodyning. By simply changing the resonator length of GTR, the microwave phased array antenna can be steered.

V. Conclusion

There are many advantageous properties of the proposed LIPSA-based phased array antenna / transmitter. Fist, one unique characteristic of this scheme is the absence of numerous phase shifters and its associated controllers. By simply increasing or decreasing the GTR length, it automatically adjusts the respective phase shift of other elements which subsequently steers the microwave phase array antenna. Furthermore, no sophisticated computer and advanced beam forming control algorithms are needed. All these features can drastically reduce the needed components, size and weight of PAA system.

Secondly, if GTR is assembled using E/O material, steering speed at nanosecond range is also possible. Thirdly, the effective microwave frequency shift will be doubled because of the double-pass propagation of the laser beam in MI. This arrangement allows the typically low frequency (~ 800MHz) acousto-optic (AO) modulator to be used for higher microwave (~1.6GHz) signal applications. In principle, the maximum scanning range $\Delta\Theta_{max}$ with good linearity is limited by coating profile, and maximum channel number. However, by cascading two or more LIPSA devices, it is possible to increase the range of $\Delta\Theta_{max}$. Construction of the device and its 2-D version using bulk, planar waveguide circuit, and MEMS technologies are straightforward. Lastly, we note that the device can also function as true-time delay element[7].

References

[1]. N. Riza, Ed. *Selected papers on Photonic Control Systems for Phased Array Antennas*, SPIE Press, 1997.

[2]. H. Zmunda and E. N. Toughlian, *Photonic aspects of Modern Radar* (Artech House, Norwood, Mass.,1994).

[3]. B. Dingel, M. Izutsu, and K. Murakawa, "Optical wavefront transformer using the multiple-reflection interference effect inside a resonator", Opt. Lett. Vol. **22**, No. 19, 1449, 1997.

[4]. F. Gires and P. Tournois, C.R. Acad. Sci. **258 (5)**, 612 (1964).

[5]. S. De Silvestri, P. Laporta, V. Magni, and O.Svelto, "Radially variable reflectivity output coupler of novel design for unstable resonator", Opt. Lett. **12**, 84 (1987).

[6]. R. Soref, "Voltage-Controlled Optical Phase Shifter", J. Lightwave Tech. **3**, 992, 1985.

[7]. B. Dingel, and M. Izutsu, "New True-Time Optical Delay Line using Single Resonator with Spatially Varying Finesse as Discrete Time Storage for Microwave Phased Array Transmitter", Proc. 1998 Asia-Pacific Microwave Conference (APMC), to held at Yokohama, Japan, Dec. 8-11, 1998 (accepted).

Double heterodyne filtering of received signals in optically time–delay controlled antennas

S.Tonda–Goldstein, L.Pastur, D.Dolfi, J.P.Huignard, T.Merlet †, O.Maas †, J.Chazelas ‡

Thomson–CSF, Laboratoire Central de Recherches
F–91404 Orsay CEDEX, France

ABSTRACT

We propose and experimentally demonstrate an optical architecture, performing processing of the transmit/receive modes of a phased array antenna. It is based on the optical generation and distribution of a microwave local oscillator, matched in frequency and direction, to the received signal.

1 INTRODUCTION

For optically time–delay controlled antennas, opto–electronic elements must be able to handle high power microwave signals. On the other hand, they have to be able to detect very low target signals. Such two antagonist characteristics are difficult to attain over large bandwidth with currently available opto–electronic components. In order to overcome the dynamic range limitation, we have developped the matched local oscillator architecture (MLOA), in which an optically carried microwave LO is used for mixing with the received microwave signals.[1] The operating principle is shown on figure 1. In the transmit mode, two cross–

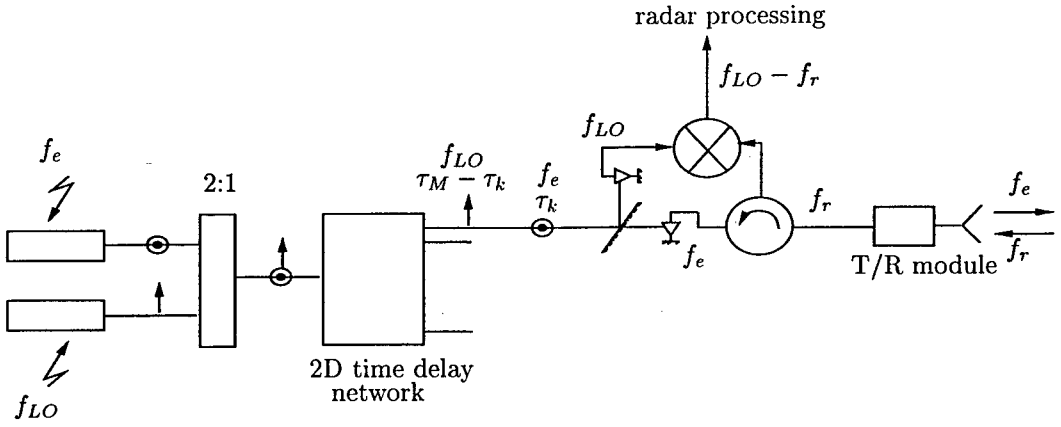

polarized optical beams are excited by two microwave signals at frequencies f_e and f_{LO} respectively. These carriers travel through a 2D time delay network, similar to the one of reference.[2] It is a set of spatial light modulators (SLM), polarizing beam splitters (PBS) and prisms. The pixels of the SLMs act as polarization switches, the PBSs swith the beam along one of the possible paths towards or not the prisms. The delay is determined by the position of the prism. The delay law applied by this network controls the scan angle of the transmitted signal and the antenna far–field pattern. The delay law experienced by the LO is chosen to be complementary to the transmitted signal, so that wether one of the two beams (carrier of frequency f_e or f_{LO}) is delayed by τ_k along channel k, the other (cross-polarized) is delayed by $\tau_M - \tau_k$, τ_M is the maximum time delay. At the output of the 2D time delay network, all the carriers are splitted in two paths. One will provide the signal to transmit, the other one the microwave LO signal to be mixed with the received signal.

0-7803-4936-9/98/$10.00

2 THE CASCADED DOUBLE–MIXING

In radar applications, because of jamming, the LO frequency must stand out of the radar bandwidth Δf. Unlike the ideal homodyne detection, there is, in the receive mode, a phase difference between channels, which disables all the channels to be added in phase. An original approach to minimize this phase difference is to use a cascaded double mixing. This leads to a lower intermediate frequency than this of the single mixing. We propose to generate the LO in two successive steps (Figure 2). The first step will provide

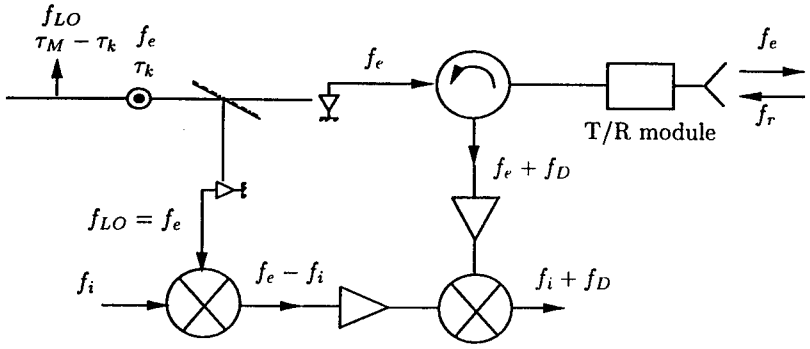

the channelized LOs with $f_{LO} = f_e$. Then, these signals are mixed with in–phase microwave signals at an intermediate frequency $f_i > \Delta f$. It provides on channel k a resulting LO of phase:

$$\phi_k^{LO}(t) = 2\pi(f_e - f_i)t - 2\pi f_e(\tau_M - \tau_k) \quad (1)$$

which is mixed, in the second step, to the corresponding component of the received signal. The result of this double mixing is a signal of phase:

$$\phi_k(t) = -2\pi(f_D + f_i)t - 2\pi f_e(\tau_M - 2T) + 2\pi f_D(2T - \tau_k) \quad (2)$$

The phase difference between two channels j and k is now reduced to:

$$\delta\phi_{jk} = 2\pi f_D(\tau_k - \tau_j) \quad (3)$$

with f_D the Doppler frequency due to the target velocity (f_D of the order of 10 kHz). Thus, the phase difference remains smaller than 1 mrad, to be compared to a prohibitive maximum phase error of 4π, in case of a single mixing with a 32 × 32 elements antenna at central frequency f_o= 3 GHz, bandwidth $\Delta f/f$ of 30% and scan angle of ±30 degrees.

3 EXPERIMENTAL RESULTS

We have implemented an experimental setup equivalent to an antenna which consists of two transmit/receive modules and two delay blocks (giving four different delay values). On each channel, a single frequency laser beam is modulated at the appropriate RF frequency by an acousto–optic Bragg cell. The beating signals are detected by fiber pigtailed photodiodes, amplified and displayed onto an digital oscilloscope. The received signals were directly generated using time delays that simulate propagation towards the target and reflection towards the antenna. The phase difference between the longest and the shortest paths is smaller than 10 ps (limit of range of the oscilloscope) and so, permits in–phase addition of the received signals.

4 REFERENCES

[1] R. R. Stephens, J.J. Lee, G.L. Tangonan, H.T. Newberg, and Wang, "Photonic rf mixing feed for multibean arrays," in *Leos Topical meetings on microwave photonics MWP97, WE 1–6*, Proc. IEEE (1997).

[2] D. Dolfi, P. Joffre, J. Antoine, J.P. Huignard, D. Philippet, and D. Granger, "Experimental demonstration of a phased–array antenna optically controlled with phase and time delays," Appl. Opt. **35**, 5293–5300 (1996).

† Thomson–CSF/Airsys, ‡ Thomson–CSF/Radars et Contre–Mesures.

Advanced Microwave Photonic Devices for Analog Optical Links

(invited paper)

Dieter Jäger, Andreas Stöhr, and Robert Heinzelmann

[1] Gerhard-Mercator-Universität, FB9 - Optoelektronik, Kommandantenstraße 60, 47057 Duisburg, Germany
Phone: +49 203 379 - 2341, Fax: +49 203 379 - 2409, E.mail: jaeger@optorisc.uni-duisburg.de

Introduction

The ultra-wideband and low loss transmission capabilities of optical fibers has led to rapid progress in the area of optical interconnections for microwave and millimeterwave systems, such as optically fed antenna systems, millimeterwave wireless communication, distribution of CATV or multimedia services, high-speed LANs and computer networks [1,2].
In this paper we discuss advanced microwave photonic devices to be used as optical/electrical or electrical/optical power converters. Special emphasis is laid upon high-speed and high-efficiency components providing optical link gain, as well as upon multifunctional and SEED devices leading to a largely simplified link design.

Broadband optical links

The fundamental concept of a unidirectional millimeterwave optical link system is sketched in Fig. 1. The basic building blocks are the electrooptical (E/O) modulator and the optoelectronic (O/E) detector both used as power converters. A key idea of this system is the use of two laserdiodes (LD), LD1 to provide the optical carrier for the signal transfer and LD2 to provide dc power transfer for the amplifier (A) and the O/E converter via the photovoltaic cell (PVC).

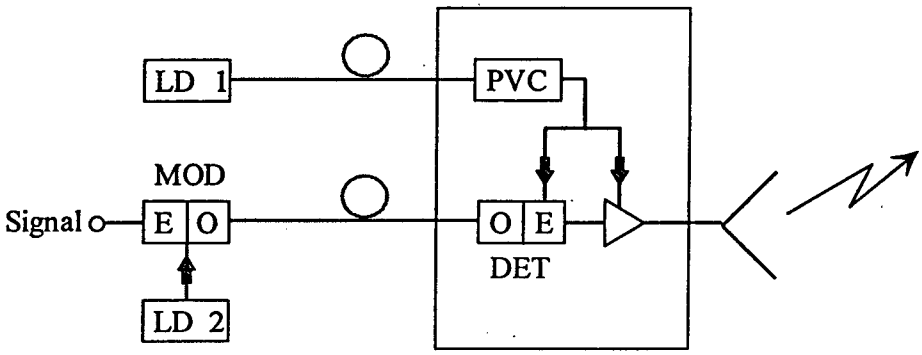

Fig. 1: Optical millimeterwave downlink

Defining the slope efficiencies of the converters of an IMDD link according to Cox et al. [3] by

$$S_{E/O} = (\Delta P / \Delta I)_{in} \quad \text{and} \quad S_{O/E} = (\Delta I / \Delta P)_{out} \tag{1}$$

where ΔP and ΔI are the change of optical power and electrical current, respectively, we obtain

0-7803-4936-9/98/$10.00

the link gain from

$$g = \frac{R_{DET}}{R_{MOD}} (S_{E/O} S_{O/E})^2 \tag{2}$$

with the resistance of the detector, R_{DET}, and the modulator, R_{MOD}. It has further been pointed out, that in case of an MZI modulator link gain can be achieved because $S_{E/O} \sim P_{opt}$, the optical input power. Using an EA modulator instead, we obtain

$$S_{E/O} = M \cdot R_{MOD} \cdot P_{opt} \tag{3}$$

with

$$M = t_M \exp(-\alpha L) \frac{d(\alpha L)}{dV} \tag{4}$$

where t_M is the fiber-to-fiber coupling efficiency, α the absorption coefficient and L the device length.

Microwave photonic devices

Because of their inherent capabilities of high input powers and high power conversion efficiencies in an ultra-broadband frequency range at a tunable characteristic impedance we have studied especially the behavior of traveling wave (TW) devices as shown in Fig. 2.

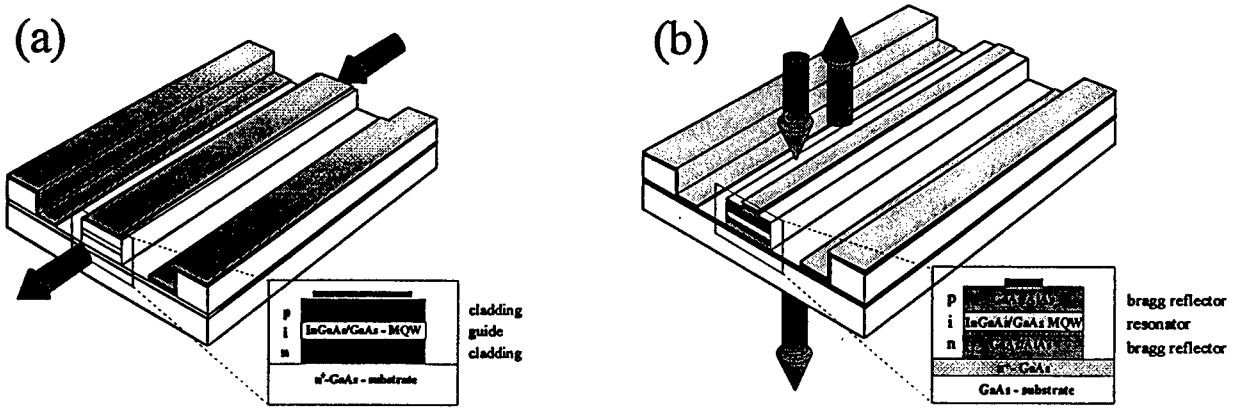

Fig 2: Traveling-wave photonic devices for high-speed ultra-broadband operation: (a) waveguide and (b) vertical structure

Optically, two concepts have been studied, the optical waveguide and the vertical structure incorporating a microcavity between two Bragg mirrors [4]. A TW-MOD has been realized with cut-off frequencies > 60 GHz [5]. This device exhibits a value of M=0,5 V^{-1} at P_{opt}=10mW. Vertical electroabsorption TW-MOD have shown cut-off frequencies >40 GHz and a pronounced linearity with M=0,05 V^{-1} in eq. (3), [6]. Additionally, TW-DET have been developed exhibiting a value of $S_{O/E}$ > 0,3 A/W in the range 20-60 GHz [7].

Using a TW-Photoconductor as a DET element, the dc power can also be converted into millimeterwave power and the devices behave as an optically controlled electrical modulator. In this case we calculate

$$S_{O/E} \doteq D\frac{V_{dc}}{R_{DET}} \tag{5}$$

with

$$D = t_D \exp(\alpha_M L)\frac{d(\alpha_M L)}{dP_{opt}} \tag{6}$$

Here $t_D=\exp(-\alpha_M L)$ are the microwave losses and α_M the microwave absorption. In the above mentioned TW-DET we have D=0.1 mW^{-1} at V_{dc}=10V. The overall link gain would be g=25 for $R_{MOD}=R_{DET}=50\ \Omega$.

Multifunctional and SEED devices

When the optical link of Fig. 1 is to be used as a bidirectional system, four different element functions are are used: Two E/O and two O/E converters each for the transmit and receive mode. The situation is sketched in Fig. 3. For the transmit mode as described above the elemtents of Figs. 3 (a) and (b) are required, whereas in the receive mode the elements of Figs. 3 (c) and (d) are needed. Note that all elements of Fig. 3 are „hybrid" transistor structures, e.g. (a) optical modulator in transmission with optical bias and electrical control, (b) electrical modulator with electrical bias and optical control, (c) optoelectronic detector with optical bias and control, and (d) electrooptic modualtor with electrical bias and control. Note further that the above mentioned EA modulator, waveguide or vertical, behaves simultaneously as a photodetector here as a photoconductor. A measured characteristic of a device is shown in Fig. 4 where $S_{O/E}$ has been determined from the photocurrent arising from the optical absorption. Such a multifunctional device can be used as a transceiver in the basestation [8]. Moreover, as a result of this self-interaction process a device with a positive internal feeedback results leading to a clear nonlinearity, of the physical mechanism in a transistor. Such a device is sketched in Fig. 5 where P_{in} and P_{out} are two optical ports and V and I two electrical

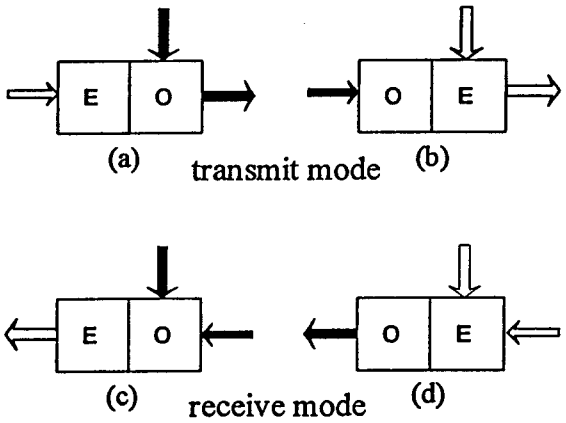

Fig. 3: Multifunctional devices for bidirectional links with optical/electrical input and output ports

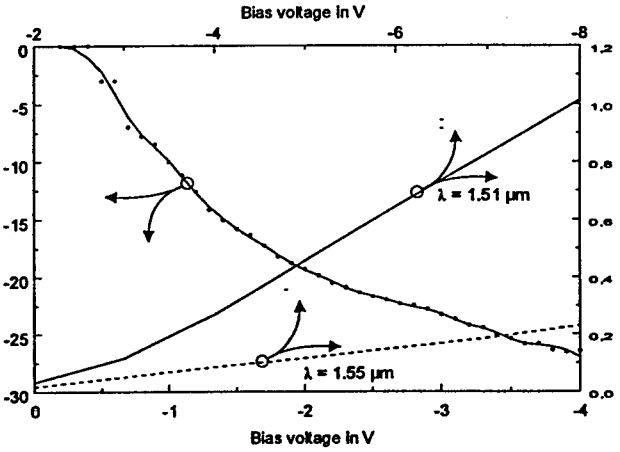

Fig. 4: EA modulator used as a detector

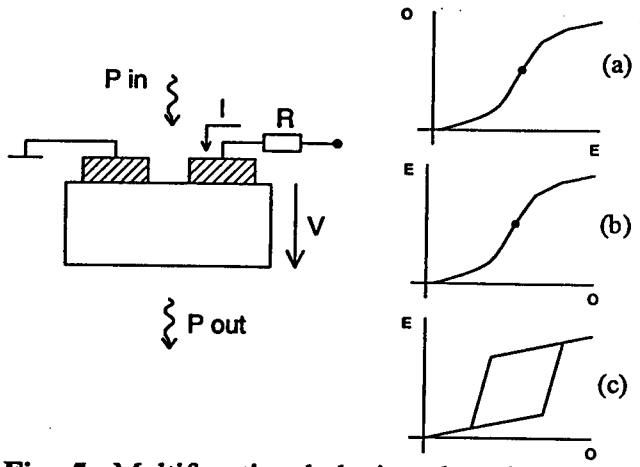

Fig. 5: Multifunctional devices based upon an EA MOD with internal feedback. O/E (a) and E/O (b) characteristics and optical/electrical bistability in (c).

parameters. Such a device is well known from nonlinear optics and called „SEED" (=self electrooptic effect device) [9].Such a device can provide high internal gain when used as an O/E or E/O converter (Figs. 5 (a) and (b) or even as an „optical transistor". Corresponding experiment have been published over 10 years ago [10]. We propose here to use the TW EA modulator from Fig. 2 as a TW-SEED for all functions of Fig. 3 leading to interesting system concepts for bidirectional optical links with gain. Additionally, because of ultrafast bistability found in those devices, of Fig. 5 (c), such a TW-SEED may become a key element in digital links.

Conclusion

In summary, advanced microwave photonic devices for optical links have been studied in this paper. A key device is the EA modulator which can provide multiple functions in a transceiver. Additionally it can lead to high gain similarly to a hybrid transistor, where both analog and digital applications are foreseen.

References

[1] —, Proceedings of the International Topical Meeting on Microwave Photonics MWP'97

[2] R.P. Braun et al., *„Optical Microwave Generation and Transmission Experiment in the 12- and 60-GHz Region for Wireless Communication"*, IEEE Transactions on Microwave Theory and Techniques, Vol. 46, No. 4, pp. 320-330, 1998

[3] C.H. Cox, *„Gain and noise figure in analogue fibre-optic links"*, IEE Proc.-J, Vol. 139, pp. 238-242, 1992

[4] A. Stöhr et al., *„InGaAs/GaAs multiple-quantum-well modulators and switches"*, Optical and Quantum Electronics, Vol. 25, pp. 865-883, 1993

[5] R. Heinzelmann et al., *"EMC measurements using electrooptic waveguide modulators"*, International Topical Meeting on Microwave Photonics '96, Conference Proceedings, Kyoto, Dezember 1996

[6] S. Zumkley et al., *"Vertical n-i-n multiple-quantum-well electrooptical modulators for high-speed applications"*, IEEE Photonics Technol. Lett., Vol. 5, No. 2, pp. 178-180, 1993

[7] M. Alles et al., *"High-speed traveling-wave photodetectors for wireless optical millimeter wave transmission"*, Int. Top. Meet. on Microwave Photonics, pp. 103-106, Duisburg, 1997

[8] A. Stöhr et al., *" Error Free Full Duplex Optical WDM-FDM Transmission using an EA-Transceiver"*, Int. Top. Meet. on Microwave Photonics, 1998 (submitted)

[9] D.A.B. Miller et al., *„Novel hybrid optically bistable switch: the quantum well self-electro-optic effect device"*, Appl. Phys. Lett., Vol. 45, pp13-15, 1984

[10] D. Jäger et al., *„Low-power optical bistability and multistability in a self-electro-optic silicon interferometer"*, IEEE J. of Quantum Electronics, Vol. QE-21, pp. 1453-1457, 1985

BROADBAND, DIRECTLY MODULATED ANALOG FIBER LINK WITH POSITIVE INTRINSIC GAIN AND REDUCED NOISE FIGURE

C. H. Cox, III, H. V. Roussell, R. J. Ram* and R. J. Helkey
M.I.T. Lincoln Laboratory
Lexington, MA, USA

*Department of Electrical Engineering and Computer Science, M.I.T.
Cambridge, MA, USA

Abstract

We report the concept and first demonstration of a broadband amplifierless, directly modulated analog fiber-optic link with an intrinsic gain of +3.8 dB, based on a series connection of diode lasers and a *pin* photodiode

I. Introduction

The RF gain of a fiber-optic link is an important parameter, not only for its own sake, but also because it has been shown to set a lower limit on the noise figure of the link [1]. One approach to increasing the gain is to reduce the bandwidth. Tuned or bandpass links with positive intrinsic gain have been demonstrated using either external [2] or direct [3] modulation. External modulation also offers the option of increasing the gain without a gain-bandwidth trade; consequently broadband external modulation links with positive intrinsic gain have been demonstrated [4], [5]. However, to date the limit on diode laser slope efficiency imposed by energy conservation has limited the intrinsic gain of directly modulated links to be negative, *i.e.* to have loss.

A previous attempt to increase the diode laser slope efficiency was the gain lever laser [6]. However, device difficulties prevented demonstration of a directly modulated link with positive intrinsic gain; further the highly non-linear nature of the gain lever's light-current curve would have limited the dynamic range to unusable levels for analog links. More recently the cascade laser has been proposed as a laser with increased slope efficiency [7], [8]. In this paper we report the first link measurements on a series connection of commercially available, fiber coupled diode lasers. The results confirm that the series connection of lasers, which duplicates the cascade lasers, does indeed increase the intrinsic link gain. Here we demonstrate that this technique permits a broadband, directly modulated link with positive intrinsic gain. In additional, by biasing the laser cascade near but above threshold the correlation among the RIN of the lasers can be reduced, thereby reducing then noise figure.

II. Theory

Consider the link shown in Fig. 1. We assume that the laser resistance, R_{Li}, and the number of lasers, N, are chosen such that $\sum_{i=1}^{N} R_{Li} = R_s$, *i.e.* there is a resistive match with the modulation source. The modulated optical

0-7803-4936-9/98/$10.00 © 1998 IEEE

output from each laser, p_{oi}, is related to the current flowing through all lasers, i_l, by the slope efficiency of that laser, s_{li}; $p_{oi}=s_{li}*i_l$. The optical outputs from all the lasers falls on a common photodiode; consequently $p_{od} = \sum_{i=1}^{N} p_{li} = i_l \sum_{i=1}^{N} s_{li}$. The photodiode current, i_d, is related to the photodiode optical power by the photodiode slope efficiency, s_d; $i_d=s_d* p_{od}$. Combining these equations we obtain an expression for the ratio of the photodiode current to the laser modulation current: $\frac{i_d}{i_l} = s_d \sum_{i=1}^{N} s_{li}$. When the photodiode load resistance, R_{LOAD}, is equal to the modulation source resistance, the intrinsic gain, g_i, is simply equal to the square of the laser and photodiode slope efficiencies:

$$g_i = s_d^{\,2} \left(\sum_{i=1}^{N} s_{li} \right)^2 \tag{1}$$

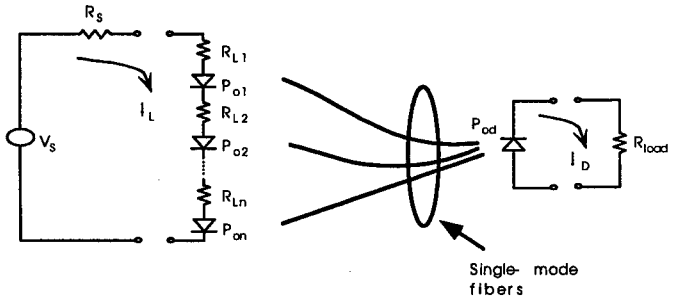

Fig. 1 Directly-modulated analog link with series-connected lasers

III. Experiment

To test the above model, six commercially available, fiber-coupled distributed feedback (DFB) diode lasers were purchased, mounted and electrically isolated from one another on a common metal plate. The lasers contained an internal, 25 Ω series resistor, which was shorted out for these measurements. The resulting resistance of each laser was measured and found to be about 5 Ω. A match to the 50 Ω source resistance was achieved by terminating the laser with a 20 Ω chip resistor to ground. The fiber outputs of all six lasers were arranged to fall on a common, large area photodiode, *i.e.* no fiber coupler was used.

The link gain and frequency response were measured using a network analyzer connected to the lasers and photodiode. For link measurements with only a subset of the lasers, the fibers of the unused lasers were bent to reduce the contribution of those lasers by at least 20 dB.

The data plotted in Fig. 2 show the gain vs. frequency with the number of lasers as the parameter. As predicted the microwave gain increases, *i.e.* the loss decreases, as the number of lasers increases. Transparency, *i.e.* $g_i=1$, is reached with 4 lasers and positive intrinsic gain is achieved with all six lasers.

To compare these measured results with theory, we need the laser and photodiode slope efficiencies. The laser slope efficiency was provided by the manufacturer. The photodiode slope efficiency contained the uncertainty

caused by the unknown fiber coupling efficiency from the fiber bundle to the photodiode. We elected to select a photodiode slope efficiency that matched the measured link gain with a particular laser, then use that same slope efficiency for all the remaining calculations. The approach permitted us to confirm the relative improvement of adding additional lasers in series. The results of calculations base on this approach are listed in Table 1. The agreement between the measured and calculated gains is very good.

The 3-dB bandwidth of the individual lasers was greater than 3 GHz; the bandwidth of the photodiode was greater than 1 GHz. However, the measured link bandwidth was about 60 MHz. The limited bandwidth of the measurement is due to the parasitics of the series connected lasers, which were in commercial butterfly packages. In principle the bandwidth of a monolithically integrated version would not suffer from these limitations and hence have a bandwidth much closer to the bandwidth of the individual components.

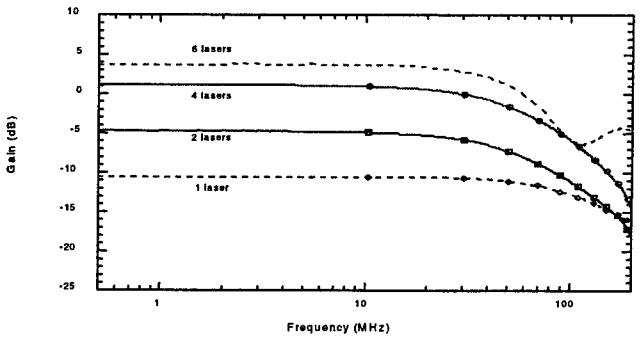

Fig. 2 Intrinsic gain vs. frequency to lasers listed in Table 1

Table 1 Measured Link Parameters

# of Lasers	Slope efficiency (W/A)	Intrinsic gain (dB)		Noise Figure (dB)
		Measured	Predicted	
1	.360	-10.52	-10.52	23.80
2	.667	-4.98	-5.16	21.23
3	.980	-1.50	-1.82	19.70
4	1.315	+0.86	+0.73	18.75
5	1.633	+2.46	+2.61	18.48
6	1.892	+3.78	+3.89	17.81

The noise figure of the link as a function of the number of lasers was also measured and is listed in Table 1. It is known that the RIN of multiple lasers is less than the RIN of an individual laser [9]. Applying this result to the present case implies that in RIN-dominated links such as these, the noise figure should decrease as the number of lasers is increased, which is confirmed by the noise figure data in Table 1. The basis for this effect is the fact that since the RIN of each laser is uncorrelated from the others, the combined RIN adds incoherently, while the signal adds coherently.

IV. Conclusion

We have demonstrated a directly modulated link with positive intrinsic gain. The bandwidth limitation of the present experimental setup can be avoided by a monolithically integrated version of the series connected laser.

Acknowledgements

The authors thank Mike Corcoran for assistance in obtaining some of the experimental link data we have reported. This work was sponsored by DARPA under Air Force Contract F19628-95-C-0002. The views expressed in this paper are those of the authors and do not reflect the official policy or position of the U.S. Government.

References

[1] C. Cox, E. Ackerman, and G. Betts, "Relationship Between Gain and Noise Figure of an Optical Analog Link", IEEE Microwave Theory Tech. Symp. Dig., pp. 1551-1554, 1996.

[2] C. Cox, G. Betts, and L. Johnson, "An Analytic and Experimental Comparison of Direct and External Modulation in Analog Fiber-Optic Links", IEEE Trans. Microwave Theory Tech., vol. 38, pp. 501-509, 1990.

[3] E. Ackerman, D. Kasemset, S. Wanuga, D. Hogue, and J. Komiak, "A High-Gain Directly Modulated L-Band Microwave Optical Link", IEEE Microwave Theory Tech. Symp. Dig., pp. 153-155, 1990.

[4] C. Cox *et al.*, "Incrementally Lossless, Broad-Bandwidth Analog Fiber-Optic Link", IEEE LEOS Summer Topical on Broadband Analog Optoelectronics, p. 15-16, 1990.

[5] K. Williams, L. Nichols, and R. Esman, "Photodetector Non-Linearity Limitations on a High-Dynamic-Range 3 GHz Fiber Optic Link", IEEE J. Lightwave Technol., vol. 16, pp. 192-199, 1998.

[6] K. Vahala, M. Newkirk and T. Chen, "The Optical Gain Lever: A Novel Gain Mechanism in the Direct Modulation of Quantum Well Semiconductor Lasers", Appl. Phys. Lett., vol. 54, pp. 2506-2508, 1989.

[7] O. Sahlen, L. Lundqzist and J. Terlecki, "A 4-Channel, 10 GB/s DFB-Cascade Laser", Proc. 8th European Conf. On Integrated Optics, April 2-4, pp. 204, 1997.

[8] J. Ch. Garcia, E. Rosencher, A. Collot, H. Laurent, J. L. Guyaux, B. Vinter and J. Nagle, "Epitaxially Stack Lasers with Esaki Junctions; a Bipolar Cascade Laser", Appl. Phys. Lett., vol. 71, no. 26, pp. 3752, 1997.

[9] P. Ramadas, E. Garmire and P. Menendez-Valdes, "Relative Intensity Noise of Laser-Diode Arrays", IEEE Photon. Technol. Lett., vol. 33, no. 11, pp. 968.

NOVEL INTEGRATED LASER DEVICES WITH GREATLY ENHANCED QUANTUM EFFICIENCY AND INTRINSIC RF MATCHING FOR LOW LOSS, BROAD BAND OPTO-MICROWAVE APPLICATIONS

S.G. Ayling , D.R. Wight, M.B. Allenson, K.P. Hilton & G.W. Smith

Defence Evaluation Research Agency Malvern, St.Andrews Rd, Malvern, WORCS, WR14 3PS, United Kingdom.

Email: sayling@dera.gov.uk Tel: +44 (0) 1684 895 860 FAX: +44(0) 1684 895 774

ABSTRACT

Fibre-optic analogue links and optically coupled transistors are inherently lossy unless narrow band matched. We demonstrate two novel laser devices with enhanced quantum efficiency to overcome these losses and produce links and transistors with RF gain.

I. INTRODUCTION

In directly modulated opto-microwave links the RF transmission efficiency is dependent upon the quantum efficiency of the laser (η_{LD}) and photodetector (η_{PD}), and the collection and transmission efficiency of the optics (η_{opt}) plus some additional RF matching factors. The current transfer from laser (I_{in}) to photodiode (I_{out}) is

$$I_{out}=(\eta_{LD}.\eta_{FO}.\eta_{PD}).I_{in} \quad (1).$$

While much effort has been expended upon increasing the efficiency of the optics and photodiodes the laser efficiency has been largely constrained by the need for a high modulation frequency. Systems based upon the alternative architecture of a CW laser sources with external optical modulator can show superior performance to directly modulated laser systems but require high power laser sources and are more complex to implement [1, 2]. The RF loss in a simple fibre optic link is typically 20dB which is dominated by the optical coupling losses, which are difficult to reduce without using lens ended fibres or bulk optics which may not be physically robust and are more costly to implement.

Where 50 Ohm impedance is important narrow band matching of the laser can compensate for the optical losses. However, this is unsuitable for broad band systems, for example receivers for broad band antennas. For broad band applications lasers are normally matched by using a series resistance which results in considerably reduced RF laser currents with most of the RF power being dissipated within the matching load. A related problem is found in high power electronic transistor amplifiers. To achieve high frequencies the transistor gate has to be small to reduce thermal and capacitance effects. This reduces the current handling capability and hence the maximum power output. To recover power many gates are used and combined in parallel in a common base configuration. This has the result of reducing the input impedance of the transistor which makes wide band matching difficult. In addition common base transistors do not allow current gain, only power gain through impedance transformation which is not be possible if constrained to have a 50 Ohm input impedance.

We describe here two novel series laser configurations which increase the laser quantum efficiency by factors of 10 and 4. The configuration also results in lasers with approximately 50 Ohm impedances which enable simplified broad band matching for fibre optic links or optically coupled with current gain in 50 Ohms configurations.

II. SERIES ARRAY LASER

An array of AlGaAs laser diodes were fabricated on a semi-insulting GaAs substrate as shown in Fig. 1 with each device electrically isolated from its neighbour. The devices are then connected in series by means of patterned and plated gold contact such that the n-side of one laser is connected to the p-side of its neighbour. The threshold of the array was 21mA,

0-7803-4936-9/98/$10.00

the same as for an individual device. The RF transmission efficiency is now given by

$$I_{out}=N.\eta_{LD}.\eta_{opt}.\eta_{PD}.\ I_{in} \quad (2)$$

where N is the number of lasers connected in series. The resultant laser array has an impedance and forward voltage that is the sum of the individual device characteristics. For 500μm long lasers, which have a typical resistance of 5 Ohms, 10 lasers are required for matching to 50 Ohms. The array was tested with a large area Si photodiode as shown in the circuit diagram Fig. 2 which is equivalent to an RF fibre optic link or an optically coupled transistor.

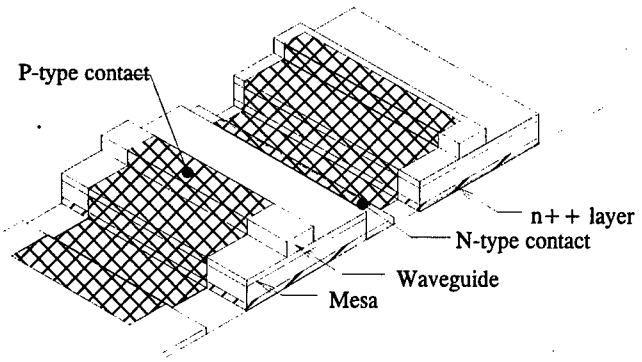

Figure 1 Series array laser. Each laser is electrically isolated on a semi-insulting GaAs substrate but connected to its neighbours via plated metal contacts.

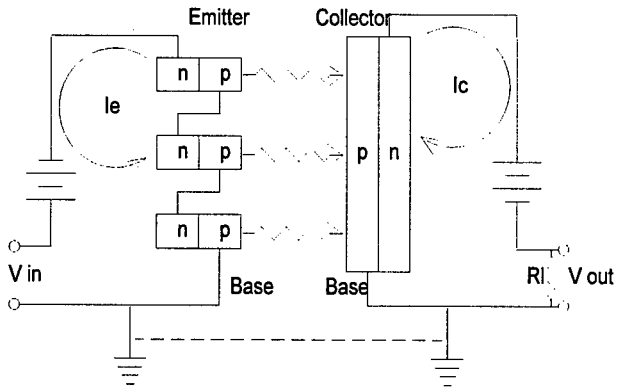

Figure 2 Series array laser with a single large area photodiode as an RF optical link and optically coupled common base transistor.

An RF current gain of 3dB was measured in a 50 Ohms load for this transistor type configuration, Fig. 3. A current gain of 6 dB would be possible if light from both facets were collected or if a high reflection facet coating was applied to one end of the laser array (i.e. η_{opt}= 50% in this demonstration).

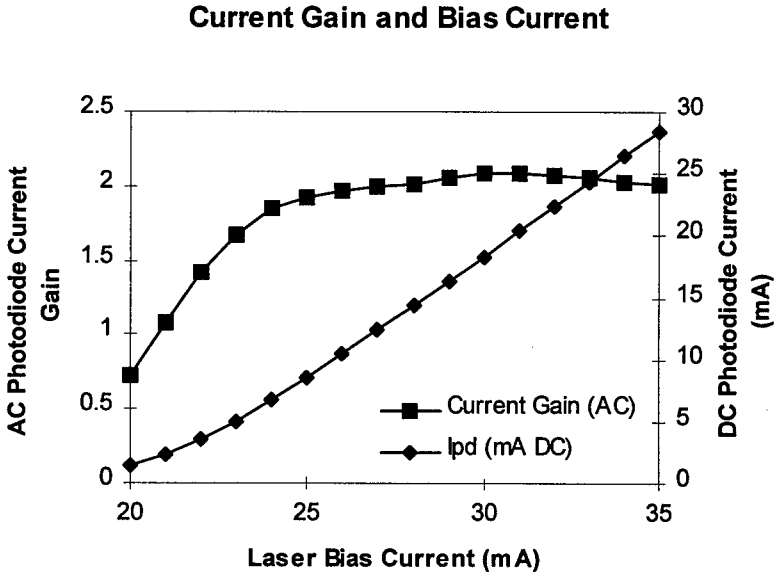

Figure 3. Current transfer results showing how the current gain depends upon the laser bias. A current gain of 3dB was measured which corresponds to a 6 dB power gain in this 50 Ohm environment.

The device required no additional heatsinking as the heat generated is the same as for a single laser with a 45 Ohm matching resistor. The only requirement was for a high voltage bias supply (20 Volts instead of 2V) rather than a high current supply (35mA instead of 350mA for a parallel connected array). The 20dB additional power is 'free' because the laser array is 10 times more efficient at converting the RF power into optical modulation than in a traditional resistive matching technique where most of the DC and RF power are dissipated as heat within the matching resistor. The array

modulation efficiency and impedance were found to flat over the bandwidth of the test equipment (DC to 400 MHz), Fig. 4. This is the first time that an optically coupled common base transistor has been demonstrated with both power and current gain in a 50 Ohm circuit.

For fibre optic links a fibre ribbon is required to connect each laser to a remote photodiode. Using individual photodiodes is preferred as these will have a higher response frequency and will avoid mode noise that would result from the lasers beating against each other. Such a laser array would have applications in short haul microwave links that are required to deliver moderate RF power. Because the link can supply RF power this removes the need for an microwave power amplifier to be attached to the antenna. This make the antenna smaller, lighter, more robust, easier to maintain and cheaper to construct due to the weight and component savings. In phased array and conformal antennas where fibre optics are being considered for LO distribution the laser array removes the need to pre-amplify the optical LO before distribution as this can now be done without loss. This can bring about significant reductions in the total power requires for such antenna systems.

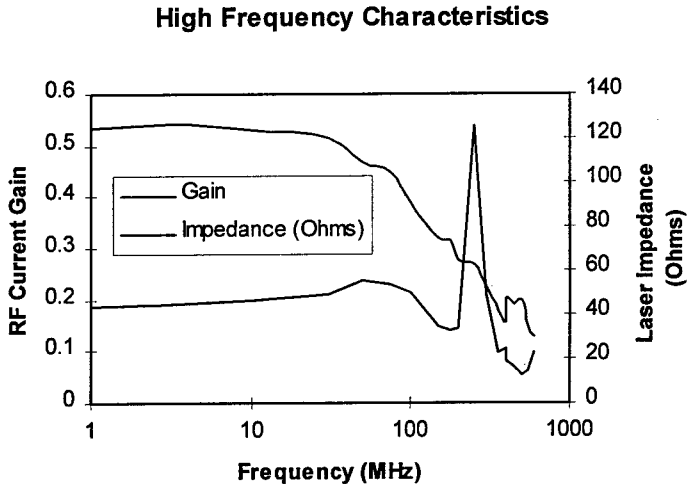

Figure 4. High frequency measurements using a 15 element 750 μm long laser array. The fall in the current gain is thought to be due to the roll off of the photodiode and the oscilloscope used to make the measurements. The impedance resonance at 300 MHz is an artefact of the current probe and not the laser array.

III. SERIES IN-LINE LASER

In this alternative configuration a single laser is subdivided into many sections all sharing one common waveguide, Fig. 5. The n-side of one section is connected to the p-side of the neighbouring section and so on down the laser. When the laser is subdivided the impedance increases as the square of the number of sections. The current can be thought of as being recycled in the laser sections so the threshold should decrease in proportion to the number of sections while the quantum efficiency and forward voltage should increase in proportion. The subsections were designed to have good optical coupling which lead to a high leakage between sections.

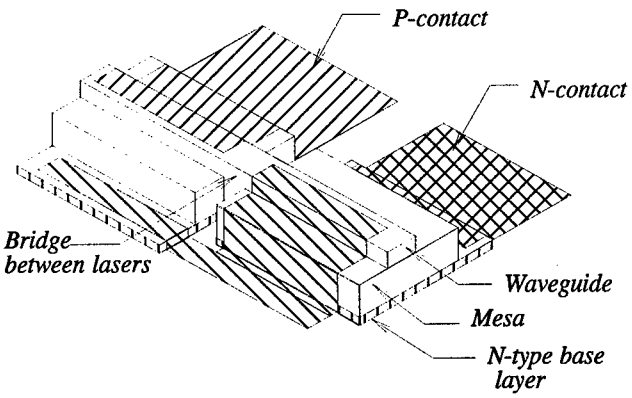

Figure 5 Series in-line laser. The n-side of one section is connected to the p-side of the next and so on down the laser

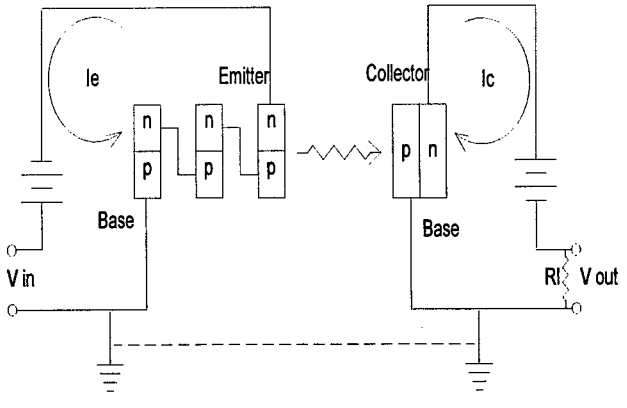

Figure 6 Series in-line laser with a photodiode as an RF optical link and a common base transistor

Number of Sub-sections	Threshold Current Ith (mA)	External Slope Efficiency η (W/A)	Forward Voltage V_f (V)	Dynamic Series Resistance(Ω)
1	27	0.34	1.8	4
2	30	0.78	3	17
3	32	0.94	4.5	25
4	21	1.17	5.6	51
5	32	0.83	7.9	57

Table 1. Preliminary results for the in-line lasers showing the expected increase in slope efficiency, forward voltage and dynamic resistance. The threshold current does not reduce as expected because of leakage currents between the different sections.

Table 1 shows the preliminary results for the series in-line connected laser. The threshold current and resistance do not follow the expect variation due to a leakage current between the sections and a variable probe resistance during testing. The leakage current has subsequently be shown to be completely eliminated by proton isolation in the connecting waveguide bridge between sections.

This device has the advantage of requiring only a single optical fibre connection for RF fibre optic links. As such it is a direct replacement for current lasers and has the advantages of a high slope efficiency and low threshold current combined with a broad band 50 Ohm impedance for simple RF matching. Unlike an integrated laser and semiconductor amplifier this device does not suffer from low frequency gain modulation and so is suitable for CATV applications and low power receivers.

IV. CONCLUSIONS

We have demonstrated two novel laser devices suitable for high efficiency RF transmission on fibre or for integrated optical transistors. These devices enable fibre optic links and optical transistors to be made with broad band gain for the first time.

V. ACKNOWLEDGEMENTS

This work was supported by the United Kingdom Ministry of Defence. The devices described in this paper were processed by S. Jones of the Electronics Sector, DERA Malvern.

VI. REFERENCES

[1] J. B. Georges, D.M. Cutrer, O. Solgaard & K.Y. Lau "Optical transmission of narrow band millimetre-wave signals", IEEE Trans. Microwave Theory and Techniques, Vol. 43, No. 9, pp. 2229-2240, 1995.

[2] C.H. Cox, G.E. Betts & L.M. Johnson, "An analytic and experimental comparison of direct and external modulation in analog fibre-optic links", IEEE Trans. Microwave Theory and Techniques, Vol. 38, No. 5, pp. 501-509, 1990.

TWO-SECTION INTEGRATED QUANTUM-CONFINED STARK EFFECT TUNED LASER WITH UNIFORM FREQUENCY MODULATION RESPONSE FROM 30KHZ TO 6GHZ

X. Huang(1), A. J. Seeds(1), *Fellow, IEEE*, J. S. Roberts (2), A. P. Knights(3)

(1)Department of Electronic & Electrical Engineering, University College London, London WC1E 7JE, UK
(2)EPSRC III-V Semiconductor Facility, University of Sheffield, Sheffield S1 3JD, UK
(3)EPSRC Ion Beam Centre, University of Surrey, Guildford GU2 5XH, UK

Abstract

We report the first post-growth band-gap engineered, quantum-confined Stark effect (QCSE) tuned tw-section ridge waveguide laser, having the widest and most uniform frequency modulation bandwidth (30kHz to 6GHz ±3dB) yet reported for field effect tuned lasers.

I. Introduction

Tunable semiconductor lasers with uniform frequency modulation (FM) response are key components in microwave over fibre analogue links using optical frequency modulated transmitters [1,2]. They are also key components in optical phase lock loops (OPLL) for high spectral purity microwave signal generation [3,4]. Conventional tunable semiconductor lasers employ current injection to achieve tuning by the carrier induced effect (CIE)[5]. Whilst this is a convenient method, it suffers from the intrinsic limitation that thermal tuning mechanisms which are dominant at low modulation frequencies (<10 MHz) have the opposite sign from plasma and band filling tuning mechanisms which pre-dominate at higher frequencies, leading to an highly non-uniform FM response [6]. Although very flat FM response over the modulation frequency range 10kHz to 20GHz has been achieved by a CIE tuned complex coupled DFB laser [7], precise adjustment of the bias current is required and the FM response uniformity and sensitivity are bias current dependent. In contrast, an intrinsically uniform FM response can be obtained by using the electro-optic (EO) effect in the tuning section, as the EO effect involves no carriers, thereby eliminating thermal effects. However, the EO effect in bulk semiconductor materials gives a small refractive index change relative to CIE. Quantum confined Stark effect (QCSE) in an MQW structure [8] provides a comparable refractive index change to CIE [9], even for wavelength detunings of 10-40nm to the red side of the e1-hh1 absorption exciton peak. Field effects in significantly reverse biased multiple quantum well (MQW) structures can offer response times in the picosecond region [10]. In earlier work, we demonstrated for the first time the use of QCSE as a semiconductor laser tuning method, using an external cavity configuration [11,12]. More recently, a twin guide structure laser using QCSE tuning [13] (FM response uniform within 15dB from 300kHz to 4GHz) and a butt-jointed DBR structure laser tuned by the related Wannier-Stark effect [14] (no uniformity data, cut-off frequency less than 4GHz) have been reported, both with very complicated fabrication requirements. Using a simple two-section integrated ridge waveguide laser structure, we have demonstrated the highly uniform FM response capability of a QCSE tuned laser (±0.7dB from 10kHz to 100MHz), free from thermal effect [15]. We now report results on QCSE tuned lasers fabricated on a semi-insulating (SI) GaAs substrate with post-growth band-gap detuning and low parasitic capacitance air-bridged contacts, offering simple fabrication requirements, highly uniform FM response, high cut-off frequency, independent control of output power, and suitability for applications where an uniform FM response over a limited tuning range is required.

II. Device fabrication and assessment

Fig.1 shows the schematic cross section of the device. The GaAs/AlGaAs MQW active layer is grown on a (100) SI GaAs substrate by MOVPE in a single epitaxy step and contains 5 quantum wells, a number being chosen to optimise the relation between the modal gain, the threshold current of the gain section and the refractive index

0-7803-4936-9/98/$10.00

change of the tuning section. Gain and tuning sections share a single cavity optically, but are isolated from each other electrically by a 30 μm wide etched isolation gap in the contact and cladding layers between them.

In order to reduce cavity loss, the impurity-free vacancy diffusion technique [16] was used to blue-shift the exciton peak of the tuning section by about 10 nm. This was implemented by coating the tuning section with ~200nm thick SiO_2 and treating the uncapped gain section in an argon plasma chamber for 5 minutes, before annealing at 940°C for 60 seconds. Wafers were then processed into metal-clad ridge guide laser on a 24μm wide mesa, with one-side etched to access the n+ GaAs contact layer, and the other side etched in a 10μm wide channel surrounding the bonding pads down to the SI substrate. Air-bridges were fabricated to connect the ridge to the bonding pads. The laser was mounted on a microwave sub-mount. The threshold current for a laser having a gain section length of 400μm and a tuning section length of 200 μm was 35mA, with only the gain section pumped. The measured tuning section capacitance was 1pF at 0V bias. The mode suppression ratio (MSR) was better than 20dB at pumping currents greater than $2I_{th}$. Continuous tuning of 22.5 GHz (red shift) was obtained for a change in tuning section reverse bias from 0V to 1.8V, corresponding to a tuning sensitivity of 12.5GHz/V. The linewidth changed only slightly with tuning section reverse bias, from 8MHz at 0V to 12MHz at 1.8V, due to the low loss of the band-gap shifted tuning section.

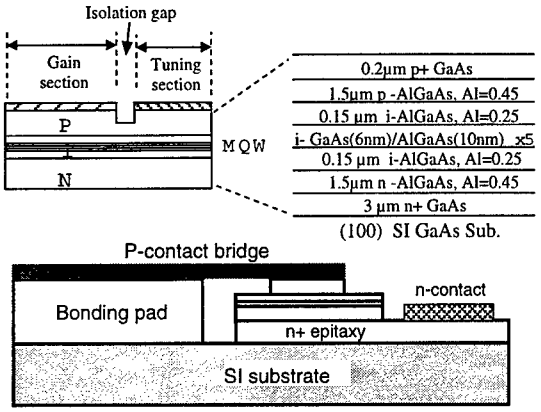

Fig.1 Structure of two-section QCSE tuned laser.

III. Dynamic response measurement and discussion

The FM response [6] was obtained using a Michelson interferometer combined with an 18GHz bandwidth GaAs photodiode and an HP8753D network analyser. A 50Ω shunt resistance was used to terminate the microstrip line feeding the tuning section. Sinusoidal RF drive at –5dBm power level was fed to the tuning section via a bias-tee. The tuning section was operated at 0.4V reverse bias, to ensure that it is remained reverse biased throughout the modulation cycle. Fig.2 shows the FM sensitivity and FM phase of the laser as a function of modulation frequency from 30kHz to 6GHz at two different gain section pumping currents. It is seen that the FM response is uniform within ±3dB up to 6GHz, and the FM phase response is uniform and in phase with the RF signal showing that red-shift tuning mechanisms are dominant. Due to the band gap detuning, the lasing wavelength is located at the red side of the exciton peak of the tuning section. Consequently, the refractive index change at the lasing wavelength increases with increasing electric field, resulting in a red shift with increasing reverse bias, in agreement with the measured results. To compare this QCSE tuning with CIE tuning, the CIE tuned FM response of the same laser was measured by applying an RF signal (-15dBm power level) to the gain section through a bias-tee, as shown in Fig.3. Here, due to the carrier injection effects, thermal tuning (red shift with increasing current) dominates at low frequencies, while plasma and band filling effects which produce blue shift with increasing current dominate at higher frequencies [6], thus an highly non-uniform FM response (> ±10dB

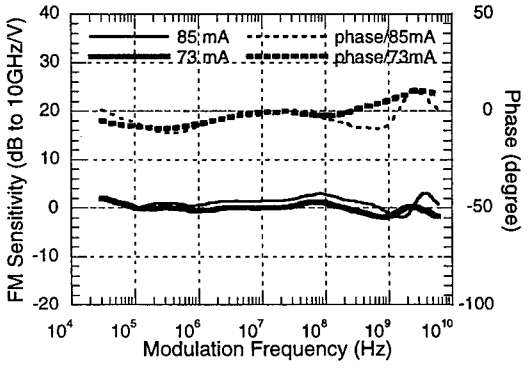

Fig.2 FM responses (magnitude and phase) of QCSE tuned laser at gain section pumping currents 73mA and 85mA.

from 30kHz to 6GHz) is obtained. The corresponding FM phase varies from anti-phase at low frequencies to in-phase at high frequencies, confirming the presence of opposite sign tuning mechanisms in the CIE tuned laser.

The residual intensity modulation (IM) for both tuning methods has also been measured. For QCSE tuning, a 4.5GHz peak frequency deviation gives a residual IM index of 0.05, while for CIE tuning, a 3.8GHz peak frequency deviation gives an IM index of 0.09, both at a modulation frequency of 100kHz. The IM response in both cases is uniform within ±2dB over the modulation frequency range 30kHz to 6GHz, with a photon-electron resonance peak at about 3GHz.

Comparing these results with our earlier work [15], where the band gap of the tuning section was not shifted, the FM sensitivity was 20GHz/V (500μm laser with 200μm tuning section length) and 4GHz peak frequency deviation gave an IM index of 0.05, the residual IM index per unit bias applied is improved by a factor of 1.8 (from 0.25/V to 0.14/V), indicating the success of band-gap engineering in reducing the tuning section absorption loss. However, the residual IM index improvement per unit frequency deviation is smaller, from 0.013/GHz to 0.011/GHz, or by a factor of 1.13. This is expected as although absorption change, $\Delta\alpha$, in the tuning section decreases with increasing bandgap blue-shift, it increases with increasing electric field change [9,17]. The refractive index change per unit electric field change, Δn, decreases with increasing bandgap blue-shift, resulting in lower FM sensitivity. Larger electric field change is therefore needed to produce the same frequency deviation.

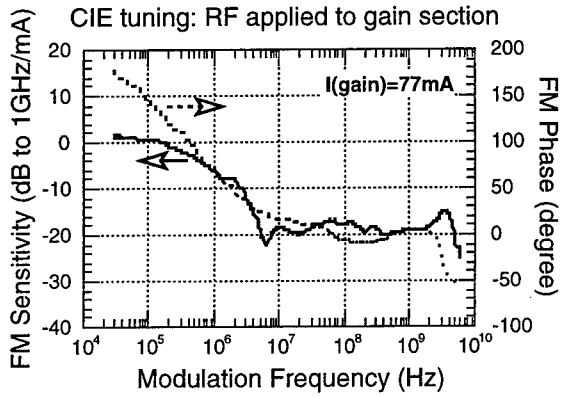

Fig.3 FM response for laser of Fig.2 using CIE tuning.

The uniform FM response of the QCSE tuned laser is almost independent of gain section pumping current, as shown in Fig.2. It is therefore possible to control the laser output power independently. All lasers characterised displayed FM response uniformity within ±3dB over the frequency range 30kHz to 6GHz, illustrating the intrinsically uniform FM response and the high reproducibility obtainable from the QCSE tuning mechanism.

The present laser has a junction width of 24μm and 1pF tuning element capacitance, leading to a calculated –3dB cut-off frequency of 6.4GHz in a 50Ω system. Using special low parasitic capacitance fabrication techniques, an RC limited bandwidth of ~40 GHz can be achieved [18]. The ultimate limit to tuning speed arises from the round trip delay effect in the laser cavity [12]. For a laser having a tuning section optical length L_t and total cavity optical length L, the relative frequency deviation response at modulation frequency ω due to the round trip effect is given by

$$\frac{\Delta f(\omega)}{\Delta f(0)} = \frac{sinc(\omega L_t / c)}{sinc(\omega L / c)}$$

where c is the velocity of light in vacuo, giving a +3dB modulation frequency limit of 20 GHz for our 600 μm long laser with 200μm tuning section length.

IV. Conclusion

We have shown the successful use of a QCSE tuning section integrated in an MQW ridge guide laser to give an intrinsically highly uniform FM response over a wide modulation frequency range (±3dB from 30kHz to 6GHz). The response is independent of gain section pumping current and reproducible from laser to laser. The use of post-growth band gap blue-shift on the tuning section reduces the residual absorption loss. It should be a straight-forward matter to extend the QCSE tuning technique described here to lasers based on InP material system for operation in the second and the third optical communication windows.

ACKNOWLEDGEMENTS

This work was supported by Nortel, the UK EPSRC and the US AFOSR. One of the authors (XH) gratefully acknowledges receipt of an ORS award and the Dean's Scholarship award from University College London.

REFERENCES

[1] A. J. Seeds, "Microwave opto-electronics", *Optical and Quantum Electronics*, Vol.25, pp. 219-229, 1993.

[2] B. Cai and A. J. Seeds, "Optical frequency modulation links: theory and experiments", *IEEE Trans. Microwave Theory and Techn.*, Vol.45, pp. 505-511, 1997.

[3] R. T. Ramos and A.. J. Seeds, "Fast heterodyne optical phase-lock loop using double quantum well laser diodes", *Electron. Lett.*, Vol. 28, pp. 82-83, 1992.

[4] U. Gliese, T. N. Nielsen, M. Bruun, E. L. Christensen, K. E. Stubkjaer, S. Lindgren and B. Broberg, "A wideband heterodyne optical phase-lock loop forgeneration of 3-18GHz microwave carriers", *IEEE Photon. Technol. Lett.*, Vol. 4, pp. 936-938, 1992.

[5] C. H. Henry, R. A. Logan and K. A. Bertness, "Spectral dependence of the change in refractive index due to carrier injection in GaAs lasers", *J. Appl. Phys.*, Vol.52, pp. 4457-4461, 1981.

[6] S. Kobayashi, Y. Yamamoto, M. Ito and T. Kimura, "Direct frequency modulation in AlGaAs semiconductor lasers", *IEEE J. Quantum Electron.*, Vol. QE-18, pp. 582-595, 1982.

[7] M. Okai, M. Suzuki and M. Aoki, "Complex coupled λ/4-shifted DFB lasers with a flat FM response", *IEEE J. Selected Topics on Quantum Electron.*, Vol. 1, pp. 461-465 1995.

[8] D. A. B. Miller, D. S. Chemla, T. C. Damen, A. C. Gossard, W. Wiegmann, T. H. Wood and C. A. Burrus, "Bandedge electroabsorption in quantum well structures: The quantum-confined Stark effect", *Phys. Rev. Lett.*, Vol. 53, pp. 2173-2177, 1984.

[9] J. E. Zucker, T. L. Hendrickson and C. A. Burrus, " Low voltage phase modulation in GaAs/AlGaAs quantum well optical waveguide," *Electro. Lett.*, Vol. 24, pp. 112-113, 1988.

[10] A. M. Fox, D. A. B. Miller, G. Livescu, J. E. Cunningham, W. Y. Jan, "Quantum well carrier sweep out: Relation to electroabsorption and exciton saturation", *IEEE J. Quantum Electron.*, Vol. QE-27, pp. 2281-2295, 1991.

[11] B. Cai, A. J. Seeds, A. Rivers and J. S. Roberts, "Multiple quantum well-tuned GaAs/AlGaAs laser", *Electron. Lett.*, Vol. 25, pp. 145-146, 1989.

[12] B. Cai, A. J. Seeds and J. S. Roberts, "MQW tuned semiconductor lasers with uniform frequency response", *IEEE Photon. Technol. Lett.*, Vol. 6, pp. 496-498, 1994.

[13] T. Wolf, K. Drogemuller, B. Borchert, H. Westermeier, E. Veuhoff and H. Baumeister, "Tunable twin-guide laser with flat frequency modulation response by quantum confined Stark effect", *Appl. Phys. Lett.*, Vol. 60, pp. 2472-2474, 1992.

[14] J. Langanay, E. Gaumont-Goarin, J. Y. Emery, C. Labourie, J. G. Provost, C. Starck, O. Le Gouezigou and D. Lesterlin, "High FM bandwidth of DBR laser including butt-jointed electro-optical wavelength tuning sections", *Electron. Lett.*, Vol. 30, pp. 311-312, 1994.

[15] X. Huang, A. J. Seeds and J. S. Roberts, "Reverse bias tuned multiple quantum well ridge guide laser with uniform frequency modulation response", *Appl. Phys. Lett.*, Vol. 71, pp. 765-766, 1997.

[16] I. Gontijo, T. Krauss, J. H. Marsh, and R. M. De La Rue, "Post growth control of GaAs/AlGaAs quantum well shapes by impurity-free vacancy diffusion", *IEEE J. Quantum Electron.* Vol. QE-30, pp. 1189-1195, 1994.

[17] U. Koren, T. L. Koch, H. Presting and B. I. Miller, " InGaAs/InP MQW waveguide phase modulator", *Appl. Phys. Lett.*, Vol. 50, pp. 368-370, 1987.

[18] O. Mitomi, I. Kotaka, K. Wakita, S. Nojima, K. Kawano, Y. Kawamura and H. Asai, "40GHz bandwidth InGsAs/InAlAs multiple quantum well optical intensity modulator", *Appl. Optics*, Vol. 31, pp. 2030-2034, 1992.

CLOCK SOURCE-LIMITED LOW JITTER, SUBTERAHERTZ SIGNAL GENERATION FROM MODE-LOCKED SEMICONDUCTOR LASER CONTROLLED BY PHASE LOCKED LOOP (PLL) WITH PHOTONIC DOWNCONVERSION

Etsu Hashimoto[1], Atsushi Takada[1], and Yoshitada Katagiri [2]

[1] NTT Optical Network Systems Labs.
1-1, Hikarino-oka, Yokosuka-shi, Kanagawa, 239-0847, Japan.
[2] NTT Opto-electronics Labs.
3-9-11, Musashino-shi, Tokyo, 180-0012, Japan.

abstract

Reference clock-limited low jitter of 0.14 ps, 197 GHz signal generation is successfully demonstrated from a harmonic colliding pulse mode-locked laser diode controlled by a PLL with photonic down-conversion using high order modulation side bands.

I. Introduction

The generation of a low-jitter high repetition rate optical pulse train, whose repetition frequency is over 100 GHz, is important for realizing both ultra-high speed optical communication networks [1] and microwave photonics transmission networks [2]. To generate an ultra-high repetition optical pulse train, passively mode-locked laser diodes (PML-LD), especially colliding pulse mode-locked laser diodes (CPM-LD), are very attractive because they can generate pulses beyond the subterahertz region without high-frequency electric circuits [3]. However, the pulses phase of a free-running PML-LD disperse and have no carrier component, so the pulses are not synchronized to the electrical reference clock.

A phase-lock loop (PLL) technique was adopted to synchronize the optical pulses from a PML-LD to a reference signal [4-5]. Photonic downconversion [6] has also been incorporated with the PLL controlling a PML-LD to expand the operation frequency beyond the frequency band limitation due to the optical detector and electrical frequency-down convertor [7]. We recently demonstrated the synchronization of 192 GHz optical pulses from a harmonic CPM-LD by a photonic down-conversion PLL using the 10th-order harmonic modulation sidebands generated by an electroabsorption modulator (EAM) [8]. However, the timing jitter was relatively large (0.6 ps) and the factor limiting the suppression of the timing jitter was not clarified.

In this paper, we achieve clock source limited, timing jitter as low as 0.14 ps from 197 GHz signal by improving the PLL configuration and report detailed characteristics of phase noise power spectrum.

II. Timing jitter and SSB phase noise spectrum in photonic downconversion PLL using harmonic modulation side bands of a high order

The diagram of the PLL with photonic downconversion using high-order modulation side bands is shown in Fig. 1. The loop consists of a phase comparator (PC), a loop filter (LF), a high frequency voltage controlled oscillator (VCO: CPM-LD in this

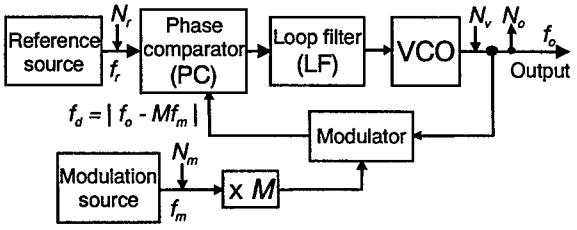

Fig. 1 Diagram of photonic down-conversion PLL

0-7803-4936-9/98/$10.00 © 1998 IEEE

case), and an optical modulator. The part of VCO output with frequency of f_0 is modulated by the optical modulator which has nonlinear response against the applied signal. When the modulator is driven with a sinusoidal signal with frequency of f_m , side bands are generated at the optical frequency of $\nu = \nu_0 \pm M f_m$ (ν_0: original optical frequency, M : natural number). The detected signal output by the optical detector then includes the frequency of f_d (= $|f_o - M f_m|$) allowing electrical control to be easily processed. The phase of downconverted signal with frequency of f_d is compared with that of the reference clock source frequency f_r at the phase comparator. The filtered output is put into the VCO to decrease the phase error. The phase of output signal with frequency f_o of the VCO is thus stabilized to the phase decided by both of the reference and modulation sources.

When the PLL is closed, spectral frequency noise power density N_o of the VCO is given by

$$N_o = (N_r + M^2 N_m)\left|\frac{G(j\omega)}{1+G(j\omega)}\right|^2 + N_v\left|\frac{1}{1+G(j\omega)}\right|^2 \quad (1)$$

where, N_r, N_m and N_v are the phase noise associated with reference clock, modulation clock source, and the VCO, respectively. $G(j\omega)$ is the open loop gain given by

$$G(j\omega) = K_d K_v \frac{F(j\omega)}{j\omega}. \quad (2)$$

Coefficients K_d , K_v and $F(j\omega)$ are the response of the PC, the response of VCO, and the transmission function of the filter, respectively. Because thermal noises from the PC and filter are assumed to be small compared to the phase noise of N_r and N_m around the carrier frequency, these noise components are neglected. Within the PLL cut-off frequency, the conditions

$$\left|\frac{G(j\omega)}{1+G(j\omega)}\right|^2 \approx 1 \quad \text{and} \quad \left|\frac{1}{1+G(j\omega)}\right|^2 \approx 0 \quad (3)$$

are considered to stand. Thus the phase noise of output VCO approaches

$$N_o = N_r + M^2 N_m. \quad (4)$$

When the phase noise of the reference and modulation clock source are nearly the same and the order of harmonics is large (>10), N_o becomes $M^2 N_m$. This means that the limit value of absolute timing jitter of the VCO is the same as that of the modulation source used, assuming that the noise power density is proportional to the square of the carrier frequency because $f_o \approx M f_m$.

At this limit condition, the phase noise density of the output signal from the optical modulator used inside the PLL falls far below the level of $M^2 N_m$ and approaches the noise density of the reference clock because the VCO output signal has the nearly equal phase noise power density as $M^2 N_m$ and its phase is out-of phase as compared with added noise by the modulator. Thus the phase noise of the VCO output signal is canceled out by the modulation. Therefore, clock noise limited low jitter signal generation can be confirmed also by measuring lower noise power density

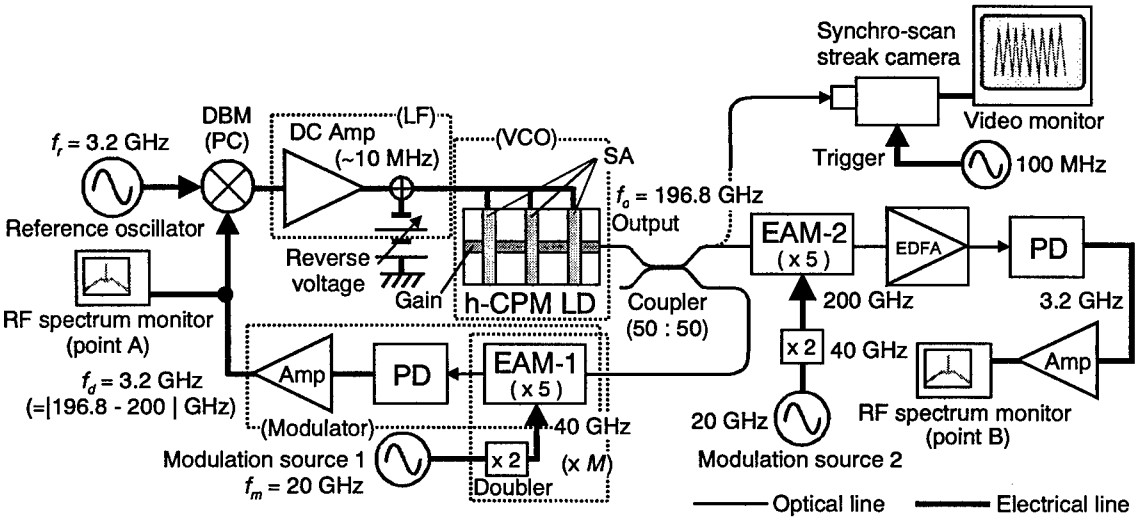

Fig. 2 Experimental setup of sub-THz signal generation using photonic down-conversion PLL

of the modulator-output signal than $M^2 N_m$.

III. Experiment

The experimental setup is shown in Fig. 2. The configuration is the almost same as Ref. [8] except for the loop delay and loop gain optimization. The EDFA with length of 9 m, used in Ref. [8], could be removed from the loop by increasing electrical gain and using a low loss, high efficiency electroabsorption modulator (EAM-1). A harmonic colliding pulse mode-locked laser (h-CPM LD) with 196.8 GHz repetition frequency [9] was used as the VCO. A part of the optical pulse train is modulated by the EAM-1 in the PLL. The drive signal applied to the optical modulator with frequency of 40 GHz, was generated by doubling a 20 GHz signal from an RF synthesizer. The optical spectrum of modulated mode-locked pulses is shown in Fig. 3. The generated sidebands lie between the original modes with the spacing of 40 GHz. Detection of the modulated optical pulses by a PD with 50 GHz bandwidth yielded electrical signals with frequencies of 3.2 GHz, 36.8 GHz, and 43.2 GHz. The signal with 3.2 GHz frequency was assumed to be the beat note between the 10-th order sideband (M = 10) of the original modulation clock frequency (f_m = 20 GHz) and the neighboring original locked-mode. The 3.2 GHz signal was phase-compared with a reference clock oscillator having frequency f_r of 3.2 GHz by a double balanced mixer (DBM). The output voltage, which is proportional to the phase error, was then amplified by the D.C. amplifier with a bandwidth of 10 MHz, superimposed on the reverse bias voltage, and applied to the saturable absorption region of the h-CPM-LD to decrease the error signal. The output frequency was thus stabilized at 196.8 GHz ($f_o = |f_r - M f_m|$). The optical signal output from the PLL was also down converted by EAM-2 driven by a 40 GHz signal from another clock source to measure the phase noise characteristics by RF spectrum analyzer. The down converted signal was also centered at 3.2 GHz. The temporal waveform was measured by a synchro-scan streak camera (SSSC) with time resolution of 3 ps.

Figure 4 shows the RF spectrum of the downconverted signal at 3.2 GHz when the PLL was closed. The carrier to noise ratio (CNR) was 96 dBc/Hz at 500 kHz offset. The inset shows the temporal trace measured by the SSSC. The phase dispersion is suppressed and the carrier note and about 200 GHz repetitious waveform are clearly observed. The SSB noise power density of output pulses outside the PLL (point B in Fig.2) is shown in Fig. 5. It was confirmed by quadrature phase detection method that the phase noise power density is almost the same as total noise power density. The SSB noise spectrum of the phase locked h-CPM LD is close to 100 (M^2) times larger than that of the reference oscillator under 100 kHz offset. Therefore, we expect timing jitter of the optical pulse train from the LD is well suppressed. The rms timing jitter is calculated to be 0.14 ps from a 25 to 1 MHz bandwidth, which approaches the clock limited value of 0.13 ps from the modulation source.

Figure 6 shows the SSB noise power density of the signal from the EAM used inside the PLL (point

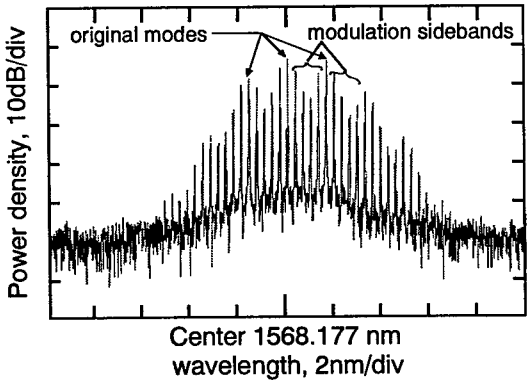

Fig. 3 Optical spectrum of h-CPM LD pulses modulated at 40 GHz by EAM.

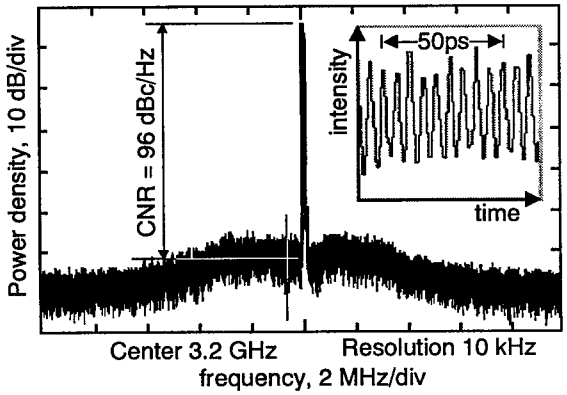

Fig. 4 Synchronized 196.8 GHz signal down-converted to 3.2 GHz. Inset shows temporal trace.

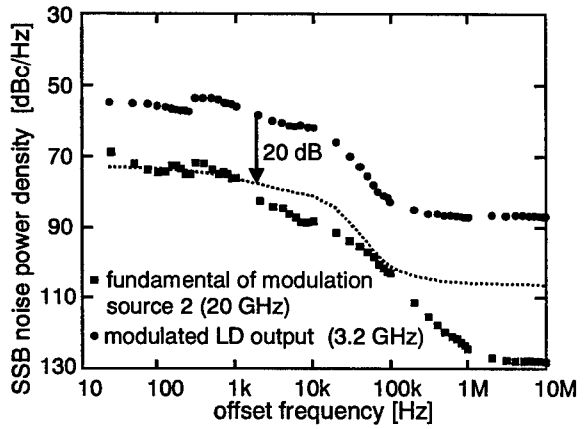

Fig. 5 Phase noise characteristics measured at point B of Fig.2.

A in Fig.2). The noise power of the tenth harmonic (200 GHz) of the modulation clock source 1 (20 GHz), which is 100 times (20 dB) large as that of the 20 GHz clock source 1, is shown as a broken line. The noise power of the modulated signal of h-CPM LD is about 30 dB smaller than that of the tenth harmonic in the range under 100 kHz. This also indicates that the phase noise of the signal from h-CPM-LD is well suppressed to approach that of the tenth harmonic.

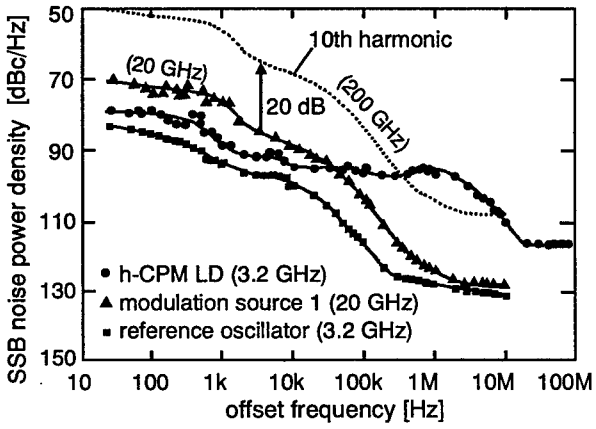

Fig. 6 Phase noise characteristics of h-CPM LD measured at point A of Fig.2.

IV. Conclusion

The dominant factor limiting the phase noise of a VCO in a PLL with photonic downconversion using high order modulation sidebands was clarified to be the noise of the harmonics of the modulation source. In experiments, the phase noise of a 197 GHz signal from a h-CPM LD was suppressed by the PLL with photonic downconversion and the rms timing jitter of 0.14 ps, limited by the modulation source, was achieved.

References

1. M. Saruwatari, "High-speed optical signal processing for communications systems", IEICE Trans. Commun., E78-B, pp.635-643, 1995.
2. K. Y. Lau, "High speed photonic devices for millimeter wave systems", Int. topical meeting on microwave photonics (MWP'96) tech. digest, pp.1-4, Dec. 1996.
3. Y.Chen and M. Wu "Monolithic colliding-pulse mode-locked quantum well lasers", IEEE Quantum Electron., QE-28 (10), pp.2176-2185, 1992.
4. R. J. Helkey, D. J. Derickson, A. Mar, and J. G. Wasserbauer, "Repetition frequency stabilisation of passively mode-locked semiconductor lasers," Electron. Lett., vol.28, pp.1920-1921, Sep. 1992.
5. L. A. Buckman, J. B. Georges, J. Park, and D. Vassilovski, "Stabilization of millimeter-wave frequencies from passively mode-locked semiconductor lasers using an optoelectronic phase-locked loop," IEEE Photon. Tech. Lett., vol. 5, pp.1137-1140, Oct. 1993.
6. R. T. Logan Jr and E. Gertel, "Millimeter-wave photonic downconvertors: Theory and demonstrations," Proc. SPIE Conf. on Opt. Technol. for Microwave Appl. VII, vol. 2560, pp.58-69, 1995.
7. Y. Katagiri and A. Takada, "Synchronized pulse-train generation from passively mode-locked semiconductor lasers by a phase-locked loop using modulation sidebands," Electron. Lett., vol. 32, pp.1892-1893, Sep. 1996.
8. E. Hashimoto, A. Takada, and Y. Katagiri, "Synchronization of subteraherts optical pulse train from PLL-controlled colliding pulse modelocked semiconductor laser," Electron. Lett., vol. 34, pp.580-582, Mar. 1998.
9. Y. Katagiri and A. Takada, "A harmonic colliding-pulse mode-locked semiconductor laser for stable subteraherts pulse generation," IEEE Photon. Tech. Lett., vol. 9, pp.1442-1444, Nov. 1997.

Distributed Millimeter-Wave InGaAs Metal-Semiconductor-Metal Photodetector

E. Dröge [1], E. H. Böttcher [1], St. Kollakowski [1], A. Strittmatter [1], O. Reimann [2], R. Steingrüber [3], A. Umbach [3], and D. Bimberg [1]

[1] Institut für Festkörperphysik, Technische Universität Berlin, Hardenbergstr. 36, 10623 Berlin, Germany

[2] Brandenburgische Technische Universität Cottbus, Lehrstuhl Theoretische Elektrotechnik, Universitätsplatz 3-4, 03044 Cottbus, Germany

[3] Heinrich-Hertz-Institut für Nachrichtentechnik Berlin GmbH, Einsteinufer 37, 10587 Berlin, Germany

Abstract

A 78-GHz traveling-wave photodetector for the long-wavelength range has been realized by periodically distributing four InGaAs/InP metal-semiconductor-metal detectors with sub-half-micrometer feature sizes electrodes on top of an InAlGaAs-core optical waveguide.

I. Introduction

During the past few years, traveling-wave concepts have been increasingly applied to photodetectors in order to improve the bandwidth performance and/or the capability to handle high-optical power levels (1-4). Photodetectors which meet both demands are of great importance for microwave links, optical heterodyne detection, and opto-electronically generated millimeter waves and microwaves. In this context, a distributed configuration comprising several individual detector elements, the photocurrents of which are coherently superimposed, represents an attractive approach since it gives rise to an enlarged absorption volume without sacrificing the bandwidth performance. Distributed configurations with periodically arranged discrete photodetectors along a microwave transmission line have been recently realized by means of hybrid technology for operation in the long-wavelength range (5) as well as monolithically integrated devices on the GaAs/GaAlAs material system (3). A 3-dB bandwidth of about 20 and 50 GHz, respectively, has been reported.

Here, we report on the design, fabrication and characterization of InP-based monolithically integrated distributed photodetectors. The devices exhibit a 3-dB bandwidth of almost 80 GHz at 1.55-μm wavelength.

II. Design

A schematic view of the distributed metal-semiconductor-metal (MSM) detector is shown in Fig. 1. It comprises four vertically-coupled waveguide-integrated metal-semiconductor-metal (MSM) detectors (6) distributed along a coplanar strip (CPS) transmission line.

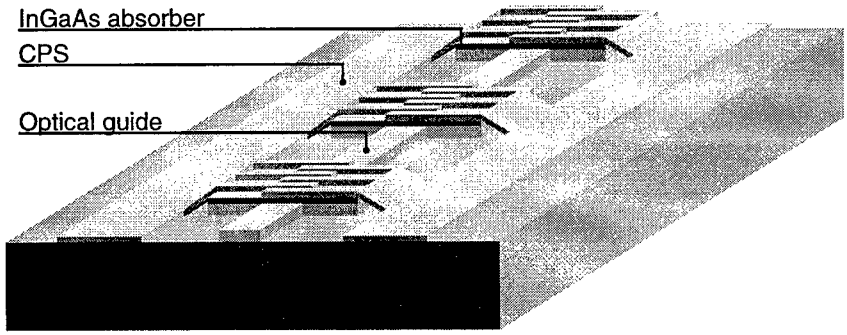

Figure 1: Schematic view of the distributed InGaAs MSM detector

0-7803-4936-9/98/$10.00

The feature size of the interdigitated electrode pattern ranges between 100 nm. and 300 nm. The devices are termed velocity-matched if the periodically arranged interdigitated MSM structures contribute exactly that amount of shunt capacitive loading to the CPS line which is required for matching the speed of the electrical wave to that of the optical one (7). The design of the coplanar slow-wave transmission line is based on a quasi static approach that has been described previously (8). The nominal characteristic impedance of the line is chosen to be 50 Ω for 0.2 and 0.3-μm electrodes and 40 Ω for 0.1-μm electrodes. The separation of the strips is 20 μm and the length of one period is about 55 μm corresponding to a total length of the distributed detector of about 220 μm.

The input end of the transmission line is open. This means that the part of photocurrent signal which travels toward the input end is fully reflected at the input. In this case, an exact velocity matching is not necessarily needed for optimizing the detector bandwidth (4). Microwave loss is more critical in this context. The simulation calculations show that it can be kept fairly low if the metallization of the conductor strips is several micrometer thick. The attenuation constant at 100 GHz, for example, is found to be 0.5 dB/mm for a metal thickness of 3 μm while it increases to 2.5 dB/mm for a metal thickness of 0.1 μm. A large metal thickness also results in a low dispersion of the phase velocity in the low frequency range. Accordingly, the variation of the phase velocity is found to be less than 2% in the frequency range from 1 GHz to 100 GHz for a metal thickness of the strips of 3 μm.

The beam propagation method (BPM) is applied to simulate the evanescent coupling from the optical waveguide to the photoabsorbing InGaAs. The modal extinction can be adjusted over a wide range by varying the Al content and the thickness of the InGaAlAs waveguide core. The devices are designed for an internal quantum efficiency of about 60 %.

III. Fabrication

The epitaxial layer sequence is grown by MOCVD and consists of a 150 nm thick InP buffer layer, a 650 nm thick $In_{0.53}Al_{0.31}Ga_{0.16}As$ core layer (λ_g=1180 nm), a 50 nm InP etch stop layer, a 145 nm thick InGaAs absorption layer, and a 50 nm thick InP cap layer. All layers are Fe-doped in order to obtain semiinsulating behavior. The interdigitated electrode structures with finger separations of 0.1, 0.2 and 0.3 μm are delineated by electron beam lithography using a two-layer resist process. The Schottky metallization consists of Pt (50 nm) and Au (50 nm) deposited by e-beam evaporation. The width and separation of the electrode fingers are nominally identical. The fingers overlap by 4.4 μm. The magnitude of the overlap exceeds the width of the optical waveguide (2 μm) in order to avoid photocarriers to be generated in a region of low electric field strength. The patterning of the mesas and the strip-type optical waveguide is performed by reactive ion etching (RIE). Details of the etching procedure have been described elsewhere (9). The metal thickness of the coplanar strips is increased to about 4 μm by means of electroplating. Simultaneously, airbridge interconnects between the coplanar line and the contact pads on the detector mesa are fabricated. The InP substrate is thinned from 350 μm to about 80 μm, order to avoid excitation of parasitic microwave modes in the substrate.

In order to permit high-performance time-domain characterization by internal electro-optical sampling, the transmission line of a certain number of devices is extended with a monolithically integrated 2.9-mm long slow-wave CPS line. Thereby, electrical reflections at the detector output are avoided. The characteristic impedance of this line, which makes use of 3 μm feature-size finger electrodes, is nominally matched to that of the distributed detector. The cross-sectional dimensions of the strips of both lines are equal. Thus, modal mismatch at the junction of the transmission lines is minimized.

IV. Device Characteristics

The static and dynamic response characteristics are measured by coupling 1.55-μm light into the 400-μm long feeding waveguide. The external quantum efficiency for optimally polarized light is found to be 7.5 %. The polarization dependence of the response is $< \pm 1$ dB. It may be chiefly attributed to the polarization-dependent fiber-to-chip coupling efficiency. Note that the external efficiency can be increased to about 10 % if an AR-coating is applied to the waveguide facet and by using a lensed fiber with smaller spot size.

Short laser pulses of about 0.65 ps FWHM at 1.55 μm wavelength are employed for characterizing the time domain response. The resulting transient voltage is measured by means of internal electro-optical sampling. A detailed description of the electro-optical sampling system will be given elsewhere (10). The signal is sampled at a distance of about 300 μm from the output end of the distributed detector. The time response of a detector with 0.2 μm finger electrodes at 3.5 V bias is shown in Fig. 2. The pulse response is characterized by a FWHM of 4.7 ps, a rise time of 3.0 ps, and a fall time of 5.0 ps.

The frequency response is obtained by Fourier transform of the pulse response shown in Fig. 2. The frequency response is then corrected for the finite duration of the laser pulses used for exciting the detector and sampling of the waveform.

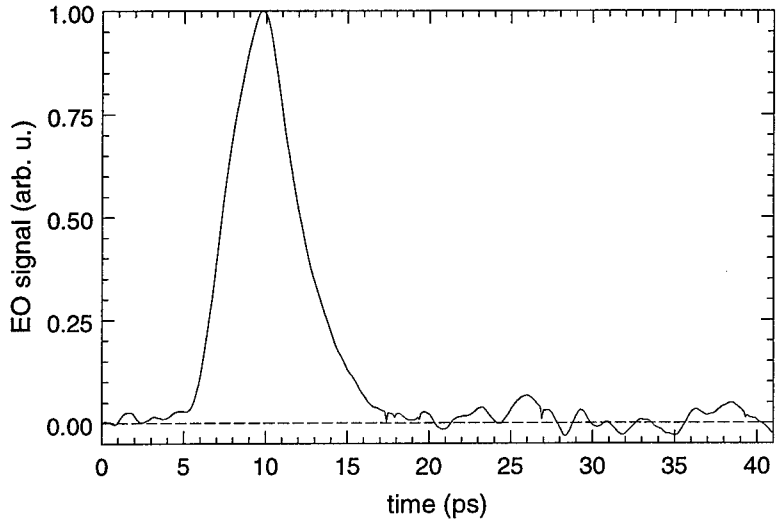

Figure 2: Pulse response at 1.55-μm light measured by electro-optical sampling.

The Fourier transforms of the measured autocorrelation traces are used for this purpose. Moreover, the finite transit time of the sampling pulse in the electro-optically active InP substrate is taken into account. Its effect on the frequency response is calculated by describing the spatial distribution of the electric field of the CPS line assuming quasi TEM behavior of the propagating signal. The corrected frequency response is shown in Fig. 3. Up to about 65 GHz the roll-off of the response is less than 1.5 dB. Then the response starts to drop fairly sharply. A 3-dB bandwidth of 78 GHz is achieved.

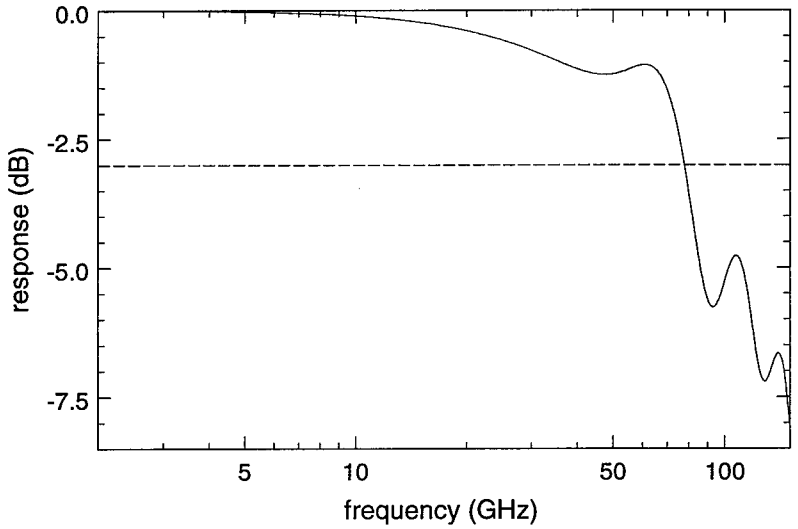

Figure 3: Corrected frequency response at 1.55-μm obtained from the pulse response shown in Fig. 2.

V. Discussion

With respect to both, bandwidth and external efficiency, the distributed detector possesses a considerable potential for further improvement. As far as the improvement of the external efficiency is concerned, the fiber-to-chip coupling efficiency can be substantially increased by integrating a spot-size transformer. Recently, we have successfully realized waveguide-integrated MSM detectors where the optical guide is fully embedded by regrown InP:Fe (11). Such a device configuration is compatible with the fabrication process of the low-loss on-chip spot-size transformers described in (12) which give rise a reduced fiber-to-chip coupling loss of about 1.5 dB.

Our recent results on the frequency response characteristics of top-illuminated InGaAs MSM detectors (13) indicate that the transit-time limited bandwidth of 0.2-μm feature size devices with 150-nm active layer thickness exceeds 150 GHz. Consequently, one can estimate the transit-time limit of vertically coupled detectors to be larger than 75 GHz. Simulation calculations show that an increase of the transit-time limited bandwidth by about a factor of two can be obtained if the dimensions of the active layer thickness and the finger electrodes are reduced simultaneously by a factor of two. As mentioned above, the distributed detector is operated with an open-circuit input termination. A considerably higher bandwidth can be obtained if the input end of the transmission line is matched. .From device modeling (7) (4), we have found that the effect of the transmission line loss on the bandwidth becomes negligibly small for a matched input in comparison to the transit-time effect as long as the device length does not exceed about 1 mm. In this case, a bandwidth close to the transit-time limit of ≥ 150 GHz is expected for devices with 80-nm active layer thickness and 100-nm feature size electrodes. The reduction of the vertical coupling efficiency due to the reduced active layer thickness can be compensated without loss to bandwidth by a corresponding increase of the device length. Our future activities will thus focus on a configuration of the distributed detector which incorporates a wide-band terminating network. Its feasibility has been recently demonstrated up to 110 GHz (14).

Very recently, an InP-based long-wavelength distributed MSM photodetector with a high external quantum efficiency has been reported. The device which makes use of a large-core optical waveguide exhibits a responsivity of 0.42 A/W and a 3 dB bandwidth of 18 GHz (15). The comparatively low bandwidth is assumed to be determined by the electrode spacing of 1.5 μm.

VI. Conclusion

A distributed millimeter-wave photodetector for the long-wavelength regime has been reported. It is based on waveguide-integrated InGaAs MSM detectors which are periodically distributed along a coplanar strip transmission line. A response time of 4.7 ps FWHM and a 3-bB bandwidth of 78 GHz at 1.55-μm light has been achieved.

VII. Acknowledgment

The authors thank D. Huhse for providing and operating the ultrashort optical pulse source, K. Schatke for her help in the epitaxial growth, A. Seeger, K. Janiak, and H.-J. Hensel for assistance in device fabrication, and G. Urmann for taking SEM pictures. This work was supported in part by the German Research Foundation (DFG) under contract number Bi 284/16-2.

References

(1) K.S. Giboney, M.J.W. Rodwell and J.E. Bowers, IEEE J. Select. Topics Quantum Electron., Vol. 2 pp. 622-629, 1996.

(2) D. Jäger and R. Kremer, IEEE MTT-S Topical Meet. on Optical Microwave Interactions, pp. 11-14, 1994.

(3) L.-Y. Lin, M.C. Wu, T. Itoh, T.H.Vang, R.E. Muller, D.L. Sivco and A.Y. Cho, IEEE Trans. Microwave Theory Tech., Vol. 45, pp. 1320-1331, 1997.

(4) E.H. Böttcher, E. Dröge and D. Bimberg, Inst. Phys. Conf. Ser. No 155: Chapter 2, pp. 55-60, 1997.

(5) C.L. Goldsmith, G.A. Magel and R.J. Baca, IEEE Trans. Microwave Theory Tech., Vol. 45, pp. 1342-1350, 1997.

(6) St. Kollakowski, E.H. Böttcher, A. Strittmatter and D. Bimberg, Electron. Lett., Vol. 36, pp. 587-588, 1998.

(7) E.H. Böttcher and D. Bimberg, Appl. Phys. Lett., Vol. 66, pp. 3648-3650, 1995.

(8) E.H. Böttcher, H. Pfitzenmaier, E. Dröge and D. Bimberg, Electron. Lett., Vol. 32, pp. 1377-1378, 1996.

(9) Ch. Lemm, St. Kollakowskit, D. Bimberg and K. Janiak, J. Electrochem. Soc., Vol. 144, L255-L257, 1997.

(10) O. Reimann, D. Huhse, E. Dröge, E.H.Böttcher and D. Bimberg, Conf. Proc. LEOS'98, accepted.

(11) St. Kollakowski, A. Strittmatter, E. Dröge, E.H. Böttcher, O. Reimann and. D. Bimberg, Appl. Phys. Lett., submitted.

(12) R. Zengerle, O. Leminger, W. Weiershausen, K. Faltin and B. Hübner, IEEE Photon. Technol. Lett., Vol. 7, pp. 532-534, 1997.

(13) E. Dröge, E.H. Böttcher, D. Bimberg, O. Reimann and R. Steingrüber, Electron. Lett., Vol. 34, pp. 1421-1422, 1998.

(14) H. Pfitzenmaier, E.H. Böttcher, E. Dröge and D. Bimberg, Conf. Proc. LEOS'97. Vol. 1, pp. 218-219, 1997.

(15) T. Chau, L. Fan, D.T.K. Tong, S. Mathai, M.C. Wu, D.L. Sivco and A.Y. Cho, Electron. Lett., Vol. 34, pp. 1422-1424, 1998.

Distributed Balanced Photodetectors for High Performance RF Photonic Links

M. S. Islam, T. Chau, A. Nespola*, A. R. Rollinger, S. Mathai, W. R. Deal, T. Itoh and M. C. Wu

UCLA, Electrical Engineering Department, 66-147D Engineering IV, 405 Hilgard Ave. Los Angeles, CA 90095-1594
Tel: (310) 825-6859, Fax: (310) 825-6954, email: wu@ee.ucla.edu
*Politecnico di Torino, Dipartimento di Elettronica, Corso Duca degli Abruzzi 24, I-100129 Torino. Italy

Balanced photodetectors are of great interest to analog fiber optic links because they can suppress laser relative intensity noise (RIN) and amplified spontaneous emission noise (ASE) from erbium-doped fiber amplifiers (EDFA) [1]. Because balanced photodetectors can achieve shot noise-limited link performance, the noise figure and spurious-free dynamic range of the link continue to be improved by increasing the power of the optical carrier. Therefore, balanced photodetectors with broad bandwidth and high saturation photocurrents are particularly important for analog fiber optic link applications. Previously, we have reported a velocity-matched distributed photodetector (VMDP) with a peak saturation photocurrent of 56 mA and a 3-dB bandwidth of 49 GHz [2]. Compared with other photodetector structures, the VMDP is more suitable for implementing the balanced photodetection since it has separate optical and microwave waveguides. Here, we demonstrate a novel distributed balanced photodetector that can achieve high saturation photocurrent and large bandwidth simultaneously. A 3-dB frequency of 16 GHz and a responsivity of 0.64 A/W have been achieved.

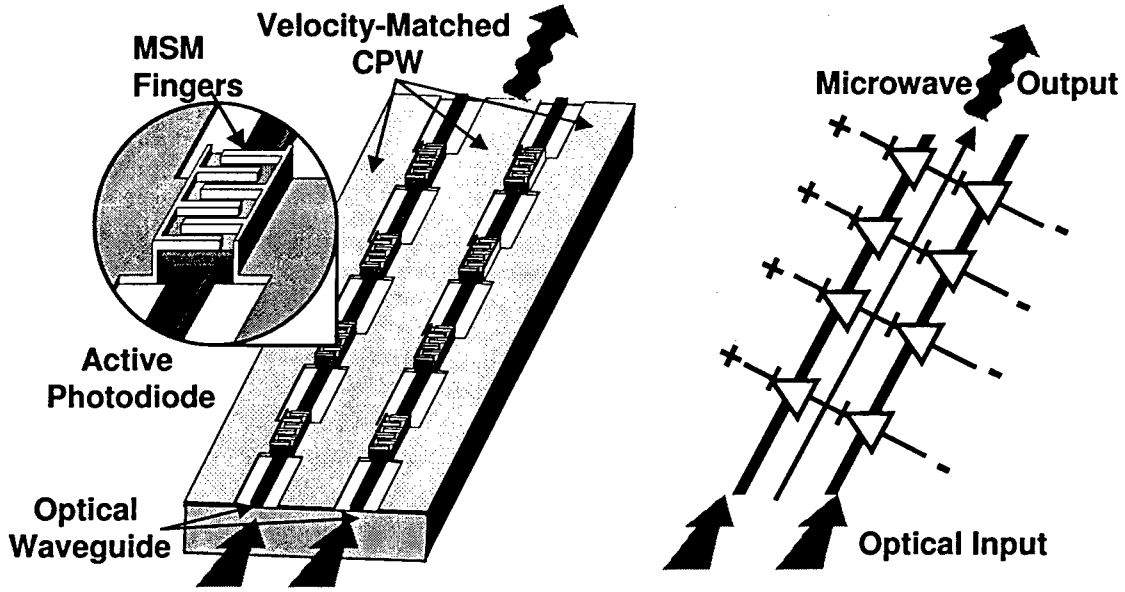

Figure 1. Schematic structure of the distributed balanced photodetector. The inset shows the active region with an MSM photodiode. Figure on the right shows the photodiodes connected to the optical waveguide in balanced detection mode.

Figure 1 shows the schematic of the balanced distributed photodetector. It consists of two input optical waveguides, two arrays of high-speed metal-semiconductor-metal (MSM) photodiodes distributed along the optical waveguides, and a 50Ω coplanar waveguide (CPW) output transmission line. Beam propagation simulation results indicate no crosstalk between the parallel optical waveguides, and the absorption per photodiode and the optical coupling loss between photodiodes are 8.8% and 3.2%, respectively. The diodes are 23 μm long and 5 μm wide. The MSM fingers are patterned by optical lithography. The central conductor of the CPW has a width of 55 μm and the separation between the central conductor and the ground conductors is 85 μm. The finger overlap of 10.5 μm is designed to provide the required capacitance loading for velocity matching. The matching ensures broadband operation. Unlike previously reported slow-wave CPW [3] that ignored the resistance of the MSM photodiode

0-7803-4936-9/98/$10.00

fingers, finite metal thickness and transmission line discontinuities in their quasi-static calculations, we used a full-wave analysis to achieve the velocity and impedance matching.

The unique advantage of the receiver is that it has monolithically integrated two high power distributed photodetectors with a velocity-matched 50Ω CPW. Most of the reported integrated balanced receivers suffer from low saturation power and are not suitable for analog links. In our design, the absorbing layer is designed to be on the top surface and evanescently coupled to a large-core passive waveguide. As the MSM photodiodes always remain below saturation by coupling only a small portion of the light from the passive waveguide, the receiver has the potential of exceeding the existing saturation photocurrents of conventional balanced photodetectors.

The dark currents of the balanced VMDP is minimized by passivating the mesa walls and placing the MSM finger tips above a silicon nitride layer [4]. The dark current of individual diode is measured to be below 0.5 nA, which is almost equal to the theoretically calculated dark current level. By coupling light directly from a lensed fiber to the waveguide facet of the receiver, the DC responsivity was measured for several different voltages and found to vary from 0.05 to 0.45 A/W as the diodes are biased from 0.5 volts to 8 volts. With anti-reflection coating, the responsivity at 8 V can be increased to 0.64 A/W.

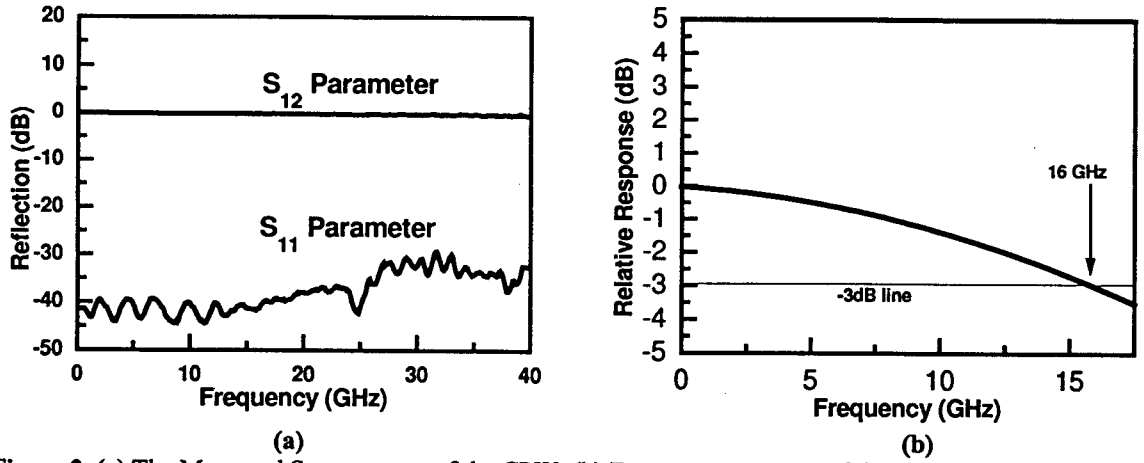

Figure 2. (a) The Measured S parameters of the CPW. (b) Frequency response of the balanced VMDP when only one waveguide is illuminated.

An HP 8510C network analyzer was used to measure the characteristic impedance and the microwave return loss (S_{11}) of the balanced receiver. Figure 2 (a) shows the S parameters of the loaded CPW. The characteristic impedance of the receiver is very well matched to 50Ω. The S_{12} is almost zero, ensuring a smooth transmission without loss. S_{11} is as low as -30 dB from DC to 40GHz. The experimental results verify the design for impedance matching.

The frequency response of the balanced VMDP was first characterized with light coupled to one waveguide only. Using optical heterodyne technique with two external cavity tunable lasers at 1.55 μm, the frequency response was measured and the 3-dB bandwidth was found to be 16 GHz. The bandwidth is currently limited by the carrier transit time of the MSM photodiodes with 1μm finger spacing. Since our bandwidth of the capacitance loaded CPW is much greater than 40 GHz (Fig. 2(a)), the bandwidth of the balanced VMDP can be increased by scaling down the MSM photodiodes. Theoretical simulation indicates that bandwidth > 100 GHz is achievable.

Figure 3 depicts the experimental setup for balanced detection. A distributed feebback laser with wavelength of 1542 nm is employed as optical source. The output is amplified by an EDFA and then filtered by an optical bandpass filter with 2 nm bandwidth. The microwave signal was modulated onto the optical carrier by an X-coupled Mach-Zehnder modulator, which produces two complimentary outputs for the balanced VMDP. The outputs were coupled to the VMDP by two single mode lensed fibers individually held by two silicon V-grooves separated by 140 μm. Since the accuracy of cutting optical fiber lengths is about 1 mm [5], a variable delay line was used to ensure equal optical path lengths between the two fibers, which is necessary to produce the broadband 180°

out-of-phase RF signals for balanced VMDP. The output from the balanced VMDP was measured using a spectrum analyzer.

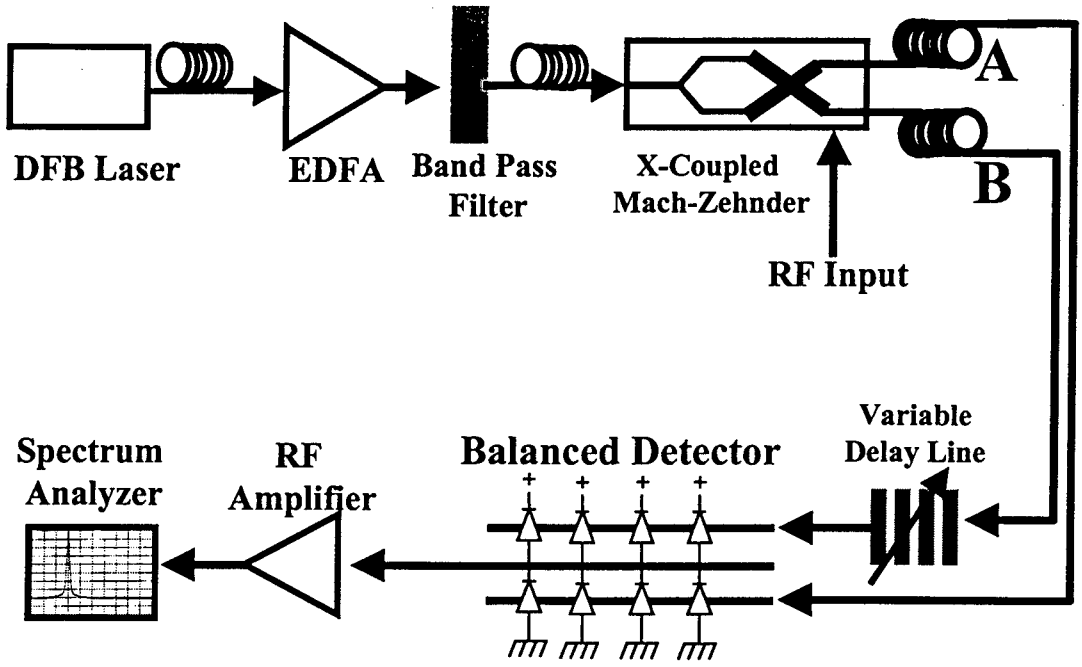

Figure 3. Balanced detection setup. The complimentary input signals are produced by the X-coupled MZ modulator.

The device was biased in balanced mode by biasing one of the ground electrodes of the CPW at 8Volts. We used a custom made probe with integrated DC-blocking capacitor on the ground that connects to the CPW ground biased at higher voltage. To verify the balanced detection, we modulated the optical input at 8GHz and tuned the fiber optic delay line from 0 to 5mm delay. Figure 4 shows the RF signal verses the delay. When the RF signals have 0° phase difference, the AC output is cancelled in balanced mode. At 180° phase difference, the RF signal is amplified, the extinction ration is more than 44dB.

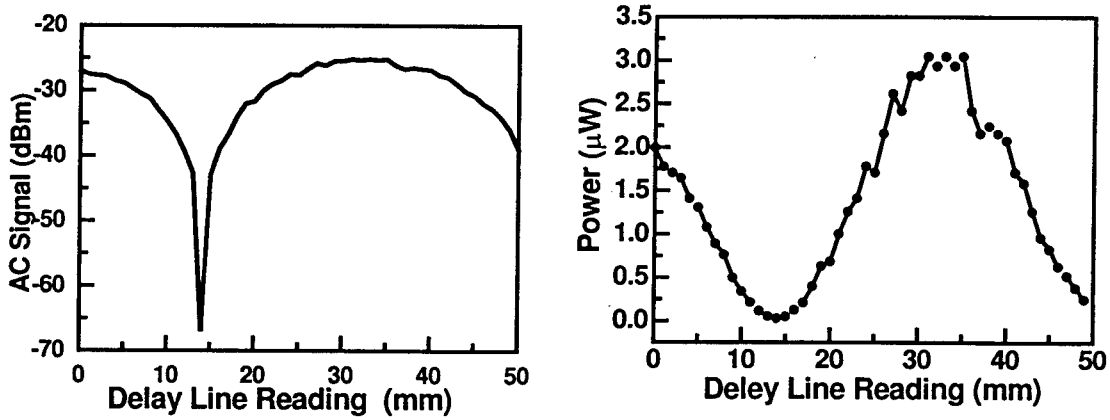

Figure 4. (a) Peak power of AC signal in balanced mode versus the delay. For RF signal at 8 GHz, the period was measured to be 38.75 mm, which is very close to the theoretical value. The power difference between 0° and 180° phase difference is more than 44-dB. (b) The same plot in linear scale.

Figure 5 shows the RF spectrum of the output from the balanced VMDP in the non-balanced (only one waveguide is illuminated) and balanced mode. Suppression of the noise floor by 12-dB has been observed in the balanced mode over a wide frequency range from 6 to 15 GHz. The signal is also enhanced by 6-dB. Typical balance between the VMDP was within 2% of the total photocurrent reading, which was limited to 2 mA in our preliminary experiments. For bandwidths lower than 6 GHz, the fiber length for one RF period is longer than 5 mm, the maximum delay length in our current setup. We are currently working on a new setup with two fiber delay lines to achieve exactly equal optical path lengths for broad band operation without any tuning of the delay line. This will allow us to measure the AC responsivity of the device in balanced mode.

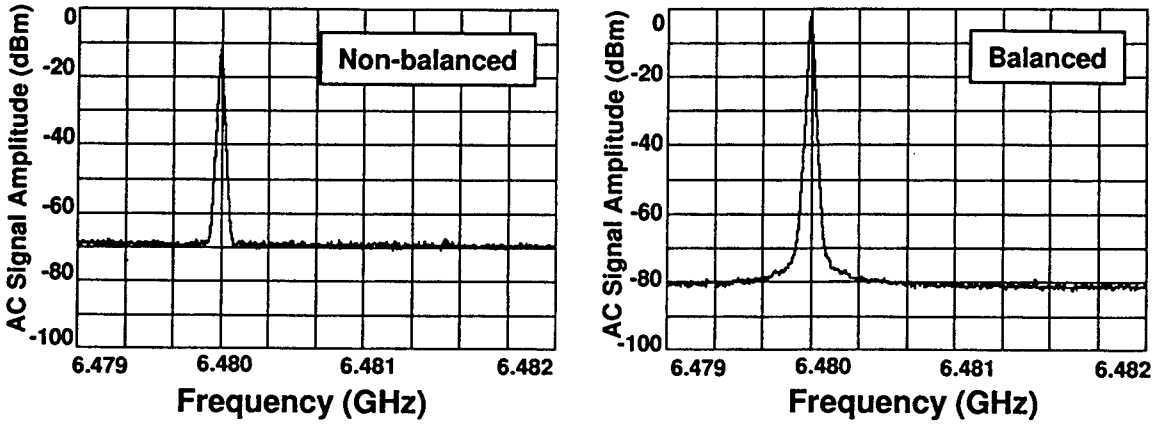

Figure 5. The AC signal in non-balanced (a) and balanced (b) detection modes are plotted separately. The balanced output is almost 6-dB higher in amplitude than the non-balanced signal. Preliminary results show a noise suppression level greater than 12-dB.

In conclusion, a balanced velocity-matched distributed photodetector (VMDP) with both impedance and velocity matching has been designed and successfully fabricated. Preliminary experimental results shows that the relative intensity noise has been suppressed by 12-dB, and the signal has been enhanced by 6-dB. This was the first integration of high power and high speed balanced detectors with a slow microwave transmission line to be used in high performance RF photonic links.

Acknowledgment

This project is supported in part by ONR MURI on RF Photonics, National Radio Astronomy Observatory, JESP and UC MICRO.

Reference:

[1] L. T. Nichols, K. J. Williams, R. D. Esman, "Optically amplified down converting link with shot-noise limited performance,"*IEEE Transaction on Microwave Theory and Techniques*, vol. 45, no. 8, pp. 1384 -1389, 1997.

[2] L. Y. Lin, M. C. Wu, T. Itoh, T. A. Vang, R. E. Muller, D. L. Sivco, and A. Y. Cho, "Velocity-matched distributed photodetectors with high-saturation power and large bandwidth," *IEEE Photon. Technol. Lett.*, vol. 8, no. 10, pp. 1376 - 1378, 1996.

[3] E. H. Bottcher, H. Pfitzenmaier, E. Droge and D. Bimberg, "Millimeter-wave coplanar waveguide slow wave transmission lines on InP," *Electronics Letters*, Vol. 32, no. 15, pp. 1377 - 1378, 1996.

[4] W. A. Wohlmuth, P. Fay, I. Adesida, "Dark current suppression in GaAs Metal-Semiconductor-Metal photodetectors," *IEEE Photon. Technol. Lett.*, vol. 8, no. 8, pp. 1061 - 1064, 1996.

[5] S. Narimatsu, N. Takachio, Y. Inoue, M. Hosoya, H. Tsunessugu and S. Hata, "An Optical 90° Hybrid Balanced Receiver Module Using a Planar Lightwave Circuit", *IEEE Photon. Technol. Lett.*, vol. 8, no. 6, pp. 737-740, 1994.

1.55 μm ABSORPTION, HIGH SPEED, HIGH SATURATION POWER, P-I-N PHOTODETECTOR USING LOW-TEMPERATURE GROWN GaAs

Yi-Jen Chiu, Sheng Z. Zhang, Siegfried B. Fleischer, John E. Bowers
and Umesh K. Mishra
Electrical and Computer Engineering Department, University of California at Santa Barbara, Santa Barbara, CA 93117
Tel:(805)893-8081 Fax:(805)893-3262, Email: chiu@opto.ece.ucsb.edu

Abstract

By utilizing low-temperature grown GaAs (LT-GaAs) as the absorption material, subbandgap detection is possible due to mid gap defects and As precipitates. In this paper, the authors demonstrate the first 1.55 μm photodetector in GaAs based material. Due to the short carrier trapping time, a bandwidth of over 20 GHz and a saturation power exceeding 10 mW are measured in this photodetector.

Introduction

AlGaAs/GaAs is a well developed material and these photodetectors have been widely used in high performance integrated circuits, however, the high bandgap characteristics (E_g =1.42 eV, λ< 0.78 μm) limit the application to datacom communication only. For telecom communications(1.3~1.6 μm), the detectors are still fabricated and designed in Ge-, GaInAsP- or InP-based materials. Recently, it was shown that low-temperature grown GaAs (LT-GaAs) can absorb light below bandgap (1~1.6 μm) due to mid gap defects or As precipitates [1~4] and also the sub-picosecond carrier trapping time at 1.56μm excitation was observed[5]. Thus, it is possible to open up the integration of high speed receivers with GaAs electronics not only for short wavelength (~0.8 μm) but also for long wavelength (1.3~1.6 μm) systems. By using LT-GaAs, such photodetectors [6.7] with bandwidths above 500 GHz were demonstrated at wavelengths shorter than 0.82 μm. However, no high speed performance has been measured at the long wavelength regime. In this paper, we show the first 1.55μm LT-GaAs p-i-n photodetectors with high bandwidth and high saturation power performance.

Fabrication and experiment

A waveguide photodetector (WGPD) was designed and fabricated. The schematic diagram of the coupling edge is shown in Figure 1 (top). A p-i-n heterostructure (bottom of Fig. 1) forms the optical waveguide. All the material was grown in an MBE system. The active region is grown by LT-GaAs which is deposited at 215°C with As_2/Ga equivalent beam pressure ratio of 12 and subsequently *in-situ* annealed at 590°C for 10 minutes. The bottom $Al_{0.5}Ga_{0.5}As$ layer is used for the optical isolation from the bulk GaAs substrate. We used the same technique as our previous work [7] to process the standard p-i-n photodetector (including metalization, lithography, etching).

An optical component analyzer (HP 8703A, 0.13 ~ 20 GHz) was used for measuring the frequency response. The external light source was a 1.55 μm laser diode. Before coupling to the WGPD, the

0-7803-4936-9/98/$10.00

modulated light was amplified by an EDFA and filtered by an optical filter centered at 1.55 μm. The generated microwave signal was collected by a microwave probe.

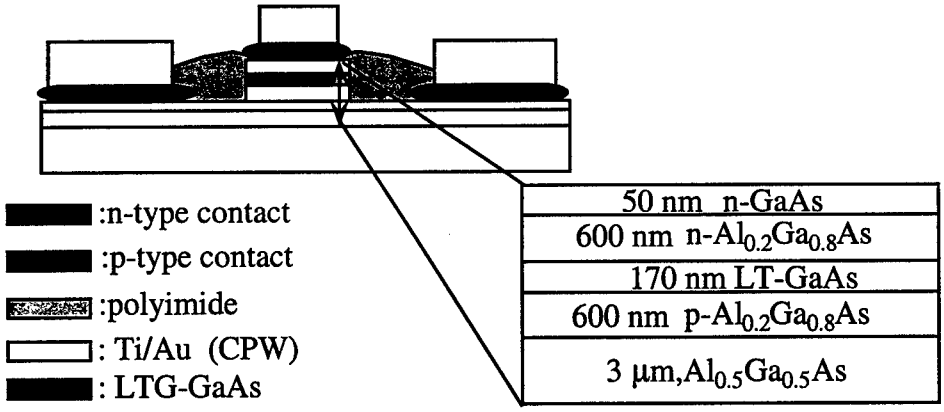

Fig. 1 (Top) the facet view of p-i-n photodetector,(bottom) the material growth structure.

Result and discussion

Two photodetectors (denoted A and B) with different lengths were fabricated and characterized. As shown in Fig.2, photodetector A (2μm wide and 35μm long) exhibits a flat frequency response within 2dB from D.C. to 20GHz. The response showed the same frequency dependence for various optical excitation powers ranging from 0.75 to 11 mW. And also, the quadratic relation (insert of Fig.2) between microwave and optical power indicates the photocurrent has linear dependence on optical power up to 20GHz. In the D.C. measurement, as shown in Fig.3, the optical power dependent photocurrent at different optical wavelengths (0.82 μm and 1.54 μm) shows a quite different saturation properties. The long wavelength shows linear detection, but the short wavelength one easily turns out to be saturated after 500 μW. However, low external quantum efficiency of 0.1% was measured. The reasons for this low efficiency are the low absorption coefficient combined with the short device length. To improve the efficiency, photodetector B (2μm wide and 300μm long) was fabricated. A quantum efficiency of 1% was obtained due to longer device (the internal quantum efficiency will be around 3% after extracting the coupling loss). The frequency response and the theoretical expectation (solid curve) are shown in Fig.4. The dependence of the frequency response on the excitation power shows ~4dB rolloff at 20GHz. It is very important to note that there are no power saturation effect up to 11 mW. The measured microwave loss is around 3.5 dB at 20GHz. Therefore, in such a long device, the microwave loss is responsible for the bandwidth limit.

It is essential to understand the limit in performance of these devices. We used a distributed photocurrent model to fit the frequency response (solid curve of Fig.4). The distributed photogenerated charge is excited as light travels through the waveguide, where the model includes the velocity mismatching between the optical wave and microwave, the carrier trapping time in LT-GaAs and microwave loss and boundary reflection of the input and output ends. The response shows little dependence on the carrier trapping times for values from 100 fs to 1 ps. It reveals that the major factor affecting the bandwidth is not the trapping time. The measured microwave loss has a 3.5 dB drop up to 20GHz and the velocity mismatch factor ($v_{optical}/v_{microwave}$) is ~2. The loss and velocity mismatch are responsible for the limited bandwidth.

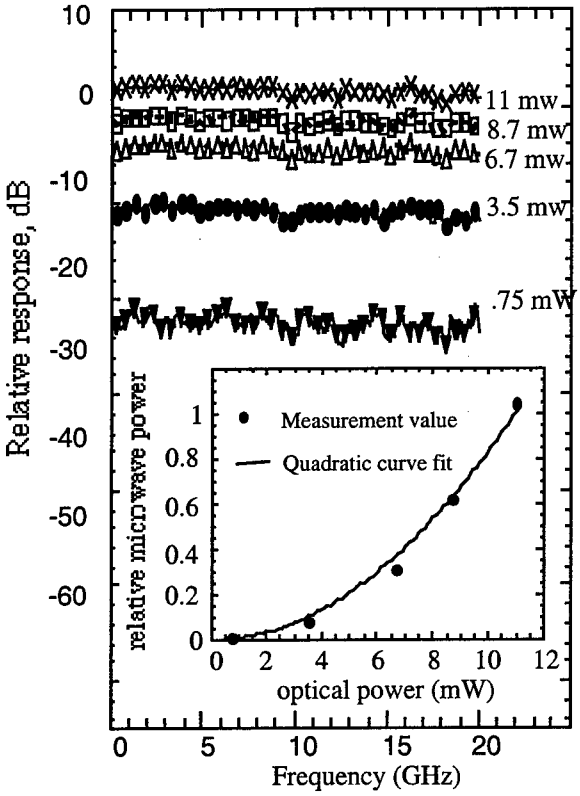

Fig. 2 Frequency response of photodetector A (30 μm long). The insert shows the quadratic relation between the microwave power and optical power.

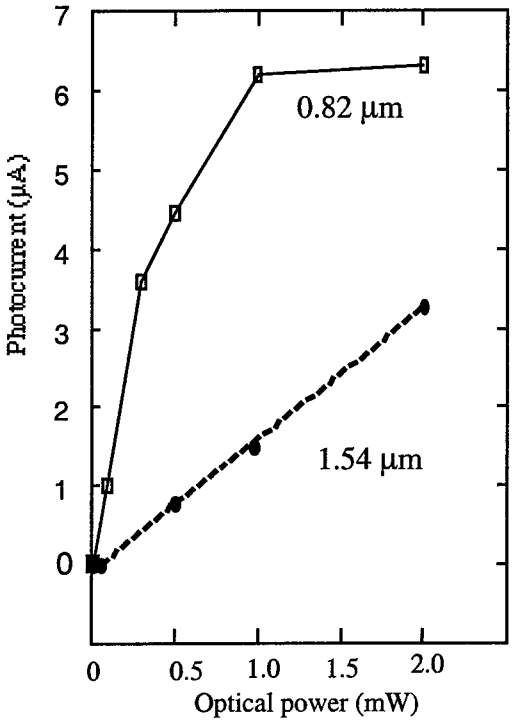

Fig. 3 D.C. photocurrent response of photodetector A (30 μm long) with different optical power at 0.82 and 1.54 μm optical wavelengths. The long wavelength detection shows a much higher saturation power.

Summary

In summary, we have successfully fabricated a novel GaAs-based p-i-n photodetector operating at 1.55 μm. The high speed (above 20 GHz) and high saturation power (above 10 mW) characteristics show that this kind of photodetector has potential application in the fields of long-wavelength-optical-fiber communication and for integration with GaAs integrated circuits.

Acknowledgments

The authors would like to thank AFOSR/PRET and DARPA Ultraphotonics projects for supporting this research.

Reference

[1]A. Srinivasan, K. Sadra, J.C. Campbell, and B.G. Streetman, "Influence of growth temperatures on the photoresponse of low temperature grown GaAs:As p-i-n diodes".,*J. of Electronic Materials*, Vol.22, no.12, pp.1457-1459, 1993

[2]A. C. Warren, J.H. Burroughes, J. M. Woodall, D.T. McInturff, R.T. Hodgson and M. R. Melloch , "1.3 μm p-i-n photodetector using GaAs with As precipitates (GaAs:As)" *IEEE Electron Device Lett.* Vol. 12, No.10 , pp. 527-529 1991.

[3]D.C. Look, "On compensation and conductivity models for molecular beam epitaxial GaAs grown at low temperature," *Journal of Applied Physics*, 1991, **70**, pp3148-51

[4]A.C. Warren, J.M. Woodall, J.L. Freeouf, D. Grischkowsky, D.T. McInturff, M.R. Melloch, and N. Otsuka ,"Arsenic precipitates and the semi-insulating properties of GaAs buffer layers grown by low-temperature molecular beam epitaxy," *Appl. Phys. Lett* 1990, **57**, pp1331-3

[5]P. Grenier and J.F. Whitaker,"Subband gap carrier dynamics in low-temperature-grown GaAs", *Appl. Phys. Lett.* Vol.70 (15), 14 April. 1997.

[6]S.Y. Chou, M.Y.Liu,"Nanoscale tera-hertz metal-semiconductor-metal photodetectors", *IEEE J. Quantum Electron*,Vol.28 No. 10, pp.2358-2368, October 1992.

[7]Y.J. Chiu, S.B. Fleischer, J.E. Bowers,"High-speed low-temperature-grown GaAs p-I-n Traveling-Wave photodetector, IEEE Photo. Technol. Lett, vol.10, no.7, pp1012-1014, July 1998.

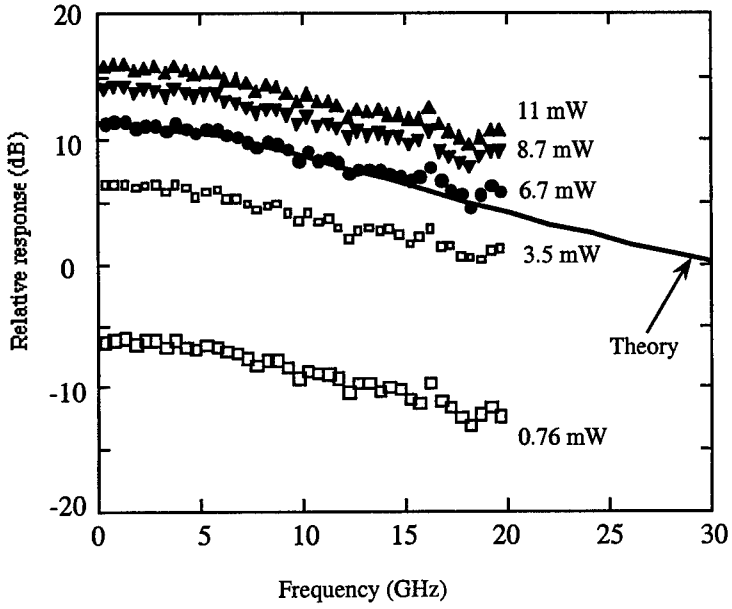

Fig. 4 Photodetector B (300 μm long) frequency response with the calculation (solid curve)

Large-Signal Compression Measurements in High-Current p-i-n Photodiodes with +11 to +20 dBm Output Microwave Power

Keith J. Williams and Ronald D. Esman
Naval Research Laboratory, Code 5670, Washington, DC 20375, USA
TEL: (202) 767-9360 FAX: (202) 404-8645 e-mail: keith.williams@nrl.navy.mil

Abstract: **We present comparisons between the small- and large-signal compression measurements for surface-illuminated p-i-n microwave photodetectors. The measured RF power provided by the photodiodes was +12, +17 and +20 dBm for bandwidths of 25, 3, and 1 GHz, respectively.**

Increasing the dynamic range and reducing the loss and noise figure of microwave externally-modulated photonic links can be realized with the use of high-current photodetectors (PDs). Increasing the output photocurrent also increases the PD output RF signal level which is particularly important in optically-steered phased array antennas since any increase in PD output signal level reduces the necessary phase- and amplitude-matched electronic gain at each antenna element. In an effort to increase the output photocurrent, a number of groups have been studying surface-illuminated (1-5), waveguide (6,7), and traveling-wave (8,9) structures as well as PD arrays (10,11). This paper compares the small- and large-signal compression characteristics in surface-illuminated p-i-n PDs.

A descriptive quantity used to characterize high-current PDs is the 1-dB small-signal compression current, $I_{1\text{-}dB,ss}$. $I_{1\text{-}dB,ss}$ has been defined (2) as the average dc photocurrent at which the RF responsivity decreases by 1 dB given that the modulation depth, m, is small (m<0.05). The RF photoresponse decreases at high average illumination levels due to space-charge screening (1). To quantify the change in RF response versus average current, measurements are performed by illuminating the PD with a small amount of RF-modulated light and adding a variable amount of unmodulated light. Measurements of $I_{1\text{-}dB,ss}$ for a 3 GHz p-side illuminated p-i-n (5), denoted PD1, and a 25 GHz n-side illuminated p-i-n, denoted PD2 (similar to those in (12), except with a 0.5-μm long intrinsic region), are shown in figure 1. Note that PD1 shows typical (1) space-charge limited behavior, with higher frequencies displaying lower $I_{1\text{-}dB,ss}$.

For large-signal operation (m~1.00) at low frequencies (low compared to 1/transit time), it is the peak current which causes the electric field collapse and, hence, compression. Thus it is expected that $I_{1\text{-}dB,ss}$ for PD1 will be approximately a factor of two larger than the large-signal 1-dB compression point, $I_{1\text{-}dB,LS}$, although, $I_{1\text{-}dB,LS}$ may be slightly higher owing to compression of only the peak portion of the sine wave. To measure $I_{1\text{-}dB,LS}$, PD1 is illuminated with a 1319-nm Nd:YAG heterodyne system (m~1.00). The frequency response at various average currents is shown in figure 2. Frequency dependent compression is exhibited since the 3 dB increase

0-7803-4936-9/98/$10.00

from 0.1 to 3 GHz at low currents decreases to 0.5 dB at 45 mA. The output microwave power generated from PD1 is seen to be +17 dBm from 0 to 3 GHz at 45 mA average current. The combined output from two 3 GHz p-i-n devices is also plotted in figure 2 at 65 mA total average current where, for a 50% decrease in bandwidth (due to the added capacitance), +20 dBm can be extracted.

To assess $I_{1\text{-}dB,LS}$, the data in figure 2 is plotted at a fixed frequency versus average current. The largest compression occurs at 3 GHz which is plotted in figure 3. Observe that $I_{1\text{-}dB,LS}$ is 26 mA (or equivalently 52 mA peak current) yielding an output 1-dB compression point, $P_{1\text{-}dB}$, of +14 dBm and a saturated output power, P_{sat}, of greater than +17 dBm. $I_{1\text{-}dB,LS}$ is nearly a factor of four higher than $I_{1\text{-}dB,ss}$ (fig. 1), which is twice the expected value if space-charge were assumed to be the only compression mechanism. At 2 GHz, $I_{1\text{-}dB,LS}$ is 42 mA ($P_{1\text{-}dB}$ = +17 dBm), and at 1 GHz, the large-signal response is only compressed 0.4 dB at 45 mA. Here again, $I_{1\text{-}dB,LS}$ is about a factor of two higher than small-signal measurements would indicate from the discussion above. This discrepancy is believed to be due to quantum efficiency nonlinearities (13) since the dc quantum efficiency of PD1 decreases as the average current increases (ref 13, PD4). Any reduction in dc and RF quantum efficiency would cause the small-signal RF response to decrease. The expected factor of two difference between small- and large-signal compression measurements results only from space-charge considerations and thus only partially explains the compression behavior. To accurately compare the two measurements, quantum efficiency nonlinearities need to be included.

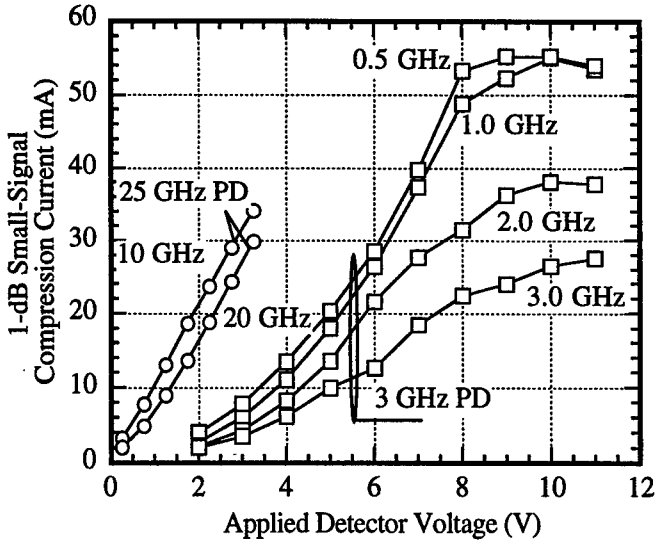

Figure 1: Measured small-signal compression current for a 3 GHz and a 25 GHz p-i-n photodetector. The test frequencies for the 3 GHz PD are 0.5, 1, 2, and 3 GHz and for the 25 GHz PD are 10 and 20 GHz.

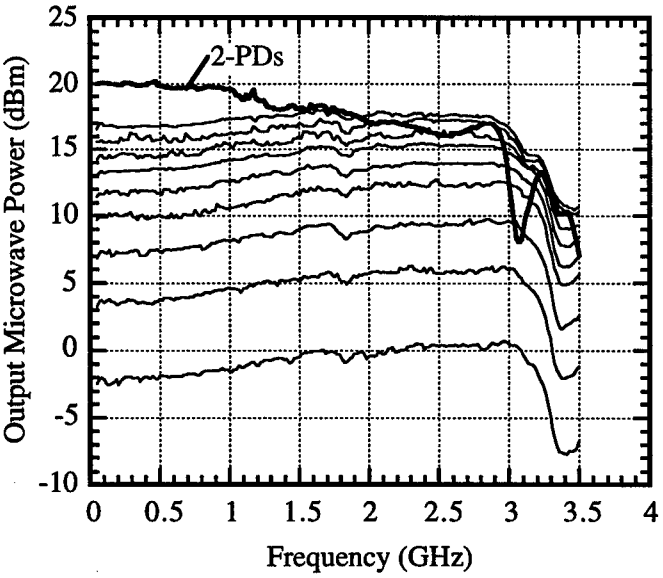

Figure 2: Measured large-signal output signal from PD1 for average photocurrents of (bottom to top) 5, 10, 15, 20, 25, 30, 35, 40, and 45 mA and for PD1 plus another similar device in parallel at 65 mA.

For higher frequency operation PD2 is used, as it maintains a bandwidth greater than 20 GHz while detecting over 30 mA at 3.25 V bias (fig. 1). Large-signal frequency response measurements for PD2 (fig. 4) show that over +12 dBm output power from 0.05 to 20.5 GHz at 25 mA average current is obtained. For PD2, $I_{1\text{-}dB,LS}$ at 10, 15, 20 and 25 GHz is deduced from figure 4 to be 25, 20, 17.5, and 19 mA, respectively. Comparisons between $I_{1\text{-}dB,LS}$ (doubled) and $I_{1\text{-}dB,ss}$ are much closer in PD2 than PD1 since the quantum efficiency of PD2 does not decrease at higher currents. Rather, the quantum efficiency of PD2 increases 0.45 dB at 25 mA (12) due to additional photocurrent from the p-region at high currents. Thus, $I_{1\text{-}dB,ss}$ for PD2 would be slightly lower when accounting for quantum efficiency nonlinearities.

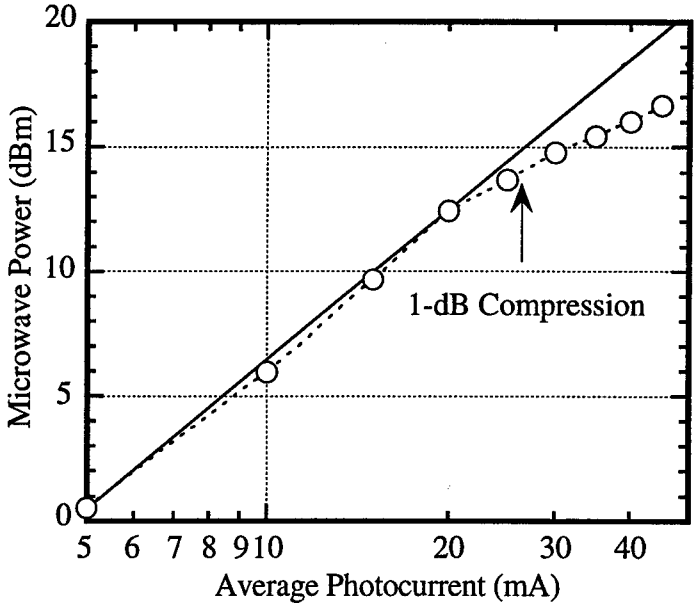

Figure 3: Measured 1-dB large-signal compression current for PD1 at 3 GHz. The solid line represents a linear response. The bias voltage is 10V.

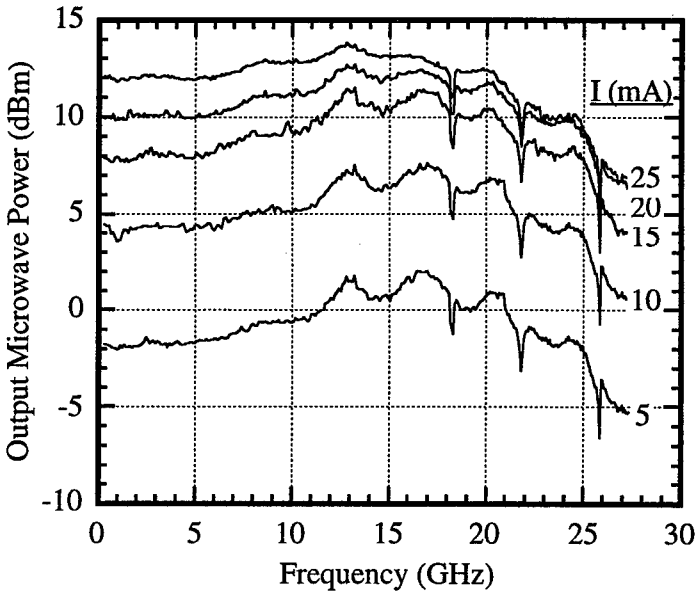

Figure 4: Measured large-signal output signal from PD2 for average photocurrents of 5, 10, 15, 20, and 25 mA. The modulation depth is 100% and the bias voltage is 4V.

Considerations for the voltage drop across the 50Ω load must also be made when comparing the small- and large-single data of high speed PDs. For PD1, a 2 V (50Ω load x 40mA photocurrent) drop only marginally affects $I_{1\text{-}dB,ss}$ since it is relatively insensitive to bias voltage variations above 8 V. However, for PD2, a 1.25 V voltage drop (at 25 mA) can cause a larger fractional change in both the applied bias and $I_{1\text{-}dB,ss}$, thus making direct comparisons between large- and small-signal measurements difficult. This becomes important when extrapolating to higher-frequency PDs since they tend to operate at lower bias voltages.

In conclusion, we have made comparisons between the large-and small-signal compression currents in microwave photodetectors. Large- and small-signal compression measurements are consistent when quantum efficiency nonlinearities are accounted for. The large-signal 1-dB com-

pression currents (1-dB output RF power compression points) obtained were greater than 75 mA (+20 dBm), 42 mA (+17 dBm), 26 mA (+14 dBm), 25 mA (+12 dBm), and 17.5 mA (+11 dBm) at frequencies of 1, 2, 3, 10, and 20 GHz, respectively.

Acknowledgement

The authors would like to thank R. Wilson and J. Kulick at AMP for supplying photodetectors. This research was supported by the Office of Naval Research.

References

(1) K.J. Williams, R.D. Esman, and M. Dagenais, "Effects of High Space-Charge Fields on the Response of Microwave Photodetectors," *IEEE Photonics Tech. Lett.*, vol. 6, no. 5, pp. 639, 1994.

(2) G.A. Davis, R.E. Weiss, R.A. LaRue, K.J. Williams and R.D. Esman, "A 920-1650 nm High-Current Photodetector," *IEEE Photon. Tech. Lett.*, **PTL-8**, pp. 1373-1375, 1996.

(3) J. Paslaski, P.C. Chen, J.S. Chen, C.M. Gee, and N. Bar-Chaim, "High-Power Microwave Photodiode for Improving Performance of RF Fiber Optic Links," *Proc. SPIE, Photonics and Radio Frequency,* Vol. 2844, 1996 Denver CO, pp. 110-119.

(4) N. Shimizu, N. Watanabe, T. Furuta, and T. Ishibashi, "InP-InGaAs Uni-Traveling-Carrier Photodiode With Improved 3-dB Bandwidth of Over 150 GHz," *IEEE Photon. Tech. Lett.*, vol. 10, no. 3, pp. 412-414, 1998.

(5) K.J. Williams, R.D. Esman, R.B. Wilson, and J.D. Kulick, "Differences in p-side and n-side Illuminated p-i-n Photodiode Nonlinearities," *IEEE Photon. Tech. Lett.*, vol. 10, no. 1, pp. 132-135, 1998.

(6) A.R. Williams, A.L. Kellner, and P.K.L. Yu, "High Frequency Saturation Measurements of an InGaAs/InP Waveguide Photodetector," *Electronics Lett.*, vol. 29, no. 14, pp. 1298-1299, 1993.

(7) S. Jasmin, N. Vodjdani, J-C. Renaud, and A. Enard, "Diluted- and Distributed-Absorption Microwave Waveguide Photodiodes for High Efficiency and High Power," *IEEE Trans. Microwave Theory and Tech.*, vol. 45, no. 8, pp. 1337-1341, 1997.

(8) V.M. Hietala, G.A. Vawter, T.M. Brennan, and B.E. Hammons, "Traveling-Wave Photodetectors for High-Power, Large-Bandwidth Applications," *IEEE Trans. Microwave Theory and Tech.*, vol. 43, no. 9, pp. 2291-2298, 1995.

(9) K.S. Giboney, M.J.W. Rodwell, and J.E. Bowers, "Traveling-Wave Photodetector Design and Measurements," *IEEE J. of Selected Topics in Quantum Electronics*, vol. 2, no. 3, pp. 622, 1996.

(10) L.Y. Lin, M.C. Wu, T. Itoh, T.A. Vang, R.E. Muller, D.L. Sivco, and A.Y. Cho, "High-Power High-Speed Photodetectors—Design, Analysis, and Experimental Demonstration," *IEEE Trans. Microwave Theory and Tech.*, vol. 45, no. 8, pp. 1320-1331, 1997.

(11) C.L. Goldsmith, G.A. Magel, B.M. Kanack, and R.J. Baca, "Principles and Performance of Traveling-Wave Photodetector Arrays," *IEEE Trans. Microwave Theory and Tech.*, vol. 45, no. 8, pp. 1342-1350, 1997.

(12) P. Hill, *et al.*,, "Measurement of Hole Velocity in n-Type InGaAs," *Appl. Physics Lett.*, **50**, p. 1260, 1987.

(13) K.J. Williams and R.D. Esman, "Photodiode DC and Microwave Nonlinearity at High Currents Due to Carrier Recombination Nonlinearities," *IEEE Photonics Tech. Lett.*, vol. 10, no. 7, pp. 1015-1017, 1998.

12dB CURRENT MODULATION BY 1.55μm LIGHT IRRADIATION IN INTEGRATED OPTICALLY CONTROLLED HEMT

Kazuhiko Shimomura Takayuki Sakai and Yuichi Nitta

Department of Electrical and Electronics Engineering, Sophia University
7-1 Kioi-cho, Chiyoda-ku, Tokyo 102-8554, Japan
Tel +81-3-3238-3422 Fax +81-3-3238-3321
E-mail: shimo@shige.ee.sophia.ac.jp

I. Introduction

High-speed photoreceiver that converts optical signal directly to microwave signal is a key component to realize fiber optic microwave transmission systems. We have demonstrated an integrated type optically controlled field-effect transistors (FETs) for such a system.[1-4] This device has the FET region and the light absorption region, and these two regions are monolithically integrated. The light absorption region is the gate of the FET and it is controlled by input light power. The structural merits of this device are the following: the operational speed of the device has no limitation of the diffusion time of the photo generated carriers and the speed can be increased up to 60GHz[1], and furthermore it can be obtained high optical-to-electrical conversion efficiency by the electric field modulation of the gate in the FET caused by the drift of photogenerated carrier.[3,4] In the last report, we have demonstrated the integrated optically controlled FET that was the GaAs FET region and GaInAs/InP light absorption region which were directly-bonded [3]. To obtain the high optical-to-electrical conversion efficiency and to increase the speed of the device, it is efficient to use the high transconductance material for the channel of FET. Hence we applied the HEMT structure using the two-dimensional electron gas for the FET region to achieve the high transconductance of FET and high optical response characteristics. In this paper, we show the structure of the device, and the improvements of the optical characteristics of the device such as current on/off ratio and responsivity of the device.

II. Device Structure and Fabrication Process

The structure of this device is shown in Fig.1. This device consisted of two parts. The upper part was the light absorption region and the lower was the FET region. The absorption region was composed of GaInAs/InP materials and the FET region was the AlGaAs/GaAs HEMT structure in place of GaAs MESFET structure [3]. This device had four electrodes that were gate and n-electrode at the absorption region, and the drain, source at the FET region. The two electrodes at the absorption region were used to separate the photo-generated carriers and to pull out from the external bias.

The operation of this device is as follows. When laser light with a long wavelength is absorbed in the absorption region, the light energy generates pairs of electrons and holes. These electrons and holes drift towards the n-layer and the p-layer of the p-i-n photodiode due to the electric field that is generated by the applied gate voltage. Then, the electric field of the gate voltage is reduced by a photogenerated electric field of electrons and holes. Due to the original electric field change, the applied voltage for the HEMT channel increases. The drain-to-source current is modulated as a result of gate voltage control by the illumination of light.

0-7803-4936-9/98/$10.00

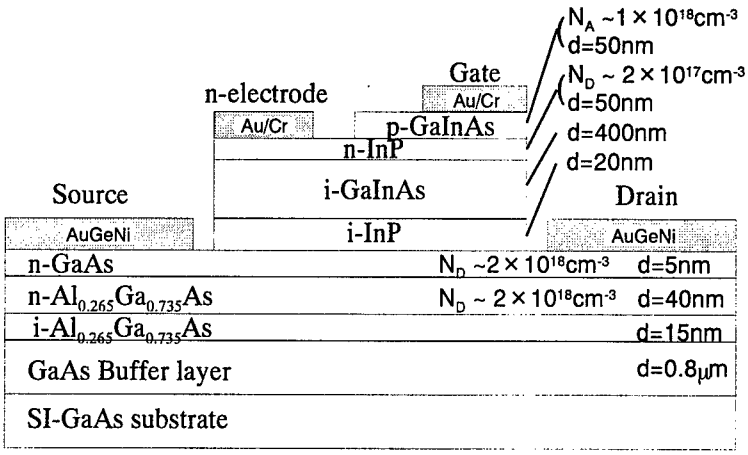

Fig. 1. Device Structure.

In this device, the operation speed was limited by the RC time constant and the drift speed of the photogenerated carriers in the absorption region, and the cut-off frequency of the FET channel. If the gate length and p-n junction area are assumed to be 1 μm × 200 μm, the drift speed of the photogenerated carriers limits the device speed, and we can estimate about 70 GHz cut-off frequency.

The fabrication process of this device is as follows. At first, HEMT that has a channel length of 20 μm and a channel width of 170 μm was fabricated. The absorption region was then directly bonded on to the HEMT. The direct bonding procedure can be summarized as follows: The InP and GaAs surfaces were treated with a H_2SO_4:H_2O_2:H_2O solution and were then rinsed in deionized water. The wafers were brought into contact just after they had finished drying. The wafers adhered to each other, although weakly, even at room temperature. This adhesion is believed to be the result of the hydrogen bonding between the OH groups that were absorbed on to the wafers' surfaces during pretreatment. They were then loaded into an annealing furnace and heated at 620℃ in a H_2 atmosphere for 30min. In the previous paper, we measured the bonding temperature dependence on the electrical and optical characteristics of the device [3]. In that experiment, the bonding temperature of 620℃ had no degradation for the performance of the device. Then the bonded substrate of the absorption region was lapped to a thickness of about 20 μm for the shaping of the absorption region. After lapping, SiO_2 film was deposited on the absorption region. Then the absorption region was patterned and etched as a mesa structure by wet chemical etching. After the etching of the absorption region, the SiO_2 film was etched in order to make electrode. Finally, the drain and the source electrodes and the n-electrode of the absorption region were formed as an ohmic contact by AuGeNi, and the p-electrode of the absorption region was formed as an ohmic contact by AuCr.

III. Experimental Results

The characteristics of optically controlled HEMT were measured by applying gate voltage V_{GS} to the absorption region and by applying drain voltage V_{DS} to the HEMT region. The optical characteristic of the device was measured using a semiconductor laser light with a wavelength of 1.55 μm, which was coupled to a single-mode optical fiber. The light from the end of the fiber was irradiated directly on to the device. Light input power P_{in} was equal to the output power from the

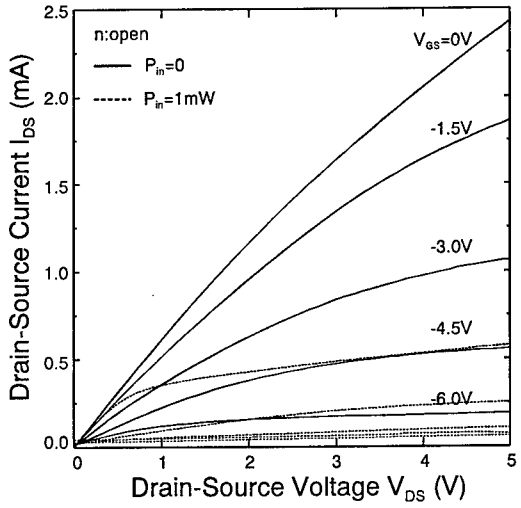

Fig. 2. I_{DS}-V_{DS} characteristics.

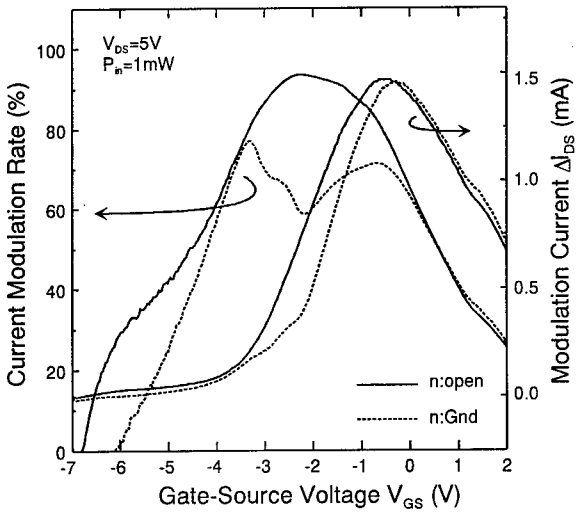

Fig. 3. Relation between Current Modulation and V_{GS}

optical fiber. Typical current-voltage characteristics were obtained when the gate voltage V_{GS} was applied to the absorption region as shown in the Fig.2 of solid line. On the other hand, when the light was irradiated to the device, the current was decreased significantly as shown in the dashed line. The decrease of the drain current was due to the increase of the field of channel region. And this was caused by the reduction of the applied voltage to the absorption region because of the field screening by the photogenerated carriers.

Figure 3 shows the relation between the current modulation and applied voltage to the absorption region V_{GS}. The modulation current is the current difference between with and without irradiated light power that is defined as $\Delta I_{DS}=I_{DS}(P_{in}=0)-I_{DS}(P_{in})$, and the current modulation rate is defined as $[I_{DS}(P_{in}=0)-I_{DS}(P_{in})]/ I_{DS}(P_{in}=0)$. The maximum current modulation rate over 90% was obtained when the V_{GS}=-2.3V, and this voltage corresponded to the voltage where the maximum transconductance of FET was obtained.

Figure 4 shows the ralation between on/off ratio and P_{in} under the V_{GS}=-2.3V. The on/off ratio was calculated from the ratio of the current with and without input light power calculated by $10\log_{10}[I_{DS}(P_{in})/I_{DS}(P_{in}=0)]$. The solid line is that the optically controlled HEMT and the dashed line is that the last reported optically controlled FET whose channel was bulk GaAs. In the case of the bulk channel, the on/off ratio was saturated around 4dB. On the other hand, 12dB on/off ratio was obtained in the optically controlled HEMT, and this is 3 times larger than that of bulk channel. This is highly influenced by the improvement of the transconductance of channel in the optically controlled HEMT. In this figure, increasing the input light power saturated the on/off ratio. This is because of the saturation of the modulation current caused by the absorption saturation.

Figure 5 shows the irradiated light power P_{in} dependence of responsivity *R*. The responsivity is defined as the ratio of the modulation current and input light power calculated by $[I_{DS}(P_{in}=0)-I_{DS}(P_{in})]/P_{in}$. The solid line is that the optically controlled HEMT, and the dashed line is that the optically controlled FET with a bulk channel. From this figure, maximum responsivity of 305(A/W) was obtained at P_{in}=1μW. As compared with the optically controlled MESFET structure [3], the responsivity was improved in HEMT structure. In the low power irradiation, the responsivity in

HEMT was two times higher than MESFET (R=152A/W). And under the higher power irradiation (P_{in}~1mW), the responsivity in HEMT was more than five times higher. From these measurement, the characteristics of the integrated type optically controlled FET was improved by the application of HEMT structure.

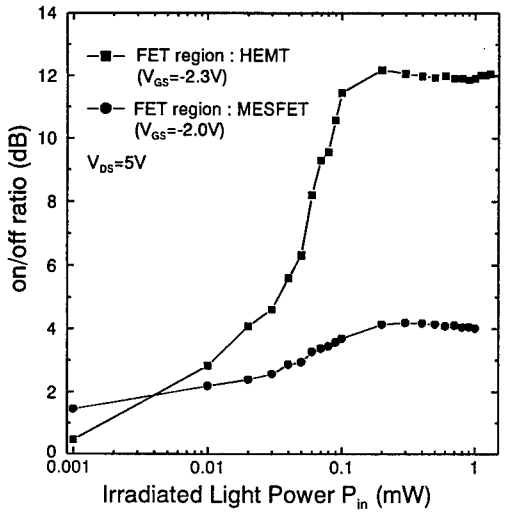

Fig. 4. Relation between On/Off Ratio and Irradiated Light Power.

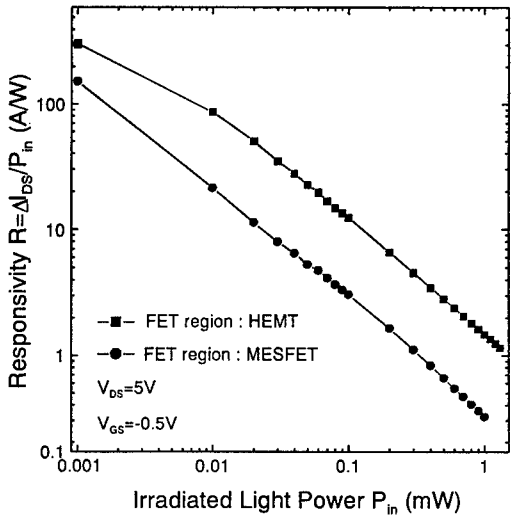

Fig. 5. Relation between Responsivity and Irradiated Light Power.

IV. Conclusion

We demonstrated an integrated optically controlled HEMT. By comparing the optically controlled FET using bulk GaAs channel, the optical response characteristics was highly improved in the optically controlled HEMT because of the increase of transconductance of FET's channel. We obtained maximum on/off ratio of 12dB and maximum responsivity of 305A/W. It was confirmed that the application of HEMT structure to the integrated optically controlled FET was effective for the improvement of device characteristics.

References

[1]K.Shimomura, "Proposal of field-effect-type photo-detector using field-screening effect in the absorption of light ," *Jpn. J. Appl. Phys.*, 1992, 12B, pp.L1757-L1759.

[2]Y.Shimizu and K.Shimomura, "Current modulation characteristics in optically-controlled field-effect transistor," *IEEE Photon. Technol. Lett.*, 1994, 6, pp.1338-1340.

[3]T.Sakai and K.Shimomura, "Bonding temperature dependence in optically controlled field-effect transistor fabricated by direct wafer bonding technique," *Jpn. J. Appl. Phys.*, 1996, 35, pp.L835-837.

[4]T.Yamagata and K.Shimomura, "Optically controlled metal-oxide semiconductor field-effect transistor operated by long-wavelength light" *Jpn. J. Appl. Phys.*, 1996, 35, pp.L1589-1592.

Bandwidth Characteristics of InP/InGaAs Uni-Traveling-Carrier Photodiodes

Naofumi Shimizu, Noriyuki Watanabe*, Tomofumi Furuta*, and Tadao Ishibashi*

NTT Optical Network Systems Laboratories, 1-1 Hikarinooka, Yokosuka 239-0847, Japan
Phone/Fax: +81-468-59-2094/3396, E-mail: nshimizu@exa.onlab.ntt.co.jp
*NTT System Electronics Laboratories, 3-1 Morinosato-Wakamiya, Atsugi 243-0198, Japan

1. Introduction

Uni-traveling-carrier photodiodes (UTC-PDs) have been proposed as high-speed and high-saturation-output photodetectors[1]. Among photocarriers generated in the p-type neutral absorption layer of the device, only minority electrons are injected into the collector and holes do not behave as active carriers. Thus, the photoresponse is primarily dominated by electron transport. In optimizing UTC-PD performance, such as bandwidth and efficiency, the thickness and doping level of the photo-absorption layer is of prime importance. However, a critical parameter, electron diffusivity in p-InGaAs, has not been studied yet, except for a heavily doped region[2].

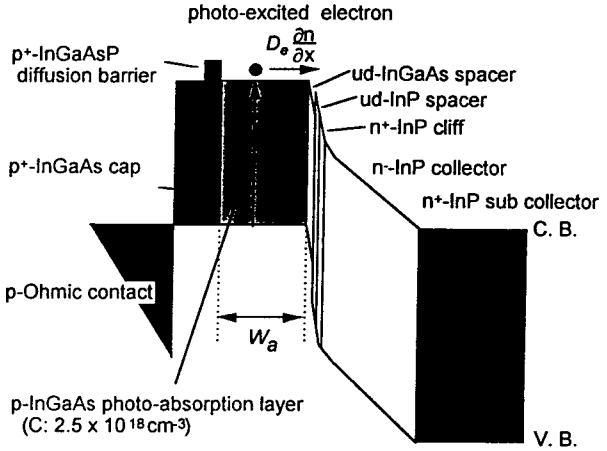

Fig. 1: Schematic band-diagram of a UTC-PD

In this paper, we report on the photoresponse of UTC-PDs for different absorption layer thicknesses. The result indicates that the bandwidth is described by a constant diffusion coefficient, which is as high as that for majority electrons. This is contrary to the theoretical analysis, which predicts a 50% reduction in electron mobility due to coupled polar-phonon plasmon scattering in the 10^{18}-cm^{-3} doping range[3].

2. Experiment

A schematic band-diagram of the InP/InGaAs UTC-PD is shown in Fig. 1. We studied structures with photo-absorption layer widths (W_a) of 220, 280, 360, and 420 nm. The absorption layer doping concentration was p = 2.5 x 10^{18} cm^{-3}. The depleted InP collection layer thickness was in the range of 150 - 220 nm. The electrical 3-dB bandwidth (f_{3dB}) of the devices was evaluated from their photoresponse to a laser input pulse (1.55 μm, 880 fs, 100 MHz) as measured by an electro-optic sampling technique[4]. To maintain a small-signal condition, we kept the input laser power level low at 0.15 pJ/pulse, where the photogenerated carrier density is much lower than the background hole density. Because the CR-time constant of the fabricated devices was 0.7 ps, it had no significant effect on the measured f_{3dB}'s.

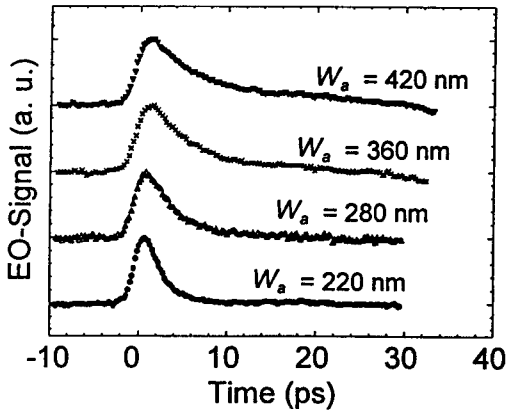

Fig. 2: Pulse response of UTC-PDs with four different W_a's.

3. Results and Discussion

Figure 2 shows the measured response at a bias voltage (V_{bias}) of -1.5 V. The exponential-tail in the

response curve was significantly lengthened as W_a increased. The f_{3dB}'s determined from the response curves are shown in Fig. 3 as a function of the neutral absorption layer thickness W_a - Δ. Here, Δ is the InGaAs depletion thickness at the interface between the photo-absorption and collector layers and is estimated to be 20 nm (5 - 9% of W_a) by numerical calculation of the band profile. As shown in the figure, f_{3dB} was found to be approximately proportional to $1/(W_a - \Delta)^2$, indicating that the response was dominated by the diffusive transport of electrons in the absorption layer.

Basically, the total response of the UTC-PD is a function of the absorption layer response and the electron traveling time in the collector layer τ_c. The effect of τ_c on the total response is, however, negligibly small because the electron velocity in InP is around 2 - 4 x 10^7 cm/s depending on the applied field[5], and W_a of the UTC-PDs studied was wide enough. Actually, the deviation in f_{3dB}'s derived for more negative V_{bias}'s was within the measurement accuracy of 5%, which meant that τ_c had little effect on f_{3dB}. In this situation, the small-signal response of the UTC-PD is given by[1]

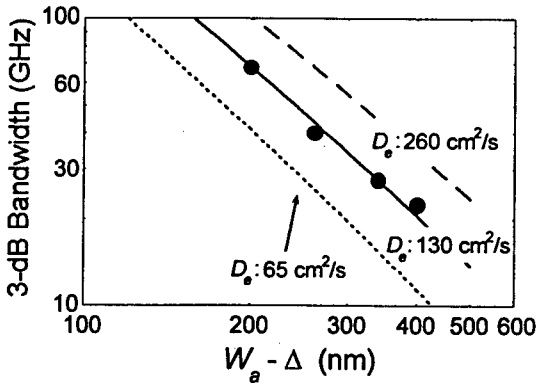

Fig. 3 f_{3dB} versus W_a - Δ (see text). The solid line represents the best-fit curve. The dotted and broken lines represent the calculated f_{3dB} with D_e of half and twice the best-fit result, respectively.

$$\frac{J(\omega)}{J(0)} = \left\{1 + j\omega\left(\frac{W_a^2}{2D_e} + \frac{W_a}{v_{th}}\right)\right\}^{-1} \quad (1)$$

Here, ω, D_e, and v_{th} are the angular frequency, the electron diffusion coefficient in the photo-absorption layer, and the electron thermionic emission velocity (2.5 x 10^7 cm/s in the InGaAs at 300 K), respectively.

We derived D_e by fitting the measured bandwidth of the UTC-PDs with Eq. (1). A diffusion coefficient of 130 cm^2/s for p = 2.5 x 10^{18} cm^{-3} was obtained from the best-fit curve for f_{3dB} vs. W_a - Δ. This D_e corresponds to an electron mobility μ_e of 5200 cm^2/Vs at 300 K, which is close to the majority mobility. This result is much different from the theoretical prediction[3] that D_e is as low as 60 cm^2/s (corresponding to μ_e of 2400 cm^2/Vs) and coupled polar-phonon plasmon scattering is the dominant factor in determining D_e.

5. Conclusion

We have studied how the bandwidth of InP/InGaAs UTC-PDs changes with respect to photo-absorption layer thickness. An electro-optic sampling technique was successfully used to accurately determine the bandwidth. The derived bandwidth is consistent with diffusive electron transport in the p-InGaAs. Contrary to the theoretical prediction, the measured minority electron diffusion coefficient, 130 cm^2/s at p = 2.5 x 10^{18} cm^{-3}, was close to that of the majority electrons.

References

1 T. Ishibashi, et al.; *Ultrafast Electronics and Optoelectronics* Technical Digest (Optical Society of America, Washington DC, 1997) 166.

2 E. S. Harmon, et al.; Appl. Phys. Lett., **63**, 636 (1993).

3 T. Kaneto, et al; Appl. Phys. Lett., **63**, 48 (1993).

4 N. Shimizu, et al.; *Jpn. J. Appl. Phys*, **37**, 1424 (1998).

5 K. Kurishima, et Al; *IEEE. Trans. Electron Devices*, **41**, 1319 (1994).

The Opto-Electronic Oscillator: Prospects for Extending the State of the Art in Reference Frequency Generation

L. Maleki

Manuscript unavailable at time of Digest printing

0-7803-4936-9/98/$10.00

Photonic Time-Stretch: A Potential Solution for Ultrafast A/D Conversion

B. Jalali, A.S. Bhushan and F. Coppinger
Electrical Engineering Department, UCLA, Los Angeles, CA 90095-1594
Voice: 310-825-9655, Fax: 310-206-2239, Email: jalali@ucla.edu

While the performance of conventional analog-to-digital converters (ADCs) continues to improve, the rate of improvement is too slow to satisfy the requirements of advanced communication and radar systems in the foreseeable future. Hence it is widely recognized that new concepts leading to major advances in the A/D technology are needed.

A signal can be stretched in time by subjecting it to sequential dispersion/chirp/dispersion steps [1]. Optics provides an ideal medium for performing this function as it provides ultrawide bandwidth dispersion [2] and chirp sources [3]. A new class of ADC systems can be realized by stretching the analog signal in time prior to sampling and quantization [4]. By reducing the signal bandwidth, time stretching increases the effective ADC sampling rate, input bandwidth and resolution. The system can operate with both pulsed and continuous-time signals. In the latter case, the signal is first segmented and interleaved into M parallel channels and each segment is stretched by M. This ensures that no signal is lost upon time transformation.

Figure 1 shows the general concept of time stretching using chirped optical pulses. A linearly chirped optical carrier is intensity modulated by the electrical signal in an electrooptic modulator. After traveling through a linear dispersive element, both electrical carrier and its modulation are slowed down in time. The ability to slow down the microwave carrier and its modulation is of paramount importance in digital receivers wherein the ADC must capture the received signal before down conversion. The optical carrier is chirped however this is of no consequence as optical field oscillations are filtered out by the photodetector.

Figure 2 shows the experimental setup. To generate the chirped pulse, a 160fs pulse from a Mode-Locked Erbium doped Fiber Ring Laser (ML-FRL) is dispersed in length L_1 of Single Mode Fiber (SMF) generating a linearly chirped optical signal. The pulse has approximately 60nm (7.5THz) bandwidth. The chirped signal is intensity modulated by the electrical waveform in a $LiNbO_3$ modulator producing an optically chirped copy of the analog waveform. The latter is linearly stretched in time by a 2nd dispersion stage consisting of length L_2 of SMF. The stretch factor is given by $M = (L_1 + L_2)/L_1$. An arbitrary analog waveform was generated by biasing the modulator at $V\pi$ and applying a pulse to it. Figure 3 shows the experimental results for various stretch factors ranging from 1 to 8 obtained by keeping L_1 fixed and using different lengths of fiber for L_2.

For a single tone modulation signal of frequency f_m and amplitude a, the output intensity is given by: $I = \frac{2a}{M}\cos\left(\frac{2\pi f_m}{M}t\right)\cos\left(\frac{\pi f_m^2 \beta_2 L_1}{2}\left(1-\frac{1}{M}\right)\right)$, where M is the stretch factor and β_2 is the linear dipsersion paramter. The second term describes the dispersion penalty due to L_2. For a fixed temperal apperture (fixed L_1), the dispersion penalty increases with M. However the resulting time transformation ensures that the penalty is negligible compared to that in conventional analog transmission over the same fiber length, L_2. This concept is shown in Figure 3.

In the case of a Nyquist rate ADC, time stretching increases the effective sampling rate and input bandwidth. In addition, since the signal bandwidth is reduced, the sampling jitter noise diminishes. In the case of Σ–Δ oversampling ADCs the advantages are much greater. This occurs due to the noise shaping property of these systems. As an example, in a 2nd order Σ–Δ modulator, the resolution increases by a significant 2.5bits for every octave of time stretch!

0-7803-4936-9/98/$10.00

References:
[1] W.J Caputi, "Stretch: a time-transformation technique", *IEEE Trans. Aerospace Electron. Syst.*, 1971, vol. AES-7, pp. 269-278.

[2] C.V. Bennet, E.P. Scott, and B.H. Kolner, "Temporal magnification and reversal of 100 Gb/s optical data with an up-conversion time microscope", *Appl. Phys. Lett.*, 1994, vol.65, no. 20, pp. 2513-2515.

[3] F. Coppinger, A.S. Bhushan, and B. Jalali, "Time magnification of electrical signal using chirped optical pulse", *Electronics Letters*, vol. 34, No. 4, pp. 399-400, 1998.

[4] A.S. Bhushan, F. Coppinger and B. Jalali, "Time-stretched analog-to-digital conversion," Electronic Letters, vol. 34, No. 11, pp. 839-841, 1998.

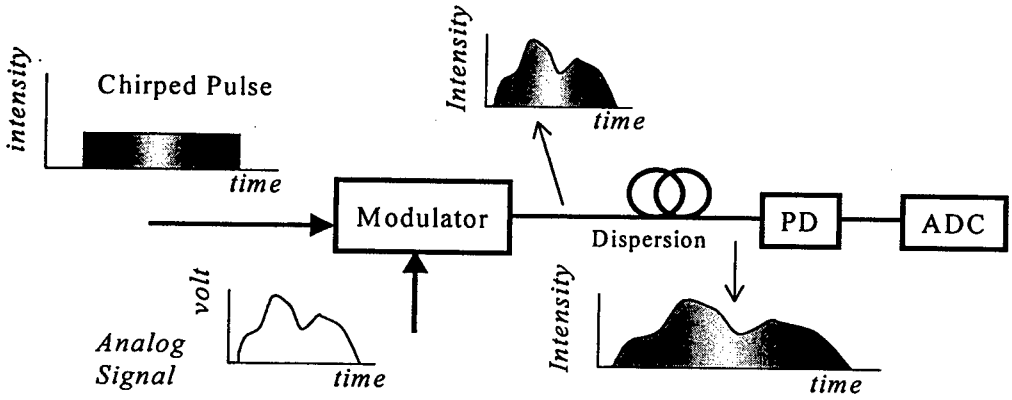

Figure 1 Schematic illustration of the chirped-pulse time-stretch system.

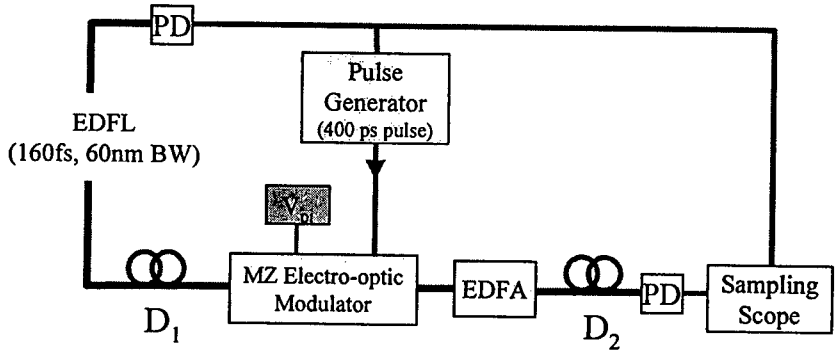

Figure 2 Experimental setup.

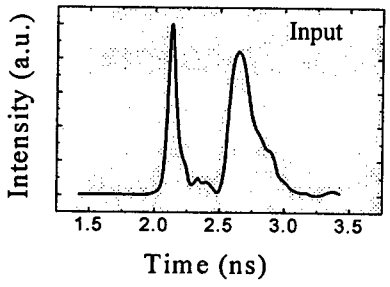

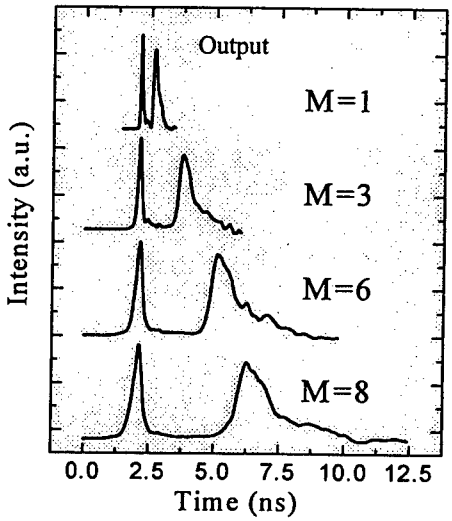

Figure 3 Preliminary experimental results for time stretching. (a) before and (b) after time stretching by various factors.

PHOTONIC RF FREQUENCY SHIFTER BASED ON HIGHLY CHIRPED MODE-LOCKED FIBER LASER

Jin U. Kang, Michael Y. Frankel, and Ronald D. Esman

Code 5672, Naval Research Laboratory
4555 Overlook Ave., S. W., Washington, D. C. 20375-5338

Abstract: We demonstrate novel photonic RF frequency shifter using a highly-chirped mode-locked fiber laser where we show frequency shifting of an RF signal from 10 GHz down to 5 GHz and up to 25 GHz.

Optical processing of microwave signals has gained much attention in recent years for its broadband, remoting, and system flexibility potentials. Such advantages have been proven in recent demonstration of such photonic functions as microwave beamforming[1], microwave links[2], and RF downconverters[3]. The typical photonic RF downconverters use mixing between the LO and RF to generate downconverted signal. Applications that require remoting such that the LO and RF sources are located apart, the typical photonic downconverters require two electro-optic(E-O) modulators. In this paper, we will present a novel photonic technique that can be used to arbitrary shift RF signal frequencies without the need for the LO source and the second E-O modulator. The technique is based on the dispersive chirping of amplitude-modulated, broadband, and pre-chirped optical carrier propagating through a dispersive fiber. We show that this effect can be used to produce a microwave frequency shift of the original signal with shifts of over tens of GigaHertz. Such capability is of great interest for many applications that require frequency shifting and may be hard to obtain using conventional methods.

In order to analyze the effect on the modulation frequency as the chirped, amplitude-modulated optical carrier propagates through a dispersive link, we analytically solved propagation of RF-modulated chirped pulse in the dispersive medium. The RF-modulated chirped optical Gaussian pulse can be written as [4]:

$$u(0,t) = E_0 \cos(\omega_m t)\exp\left(-\frac{(1+iC)}{2}\frac{t^2}{t_0^2}\right) \tag{1}$$

where E_0 is an amplitude, ω_m is the RF modulation frequency, C is a chirp parameter defined as $C = (\Delta\omega^2 t_0^2 - 1)^{0.5}$, t_0 is the initial linearly-chirped pulse width and $\Delta\omega$ is the bandwidth of the laser. The governing equation that describes the propagation of such pulses in the second-order dispersive medium, neglecting losses, can be written as:

$$i\frac{\partial u}{\partial z} - \frac{1}{2}\beta_2\frac{\partial^2 u}{\partial t^2} = 0 \tag{2}$$

where β_2 is a group-velocity dispersion parameter. By substituting equation (1) into (2) and analytically solving the equation, the output pulse can be written as:

$$u(z,t) = E_{0,z}\cos\left(\frac{\omega_m}{4A\delta}t\right)\exp\left(\frac{t^2}{4\delta^2}\right) \tag{3}$$

where, $E_{0,z}$ is the new amplitude after propagation, $A = (1+iC)/(2t_0^2)$, and $\delta = \frac{i}{2}\beta_2 z - \frac{1}{4A}$. From (3), it can be seen that the new RF modulation frequency due to the chirping is $\omega=\omega_m/(4A\delta)$. In the case of highly chirped pulses (e.g., $\Delta\omega >> 1/t_0$), the new RF modulation frequency can be simply written as:

$$\omega = \omega_m\sqrt{\frac{1}{1\pm\frac{2\Delta\lambda D z}{t_0}}} \tag{4}$$

where $\Delta\lambda$ is a pulse spectral bandwidth, D is the propagation medium dispersion, and z is the propagation distance. From (4), it can be easily seen that the amount of RF modulation frequency shift depends on the total dispersion and

0-7803-4936-9/98/$10.00

the amount of initial chirp of the carrier. The sign is "+" or "-", depending on whether the initial pulses are chirped in the anomalous dispersion regime and normal dispersion regime, respectively. From the equation, it can be seen that larger chirping results in larger frequency shifting while the direction of the shift depends on the sign of the chirping. Also, given the same length of dispersive fiber for frequency shifting, if the initial chirped pulse widths are the same, the pulse with broader laser bandwidth results in larger amount of chirping and thus results in larger amount of frequency shift.

The analysis was verified experimentally with a system shown schematically in Fig. 1. A stretched-pulse mode-locked fiber laser generating spectrally wide (~30 nm) 1-2 ps pulses at 1.55μm with a 40 MHz repetition rate was used as a source. The laser beam was end-fire coupled

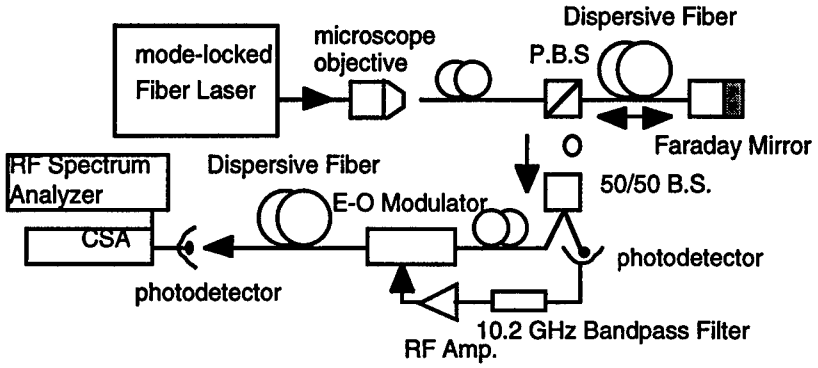

Figure 1 Schematic of the photonic RF frequency shifter set-up.

into one port of a polarizing beamsplitter, propagated through a 1.5 km long standard SMF-28 fiber (D~ 19 ps/nm.km) reflected off a Faraday mirror at the end of the fiber and coupled out from the other port of the polarizing beamsplitter. Double passing through the SMF-28 fiber linearly chirps the pulses to approximately ~2.2 ns forming a quasi-CW source for our photonic RF frequency shifter measurements. The chirped optical carrier was

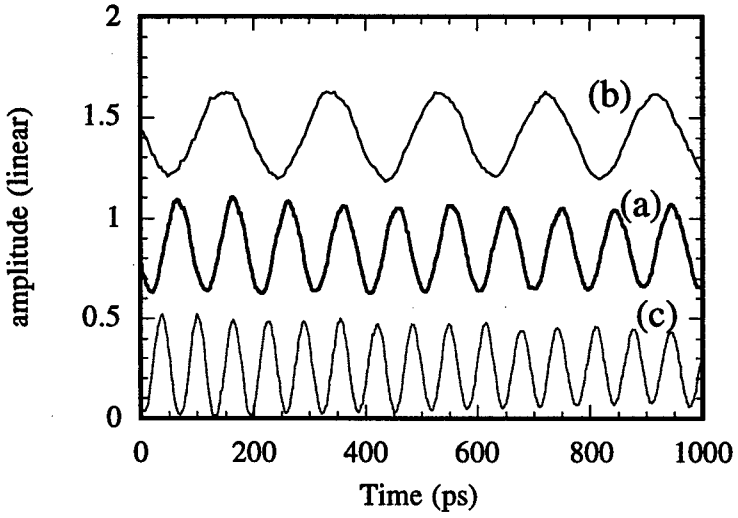

Figure 2 Temporal traces of (a) unshifted RF signal, (b) downshifted RF signal, and (c) upshifted RF signal using a 50 GHz sampling scope.

amplitude modulated with a 10.2 GHz signal in a wideband integrated electro-optic modulator (IEOM). Frequency shifting was achieved by propagating amplitude modulated optical pulses through various dispersive fiber segments. For frequency upshifting, dispersion compensating (DC) fiber was used (D~ -95 ps/nm.km) which effectively compress the optical pulses. Downshifting was achieved using SMF-28 fibers, which further chirps the optical pulses. The frequency shifted RF signal is recovered by a fast PIN detector.

To verify frequency shifts, both an RF spectrum analyzer and a 50 GHz sampling scope were used to monitor the RF signal in the frequency and time domain, respectively. In order to generate the ~10 GHz signal, a portion of the optical power was converted into RF signal using fast photodetector followed by a bandpass filter at ~10.2 GHz to select a 255^{th} harmonic of the laser frequency. A RF amplifier was used to amplify the RF signal and drive the IEOM. Because of the large bandwidth of the RF bandpass filter, several harmonics around 10.2 GHz were present. The average optical power through the IEOM was approximately 0.3 mW. In order to achieve

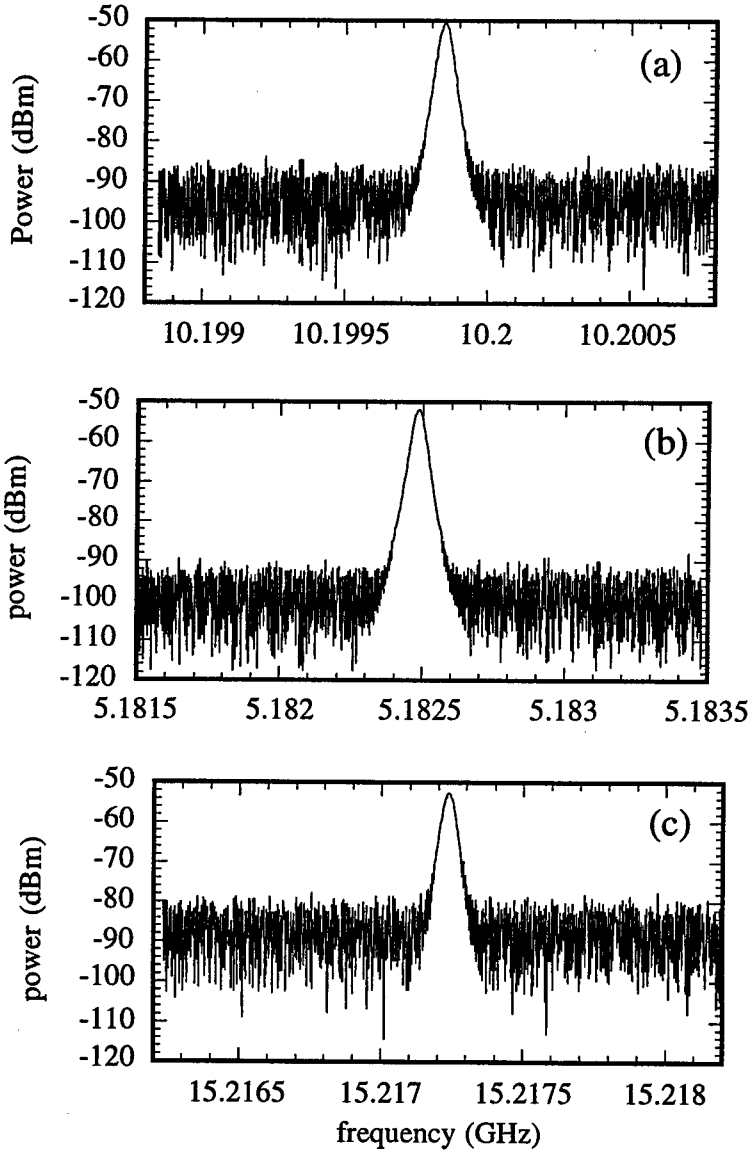

Figure 3 RF spectra corresponding to temporal signals shown in Fig. 2.

downshifting, 3 km of SMF-28 was used to further chirp the modulated optical pulses. For upshifting, 200 m long DC fiber was used to compress the optical pulses. Figure 2 shows the time traces of the 10 GHz original signal measured without dispersive fiber (a), the ~5.2 GHz signal using 3 km long SMF-28 fiber (b), and the upshifted ~15.2 GHz signal using 200 m long DC fiber (c). Corresponding RF spectrums are also shown in Figure 3. The recovered frequency shifted signals were approximately -60 dB down from the original signal used to drive the modulator, which is consistent with the IEOM half-wave voltage V_π of 20 V and photodetector current of 0.12 mA. Higher optical power and better IEOMs can significantly improve the link loss[2].

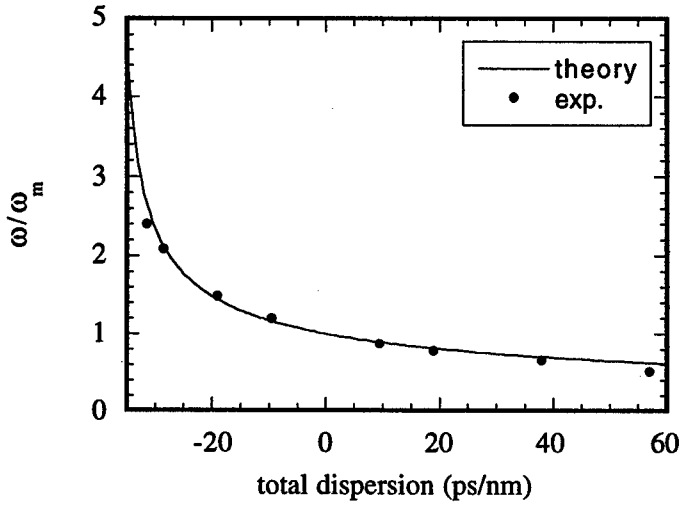

Figure 4 The ratio between the shifted and the initial RF modulation frequencies as a function of total dispersion of the fibers. Dots represent experimental data and line represent theoretical results.

Further experiments were performed with different lengths of fibers representing different total dispersions and frequency shifts up to 25 GHz were obtained. These results are summarized in Fig. 4 where the ratio between the new to the initial RF frequency is plotted as a function of total dispersion of the fibers. For theoretical fit, t_0 of 2.2 ns and $\Delta\lambda$ of 30 nm was used. The experimental results are in excellent agreement with the theoretical prediction. The small discrepancy between the theory and the experiment is partly because our pulse shape deviates from the ideal Gaussian case in addition to the uncertainty in the total dispersion of the fibers.

In conclusion, we analyzed the propagation of amplitude-modulated chirped optical signals through dispersive media. The results predict a shift in the output RF frequency and were experimentally verified, with demonstrated RF frequency shifts of a 10 GHz down to 5 GHz and up to 25 GHz. The amount of RF frequency shift depends on the total dispersion of the fiber that compresses or stretches the amplitude-modulated chirped optical carrier. This method can be used to produce extremely large RF frequency tunability with the generated RF signals in excess of 100 GHz.

This work was supported by the Office of Naval Research.

References

[1] M. Y. Frankel, P. J. Matthews, and R. D. Esman, IEEE Trans. Microwave Theory Technol. **44**, 2696 (1996)
[2] Lee T. Nichols, Keith J. Williams, and Ronald D. Esman, IEEE Trans. Microwave Theory Technol. **45**, 1384 (1997)
[3] K. J. Williams and R. D. Esman, IEEE Photon. Tech. Lett., **8**, 148 (1996)
[4] G. P. Agrawal, Nonlinear Fiber Optics, 2nd edition (Academic Press, San Diego, 1995)

A NOVEL TOPOLOGY OF TUNEABLE OPTICAL RADIO FREQUENCY NOTCH FILTER USING A CHIRPED FIBRE GRATING

W. Zhang, J. A. R. Williams, and I. Bennion

Electronic Engineering and Computer Science Division
Aston University, Aston Triangle, Birmingham, B4 7ET, UK
e-mail: w.zhang@aston.ac.uk

Abstract

We present a novel topology of tuneable optical radio frequency notch filter using a chirped fibre grating. An effective doubling of the linear, continuous tuning range is obtained within the bandwidth of the chirped grating compared to a previous topology.

I. Introduction

Photonic signal processing for radio frequency system is attractive because it can overcome many limitations imposed by conventional electrical signal processing. Many applications such as communication or radar system, require a wide dynamic range, high resolution notch filter to filter unwanted noise and clutter. There have been several kinds of tuneable optical notch filters proposed [1]-[5]. Most of which use several optical fibre delay lines of differing lengths to give out stepped time delay. Some reported schemes which may be tuned continuously either result in changing inserted loss or need multiple tuneable lasers.

Linearly chirped fibre gratings have either a linearly chirped grating period or linearly chirped effective refractive index distribution. The light intensity for different wavelength reflects from different spatial regions along the grating, introducing a time delay that is wavelength dependent and thus tuneable by varying the operating optical wavelength [6]. Although the chirped grating is a notch filter by itself, its free spectral range (FSR), generally very large, depends on the chirp rate of the grating. Due to the requirement of very wide chirp bandwidth it is difficult to make its FSR down to megahertz range where the operating frequencies of many applications are located. Besides, limited by chirped grating fabrication technology, its spectrum response is still not smooth enough to give a precise tuning of notch frequency. We describe here a novel topology of tuneable optical notch filter using a linearly chirped fibre grating which provides doubled time delay of the grating, linearly and continuously tuning either by simply changing the wavelength of the optical carrier or by tuning the temperature of the grating.

II. Principle

The topology of the tuneable optical radio frequency notch filter is shown in Fig.1a. The notch frequencies of the filter are given by,

$$f_{notch} = (k+\frac{1}{2})\frac{1}{\tau_d} \quad k = 0,1,2,\cdots \tag{1}$$

where τ_d is the difference of the time delays between two light beams, consisting of a fixed time delay difference and a tuneable time delay difference. When τ_d is changed, the shift of the notch frequencies is,

$$\Delta f_{notch} = (k+\frac{1}{2})\frac{\Delta\tau}{\tau_d^{\,2}} \tag{2}$$

0-7803-4936-9/98/$10.00

where $\Delta\tau$ is the change of the time delay difference which here is provided by a linearly chirped grating. If the fixed time delay difference is much larger than the tuneable time delay, the shift of the notch frequencies can be tuned linearly and precisely by changing $\Delta\tau$, meanwhile the free spectral range (FSR) defined by the notch spacing is kept nearly unchanged. This offers a large flexibility for real time signal processing.

Since chirped gratings can exhibit positive or negative time delay change with regard to wavelength, with same magnitude depending on the orientation of the grating, it offers a possibility to increase the obtainable time delay and thus the tuneable frequency range by connecting the chirped grating between two arms of the optical fibre Mach-Zehnder section. This makes full use of time delay characteristics of the chirped grating.

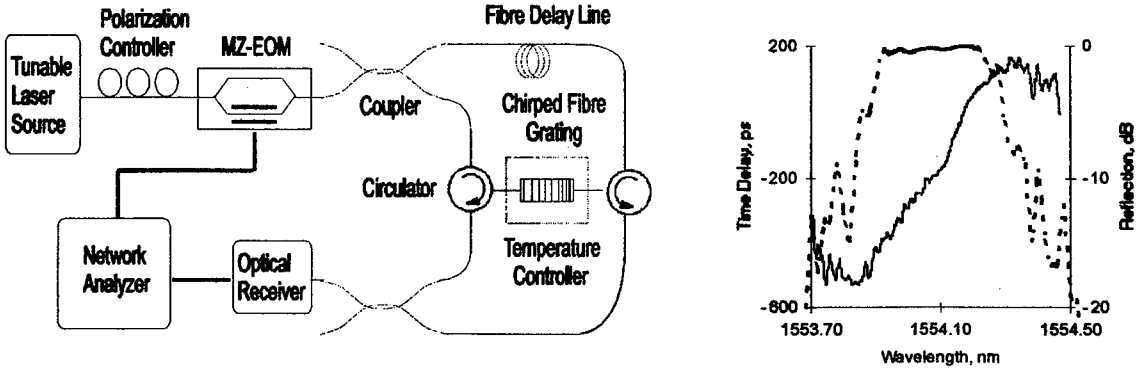

Fig.1 (a) the experimental arrangement, (b) the spectral response of the chirped grating.

III. Experiment and Results

A linearly chirped fibre grating with a length of 5cm was used to introduce a time delay that is wavelength dependent and thus tuneable by varying either the operating optical wavelength or the temperature applied to the grating [6]. Fig.1b gives the measured spectra of reflection and time delay. Within the grating bandwidth of about 0.3nm the reflectivity was larger than 99%. A temperature controller with a temperature control accuracy up to 0.01 °C, was used to stabilise the grating's response. A fixed length of standard single mode fibre (450m long) was used in our experiment, which gives a fixed time delay difference to the final resultant signal. The tuneable laser was operated with a coherence length significantly less than the optical path difference of the notch filter. The effect of linearly chirped grating on the microwave response of the optical notch filter was observed using a lightwave component analyzer (LCA). The chirped grating was connected between the two arms of Mach-Zehnder section through two circulators. Such a topology doubles the tuneable time delay within the grating's bandwidth of nearly total reflection, illustrated as Fig.2.

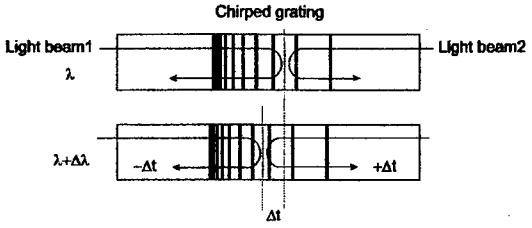

Fig.2 The variation of time delay induced by the chirped grating with wavelength

The free spectral range (FSR) of the filter is about 440 kHz for the fixed length of 450m. In the case that the grating is connected with only one arm [7], the shifts of the notch frequencies by changing source wavelength from 1553.9 nm to 1554.2 nm, are 100 kHz at around 500 MHz. The shift of the notch frequencies increases to 400 kHz when the filter operates at around 2 GHz, since the shift of the notch frequencies increases with the increase of operating frequency, according to (2). When the grating is connected between two arms, the obtainable frequency shifts are ~200 kHz and 780 kHz, respectively, giving a nearly doubled time delay as expected. Fig.3a gives the experimental results of the microwave frequency response of the optical notch filter operating at around 2 GHz. The relationship between notch frequency shift and source wavelength is shown in Fig.3b. The experimental data at the sampled wavelengths are very close to the regressed straight line, and exhibits a good linearity.

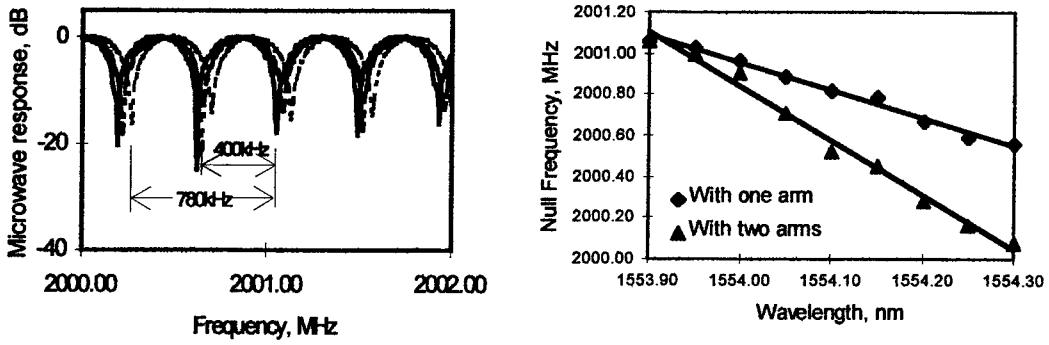

(a) (b)

Fig.3 The experimental results of the optical notch filter

Reducing the length of the fixed fibre delay line gives rise to increasing the FSR of the filter. An FSR of 11.8 MHz was obtained in our experiment where the fixed fibre delay line length was reduced to 35 m, consequently giving a tuneable range of ~11 MHz when operated at around 2 GHz.

It should be pointed out that for the configuration with the doubled time delay, the wavelength of the light source is necessarily confined within the bandwidth of the grating. When the wavelength of the light source operates far from the bandwidth, there is no reflection from the grating, the light beam of each arm swaps the travelling path through the circulator, and this topology acts as a notch filter with the fixed time delay provided by the fibre delay line. When the wavelength is close to the bandwidth, the notch frequency varies irregularly with the wavelength due to the complicated dispersion response of the grating in this region.

The fixed time delay can be altered by changing the length of the fibre delay line to provide the larger FSR of the notch filter, depending on the practical application. However, the optical coherence of the source must be accounted for as it will play a significant role in the device response. When the FSR is increased to the order of GHz, the frequency response becomes more complicated than indicated in (1) due to the effect of the grating dispersion on the sidebands [8].

IV. Conclusion

A novel topology of optical notch filter employing a chirped fibre grating has been demonstrated. Its low cost, compactness and flexibility makes it suitable for real time signal processing in radio frequency systems. More complex geometry of such delay lines will allow for the synthesis of more complex filter responses.

Acknowledgements

This work is funded under EPSRC Grant GR/L37403.

References

[1] J. E. Bowers, S. A. Newton, and H. J. Shaw, "Fiber-optic variable delay lines", *Electron. Lett.* Vol.**18**, pp.999-1000, 1982

[2] M. Y. Frankel and R. D. Esman: "Fiber-optic tuneable microwave transversal filter", *Optical Fiber commun. Conf., OFC' 95 Tech. Dig.*, San Diego, CA, Feb. 26-Mar. 3 pp.124-125, 1995

[3] F. Coppinger, S. Yegnanarayanan, P. D. Trinh, B. Jalali, and I. L. Newberg, "Nonrecursive tunable photonic filter using wavelength-selective true time delay", *IEEE Photonics Technol. Lett.*, vol.**8**, no.9, pp.1214-1216, 1996

[4] F. Coppinger, S. Yegnanarayanan, P. D. Trinh, and B. Jalali, "Continuously tunable photonic radio-frequency notch filter", *IEEE Photonics Technol. Lett.*, vol.**9** no.3, pp.339-341, 1997

[5] D. Norton, S. Johns, C. Keefer, and R. Soref, "Tunable microwave filtering using high dispersion fiber time delay", *IEEE Photonics Technol. Lett.*, vol.**6**, no.7, pp.831-832, 1994

[6] I. Bennion, J. A. R. William, L. Zhang, K. Sugden, and N. J. Doran, "UV-written in-fibre Bragg gratings", *Opt. Quantum Electron.*, vol.**28** pp.93 1996

[7] W. Zhang, J. A. R. Williams, L. A. Everall, and I. Bennion, "Tuneable radio frequency filtering using linearly chirped fibre grating", *Proc. ECOC'98,* Madrid, Spain, Sept. 20-24 1998

[8] H. Schmuck, "Comparison of optical millimetre wave system concepts with regard to chromatic dispersion", *Electronic Letters* **31**(21), pp. 1848-1849, 1995

SIGNAL-ASE NOISE FILTERING IN OPTICAL MILLIMETER-WAVE RADIO-OVER-FIBER LINKS

R. A. Griffin, P. M. Lane and J. J. O'Reilly

Telecommunications Group, Department of Electronic and Electrical Engineering,
University College London,
Torrington Place, London WC1E 7JE, UK.

Abstract: We consider optical amplifier noise in self-heterodyne optical mm-wave links, and propose that 0 dB noise figure can be achieved. We experimentally demonstrate 2.5 dB noise figure reduction for an EDFA using a tailored optical filter.

I. INTRODUCTION

Photonic millimeter-wave links are a promising approach for the provision of a radio-based final drop for broadband customer access networks [1], providing transport of mm-wave signals from a central base station to multiple remote antenna units. There has been considerable progress in recent years, with focus on the development of 'self-heterodyne' optical sources which allow operation at 1550 nm over standard fiber with minimal power penalty from chromatic dispersion [2-4].

Operation of radio-over-fiber systems at 1550 nm allows the utilisation of Erbium-doped fiber amplifiers (EDFAs), providing compensation for propagation and splitting loss. With continued progress, system performance will ultimately be limited by noise generated from the optical amplification process. Here we show that the optical amplifier noise figure may be reduced by 3 dB for self-heterodyne signals, potentially doubling the system capacity. We experimentally demonstrate 2.5 dB improvement in the noise figure of an EDFA.

II. THEORY

In an optical amplification process, amplified spontaneous-emission (ASE) is added to the amplified signal, degrading the carrier-to-noise ratio (CNR) of the input signal. For conventional intensity modulation, signal-ASE beat noise cannot be reduced by optical filtering, resulting in a minimum amplifier noise figure of 3 dB [5]. In optical mm-wave links, self-heterodyne optical signals are employed in preference to intensity modulation in order to avoid large power penalties due to chromatic dispersion at 1550 nm [6]. As we show below, self-heterodyne optical spectra allow filtering of signal-ASE beat noise, potentially allowing a 0 dB optical amplifier noise figure.

A mm-wave optical self-heterodyne signal has an optical power spectrum $S(f)$ given by

$$S(f)=\frac{I_0}{2}[\delta(f-f_0+f_{mm}/2)+\delta(f-f_0-f_{mm}/2)] \tag{1}$$

where f_0 is the optical center frequency. With an ideal receiver, the CNR of the generated mm-wave carrier is shot noise limited. For a photodetector with 100% quantum efficiency, the CNR of the signal generated at f_{mm} is given by

$$CNR_{in}=\frac{I_0}{4h\nu B} \tag{2}$$

where $h\nu$ is the photon energy and B is the detector bandwidth. During optical amplification, spontaneous emission is added to the signal, degrading the CNR. After optical amplification with gain G, ASE power at the output has spectral density $(G-1)n_{sp}h\nu$, where n_{sp} is the spontaneous-emission factor [5]. For $G>>1$, CNR at the output is dominated by signal-ASE beating, and is given by

$$CNR_{out}=\frac{GI_0}{8(G-1)n_{sp}h\nu B} \tag{3}$$

The noise figure NF of the amplifier for the self-heterodyne signal is then given by

0-7803-4936-9/98/$10.00

$$NF \equiv \frac{CNR_{in}}{CNR_{out}} \cong 2n_{sp} \tag{4}$$

Without optical filtering, the amplifier noise figure has a minimum value of 3 dB, when $n_{sp} = 1$, identical to the case of intensity modulation with direct detection. For the self-heterodyne spectrum, however, ASE power at frequencies $f_0 + \frac{3}{2} f_{mm}$ and $f_0 - \frac{3}{2} f_{mm}$ – *outside the signal band* – contributes to the generation of signal-ASE beat noise at the heterodyne frequency f_{mm}. Using an optical band-pass filter, the signal-ASE noise power can hence be reduced by 3dB, potentially allowing 0 dB noise figure. This effect is analogous to image filtering in electronic mixers, and has previously been demonstrated only for coherent optical systems employing a local oscillator at the receiver [7].

III. EXPERIMENT

A 30 GHz self-heterodyne optical signal was generated using optical suppressed-carrier modulation [2]. A CW 1550 nm DFB laser was externally modulating using a $LiNbO_3$ Mach-Zehnder modulator (MZM). The modulator was driven at 15 GHz and biased at V_π, the point of minimum optical transmission, suppressing the optical carrier. For moderate drive levels, the majority of the optical power resides in first-order sidebands displaced 15 GHz from the optical carrier, providing a 30 GHz self-heterodyne optical signal.

The optical mm-wave signal was attenuated and amplified using two EDFAs. To perform signal-ASE filtering, an apodised fiber Bragg grating (FBG) with peak reflectivity 99.9% and FWHM 60 GHz was employed in reflection. The measured reflection spectrum of the FBG is shown in Figure 1, together with the optical spectrum of the generated mm-wave signal. Also shown schematically is ASE power contributing to detected signal-ASE noise at 30 GHz. ASE power offset 45 GHz from the suppressed optical carrier will be strongly attenuated by the FBG filter, which is the basis for the improvement in CNR.

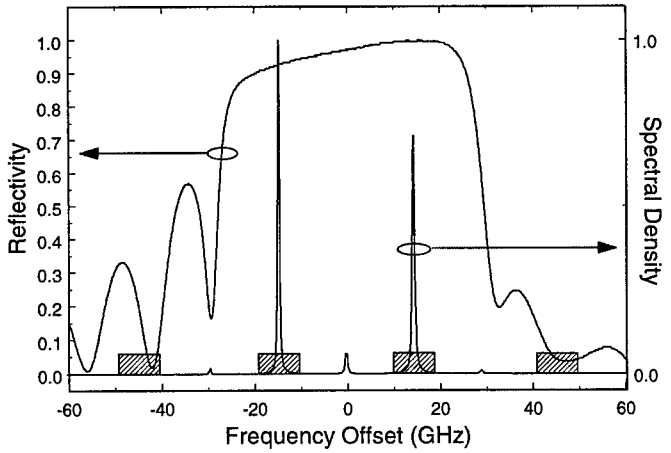

Figure 1: Spectrum of the optical mm-wave signal is shown together with the FBG reflection spectrum. Shaded areas schematically illustrate ASE power contributing to CNR reduction.

The detected 30 GHz carrier was amplified and mixed down to baseband with a broadband mixer, and the noise of the IF signal measured with a spectrum analyser. To distinguish between signal-ASE noise filtering and ASE-ASE filtering, the unpolarized nature of ASE was utilised. ASE-ASE beat noise was measured separately at the output by adjusting a polariser to null the signal term. By subtracting ASE-ASE beat noise and receiver noise from the total, signal-ASE noise could be accurately estimated. The experimental layout is shown schematically in Figure 2.

Measured CNR as a function of input optical power with and without optical filtering is shown in Figure 3. The slope of both sets of measurements is close to one, in agreement with (3) which predicts a linear relationship between CNR and input power, confirming that the measured noise is due to signal-ASE beating. Ten measurements for a fixed input power yielded an average improvement in CNR of 2.5±0.2 dB using optical filtering.

The expected noise reduction was calculated using the measured reflection spectrum of the FBG. With the optical carrier frequency centered in the FBG reflection band, we calculate a CNR improvement of 2.6 dB should be achieved for a 30 GHz signal, in good agreement with the experimental CNR measurements. The noise reduction is limited by sidelobes in the reflection spectrum of the FBG. Better apodisation would lead to CNR improvement closer to the maximum value of 3dB.

Final verification of the experiment was performed by repeating the measurements with a 14.6 GHz optical mm-wave signal. In this case, ASE power contributing to signal-ASE noise falls within the FBG reflection band, and no improvement in CNR is expected. Experimental measurement confirmed that the CNR was not improved in this case.

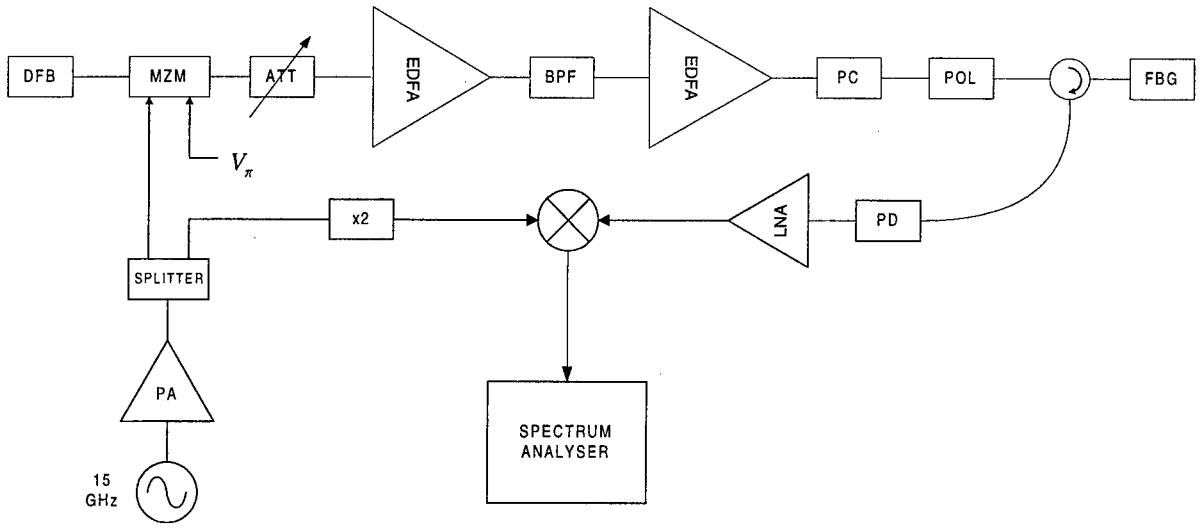

Figure 2: Schematic experimental layout for measurement of signal-ASE noise filtering. Abbreviations: PA – power amplifier; MZM – Mach-Zehnder modulator; ATT – attenuator; BPF – band-pass filter; PC – polarization controller; POL – polarizer; FBG – fiber Bragg grating; PD – photodetector; LNA – low noise amplifier.

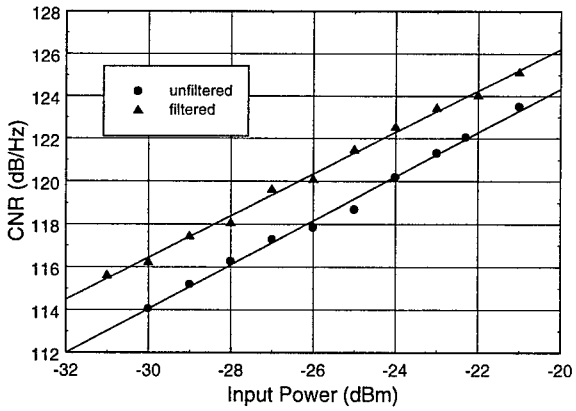

Figure 3: Measured CNR due to signal-ASE beat noise as a function of optical input power.

IV. CONCLUSION

We have demonstrated that signal-ASE noise reduction can be achieved for self-heterodyne optical mm-wave signals using passive optical filtering. We applied the technique to an optical suppressed-carrier signal, but noise reduction can be

achieved for other self-heterodyne signals, such as optical single-sideband signals [3]. An improvement of 2.5 dB in CNR was measured experimentally using a FBG. With current rapid improvement in sources and filters driven by DWDM development, we expect that CNR improvement close to 3 dB will be practically achievable.

For optical mm-wave links which are noise-limited by signal-ASE beating, noise filtering will provide significant benefit. Noise reduction of 3 dB will allow the link capacity to be doubled, providing further stimulus for the deployment of radio-over-fiber networks.

V. ACKNOWLEDGEMENTS

This work was funded by the European Commission ACTS project FRANS.

VII. REFERENCES

1. J. O'Reilly and P. Lane, "Remote delivery of video services using mm-waves and optics", *J. Lightwave Technol.*, vol. 12, pp. 369 - 375, 1994.
2. J. J. O'Reilly, P. M. Lane, R. Heidemann and R. Hofstetter, "Optical generation of very narrow linewidth millimetre-wave signals", *Electron. Lett.*, vol. 28, pp. 2309-2311, 1992.
3. G. H Smith., D. Novak and Z. Ahmed, "Technique for optical SSB generation to overcome dispersion penalties", *Electron Lett.*, vol. 33, pp. 74-75, 1997.
4. P. Braun R, G. Grosskopf, D. Rohde and F. Schmidt, "Low-phase-noise millimeter-wave generation at 64 GHz and data transmission using optical sideband injection locking", *IEEE Photon. Technol. Lett.*, vol 10, pp. 728-730, 1998.
5. G. P. Agrawal, Nonlinear Fiber Optics, 2nd Edition, Academic Press, London.
6. H. Schmuck, "Comparison of optical millimetre-wave system concepts with regard to chromatic dispersion", *Electron. Lett.*, vol 31, pp. 1848-49, 1995.
7. G. R. Walker, R. C. Steele, and N. G. Walker, "Optical amplifier noise figure in a coherent optical transmission system", *J. Lightwave Technol.*, vol. 8, pp. 1409-1413, 1990.

Coherent Fiber-Optic Links for Transmission and Signal Processing in Microwave and Millimeter-Wave Systems

U. Gliese

Center for Broadband Telecommunications, Department of Electromagnetic Systems,
Technical University of Denmark, Building 348, DK-2800 Lyngby, Denmark
Phone: +45 45 88 14 44, Fax: +45 45 93 16 34, E-mail: ug@emi.dtu.dk

Abstract

The principles of coherent fiber-optic links are presented and the transmission and signal processing capabilities offered to microwave and millimeter-wave systems are discussed. Furthermore, an overview of implemented transmitter types and link experiments is given.

1. Introduction

Fiber-optic links are gaining increasing interest for implementation of transmission as well as signal processing functions in microwave and millimeter-wave systems.

The basic outline for a fiber-optic link is shown in Fig. 1. Basically, the link transports a signal from its input to its output. If the signal remains unaltered, the link is transparent and its only function is signal transmission. On the other hand, if the signal is intentionally altered by the link, it also performs signal processing. This added functionality may be desirable in many systems and may enable a number of new applications. At present, the potential of such multifunctional links is increasingly recognized [1]-[6]. In coherent links, the signal processing functions can most often be obtained without significant added complexity and cost and without degradation of the transmission performance.

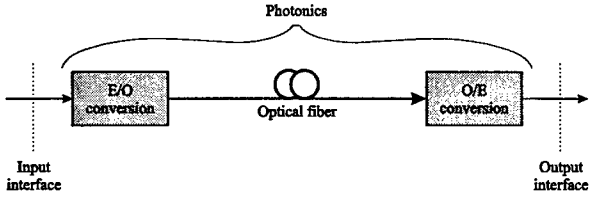

Figure 1: Schematic for the fiber-optic link.

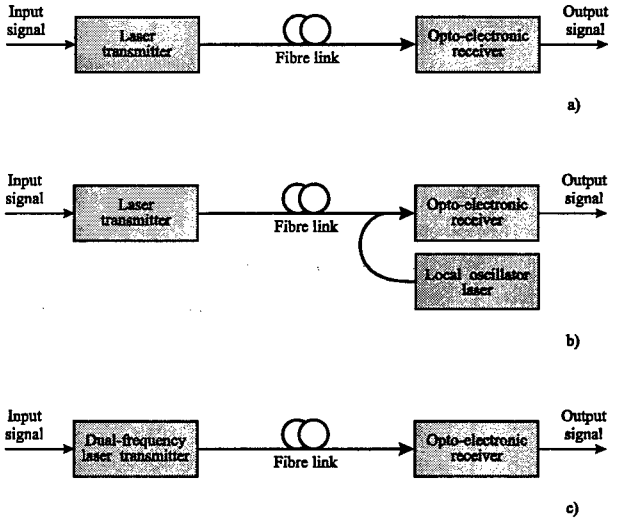

Figure 2: Schematics for a) IM-DD links, b) HD coherent links, and c) RHD coherent links.

2. Principles of coherent links

Fiber-optic links may be implemented with coherent or non-coherent techniques. The three resulting link types are shown in Fig. 2. A detailed description of the non-coherent intensity modulated direct detection (IM-DD) link type can be found in [7], [8]. In the heterodyne detection (HD) and the remote heterodyne detection (RHD) links, the interaction between two laser signals form the basis for the detection process, and the detected signal current is given as

$$i_s(t) = 2R\sqrt{p_1(t)p_2(t)} \cdot \cos\left[\{\omega_1(t) - \omega_2(t)\}t + \phi_1(t) - \phi_2(t)\right]$$

where R is the responsivity of the photodetector,

0-7803-4936-9/98/$10.00 © 1998 IEEE

t is the time, and $p(t)$ is the instantaneous power, $\omega(t)$ is the instantaneous frequency and $\phi(t)$ is the instantaneous phase of the laser signals. The equation shows that it is necessary to maintain a well defined correlation between the frequency and phase of the two signals. This makes coherent links more complex than non-coherent links. However, as discussed in this paper, it also offers a number of advantages. More detailed descriptions of the HD principle can be found in [9] and of the RHD principle in [5], [6], [8].

This paper is focused on RHD coherent links. In these, both laser signals are generated at the transmitter end of the link. This makes it significantly easier to maintain frequency and phase correlation as compared to HD links.

3. Transmission capabilities

The transmission properties and capabilities of coherent RHD links are, in many respects, different from those of the IM-DD links. The higher complexity of coherent links pays off in terms of:

- Higher link gain [10].
- Comparable or higher linearity [10].
- Comparable or higher CNR [10].
- Lower sensitivity to chromatic dispersion [8].

The link gain can be much higher since a modulation depth of unity can be achieved without degradation of linearity (see the equation) and since the power from two lasers is often involved. The CNR improvement depends on the involved noise sources. Incorporation of optical preamplifiers in the DD receivers will reduce the CNR advantage offered by the coherent detection.

4. Signal processing capabilities

In addition to attractive transmission capabilities, the coherent links readily offer photonic signal processing possibilities. This is evident from the equation where it is seen that changes in either amplitude, frequency or phase applied to one of the laser signals will result in proportional changes of the signal at the output of the link.

This feature opens up for photonic implementation of a variety of functionalities in microwave and millimeter-wave systems:

- Transmission.
- Amplitude control.
- Frequency control.
- Phase control.
- Time delay control.
- Filtering.
- Modulation and demodulation.
- Frequency conversion.
- Signal recovery.

Photonic implementation of these functionalities may be advantageous in some existing applications and may open up for new applications that were not possible beforehand.

All of the listed functionalities are, to a large extent, equally important. It is, however, impossible to give a complete survey of them all. In the remainder of the paper, which deals with experimental results, the focus is placed on transmitter concepts and RHD link experiments demonstrating transmission, modulation, frequency conversion and signal recovery.

5. Dual-frequency laser transmitters

The RHD links require dual-frequency laser transmitters. These can be implemented in different ways and a significant number of concepts have been proposed and experimented:

- Dual mode laser (DML) transmitters [11].
- Pulsed laser (PL) transmitters [12].
- Optical frequency shifter (OFS) transmitters:
  - Splitting and shifting (SS) [13], [14].
  - SSB modulation [15]-[17].
  - Suppressed carrier DSB modulation [18].
- Optical injection locked loop (OILL) transmitters [19]-[21].
- Optical phase locked loop (OPLL) transmitters [22]-[25].
- Optical feedforward modulator (OFFM) transmitters [26].

The above transmitters, some of which are conceptually very different, basically generate two phase correlated optical signals that can be separately altered in intensity, frequency and phase. All of them have been successfully used in link experiments.

Table 1: Overview of RHD link transmission and signal processing experiments.

Functionality	Tx concept	LF	IF	RF	Modulation	Year	Ref.
Modulation	OPLL	1 Gb/s		9 GHz	1 Gb/s QPSK	1994	[27]
Modulation	OFS-DSB	140 Mb/s		36 GHz	140 Mb/s BPSK	1994	[28]
Up-conversion	OFS-SSB		50 MHz	650 MHz	No modulation	1994	[29]
Up-conversion	OPLL		2 GHz	9 GHz	100 Mb/s DPSK	1994	[30]
Up-conversion	PL		2 GHz	58 GHz	155 mb/s BPSK	1996	[31]
Up-conversion	OFS-SSB		2 GHz	39 GHz	155 mb/s BPSK + AM-VSB	1997	[32]
Up-conversion	OILL		140 MHz	19 GHz	140 Mb/s OQPSK	1997	[20]
Up-conversion	OILL		1 GHz	64 GHz	140 Mb/s OQPSK	1998	[33]
Transparency	OFFM			39 GHz	300 Mb/s BPSK	1994	[34]
Transparency	DML			60 GHz	No modulation	1996	[11]
Transparency	OFS-SSB			12 GHz	51.8 Mb/s BPSK	1997	[35]
Transparency	OFS-SSB			38.1 GHz	155 Mb/s BPSK	1997	[36]
Transparency	OFS-SSB			10 GHz	2.49 Gb/s BPSK	1997	[37]
Transparency	DML			36.8 GHz	51.8 Mb/s PSK	1998	[38]
Signal recovery	OPLL			7.6 GHz	27 MHz FM	1994	[39]

6. Link experiments

An overview of the link experiments that have been carried out using coherent RHD is given in Table 1. A large number of different functionalities, transmitter concepts and signal formats have been experimented with excellent results. For all of the experiments, the indicated functionality describes the signal processing that is carried out by the link in addition to transmission.

All of the transmitter concepts have been applied although not for all functionalities. As an example, it is only the OPLL transmitter that can be used for transparent signal recovery of a microwave signal that has been degraded by additive noise [5], [39].

The SSB modulation transmitter is by far the most popular. This is because of its lower complexity as compared to especially the OILL and OPLL transmitters. However, the latter do enable a better performance in terms of link gain and CNR without the addition of optical amplifiers. This is because the full power from two separate lasers is ideally available for transmission. Furthermore, the two laser signals are readily available for individual photonic processing.

The experiments clearly demonstrate the feasibility of coherent fiber-optic RHD links. As evident, most focus on transparent transmission and frequency conversion. However, the photonic signal processing potential of coherent links can be taken much further. This may lead to many new innovative system applications.

7. Conclusion

Coherent fiber-optic RHD links exhibit attractive transmission capabilities as compared to IM-DD links. In addition, they also offer the capabilities to perform a large number of different signal processing functionalities. An overview of link experiments demonstrating, modulation, frequency conversion, and signal recovery has been given. In many applications, such links may be much more desirable than transparent links. As opposed to the conventional DD links, the RHD links can in many cases be optimized to the specific application. This may significantly influence performance, cost, power consumption, etc. When comparing DD links and RHD links this must be taken into account, and the entire system must be evaluated in its entirety from end-to-end.

References

[1] G.K. Gopalakrishnan, et. al., "A low-loss downconverting analog fiber-optic link," IEEE Trans. MTT, vol. 43, no. 9, 1995, pp. 2318-2323.

[2] U. Gliese, "Multi-functional fibre-optic microwave and millimeter-wave links," Proc. URSI General Assembly, Lille, France, August, 1996, pp. 638.

[3] L. Noël, et. al., "Novel techniques for high-capacity 60-GHz fiber-radio transmission systems," IEEE Trans. MTT, vol. 45, no. 8, 1997, pp. 1416-1423.

[4] K.J. Williams, et. al., "Photonic Microwave Signal Processing," Proc. IEEE MWP, September, 1997, Dusiburg, Germany, pp. 187-190.

[5] U. Gliese, et. al., "Multi-functional fibre-optic microwave links based on remote heterodyne detection," IEEE Trans. MTT, vol. 46, no. 5, 1998.

[6] U. Gliese, "Multi-functional fibre-optic microwave links," Opt. and Quan. Elec., 1998

[7] C. Cox III, et. al., "Techniques and performance of intensity-modulation direct-detection analog optical links," IEEE Trans. MTT, vol. 45, no. 8, 1997, pp. 1375-1383.

[8] U. Gliese, et. al., "Chromatic dispersion in fiber-optic microwave and millimeter-wave links," IEEE Trans. MTT, vol. 44, no. 10, 1996, pp. 1716-1724.

[9] R. Gross, et. al., "Multichannel coherent FSK experiments using subcarrier multiplexing techniques," IEEE JLT, vol. 8, no. 3, 1990, pp. 406-414.

[10] T.N. Nielsen, et. al., "Performance evaluation of fibre-optic microwave links," ESA, ESTEC Contract Report, Contract No. 134212, Technical University of Denmark, Department of Electromagnetic Systems, R590, October, 1994.

[11] D. Wake, et. al., "Transmission of 60-GHz signals over 100 km of optical fiber using a dual-mode semiconductor laser source," IEEE PTL, vol. 8, no. 4, 1996, pp. 578-580.

[12] D.Y. Kim, et. al., "Ultrastable millimetre-wave signal generation using hybrid modelocking of a monolithic DBR laser," IEE Elec. Lett., vol. 31, no. 9, 1995, pp. 733-734.

[13] M. Tamburrini, et. al., "Optical feed for a phased array microwave antenna," IEE Elec. Lett., vol. 23, no. 13, 1987, pp. 680-681.

[14] C.L. Wang, et. al., "Permanent magnet-based guided-wave magnetooptic Bragg cell modules," IEEE JLT, vol. 10, no. 5, 1992, pp. 644-648.

[15] M. Izutsu, et. al., "Integrated optical SSB modulator/frequency shifter," IEEE JQE, vol. 17, no. 11, 1981, pp. 2225-2227.

[16] R.F. Kalman, et. al., "A novel analog optical link with high dynamic range," IEEE PTL, vol. 5, no. 6, 1993, pp. 725-728.

[17] G.H. Smith, et. al., "Technique for optical SSB generation to overcome dispersion penalties in fiber-radio systems," IEE Elec. Lett., vol. 33, no. 1, 1997, pp. 74-75.

[18] J.J. O'Reilly, et. al., "Optical generation of very narrow linewidth millimetre wave signals," IEE Elec. Lett., vol. 28, no. 25, 1992, pp. 2309-2311.

[19] L. Goldberg, et. al., "Microwave signal generation with injection-locked laser diodes," IEE Elec. Lett., vol. 19, no. 13, 1983, pp. 491-493.

[20] R.-P. Braun, et. al., "Microwave generation for bidirectional broadband mobile communications using optical sideband injection locking," IEE Elec. Lett., vol. 33, no. 16, 1997, pp. 1395-1396.

[21] L. Noël, et. al., "Optical millimetre-wave generation technique with high efficiency, purity and stability," IEE Elec. Lett., vol. 32, no. 21, 1996, pp. 1997-1998.

[22] R.C. Steele, "Optical phase-locked loop using semiconductor laser diodes," IEE Elec. Lett., vol. 19, no. 2, 1983, pp. 69-70.

[23] K.J. Williams, et. al., "6-34 GHz offset phase-locking of Nd:YAG 1319 nm nonplanar ring lasers," IEE Elec. Lett., vol. 25, no. 18, 1989, pp. 1242-1243.

[24] R.T. Ramos, et. al., "Fast heterodyne optical phase-lock loop using double quantum well laser diodes," IEE Elec. Lett., vol. 28, no. 1, 1992, pp. 82-83.

[25] U. Gliese, et. al., "A wideband heterodyne optical phase locked loop for generation of 3-18 GHz microwave carriers," IEEE PTL, vol. 4, no. 8, 1992, pp. 936-938.

[26] O. Solgaard, et. al., "Millimeter-wave, multigigahertz optical modulation by feedforward phase noise compensation of a beat note generated by photomixing of two laser diodes," IEEE PTL, vol. 5, no. 5, 1993, pp. 574-577.

[27] T.N. Nielsen, et. al., "A Gbit/s QPSK optical microwave transmitter based on a semiconductor optical amplifier phase modulator and phase locked DFB lasers," Tech. Dig. OFC, February, 1994, San Jose, California, pp. 114-115.

[28] H. Schmuck, et. al., "Advanced fibre-optic distribution of 140 Mbit/s mm-wave signals at 36 GHz," Proc. ECOC, Firenze, Italy, 1994, pp. 39-44.

[29] R.F. Kalman, et. al., "Demonstration of an analog heterodyne interferometric phase-modulated (HIMP) link," IEEE PTL, vol. 6, no. 10, 1994, pp. 1271-1273.

[30] U. Gliese, et. al., "Frequency Up-Shifting Fiber-Optic Microwave Link," Proc. IEEE MWP, November, 1994, Abbaye de Vaux de Cernay, France, pp. 137-139.

[31] C.H. von Helmolt, et. al., "58-GHz fiber-optic upconverter applicable to wireless communication systems," Tech. Dig. OFC, San Jose, California, 1996, pp. 209-210.

[32] G.H. Smith, et. al., "Full-duplex broadband millimetre-wave optical transport system for fibre-wireless access," IEE Elec. Lett., vol. 33, no. 13, 1997, pp. 1159-1160.

[33] R.-P. Braun, et. al., "Fiber optic millimeter-wave generation at 64 GHz and spectral efficient data transmission for mobile communications," Tech. Dig. OFC, San Jose, California, 1998, pp. 17-18.

[34] J.B. Georges, et. al., "Transmission of 300 Mbit/s BPSK at 39 GHz using feedforward optical modulation," IEE Elec. Lett., vol. 30, no. 2, 1994, pp. 160-161.

[35] G.H. Smith, et. al., "Overcomming chromatic-dispersion effects in fiber-wireless systems incorporating external modulators," IEEE Trans. MTT, vol. 45, no. 8, 1997, pp. 1410-1415.

[36] G.H. Smith, et. al., "Full-duplex fiber-wireless system using electrical and optical SSB modulation for efficient broadband millimeter-wave transport," Proc. IEEE MWP, September, 1997, Dusiburg, Germany, pp. 223-226.

[37] K. Kitayama, "Highly spectral efficient OFDM wireless networks by using optical SSB modulation," Proc. IEEE MWP, September, 1997, Dusiburg, Germany, pp. 231-234.

[38] C. Lim, et. al., "Implementation of an upstream path in a millimeter-wave fiber-wireless system," Tech. Dig. OFC, San Jose, California, 1998, pp. 16-17.

[39] T.N. Nielsen, et. al., "Highly Linear and Transparent 3-18 GHz Optical Microwave Link," Tech. Dig. IEEE MTT-S, May, 1994, San Diego, California, pp. 491-494.

2-Gbit/s Phase Shift Keying Based on Optical Delay Switching for Microwave Optical Link

Seiji Fukushima, Tetsuichiro Ohno, Yoshiyuki Doi,
Yutaka Matsuoka, Hiroaki Takeuchi
NTT Optoelectronics Laboratories
3-1 Morinosato Wakamiya, Atsugi, Kanagawa 243-0198 Japan

Binary phase shift keying is demostrated with the modulation performed by switching optical delays between 0 and π. We achieved modulation up to 2 Gbit/s and error-free transmission through a 5-km single-mode fiber.

I. Introduction

Optics is highly advantageous for generation, modulation, fiber transmission, and amplification in microwave links as well as optical fiber communications. Microwave optical links that carry phase shift keying (PSK) signals have been demonstrated.[1,2] However, the electric PSK modulators used in previous experiments limited the bit rates to a few hundred Mbit/s.We propose novel binary PSK modulation based on optical delay switching, where, except for an optical millimeter-wave (mm-wave) source, high-speed devices operating at a carrier frequency are not needed. This paper also demonstrates a transmission of 2-Gbit/s PSK signal in a microwave optical link.

II. Principle

PSK modulation is made possible by giving phase shifts to a carrier with a delay line, although this has not been widely used because in the conventional frequency ranges the delay line is very long, making it inappropriate for monolithic integration. Now, it has become possible in the mm-wave range.

The proposed PSK modulator configuration is shown in Fig. 1. Key components are the π-delay line and 2x1 switch. Phase delay π is defined in a mm-wave frequency, but not in a light frequency. The optical pulses are divided into two paths. The delay line provides a π-delay only in the upper path. Hence, the phases in the two paths are opposite. The upper path is referred to as '1' and the lower one as '0.' The 2x1 switch selects only one path, according to the input data. This configuration can be easily implemented by using a delay line and two intensity modulators. Its main features are that (a) only performance at the data bit rate is required for the electronic drivers and light modulators, and (b) there are no practical limitations on the carrier frequency. A demerit of this configuration is that the modulator is designed for a certain carrier frequency unless the delay line length is tunable.

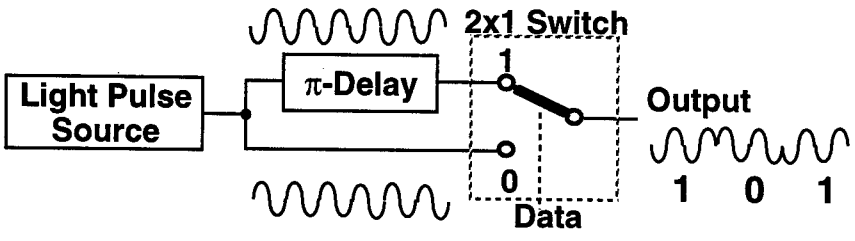

Fig. 1 Block diagram of the PSK modulator.

0-7803-4936-9/98/$10.00 © 1998 IEEE

III. Experiments

A. Setup

Figure 2 shows the experimental setup, which includes three stations--a central station, an access station, and a terminal. A practical application uses antennas between an access station and a terminal, whereas they were directly connetced in this experiment. An integrated light source (ILS)[3,4] consisting of a distributed feedback laser diode (DFB-LD) and an electroabsorption light modulator (EA-Mod) was empolyed to generate optical pulses with mm-wave frequencies. The internal EA modulator has a modulation capability of up to 40 Gbit/s. The light pulses are divided into two paths. The upper path has a variable delay line. A $LiNbO_3$ Mach-Zender intensity modulator (MZ-Mod) is placed in each path, and only one of the switches is ON, according to the input data. The light pulses are combined and amplified by an Erbium-doped fiber amplifier (EDFA). Microwave multiplexing light is transmitted to the access station through an optical fiber. A photodiode (PD) converts light signal into mm-wave one. The signal is demodulated and its error rate is measured at the terminal.

B. Results

PSK modulation was confirmed as oscilloscope traces without fiber transmission, where the sampling oscilloscope replaced the error detector. The carrier and modulation data were fed to the EA-Mod in the ILS and to the two MZ-Mods, respectively. Figure 3(a) shows a response of a 9.54-GHz carrier to a 1.06-GHz

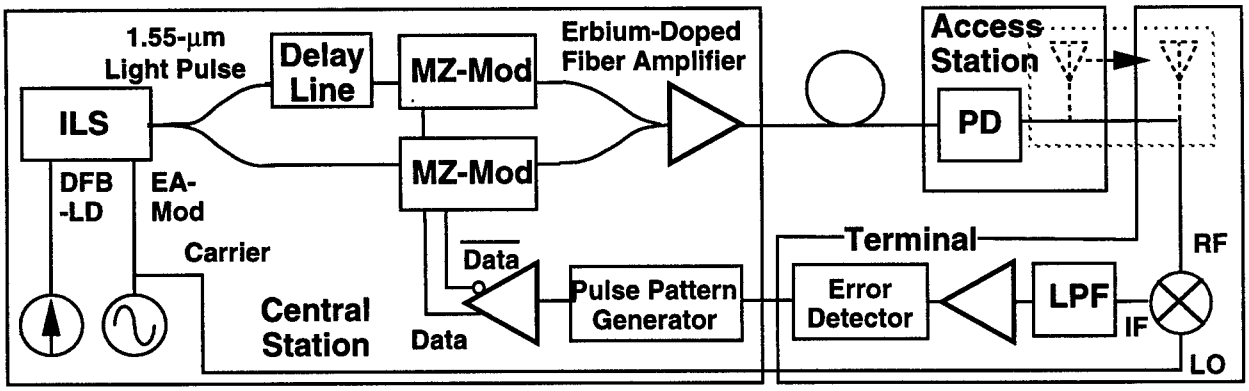

Fig. 2 Experimental setup of an optical PSK modulator and a demodulating apparatus.

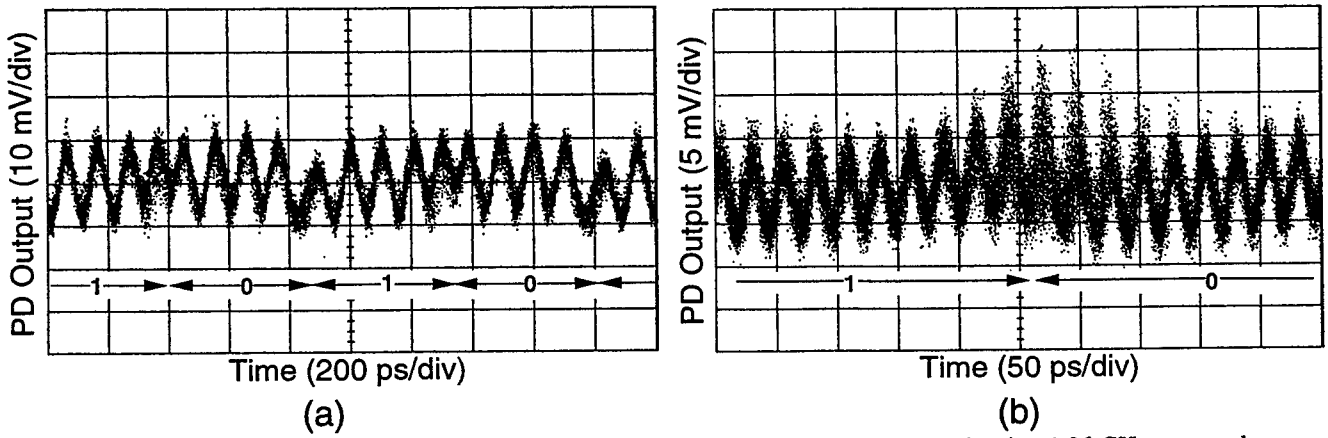

Fig. 3 PSK-modulated light pulses. (a) The carrier frequency is 9.54 GHz and the input data is a 1.06-GHz rectangular wave. (b) The carrier frequency is 38.16 GHz. Phase change is seen near the center. The output voltage in (b) is lower than that in (a) because of the frequency characteristic of PD.

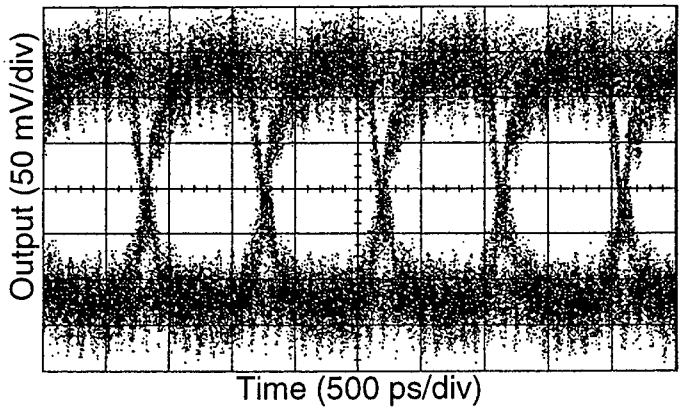

Fig. 4 Eye pattern of the demodulated signal. The carrier frequency is 9.54 GHz and the data is a 1.06-Gbit/s PRBS signal.

rectangular wave. The trace shows that the carrier is PSK-modulated. Phase delays 0 and π appear, corresponding to the input data. PSK modulation was confirmed up to a carrier frequency of 38.16 GHz, as shown in Fig. 3(b). The loss in this modulator section was -15 dB, and it can be compensated by the EDFA.

The PSK signals are demodulated at the terminal. The demodulation was performed by mixing the original carrier and the modulated signal. The eye pattern was observed at the low-pass filter (LPF) input, as shown in Fig. 4. The 9.54-GHz carrier is residual in the eye pattern, but is eliminated at the LPF. Error-free transmission was experimentally confirmed using a 5-km single-mode fiber. At the central station, a 2.12-Gbit/s pseudo-random bit stream (PRBS) was converted to PSK-modulated signal on a 9.54-GHz carrier, and the signal was well demodulated at the terminal after the 5-km transmission. The bit error rate dependence on the light power is shown in Fig. 5. The error rate was 1×10^{-10} at -10 dBm, where the light power was measured at the PD input. The carrier frequency could be higher: it was limited by the mixer performance in the present experiment.

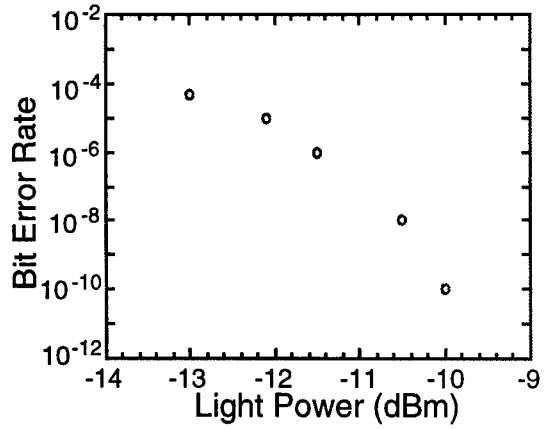

Fig. 5 Bit error rate dependence on the light power.

IV. Summary

In summary, we proposed a binary PSK modulator for a microwave optical link and achieved 2.12-Gbit/s modulation. In a practical demonstration, a mode-locked LD[5] and a uni-travelling-carrier waveguide PD[6] will be used as the source and detector, respectively, because of their capability for high-frequency, high-power operation. This PSK-modulator configuration would be a powerful monolithic integration.

V. Acknowledgment

The authors would like to thank H. Iwamura for his encouragement.

References

1. Z. Ahmed. D. Novak, R. B. Waterhouse, and H.-F. Liu, IEEE Trans. Microwave Theory Tech. 45, 1431 (1997).

2. G. H. Smith, D. Novak, and Z. Ahmed, IEEE Trans. Microwave Theory Tech. 45, 1410

(1997).
3. H. Takeuchi, K. Tsuzuki, K. Sato, M. Yamamoto, Y. Itaya, A. Sano, M. Yoneyama, and T. Otsuji, IEEE Photon. Technol. Lett. 9, 572 (1997).
4. S. Fukushima, E. Sano, Y. Yamane, K. Genda, and T. Matsumura, IEEE Photon. Technol. Lett. 10, 227 (1998).
5. K. Sato, K. Wakita, I. Kotaka, Y. Kondo, and M. Yamamoto, Appl. Phys. Lett. 65(1), 1 (1994).
6. Y. Muramoto, K. Kato, M. Mitsuhara, O. Nakajima, Y. Matsuoka, N. Shimizu, and T. Ishibashi, Electron. Lett. 34, 122 (1998).

SIMULTANEOUS ELECTRO-OPTICAL UPCONVERSION TO 60 GHz OF UNCODED OFDM SIGNALS

Michael Sauer, Konstantin Kojucharow, Heiko Kaluzni, Dirk Sommer, and Walter Nowak

Dresden University of Technology, Communications Laboratory, D-01062 Dresden, Germany

Phone: +49 351 463 5295, Fax: +49 351 463 7163, E-mail: sauer@ifn.et.tu-dresden.de

Abstract

The transmission of 46 MBit/s DQPSK-OFDM signals by simultaneous electro-optical upconversion to 60 GHz has been successfully demonstrated. Bit error rates $<10^{-7}$ were obtained for each of two optical channels.

I. Introduction

Due to the high air link loss at millimeter-wave frequencies, numerous picocells are created in mobile broadband communications systems. In [1], a system concept and transmission experiments are reported using an optical WDM system and simultaneous external modulation with a master local oscillator signal for generating the 60 GHz transmission signal at the base stations electrically. However, for greatly simplifying base station design, optical mm-wave signal transmission is desired.

Many techniques have been proposed for optical mm-wave carrier generation. Simultaneous electro-optical upconversion of IF signals in a WDM system [2] reduces the effort for mm-wave carrier generation significantly by using only one high-speed modulator for several optical channels. In this paper, we report on recent experimental results of optical millimetric upconversion (60 GHz) of two channels each carrying 46 MBit/s OFDM signals. Using this technique, uncoded bit error rates (BER) of $5.6 \cdot 10^{-8}$ have been obtained.

II. System setup for simultaneous upconversion

In order to generate an optical mm-wave signal for direct detection at the base station's site in mobile broadband communications systems, external modulation of laser diodes is a simple, but powerful technique. Whereas in most system demonstrations the laser is merely used as light source emitting a CW signal and the mm-wave carrier as well as the datas are imprinted by means of external modulation, IF signal upconversion of a directly modulated laser diode was demonstrated in [3]. This technique is attractive, since DFB lasers show excellent modulation characteristics in terms of linearity (low IMD distortion), power and bandwidth. By use of an external electro-optical modulator (EOM), this optical IF modulation can be easily upconverted to mm-wave frequencies without signal distortion. The strong nonlinear electro-optical characteristic of external modulators generates only harmonics of the modulation frequency applied to the device, but does not distort the optical signal fed into the EOM.

Due to the high number of picocells in mm-wave communications systems, cost-effective solutions for feeding the base stations are required. If external upconversion is simultaneously applied by a single EOM to a number of optical WDM channels carrying individual IF signals, a significant reduction of high-speed components within the system is achieved. In such a system, the optical channels are assigned to certain base stations by their wavelengths. All components (apart from the high-speed EOM) within the optical network - multiplexers, demultiplexers as well as wavelength-selected laser diodes - are standard WDM components being readily available. Furthermore, optical amplification can be appied by use of a single erbium-doped fiber amplifier (EDFA) for all channels. However, in spite of using a single EOM for the several channels, system flexibility is not affected. Individual transmission frequencies within picocells are achieved by individual IF frequencies and there is no crossstalk due to the simultaneous external modulation. In uplink mode, a stable mm-wave tone at the base station site for electrically downconverting the received signal can be easily obtained by

0-7803-4936-9/98/$10.00

switching off the IF modulation and using the laser diode as CW light emitter and the EOM for imprinting the mm-wave tone. There is no synchronization required between the different channels.

A block diagram of the experimental setup is shown in Fig. 1. Two DFB laser diodes (LD 1 and LD 2) with slightly different emission wavelengths ($\Delta\lambda$ = 1.6 nm) were directly modulated with a 46 MBit/s OFDM signal at f_{IF} = 2.268 GHz. Signal decorrelation of the two optical channels was obtained by introducing 50 m of optical fiber after laser diode LD 1. After individual polarization control of the optical signals (not shown in Fig. 1), being required by the electro-optical modulator, the signals were combined using a 50/50 coupler. Then, the optical signals were fed into a high-speed Mach-Zehnder intensity modulator for simultaneous electro-optical upconversion to 60 GHz.

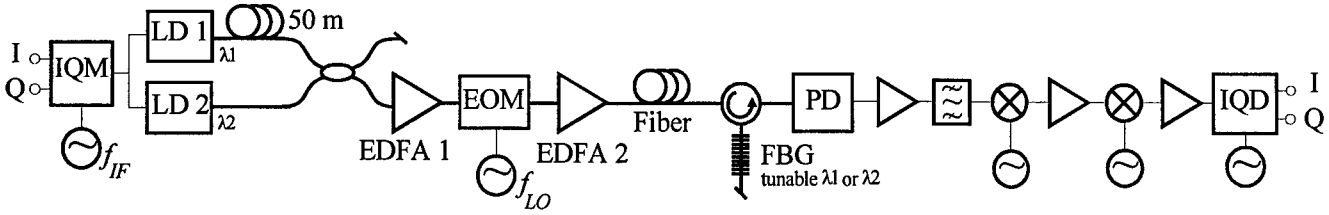

Fig. 1: Experimental setup for transmission experiments using simultaneous upconversion of two optical channels.

In general, any external modulation scheme can be applied. This could be modulation with a 60 GHz tone with the EOM biased at quadrature. Apart from the very high modulation frequency (and very high-speed EOM required), signal transmission would be highly dispersion-dependent [4]. This could be overcome by external single-sideband modulation [5]. In order to reduce the modulation frequency, in this paper double-sideband modulation with suppressed carrier has been used. The device was biased at V_π and modulated with a f_{LO} = 28.800 GHz tone. This results after detection in a mm-wave signal at $2 \cdot f_{LO} + f_{IF}$ = 59.868 GHz for each of the optical channels. However, for future transmission experiments, a technique for dispersion-independent mm-wave transmission using phase modulation at Ka-band and optical filtering [6] will be used. By direct detection, a mm-wave data signal having 6 dB more power (at the same modulation depth) compared to a Mach-Zehnder device is received.

In order to increase the power detected, optical amplification before and after the EOM was used. A tunable fiber Bragg grating with a transmission bandwidth of Δf_{-1dB} = 67.3 GHz and a side lobe suppression of >25 dB in combination with an optical circulator was used as demultiplexer. By tuning the Bragg grating, either the channel at λ1 or the channel at λ2 could be selected without any change of the experimental setup. The optical mm-wave signal was received by a high-speed photodetector followed by a low-noise V-Band amplifier (NF = 6 dB) and a double-conversion receiver with subsequent quadrature-demodulation, baseband filtering, A/D-sampling and further baseband processing. The bit error rate was detected utilizing a pseudo-random bit sequence of length $2^{32}-1$.

III. Experimental results and discussion

The OFDM signal modulation format utilized throughout the experiments was 512 carrier differential π/4-PSK being generated by means of a vector modulator (at f_{IF}). No signal coding and/or error correction were used in order to evaluate the optical link performance as well as RF and baseband components.

For first transmission experiments, only one optical channel was used. Apart from the 50/50 coupler and EDFA 1, the setup was the same as shown in Fig. 1. A maximum modulation power of +7 dBm could be applied for modulating the laser diode in order to avoid an increased BER due to intermodulation distortion. For modulating the external Mach-Zehnder modulator, a drive power of approximately +19 dBm was available at f_{LO} = 28.800 GHz. This resulted in a low EOM modulation index. Increased modulation power would result in improved detected power without generation of signal intermodulation distortion within the IF channel bandwidth, but harmonics of the 28.8 GHz modulation tone. However, these harmonics are uncritical since they are filtered out by the demultiplexer.

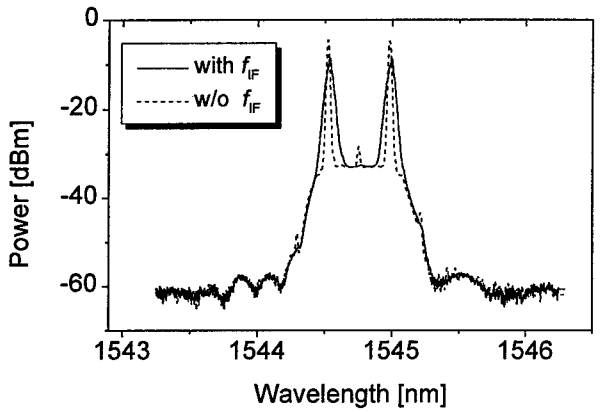

Fig. 2: Optical spectrum before detection.

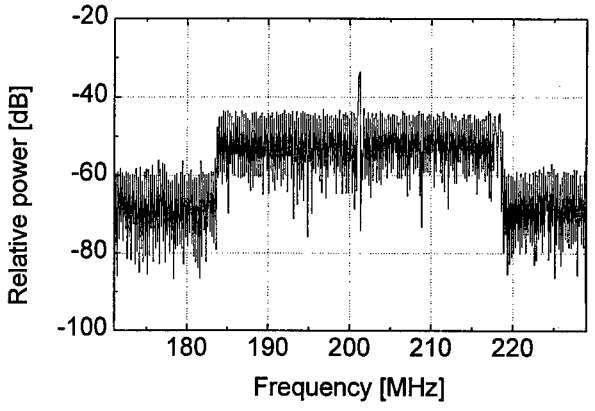

Fig. 3: Received OFDM spectrum @ BER < 10^{-7}

In order to increase the detected mm-wave power, optical amplification ($G = 30.3$ dB) after external modulation was used. The received optical spectrum with one optical channel (after amplifier noise filtering using the demultiplexer Bragg grating) is shown by the solid line in Fig. 2. The optical carrier is strongly suppressed and only the f_{LO} modulation sidebands appear. The IF modulation cannot be resolved, but the dashed line shows the spectrum at switched-off IF modulation for comparison. The total electrical power detected at $2 \cdot f_{LO} + f_{IF} = 59.868$ GHz was –64 dBm for an uncoded bit error rate of $7.8 \cdot 10^{-8}$. The OFDM spectrum received and downconverted to 200 MHz is shown in Fig. 3. The occupied bandwidth is 35 MHz, with a subcarrier spacing of $\Delta f = 78.125$ kHz. In Fig. 4, the BER vs. SNR, measured at baseband subsystem, is depicted.

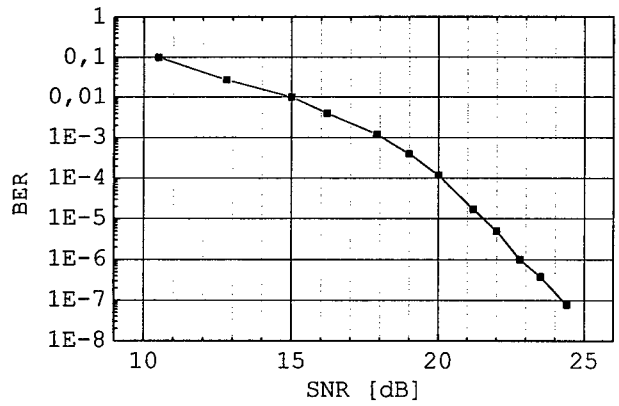

Fig. 4: BER vs. SNR for one optical carrier.

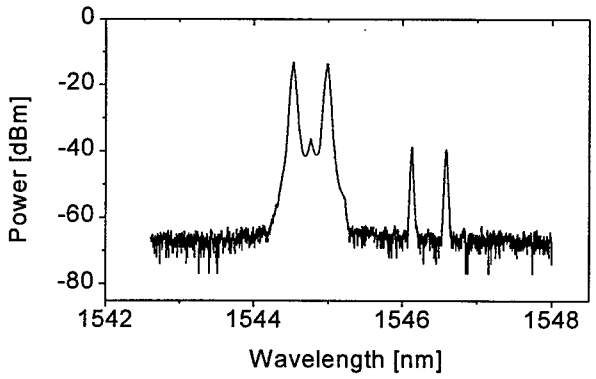

Fig. 5: Received optical spectrum with two channels.

Further experiments with two optical carriers (channel spacing 200 GHz) were carried out demonstrating simultaneous upconversion, see Fig. 1. In this case, an additional optical amplifier (EDFA1) had to be introduced for loss compensation. The received optical spectrum is shown in Fig. 5. As can be seen, one optical channel is suppressed by approximately 25 dB due to demultiplexing. Measurements for both optical channels were obtained by tuning the Bragg grating's center wavelength either to $\lambda 1$ or to $\lambda 2$. For channel 1 as well as channel 2, uncoded BER of $<10^{-7}$ were obtained simply by

tuning the Bragg filter. For channel 1, a BER of $5.6 \cdot 10^{-8}$ was reached with a SNR of 28 dB, which is a penalty of approximately 3 dB compared to the experiments with one laser diode.

IV. Conclusions

Electro-optical upconversion to 60 GHz of an optical signal carrying uncoded 46 MBit/s DQPSK-OFDM modulation at $f_{IF} = 2.268$ GHz has been successfully demonstrated. A complete mm-wave system setup has been realized including signal modulation, electro-optical upconversion, optical amplification, demultiplexing, photodetection, and electrical downconversion. In transmission experiments, BER $<10^{-7}$ have been obtained. Further experiments using two laser diodes for simultaneous electro-optical upconversion and alternatively receiving channel 1 or channel 2 showed the feasibility of this technique. A BER of $5.6 \cdot 10^{-8}$ was achieved with a SNR of 28 dB.

Acknowledgment

The project is supported by German Research Council (DFG) under contract INK 13.

References

[1] K. Kojucharow, H. Kaluzni, M. Sauer, W. Nowak: "A Wireless LAN at 60 GHz - Novel System Design and Transmission Experiments", IEEE MTT-S International Microwave Symposium, TH3C-2, Baltimore, USA, 1998

[2] M. Sauer, W. Nowak: "Simultaneous upconversion of several channels in mm-wave subcarrier transmission systems for wireless LANs at 60 GHz", International Topical Meeting on Microwave Photonics (MWP), FR1-1, Duisburg/Essen, Germany, 1997

[3] J. Park, M. S. Shakouri, K. Y. Lau: "Millimetre-wave electro-optical upconverter for wireless digital communications", *Electronics Letters*, vol. 31, no. 13, pp. 1085-1086, 1995

[4] H. Schmuck: "Comparison of optical millimetre-wave system concepts with regard to chromatic dispersion", *Electronics Letters*, vol. 31, no. 21, pp. 1848-1849, 1995

[5] G. H. Smith, D. Novak, Z. Ahmed: "Technique for optical SSB generation to overcome dispersion penalties in fibre-radio systems", *Electronics Letters*, vol. 33, no. 1, pp. 74-75, 1997

[6] M. Sauer, W. Nowak: "Simultaneous upconversion by phase modulation for dispersion-independent optical mm-wave transmission", 24th European Conference on Optical Communication (ECOC), TuD15, Madrid, Spain, 1998

FADING-FREE TRANSPORT OF 60GHz-OPTICAL DSB SIGNAL IN NON-DISPERSION SHIFTED FIBER USING CHIRPED FIBER GRATING

Ken-ichi Kitayama

Communications Research Laboratory
Ministry of Posts and Telecommunications
4-2-1, Nukui-Kitamachi, Koganei-shi, Tokyo 184-8795, Japan
Phone: 81-42-327-6209, Fax: 81-42-327-7035, Email: kitayama@crl.go.jp

I. Introduction

In radio-on-fiber mm-wave wireless access networks, the external modulation technique is promising. Because it will potentially provide low-cost antenna base stations due to its simplicity, compared to the other techniques including optical self-heterodyning and electrical or optical frequency up- and down-conversion techniques[1]. However, the external modulation basically generates the optical double sideband(DSB) signal. Its transmission over non-dispersion shifted single-mode fiber(SMF) causes periodic fading of mm-wave signal along the fiber due to the fiber dispersion. Optical single sideband(SSB) signal can overcome this fading problem[2]~[5]. However, there still remain some difficulties in the generation techniques of optical SSB signal.

In this paper, fading cancellation for 60GHz optical DSB signal transmission in a long non-dispersion shifted SMF in 1550nm wavelength region is experimentally demonstrated for the first time by using a chirped FGR. Hence, the optical DSB signal transmission will become one of the most practical options for mm-wave radio-on-fiber wireless access systems.

II. Principle

As shown in Fig.1, in a non-dispersion shifted SMF the lower sideband(LSB) wave of the optical DSB signal lags behind the upper sideband(USB) wave during the propagation in the longer wavelength region above 1300nm. The square-law detection of the optical DSB signal generates the beat of the two mm-waves which are originated from the LSB and USB. The beat causes the fading of the mm-wave signal periodically along the fiber axis[6].The basic mechanism of the dispersion compensation using the FGR is schematically shown in Fig.2. In the chirped FGR, the period of grating almost linearly changes along the fiber axis. Assume that the gratings with the periods of Λ^- and Λ^+, which reflect off the LSB and USB of the optical DSB signal, be positioned near the input end and the far end, respectively. The periods $\Lambda^{\pm}$ must satisfy the diffraction condition;

$$\Lambda^{\pm} = \frac{\lambda}{2n_e} = \frac{c}{2n_e(f_0 \pm f_m)} \tag{1}$$

where λ , f_0 , n_e, and f_m, are the wavelength and the optical frequency of light source, the effective refractive index of FGR, and the mm-wave subcarrier frequency, respectively. By inserting the FGR in the optical fiber link, therefore, the group delay difference between the LSB and USB caused by the fiber dispersion can be compensated.The length of FGR has to be determined in the following manner.

Suppose that the electric field of intensity-modulated lightwave be written[7]

$$E = \sqrt{I}e^{j\phi(I)} \quad , \quad I = I_0\left(1 + m\cos 2\pi f_m t\right) \tag{2}$$

where I is the intensity, $\phi(I)$ the phase of the lightwave, and m the modulation depth. After propagating in the optical fiber and the FGR, the mm-wave signal power is given by

$$P = 2mI_0\sqrt{1+\alpha_H{}^2}\cos\left\{\frac{\pi\lambda^2 f_m{}^2}{c}\left(DL + \tilde{D}l\right) + \tan^{-1}\alpha_H\right\} \tag{3}$$

0-7803-4936-9/98/$10.00

where D and $\tilde{D}$ and L and l denote the dispersions and the lengths of the fiber and FGR, respectively, and α_H the chirp parameter. Here the dispersion slopes, that is, quadratic dispersions, of both the fiber and FGR are neglected. The separation between the above two gratings has to satisfy the following condition;

$$\frac{c}{\lambda^2 f_m^{\,2} D}\left(DL+\tilde{D}l\right)+\tan^{-1}\alpha_H = q\pi,\ (q=1,2,...). \quad (4)$$

In the practical system design, given a fiber length L and a mm-wave frequency f_m a perfect compensation for the fiber dispersion can be made by choosing the overall dispersion value $\tilde{D}l$ of FGR across the frequency span of $2f_m$ so that Eq.(4) is satisfied. Therefore, it is practically important to evaluate the tolerance of the regenerated mm-wave signal power to the deviations of length Δl and dispersion $\Delta\tilde{D}$ of FGR. From Eq.(3) the relation between these deviations and the normalized signal power can be derived as

$$\eta = \cos\left\{\frac{\pi\lambda^2 f_m^{\,2}\tilde{D}l}{c}\left(\frac{\Delta l}{l}+\frac{\Delta\tilde{D}}{\tilde{D}}\right)\right\}\ (0\leqq\eta\leqq 1). \quad (5)$$

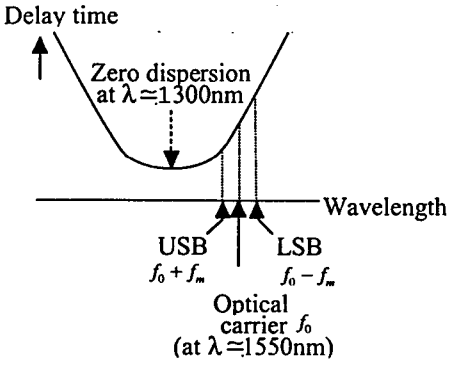

Fig.1 Group delays of the LSB and USB of optical DSB signal in non-dispersion shifted single-mode fiber in 1550nm wavelength region.

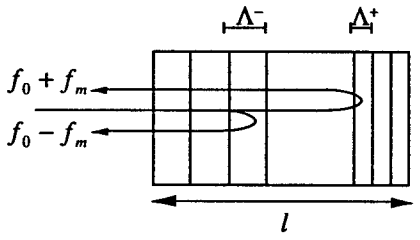

Fig.2 Schematic of chirped fiber grating and the compensation of the group delay differenece between the LSB and USB of optical DSB signal.

To maintain, for example, η of 0.9, the sum of $\Delta l/l$ and $\Delta\tilde{D}/\tilde{D}$ must be smaller than 0.83%. For the test FGR used in the experiment, $\Delta l/l$ of 0.83% amounts to 0.12mm, and this could be within a control in the FGR fabrication process. In the calculations of Eq.(5), the dispersion of fiber grating is assumed to be 600ps in the frequency span of $2f_m$=120GHz, and λ=1550nm. The relation between the wavelength deviation Δl of light source and the normalized signal power η is expressed as

$$\eta = \cos\left\{\left(\frac{2\Delta\lambda}{\lambda}+1\right)q\pi\right\} \quad (6)$$

The wavelength deviation causes little signal degradation; η's are kept to be 0.995 and 0.95 for $\Delta\lambda/\lambda$=0.9x10^{-3} and 3.0x10^{-3}. These values correspond to significantly large wavelength deviations of 1.4nm and 4.7nm at λ =1550nm, respectively . Therefore, the wavelength deviation of light source will not be a serious problem provided that the quadratic dispersion of FGR is neglected.

III. Experiment

The experimental setup for the bit error rate(BER) measurement is shown in Fig.3. The FGR may be inserted anywhere from the input to the output of the optical fiber link. The measured group delay of the test FGR is plotted as a function of the wavelength in Fig.4(a). The group delay of test 36km-long SMF is also plotted. The group delay difference of 600ps between the LSB and USB over the frequency span of 120GHz (=0.96nm) should be compensated by setting the wavelength of light source at λ =1548.8nm. The measurement result of reflectivity of the FGR is also plotted as a function of the wavelength in Fig.4(b).The chirped grating extends over 14.5mm along the fiber axis. The overall insertion loss including the optical circulator loss is as low as 1.5dB. A specially designed 60GHz-band InGaAsP electroabsorption(EA) modulator module is used as the EO converter[5]. A cw DFB laser diode is used as the light source. The input optical power to the EA modulator is 6dBm. A pin photodiode having 3dB

bandwidth of 50GHz is used as the OE converter.

The BER measurements are made for the fiber lengths of around 36km. NRZ 2^{23}-1 PRBS 156Mbit/s signal in a DPSK format at the intermediate frequency(IF) of 2.6GHz is combined and upconverted by mixing with the local oscillator(LO) of 57.0GHz. The mm-wave data signal is applied to the EA modulator, and then the optical DSB signal is produced. The RF power of 5dBm is applied to the EA modulator. Both the optical DSB signal spectra and RF spectra of 59.6GHz carriers with and without FGR after the propagation are shown in Figs.5(a) and (b), respectively. In Fig.5(a) the RF carrier intensity at f_m=59.6GHz is maximized for L=35.0km without the FGR.

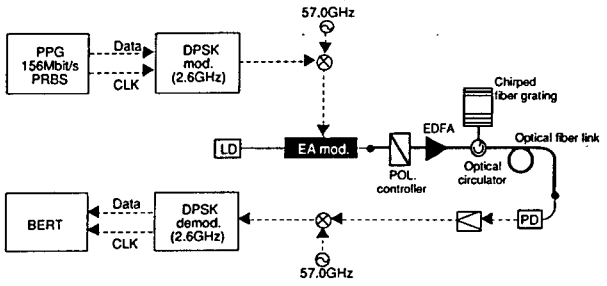

Fig.3 Experimental setup for measuring BER.

Measured BER's with and without FGR are plotted as a function of the received optical power in Fig.6. Without the FGR, no signal is detected at L=36.0km, and the BER is minimized for L=35.0km. With the FGR, on the contrary, BER<10^{-9} is obtained even at L=36.0km, and BER only slightly degrades as the fiber length becomes shorter. Thus, the fading-free transmission by using FGR is confirmed.

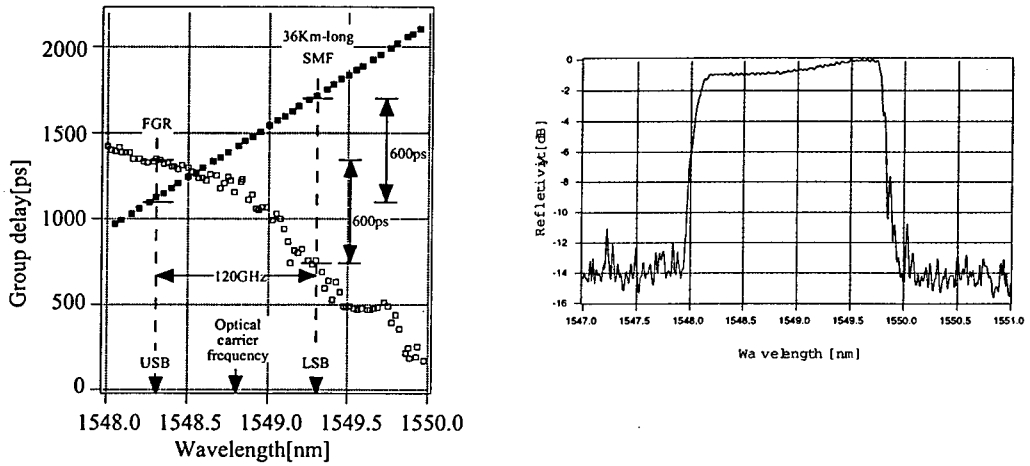

Fig.4 Characteristics of the test FGR; (a)Measured group delays of FGR and test 36.0km-long non-dispersion shifted SMF vs. wavelength, and (b)measured reflectivity vs. wavelength.

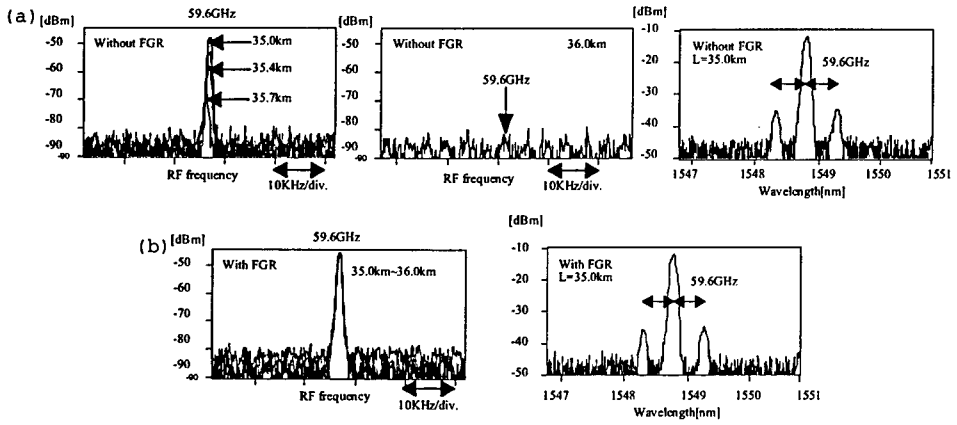

Fig.5 Optical spectra of optical DSB signal and RF spectra of 59.6GHz carriers after the propagation, (a)with and (b)without the FGR.

IV. Conclusion

Fading-free transmission of 60GHz optical DSB signal over a chirped FGR-inserted 36.0km-long non-dispersion shifted SMF link in 1550nm wavelength region has been experimentally demonstrated. Due to the low insertion loss and 1.5nm wide utilizable spectral range of FGR as well as the simple system configuration of the external modulation, the optical DSB signal transmission by using the chirped FGR will become a very practical option for radio-on-fiber mm-wave wireless systems.

Finally, an EA modulator is particularly suitable for the external modulation. Recent progress in simultaneous operation of EA transceiver as the OE- and EO conversions[8],[9], along with a potential progress of MMIC technologies[10] in near future will strongly suggest that the cost of the antenna base stations of micro- or picocellular mm-wave radio-on-fiber wireless access systems can be driven down to reasonable prices so as to accelerate a huge number of the initial deployments.

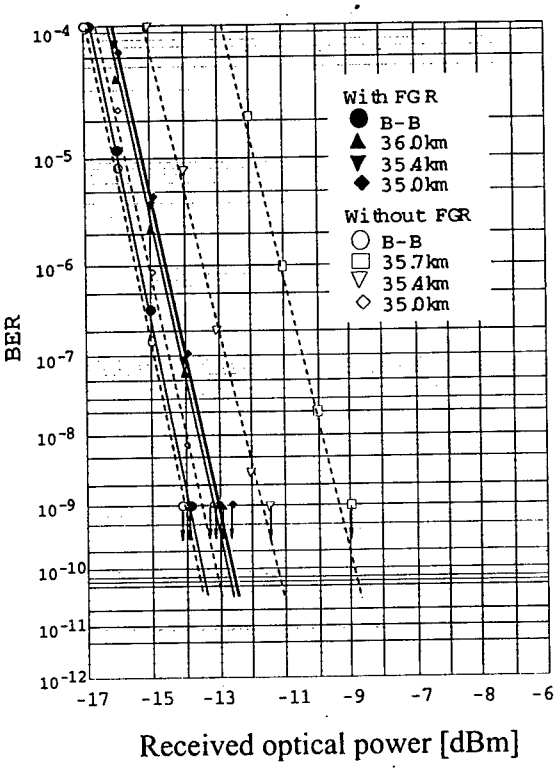

Fig.6 Measured BER's with and without FGR vs. received optical power.

Acknowledgment

The author would like to thank R. Yamauchi and A. Wada of Fujikura Ltd. for providing the fiber grating and their useful discussions. His thank is also due to H.Fukuchi and Y.Furuhama of CRL for their encouragement.

References

[1] K. Kitayama, "Architectural considerations of radio-on-fiber millimeter-wave wireless access systems," to be present in *ISSSE'98*,1998 (Pisa).

[2] G. H. Smith, D. Novak, and Z. Ahmed, "Technique for optical SSB generation to overcome fiber dispersion penalties in fibre-radio system," *Electron. Lett.*, vol. 33, pp. 74-75, 1997.

[3] K. Kitayama, "Highly Spectral Efficient OFDM/PDM Wireless Networks by using Optical SSB Modulation," *J. Lightwave Technol.*, vol. 16, pp.969-976, 1998.

[4] J. Park, W. V. Sorin, and K. Y. Lau, "Elimination of the fibre chromatic dispersion penalty on 1550nm millimetre-wave optical transmission," *Electron. Lett.*, vol. 33, pp. 512-513, 1997.

[5] K. Kitayama, T. Kuri, and Y. Ogawa, "Error-free optical 156Mb/s millimeter-wave wireless transport through 60GHz external modulation," *OFC'98*, TuC2,1998 (San Jose).

[6] R. Hofstetter, H. Schmuck, and R. Heidemann, "Dispersion effects in optical millimeter-wave systems using self-heterodyne method for transport and generation," *IEEE Trans. Microwave Theory Tech.*, vol. 43, pp. 2263-2269, 1995.

[7] F.Devaux, Y.Sorel, and J.F.Kerdiles, "Simple measurement of fiber dispersion and of chirp parameter of intensity modulated light emitter," *J.Lightwave Technol.*, vol.11, pp.1937-1940, 1993.

[8] L. Noël, D.Wake, D.G.Moodie, D.D.Marcenac and D.Nesset, "Novel Techniques for High-Capacity 60GGHz Fiber-Radio Transmission Systems," *IEEE Trans. on Microwave Theory and Technol.*, vol.45, pp.1416-1423, 1997.

[9] A. Stöhr, K. Kitayama, and D. Jäger, "Error free full duplex optical WDM-FDM transmission using an EA-transceiver," to be presented in *MWP'98*,1998.

[10] L. Raffaelli, "Millimeter-wave automotive radars and related technology," *1996 IEEE-MTT-S International Micro wave Symposium Digest*, pp.36-39, 1996.

Generation, Routing, and Detection of 100 GSa/s Arbitrary Analog Optical Waveform Packets Using Analog Optical TDM

Paul Toliver, Robert J. Runser, Kung-Li Deng, Ivan Glesk, and Paul R. Prucnal
Department of Electrical Engineering, Princeton University, Princeton, NJ 08544
Tel: 609-258-2041 Fax: 609-258-2158 email: ptoliver@ee.princeton.edu

I. Introduction

The recent advances and innovations in digital fiber optics have significantly increased the potential use of lightwave technology for a variety of microwave photonics applications. Examples include ultrafast analog optical communication networks, high-bandwidth CATV distribution networks, remote antenna routing and processing, and phased array antenna signal generation and processing. For the more complex system applications that are required to control the routing of either the distribution or the reception and processing of analog waveforms, a number of key subsystems are required in the network. Depending upon the application, some of the subsystems required may include optical packet generation at the source, all-optical routing within the network, and finally ultra high-speed detection and sampling at the destination. This paper presents a few examples of devices and systems that enable the generation, routing, and processing of 100 GSa/s arbitrary waveform packets using a novel technique referred to as analog optical time-division multiplexing (AOTDM).

II. System Overview

Recently, a packet-switched optical networking demonstration (*POND*) node was constructed at Princeton University to demonstrate the capabilities of ultrafast optical TDM (OTDM) techniques for fiber optic networks [1]. The initial demonstrations of the network were geared towards high-speed digital computer interconnection networks in which data is maintained in the all-optical form from source to destination. In this work, however, we explore the use of the *POND* network for analog applications by combining a 100 Gbit/s digital packet header with a 100 GSa/s analog payload resulting in an analog optical TDM packet. Each node in the mesh-based network topology has the capability to route incoming optical packets to the node's output ports based upon the digital packet header information as well as generate local packets of its own. When a packet that is traversing the network finally reaches its destination, the analog packet payload must be received at that node and the packet is removed from the network.

The optical packet format for the network demonstration of analog packet routing is illustrated in Fig. 1. It consists of a digitally modulated packet address header followed by an analog-modulated packet payload. The envelope of the packet information is encoded onto a high repetition rate optical pulse stream. In order to generate 100 GSa/s analog packets, it is necessary for the inter-pulse spacing to be exactly 10 ps. For this spacing, the maximum pulse width is limited to approximately 2 ps to prevent significant pulse overlap that would cause inter-symbol crosstalk. Since no laser sources are currently available with 100 GHz repetition rates, and in addition, there are currently no modulators that are able to encode information onto such a high repetition rate pulse stream, it is necessary to devise a scheme to create the required high-

0-7803-4936-9/98/$10.00

bandwidth packets. Therefore, our lab has developed a novel packet compression device [2], as illustrated in Fig. 2, in order to create the 100 GSa/s AOTDM packets.

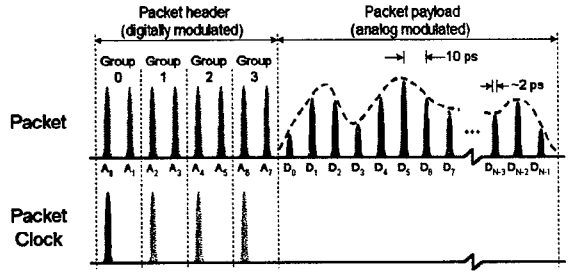

Fig. 1: Packet composed of digital header followed by analog packet payload

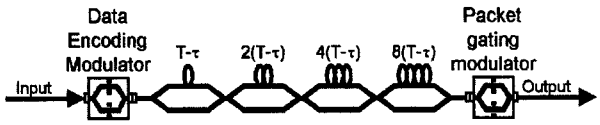

Fig. 2: Packet compression device for creating arbitrary 16-sample waveforms

The packet compressor design shown allows the compression of an arbitrary 16-sample packet at 100 MSa/s into an ultra high-speed 100 GSa/s packet. This operation of the device is illustrated schematically in Fig. 3. For reference, the variable T represents the pulse spacing of the slow (i.e. 10 ns) input pulse steam, and τ is the pulse spacing of the fast (i.e. 10 ps) output pulse stream. The uppermost waveform represents a relatively slow modulation envelope being encoded onto a 100 MHz optical pulse stream using the data encoding modulator of the packet compressor. By using a series of feed-forward fiber optic delay lines, each pulse at the output of the data encoding modulator is replicated 16 times with a spacing (T-τ) between each identical copy. In Fig. 3, a few sets of pulse copies from pulses 1, 2, and 16 of the original 100 MHz input packet are shown along with there relative timing relationships. The net result seen at the output of the delay line structure is a superposition of all the individual pulse copies. In the illustration, it is clear that it is necessary to provide a packet gating function to allow only the packet of samples which contains all of the original 16-samples in the correct sequence, although they are packed 1000 times tighter. The packet gating modulator provides this functionality. Finally, the lower signal in Fig. 3 illustrates the desired 100 GSa/s arbitrary waveform that is generated at the output.

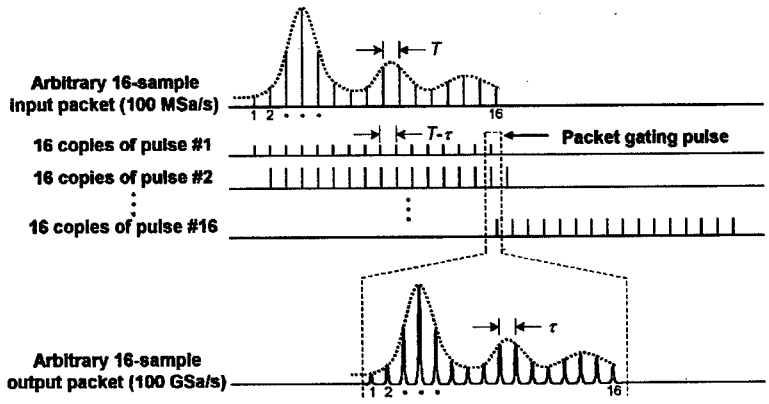

Fig. 3: Illustration showing operation of the optical packet compressor. The input signal of the device is shown at the top of the figure, and the compressed output waveform is shown at the bottom.

Once the packet has been generated, it is necessary to read the ultra high-speed header bits at intermediate nodes of the network to control the routing of the packet as well as extract the analog packet payload once it finally reaches its destination. The terahertz optical asymmetric demultiplexer (TOAD), illustrated in Fig. 4, is a high speed all-optical switching device and can perform the tasks of both an ultrafast digital packet header demultiplexer [3], as well as an ultrafast analog optical sampling gate [4]. The TOAD is a nonlinear interferometer that takes advantage of semiconductor nonlinearities in order to create an ultrafast switching window in time, which allows incoming data to be gated to the output only when a clock pulse is present. Fig. 5 illustrates a typical example of the time-resolved switching window achievable with the TOAD. This illustration shows a switching window with a FWHM of approximately 13 ps; however, we have demonstrated switching windows as short as 4 ps experimentally [3].

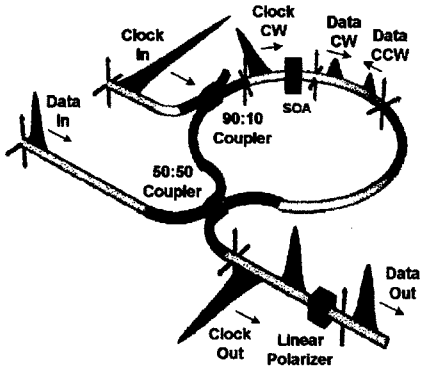

Fig. 4: Illustration of terahertz optical asymmetric demultiplexer (TOAD) and its operation.

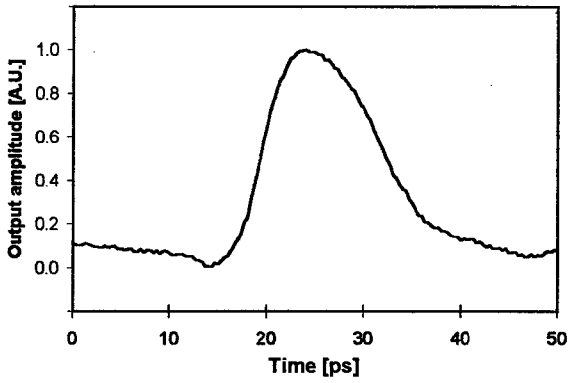

Fig. 5: Typical time-resolved switching window achievable with the TOAD.

III. Experimental Demonstration

A simplified block diagram illustrating the major subsystems of the *POND* network to enable the generation, routing, and detection of 100 GSa/s arbitrary analog waveforms is shown in Fig. 6.

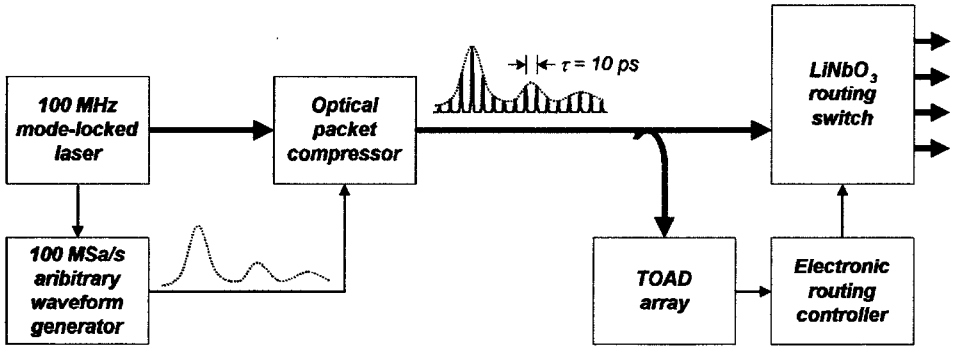

Fig. 6: Block diagram of the major subsystems in the network.

Two examples of experimental demonstrations to generate and sample an arbitrary analog packet waveform are illustrated in Fig. 7. The dashed lines in the figures represent the original analog modulation envelopes whereas the solid lines correspond to the output detected from the TOAD. The first figure demonstrates the generation and sampling of a compressed 12.5 GHz sinusoidal waveform, and the second figure illustrates the technique using a 12.5 GHz sawtooth waveform. The detected waveforms were obtained using a TOAD with a 10 ps gating window and moving the TOAD clock pulse in time relative to the packet in order to map out the detected waveform intensity.

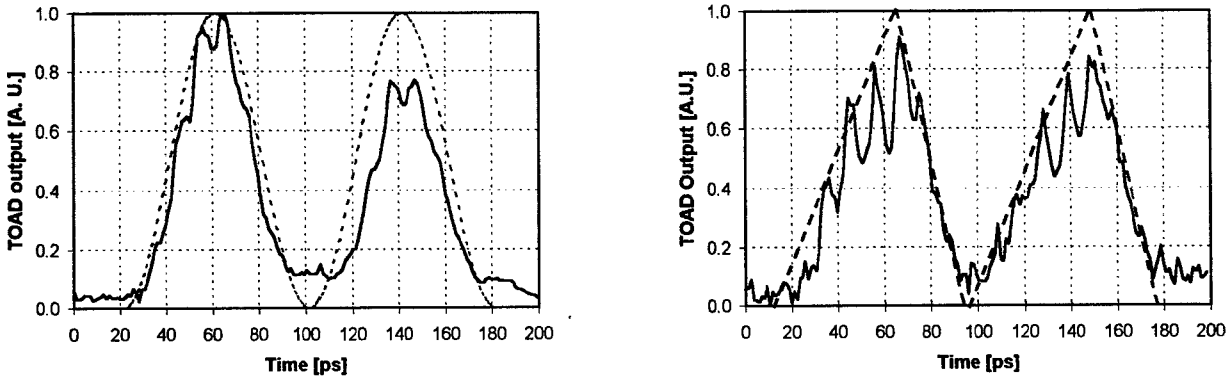

Fig. 7: Examples of detected 100 GSa/s arbitrary analog packet payloads

IV. SUMMARY

This paper has introduced the concept of applying ultrafast optical TDM techniques to enable the generation and detection of high-bandwidth analog waveform packets. Initial experiments with the analog optical TDM (AOTDM) system shows that these techniques can provide a great deal of control on the waveform profile. In addition, by appending the analog waveform to a high-speed digital header, more complex system functions, such as self-routing of analog waveforms throughout an interconnection network, are made possible.

REFERENCES

1. B. Y. Yu, P. Toliver, R. J. Runser, K. Deng, D. Zhou, I. Glesk, and P. R. Prucnal, "Packet-switched optical networks," *IEEE Micro*, vol. 18, pp. 28-38, Feb. 1998
2. K. L. Deng, K. I. Kang, I. Glesk, P. R. Prucnal, and S. Shin, "Optical packet compressor for ultrafast packet-switched optical networks", *Electron. Lett.*, vol. 33, pp. 1237-1238, July 1997
3. I. Glesk, J. P. Sokoloff, and P. R. Prucnal, "Demonstration of all-optical demultiplexing of TDM data at 250 Gbit/s," *Electron. Lett.*, vol. 30, pp. 1322-1323, Feb. 1994
4. K. L. Deng, R. J. Runser, I. Glesk, and P. R. Prucnal, "Single-shot optical sampling oscilloscope for ultrafast optical waveforms", *IEEE Photon. Technol. Lett.*, vol. 10, pp. 397-399, March 1998

State of the Art Laser Sources for High Bit Rate, Long Haul Fiber Optic Communications Systems

W. D. Johnston, Jr.

Lucent Technologies—Bell Labs
Murray Hill, NJ USA

The worldwide voice and data telecommunications network operates over optical fiber cable using semiconductor lasers emitting at wavelengths near 1.55 micrometer wavelength. Spans up to 640 kilometers are served, without electronic regeneration, using erbium-doped optical fiber amplifiers. Typically, a number of wavelength "channels" are multiplexed together and sent over a single fiber strand. The number of channels so multiplexed has grown from 8 to 16 in systems installed in 1997, to 40 for systems in 1998 to 80 or more in 1999 systems. Each channel carries 2.5 or 10 Gbits/sec. of information.

Such systems require semiconductor lasers in the optical transmitter assemblies with precisely controlled properties. The channels are spaced by as little as 50 GHz, and the optical frequency must be controllable and stable to a small fraction of this number over a projected system lifetime of ~25 years. At the same time the high frequency stability of the laser transmitter output (freedom from "chirp") under modulation is essential so that residual dispersion in the fiber does not degrade the signal beyond system limits.

These requirements are being met today for 10 Gb systems with highly stable DC lasers and external $LiNbO_3$ modulators. For 2.5 Gb systems, a laser chip integrating a DC-operated Distributed Feedback (DFB) laser with an electroabsorption modulator on a single InP abased chip provides a compact and cost effective alternative. This structure typically is fabricated using selected area metallorganic CVD epitaxy and incorporates a sophisticated strained multi-quantum well structure in both laser and modulator sections. Control of the composition of the quaternary InGaAsP layer compositions to a fraction of an atomic percent, and of many of the twenty-odd layer thicknesses to a few tenths of a nanometer is mandatory for acceptable performance.

From a research point of view, the challenges posed by the needs for such single wavelength electroabsorption modulated laser (EML) devices have all been solved, but there remain significant engineering issues centered around the manufacturability of such sophisticated designs. The world market for these devices is highly competitive, and there are significant business challenges as well. For the future, still higher bit rates, and/or more wavelengths/channels spaced more closely will be required. Meeting these challenges will require further optoelectronic integration at the chip level, and possibly new, multiple selectable wavelength or tunable wavelength designs, as well as ever more precise control of the manufacturing technology and processes.

0-7803-4936-9/98/$10.00

WDM

Goals for Signal Source:

- All ITU Wavelengths
- Accurate to 1 part in 15,000
- With high-speed digital data on each wavelength and low chirp
- Wavelengths stable to 2 parts in 15,000 for 25 years

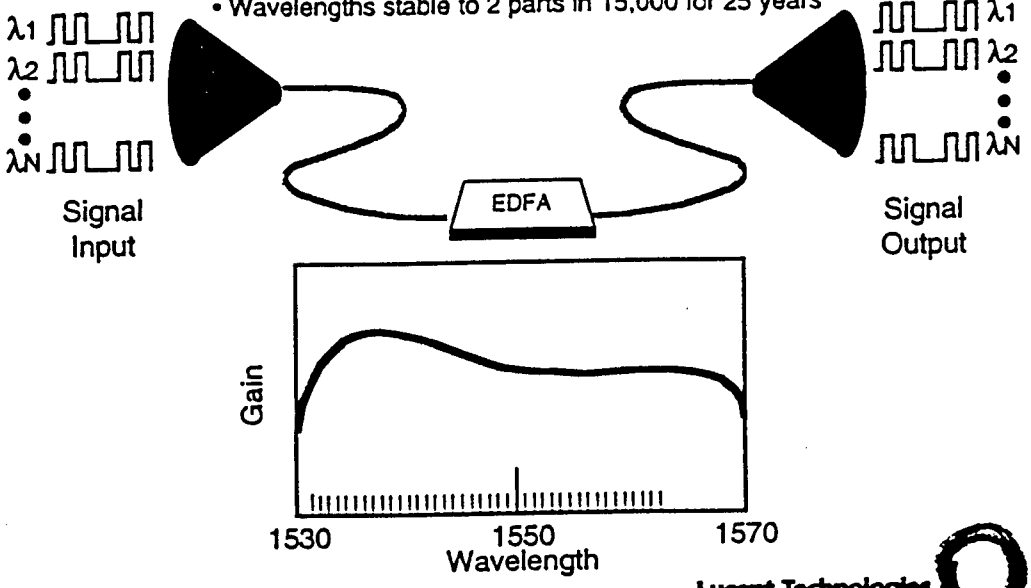

Lucent Technologies
Bell Labs Innovations

OE7373CG017

Lithium Niobate High-Speed Intensity Modulator

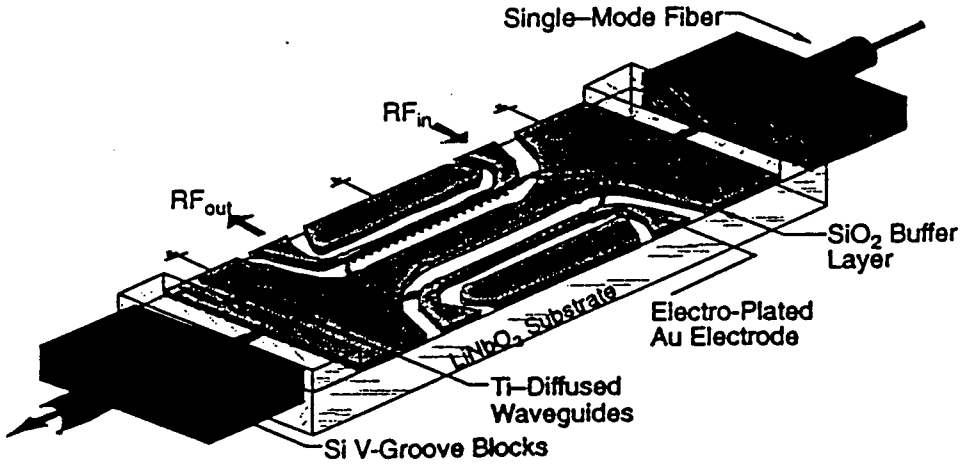

Lucent Technologies
Bell Labs Innovations

OE8058mkg016

Sources With Modulators
Requirements

- *Very Stable Wavelengths - Total variation in 25 years ≤ 2Å*
- *High Reliability - This device has a median time to failure greater than 36 years*
- *Assured Supply at all ITU Wavelengths*
- *Competitively Priced*

microelectronics group

Sources With Modulators
Requirements

- *Low Chirp - Maximum wavelength variation with signal ≤ 0.2Å. During the "on state - the one's bit" ≤ 0.1Å (one part in 150,000)*
- *Precisely controlled wavelengths - Each module meets a specified ITU wavelength (λ) within 1Å (one part in 15,000)*
- *High Speed - Rise and Fall times from 120psec (picoseconds) for 2.5Gb/s to 40psec for 10Gb/s*

Integrated Functionality on a Laser Chip

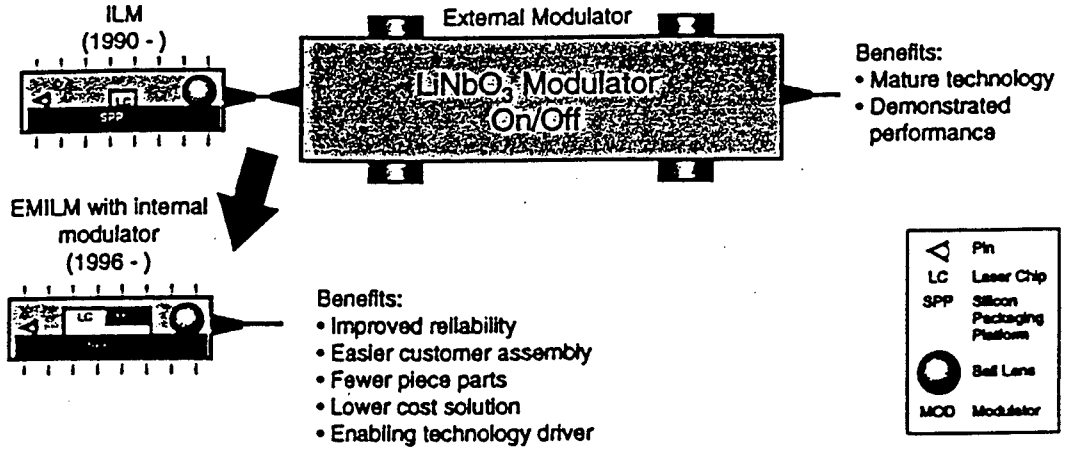

Lucent Technologies
Bell Labs Innovations

OE7373CG020

Lucent Technologies Electroabsorption Modulated Laser

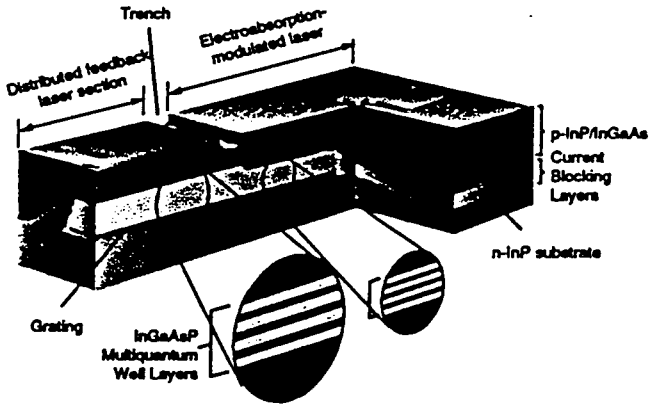

Advantages

- **High reliability:** active MQW layers grown with one process
- **Low chirp:** modulator & facet coating designed to reduce reflections by a factor of one million
- **High speed:** modulator with blocking layers designed to reduce parasitics
- **High yield & power:** folded cavity design for mature processes & high power

Lucent Technologies
Bell Labs Innovations

OE7373CG022

Workshop on $LiNbO_3$ Broadband Modulators

W. K. Burns

Code 5671
Naval Research Laboratory
Washington, DC 20375
202-767-4928
fax 202-767-0966
burns@ccf.nrl.navy.mil

Abstract

This workshop will look at the current status of $LiNbO_3$ broadband modulators and explore approaches and future potential for producing low drive voltage broadband devices.

Summary

Recent progress in the development of velocity matched broadband $LiNbO_3$ modulators has opened new opportunities for the demonstration of low drive voltage devices.

Velocity matched traveling wave devices in $LiNbO_3$ require the reduction of the microwave phase velocity so that it equals the optical phase velocity. Generally this is done by manipulating the geometric structure and layer thicknesses of the electrodes and buffer layers making up the electrode structure. Early velocity matched devices[1-3] tended to achieve velocity matching at the expense of impedance matching which in turn results in some degradation in performance. The difficulty in achieving simultaneous velocity and impedance matching arises from the high dielectric constant of $LiNbO_3$. Progress in overcoming this problem and achieving improved device operation has come from two developments: First, the use of ridge waveguide strutures[4] which use physical etching to remove the high dielectric constant $LiNbO_3$ material, and thus add an additional degree of freedom in the design problem. Second, the realization that increasing the electrode gaps can actually improve device performance even though the field across the waveguides is reduced[5,6]. This occurs because the improvement in electrode loss at the larger gap gives a larger benefit than the negative effect of the simultaneous increase in voltage-length product. These improvements have allowed the demonstration by NTT of simultaneous velocity and impedance matched devices with very large (>100 Ghz) bandwidth[7]. As there is an inherent trade-off between bandwidth and drive voltage in the design of these devices, one can exploit these approaches to obtain lower drive voltages in devices with limited bandwidth, in theory approaching 2-3V levels. Additional developments in the demonstration of long and reflection devices with long effective interaction lengths also offers promise for low drive voltage devices[8]. This workshop will explore the current status and future potential of low drive voltage, broadband device development.

0-7803-4936-9/98/$10.00

References:

1. M. Seino, N. Mekada, T. Yamane, Y. Kubota, and M. Doi, Tech. Dig. ECOC'90, paper ThG1-5(1990).

2. G. K. Gopalakrishnan, C. H. Bulmer, W. K. Burns, R. W. McElhanon, and A. S. Greenblatt, Electron. Lett. 28, 826(1992)

3. D. W. Dolfi and T. R. Ranganath, Electron. Lett. 28, 1197(1992).

4. K. Noguchi, O. Mitomi, H. Miyazawa, and S. Seki, J. Lightwave Tech 13, 1164, 1995.

5. O. Mitomi, K. Noguchi, and H. Miyazawa, Tech. Dig. LEOS'95, paper 104.1(1995).

6. R. Madabhushi, Tech. Dig. OFC'96, paper ThB3(1996).

7. K. Noguchi, O. Mitomi, and H. Miyazawa, Tech. Dig. OFC'96, paper ThB2(1996).

8. W. K. Burns, M. M. Howerton, R. P. Moeller, A. S. Greenblatt, and R. W. McElhanon, Photon. Tech. Lett. 10, 805-806, 1998.

Recent Progresses in High Frequency, High Power Photodetectors

M. C. Wu, T. Itoh, T. Chau, S. Islam, S. Mathai, A. Rollinger, and A. Nespola

Department of Electrical Engineering
University of California, Los Angeles
Los Angeles, CA 90095-1594, U.S.A.
E-mail: wu@ee.ucla.edu

High power, high frequency photodetectors play a key role in determining the performance of analog and microwave fiber optic links. The high power photodetectors allows the use of high power laser sources in externally modulated links. This can significantly reduce the RF insertion loss, and increase the spurious free dynamic range and signal-to-noise ratio of the link [1]. High power photodetectors are particularly important for high frequency links because the electro-optic modulators with low V_π (half-wave voltage) become more difficult to achieve. They are also useful for optoelectronic generation of millimeter-waves and submillimeter waves for local oscillators in radio astronomy [2,3]. Though significant progress has been made in high speed photodetectors, the conventional photodetectors tend to saturate at very low optical powers because they employ small absorption volume (typically on the order of 1 μm^3) to reduce transit time and parasitic capacitance. Recently, large-core waveguide photodetectors have been proposed to increase the saturation power [4]. Traveling-wave photodetectors can further extend the absorption volume and achieve even higher saturation power [5-7].

In this paper, we will review the recent progress in high speed, high power photodetectors. The design trade-offs among the saturation power, 3-dB bandwidth, and quantum efficiency will be described. The fundamental limit of saturation powers for various types of photodetectors, including surface-illuminated p-i-n photodetectors, waveguide photodetectors, traveling-wave photodetectors, and velocity-matched distributed photodetectors, will be derived and compared. In particular, the figure-of-merit (FOM) for high power, high frequency photodetector will be defined [5]. We will also present the recent experimental results of the long-wavelength velocity-matched distributed photodetectors (VMDP) fabricated at UCLA.

The VMDP consists of an array of localized photodiodes serially connected by a passive optical waveguide, and the photocurrents are collected in phase by a separate output microwave transmission line. The microwave transmission line has an impedance of 50 Ω and is velocity-matched to the optical waveguide, which allows the VMDP to extend its absorption length to several hundred micrometers without penalizing its bandwidth. Therefore, the saturation power is greatly enhanced while the bandwidth is essentially the same as that of a single photodiode. Another unique advantage of the VMDP is that the optical waveguide, active photodiodes, and the microwave transmission line can be independently optimized. A VMDP with nanoscale metal-semiconductor-metal photodiodes and coplanar strips transmission line has been designed and fabricated at UCLA. Long-wavelength photodetectors are also being developed at UCLA and other laboratories [7].

Another important development is high power balanced photodetectors. At high photocurrent, the receiver noise of externally modulated links is dominated by the relative intensity noise

0-7803-4936-9/98/$10.00

(RIN). Since balanced photodetectors can cancel out the RIN and the amplified spontaneous emission (ASE) noise from erbium doped fiber amplifiers (EDFA), there are great interests to develop high power balanced photodetectors. Recently, NRL has demonstrated the shot noise-limited performance by using balanced receivers with discrete photodiodes [8]. However, monolithic devices will be required for higher frequency links. UCLA is currently developing a high power balanced photodetectors based on the VMDP structures [9]. The experimental results and their implications on systems will be discussed in the conference.

Another important issue of high power photodetectors is their reliability. Because of the large power consumption and the resulting heat generated in the device, the reliability of high power photodetectors is worse than the conventional photodetectors. In RF photonic links, the photodetectors are often biased at high voltage to reduce their nonlinearity. This further increases the electrical power consumption in the devices. Theoretical study shows that thermal run-away and catastrophic damage could occur for high power photodetectors. Detailed results will be presented in the conference, and their implication on the design of high power photodetectors will also be addressed.

Acknowledgment:

The authors would like to thank Drs. T. Vang, D. Scott, and J. Elliott of TRW for collaborations, Dr. L. Y. Lin of AT&T Research Labs for valuable contributions, and ONR MURI on RF Photonics for supporting this project.

References:

1. C. H. Cox, III, "Gain and noise figure in analogue fiber-optic links," *IEE Proceedings-J*, Vol. 139, pp. 238-242, 1992.
2. S. Verghese, K.A. McIntosh, and E.R. Brown, "Optical and terahertz power limits in the low-temperature-grown GaAs photomixers," Applied Physics Letters, vol.71, pp.2743-5, 1997.
3. J.M. Payne, L. D'Addario, D.T. Emerson, A.R. Kerr, B. Shillue, "Photonic local oscillator for the Millimeter Array," Proc. SPIE, Kona, Hawaii, 1998.
4. A. R. Williams, A. L. Kellner, and P. K. L. Yu, "Dynamic range performance of a high speed, high saturation InGaAs/InP pin waveguide photodetector," Elec. Lett., Vol. 31, no. 7, p. 548-549, 1995.
5. L. Y. Lin, M. C. Wu, T. Itoh, T. A. Vang, R. E. Muller, D. L. Sivco, and A. Y. Cho, "High-power High-Speed Photodetectors. Design, Analysis, and Experimental Demonstration," IEEE MTT, Vol. 45, pp1320-1331, 1997
6. T. Chau, L. Fan, D. T. K. Tong, S. Mathai, and M. C. Wu, "Long Wavelength Velocity-Matched Distributed Photodetectors," Proc. Conference on Lasers and Electro-Optics (CLEO), San Francisco, CA, May 3-8, 1998.
7. Up-to-date references on travelling wave photodetectors and high power photodetectors can be found in the proceeding of the 1998 Microwave Photonics Conference (MWP 98).
8. K. J. Williams, R. D. Esman, "Optically amplified down converting link with shot-noise-limited performance," IEEE Photon. Technol. Lett., vol. 8, pp. 148-52, 1996.
9. M. S. Islam, et al., to be presented in MWP 98.

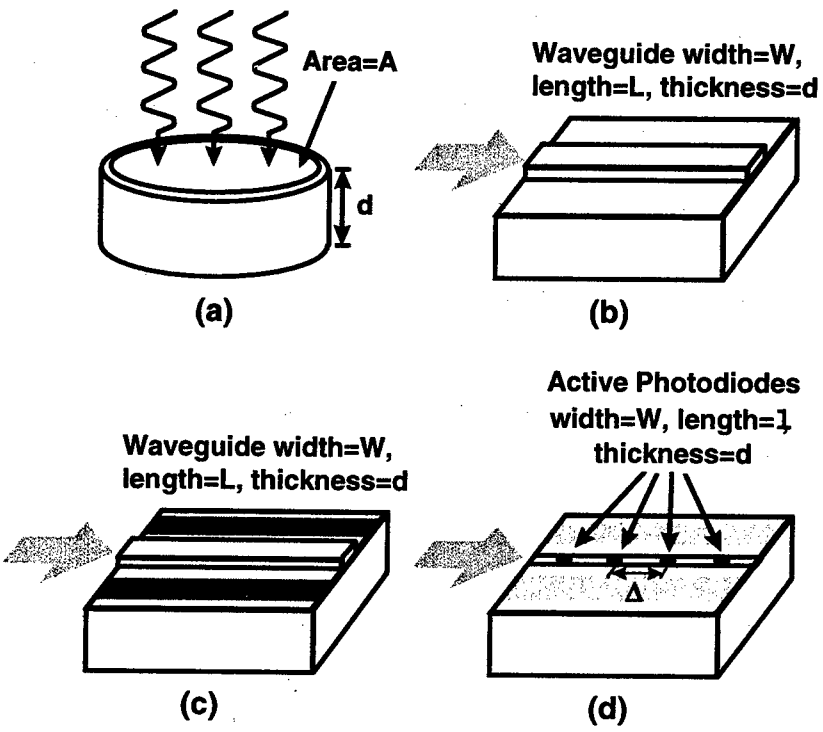

Figure 1. Various structures of high power photodetectors: (a) surface-illuminated photodetectors, (b) waveguide photodetectors, (c) traveling wave photodetectors, and (d) velocity-matched distributed photodetectors. (a) and (b) are lumped photodetectors, while (c) and (d) are traveling wave devices.

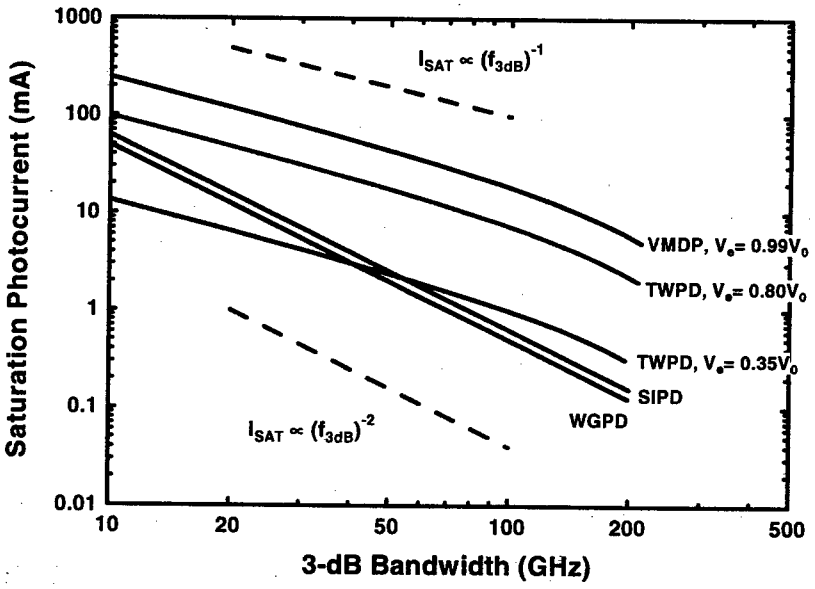

Figure 2. The calculated maximum saturation photocurrent versus the 3-dB bandwidth for the photodetectors shown in Fig. 1.

45 GHz Wide Bandwidth InGaAs/InP Photoreceiver

Abhay Joshi, Xinde Wang, and Dan Mohr
Discovery Semiconductors, Inc.

Arthur Paollela
Lockheed Martin CPC

William Stacey
Raytheon Advanced Device Center

Discovery Semiconductors has developed a 45 GHz "Dual-depletion InGaAs/InP Photodetector." The PIN operates at -3V reverse bias and has minimum responsivity of 0.5 A/W at 1.3 and 1.55 μm wavelength. The Ripple Factor is less than ±1 dB for a wide band of frequencies, DC to 45 GHz. The salient feature of the PIN is an on-chip co-planar waveguide output for proper impedance matching. Discovery Semiconductors has also designed Monolithic InGaAs PIN/InP p-HEMT Amplifier Photoreceiver Opto-electronic Integrated Circuit (OEIC). The combination of optical, microwave, and digital functions on the same chip is a technology that has significant potential for commercial applications such as ethernet fiber local area networks and optical communications systems (Synchronized Optical Network SONET, ISDN, telephony and digital CATV). Important inter-service military applications are optically fed phased array systems and optically controlled microwave networks for airborne and spaceborne systems.

0-7803-4936-9/98/$10.00

45 GHz Wide Bandwidth, 1.3/1.55um InGaAs Photodiode with Co-planar Waveguide

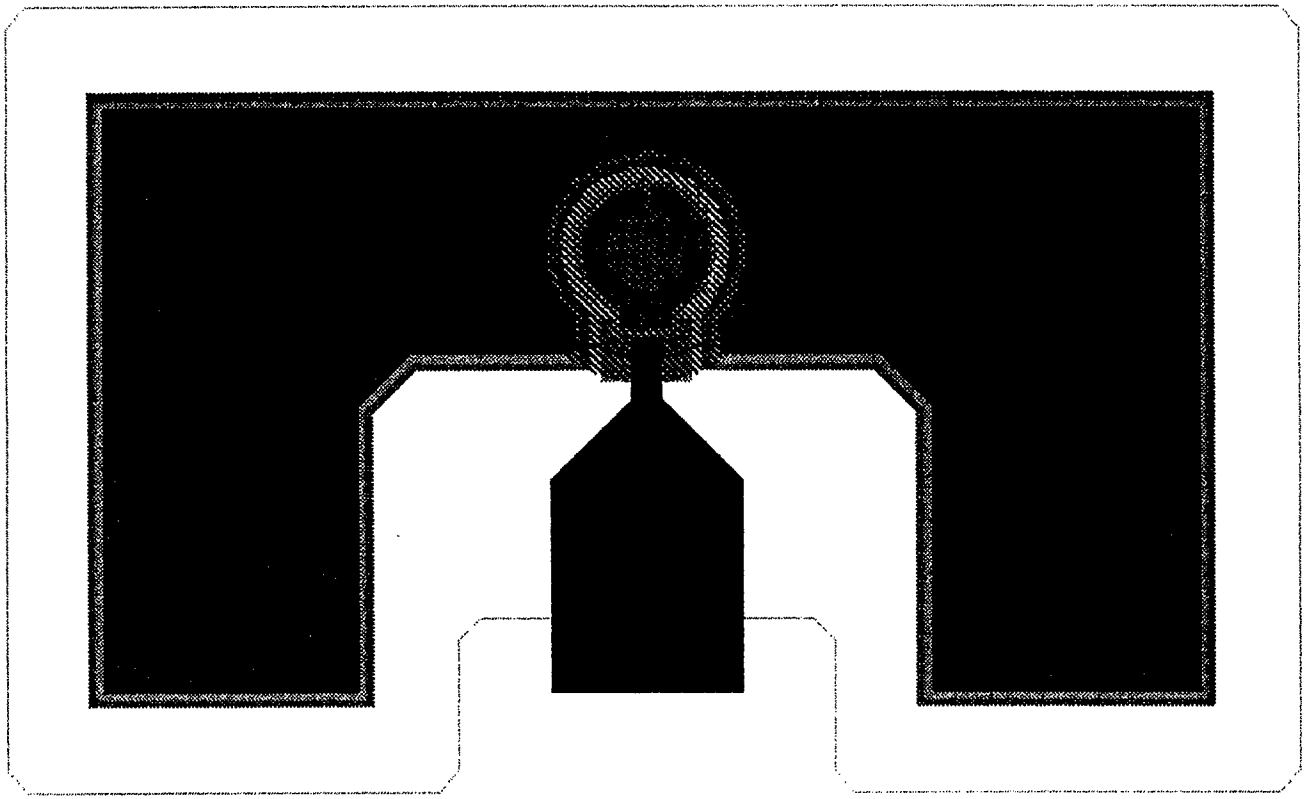

Frequency Response Curve of Discovery's Wide Bandwidth InGaAs Photodiode

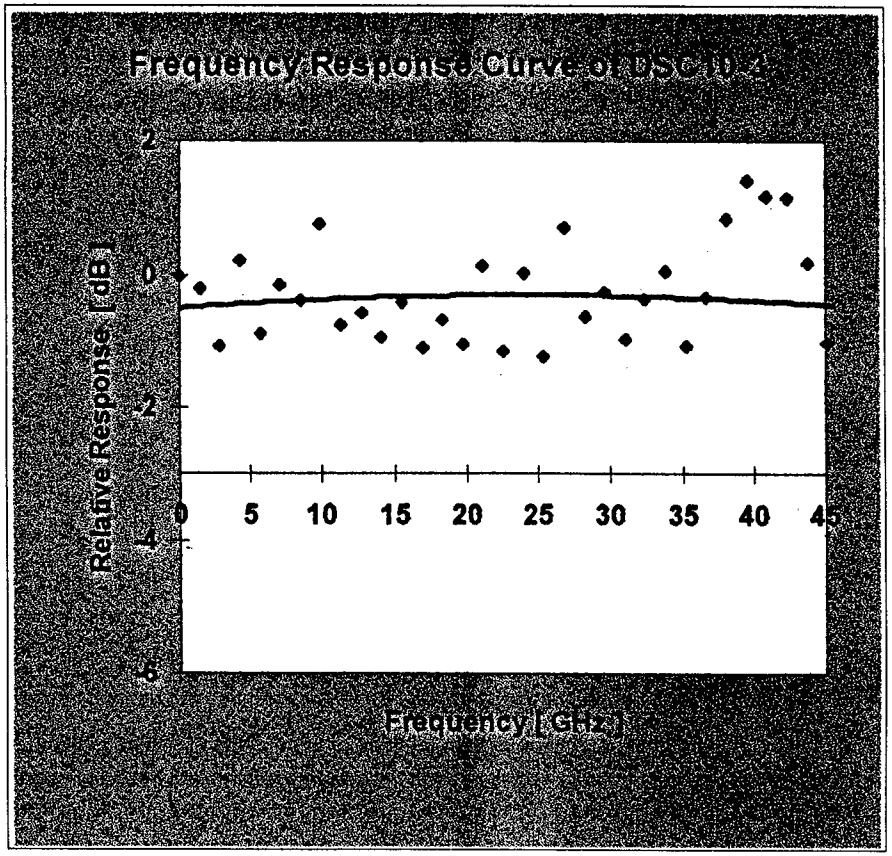

Discovery's Wide Bandwidth InGaAs/InP Pigtailed Photodiode with RF Connector

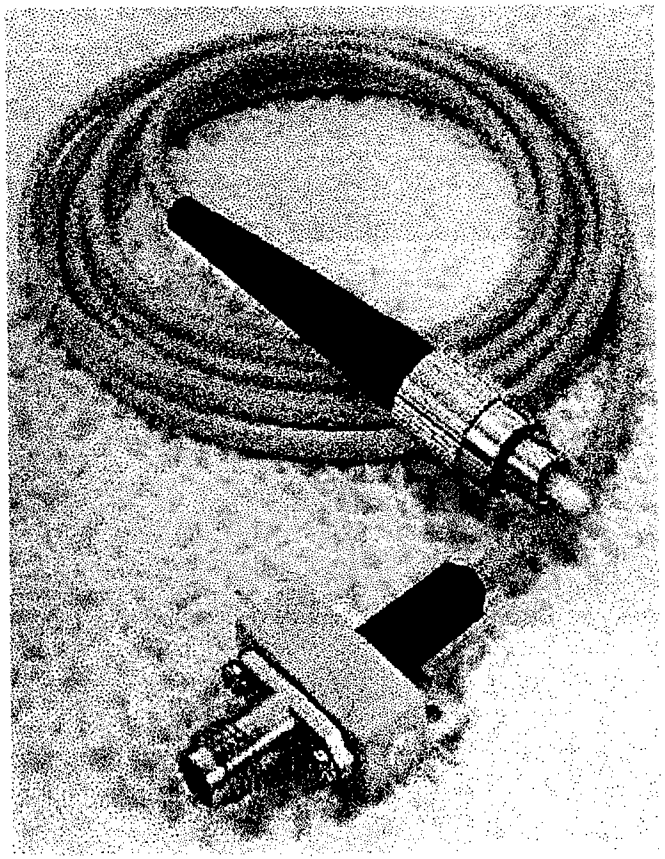

A Quad InGaAs Detector Array for Wavelength Division Multiplexing (WDM)

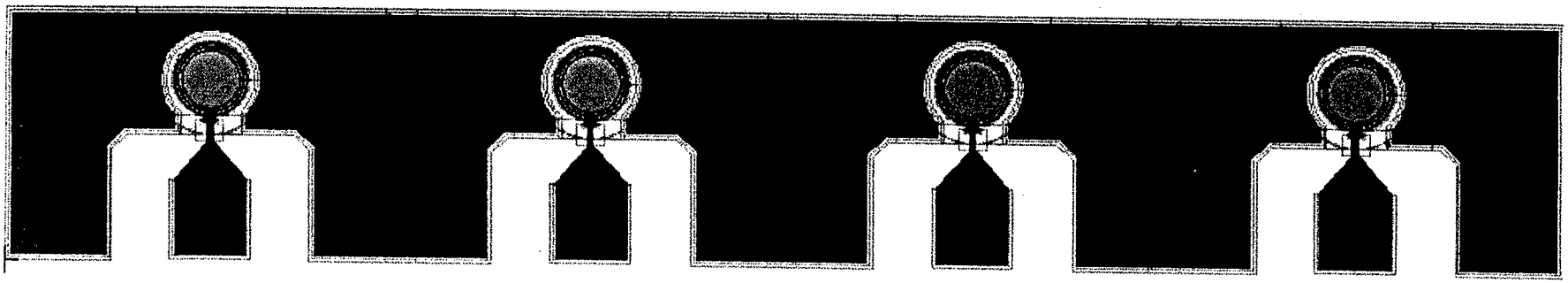

DC to 45 GHz Wide Bandwidth InGaAs/InP 3-Stage Common Source Cascode OEIC

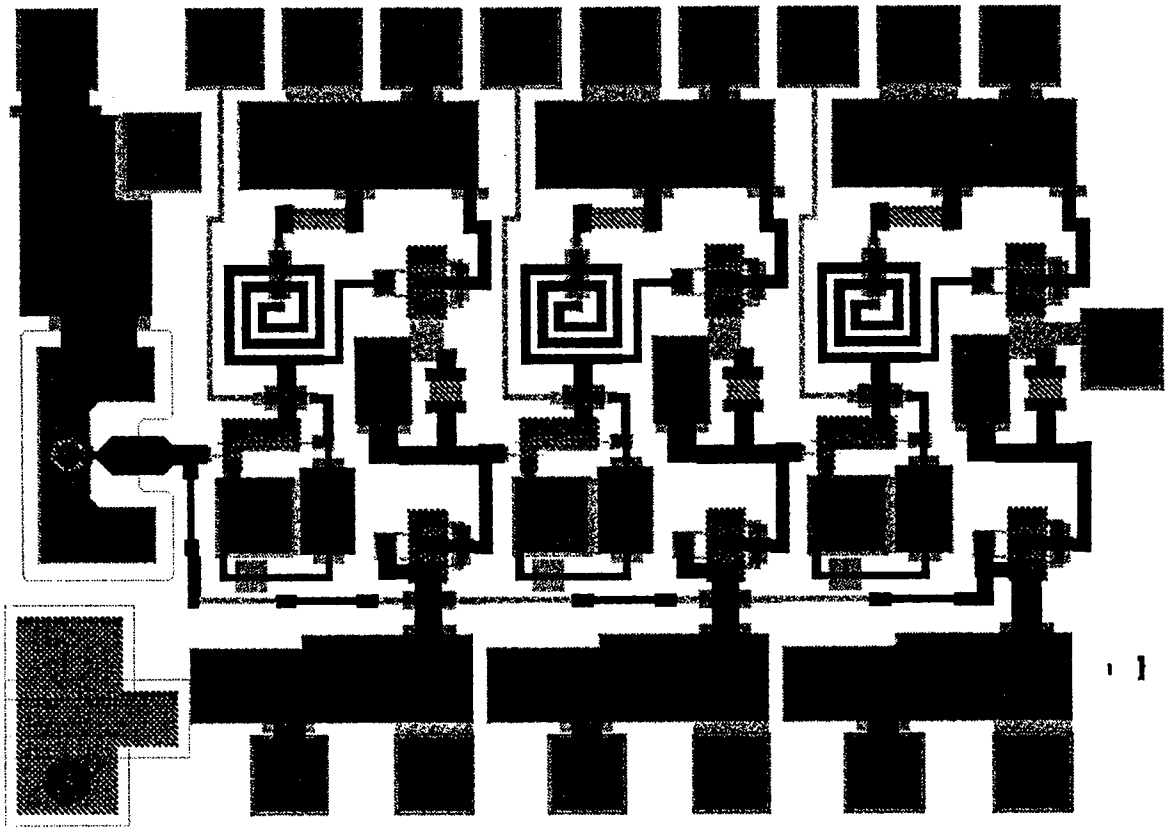

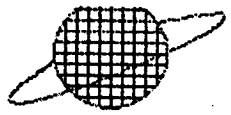

Conclusions

- 45 GHz InGaAs PIN Diodes Fabricated with CPW Output on Semi-Insulating InP.
- Methodology & Process to Monolithically Integrate InGaAs PINs with InP p-HEMT Amplifiers has been fully developed.
- 8 Different OEIC Circuits Currently Being Processed for Yield and Statistical Analysis to Eventually Manufacture for OC-192/768.

Author Index

Abraham, P. 33
Ackerman, E. 45
Allenson, M. 161
Auker, G. 25
Ayling, S. 161

Bennion, I. 203
Benoist, K. 131
Berceli, T. 63
Bhusan, A. 197
Biernacki, P. 137
Bimberg, D. 173
Bottcher, E. 173
Bouchoule, S. 13
Bowers, J. 33, 181
Brown, R. 135
Burns, W. 235

Cadiou, J. 13, 59
Carr, A. 123
Chang, Y. 115
Chau, T. 107, 177, 237
Chazelas, J. 151
Chen, W. 29
Chiu, Yi-Jen 33, 181
Chiu, Yun 49
Cho, A. 107
Chuyanov, V. 85
Contarino, V. 90
Coppinger, F. 197
Corral, J. 99
Cox, C. 157
Craven, J. 21
Cusick, T. 111

Deal, W. 177
Deng, K. 227
Dingel, B. 147
Doi, Y. 215
Dolfi, D. 151
Droge, E. 173
Dubovitsky, S. 85

Edge, C. 141
Elamaran, B. 55
Elkin, M. 141
Esman, R. 137, 185, 199

Fetterman, H. 115
Fleischer, S. 181
Frankel, M. 199
Freude, W. 95
Fukushima, S. 215
Funk, E. 21
Furuta, T. 193
Fuster, J. 99

Garner, S. 85
Glesk, I. 227
Gliese, U. 141, 211
Gopinath, A. 41
Griffin, R. 93, 207

Hashimoto, E. 169
Heinzelmann, R. 153
Helkey, R. 157
Henion, S. 135
Herczfeld, P. 90
Hilt, A. 63
Hilton, K. 161
Hoshida, T. 75
Huang, X. 141, 165
Huignard, J. 151

Iezekiel, S. 55, 111
Ishibashi, T. 5, 193
Islam, M. 177, 237
Itoh, T. 107, 177, 237
Izutsu, M. 147

Jaffre, P. 59
Jager, D. 37, 153
Jalali, B. 197
Jalali, B. 49
Jaro, G. 63
Johnston, W. 231
Joshi, A. 241

Kaluzni, H. 219
Kang, J. 199
Katagiri, Y. 169
Kazmierski, C. 13
Kiruluta, A. 103
Kitayama, K. 17, 37, 223
Knights, A. 165
Kojucharow, K. 219
Kollakowski, St. 173
Komaki, S. 83
Kriehn, G. 103
Kuri, T. 17

Laliew, C. 41
Lane, P. 93, 207
Langley, L. 141
Lee, C. 21
Legaud, P. 13
Lewis, M. 143
Li, G. 29
Liu, Y. 29
Lovseth, S. 41

Maas, O. 151
Maat, D. 131
Mahric, M. 71
Maleki, L. 195
Marozsak, T. 63
Marti, J. 99
Mathai, S. 107, 177, 237
Mathoorasing, D. 13, 59
Matsuoka, Y. 215
Merlet, T. 151
Mihaly, S. 63
Miles, R. 111
Mishra, U. 181
Mohr, D. 241
Munro, J. 127

Nagatsuma, T. 5
Nawaz, M. 87
Nespola, A. 177, 237
Newberg, I. 51, 115
Nguyen, R. 29
Nichols, L. 137
Nirmalathas, A. 79
Nirmalathas, A. 9
Nishikawa, K. 75
Nitta, Y. 189
Novak, D. 9, 79
Nowak, W. 219

Author Index

O'Reilly, J. 93, 207
Obata, S. 83
Ogawa, Y. 17
Ohno, T. 215
Onnegren, J. 119

Palai, P. 95
Panaretos, S. 115
Paollela, A. 241
Pappert, S. 29
Pastur, L. 151
Penard, E. 13, 59
Pescod, C. 25
Pettersson, L. 119
Pollard, R. 55
Polo, V. 99
Prince, J. 127

Ram, R. 157
Ramos, F. 99
Ramsey, S. 21
Reimann, O. 173
Roberts, J. 165
Rollinger, A. 107, 177, 237
Roussell, H. 157
Runser, R. 227

Sahri, N. 5
Sakai, T. 189
Sample, P. 143
Sato, K. 5
Sauer, M. 219
Schaffer, C. 67
Schmuck, H. 59
Schulz, P. 135
Scott, D. 107
Seeds, A. 1, 141, 165
Sharp, P. 25
Shimizu, N. 5, 193
Shimomura, K. 189
Silveira, P. 103
Sirett, R. 25
Sivco, D. 107
Slawsby, N. 127
Smit, M. 13
Smith, G. H. 9, 79
Smith, G. W. 161
Sommer, K. 219
Sparks, R. 127
Stacey, W. 241
Steier, W. 85
Steingruber, R. 173
Stohr, A. 37, 153
Strittmatter, A. 173
Stulemeijer, J. 131
Sukhoivanov, A. 95
Sun, C. 29

Takada, A. 169
Takeuchi, H. 215
Tanguy, D. 13, 59
Tittensor, P. 123
Toliver, P. 227
Tonda-Goldstein, S. 151
Tsap, B. 115
Tsuchiya, M. 75
Tsukamoto, K. 83

Udvary, E. 63
Umbach, A. 173

van Vliet, F. 131
Vang, T. 107
Varga, Z. 63
Vergnol, E. 59

Wagner, K. 103
Wale, M. 141
Wang, X. 241
Ward, A. 137
Watanabe, N. 193
Weaver, S. 103
Welstand, R. 29
Wight, D. 161
Williams, J. 203
Williams, K. 185
Wilson, R. 143
Wu, M. 107, 177, 237

Yaita, M. 5
Yost, T. 90
Young, T. 25, 87
Yu, P. 29

Zhang, S. 33, 181
Zhang, W. 203
Zhang, X. 41
Zhu, J. 29
Zolomy, A. 63

NOTES